METABOLISM AND CHROMATIN MODIFICATION IN CANCER

EDITED BY: Guillermo Barreto, Yongbin Chen, Huafeng Zhang and Yongguang Tao

PUBLISHED IN: Frontiers in Cell and Developmental Biology and Frontiers in Oncology

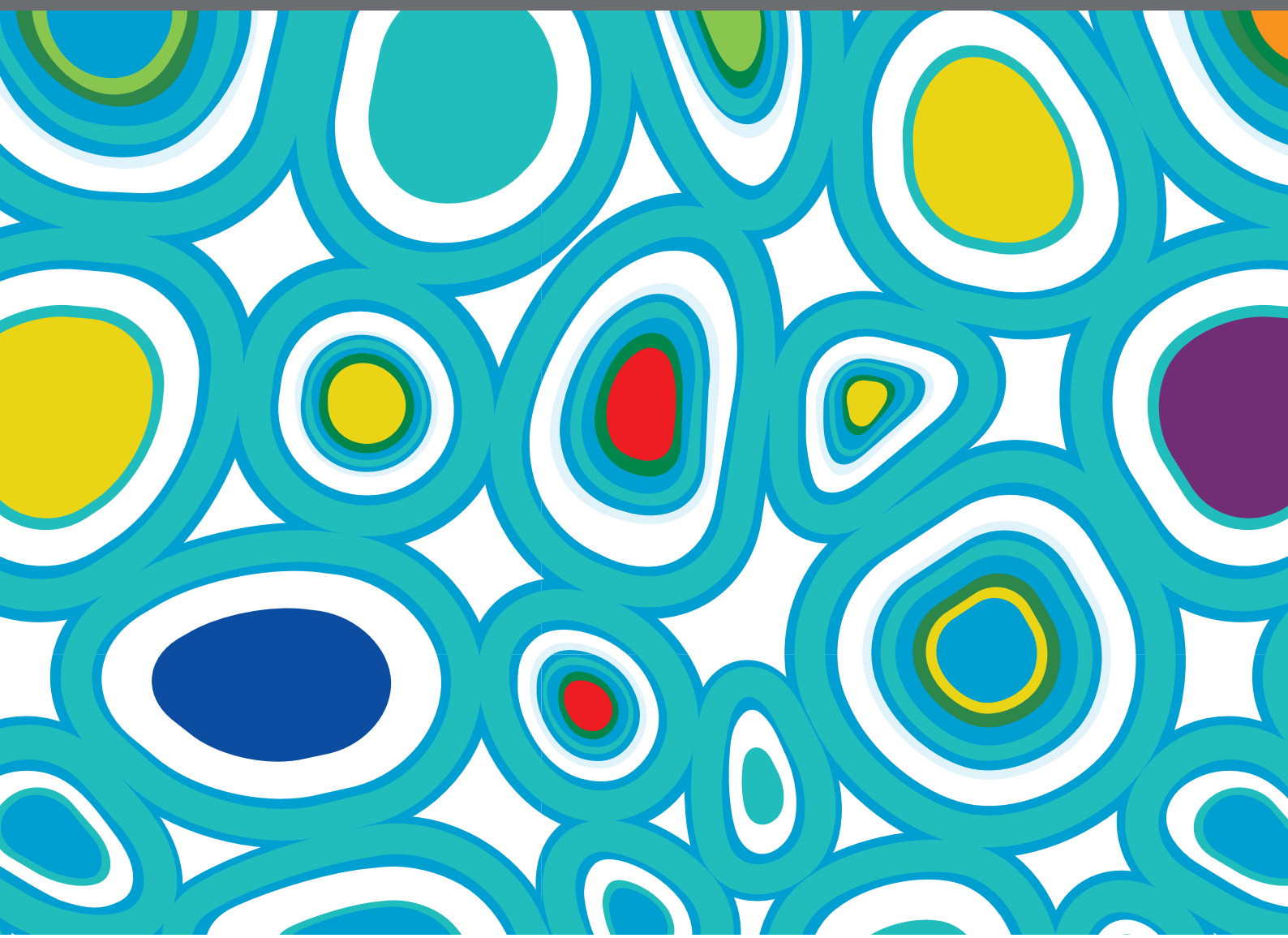

frontiers Research Topics

frontiers

ISSN 1664-8714
ISBN 978-2-88976-943-8
DOI 10.3389/978-2-88976-943-8

About Frontiers

Frontiers is more than just an open-access publisher of scholarly articles: it is a pioneering approach to the world of academia, radically improving the way scholarly research is managed. The grand vision of Frontiers is a world where all people have an equal opportunity to seek, share and generate knowledge. Frontiers provides immediate and permanent online open access to all its publications, but this alone is not enough to realize our grand goals.

Frontiers Journal Series

The Frontiers Journal Series is a multi-tier and interdisciplinary set of open-access, online journals, promising a paradigm shift from the current review, selection and dissemination processes in academic publishing. All Frontiers journals are driven by researchers for researchers; therefore, they constitute a service to the scholarly community. At the same time, the Frontiers Journal Series operates on a revolutionary invention, the tiered publishing system, initially addressing specific communities of scholars, and gradually climbing up to broader public understanding, thus serving the interests of the lay society, too.

Dedication to Quality

Each Frontiers article is a landmark of the highest quality, thanks to genuinely collaborative interactions between authors and review editors, who include some of the world's best academicians. Research must be certified by peers before entering a stream of knowledge that may eventually reach the public - and shape society; therefore, Frontiers only applies the most rigorous and unbiased reviews.
Frontiers revolutionizes research publishing by freely delivering the most outstanding research, evaluated with no bias from both the academic and social point of view. By applying the most advanced information technologies, Frontiers is catapulting scholarly publishing into a new generation.

What are Frontiers Research Topics?

Frontiers Research Topics are very popular trademarks of the Frontiers Journals Series: they are collections of at least ten articles, all centered on a particular subject. With their unique mix of varied contributions from Original Research to Review Articles, Frontiers Research Topics unify the most influential researchers, the latest key findings and historical advances in a hot research area! Find out more on how to host your own Frontiers Research Topic or contribute to one as an author by contacting the Frontiers Editorial Office: frontiersin.org/about/contact

METABOLISM AND CHROMATIN MODIFICATION IN CANCER

Topic Editors:
Guillermo Barreto, UMR 7365 CNRS-Université de Lorraine, Biopôle de l'Université de Lorraine, France
Yongbin Chen, Key Laboratory of Animal Models and Human Disease Mechanisms, Kunming Institute of Zoology, Chinese Academy of Sciences (CAS), China
Huafeng Zhang, University of Science and Technology of China, China
Yongguang Tao, Central South University, China

Citation: Barreto, G., Chen, Y., Zhang, H., Tao, Y., eds. (2022). Metabolism and Chromatin Modification in Cancer. Lausanne: Frontiers Media SA.
doi: 10.3389/978-2-88976-943-8

Table of Contents

frontiers in Cell and Developmental Biology

ORIGINAL RESEARCH
published: 30 September 2020
doi: 10.3389/fcell.2020.579629

Fra-1 Inhibits Cell Growth and the Warburg Effect in Cervical Cancer Cells via STAT1 Regulation of the p53 Signaling Pathway

Manying Zhang[1,2], Lin Liang[1,2], Junyu He[1,2], Zhengxi He[1,2], Chunxue Yue[1,2], Xi Jin[1,2], Mengxiang Gao[1,2], Songshu Xiao[3] and Yanhong Zhou[1,2]**

[1] Hunan Cancer Hospital and The Affiliated Cancer Hospital of Xiangya School of Medicine, Central South University, Changsha, China, [2] NHC Key Laboratory of Carcinogenesis, Hunan Cancer Hospital and The Affiliated Cancer Hospital of Xiangya School of Medicine, Central South University, Changsha, China, [3] Department of Gynecology and Obstetrics, The Third Xiangya Hospital, Central South University, Changsha, China

OPEN ACCESS

Edited by:
Yongbin Chen,
Kunming Institute of Zoology (CAS), China

Reviewed by:
Jian Zhang,
Fourth Military Medical University, China
Yong Peng,
Sichuan University, China
Huafeng Zhang,
University of Science and Technology of China, China

***Correspondence:**
Songshu Xiao
287932636@qq.com
Yanhong Zhou
zhouyanhong@csu.edu.cn

Specialty section:
This article was submitted to Molecular and Cellular Oncology, a section of the journal Frontiers in Cell and Developmental Biology

Received: 03 July 2020
Accepted: 08 September 2020
Published: 30 September 2020

Citation:
Zhang M, Liang L, He J, He Z, Yue C, Jin X, Gao M, Xiao S and Zhou Y (2020) Fra-1 Inhibits Cell Growth and the Warburg Effect in Cervical Cancer Cells via STAT1 Regulation of the p53 Signaling Pathway. Front. Cell Dev. Biol. 8:579629. doi: 10.3389/fcell.2020.579629

The oncogenesis of cervical cancer is a multi-factor and multi-step process, and major risk factors include oncogene activation with tumor suppressor gene inactivation, viral factors, and immune factors. For example, the human papillomavirus (HPV) has been linked to the occurrence of cervical cancer. At present, the pathogenesis of cervical cancer remains unclear. Fra-1 (Fos-related antigen 1, also known as FOSL1) is a member of the Fos family and an important nuclear transcription factor that regulates normal cell growth, differentiation, and apoptosis. In the present study, we found that Fra-1 inhibited the proliferation of cervical cancer cells while also promoting apoptosis and affecting cell cycle distribution. Moreover, Fra-1 up-regulated STAT1 expression and modulated p53 signal pathway activity in cervical cancer cells. Overexpression of Fra-1 inhibited cell senescence by altering sirtuin 1 (SIRT1) expression in HeLa cells, and Fra-1 overexpression restored mitochondrial disorder and suppressed metabolic reprogramming in HeLa cells. Silencing of STAT1 impaired the inhibitory effect of Fra-1 on cervical cancer cell growth, while knock-down of STAT1 reversed the effect on cell senescence and mitochondrial dysfunction caused by Fra-1 in HeLa cells. Silencing of STAT1 also recovered metabolic reprogramming in cervical cancer cells. In summary, our results show that Fra-1 inhibited cervical cancer cell growth and the Warburg effect via STAT1-mediated regulation of the p53 signaling pathway.

Keywords: Fra-1, STAT1, cervical cancer, cell growth, Warburg effect

INTRODUCTION

Among Chinese women aged 15–44 years, cervical cancer is the second most common cancer and the most common gynecological malignancy (Liou et al., 2016; Gu et al., 2017; Vu et al., 2018). The typical age range for onset of carcinoma *in situ* is 30–35 years, and that for invasive cancer is 45–55 years. In recent years, the incidence of cervical cancer in younger patients has increased

Abbreviations: CDK4, cyclin-dependent kinase 4; FOSL1 (also known as Fra-1), FOS-like antigen 1; GDH, glutamine dehydrogenase; IDH2, isocitrate dehydrogenase 2; MDM2, MDM2 proto-oncogene, E3 ubiquitin protein ligase; MnSOD2, Mn superoxide dismutase 2; PKF, G6-phosphofructokinase; PKM2, pyruvate kinase muscle isozyme 2; SIRT3, sirtuin 3; STAT1, signal transducer and activator of transcription 1; TP53, tumor protein p53.

(Schwarz et al., 2009; Cao et al., 2010; Liu et al., 2015). Most cervical cancer cases (∼99.7%) are accompanied by high-risk human papillomavirus (HPV) infection, and persistent infection with high-risk HPV has been shown to be a major risk factor for cervical cancer. The incubation period for HPV is long, with oncogenesis commonly occurring 8–10 years after infection. While HPV infection is a known cause of cervical cancer, it does not fully explain the occurrence of cervical cancer. Other factors are important in the malignant transformation of high-grade HPV infection (Kaliff et al., 2018; Farazi et al., 2019; So et al., 2019). The key events leading to oncogenesis are mediated by many factors, which need to be further understood (Ramdass et al., 2013; Karim et al., 2018; Mirbahari and Sadeghi, 2018). Many gaps in knowledge regarding cervical cancer pathogenesis and the corresponding treatment mechanism remain to be filled.

Tumor cells commonly achieve enhanced proliferation, growth, survival, and long-term maintenance via alteration of their metabolism. The rate of glucose uptake and lactate production is increased dramatically in many tumors cells, which requires sufficient oxygen and fully functioning mitochondria. This is known as the Warburg Effect and has been explored extensively (Nagao et al., 2019), since Otto Warburg first described this phenomenon in the 1920s, with studies producing both supportive and opposing evidence (He et al., 2016).

Fra-1 (Fos-related antigen 1, also known as FOSL1) is a member of the Fos family and an important nuclear transcription factor that regulates normal cell growth, differentiation, and apoptosis (Annis et al., 2018; Xu et al., 2018). Fra-1 is highly expressed in many malignant tumors and plays an important role in cell transformation, proliferation, invasion, and metastasis (Annis et al., 2018; Wang et al., 2018). Fra-1 activity is regulated at both the transcriptional and translation levels (Xiao et al., 2015; Belguise et al., 2017). Our preliminary studies suggested that Fra-1 can inhibit the proliferation of cervical cancer cells (Xiao et al., 2015), but the underlying mechanism remained unclear. Therefore, in the present study, we investigate the effects and possible mechanisms of Fra-1 on the proliferation, apoptosis, and senescence of cervical cancer cells.

Signal transducer and activator of transcription 1 (STAT1) has been reported to act as a tumor suppressor. Studies have shown that STAT1 plays an important role in apoptotic and anti-apoptotic signaling, demonstrating that it can regulate apoptosis by inhibiting non-transcriptional mechanisms such as anti-apoptotic protein nuclear factor (NF)-kappa B (Zhang et al., 2018). In renal cell carcinoma cells, down-regulation of STAT1 expression can slow cell growth (Ah-Koon et al., 2016). Additional research has linked STAT1 with the development of many malignant tumors, including breast cancer, myeloma, and renal cancer (Suyama et al., 2016; Chen et al., 2017; Qu et al., 2017; Josahkian et al., 2018). Specifically, STAT1 was shown to regulate p53 activity by inducing phosphorylation of p53 (Chen et al., 2017). Through such interaction with p53, STAT1 promotes apoptosis, and STAT1 also interacts with the p53 inhibitor MDM2 (Chen et al., 2017). Therefore, we explored whether the potential effects of Fra-1 on cervical cancer cell growth and the Warburg effect in these cells are mediated by STAT1 regulation of the p53 signaling pathway.

Here we first investigated the effect of Fra-1 on cell growth and the Warburg effect in cervical cancer cells. Then, we determined the influence of Fra-1 on STAT1 expression. Finally, we confirmed that the inhibition of cell growth and the Warburg effect in cervical cancer cells by Fra-1 is mediated via STAT1.

MATERIALS AND METHODS

Cell Culture

HeLa cells, a human cervical cancer cell line, were purchased from the ATCC (Manassas, VA, United States) and maintained by our laboratory. The HeLa cells were cultured in RPMI-1640 supplemented with 10% fetal bovine serum (FBS; Gibco Life Technologies, Grand Island, NY, United States) in a 5% CO_2 incubator at 37°C.

Construction of pEGFP-N1-Fra-1 Vector and Cell Transfection

The coding region of the Fra-1 gene was amplified by polymerase chain reaction (PCR). The primer sequences for the Fra-1 gene were 5′-atactcgaatgaacctggccatcagcat-3′ and 5′-gcggaattctcacagggacatgaaatccg-3′. The conditions for PCR amplification were one cycle for 5 min at 94°C; 30 cycles for 45 s at 94°C, 45 s at 55°C, and 90 s at 72°C, and a final cycle for 10 min at 72°C. The coding region fragments of the Fra-1 gene were cloned into the TA vector (Promega, Fitchburg, WI, United States) for transformation in *Escherichia coli* JM109 (Takara, Dalian, China). In the TA vector, restriction endonuclease xhoi and ecor1 (Promega) were used to cut the required DNA fragments, which were then subcloned into the pEGFP-N1 vector. The accuracy of the cloned sequence was confirmed by DNA sequencing using an ABI 3730 instrument (Applied Biosystems, Foster City, CA, United States).

To construct a stable cervical cancer cell line overexpressing Fra-1, we transfected HeLa cells with the pEGFP-N1/Fra-1 or pEGFP-N1 (blank control vector) using Lipofectin (Invitrogen, Carlsbad, CA, United States) according to the manufacturer's instructions as described previously (Xiao et al., 2015). This was followed by G418 selection. Western blotting was performed to detect the expression level of Fra-1 protein to verify successful establishment of the stable cell line.

Colony Formation and CCK8 Assay

Cell proliferation was evaluated using colony formation and CCK8 assays. For the colony formation assay, 1,000 cells were seeded in each well of six-well plates and cultured at 37°C. After 14 days in culture, the cells were fixed in 4% paraformaldehyde solution and stained with 0.1% crystal violet solution. Colonies were counted and photographed. For the CCK8 assay, cells were seeded in 96-well culture plates at a density of 1,000 cells/well in 200 μl medium. After culture at 37°C for 6 days, we analyzed the cell density in each well every 24 h using the 7Sea-Cell Counting Kit (7Sea Biotech, Shanghai, China). Briefly, 20 μl of CCK8 solution was added to each well and incubated for 2 h at 37°C before the absorbance at 450 nm was measured by a Paradigm Detection System (Beckman Coulter, Brea, CA, United States).

Flow Cytometric Analysis of Cell Cycle Distribution and Apoptosis

Prior to flow cytometric analyses, cells (5×10^5/well) were seeded in 6-well cell culture plates and cultured in a humidified atmosphere of 5% CO_2 at 37°C for 24 h before harvesting with 0.5% trypsin and centrifugation. For cell cycle analysis, cells were fixed in ice-cold 70% ethanol overnight at 4°C. The fixed cells were then resuspended in 500 μl phosphate-buffered saline (PBS) to which 10 μl RNase A was added for a 5-min incubation followed by three washes with cold PBS. Next, 10 μl propidium iodide (PI) solution was added to the resuspended cell solution for incubation at 4°C for 30 min. Finally, the cells were washed twice with PBS before flow cytometric analysis of cell cycle distribution. For flow cytometric detection of apoptotic cells, the Hoechst 33342/PI Apoptosis Assay Kit (BestBio, Shanghai, China) was used. Briefly, the harvested cells were washed twice with ice-cold PBS and resuspended in 500 μl staining buffer. Then, the resuspended cell solution was incubated with 5 μl Hoechst 33342 and 5 μl PI solution in darkness for 20 min at 4°C. Finally, the cells were washed twice with PBS before flow cytometric analysis of cell apoptosis. All flow cytometric analyses were performed using a MoFlo^{TM} XDP High-Performance Cell Sorter (Beckman Coulter). The data for cell cycle distribution and apoptosis were analyzed using Summit v5.2 Software (Beckman Coulter).

Quantitative Real-Time PCR

The total RNA of HeLa cells was isolated using TRIzol reagent (Invitrogen), and cDNA was then generated by reverse transcription from 1 μg total RNA using the HiScript II Q RT SuperMix for qPCR (Vazyme, Nanjing, China). Quantitative real-time PCR was carried using ChamQTM SYBR® qPCR Master Mix (Vazyme, Nanjing, China). The primers used for real-time PCR are listed in **Table 1**.

TABLE 1 | List of the human-specific primer sequences used for qPCR analyses.

Gene	Primer Sequence		T_m (°C)
	Forward	Reverse	
STAT1	5′-ttcaggaagacccaatccag-3′	5′-tgaatattccccgactgagc-3′	60
p53	5′-gttccgagagctgaatgagg -3′	5′-tctgagtcaggcccttctgt-3′	60
Bcl-2	5′-atgtgtgtggagagcgtcaa-3′	5′-acagttccacaaaggcatcc-3′	60
p38	5′-tgactcagatgccgaagatg-3′	5′-atcataaggatcggccactg-3′	60
p21	5′-ggaagaccatgtggacctgt-3′	5′-ggattagggcttcctcttgg-3′	60
MDM2	5′- ggtgggagtgatcaaaagga-3′	5′-gtggcgttttctttgtcgtt-3′	60
CDK4	5′-cccgaagttcttctgcagtc-3′	5′-ctggtcggcttcagagtttc-3′	60
Cyclin D1	5′- cctgtcctactaccgcctca -3′	5′- cacctcctcctcctcctctt -3′	60
IL-6	5′-actcacctcttcagaacgaattg-3′	5′-ccatctttggaaggttcaggttg-3′	60
IL-8	5′-actgagagtgattgagagtggac-3′	5′-aaccctctgcacccagttttc-3′	60
GLUT1	5′-gcgggttgtgccatactcatgacc-3′	5′-aggccacaaagccaaagatggcc-3′	59
HK II	5′-gagccaccactcaccctact-3′	5′-ccaggcattcggcaatgtg-3′	60
LDHA	5′-ttgacctacgtggcttggaag-3′	5′-ggtaacggaatcgggctgaat-3′	60
β-tubulin	5′-aagatccgagaagaataccctga-3′	5′-ctaccaactgatggacggaga-3′	60

STAT1, signal transducer and activator of transcription 1; Bcl-2, B-cell lymphoma 2; CDK4, cyclin dependent kinase 4; IL-6, interleukin 6; IL-8, interleukin 8; Glut1, glucose transporter 1; LDHA, lactate dehydrogenase A.

Detection of Cellular Senescence by β-Galactosidase Staining

HeLa cells were washed three times in six-well plates with 1 × PBS and fixed with 4% paraformaldehyde at room temperature for 15 min. The plate was rinsed two times with 1 × PBS, and 1 ml of staining solution was added to each well. The plate was incubated overnight at 37°C without CO_2. Cellular senescence was detected using a Senescence-associated β-Galactosidase Staining Kit (C0602, Beyotime, China). On images captured with a light microscope (CKX41, Olympus, Japan), β-galactosidase–positive cells (blue staining) were considered senescent cells.

Intracellular Ca^{2+} Concentration Assay

The fluorescent dye Fura-2 AM (Beyotime Institute of Biotechnology, Haimen, China) penetrates the cell membrane and binds calcium ions to produce strong fluorescence under 330–350 nm excitation light and weak fluorescence under 380 nm excitation light. The ratio of 340 and 380 nm fluorescence is routinely used to evaluate the intracellular calcium concentration. Fura-2 staining was performed according to the manufacturer's instructions in the present study. Afterward, the cells were washed twice and resuspended in PBS for fluorescence-activated cell sorting (FACS) analysis (Beckman Coulter). The Ca^{2+} concentration data were analyzed using Summit v5.2 software (Beckman Coulter).

Intracellular Reactive Oxygen Species (ROS) Measurement

HeLa cells were trypsinized, counted, and then resuspended in culture medium (1×10^6/ml/tube). To 1 ml of cell suspension, we added 1 μl of 10 mM DCFH-DA active oxygen fluorescence probe solution (Applygen, Beijing, China). For the negative control group, 1 μl dimethyl sulfoxide (DMSO) solution was added, and for the positive control group, 1 μl active oxygen positive control solution and 1 μl of 10 mM DCFH-DA active oxygen fluorescence probe solution was added. For all groups, the mixtures were incubated at 37°C for 20 min, with pipetting of the probe solution and mixing every 3–5 min to ensure good distribution of the cells. After washing with 1 × PBS solution two or three times, the cells were resuspended in a proper volume of 1 × PBS (generally 400–500 μl) for testing of reactive oxygen species (ROS) levels. The cells were then washed twice with cold PBS and resuspended in PBS for analysis of the intracellular ROS concentration by FACS (Beckman Coulter).

Determination of Mitochondrial Membrane Potential Using JC-1

The effect of Fra-1 of mitochondrial membrane potential was assessed by flow cytometry using the sensitive and relatively mitochondrion-specific lipophilic cationic probe

fluorochrome JC-1. JC-1 accumulates to form J-aggregates and emits red fluorescence in mitochondria with a high membrane potential, yet dissociates into monomers and emits green fluorescence in mitochondria that have lost their cross-membrane electrochemical gradient. The groups of HeLa cells were suspended in 1 ml warm staining buffer at approximately 1×10^6 cells/ml and incubated at 37°C for 5 min. Then 1 μl of 2 mM JC-1 (2 μM final concentration; MultiSciences Biotech, Co., Ltd., Hangzhou, China), and the cells were incubated at 37°C in 5% CO_2, for 15–30 min. Afterward, the cells were pelleted by centrifugation and resuspended by gentle tapping of the tubes, and then 500 μl PBS was added to each tube. Mitochondrial membrane potential was assessed by FACS (Beckman Coulter).

Small Interfering RNA-Based Silencing of STAT1

The siRNAs were designed and synthesized by Guangzhou RiboBio (RiboBio, Guangzhou, China). The siRNAs targeting on STAT1 gene were designed and synthesized, and the most effective siRNA (STAT1) identified by qPCR was applied in further experiments. Twenty-four hours prior to transfection, cells were plated onto a six-well plate (Greiner, Germany) at 40–60% confluence. Transfection was performed with Lipofectamine 2,000 (Invitrogen) according to the manufacturer's protocol. The medium was replaced 4–6 h after transfection with new culture medium.

Measurement of NAD^+/NADH Ratio

To assess mitochondrial function by evaluation of the NAD^+/NADH ratio, NAD^+ and NADH were extracted from cells. For NAD^+ extraction, 1×10^6 cells were collected in a centrifuge tube. The supernatant was discarded, and 0.9 ml was added acid extract, followed by sonication of the solution for 1 min (intensity 40%, 4 s, stop for 2 s). The solution was then boiled for 5 min, cooled in an ice bath, and centrifuged for 10 min at 10,000 × *g* at 4°C. The supernatant was transferred to another new centrifuge tube to which an equal volume of alkaline extract was added to neutralize the solution. Centrifugation at 10,000 × *g* at 4°C for 10 min was repeated, and the supernatant was collected and stored on ice for testing. For NADH extraction, 4–5 million cells were collected in a centrifuge tube. The supernatant was discarded, 0.9 ml alkaline extract was added, followed by sonication of the solution for 1 min (40%, 4 s, stop for 2 s). The solution was then boiled for 5 min, cooled in an ice bath, and centrifuged for 10 min at 10,000 × *g* at 4°C. The supernatant was transferred to another new centrifuge tube to which an equal volume of acidic extract was added to neutralize the solution. Centrifugation at 10,000 × *g* at 4°C for 10 min was repeated, and the supernatant was collected and stored on ice for testing.

For testing of NAD^+ and NADH levels, the solutions were centrifuged at 20,000 × *g* at 4°C for 5 min. The supernatant was discarded, and precipitation solution (Nanjing Jiancheng Bioengineering Institute, Nanjing, China) was added for measurement of the solution absorbance at 570 nm.

Measurement of Lactic Acid Content and Production

Lactic acid content within the cells and within the media was detected in samples of approximately 5×10^5 HeLa cells cultured for 48 h. The cells were homogenized by ultrasonic fragmentation, and the lactic acid measurement kit reagents (Nanjing Jiancheng Bioengineering Institute, China) were added according to the manufacturer's instructions for sample loading. The absorbance in each well was measured at 530 nm using the Paradigm Detection Platform (Beckman Coulter). Lactic acid measurements were normalized to total protein concentration, which was tested using the BCA assay (Thermo Fisher Scientific), for each sample.

Measurement of Glucose Concentration

HeLa cells were plated in 6-well culture plates (1×10^6 cells per well) and incubated at 37°C in 5% CO_2 for 24–48 h. When the cells reached approximately 80% confluency, the culture medium was transferred to a new centrifuge tube and centrifuged at 1,000 × *g* for 5 min at 4°C to remove insoluble materials. The supernatant was transferred to specific tubes for the detection of glucose concentration in the medium by the ADVIA 1,650 automatic biochemical analyzer (SIEMENS, Berlin, Germany). Meanwhile, the cells on the culture plate were trypsinized, washed with cold 1 × PBS, and resuspended in microcentrifuge tubes. After 3 min of ultrasonication on ice, the samples were centrifuged at 12,000 × *g* for 20 min at 4°C. This supernatant was then transferred to specific tubes for intracellular glucose concentration detection by the ADVIA 1,650 automatic biochemical analyzer. All values were normalized according to protein concentration, which was determined by the BCA assay.

Measurement of Glutamine Production

For measurement of glutamine production, aliquots of 1×10^6 HeLa cells were seeded and cultured for 24 h before harvesting, washing with cold PBS, and resuspension in 100 μl of Hydrolysis Buffer (BioVision, Milpitas, CA, United States). The cells were quickly homogenized by rapid pipetting up and down several times. The glutamine content was then assessed using the glutamine colorimetric assay kit according to the manufacturer's instructions (BioVision, Milpitas, CA, United States) and normalized according to the protein concentration, which was determined by the BCA assay for each sample.

Western Blotting Analysis

For western blot analysis of protein expression levels, HeLa cells were lysed in radioimmunoprecipitation (RIPA) buffer (CWBio, Beijing, China). Then 50 μg lysate was electrophoresed on 10% separation gel and transferred to a polyvinylidene difluoride membrane (HyClone Laboratories, Logan, UT, United States), which was sealed with 5% non-fat milk diluted in PBS-Tween20 for ∼2 h. Primary antibody solution was then added for incubation at 4°C for 12 h. The primary antibodies used were: anti-sirtuin 3 (SIRT3, dilution ratio: 1:500), anti-Mn superoxide dismutase 2 (MnSOD2, dilution ratio: 1:1,000), anti-isocitrate dehydrogenase 2 (IDH2, dilution ratio: 1:500),

anti-liver kinase B1 (LKB1, dilution ratio: 1:500), anti-p-AMP-activated protein kinase (AMPK, dilution ratio: 1:1,000), anti-pyruvate kinase muscle isozyme 2 (PKM2, dilution ratio: 1:1,000), anti-phosphofructose kinase 1 (PFK1, dilution ratio: 1:1,000), anti-pyruvate dehydrogenase (PDH, dilution ratio: 1:1,000), anti-FOS like 1, AP-1 transcription factor subunit (FOSL1, Fra-1, Abcam, Cambridge, MA, United States, dilution ratio: 1:500), anti-signal transducer and activator of transcription 1 (STAT1, dilution ratio: 1:500), anti-c-Rel (c-Rel, dilution ratio: 1:1,000), anti-lactate dehydrogenase A (LDHA, dilution ratio: 1:1,000), anti-sirtuin 1 (SIRT1, dilution ratio: 1:500), anti- B-cell lymphoma-2 (Bcl-2, dilution ratio: 1:1,000), anti-NF kappa-B (NF-κB/p65, dilution ratio: 1:1,000, Immunoway Technology, Newark, DE, United States), anti-TP53 (p53, dilution ratio: 1:1,000), anti-cyclin-dependent kinase 4 (CDK4, dilution ratio: 1:1,000), anti-cyclin D1 (dilution ratio: 1:1,000), anti-p21 (dilution ratio: 1:1,000), anti-MAPK14/p38 (dilution ratio: 1:1,000), and anti-MDM2 (dilution ratio: 1:1,000) anti-p16 (dilution ratio: 1:1,000, Boster Technology, Wuhan, China). After three washes on a shaker with PBS-Tween20, the membranes were incubated with anti-rabbit or anti-mouse horseradish peroxidase (HRP)-conjugated secondary antibody (Santa Cruz Biotechnology, Santa Cruz, CA, United States, 1:3,000 dilution) for 1 h at 37°C). Finally, the protein bands were developed using the Luminata Forte western HRP substrate (Millipore, Billerica, MA, United States). Anti-β-tubulin (Santa Cruz Biotechnology) expression was used for normalization.

Cervical Cancer Tumor Growth *in vivo*

The study protocol was approved by and conducted in accordance with the Committee of the Use of Live Animals in Teaching and Research at the Central South University. Twelve four-week-old BALB/c-nu female nude mice were purchased from the animal institutes of the Chinese Academy of Medical Sciences and Peking Union Medical College (CAMS and PUMC). We divided the mice into three groups (n = 4 each). HeLa cells transfected with the control vector (HeLa vector), HeLa cells transfected to overexpress Fra-1 (HeLa/Fra-1), and HeLa cells with overexpression of Fra-1 and silencing of STAT1 (HeLa/Fra-1/siSTAT1) of good cell status were inoculated into the right armpit of the mice in the three respective groups at a concentration of 6×10^6 cells/150 μl. The mice were monitored twice weekly for palpable tumor formation and euthanized 15 days after transplantation for assessment of tumor formation. Tumors were measured using a Vernier caliper, weighed, and photographed.

Statistical Analysis

All data were presented as mean ± standard deviation (SD) values obtained from three independent experiments and analyzed by one-way analysis of variance (ANOVA). Then two-way ANOVA followed by Tukey's multiple comparison test for multiple comparisons was performed. GraphPad Prism 5.0 (GraphPad Software, La Jolla, CA, United States) was used for all analyses, and a value of $P < 0.05$ indicated a statistically significant difference.

RESULTS

Fra-1 Inhibited Proliferation, Promoted Apoptosis, and Altered the Cell Cycle Distribution of Cervical Cancer Cells

Our previous research demonstrated lower Fra-1 expression in cervical carcinoma tissues compared to adjacent normal tissues. To further investigate this feature of cervical cancer cells, we established a stable Fra-1–overexpressing HeLa cell line using lentivirus transfection technology. The results of the CCK8 test showed that the proliferation rate of HeLa cells overexpressing Fra-1 was significantly reduced compared to that of vector group (**Figure 1A**). Furthermore, Fra-1–overexpressing HeLa cells formed fewer colonies than did the control cells (**Figures 1B,C**). Thus, these assays demonstrated that Fra-1 overexpression inhibited HeLa cell proliferation. We also examined the effect of Fra-1 overexpression on the cell cycle distribution of HeLa cells by flow cytometry and found that the percentage of cells in S phase was 13.32% among Fra-1–overexpressing HeLa cells, which was lower than that of 24.57% among the control cells (**Figure 1D**). Therefore, we conclude that Fra-1 overexpression significantly induced S-phase arrest in HeLa cells. Furthermore, we detected the effect of Fra-1 overexpression on cell apoptosis by flow cytometry with Hoechst 33342/PI double staining. The results showed that the proportion of early apoptotic cells among the Fra-1–overexpressing HeLa cells was 6.01%, while that in the control group was only 2.99% (**Figure 1E**). Thus, overexpression of Fra-1 promoted apoptosis among HeLa cells.

Fra-1 Up-Regulated STAT1 and Altered p53 Signaling in Cervical Cancer Cells

To explore the mechanism by which Fra-1 overexpression altered key activities of cervical cancer cells, we performed the real-time PCR and western blot analyses to examine the effects on STAT1 expression and performed an mRNA microarray analysis to identify differentially activated signaling pathways. Our results showed that STAT1 protein was significantly up-regulated in Fra-1–overexpressing HeLa cells compared with the control cells, and the results of real-time PCR for STAT1 gene expression were consistent. Through Kyoto Encyclopedia of Genes and Genomes (KEGG) analysis, we observed obvious differences in signal pathway activity between Fra-1–overexpressing HeLa cells and control cells (**Figure 2A**). The p53 pathway was specifically identified and is strongly linked to the proliferation and apoptosis of cancer cells. Previous research has shown that STAT1 regulates the p53 activity and induces phosphorylation of p53 (McDermott et al., 2005). Therefore, we further tested the expression levels of key molecules involved in the p53 signaling pathway. We found that p53 was significantly up-regulated in Fra-1–overexpressing HeLa cells compared with the control cells, and p38 (MAPK) and p21 also were up-regulated in Fra-1–overexpressing HeLa cells. Conversely, MDM2, Bcl-2, CDK4, and cyclin D1 were down-regulated in Fra-1–over-expressing HeLa cells (**Figure 2B**). To confirm the differential expression of these proteins, we also detected the expression of the corresponding genes by real-time PCR. The results confirmed that p53, p38, and p21 were

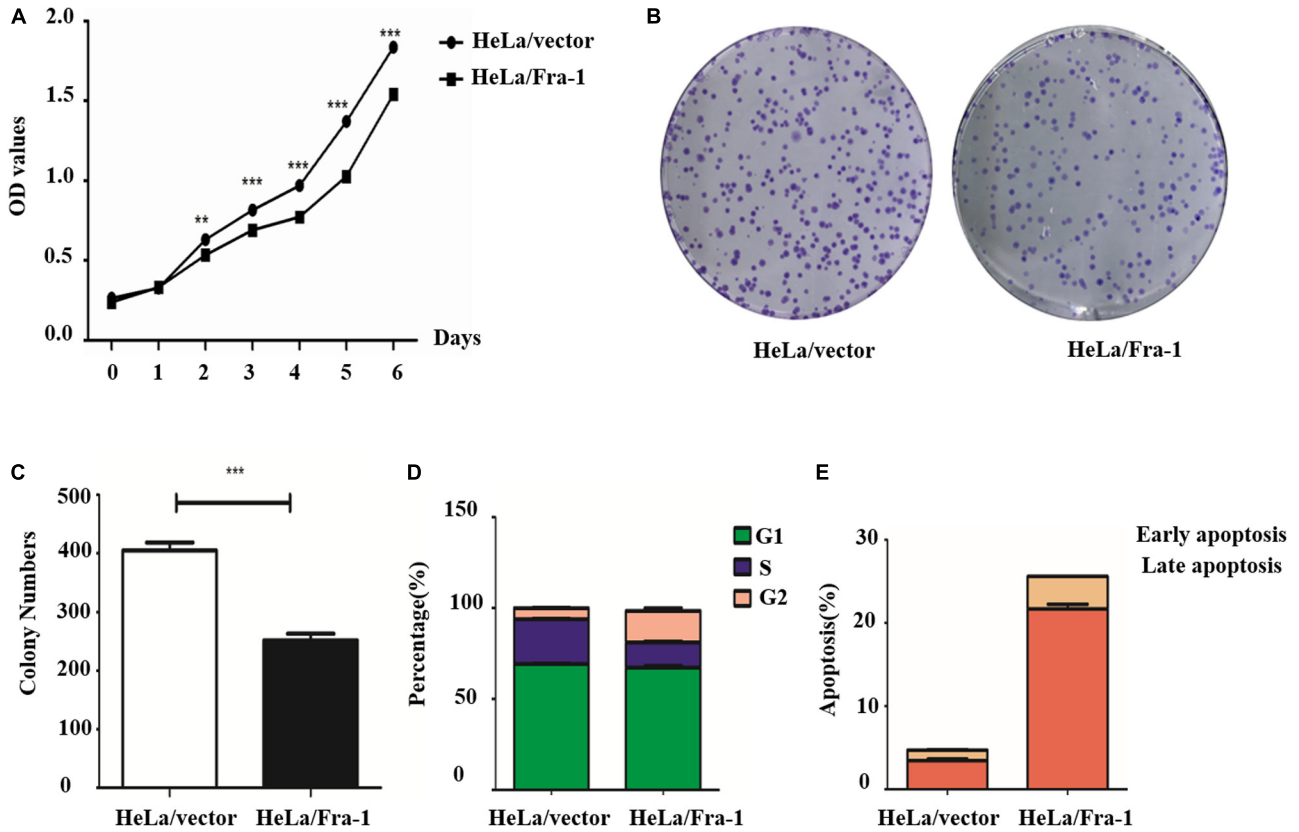

FIGURE 1 | Fra-1 inhibited the proliferation and promoted apoptosis of cervical cancer cells. **(A)** Cell viability of HeLa cells transfected with control vector (HeLa/vector) and HeLa cells transfected with Fra-1 overexpression vector (HeLa/Fra-1) cells determined by CCK8 assay. **(B)** Colony forming ability of HeLa/vector and HeLa/Fra-1 cells. **(C)** Colony numbers formed by HeLa/vector and HeLa/Fra-1 cells. **(D)** Cell cycle distribution among HeLa/vector and HeLa/Fra-1 cells as determined by flow cytometry. **(E)** Flow cytometric analysis of apoptosis among HeLa/vector and HeLa/Fra-1 cells. Data means ± standard deviation (SD). Each representative experiment was repeated three times with similar results. $^{**}P < 0.01$; $^{***}P < 0.001$, $n = 3$.

up-regulated at the mRNA level, while MDM2, Bcl-2, CDK4, and cyclin D1 were down-regulated at the mRNA level in Fra-1–over-expressing HeLa cells compared with the control cells (**Figure 2C**).

Fra-1 Overexpression Restored Mitochondrial Disorder in Cervical Cancer Cells

To further study the effect of Fra-1 on cervical cancer cell senescence, we simulated the aging process of normal cells. Taking advantage of the reproductive senescence characteristic of the cells, we cultured the primary cells until they experienced senescence using the method of serial sub cultivation, and we finally used the 30th generation of cells for experiments evaluating mitochondrial disorder. Cell senescence was measured using a β-galactosidase staining assay, and the results showed that Fra-1 promoted HeLa cell senescence (**Figure 3A**). We also investigated whether Fra-1 affected the expression of senescence-related molecules and observed a significant reduction in SIRT1 expression in Fra-1–overexpressing HeLa cells. p65 is a key regulator of the process of senescence, and SIRT1 inhibits NF-κB activity mainly by deactivating p65. Our results showed that Fra-1 overexpression promoted the expression of NF-κB and p16, but decreased c-Myc expression in HeLa cells (**Figure 3B**).

Disturbance of intracellular calcium homeostasis can affect mitochondrial membrane potential and result in tumorigenesis (Vasileiou et al., 2019). Thus, we investigated whether the intracellular Ca^{2+} concentration is altered in Fra-1–overexpressing HeLa cells. We found a higher Ca^{2+} concentration in Fra-1–overexpressing HeLa cells than in control cells, as demonstrated by the mean fluorescence intensity (MFI) data (**Figure 3C**). ROS play crucial roles in many cell biological functions and in mitochondria. We examined the effect of Fra-1 overexpression on ROS levels and observed a significant decrease in the ROS level in Fra-1–overexpressing HeLa cells compared with that in control cells, with a corresponding decrease in the MFI from 6,973 ± 181.9 to 2,478 ± 175.1 (**Figure 3D**). A reduction in mitochondrial membrane potential ($\Delta\psi m$) is considered to be an early event during apoptosis and metabolism. Therefore, we also examined the mitochondrial membrane potential in Fra-1–overexpressing HeLa cells by JC-1 staining. A decrease in the mitochondrial membrane potential during apoptosis was represented by a decrease in red

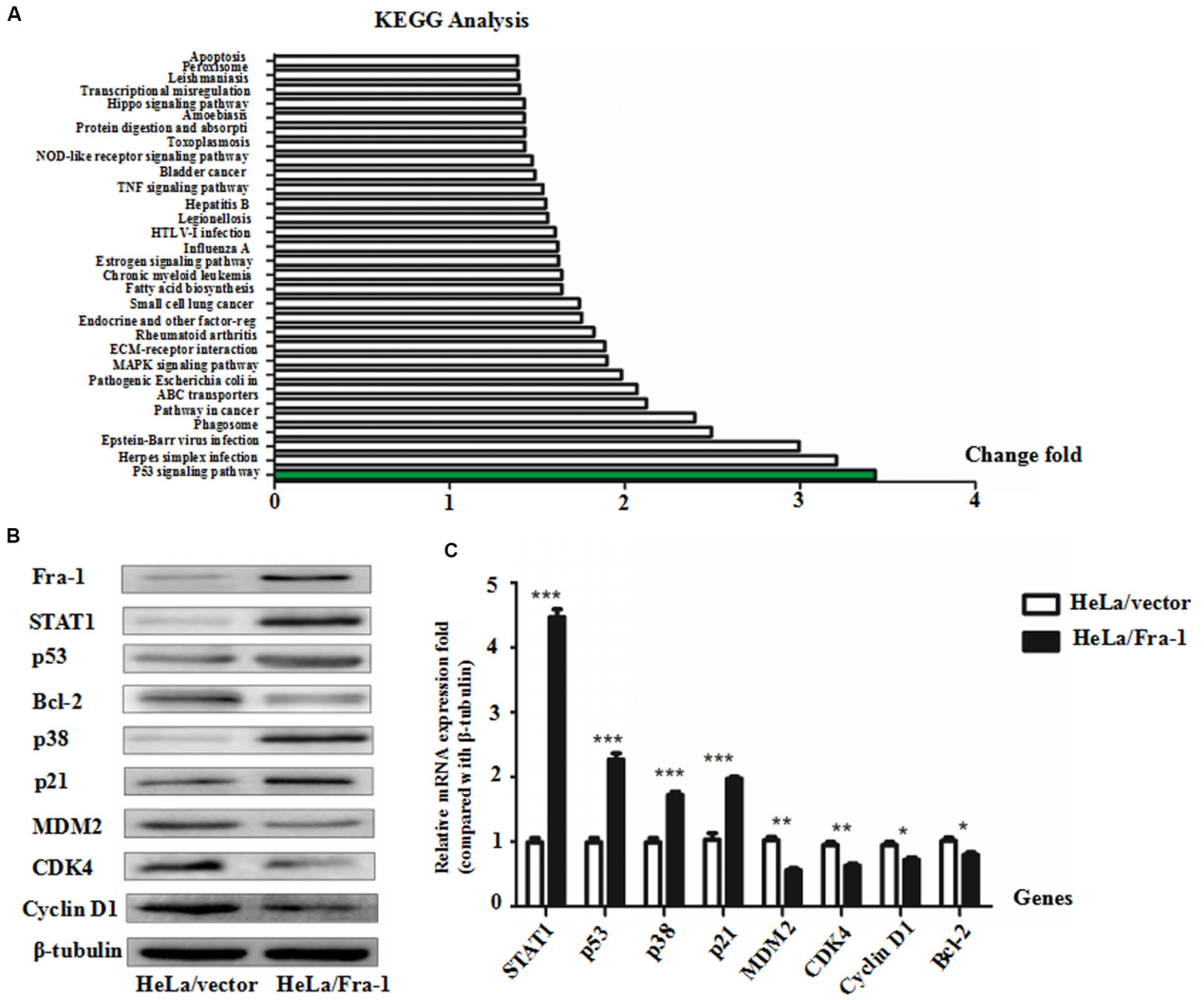

FIGURE 2 | Fra-1 regulated p53 signaling pathway activity in cervical cancer cells. **(A)** mRNA chip analysis in HeLa/vector and HeLa/Fra-1 cells revealed differences in mRNA expression between the two groups. Differentially active signaling pathways were identified by gene ontology analysis. **(B)** Western blotting analysis of signal transducer and activator of transcription 1 (STAT1), p53, Bcl-2, p38, p21, MDM2, CDK4, and cyclinD1 protein levels in HeLa/vector and HeLa/Fra-1 cells. **(C)** Real-time polymerase chain reaction (PCR) analysis the mRNA expression levels of STAT1, p53, Bcl-2, p38, p21, MDM2, CDK4, and cyclinD1 in HeLa/vector and HeLa/Fra-1 cells. $^{*}P < 0.05$; $^{**}P < 0.01$; $^{***}P < 0.001$, $n = 3$.

fluorescence intensity and an increase in green fluorescence intensity. Among the Fra-1–overexpressing HeLa cells, the percentage of cells with $\Delta\psi m$ loss was greater than that among the control cells. The percentage decrease in the mitochondrial membrane potential was 9.94% with Fra-1 overexpression compared with 5.06% in control cells (**Figure 3E**).

We next investigated the possible mechanism for the effects of Fra-1 overexpression on mitochondrial function. It is well known that during oxidative phosphorylation, the electron transport chain in the mitochondrial inner membrane converts NADH to NAD^+ through five complexes and produces oxygen and ATP. Thus, an increased NAD^+/NADH ratio represents an increase in mitochondrial function. We found that the NAD^+/NADH ratio was increased in Fra-1–overexpressing HeLa cells (**Figure 3F**). Western blot analysis revealed elevated expression of SIRT3, MnSOD2, and IDH2 in Fra-1–overexpressing HeLa cells (**Figure 3G**). Together these results revealed that Fra-1 overexpression restored mitochondrial function in HeLa cells.

Fra-1 Suppressed the Warburg Effect in Cervical Cancer Cells

The Warburg effect is a key characteristic of cancer cell metabolism, in which cancer cells are more inclined to glycolysis and glutamine metabolism. Therefore, we explored whether Fra-1 overexpression affected the Warburg effect in HeLa cells. First, we detected the effects of Fra-1 overexpression on the expression levels of key enzymes involved in aerobic glycolysis by Western blot and q-PCR analyses. The results showed that Fra-1 significantly inhibited the expression of rate-limiting

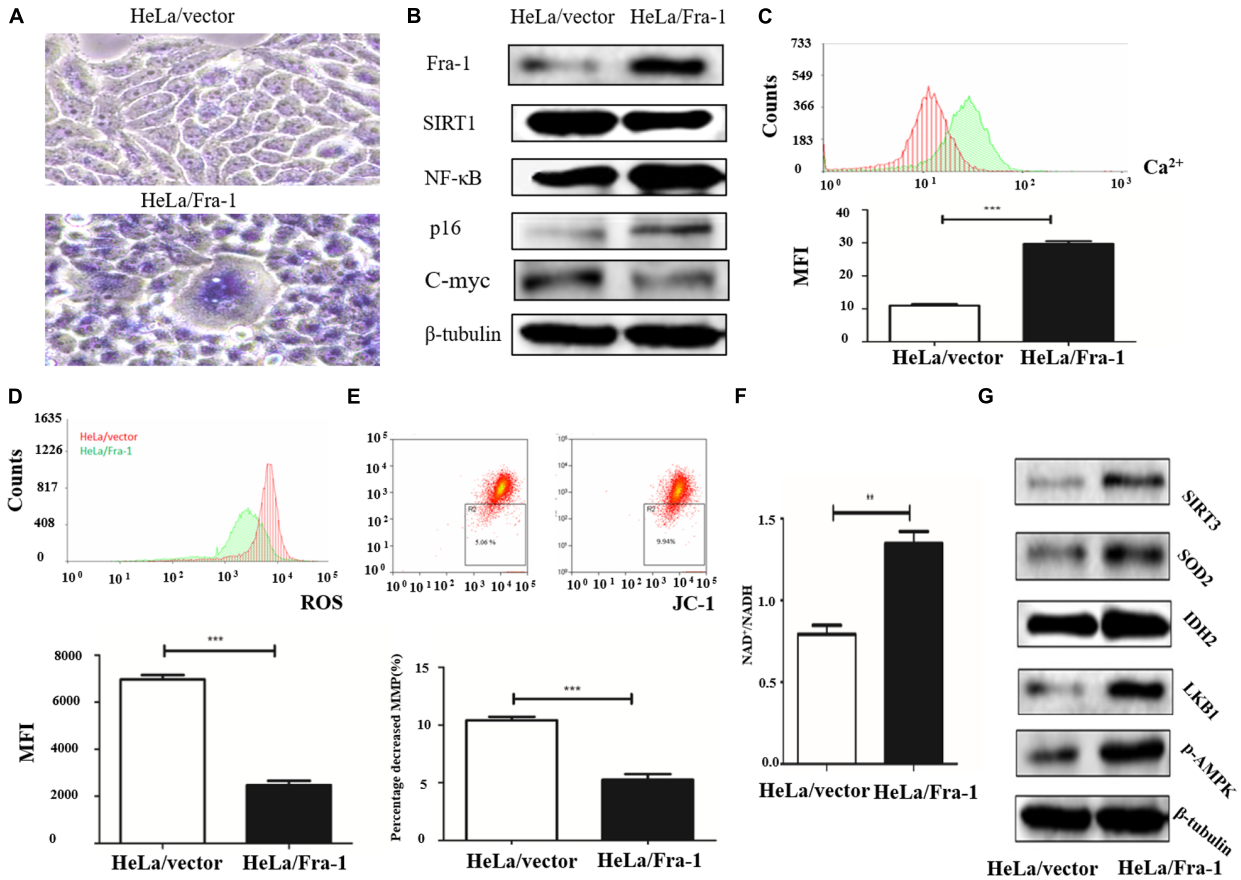

FIGURE 3 | Fra-1 promoted cell senescence and restored mitochondrial disorder in cervical cancer cells. **(A)** β-Galactosidase assay for cell senescence in HeLa/vector and HeLa/Fra-1 cells. **(B)** Western blot analysis of Fra-1, SIRT1, NF-κB, p16, and c-Myc protein expression in HeLa/vector and HeLa/Fra-1 cells. **(C)** Flow cytometric analysis of intracellular Ca^{2+} concentration. Red color represents HeLa/vector group and green color represents HeLa/Fra-1 group. **(D)** Flow cytometric analysis of intracellular reactive oxygen species (ROS) concentration. Red color represents HeLa/vector group and green color represents HeLa/Fra-1 group. **(E)** Flow cytometric analysis of mitochondrial membrane potential ($\Delta\psi m$) in HeLa/vector and HeLa/Fra-1 cells. **(F)** NAD^+/NADH ratio in HeLa/vector and HeLa/Fra-1 cells. **(G)** Western blot analysis of sirtuin 3 (SIRT3), SOD2, IDH2, LKB1, and p-AMPK expression in HeLa/vector and HeLa/Fra-1 cells. $^{**}P < 0.01$; $^{***}P < 0.001$, $n = 3$.

enzymes in glycolysis, PFK1 and PKM2, while promoting the expression of PDH, which catalyzes pyruvate to produce acetyl-CoA (**Figure 4A**). Moreover, Fra-1 inhibited the expression of another glycolytic rate-limiting enzyme, HK II, in cervical cancer cells. Likewise, expression of glucose transporter 1 (Glut1), which is responsible for transporting glucose into cells, also was decreased in Fra-1-overexpressing HeLa cells. A significant reduction was observed in the mRNA level of LDHA, which converts pyruvate to lactate (**Figure 4B**). Finally, we examined the effect of Fra-1 overexpression on intracellular lactate levels and found less lactic acid accumulation in Fra-1–overexpressing HeLa cells than in control cells (**Figure 4C**). We also confirmed that the glucose level was decreased in Fra-1–overexpressing HeLa cells (**Figure 4D**).

The Warburg effect is often accompanied by abnormal glutamine metabolism and fatty acid synthesis. Our western blot results showed that glutamine dehydrogenase (GDH), which drives glutamine entry into the TCA cycle as α-KG, was significantly down-regulated in Fra-1–overexpressing HeLa cells. Moreover, Fra-1 overexpression was associated with a decreased glutamine concentration (**Figure 4E**).

All of the results described above indicate that Fra-1 likely suppresses the Warburg effect and fatty acid synthesis while also enhancing mitochondrial function and repairing mitochondrial dysfunction. Overall, Fra-1 plays key roles in the metabolic reprogramming of cervical cancer cells.

Silencing of STAT1 Impaired the Inhibitory Effect of Fra-1 on Cervical Cancer Cell Proliferation

Because we found that Fra-1 inhibited HeLa cell proliferation and up-regulated STAT1 expression, we investigated whether silencing STAT1 using siRNAs designed specifically for STAT1 could alter the inhibitory effect of Fra-1 on cervical cancer cell growth. Upon silencing of STAT1 in Fra-1–overexpressing HeLa cells, we found that the proliferation rate of Fra-1–overexpressing

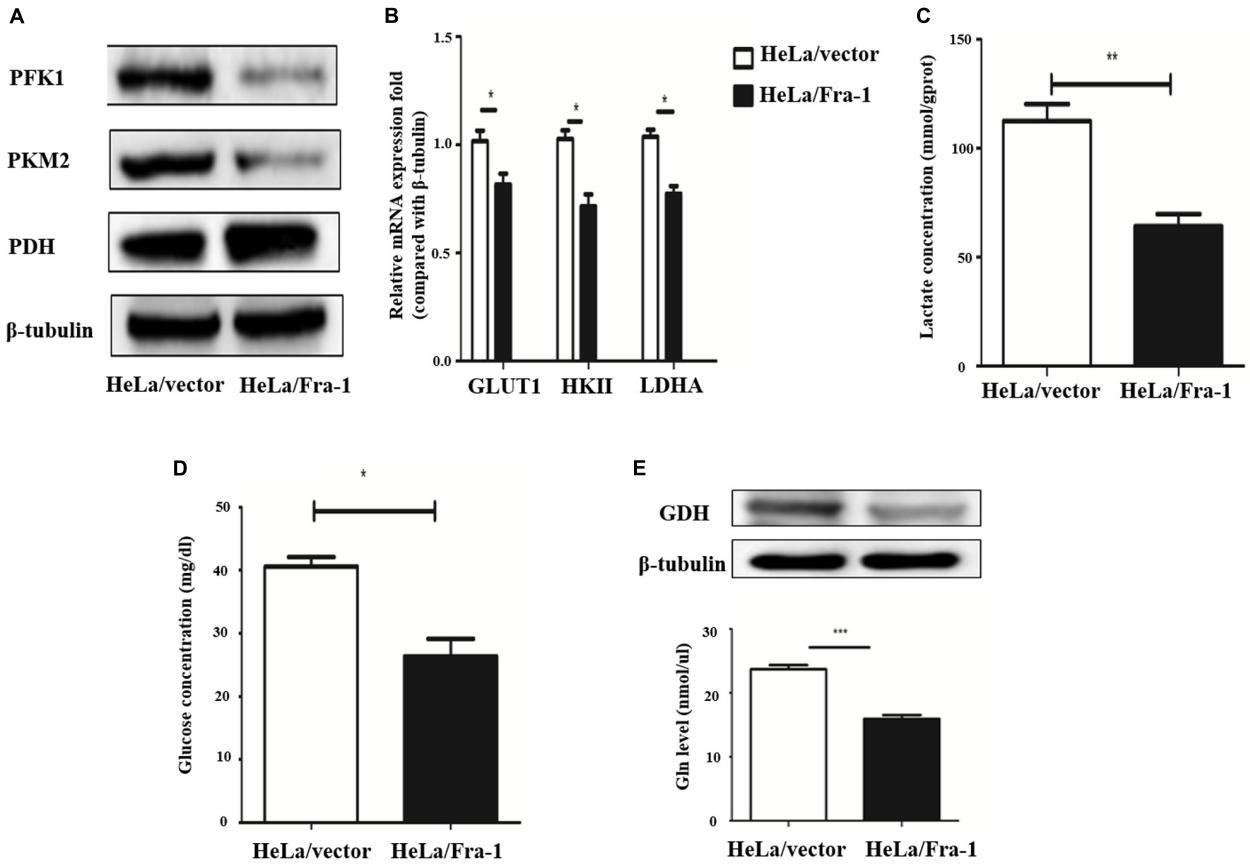

FIGURE 4 | Fra-1 suppressed metabolic reprogramming in cervical cells. **(A)** Western blot analysis of the expression of key glycolysis enzymes PFK1, PKM2, and PDH in HeLa/vector and HeLa/Fra-1 cells. **(B)** Real-time polymerase chain reaction (PCR) analysis of the expression of glycolysis enzymes GLUT1, HK II, and LDHA in HeLa/vector and HeLa/Fra-1 cells. **(C)** Lactate concentration in HeLa/vector and HeLa/Fra-1 cells. **(D)** Glucose concentration in HeLa/vector and HeLa/Fra-1 cells. **(E)** Glutamine dehydrogenase (GDH) protein level and glutamine concentration in HeLa/Fra-1 and HeLa/vector cells. $^{*}P < 0.05$; $^{**}P < 0.01$; $^{***}P < 0.001$, $n = 3$.

HeLa cells was restored based on CCK8 assay results as well as the colony forming assay (**Figures 5A–C**).

To verify the observed effects of STAT1 silencing *in vivo*, we compared the growth of tumors formed by HeLA/vector, HeLa/Fra-1, and HeLa/Fra-1/siSTAT1 cells in BALB/c-nu mice Tumor formation was significantly diminished in the HeLa/Fra-1 group compared with that in the HeLa/vector control group. However, tumorigenicity was significantly increased for HeLa/Fra-1/siSTAT1 cells. These findings suggest that Fra-1 inhibited the tumorigenicity of HeLa cells in nude mice via STAT1 (**Figure 5D**).

To explore the possible mechanism underlying the observed phenotypic changes, we analyzed the expression levels of several molecules closely related to the cell cycle distribution and apoptosis by western blotting and real-time PCR experiments. The results showed that, compared with the corresponding expression levels in Fra-1–overexpressing HeLa cells, the changes in p53, Bcl-2, p38, p21, MDM2, CDK4, and cyclin D1 expression were reversed by silencing of STAT1 in Fra-1–overexpressing HeLa cells. Specifically, p53, p38, and p21 were down-regulated at the protein level, and MDM2, CDK4, Bcl-2, and cyclin D1 were up-regulated at both the mRNA and protein levels after silencing of STAT1. The real-time PCR analysis revealed similar trends. Moreover, the expression levels of some of these proteins were even renewed to their levels in control HeLa cells (**Figures 5E,F**).

Together our results demonstrated that silencing of STAT1 impaired the inhibitory effect of Fra-1 on cervical cancer cell growth.

Silencing of STAT1 Reversed the Effect of Fra-1 on Cell Senescence and Mitochondrial Dysfunction in Cervical Cancer Cells

β-galactoside staining revealed that STAT1 silencing inhibited the senescence of Fra-1–overexpressing HeLa cells, restoring it to almost the background level (**Figure 6A**). These results indicate that STAT1 promoted senescence in Fra-1–overexpressing HeLa cells. We next explored STAT1 silencing affected the expression of senescence-related molecules in cervical cancer cells. Western blot analysis showed that the expression levels of SIRT1 and c-Myc oncogene were significantly up-regulated with STAT1 silencing, whereas the expression levels of p16 and NF-κB were down-regulated (**Figure 6B**). We detected changes in staining

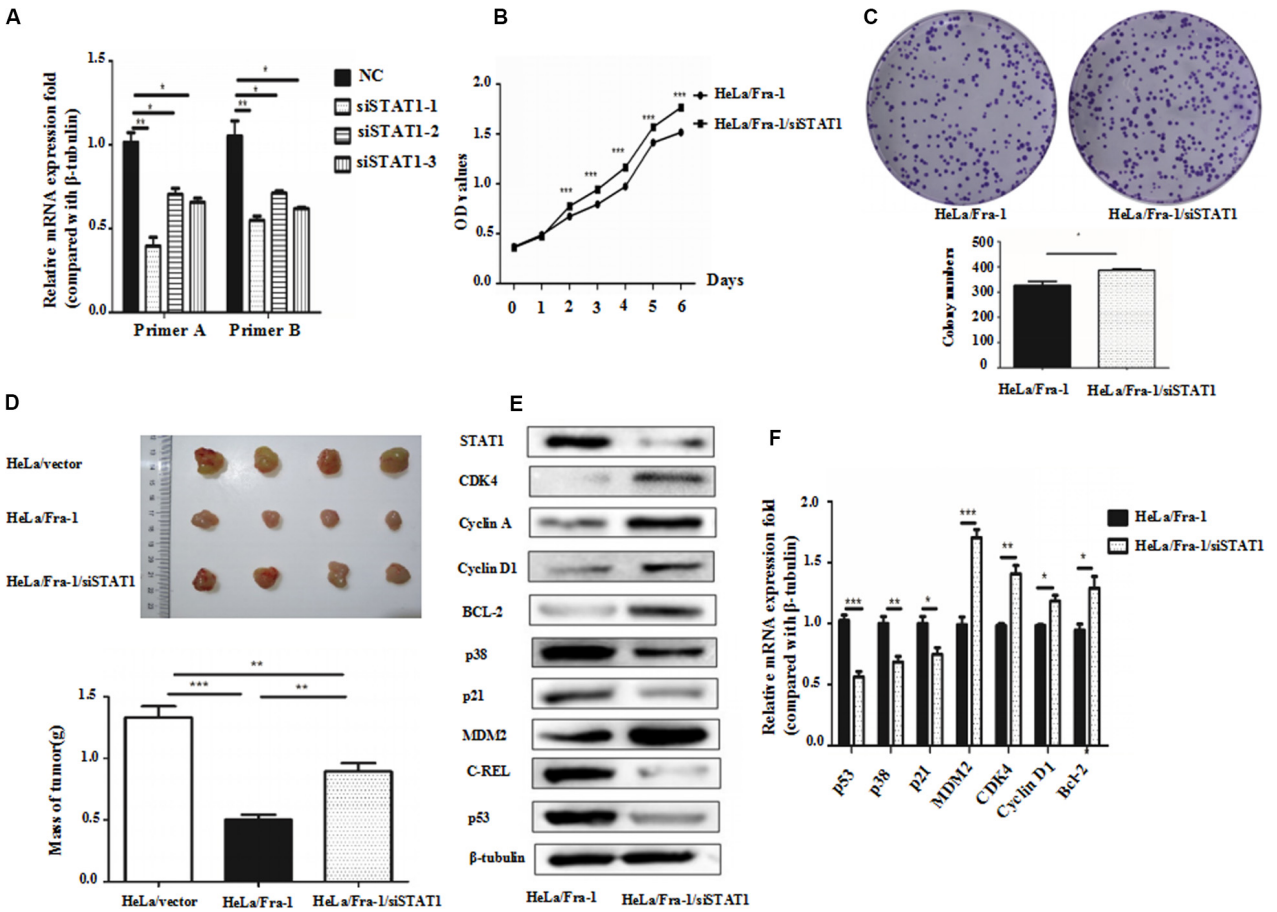

FIGURE 5 | Silencing of signal transducer and activator of transcription 1(STAT1) by small interfering RNA promoted proliferation of cervical cancer cells via activation of the p53 signal pathway. **(A)** Real-time polymerase chain reaction (PCR) analysis of the silencing effects of three siRNAs for STAT1 in HeLa/Fra-1 cells. **(B)** Cell viability of HeLa/Fra-1 and HeLa/Fra-1/siSTAT1 cells according to CCK8 assay. **(C)** Colony forming ability of HeLa/Fra-1 and HeLa/Fra-1/siSTAT1 cells. **(D)** *In vivo* analysis of subcutaneous implanted tumor growth to compare the tumorigenic abilities of HeLa/vector, HeLa/Fra-1, and HeLa/Fra-1/siSTAT1 cells in mice. **(E)** Western blot analysis of protein expression of STAT1, CDK4, cyclin A, cyclin D1, p53, Bcl-2, c-REL, p38, p21, and MDM2 in HeLa/Fra-1 and HeLa/Fra-1/siSTAT1 cells. **(F)** Real-time PCR analysis of mRNA expression of STAT1, CDK4, cyclin D1, p53, Bcl-2, p38, p21, and MDM2 in HeLa/Fra-1 and HeLa/Fra-1/siSTAT1 cells. $^{*}P < 0.05$; $^{**}P < 0.01$; $^{***}P < 0.001$, $n = 3$.

for Ca^{2+}, ROS, and JC-1 in Fra-1–overexpressing HeLa cells with STAT1 silencing by flow cytometry. The results showed that STAT1 silencing did not change the level of the important intracellular messenger Ca^{2+} in Fra-1–overexpressing HeLa cells (**Figure 6C**). However, the ROS level was increased upon STAT1 silencing (**Figure 6D**), with the MFI data indicating an obvious increase in ROS (**Figure 6E**). JC-1 staining showed that STAT1 silencing had little effect on the mitochondrial membrane potential ($\Delta\psi m$) in Fra-1–overexpressing HeLa cells (**Figure 6F**).

Silencing of STAT1 Recovered Metabolic Reprogramming in Cervical Cancer Cells

We first examined the effect of STAT1 silencing on mitochondrial metabolism in Fra-1–overexpressing HeLa cells. The NAD^{+}/NADH ratio was decreased obviously by STAT1 silencing (**Figure 7A**), indicating that STAT1 caused mitochondrial dysfunction in HeLa cells. After silencing of STAT1, the major mitochondrial deacetylase SIRT3 was down-regulated, and the expression of the crucial anti-oncogene LKB1 was significantly reduced, which thereby inhibited the activity of AMPK (**Figure 7B**). The reduction in AMPK expression further led to an increase in ACC, a rate-limiting enzyme for fatty acid synthesis.

Then we tested the influence of STAT1 silencing on the Warburg effect. The expression of PFK1 and PKM2, the rate-limiting enzymes of glycolysis, were shown to be decreased significantly (**Figure 7C**), and at the mRNA level, the change in HK II expression that occurred with Fra-1 overexpression was significantly reversed after silencing STAT1. In addition, the expression levels of glycolytic enzymes GLUT1 and LDHA were also significantly restored (**Figure 7D**). Further experiments showed that silencing of STAT1 significantly promoted the uptake of glucose in Fra-1–overexpressing HeLa cells (**Figure 7E**), and the intracellular content of lactate also

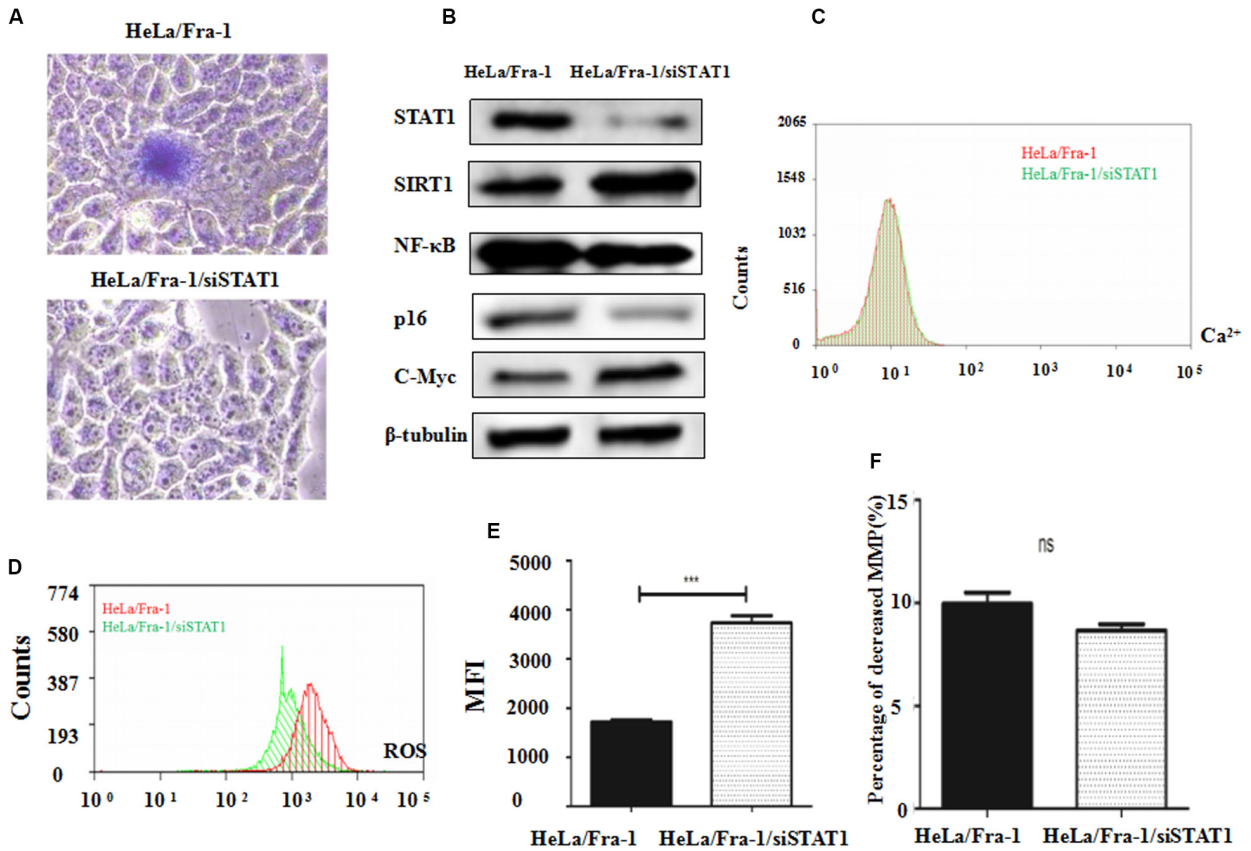

FIGURE 6 | Silencing of signal transducer and activator of transcription 1 (STAT1) inhibited senescence and promoted mitochondrial dysfunction in cervical cancer cells. **(A)** β-Galactosidase assay for cell senescence in HeLa/Fra-1 and HeLa/Fra-1/siSTAT1 cells. **(B)** Western blot analysis of protein expression of c-Myc, SIRT1, NF-κB, and p16 in HeLa/Fra-1 and HeLa/Fra-1/siSTAT1 cells. **(C)** Flow cytometric analysis of intracellular Ca^{2+} concentration. Red color represents HeLa/Fra-1 group and green color represents HeLa/Fra-1/siSTAT1 group. **(D)** Flow cytometric analysis of intracellular reactive oxygen species (ROS) levels. Red color represents HeLa/Fra-1 group and green color represents HeLa/Fra-1/siSTAT1 group. **(E)** MFI data reflecting changes in the intracellular ROS concentration in HeLa/Fra-1 and HeLa/Fra-1/siSTAT1 cells. **(F)** Flow cytometric analysis of mitochondrial membrane potential ($\Delta\psi m$) in HeLa/Fra-1 and HeLa/Fra-1/siSTAT1 cells. $^{*}P < 0.05$; $^{**}P < 0.01$; $^{***}P < 0.001$, $n = 3$.

was increased (**Figure 7F**). However, silencing of STAT1 had little effect on GDH in HeLa cells. The glutamine concentration also showed a slight increase in Fra-1–overexpressing cells (**Figure 7G**). These results showed that STAT1 silencing recovered mitochondrial dysfunction in HeLa cells and reversed the Warburg effect caused by Fra-1.

In summary, our results showed that Fra-1 inhibited cervical cancer cell growth and repaired metabolic dysfunction via STAT1, and these effects involved the Warburg effect and fatty acid metabolism in cervical cancer cells.

DISCUSSION

The Fra-1 and Jun proteins form heterodimers, resulting in a leucine zipper protein activator protein 1 (AP-1; Tolza et al., 2019). Fra-1 was shown to be closely related to the tumorigenesis of many tumors (He et al., 2015; Oliveira-Ferrer et al., 2015), and additional research identified Fra-1 as an oncogene-encoded transcription factor plays a crucial role in cancer invasion and metastasis (Luo et al., 2010). However, Fra-1 is down-regulated in the tumorigenic cell lines CGL3 and HeLa compared to non-tumorigenic cells, and it specifically inhibits the tumorigenicity of cervical carcinoma cell lines (Kehrmann et al., 2013). Our previous study showed that Fra-1 is expressed at low levels in cervical carcinoma tissues compared to adjacent normal tissues (Xiao et al., 2015). Therefore, the role of Fra-1 in cervical carcinoma needed to be investigated further.

The results of the present study show that Fra-1 overexpression inhibited cell proliferation, while promoting cell apoptosis and senescence in HeLa cervical cancer cells. Moreover, Fra-1 overexpression in these cells inhibited subcutaneous tumor formation in our *in vivo* experiment. Overall, Fra-1 overexpression in cervical cancer cells exerted a tumor suppressing effect based on our *in vitro* analyses of cell proliferation, cell cycle distribution, apoptosis, and senescence as well as in our xenograft tumor model.

Metabolic reprogramming is required to meet the different metabolic needs of cancer cells during tumorigenesis (Allison et al., 2017). Altered metabolism is a major feature

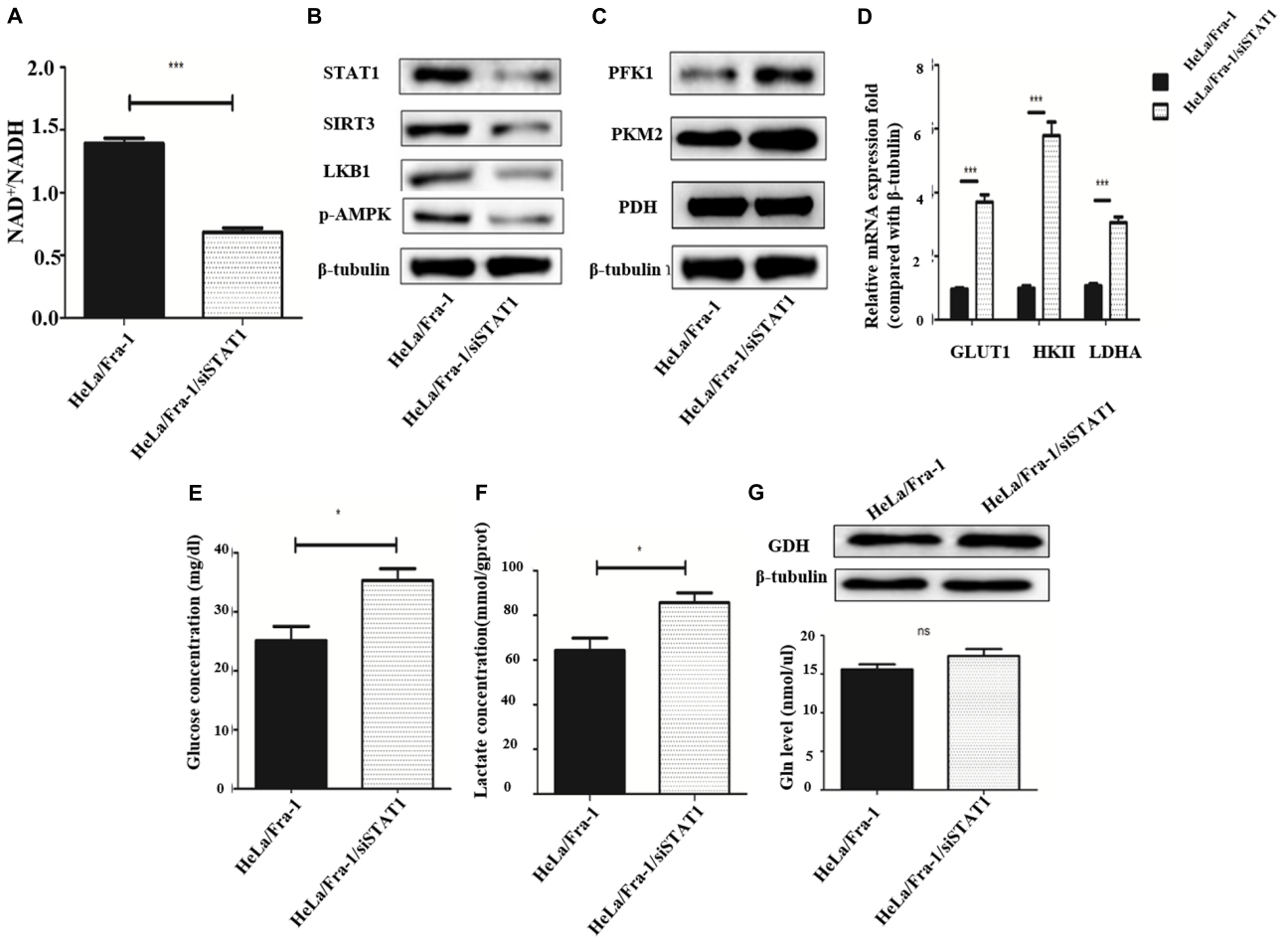

FIGURE 7 | Silencing of signal transducer and activator of transcription 1(STAT1) recovered metabolic reprogramming in cervical cancer cells overexpressing Fra-1. **(A)** NAD + /NADH ratio in HeLa/Fra-1 and HeLa/Fra-1/siSTAT1 cells. **(B)** Western blot analysis of STAT1, sirtuin 3 (SIRT3), LKB1, and p-AMPK expression in HeLa/Fra-1 and HeLa/Fra-1/siSTAT1 cells. **(C)** Western blot analysis of the expression of key glycolysis enzymes PFK1, PKM2, and PDH in HeLa/Fra-1 and HeLa/Fra-1/siSTAT1 cells. **(D)** Real-time polymerase chain reaction (PCR) analysis of mRNA expression of glycolysis enzymes Glut1, HK II, and LDHA in HeLa/Fra-1 and HeLa/Fra-1/siSTAT1 cells. **(E)** Glucose concentration in HeLa/Fra-1 and HeLa/Fra-1/siSTAT1 cells. **(F)** Lactate concentration in HeLa/Fra-1 and HeLa/Fra-1/siSTAT1 cells. **(G)** Protein expression of glutamine dehydrogenase (GDH) and glutamine concentration in HeLa/Fra-1 and HeLa/Fra-1/siSTAT1 cells. NS: No statistical difference; $P < 0.05$; $^{**}P < 0.01$; $^{***}P < 0.001$, $n = 3$.

of tumor cells, commonly including the Warburg effect and up-regulation of glutamine metabolism to convert carbon sources (Mills and O'Neill, 2016). In addition, mitochondrial function is often impaired, and mitochondrial metabolism is weakened. Mitochondria produce ATP via oxidative phosphorylation using pyruvate and fatty acids (Li et al., 2017). Cells with damaged mitochondria cannot generate enough ATP from mitochondrial oxidative phosphorylation and then are forced to rely on glycolysis for ATP generation (Lavie et al., 2018). In the present study, we explored whether Fra-1 caused these metabolic changes in HeLa cells. The mitochondrial membrane potential, Ca^{2+} concentration, and ROS level are closely related to cell metabolism. Changes in mitochondrial membrane potential modulate the activity of important enzymes in mitochondria, and the mitochondrial membrane potential, or $\Delta\Psi$, is a reflection of mitochondrial metabolic status (Arfaoui et al., 2018). Additionally, Ca^{2+} regulates cell metabolism together with ROS (Zhou et al., 2017). Our results indicated that Fra-1 overexpression increased the intracellular Ca^{2+} concentration, but decreased the ROS level and mitochondrial membrane potential in HeLa cells. These changes indicate that Fra-1 was related to metabolic changes in cervical cancer cells, and thus, we next sought to understand how Fra-1 causes metabolic reprogramming.

Sirtuin 3, a member of the NAD^+-dependent deacetylases, is an important deacetylase in mitochondria. SIRT3 inhibits ROS production through two important target molecules, IDH2 and SOD2 (Yamato et al., 2016). Therefore, we examined the effect of Fra-1 overexpression on SIRT3, IDH2, and SOD2 expression in cervical cancer cells. We found that Fra-1 overexpression restored mitochondrial function in cervical cancer cells via the SIRT3 signaling pathway, and Fra-1 increased the expression

of IDH2 and SOD2. The results indicated that Fra-1 up-regulated the expression of SIRT3, which led to changes in IDH2 and SOD2 expression as downstream molecules, and finally reduced the ROS content in cervical cancer cells. NAD^+ and NADH are two coenzymes necessary for cellular energy metabolism. A low NAD^+/NADH ratio leads to metabolic imbalance, and an increase in the NAD^+/NADH ratio can ameliorate the metabolic imbalance (Pillai et al., 2010). Our results showed that Fra-1 increased the NAD^+/NADH ratio in cervical cancer cells, indicating that Fra-1 repaired some functions of mitochondrial in HeLa cells.

Sirtuin 3 deacetylates and activates LKB1, thereby augmenting the activity of the LKB1-AMPK pathway (Li et al., 2015). Multiple studies have identified LKB1 as a tumor suppressor gene and shown that it inhibits important metabolic pathways in cancer cells by activating AMPK (Hawley et al., 2016; Blackmore et al., 2017). AMPK is an important energy receptor in cells that regulates and maintains energy homeostasis. Activated AMPK rapidly inactivates the fatty acid synthesis rate-limiting enzyme, ACC, thereby inhibiting lipid synthesis and reducing energy consumption (Lu et al., 2018). We found that Fra-1 promoted the expression of LKB1 and p-AMPK, which in turn reduced the expression of ACC.

We next wanted to explore the effect of Fra-1 overexpression on the Warburg effect. The Warburg effect indicates that during glycolysis, glycolysis is enhanced in tumor cells and the expression of metabolic enzymes and intermediates is increased. We found Fra-1 overexpression down-regulated glycolytic rate-limiting enzymes PFK1, PKM2, and HK II as well as the expression of important glycolytic enzymes GLUT1, LDHA, and pyruvate dehydrogenase kinase. Additionally, Fra-1 overexpression led to decreased glucose and lactate concentrations in cervical cancer cells. The Warburg effect also increases glutamine and lipid metabolism, and our results showed that Fra-1 overexpression decreased the glutamine concentration as well as the expression of GDH in cervical cancer cells. In conclusion, in the present study, Fra-1 repaired mitochondrial metabolism in cervical cancer cells, but inhibited the Warburg effect and lipid metabolism.

Signal transducer and activator of transcription 1 is an important transcription factor that has repeatedly been shown to be a tumor suppressor. STAT1 inhibits cell proliferation through immune regulation and other mechanisms (Zhang et al., 2017). Changes in the expression level of STAT1 can alter the proliferation of HeLa cell (Lei et al., 2015). We found that Fra-1 overexpression in cervical cancer cells caused very significant changes in STAT1 expression at both the protein and mRNA levels. Therefore, we explored whether the transcription factor STAT1 is involved in the effects of Fra-1 in cervical cancer cells. We found that after silencing of STAT1, the tumor suppression effect of Fra-1 overexpression disappeared through a series of *in vivo* and *in vitro* experiments. Silencing of STAT1 restored the proliferation of cervical cancer cells and the growth of xenograft tumors to some extent. The expression levels of some important molecules in the p53 signaling pathway also were altered by STAT1 silencing in Fra-1–overexpressing HeLa cells. We also investigated the effects of STAT1 on metabolic reprogramming of cervical cancer cells overexpressing Fra-1. Our results revealed that STAT1 silencing recovered the ROS level in Fra-1–overexpressing cervical cancer cells and reduced the NAD^+/NADH ratio, which increased the metabolic instability of the cervical cancer cells. Additionally, STAT1 silencing up-regulated the expression of glycolysis enzymes PFK1, PKM2, HK II, GLUT1, and LDHA as well as increased the concentrations of glycolysis products glucose and lactate. After silencing of STAT1, the expression levels of SIRT3, LKB1 and p-AMPK also were reduced. The decrease of p-AMPK expression can increase the expression of the rate-limiting enzyme ACC in fatty acid synthesis, and this was observed in our experiment. In conclusion, silencing of STAT1 caused metabolic imbalance and recovered the Warburg effect in Fra-1–overexpressing cervical cancer cells.

In summary, our results showed that Fra-1 overexpression in cervical cancer cells inhibited cell growth and repaired metabolic dysfunction, including the Warburg effect and fatty acid metabolism, via STAT1 regulation of p53 signaling.

DATA AVAILABILITY STATEMENT

The original contributions presented in the study are included in the article/supplementary material, further inquiries can be directed to the corresponding authors.

ETHICS STATEMENT

The animal study was reviewed and approved by the Committee of the Use of Live Animals in Teaching and Research at the Central South University.

AUTHOR CONTRIBUTIONS

YZ and SX conceived and supervised the study. MZ completed the main experiments of cell proliferation, ROS, lactic acid detection and cervical cancer tumor growth *in vivo*. LL performed the experiments of NAD^+/NADH, cell cycle, and cell apoptosis. JH and MG performed the experiments of western blot. ZH performed the experiments of JC-1 and Intracellular Ca^{2+} concentration assay. CY and XJ performed the experiments of siRNAs and measurement of glucose concentration and analyzed data. MZ wrote the manuscript. YZ made manuscript revisions. All authors reviewed the manuscript.

FUNDING

This work was supported by the National Natural Science Foundation of China (grant no. 81272975), the Science and Technology Foundation Survey Project of Ministry of Science and Technology of China (grant nos. 2018FY100900 and 2018FY10090004), and the Fundamental Research Funds for the Central Universities of Central South University (grant no. 2019zzts731).

REFERENCES

Ah-Koon, L., Lesage, D., Lemadre, E., Souissi, I., Fagard, R., Varin-Blank, N., et al. (2016). Cellular response to alkylating agent MNNG is impaired in STAT1-deficients cells. *J. Cell Mol. Med.* 20, 1956–1965. doi: 10.1111/jcmm.12887

Allison, K. E., Coomber, B. L., and Bridle, B. W. (2017). Metabolic reprogramming in the tumour microenvironment: a hallmark shared by cancer cells and T lymphocytes. *Immunology* 152, 175–184. doi: 10.1111/imm.12777

Annis, M. G., Ouellet, V., Rennhack, J. P., L'Esperance, S., Rancourt, C., Mes-Masson, A. M., et al. (2018). Integrin-uPAR signaling leads to FRA-1 phosphorylation and enhanced breast cancer invasion. *Breast Cancer Res.* 20:9. doi: 10.1186/s13058-018-0936-938

Arfaoui, A., El Hadrami, A., and Daayf, F. (2018). Pre-treatment of soybean plants with calcium stimulates ROS responses and mitigates infection by *Sclerotinia sclerotiorum*. *Plant Physiol. Biochem.* 122, 121–128. doi: 10.1016/j.plaphy.2017.11.014

Belguise, K., Cherradi, S., Sarr, A., Boissière, F., Boulle, N., Simony-Lafontaine, J., et al. (2017). PKCθ-induced phosphorylations control the ability of Fra-1 to stimulate gene expression and cancer cell migration. *Cancer Lett.* 385, 97–107. doi: 10.1016/j.canlet.2016.10.038

Blackmore, K., Zhou, W., and Dailey, M. J. (2017). LKB1-AMPK modulates nutrient-induced changes in the mode of division of intestinal epithelial crypt cells in mice. *Exp. Biol. Med.* 242, 1490–1498. doi: 10.1177/1535370217724427

Cao, L., Li, X., Zhang, Y., Li, X., and Wang, Q. (2010). Clinical features and prognosis of cervical cancer in young women. *Zhong Nan Da Xue Xue Bao Yi Xue Ban* 35, 875–878. doi: 10.3969/j.issn.1672-7347.2010.08.017

Chen, Y., Fang, L., Zhang, J., Li, G., Ma, M., Li, C., et al. (2017). Blockage of Glyoxalase I inhibits colorectal Tumorigenesis and tumor growth via upregulation of STAT1, p53, and Bax and downregulation of c-Myc and Bcl-2. *Int. J. Mol. Sci.* 18:570. doi: 10.3390/ijms18030570

Farazi, P. A., Siahpush, M., Michaud, T. L., Kim, J., and Muchena, C. (2019). Awareness of HPV and cervical cancer prevention among university health sciences students in cyprus. *J. Cancer Educ.* 34, 685–690. doi: 10.1007/s13187-018-1356-1352

Gu, C., Chen, W. T., Zhang, Q., Chow, K. M., Wu, J., Tao, L., et al. (2017). Exploring chinese Women's perception of cervical cancer risk as it impacts screening behavior: a qualitative study. *Cancer Nurs.* 40, E17–E25. doi: 10.1097/NCC.0000000000000400

Hawley, S. A., Ford, R. J., Smith, B. K., Gowans, G. J., Mancini, S. J., Pitt, R. D., et al. (2016). The Na+/glucose cotransporter inhibitor canagliflozin activates ampk by inhibiting mitochondrial function and increasing cellular AMP levels. *Diabetes Metab. Res. Rev.* 65, 2784–2794. doi: 10.2337/db16-0058

He, J., Zhu, G., Gao, L., Chen, P., Long, Y., Liao, S., et al. (2015). Fra-1 is upregulated in gastric cancer tissues and affects the PI3K/Akt and p53 signaling pathway in gastric cancer. *Int. J. Oncol.* 47, 1725–1734. doi: 10.3892/ijo.2015.3146

He, W., Wu, Y., Tang, X., Xia, Y., He, G., Min, Z., et al. (2016). HDAC inhibitors suppress c-Jun/Fra-1-mediated proliferation through transcriptionally downregulating MKK7 and Raf1 in neuroblastoma cells. *Oncotarget* 7, 6727–6747. doi: 10.18632/oncotarget.6797

Josahkian, J. A., Saggioro, F. P., Vidotto, T., Ventura, H. T., Candido Dos Reis, F. J., de Sousa, C. B., et al. (2018). Increased STAT1 expression in high grade serous ovarian cancer is associated with a better outcome. *Int. J. Gynecol. Cancer* 28, 459–465. doi: 10.1097/IGC.0000000000001193

Kaliff, M., Sorbe, B., Mordhorst, L. B., Helenius, G., Karlsson, M. G., and Lillsunde-Larsson, G. (2018). Findings of multiple HPV genotypes in cervical carcinoma are associated with poor cancer-specific survival in a Swedish cohort of cervical cancer primarily treated with radiotherapy. *Oncotarget* 9, 18786–18796. doi: 10.18632/oncotarget

Karim, S., Souho, T., Benlemlih, M., and Bennani, B. (2018). Cervical cancer induction enhancement potential of chlamydia trachomatis: a systematic review. *Curr. Microbiol.* 75, 1667–1674. doi: 10.1007/s00284-018-1439-1437

Kehrmann, A., Truong, H., Repenning, A., Boger, R., Klein-Hitpass, L., Pascheberg, U., et al. (2013). Complementation of non-tumorigenicity of HPV18-positive cervical carcinoma cells involves differential mRNA expression of cellular genes including potential tumor suppressor genes on chromosome 11q13. *Cancer Genet.* 206, 279–292. doi: 10.1016/j.cancergen.2013

Lavie, J., De Belvalet, H., Sonon, S., Ion, A. M., Dumon, E., Melser, S., et al. (2018). Ubiquitin-dependent degradation of mitochondrial proteins regulates energy metabolism. *Cell Rep.* 23, 2852–2863. doi: 10.1016/j.celrep.2018.05.013

Lei, R. L., Xiao, S. S., and Xue, M. (2015). Cisplatin inhibits proliferation of cervical carcinoma cell line by up-regulating Stat1 expression. *Nan Fang Yi Ke Da Xue Xue Bao* 35, 88–92.

Li, N., Huang, D., Lu, N., and Luo, L. (2015). Role of the LKB1/AMPK pathway in tumor invasion and metastasis of cancer cells (Review). *Oncol. Rep.* 34, 2821–2826. doi: 10.3892/or.2015.4288

Li, X., Han, G., Li, X., Kan, Q., Fan, Z., Li, Y., et al. (2017). Mitochondrial pyruvate carrier function determines cell stemness and metabolic reprogramming in cancer cells. *Oncotarget* 8, 46363–46380. doi: 10.18632/oncotarget.18199

Liou, Y. L., Zhang, T. L., Yan, T., Yeh, C. T., Kang, Y. N., Cao, L., et al. (2016). Combined clinical and genetic testing algorithm for cervical cancer diagnosis. *Clin. Epigenet.* 10:66. doi: 10.1186/s13148-016-0232-3

Liu, P., Wei, Z., He, X., Yu, J., Tian, X., and Chang, J. (2015). Genetic association between CD95 rs2234767 polymorphism and cervical cancer risk: a meta analysis. *Int. J. Clin. Exp. Med.* 8, 2357–2363.

Lu, Y., Yao, J., Gong, C., Wang, B., Zhou, P., Zhou, S., et al. (2018). Gentiopicroside ameliorates diabetic peripheral neuropathy by modulating PPAR- Γ/AMPK/ACC signaling pathway. *Cell Physiol. Biochem.* 50, 585–596. doi: 10.1159/000494174

Luo, Y. P., Zhou, H., Krueger, J., Kaplan, C., Liao, D., Markowitz, D., et al. (2010). The role of proto-oncogene Fra-1 in remodeling the tumor microenvironment in support of breast tumor cell invasion and progression. *Oncogene* 29, 662–673. doi: 10.1038/onc.2009.308

McDermott, U., Longley, D. B., Galligan, L., Allen, W., Wilson, T., and Johnston, P. G. (2005). Effect of p53 status and STAT1 on chemotherapy-induced, Fas-mediated apoptosis in colorectal cancer. *Cancer Res.* 65, 8951–8960. doi: 10.1158/0008-5472.CAN-05-0961

Mills, E. L., and O'Neill, L. A. (2016). Reprogramming mitochondrial metabolism in macrophages as an anti-inflammatory signal. *Eur. J. Immunol.* 46, 13–21. doi: 10.1002/eji.201445427

Mirbahari, S. G., and Sadeghi, M. (2018). The prevalence of genus Alpha human *Papillomavirus* in women with uterine cervical infection and/or inflammation in Western Iran. *Mater. Sociomed.* 30, 113–117. doi: 10.5455/msm.2018.30.113-117

Nagao, A., Kobayashi, M., Koyasu, S., Chow, C. C. T., and Harada, H. (2019). HIF-1-dependent reprogramming of glucose metabolic pathway of cancer cells and its therapeutic significance. *Int. J. Mol. Sci.* 20:238. doi: 10.3390/ijms20020238

Oliveira-Ferrer, L., Kürschner, M., Labitzky, V., Wicklein, D., Müller, V., Lüers, G., et al. (2015). Prognostic impact of transcription factor Fra-1 in ER-positive breast cancer: contribution to a metastatic phenotype through modulation of tumor cell adhesive properties. *J. Cancer Res. Clin. Oncol.* 141, 1715–1726. doi: 10.1007/s00432-015-1925-2

Pillai, V. B., Sundaresan, N. R., Kim, G., Gupta, M., Rajamohan, S. B., Pillai, J. B., et al. (2010). Exogenous NAD blocks cardiac hypertrophic response via activation of the SIRT3-LKB1-AMP-activated kinase pathway. *J. Biol. Chem.* 285, 3133–3144. doi: 10.1074/jbc.M109.077271

Qu, S., Guo, Y., Huang, S. T., and Zhu, X. D. (2017). Inhibition of STAT1 sensitizes radioresistant nasopharyngeal carcinoma cell line CNE-2R to radiotherapy. *Oncotarget* 9, 8303–8310. doi: 10.18632/oncotarget.19690

Ramdass, B., Chowdhari, A., and Koka, P. (2013). Cancer-initiating cells as target for prevention of recurring disease etiology: role of these malignant putative progenitor cells in relapse or metastasis of human cervical carcinoma. *J. Stem Cells* 8, 233–251.

Schwarz, T. F., Spaczynski, M., Schneider, A., Wysocki, J., Galaj, A., Perona, P., et al. (2009). Immunogenicity and tolerability of an HPV-16/18 AS04-adjuvanted prophylactic cervical cancer vaccine in women aged 15-55 years. *Vaccine* 27, 581–587. doi: 10.1016/j.vaccine.2008.10.088

So, K. A., Lee, I. H., Kim, T. J., and Lee, K. H. (2019). Risk factors of persistent HPV infection after treatment for high-grade squamous intraepithelial lesion. *Arch. Gynecol. Obstet.* 299, 223–227. doi: 10.1007/s00404-018-4936-4939

Suyama, K., Onishi, H., Imaizumi, A., Shinkai, K., Umebayashi, M., Kubo, M., et al. (2016). CD24 suppresses malignant phenotype by downregulation of SHH

transcription through STAT1 inhibition in breast cancer cells. *Cancer Lett.* 374, 44–53. doi: 10.1016/j.canlet.2015.12.013

Tolza, C., Bejjani, F., Evanno, E., Mahfoud, S., Moquet-Torcy, G., Gostan, T., et al. (2019). AP-1 signaling by Fra-1 directly regulates HMGA1 oncogene transcription in triple-negative breast cancers. *Mol. Cancer Res.* 17, 1999–2014. doi: 10.1158/1541-7786.MCR-19-0036

Vasileiou, P. V. S., Evangelou, K., Vlasis, K., Fildisis, G., Panayiotidis, M. I., Chronopoulos, E., et al. (2019). Mitochondrial homeostasis and cellular senescence. *Cells* 8:686. doi: 10.3390/cells8070686

Vu, L. T. H., Tran, H. T. D., Nguyen, B. T., Bui, H. T. T., Nguyen, A. D., and Pham, N. B. (2018). Community-based screening for cervical cancer using visual inspection with acetic acid: results and lessons learned from a pilot study in vietnam. *J. Public Health Manag. Pract.* 24(Suppl. 2), S3–S8. doi: 10.1097/PHH.0000000000000709

Wang, X., Guo, R., Lv, Y., and Fu, R. (2018). The regulatory role of Fos related antigen-1 in inflammatory bowel disease. *Mol. Med. Rep.* 17, 1979–1985. doi: 10.3892/mmr.2017.8071

Xiao, S., Zhou, Y., Yi, W., Luo, G., Jiang, B., Tian, Q., et al. (2015). Fra-1 is downregulated in cervical cancer tissues and promotes cervical cancer cell apoptosis by p53 signaling pathway in vitro. *Int. J. Oncol.* 46, 1677–1684. doi: 10.3892/ijo.2015.2873

Xu, X., Jiang, R., Gong, P., Liu, Q., Chen, Y., Hou, S., et al. (2018). Up-regulation of FOS-like antigen 1 contributes to neuronal apoptosis in the cortex of rat following traumatic brain injury. *Metab. Brain Dis.* 33, 115–125. doi: 10.1007/s11011-017-0129-7

Yamato, M., Kawano, K., Yamanaka, Y., Saiga, M., and Yamada, K. (2016). TEMPOL increases NAD(+) and improves redox imbalance in obese mice. *Redox Biol.* 8, 316–322. doi: 10.1016/j.redox.2016.02.007

Zhang, X., Li, X., Tan, F., Yu, N., and Pei, H. (2017). STAT1 inhibits MiR-181a expression to suppress colorectal cancer cell proliferation through PTEN/Akt. *J. Cell. Biochem.* 118, 3435–3443. doi: 10.1002/jcb.26000

Zhang, Y., Chen, Y., Liu, Z., and Lai, R. (2018). ERK is a negative feedback regulator for IFN-γ/STAT1 signaling by promoting STAT1 ubiquitination. *BMC Cancer* 18:613. doi: 10.1186/s12885-018-4539-4537

Zhou, Y., Chung, A. C. K., Fan, R., Lee, H. M., Xu, G., Tomlinson, B., et al. (2017). Sirt3 deficiency increased the vulnerability of pancreatic beta cells to oxidative stress-induced dysfunction. *Antioxid. Redox Signal.* 27, 962–976. doi: 10.1089/ars.2016.6859

Conflict of Interest: The authors declare that the research was conducted in the absence of any commercial or financial relationships that could be construed as a potential conflict of interest.

frontiers in Cell and Developmental Biology

REVIEW
published: 26 March 2021
doi: 10.3389/fcell.2021.651317

The Roles of 2-Hydroxyglutarate

Xin Du[1,2] *and Hai Hu*[1,2]*

[1] Guangdong Provincial Key Laboratory of Malignant Tumor Epigenetics and Gene Regulation, Sun Yat-sen Memorial Hospital, Sun Yat-sen University, Guangzhou, China, [2] Department of Oncology, Sun Yat-sen Memorial Hospital, Sun Yat-sen University, Guangzhou, China

2-Hydroxyglutarate (2-HG) is structurally similar to α-ketoglutarate (α-KG), which is an intermediate product of the tricarboxylic acid (TCA) cycle; it can be generated by reducing the ketone group of α-KG to a hydroxyl group. The significant role that 2-HG plays has been certified in the pathophysiology of 2-hydroxyglutaric aciduria (2HGA), tumors harboring mutant isocitrate dehydrogenase 1/2 (IDH1/2mt), and in clear cell renal cell carcinoma (ccRCC). It is taken as an oncometabolite, raising much attention on its oncogenic mechanism. In recent years, 2-HG has been verified to accumulate in the context of hypoxia or acidic pH, and there are also researches confirming the vital role that 2-HG plays in the fate decision of immune cells. Therefore, 2-HG not only participates in tumorigenesis. This text will also summarize 2-HG's identities besides being an oncometabolite and will discuss their enlightenment for future research and clinical treatment.

Keywords: 2-Hydroxyglutarate, epigenetics, metabolism, immunology, isocitrate dehydrogenase

OPEN ACCESS

Edited by:
Huafeng Zhang,
University of Science and Technology of China, China

Reviewed by:
Hongming Miao,
Army Medical University, China
Changliang Shan,
Nankai University, China

***Correspondence:**
Hai Hu
huhai@mail.sysu.edu.cn

Specialty section:
This article was submitted to Molecular and Cellular Oncology, a section of the journal Frontiers in Cell and Developmental Biology

Received: *09 January 2021*
Accepted: *16 February 2021*
Published: *26 March 2021*

Citation:
Du X and Hu H (2021) The Roles of 2-Hydroxyglutarate. Front. Cell Dev. Biol. 9:651317. doi: 10.3389/fcell.2021.651317

INTRODUCTION

2-Hydroxyglutarate (2-HG) is structurally similar to α-ketoglutarate (α-KG), which is an intermediate of the tricarboxylic acid (TCA) cycle; it can be generated by reducing the ketone group of α-KG to a hydroxyl group. With its C-2 being a chiral carbon, it has two enantiomers: L-2HG and D-2HG. Besides the well-known IDH1/2mt, which acquires a neomorphic catalytic activity that reduces α-KG to the D enantiomer of 2-HG (Dang et al., 2010; Ward et al., 2010), 2-HG also derives from the "promiscuity" of some enzymes (**Figure 1**); it means that apart from their primary reaction, these enzymes can catalyze an "unwanted" reaction at a low rate. For example, besides the conversion between malate and oxaloacetate, malate dehydrogenase (MDH) also reduces α-KG to L-2HG, although the catalytic efficiency is 10^7–10^8-folds lower than its primary reaction (Rzem et al., 2007). Lactate dehydrogenase (LDH) A (LDHA) (Intlekofer et al., 2017) and SerA (Zhao and Winkler, 1996), the *Escherichia coli* homolog of PHGDH, was also reported to synthesize L-2HG. As for D-2HG, PHGDH also owns the property of producing D-2HG from α-KG (Fan et al., 2015). IDH2 catalyzes the reductive carboxylation of glutamine-derived α-KG, producing citrate and NADPH (Wise et al., 2011); this process is accompanied by an accumulation of D-2HG, although whether D-2HG derives from the catalysis of IDH2 directly remains uncharted. In respect of the clearance of 2-HG, the two enantiomers are removed by L2HGDH (Rzem et al., 2004) and D2HGDH (Achouri et al., 2004) in the mitochondria. Both enzymes utilize FAD as an electron acceptor to execute the oxidation of 2-HG, thereby generating α-KG and FADH2.

2-Hydroxyglutarate did not draw much attention after being identified; this continued until the discovery of 2-hydroxyglutaric aciduria (2-HGA) (Ye et al., 2018). 2-HGA is a rare disease

characterized by an accumulation of 2-HG in body fluids; its clinical manifestations encompass a series of psychiatric and neurological symptoms such as epilepsy, and signs like hypotonia, macrocephaly, and extrapyramidal symptoms, along with neuroimaging changes (Kranendijk et al., 2012; Rodrigues et al., 2017). By which enantiomer accumulates in the body fluids, it can be classified into D-2HGA, L-2HGA, and "combined D,L-2-hydroxyglutaric aciduria" (D,L-2HGA) (Kranendijk et al., 2012). L-2HGA and the type I D-2HGA are derived from a mutation of L2HGDH and D2HGDH, respectively (Rzem et al., 2004; Struys et al., 2005); the etiology of the type II D-2HGA is the gain-of-function mutation of IDH2 (Kranendijk et al., 2010), and that of the D,L-2-HGA is the mutation of SLC25A1, which acts as a mitochondrial citrate carrier (Nota et al., 2013). The neurotoxic effect of 2-HG forms the pathophysiological basis of 2-HGA, since the accumulation of both enantiomers leads to impaired creatine kinase activity, induced oxidative stress, and a higher glutamate uptake into synaptosomes and synaptic vesicles (Junqueira et al., 2003, 2004; Kranendijk et al., 2012).

Although 2-HGA brought 2-HG to the attention of researchers, it was its identity as an "oncometabolite" made it famous. Two genomic sequencing studies published in 2008 and 2009 discovered the high mutation rate of IDH1 in glioblastoma and acute myeloid leukemia (AML), respectively (Parsons et al., 2008; Mardis et al., 2009). A series of researches after then demonstrated the existence of IDH1/2mt in 70–80% of grade II/III glioma and secondary glioblastoma, and also in about 20% of AML (Yan et al., 2009; Medeiros et al., 2017). Besides that, IDH1/2 mutation also consists in chondrosarcoma, osteosarcoma, cholangiocarcinoma, and prostate cancer (Gagné et al., 2017). These mutations mainly take place at the R132 of IDH1 and R172 of IDH2 (Ye et al., 2018). To date, D-2HG has been supposed to trigger oncogenesis by altering the methylation pattern of DNA and histone, expression and activity of DNA repair proteins, collagen maturation, and immune response (Gagné et al., 2017; Reiter-Brennan et al., 2018), although increasing attention is being paid to its antitumor effect (Fu et al., 2015; Su et al., 2018).

As for the other enantiomers, L-2HG, its accumulation has been reported in clear cell renal cell carcinoma (ccRCC), which resulted from the copy number loss of L2HGDH (Shelar et al., 2018). Increased L-2HG in ccRCC suppresses the methylcytosine dioxygenase (TET) and KDM6A, leading to hypermethylation of DNA and histone. On the other hand, overexpression of L2HGDH is issued in a lower L-2HG level and restored the altered epigenetic state, thus hindering the growth of ccRCC. Therefore, L-2HG is also regarded as an oncometabolite (Shim et al., 2014; Shelar et al., 2018).

2-Hydroxyglutarate is famous for its involvement in tumorigenesis; however, this just represents for its pathological effect. Then, does 2-HG function in other contexts? It is reported that L-2HG accumulates in hypoxia or acidic pH (Harris, 2015; Oldham et al., 2015; Nadtochiy et al., 2016); there are also researches confirming the significant role that 2-HG plays in the fate decision of immune cells (Tyrakis et al., 2016; Sun et al., 2020). It seems that 2-HG has physiological roles that extend beyond its being an oncometabolite; therefore, this text will also summarize 2-HG's identities besides its being an oncometabolite and discuss their enlightenment for future research and clinical treatment.

THE TUMORIGENIC EFFECT OF 2-HYDROXYGLUTARATE

The Oncometabolite 2-Hydroxyglutarate Inhibits α-Ketoglutarate-Dependent Dioxygenases

Transformation by IDHmt has been demonstrated in numerous researches. It was revealed that the mutation of IDH occurred earlier than the mutation of *TP53* or the loss of 1p/19q (Watanabe et al., 2009). It can also happen in the early stage of AML and be detected in a population of pre-leukemic stem cells in some patients. These facts suggest that IDH mutation represents an early event in gliomagenesis and leukemogenesis (Langemeijer et al., 2009; Corces-Zimmerman et al., 2014; Shlush et al., 2014). Introducing IDH1 R132H facilitated anchorage-independent growth of astrocytes lacking *CDKN2A*, *ATRX*, and *PTEN* (Modrek et al., 2017; Mukherjee et al., 2018; Philip et al., 2018), and the expression of IDH1/2 mutant impaired hepatocyte differentiation (Saha et al., 2014). Though it seems that IDHmt alone is not sufficient to induce tumorigenesis *in vivo* (Chaturvedi et al., 2013; Bardella et al., 2016; Philip et al., 2018), it cooperates with other oncogenes or deficiency of tumor suppressors to trigger tumorigenesis (Chaturvedi et al., 2013; Chen et al., 2013; Bardella et al., 2016; Philip et al., 2018). Discovering the neomorphic activity of IDHmt did shed light on the tumorigenic effects that IDHmt imposes. These mutations in the active site of IDH disturb the interaction between its binding pocket and the β-carboxyl of isocitrate (Dang et al., 2010; Ward et al., 2010). It was reported that IDH1 R132 substitution altered the spatial position of Y139, and then the hydroxyl moiety of Y139 occupied the space of isocitrate (Dang et al., 2010) and led to a closed conformation, thus favoring the binding of NADPH and the subsequent reduction of α-KG (Dang et al., 2010). IDH normally functions as a homodimer; the WT:MT heterodimer significantly decreases its catalytic ability compared with the WT:WT homodimer, because the two subunits alter their conformation in a co-operative way. The disability in interacting with isocitrate of the mutant subunit could impede the conformation change of the wild-type (WT) one (Zhao et al., 2009).

Elevation of L-2HG is observed in ccRCC; it takes glutamine as predominant carbon source and is generated by the promiscuous activity of MDH. L-2HG is removed by L2HGDH under physiological conditions, but a large portion of ccRCC (∼40%) undergo loss of heterozygosity (LOH) of 14q where *L2HGDH* locates in. What is more, proliferator-activated receptor gamma co-activator 1-alpha (PGC-1α), the transcription factor regulating L2HGDH expression, is usually downregulated in renal tumor cells (Brinkley et al., 2020). All of these results in L2HGDH downregulation and the subsequent accumulation of L-2HG. L2HGDH knockdown promoted malignant phenotypes,

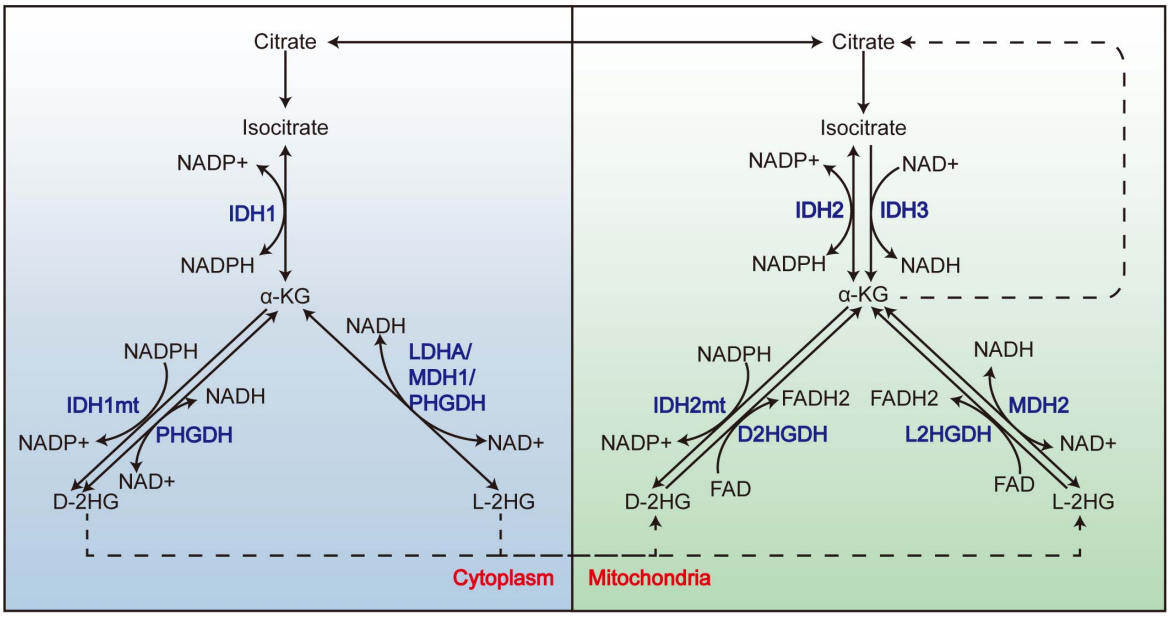

FIGURE 1 | The promiscuity of LDHA, MDH, and PHGDH and the metabolism of 2-HG. 2-HG derives from the promiscuity of LDHA, MDH1, and PHGDH in the cytoplasm and MDH2 in the mitochondria. Mutations of IDH1 and IDH2 endow them the neomorphic enzyme activity to convert α-KG to D-2HG. L-2HG and D-2HG are removed by L2HGDH and D2HGDH from the mitochondria, respectively. LDHA, lactate dehydrogenase A; MDH, malate dehydrogenase; 2-HG, 2-hydroxyglutarate.

while its expression did the opposite; moreover, its under-expression is associated with poor prognosis (Shelar et al., 2018; Shenoy et al., 2019). Therefore, L2HGDH acts a tumor suppressor in ccRCC, and the accumulated L-2HG is thought to be an oncometabolite.

Both enantiomers of 2-HG were found to inhibit α-KG-dependent dioxygenases including TET2 and Jumonji-C (JmjC) histone demethylases by completely interacting with the α-KG-binding site (Chowdhury et al., 2011; Xu et al., 2011). These oxidases vary in their sensitivity to 2-HG; for example, the IC50 of histone demethylase JMJD2C to D-2HG is 79 ± 7 μM, while the value of hypoxia-inducible factor (HIF) is 1,500 ± 400 μM (Chowdhury et al., 2011). L-2HG is significantly more potent in inhibiting these enzymes than D-2HG (Chowdhury et al., 2011; Koivunen et al., 2012). For a clear inhibition on dioxygenases, a 100-fold molar excess of 2-HG over α-KG is required (Chowdhury et al., 2011); these facts suggest that D-2HG functions as a weak antagonist of α-KG. Under physiological conditions, the level of D-2HG is too low to significantly inhibit these enzymes. When IDH is mutant, α-KG is consumed to generate a concentration as high as 3–35 mM of D-2HG (Dang et al., 2010), which far exceeds the IC50 of these α-KG-dependent dioxygenases; this provides clues to detect the mechanism of the tumorigenic effect of D-2HG, and similarly of L-2HG.

2-Hydroxyglutarate and DNA Methylation

Profiling promoter methylation of the glioblastoma samples in The Cancer Genome Atlas (TCGA) identified a distinct subset with a hypermethylated phenotype, named glioma-CpG island methylator phenotype (G-CIMP). This phenotype exhibited a tight association with IDH1 mutation (Noushmehr et al., 2010). A similar phenomenon was also discovered in AML patients, and the IDH1/2 mutation exhibited an enrichment in patients with intermediate-risk cytogenetics (Figueroa et al., 2010). Subsequently, it was uncovered that the expression of IDH1mt could mirror the G-CIMP in low-grade glioma (Turcan et al., 2012), and IDH1/2mt was found to increase the global level of 5-mC (Figueroa et al., 2010). The mutation of IDH1 and IDH2 is mutually exclusive with each other (Figueroa et al., 2010), suggesting that they transform cells in a similar way; consistent with that, the methylation change is similar between IDH1mt and IDH2mt AML samples (Figueroa et al., 2010). These facts indicate that IDH mutation defines a specific epigenome and clinical features. According to this, the 2016 WHO brain tumor classification classified (anaplastic) astrocytoma based on the existence of IDH mutation, and the diagnosis of (anaplastic) oligodendroglioma requires coexistence of IDH mutation and 1p/19q co-deletion (Preusser and Marosi, 2017).

Now that IDH1/2 acquires a neomorphic enzyme activity of converting α-KG to 2-HG, D-2HG may play a vital role in the transformation by IDHmt. Indeed, D-2HG treatment recapitulated IDH1-induced differentiation block and cytokine-independence in hematopoietic cells (Losman et al., 2013). Similarly, D-2HG supplement promoted anchorage-independent growth in glioma cells (Philip et al., 2018). To investigate the tumorigenic mechanism of D-2HG and considering that D-2HG inhibits α-KG-dependent dioxygenases, a group transfected TF-1 human erythroleukemia cell line with a pool of shRNA targeting these enzymes. A relative enrichment of shRNAs targeting TET2 but not its paralog TET1 was detected after a period

of culturing; TET2 knockdown recapitulated the transforming effect of IDH1mt and D-2HG in TF-1 cells, indicating that TET2 may mediate transformation induced by IDH1mt and D-2HG (Losman et al., 2013). Its activity converting 5mC to 5-hydroxymethylcytosine accounts for the association between IDHmt and a hypermethylated genome observed in AML and glioma samples. The co-expression of IDH1/2mt and the catalytic domain of TET1 or TET2 decrease 5-hmC to a nearly undetectable level, suggesting that IDHmt caused abnormal DNA methylation by inhibiting TETs (Xu et al., 2011). What is more, TET2 mutation is frequently observed in myeloid cancers, in about 24% of secondary AML and 22% of chronic myelomonocytic leukemia, while it is mutually exclusive with mutation in IDH (Delhommeau et al., 2009; Figueroa et al., 2010). In another study, hypermethylation of TET2 promoter was observed in a small fraction (16%) of low-grade diffuse gliomas without IDH mutation, but this phenomenon did not occur in gliomas with IDH mutation. The deficiency of TET2 induced a similar methylome with that IDHmt does in glioma (Figueroa et al., 2010). These facts all suggest that TET2 deficiency mediates the tumorigenic effects of mutant IDH and D-2HG. The abnormal *de novo* DNA methylation plays a vital role in tumorigenesis, repressing genes that are indispensable for differentiation (Klutstein et al., 2016). The infection of mutant IDH enriched 5-mC at the promoter of differentiation-associated genes and induced genes associated with stem cell (Figueroa et al., 2010; Turcan et al., 2012). Other modules can also be affected by the anomalous methylation; the hypermethylation of CTCF-binding sites comprises its binding with the insulator protein CTCF in glioma, permitting an enhancer to interact with *PDGFRA*, which is a glioma oncogene (Flavahan et al., 2016) and blocking differentiation by disassociating SOX2 from putative enhancers (Modrek et al., 2017). In conclusion, aberrant DNA methylation mediated the oncogenic effect of IDHmt and D-2HG.

L-2HG is a bona fide oncometabolite; its supplement promotes ccRCC cell line migration (Shelar et al., 2018). Both increased L-2HG and L2HGDH knockdown led to diminished 5-hmC level, which is strongly associated with tumor aggressiveness and an unfavorable prognosis, and restoring the activity of TET2 leads to inhibition of ccRCC growth both *in vitro* and *in vivo* (Shim et al., 2014; Shenoy et al., 2019). Therefore, the inhibition of L-2HG on TETs and the subsequent altered DNA methylation may mediate its oncogenic effect. It was reported that L-2HG upregulated PHLDB2 to promote vasculogenic mimicry (VM) in renal cancer cell lines in a way associated with DNA methylation; the DNA methyltransferase inhibitor counteracted with L-2HG in regulating PHLDB2 (Wang et al., 2020). Although its association with DNA methylation is well established, little is known about how L-2HG-induced DNA hypermethylation triggers tumorigenesis, so further investigation is required.

2-Hydroxyglutarate and Histone Methylation

The Jmjc histone demethylase is another member of the α-KG-dependent dioxygenase (Chowdhury et al., 2011), and it is sensitive to the perturbation of 2-HG. As reported, the mutant IDH2 or its product D-2HG compromised MyoD-driven differentiation in fibroblast cell line. Mechanistically, D-2HG induced H3K9me3 at those MyoD-binding loci, decreasing their accessibility to MyoD (Schvartzman et al., 2019). Likewise, IDH2mt expression or D-2HG treatment block adipocyte differentiation; this is correlated with an enrichment of the repressive mark H3K9me3 at some lineage-specific gene (Lu et al., 2012). Consistently, the expression of KDM4C, the demethylase for H3K9me3, is required during the differentiation of adipocyte. And it is interesting that observable changes in histone methylation preceded DNA methylation in the IDH1mt-expressing adipocyte. In another study, IDHmt inhibitor induced histone demethylation that predated DNA demethylation (Kernytsky et al., 2015). The above cases indicate that the methylation of histone is more sensitive to that of DNA in the face of D-2HG and acts as an independent factor in transformation. In line with this, inhibitors targeting IDH mutant induced differentiation by reversing the abnormal histone methylation at some genes, which are implicated in differentiation (Rohle et al., 2013; Kernytsky et al., 2015; Nakagawa et al., 2019).

As reported, L2HGDH overexpress decreased H3K27me3 and H3K9me3 in RCC cell line (Shim et al., 2014). Comparing the transcriptome of A498 RCC cell line overexpressing L2HGDH with the control group revealed that the upregulated genes showed an enrichment for the targets of polycomb repressor complex 2 (PRC2) and/or H3K27me3 target genes (Shelar et al., 2018). In accordance with that, the H3K27 histone demethylase KDM6A is frequently mutated in renal carcinoma (Dalgliesh et al., 2010), KDM6A knockdown recapitulates the malignant phenotypes that L-2HG induced, and PRC2 knockdown did the opposite. The above facts suggest that the L2HGDH/L2HG axis induces tumorigenesis through an aberrant histone methylation.

2-Hydroxyglutarate and Hypoxia-Inducible Factor Signaling

Hypoxia adaption is largely mediated by HIFs, which function as a heterodimer and consists of an α-subunit and a β-subunit. There are three families of HIF in human cells: HIF-1, HIF-2, and HIF-3. The α-subunit is oxygen-sensitive. In normoxia, it is hydroxylated by HIF prolyl hydroxylases (PHD/EGLN). Subsequently, the hydroxylated HIF-α is recognized by von Hippel–Lindau (VHL) E3 ligase for degradation through the proteasome pathway (Balamurugan, 2016). FIH can also hydroxylate HIF-α, resulting in its disability in interacting with transcription cofactors. In hypoxia, the activity of PHD and FIH is diminished. The stabilized HIF-α then translocated to nucleus and interact with the β-subunit, the HIF-1α/β heterodimer, and facilitates the transcription of its downstream targets (Balamurugan, 2016).

Although PHD, the enzyme hydroxylating HIF-1α, belongs to the α-KG-dependent dioxygenase family, the influence of 2-HG on HIF pathway seems debatable. In the research of Zhao et al. (2009) overexpression of IDH1mt or downregulation of the WT allele elevated the level of HIF-1α, while α-KG

supplement diminished this effect; they inferred that IDH1 or its mutant allele regulated HIF-1α by controlling the level of α-KG. Although D-2HG was not discussed in this research, it can be concluded that expression of IDHmt upregulated HIF-1α. However, Koivunen et al. (2012) discovered that IDH1mt expression reduced HIF-1α level, because D-2HG acted as a co-substrate of EGLN, and this was enantiomer-specific. EGLN1 knockdown comprised the proliferation of IDH1mt astrocyte while downregulating HIF-1α did the opposite; these results suggest that IDHmt-derived D-2HG activates EGLN1, and subsequent downregulation of HIF-1α may lead to the tumorigenesis of glioma (Koivunen et al., 2012). Consistently, bioinformatic analysis of 288 low-grade diffuse or anaplastic gliomas samples from TCGA revealed that those with IDHmt displayed a significant inhibition on hypoxia-mediated signaling (Kickingereder et al., 2015). The discrimination between the two enantiomers in inhibiting EGLN1 was also discovered in hematopoietic cells. D-2HG rather than L-2HG could recapture the transforming effect of IDHmt expression, and this is related to its discrimination in inhibiting EGLN1 (Losman et al., 2013). It seems that, in astrocytes and hematopoietic cells, HIF may act as a tumor suppressor, and the mutation of IDH inhibits HIF signaling through D-2HG and promotes oncogenesis. The mechanism of D-2HG to promote EGLN also remains controversial. Contradicting the opinion that D-2HG acts as a co-substrate to activate EGLN1, another group demonstrated that both enantiomers could be oxidized to α-KG non-enzymatically through a Fenton-type chemistry mediated by iron and other physiologically relevant reducing agents such as L-ascorbate and GSH (Tarhonskaya et al., 2014); the α-KG derived from 2-HG oxidation is at levels to support catalysis by PHD. They attributed the result that PHD2 catalysis proceeded in the presence of D-2HG rather than L-2HG in the research of Koivunen P. to the more potent inhibition of L-2HG than D-2HG and/or the contamination of D-2HG by α-KG (Tarhonskaya et al., 2014). Further researches are required to explore the conditions dictating the influence of D-2HG on PHD and the mechanisms behind it.

2-Hydroxyglutarate and Other α-Ketoglutarate-Dependent Dioxygenases

The *Escherichia coli* protein AlkB was demonstrated to be an α-KG-dependent dioxygenase; it works as a DNA repair enzyme, oxidizing the alkyl groups in cytotoxic lesions 1-methyladenine (m1A) and 3-methylcytosine (m3C) induced by alkylation agents (Trewick et al., 2002; Chen et al., 2017). Its homolog in human was identified as the ALKBH family, including ALKBH1-8 and FTO. ALKBH2 and ALKBH3 play the major role in restoring the alkylated DNA (Chen et al., 2017). L-2HG and D-2HG are found to inhibit ALKBH2/3 in a pathophysiologically relevant level (Chen et al., 2017), restraining their activity in repairing m1A and m3C in ssDNA and dsDNA. DNA repair deficiency may help to accumulate mutations in the genome, thereby contributing to tumorigenesis; this is consistent with the fact IDH mutation is an early event in gliomagenesis and leukemogenesis (Langemeijer et al., 2009; Watanabe et al., 2009; Corces-Zimmerman et al., 2014; Shlush et al., 2014) as well as the higher mutation load in IDmt LGG compared with IDHwt LGG in TCGA database (Kohanbash et al., 2017).

By utilizing a brain-specific IDHmt knockin mouse model, Sasaki et al. (2012) discovered that mice expressing IDHmt exhibited a deficiency in collagen maturation. This phenomenon was related to the inhibition of D-2HG on prolyl-4-hydroxylases I, II, and III (C-P4H I–III), and procollagen-lysine 2-oxoglutarate 5-dioxygenases 1, 2, and 3 (Plod1–3), which mediated collagen hydroxylation. As hydroxylation is necessary for collagen maturation, basement membrane aberrations and hemorrhage were induced in mice with IDHmt tumor (Sasaki et al., 2012; Pellegatta et al., 2015). Mutation of genes encoding collagen is frequent in glioblastoma (GBM); what is more, IDHmt seldom coexists with basement membrane-related gene mutations (Sasaki et al., 2012). Therefore, collagen immaturation mediated by D-2HG may be involved in GBM tumorigenesis. As reported, an accumulation of immature procollagen-IV in endoplasmic reticulum (ER) led to ER stress and autophagy of ER, inhibiting the autophagic degradation of the ER-caused apoptosis (Viswanath et al., 2018b). Therefore, the attenuated collagen maturation and its downstream effect may be druggable in the context of IDH mutation.

D-2-Hydroxyglutarate Modulates the Immune Microenvironment

D-2HG is not only a cancer cell-autonomous oncometabolite, but it also contributes to an immunosuppressive milieu by exerting on immune cells both directly and indirectly (**Figure 2**). By inhibiting the expression and activation of STAT1, D-2HG attenuates chemokine CXCL10 secretion in glioma cell lines, thereby suppressing cytotoxic T lymphocyte infiltration in the tumor site (Kohanbash et al., 2017). Extracellular D-2HG is five-folds higher than the intracellular level; therefore, it can be inferred that tumor-infiltrating lymphocytes are faced with a high concentration of D-2HG (Böttcher et al., 2018; Bunse et al., 2018). Although D-2HG is poorly cell-penetrative, the transporter SLC13A3 can import D-2HG into T lymphocyte. An excess of D-2HG in T lymphocyte suppresses ATPase, subsequently reducing ATP and attenuating PLC-γ phosphorylation, which both resulted in decreased nuclear translocation of the nuclear factor of activated T cells (NFAT), which is of much concern in T lymphocyte cell activation. Moreover, D-2HG also diminished putrescine, which stimulated T lymphocyte cell proliferation (Bunse et al., 2018; Zhang et al., 2018). Apart from chemotaxis, activation, and proliferation, T lymphocyte differentiation is no exception. D-2HG impairs Th17 polarization by destabilizing HIF-1; this is enantiomer-specific since L-2HG did not exert such effect (Böttcher et al., 2018), although IDHmt glioblastoma expresses significantly lower PD-L1 compared with IDHwt (Wang et al., 2016), and there is another research revealing that D-2HG induces transient *PD-L1* promoter hypermethylation, thus lowering the expression of PD-L1 (Rover et al., 2018). On the whole, D-2HG suppresses antitumor T cell immunity. Inspired by this, targeting the mutant IDH may synergize with

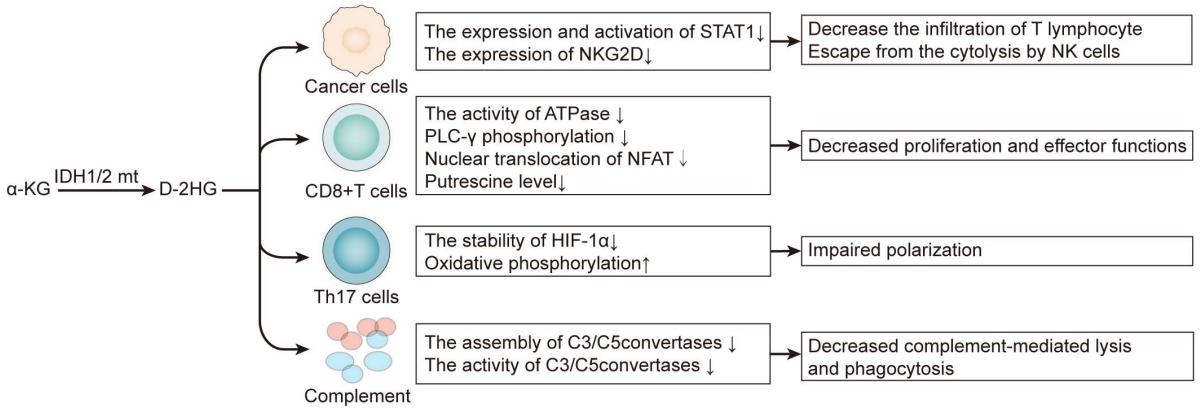

FIGURE 2 | D-2HG derived from mutant IDH is an immunosuppressive metabolite. 2-HG, 2-hydroxyglutarate.

immunotherapy. Combining IDH1 inhibitor with anti-PD-1 improved prognosis in C57BL/6J mice bearing IDH1mt glioma (Bunse et al., 2018). The IDH inhibitor IDH-C35 significantly enhances CD8 + T cell infiltration and prolongs the survival of glioma-associated antigens vaccinated mice challenged with IDHmt glioma (Kohanbash et al., 2017). Tumor vaccine is another way of immunotherapy besides blocking the immune checkpoint, and the mutant IDH is quite a tumor-specific neoantigen. Vaccination of transgenic mice expressing human major histocompatibility complexes (MHCs) with a peptide in the IDH1mt induced a CD4 + T-dependent immune response suppresses the growth of the IDH1mt sarcoma in an MHC-humanized animal model (Schumacher et al., 2014). Consistent with this, another group immunized mice bearing intracranial glioma with peptides encompassing the IDH1 mutation site, which significantly prolonged the survival of mice bearing IDH1mt and even cured 25% of them (Pellegatta et al., 2015). Therefore, besides immune checkpoint inhibitors, IDHmt-derived peptide vaccination is also a prospective therapy, and their combination may find synergy with each other. IDH1 inhibitor amplified the efficiency of glioma-associated antigens vaccination, augmented the infiltration of CD8 + T cell and improved the survival of mice challenged with IDH1mt tumor (Kohanbash et al., 2017). And in the research of Bunse et al. (2018) adoptive transfer of T cells from IDH1R132H peptide-vaccinated C57BL/6J mice only works in the presence of IDH inhibitor.

Apart from adaptive immunity, D-2HG also limits the innate defense against tumor. Via D-2HG, IDHmt astrocyte inactivates complement, for it restrains the assembly of C5 convertase and inactivates assembled C3/C5 convertases in the classical pathway of complement activation; in the meantime, it inhibits the assembly of C3/C5 convertases in the alternative pathway (Zhang et al., 2018). By those means, the glioma cell ward off complement-mediated lysis and phagocytosis (Zhang et al., 2018). Natural killer (NK) cells are also executors in excluding tumor. The receptor NK group 2D (NKG2D) activates NK cells when ligating with NKG2D ligands (NKG2DLs) on the surface of targeted cells such as tumor cells (Zhang et al., 2016). IDHmt astrocyte cell lines and patient-derived glioma stem-like cells exhibit a lower expression of NKG2D than those with IDHwt, and this is associated with the hypermethylation of NKG2D promoters. Downregulating NKG2D helps tumor cells to escape cytolysis by NK cells, and the pretreatment of D-2HG confers IDHwt astrocytes resistance to that (Zhang et al., 2016), restoring NKG2DL expression by the DNMT inhibitor decitabine, which significantly prompted NK-induced cytotoxicity.

2-HYDROXYGLUTARATE PRODUCTION CONFERS VULNERABILITIES

From the above, we can conclude that 2-HG triggers tumorigenesis through multiple mechanisms. However, its inhibition on α-KG-dependent dioxygenases and the altered epigenetic landscape also confers the tumor cells vulnerabilities (**Table 1**). For example, D-2HG sensitizes IDHmt malignancies to DNA damage. Chemotherapy combining procarbazine, CCNU/lomustine, and vincristine (PCV) attains a better prognosis in oligodendroglial patients harboring IDHmt compared with those with the WT allele (Cairncross et al., 2014). Mechanistically, among the three regimens in PCV therapy, CCNU and procarbazine are DNA alkylating agents, and the DNA repair enzymes ALKBH2/3 are inhibited by D-2HG, thereby sensitizing tumor cells to them (Wang et al., 2015). Also, the IDHmt expression gives rise to a "BRCAness" phenotype by impeding homologous recombination, rendering the tumor cells more susceptible to poly(adenosine 5′-diphosphate–ribose) polymerase (PARP) inhibitors (Sulkowski et al., 2017). ATM, encoded by the ataxia telangiectasia mutated gene (*ATM*), is also a DNA repair enzyme involved in sensing the double-strand break (DSB) and the mobilization of downstream repair machinery (Inoue et al., 2016). D-2HG attenuates the transcription of *ATM* by increasing the repressive mark H3K9me3 at its promoter, making for a susceptibility to DNA damage (Inoue et al., 2016; Molenaar et al., 2018). In addition, the inhibition of D-2HG on histone demethylase KDM4B brings about a hypermethylated state around DNA break loci; this

TABLE 1 | The production of D-2HG confers vulnerability to IDHmt tumor.

Mechanism	Vulnerability	Resulted drug susceptibility	References
D-2HG inhibits the ALKBH2/3 DNA repair enzymes	Impaired DNA repair	Alkylating agents	Wang et al., 2015
Inactivates the KDM4A and KDM4B, which are involved in DSB repair and recruitment of repair factors		PARP inhibitor	Sulkowski et al., 2017
KDM4B inhibition by D-2HG leads to abnormal H3K9 methylation surrounding DNA break loci, masking the H3K9me3 signal at break loci, which is required for homology-dependent repair			Sulkowski et al., 2020
IDH1 expression downregulates the DNA damage sensor ATM		Ionizing radiation	Inoue et al., 2016
IDH1mt lowers intracellular NAD+, the substrate for PARP-mediated DNA repair		Temozolomide (TMZ)	Lu et al., 2017
D-2HG production consumes NADPH, which is required for buffering oxidative stress	Sensitivity to oxidative stress	Ionizing radiation	Gelman et al., 2018
IDH1mt induced a dependency on Nrf2-guided glutathione *de novo* synthesis		Nrf2 inhibitor	Yu et al., 2020
D-2HG inhibits BCAT1/2, consequently increasing the dependence on glutaminase to synthesize glutathione, the pivotal metabolite in neutralizing oxygen radical		Radiation; glutaminase inhibitor	McBrayer et al., 2018
IDH1mt downregulates nicotinate. Phosphoribosyltransferase (Naprt1) resulted in a dependence on nicotinamide phosphoribosyltransferase (NAMPT), another rate-limiting enzyme of the NAD+ salvage pathway	Sensitivity to NAD+ depletion	NAMPT inhibitor	Tateishi et al., 2015
D-2HG inhibits cytochrome *c* oxidase (COX) in the electron transport chain (ETC), and this lowers the threshold for apoptosis, increasing IDH mutated cell dependence on BCL-2 for survival	A higher dependence on anti-apoptosis protein	BCL-2 inhibitor	Chan et al., 2015
D-2HG inhibits succinate dehydrogenase (SDH), which leads to mitochondrial hypersuccinylation and impaired mitochondrial function, resulting in the recruitment of BCL-2 to the mitochondrial membrane			Li et al., 2015
D-2HG destabilizes Mcl-1 through prompting its proteasome turnover, conferring its reliance on Bcl-xL to survive		Bcl-xL inhibitor	Karpel-Massler et al., 2017

masks the H3K9me3 signals required for homology-dependent repair (HDR) factor recruitment. KDM4B overexpression rescues the DNA repair deficiency in IDH mutant cell but not in IDH WT cells (Sulkowski et al., 2017; Sulkowski et al., 2020). In general, D-2HG suppresses DNA repair; as a consequence, synthetic lethal interaction can be established between IDHmt and DNA damage agents.

The process of 2-HG generation largely reprograms the metabolic landscape. To sum up, 2-HG synthesis consumes the reducing equivalent NADPH and NADH (Gilbert et al., 2014; Gelman et al., 2018; Hollinshead et al., 2018; Philip et al., 2018); downregulates lipid synthesis (Gelman et al., 2018; Viswanath et al., 2018a,b); reduces glycolysis (Chesnelong et al., 2014); stimulates glutamine metabolism (Reitman et al., 2014; Hollinshead et al., 2018; McBrayer et al., 2018); depletes the TCA flux; and impairs mitochondrial respiration (Reitman et al., 2011; Izquierdo-Garcia et al., 2015; Li et al., 2015; McBrayer et al., 2018). Some metabolic phenotypes among these confer IDHmt tumor vulnerabilities that can be exploited. 2-HG synthesis imposed an NADPH deficit, attenuating the ability to buffer oxidative stress. Both colorectal carcinoma and astrocyte cell lines expressing IDH1/2mt exhibited a hypersensitivity to ionizing radiation or H_2O_2 compared with those with IDH1/2wt (Gelman et al., 2018). Moreover, IDH1 glioma relies on nuclear factor (erythroid-derived 2)-like 2 (Nrf2)-governed glutathione synthesis pathway to maintain the intracellular redox homeostasis. Inhibiting Nrf2 by triptolide, a diterpenoid epoxide from *Tripterygium wilfordii*, compromised glutathione synthesis and caused synthetic lethality in IDHmt glioma by inducing oxidative damage (Yu et al., 2020). The vulnerability to oxidative stress also derives from the competitive inhibition of D-2HG on BCAT1/2, which lowers glutamate and prompts a dependence on the glutaminase to generate glutamate and downstream glutathione, which functions in neutralize intracellular reactive oxygen species (ROS). Hence, ablating glutaminase in IDHmt glioma extensively sensitizes cells to oxidative damage and radiation (McBrayer et al., 2018). In conclusion, the production of D-2HG is accompanied by an accessorial sensitivity to oxidative stress, and multiple layers of its antioxidant system can become druggable.

The expression of IDHmt reduces intracellular NAD+ by downregulating nicotinate phosphoribosyltransferase (Naprt1) in the NAD+ salvage pathway; a further depletion of NAD+ by targeting nicotinamide phosphoribosyltransferase (NAMPT), another enzyme in the metabolic pathway, induced a synthetic lethality with IDH mutation (Tateishi et al., 2015). Since NAD+ is a substrate for base excision repair (BER) mediated by PARP DNA repair machinery, there is a hardship for the IDHmt glioma to sustain the genomic integrity; this explains for the hypersensitivity of glioma with IDHmt to PARP inhibitors, which could synergize with a DNA alkylating agent such as temozolomide (TMZ) (Lu et al., 2017; Philip et al., 2018). D-2HG also inhibits the mitochondrial electron transport chain (ETC) by compromising the activity of cytochrome *c* oxidase (COX), resulting in a lower mitochondrial threshold to induce apoptosis, which sensitized those AML cells with IDH1mt

to the inhibitor of the anti-apoptotic protein BCL-2 (Chan et al., 2015). Similarly, in another study, IDHmt-derived D-2HG inhibits succinate dehydrogenase (SDH), the accumulated succinate hypersuccinylate mitochondria, and finally induces the mitochondrial membrane localization of BCL-2 (Li et al., 2015). Another member of the BCL-2 family, Mcl-1, is downregulated in IDH1mt glioma cells, inducing a dependence on the anti-apoptosis protein Bcl-xL and thus the synthetic lethality of IDH1mt with Bcl-xL inhibitor (Karpel-Massler et al., 2017). These researches indicate that IDHmt has a specific role in dictating cell death program, inducing a dependence on certain anti-apoptotic protein, which is a potential target.

D-2-HYDROXYGLUTARATE EXERTS TOXICITY ON CANCER CELL

Although 2-HG is identified as an oncometabolite, which facilitates tumor initiation, there is a paradox that IDHmt foreshadows a benign prognosis in glioma, and a similar trend also exists in AML (Parsons et al., 2008; Yan et al., 2009; Marcucci et al., 2010; Chou et al., 2011). Then, does 2-HG also exert toxicity on cancer cells? In the research of Fu et al. (2015) both enantiomers of 2-HG and the expression of IDHmt inhibited ATP synthase, thereby inactivating mTOR and cell growth. This uncovered the growth-suppressive effect of 2-HG on IDHmt glioma and suggested that there likely exist other mechanisms by which 2-HG exerts its potential toxicity on cancer cell. Rui Su et al., reported that exogenous D-2HG inhibited FTO, a RNA demethylase, which caused a decrease in *MYC* and *CEBPA* transcripts, suppressing tumor growth through the FTO/m6A/MYC/CEBPA axis. Exogenous L-2HG and overexpressed IDH1mt both recapitulated these effects (Fu et al., 2015). Consistent with this, in a subsequent study of the same group, targeting FTO induced a similar effect on FTO/m6A/MYC/CEBPA axis signaling through the same mechanism, leading to cell-cycle arrest in cancer stem cells (Su et al., 2020). Although D-2HG blunts immunity as a whole, it was reported that FTO inhibition decreased the expression of immune checkpoints like PD-L1, PD-L2, and LILRB, thereby counteracting the immune evasion of leukemia cells. Besides, D-2HG hinders neutrophil chemotaxis, which helps to establish an immunosuppressive ecology in the tumor microenvironment (TME) (Amankulor et al., 2017). Finally, IDHmt may induce susceptibility to some treatments. The above factors may be a proper explanation for the benign prognosis in glioma and AML with IDHmt; however, the inherent difference in genotypic milieu should not be neglected.

THE ROLES OF 2-HYDROXYGLUTARATE BEYOND ONCOMETABOLITE

L-2-Hydroxyglutarate Takes Part in the Adaption to Hypoxia

It was revealed that multiple cell lines displayed an increase of 2-HG under hypoxia (Intlekofer et al., 2015; Oldham et al., 2015). L2HGDH but not D2HGDH knockdown decreased its concentration, indicating that L-2HG builds the majority of 2-HG pool; the result of gas chromatography–mass spectroscopy (GC-MS) also confirmed so. The sensitivity of L-2HG concentration to hypoxia varies among cell lines; L-2HG in C2C12 cells was only induced twofold (about 3 μM) by 2% oxygen (Chakraborty et al., 2019), which was a drop in the bucket compared with 304 ± 81 μM in SF188 cells by 0.5% oxygen (Intlekofer et al., 2015). Besides, not all α-KG-dependent dioxygenases are susceptible to the perturbation of L-2HG in hypoxia; the research of Chakraborty et al. (2019) revealed that the inhibition of KDM6A in C2C12 cells under hypoxia was directly resulted from change in oxygen concentration rather than the effect of HIF or L-2HG. The glutamine-derived α-KG builds the primary source of L-2HG, and the enzymes manufacturing L-2HG in hypoxia are LDHA and MDH; they consume α-KG and NADH to produce L-2HG and NAD+ (Intlekofer et al., 2017). Some studies reported that LDHA had a greater contribution in generating L-2HG than MDH (Intlekofer et al., 2015), while there are also others that demonstrated the opposite (Oldham et al., 2015); maybe it depends on cell types. When it comes to the mechanism of L-2HG's accumulation, when there is a paucity of oxygen, some researchers think that the increased α-KG level and NADH/NAD+ ratio skew the reaction LDHA and MDH catalyzes toward the direction of L-2HG synthesis (Oldham et al., 2015), and downregulation of L2HGDH in hypoxia contributed to that too. An acidic intracellular environment resulted from oxygen limitation, which also favors the "promiscuous" reaction catalyzed by LDH and MDH, because an acidic pH sustains a protonated form of α-KG that binds to the substrate-binding pocket of LDHA more tightly via forming a hydrogen bond (Nadtochiy et al., 2016; Intlekofer et al., 2017). An analogous mechanism may be involved in the interaction between α-KG and MDH under acidic pH.

As described above, intracellular L-2HG elevates in the face of low-oxygen condition; it helps in alleviating hypoxia-induced reductive stress. Reductive stress is defined as an excess accumulation of reducing equivalents (specifically NADH, NADPH, and GSH) that exceeds the capacity of endogenous oxidoreductases (Xiao and Loscalzo, 2020). The oxidation of NADH by complex I is suppressed under hypoxia; this results in its accumulation, offering more electrons for one-electron reduction of oxygen that generates $O_2\bullet$- (Kussmaul and Hirst, 2006; Yang and Kahn, 2006; Clanton, 2007). Mechanisms by which reductive stress damages cells include disturbing signal transduction by ROS, inducing ER stress, and so on (Xiao and Loscalzo, 2020). In this process of reducing α-KG by NADH, L-2HG acts as a reservoir of excess reducing equivalents. L2HGDH knockdown not only mitigated mitochondrial membrane hyperpolarization but also impeded the generation of mitoSOX (Oldham et al., 2015), indicating that L-2HG metabolism was implicated in maintaining redox balance. It is explicit that being an α-KG-dependent dioxygenase, PHD, the key enzyme in regulating the stability of HIF-1α, can be suppressed by L-2HG. The IC50 value for the L form of 2-HG to PHD is 419 ± 150 μM (Chowdhury et al., 2011), which

is comparable with the concentration of L-2HG quantitated in SF188 cells (304 ± 81 μM) under hypoxia. In accordance with that, downregulating L2HGDH in aerobic condition stabilized HIF-1α (Oldham et al., 2015). Therefore, L-2HG may assist in cell's adaption to hypoxia via sustaining the activity of HIF pathway.

In summary, L-2HG partakes in acclimatizing hypoxia by regulating redox homeostasis and the activity of HIF pathway. Now that PHD can be inhibited by L-2HG, it is probable that KDM and TET are also sensitive to the perturbation of L-2HG, owing to their lower IC50. A study reported that hypoxia-induced L-2HG could inhibit KDM4C, thereby promoting the methylation of H3K9 (Intlekofer et al., 2015). Although its downstream effect remains obscure, it does suggest that besides sensing oxygen directly, TET and KDM4C can sense changes in oxygen concentration indirectly through L-2HG. In terms of D-2HG, although a study revealed a concomitant increased synthesis of D-2HG associated with IDH2-dependent carboxylation of α-KG (Wise et al., 2011), there is no definitive evidence demonstrating D-2HG's contribution in the adaption to hypoxia. A conceivable explanation is that D-2HG elevates marginally relative to L-2HG; more importantly, D-2HG functions as a weak antagonist of α-KG-dependent dioxygenase, which is far less efficient than L-2HG (Xu et al., 2011).

2-Hydroxyglutarate Is an "Immunometabolite"

Accumulated studies suggest that there is a close relationship between metabolism and the activation, differentiation, and exhaustion of immune cells (Zhang and Romero, 2018; Yerinde et al., 2019). Some subsets of T cell exhibit a distinct metabolic feature. For example, naïve CD8 + T cells metabolically rely on oxidative phosphorylation, and their activation leads to a metabolic switch to glycolysis, while memory T cells heavily depend on fatty acid oxidation (Yerinde et al., 2019). Multiple processes of CD8 + T cells such as clonal expansion and memory formation are sustained by a distinct metabolic state (Yerinde et al., 2019). Such association between metabolism and function also exists in other subsets of immune cells. What is more, the function states of immune cells are also shaped by epigenetics (Gray et al., 2017). Now that metabolism and epigenetics have such a huge impact on immune cells, the metabolites linking metabolism and epigenetics such as 2-HG, fumarate, and acetyl-CoA are predicted to be vital in immune cells. Next, we are going to discuss the role of 2-HG in immune cells.

As mentioned in the research of Tyrakis et al. (2016) CD8 + T cell produced millimolar L-2HG in response to TCR triggering, resulting in an enrichment of active H3K4me3 mark and RNA pol II at *CD62L*, polarizing it to memory subsets. Moreover, accumulating L-2HG prompted a global increase of H3K27me3 and 5mC and knockdown of H3K27me2/3 demethylase Utx; and TET2 also motivated the expression of CD62L, indicating that epigenetic inhibition somewhere else in the genome triggers the transcription of *CD62L*. Although it was a little regrettable that the study did not identify these genes, it unveiled L-2HG's identity of "immunometabolite" unprecedentedly, which mattered a lot in the fate decision of CD8 + T lymphocytes through a metabolic–epigenetic axis. A recent study further revealed that with Utx bound directly to *Prdm1*, through reduced demethylation of histone H3K27me3, its deficiency hampers the transcription of *Prdm1*-encoding Blimp1 that is an effector-associated transcription factor, triggering a memory-like phenotype (Yamada et al., 2019). Therefore, L-2HG dictates CD8 + T lymphocyte fate through the metabolism–epigenetics axis. This also uncovered the suppression on T lymphocyte in the TME from another aspect, since the carbon source of L-2HG, glutamine, is also taken as the primary nutritional source by multiple kinds of tumor.

Similar to L-2HG, D-2HG has also been demonstrated to be a mediator in T lymphocyte differentiation. In Tao Xu's study, differentiating Th17 cells sustains a ∼5–10-fold higher concentration of D-2HG than did iTreg cells, inducing a hypermethylated state of *Foxp3* loci, which is a master transcription factor in the charge of Treg differentiation. ^{15}N-labeling analysis demonstrated that D-2HG was mainly derived from glutamine, and glutamate oxaloacetate transaminase 1 (GOT1) inhibition reprogrammed Th17 differentiation toward iTreg cells (Xu et al., 2017). Similar with this, in the study of Licheng Sun, PM2.5 and indeno[1,2,3-*cd*]pyrene (IP) activated the expression of GOT1 in an AhR-dependent manner, thereby enhancing the metabolic flux from glutamine to D-2HG, bringing about a hypermethylated state of *Foxp3* loci and finally disrupted Th17/Treg ratio (Sun et al., 2020). This AhR-GOT1-D-2HG axis functions in the pathogenesis of asthma. By adopting a GOT1 inhibitor, they alleviated pulmonary inflammation in a mouse asthma model successfully.

We can conclude from the aforementioned studies that 2-HG interferes with T cell differentiation through epigenetics; they also inspire us the feasibility of regulating immune functions through the metabolism–epigenetics axis in T cells. Besides asthma, the imbalance of Th17/Treg ratio happens in a set of autoimmune diseases including psoriasis, inflammatory bowel disease, and multiple sclerosis (Lee, 2018); a similar role of D-2HG in their pathophysiology may exist. Other than modulating immune homeostasis in these diseases through drug intervention, adoptive immunotherapy is another viable choice. For instance, compared with injecting Th17 cells with control shRNA, adoptive transfer using Th17 cells infected with virus containing shGot1 significantly tempered disease severity in a mouse experimental autoimmune encephalomyelitis model (Xu et al., 2017). As regards oncotherapy, a pretreatment of L-2HG significantly exaggerated the persistence and antitumor capacity of adoptively transferred CD8 + T lymphocytes (Tyrakis et al., 2016). Therefore, benefiting from the plasticity of T lymphocyte differentiation and its reliance on epigenetics and metabolism (Kleinewietfeld and Hafler, 2013; Lee, 2018), we can take 2-HG as an entry point in maintaining the balance of immunity.

CONCLUSION

During the recent 10 years, much efforts have been paid in exploring the pathophysiology of IDHmt, leading to remarkable

achievements. Due to their excellent performance in clinical trial, the IDH inhibitors ivosidenib and enasidenib are approved by Food and Drug Administration (FDA) to treat adults with relapsed and refractory AML with IDH1/2 mutation. However, the application of IDHmt inhibitors in solid tumor seems not that effective; to crack this hard nut, a deeper insight on the relationship between IDHmt and the mutational background as well as TME is required. Besides targeting IDH directly, an alternative way is to exploit the vulnerabilities it confers, and this may be a more prospective strategy in the condition that IDHmt gradually becomes a passenger mutation from driver mutation (Waitkus et al., 2018). It is noteworthy that this strategy is incompatible with IDH inhibitor, as it depends on the activity of IDHmt. Until now, little is known with regard to the detailed tumorigenic mechanism of L-2HG, and this requires further investigation. As L-2HG is structurally analogous to D-2HG, they may share some common mechanisms such as suppressing α-KG-dependent dioxygenases. L-2HG generates in acidic environment and participates in the adaption to hypoxia. Does this also function in solid tumor, thus representing for the tumorigenic property of L-2HG from another perspective? Because the TME is quite a hypoxia and acidic milieu, L-2HG may help these areas establish an adaption to limited oxygen supply and, at the same time, generate phenotype heterogeneity, which contributes to variant therapeutic responses in the intratumoral religion through epigenetics and other mechanisms. It is surprising that in addition to oncometabolite, 2-HG also serves as immunometabolite. How the 2-HG metabolism in T lymphocyte will alter in the TME and what consequences this will bring about are worthy of exploration. What is more, does endogenous 2-HG regulate the functions of other immune cell subsets? Recently, L-2HG is demonstrated to promote axon regeneration in the central nervous system (Li et al., 2020). Therefore, 2-HG may also function in other physiological processes.

In conclusion, besides triggering tumorigenesis, 2-HG plays a significant role in adaption to hypoxia and acts as an "immunometabolite." 2-HG is just one of the numerous metabolites; its functions reflect a tight association between metabolism and epigenetics, signaling transduction and other cellular processes, and these are all the themes of present researches on metabolism.

AUTHOR CONTRIBUTIONS

XD wrote the manuscript and made the figures. HH provided direction to the review. Both authors contributed to the article and approved the submitted version.

FUNDING

This work was supported by grants from the National Natural Science Foundation of China (82025026 and 81730077 to HH), National Key R&D Program of China (2016YFC1302301), Science and Technology Program of Guangzhou (201704020095), Program for Guangdong Introducing Innovative and Entrepreneurial Teams (2016ZT06S252), and Fundamental Research Funds for the Central Universities (17ykjc14).

REFERENCES

Achouri, Y., Noel, G., Vertommen, D., Rider, M. H., Veiga-Da-Cunha, M., and Van Schaftingen, E. (2004). Identification of a dehydrogenase acting on D-2-hydroxyglutarate. *Biochem. J.* 381, 35–42. doi: 10.1042/BJ20031933

Amankulor, N. M., Kim, Y., Arora, S., Kargl, J., Szulzewsky, F., Hanke, M., et al. (2017). Mutant IDH1 regulates the tumor-associated immune system in gliomas. *Genes Dev.* 31, 774–786. doi: 10.1101/gad.294991.116

Balamurugan, K. (2016). HIF-1 at the crossroads of hypoxia, inflammation, and cancer. *Int. J. Cancer* 138, 1058–1066. doi: 10.1002/ijc.29519

Bardella, C., Al-Dalahmah, O., Krell, D., Brazauskas, P., Al-Qahtani, K., Tomkova, M., et al. (2016). Expression of Idh1(R132H) in the murine subventricular zone stem cell niche recapitulates features of early gliomagenesis. *Cancer Cell* 30, 578–594. doi: 10.1016/j.ccell.2016.08.017

Böttcher, M., Renner, K., Berger, R., Mentz, K., Thomas, S., Cardenas-Conejo, Z. E., et al. (2018). D-2-hydroxyglutarate interferes with HIF-1α stability skewing T-cell metabolism towards oxidative phosphorylation and impairing Th17 polarization. *Oncoimmunology* 7:e1445454. doi: 10.1080/2162402x.2018.1445454

Brinkley, G., Nam, H., Shim, E., Kirkman, R., Kundu, A., Karki, S., et al. (2020). Teleological role of L-2-hydroxyglutarate dehydrogenase in the kidney. *Dis. Model Mech.* 13:dmm045898. doi: 10.1242/dmm.045898

Bunse, L., Pusch, S., Bunse, T., Sahm, F., Sanghvi, K., Friedrich, M., et al. (2018). Suppression of antitumor T cell immunity by the oncometabolite (R)-2-hydroxyglutarate. *Nat. Med.* 24, 1192–1203. doi: 10.1038/s41591-018-0095-6

Cairncross, J. G., Wang, M., Jenkins, R. B., Shaw, E. G., Giannini, C., Brachman, D. G., et al. (2014). Benefit from procarbazine, lomustine, and vincristine in oligodendroglial tumors is associated with mutation of IDH. *J. Clin. Oncol.* 32, 783–790. doi: 10.1200/JCO.2013.49.3726

Chakraborty, A. A., Laukka, T., Myllykoski, M., Ringel, A. E., Booker, M. A., Tolstorukov, M. Y., et al. (2019). Histone demethylase KDM6A directly senses oxygen to control chromatin and cell fate. *Science* 363, 1217–1222. doi: 10.1126/science.aaw1026

Chan, S. M., Thomas, D., Corces-Zimmerman, M. R., Xavy, S., Rastogi, S., Hong, W. J., et al. (2015). Isocitrate dehydrogenase 1 and 2 mutations induce BCL-2 dependence in acute myeloid leukemia. *Nat. Med.* 21, 178–184. doi: 10.1038/nm.3788

Chaturvedi, A., Araujo Cruz, M. M., Jyotsana, N., Sharma, A., Yun, H., Görlich, K., et al. (2013). Mutant IDH1 promotes leukemogenesis in vivo and can be specifically targeted in human AML. *Blood* 122, 2877–2887. doi: 10.1182/blood-2013-03-491571

Chen, C., Liu, Y., Lu, C., Cross, J. R., Morris, J. P. T., Shroff, A. S., et al. (2013). Cancer-associated IDH2 mutants drive an acute myeloid leukemia that is susceptible to Brd4 inhibition. *Genes Dev.* 27, 1974–1985. doi: 10.1101/gad.226613.113

Chen, F., Bian, K., Tang, Q., Fedeles, B. I., Singh, V., Humulock, Z. T., et al. (2017). Oncometabolites d- and l-2-Hydroxyglutarate inhibit the AlkB family DNA repair enzymes under physiological conditions. *Chem. Res. Toxicol.* 30, 1102–1110. doi: 10.1021/acs.chemrestox.7b00009

Chesnelong, C., Chaumeil, M. M., Blough, M. D., Al-Najjar, M., Stechishin, O. D., Chan, J. A., et al. (2014). Lactate dehydrogenase A silencing in IDH mutant gliomas. *Neuro-Oncology* 16, 686–695. doi: 10.1093/neuonc/not243

Chou, W. C., Lei, W. C., Ko, B. S., Hou, H. A., Chen, C. Y., Tang, J. L., et al. (2011). The prognostic impact and stability of Isocitrate dehydrogenase 2 mutation

in adult patients with acute myeloid leukemia. *Leukemia* 25, 246–253. doi: 10.1038/leu.2010.267

Chowdhury, R., Yeoh, K. K., Tian, Y. M., Hillringhaus, L., Bagg, E. A., Rose, N. R., et al. (2011). The oncometabolite 2-hydroxyglutarate inhibits histone lysine demethylases. *EMBO Rep.* 12, 463–469. doi: 10.1038/embor.2011.43

Clanton, T. L. (2007). Hypoxia-induced reactive oxygen species formation in skeletal muscle. *J. Appl. Physiol. (1985)* 102, 2379–2388. doi: 10.1152/japplphysiol.01298.2006

Corces-Zimmerman, M. R., Hong, W. J., Weissman, I. L., Medeiros, B. C., and Majeti, R. (2014). Preleukemic mutations in human acute myeloid leukemia affect epigenetic regulators and persist in remission. *Proc. Natl. Acad. Sci. U.S.A.* 111, 2548–2553. doi: 10.1073/pnas.1324297111

Dalgliesh, G. L., Furge, K., Greenman, C., Chen, L., Bignell, G., Butler, A., et al. (2010). Systematic sequencing of renal carcinoma reveals inactivation of histone modifying genes. *Nature* 463, 360–363. doi: 10.1038/nature08672

Dang, L., White, D. W., Gross, S., Bennett, B. D., Bittinger, M. A., Driggers, E. M., et al. (2010). Cancer-associated IDH1 mutations produce 2-hydroxyglutarate. *Nature* 465:966. doi: 10.1038/nature09132

Delhommeau, F., Dupont, S., Della Valle, V., James, C., Trannoy, S., Masse, A., et al. (2009). Mutation in TET2 in myeloid cancers. *N. Engl. J. Med.* 360, 2289–2301. doi: 10.1056/NEJMoa0810069

Fan, J., Teng, X., Liu, L., Mattaini, K. R., Looper, R. E., Vander Heiden, M. G., et al. (2015). Human phosphoglycerate dehydrogenase produces the oncometabolite D-2-hydroxyglutarate. *ACS Chem. Biol.* 10, 510–516. doi: 10.1021/cb500683c

Figueroa, M. E., Abdel-Wahab, O., Lu, C., Ward, P. S., Patel, J., Shih, A., et al. (2010). Leukemic IDH1 and IDH2 mutations result in a hypermethylation phenotype, disrupt TET2 function, and impair hematopoietic differentiation. *Cancer Cell* 18, 553–567. doi: 10.1016/j.ccr.2010.11.015

Flavahan, W. A., Drier, Y., Liau, B. B., Gillespie, S. M., Venteicher, A. S., Stemmer-Rachamimov, A. O., et al. (2016). Insulator dysfunction and oncogene activation in IDH mutant gliomas. *Nature* 529, 110–114. doi: 10.1038/nature16490

Fu, X., Chin, R. M., Vergnes, L., Hwang, H., Deng, G., Xing, Y., et al. (2015). 2-Hydroxyglutarate inhibits ATP synthase and mTOR signaling. *Cell Metab.* 22, 508–515. doi: 10.1016/j.cmet.2015.06.009

Gagné, L. M., Boulay, K., Topisirovic, I., Huot, M. E., and Mallette, F. A. (2017). Oncogenic activities of IDH1/2 mutations: from epigenetics to cellular signaling. *Trends Cell Biol.* 27, 738–752. doi: 10.1016/j.tcb.2017.06.002

Gelman, S. J., Naser, F., Mahieu, N. G., McKenzie, L. D., Dunn, G. P., Chheda, M. G., et al. (2018). Consumption of NADPH for 2-HG synthesis increases pentose phosphate pathway flux and sensitizes cells to oxidative stress. *Cell Rep.* 22, 512–522. doi: 10.1016/j.celrep.2017.12.050

Gilbert, M. R., Liu, Y., Neltner, J., Pu, H., Morris, A., Sunkara, M., et al. (2014). Autophagy and oxidative stress in gliomas with IDH1 mutations. *Acta Neuropathol.* 127, 221–233. doi: 10.1007/s00401-013-1194-6

Gray, S. M., Amezquita, R. A., Guan, T., Kleinstein, S. H., and Kaech, S. M. (2017). Polycomb repressive complex 2-mediated chromatin repression guides effector CD8(+) T cell terminal differentiation and loss of multipotency. *Immunity* 46, 596–608. doi: 10.1016/j.immuni.2017.03.012

Harris, A. L. (2015). A new hydroxy metabolite of 2-oxoglutarate regulates metabolism in hypoxia. *Cell Metab.* 22, 198–200. doi: 10.1016/j.cmet.2015.07.016

Hollinshead, K. E. R., Munford, H., Eales, K. L., Bardella, C., Li, C., Escribano-Gonzalez, C., et al. (2018). Oncogenic IDH1 mutations promote enhanced proline synthesis through PYCR1 to support the maintenance of mitochondrial redox homeostasis. *Cell Rep.* 22, 3107–3114. doi: 10.1016/j.celrep.2018.02.084

Inoue, S., Li, W. Y., Tseng, A., Beerman, I., Elia, A. J., Bendall, S. C., et al. (2016). Mutant IDH1 downregulates ATM and alters DNA repair and sensitivity to DNA damage independent of TET2. *Cancer Cell* 30, 337–348. doi: 10.1016/j.ccell.2016.05.018

Intlekofer, A. M., Dematteo, R. G., Venneti, S., Finley, L. W., Lu, C., Judkins, A. R., et al. (2015). Hypoxia induces production of L-2-hydroxyglutarate. *Cell Metab.* 22, 304–311. doi: 10.1016/j.cmet.2015.06.023

Intlekofer, A. M., Wang, B., Liu, H., Shah, H., Carmona-Fontaine, C., Rustenburg, A. S., et al. (2017). L-2-Hydroxyglutarate production arises from noncanonical enzyme function at acidic pH. *Nat. Chem. Biol.* 13, 494–500. doi: 10.1038/nchembio.2307

Izquierdo-Garcia, J. L., Viswanath, P., Eriksson, P., Cai, L., Radoul, M., Chaumeil, M. M., et al. (2015). IDH1 mutation induces reprogramming of pyruvate metabolism. *Cancer Res.* 75, 2999–3009. doi: 10.1158/0008-5472.Can-15-0840

Junqueira, D., Brusque, A. M., Porciuncula, L. O., Rotta, L. N., Frizzo, M. E., Wyse, A. T., et al. (2004). In vitro effects of D-2-hydroxyglutaric acid on glutamate binding, uptake and release in cerebral cortex of rats. *J. Neurol. Sci.* 217, 189–194. doi: 10.1016/j.jns.2003.10.005

Junqueira, D., Brusque, A. M., Porciuncula, L. O., Rotta, L. N., Ribeiro, C. A., Frizzo, M. E., et al. (2003). Effects of L-2-hydroxyglutaric acid on various parameters of the glutamatergic system in cerebral cortex of rats. *Metab. Brain Dis.* 18, 233–243. doi: 10.1023/a:1025559200816

Karpel-Massler, G., Ishida, C. T., Bianchetti, E., Zhang, Y., Shu, C., Tsujiuchi, T., et al. (2017). Induction of synthetic lethality in IDH1-mutated gliomas through inhibition of Bcl-xL. *Nat. Commun.* 8:1067. doi: 10.1038/s41467-017-00984-9

Kernytsky, A., Wang, F., Hansen, E., Schalm, S., Straley, K., Gliser, C., et al. (2015). IDH2 mutation-induced histone and DNA hypermethylation is progressively reversed by small-molecule inhibition. *Blood* 125, 296–303. doi: 10.1182/blood-2013-10-533604

Kickingereder, P., Sahm, F., Radbruch, A., Wick, W., Heiland, S., von Deimling, A., et al. (2015). IDH mutation status is associated with a distinct hypoxia/angiogenesis transcriptome signature which is non-invasively predictable with rCBV imaging in human glioma. *Sci. Rep.* 5:16238. doi: 10.1038/srep16238

Kleinewietfeld, M., and Hafler, D. A. (2013). The plasticity of human Treg and Th17 cells and its role in autoimmunity. *Semin. Immunol.* 25, 305–312. doi: 10.1016/j.smim.2013.10.009

Klutstein, M., Nejman, D., Greenfield, R., and Cedar, H. (2016). DNA methylation in cancer and aging. *Cancer Res.* 76, 3446–3450. doi: 10.1158/0008-5472.CAN-15-3278

Kohanbash, G., Carrera, D. A., Shrivastav, S., Ahn, B. J., Jahan, N., Mazor, T., et al. (2017). Isocitrate dehydrogenase mutations suppress STAT1 and CD8(+) T cell accumulation in gliomase. *J. Clin. Investig.* 127, 1425–1437. doi: 10.1172/JCI90644

Koivunen, P., Lee, S., Duncan, C. G., Lopez, G., Lu, G., Ramkissoon, S., et al. (2012). Transformation by the (R)-enantiomer of 2-hydroxyglutarate linked to EGLN activation. *Nature* 483, 484–488. doi: 10.1038/nature10898

Kranendijk, M., Struys, E. A., Salomons, G. S., Van der Knaap, M. S., and Jakobs, C. (2012). Progress in understanding 2-hydroxyglutaric acidurias. *J. Inherit. Metab. Dis.* 35, 571–587. doi: 10.1007/s10545-012-9462-5

Kranendijk, M., Struys, E. A., van Schaftingen, E., Gibson, K. M., Kanhai, W. A., van der Knaap, M. S., et al. (2010). IDH2 mutations in patients with D-2-hydroxyglutaric aciduria. *Science* 330:336. doi: 10.1126/science.1192632

Kussmaul, L., and Hirst, J. (2006). The mechanism of superoxide production by NADH:ubiquinone oxidoreductase (complex I) from bovine heart mitochondria. *Proc. Natl. Acad. Sci. U.S.A.* 103, 7607–7612. doi: 10.1073/pnas.0510977103

Langemeijer, S. M., Kuiper, R. P., Berends, M., Knops, R., Aslanyan, M. G., Massop, M., et al. (2009). Acquired mutations in TET2 are common in myelodysplastic syndromes. *Nat. Genet.* 41, 838–842. doi: 10.1038/ng.391

Lee, G. R. (2018). The balance of Th17 versus treg cells in autoimmunity. *Int. J. Mol. Sci.* 19:730. doi: 10.3390/ijms19030730

Li, F., He, X., Ye, D., Lin, Y., Yu, H., Yao, C., et al. (2015). NADP(+)-IDH mutations promote hypersuccinylation that impairs mitochondria respiration and induces apoptosis resistance. *Mol. Cell* 60, 661–675. doi: 10.1016/j.molcel.2015.10.017

Li, F., Sami, A., Noristani, H. N., Slattery, K., Qiu, J., Groves, T., et al. (2020). Glial metabolic rewiring promotes axon regeneration and functional recovery in the central nervous system. *Cell Metab.* 32, 767–785.e7. doi: 10.1016/j.cmet.2020.08.015

Losman, J.-A., Looper, R. E., Koivunen, P., Lee, S., Schneider, R. K., McMahon, C., et al. (2013). (R)-2-Hydroxyglutarate is sufficient to promote leukemogenesis and its effects are reversible. *Science* 339, 1621–1625. doi: 10.1126/science.1231677

Lu, C., Ward, P. S., Kapoor, G. S., Rohle, D., Turcan, S., Abdel-Wahab, O., et al. (2012). IDH mutation impairs histone demethylation and results in a block to cell differentiation. *Nature* 483, 474–478. doi: 10.1038/nature10860

Lu, Y., Kwintkiewicz, J., Liu, Y., Tech, K., Frady, L. N., Su, Y. T., et al. (2017). Chemosensitivity of IDH1-mutated gliomas due to an impairment in PARP1-mediated DNA repair. *Cancer Res.* 77, 1709–1718. doi: 10.1158/0008-5472.Can-16-2773

Marcucci, G., Maharry, K., Wu, Y. Z., Radmacher, M. D., Mrozek, K., Margeson, D., et al. (2010). IDH1 and IDH2 gene mutations identify novel molecular subsets within de novo cytogenetically normal acute myeloid leukemia: a Cancer and Leukemia Group B study. *J. Clin. Oncol.* 28, 2348–2355. doi: 10.1200/JCO.2009.27.3730

Mardis, E. R., Ding, L., Dooling, D. J., Larson, D. E., McLellan, M. D., Chen, K., et al. (2009). Recurring mutations found by sequencing an acute myeloid leukemia genome. *N. Engl. J. Med.* 361, 1058–1066. doi: 10.1056/NEJMoa0903840

McBrayer, S. K., Mayers, J. R., DiNatale, G. J., Shi, D. D., Khanal, J., Chakraborty, A. A., et al. (2018). Transaminase inhibition by 2-hydroxyglutarate impairs glutamate biosynthesis and redox homeostasis in glioma. *Cell* 175, 101–116 e125. doi: 10.1016/j.cell.2018.08.038

Medeiros, B. C., Fathi, A. T., DiNardo, C. D., Pollyea, D. A., Chan, S. M., and Swords, R. (2017). Isocitrate dehydrogenase mutations in myeloid malignancies. *Leukemia* 31, 272–281. doi: 10.1038/leu.2016.275

Modrek, A. S., Golub, D., Khan, T., Bready, D., Prado, J., Bowman, C., et al. (2017). Low-grade astrocytoma mutations in IDH1, P53, and ATRX cooperate to block differentiation of human neural stem cells via repression of SOX2. *Cell Rep.* 21, 1267–1280. doi: 10.1016/j.celrep.2017.10.009

Molenaar, R. J., Radivoyevitch, T., Nagata, Y., Khurshed, M., Przychodzen, B., Makishima, H., et al. (2018). IDH1/2 mutations sensitize acute myeloid leukemia to PARP inhibition and this is reversed by IDH1/2-mutant inhibitors. *Clin. Cancer Res.* 24, 1705–1715. doi: 10.1158/1078-0432.Ccr-17-2796

Mukherjee, J., Johannessen, T. C., Ohba, S., Chow, T. T., Jones, L., Pandita, A., et al. (2018). Mutant IDH1 cooperates with ATRX loss to drive the alternative lengthening of telomere phenotype in glioma. *Cancer Res.* 78, 2966–2977. doi: 10.1158/0008-5472.CAN-17-2269

Nadtochiy, S. M., Schafer, X., Fu, D., Nehrke, K., Munger, J., and Brookes, P. S. (2016). Acidic pH is a metabolic switch for 2-hydroxyglutarate generation and signaling. *J. Biol. Chem.* 291, 20188–20197. doi: 10.1074/jbc.M116.738799

Nakagawa, M., Nakatani, F., Matsunaga, H., Seki, T., Endo, M., Ogawara, Y., et al. (2019). Selective inhibition of mutant IDH1 by DS-1001b ameliorates aberrant histone modifications and impairs tumor activity in chondrosarcoma. *Oncogene* 38, 6835–6849. doi: 10.1038/s41388-019-0929-9

Nota, B., Struys, E. A., Pop, A., Jansen, E. E., Fernandez Ojeda, M. R., Kanhai, W. A., et al. (2013). Deficiency in SLC25A1, encoding the mitochondrial citrate carrier, causes combined D-2- and L-2-hydroxyglutaric aciduria. *Am. J. Hum. Genet.* 92, 627–631. doi: 10.1016/j.ajhg.2013.03.009

Noushmehr, H., Weisenberger, D. J., Diefes, K., Phillips, H. S., Pujara, K., Berman, B. P., et al. (2010). Identification of a CpG island methylator phenotype that defines a distinct subgroup of glioma. *Cancer Cell* 17, 510–522. doi: 10.1016/j.ccr.2010.03.017

Oldham, W. M., Clish, C. B., Yang, Y., and Loscalzo, J. (2015). Hypoxia-mediated increases in L-2-hydroxyglutarate coordinate the metabolic response to reductive stress. *Cell Metab.* 22, 291–303. doi: 10.1016/j.cmet.2015.06.021

Parsons, D. W., Jones, S., Zhang, X., Lin, J. C., Leary, R. J., Angenendt, P., et al. (2008). An integrated genomic analysis of human glioblastoma multiforme. *Science* 321, 1807–1812. doi: 10.1126/science.1164382

Pellegatta, S., Valletta, L., Corbetta, C., Patane, M., Zucca, I., Riccardi Sirtori, F., et al. (2015). Effective immuno-targeting of the IDH1 mutation R132H in a murine model of intracranial glioma. *Acta Neuropathol. Commun.* 3:4. doi: 10.1186/s40478-014-0180-0

Philip, B., Yu, D. X., Silvis, M. R., Shin, C. H., Robinson, J. P., Robinson, G. L., et al. (2018). Mutant IDH1 promotes glioma formation in vivo. *Cell Rep.* 23, 1553–1564. doi: 10.1016/j.celrep.2018.03.133

Preusser, M., and Marosi, C. (2017). Neuro-oncology in 2016: advances in brain tumour classification and therapy. *Nat. Rev. Neurol.* 13, 71–72. doi: 10.1038/nrneurol.2017.3

Reiter-Brennan, C., Semmler, L., and Klein, A. (2018). The effects of 2-hydroxyglutarate on the tumorigenesis of gliomas. *Contemp. Oncol. (Pozn)* 22, 215–222. doi: 10.5114/wo.2018.82642

Reitman, Z. J., Duncan, C. G., Poteet, E., Winters, A., Yan, L. J., Gooden, D. M., et al. (2014). Cancer-associated isocitrate dehydrogenase 1 (IDH1) R132H mutation and d-2-hydroxyglutarate stimulate glutamine metabolism under hypoxia. *J. Biol. Chem.* 289, 23318–23328. doi: 10.1074/jbc.M114.575183

Reitman, Z. J., Jin, G., Karoly, E. D., Spasojevic, I., Yang, J., Kinzler, K. W., et al. (2011). Profiling the effects of isocitrate dehydrogenase 1 and 2 mutations on the cellular metabolome. *Proc. Natl. Acad. Sci. U.S.A.* 108, 3270–3275. doi: 10.1073/pnas.1019393108

Rodrigues, D. G. B., de Moura Coelho, D., Sitta, A., Jacques, C. E. D., Hauschild, T., Manfredini, V., et al. (2017). Experimental evidence of oxidative stress in patients with l-2-hydroxyglutaric aciduria and that l-carnitine attenuates in vitro DNA damage caused by d-2-hydroxyglutaric and l-2-hydroxyglutaric acids. *Toxicol. In Vitro* 42, 47–53. doi: 10.1016/j.tiv.2017.04.006

Rohle, D., Popovici-Muller, J., Palaskas, N., Turcan, S., Grommes, C., Campos, C., et al. (2013). An inhibitor of mutant IDH1 delays growth and promotes differentiation of glioma cells. *Science* 340, 626–630. doi: 10.1126/science.1236062

Rover, L. K., Gevensleben, H., Dietrich, J., Bootz, F., Landsberg, J., Goltz, D., et al. (2018). PD-1 (PDCD1) promoter methylation is a prognostic factor in patients with diffuse lower-grade gliomas harboring isocitrate dehydrogenase (IDH) mutations. *EBioMedicine* 28, 97–104. doi: 10.1016/j.ebiom.2018.01.016

Rzem, R., Veiga-da-Cunha, M., Noel, G., Goffette, S., Nassogne, M. C., Tabarki, B., et al. (2004). A gene encoding a putative FAD-dependent L-2-hydroxyglutarate dehydrogenase is mutated in L-2-hydroxyglutaric aciduria. *Proc. Natl. Acad. Sci. U.S.A.* 101, 16849–16854. doi: 10.1073/pnas.0404840101

Rzem, R., Vincent, M. F., Van Schaftingen, E., and Veiga-da-Cunha, M. (2007). L-2-hydroxyglutaric aciduria, a defect of metabolite repair. *J. Inherit. Metab. Dis.* 30, 681–689. doi: 10.1007/s10545-007-0487-0

Saha, S. K., Parachoniak, C. A., Ghanta, K. S., Fitamant, J., Ross, K. N., Najem, M. S., et al. (2014). Mutant IDH inhibits HNF-4α to block hepatocyte differentiation and promote biliary cancer. *Nature* 513, 110–114. doi: 10.1038/nature13441

Sasaki, M., Knobbe, C. B., Itsumi, M., Elia, A. J., Harris, I. S., Chio, I. I., et al. (2012). D-2-hydroxyglutarate produced by mutant IDH1 perturbs collagen maturation and basement membrane function. *Genes Dev.* 26, 2038–2049. doi: 10.1101/gad.198200.112

Schumacher, T., Bunse, L., Pusch, S., Sahm, F., Wiestler, B., Quandt, J., et al. (2014). A vaccine targeting mutant IDH1 induces antitumour immunity. *Nature* 512, 324–327. doi: 10.1038/nature13387

Schvartzman, J. M., Reuter, V. P., Koche, R. P., and Thompson, C. B. (2019). 2-hydroxyglutarate inhibits MyoD-mediated differentiation by preventing H3K9 demethylation. *Proc. Natl. Acad. Sci. U.S. A.* 116, 12851–12856. doi: 10.1073/pnas.1817662116

Shelar, S., Shim, E. H., Brinkley, G. J., Kundu, A., Carobbio, F., Poston, T., et al. (2018). Biochemical and epigenetic insights into L-2-hydroxyglutarate, a potential therapeutic target in renal cancer. *Clin. Cancer Res.* 24, 6433–6446. doi: 10.1158/1078-0432.CCR-18-1727

Shenoy, N., Bhagat, T. D., Cheville, J., Lohse, C., Bhattacharyya, S., Tischer, A., et al. (2019). Ascorbic acid-induced TET activation mitigates adverse hydroxymethylcytosine loss in renal cell carcinoma. *J. Clin. Investig.* 129, 1612–1625. doi: 10.1172/jci98747

Shim, E. H., Livi, C. B., Rakheja, D., Tan, J., Benson, D., Parekh, V., et al. (2014). L-2-Hydroxyglutarate: an epigenetic modifier and putative oncometabolite in renal cancer. *Cancer Discov.* 4, 1290–1298. doi: 10.1158/2159-8290.Cd-13-0696

Shlush, L. I., Zandi, S., Mitchell, A., Chen, W. C., Brandwein, J. M., Gupta, V., et al. (2014). Identification of pre-leukaemic haematopoietic stem cells in acute leukaemia. *Nature* 506, 328–333. doi: 10.1038/nature13038

Struys, E. A., Salomons, G. S., Achouri, Y., Van Schaftingen, E., Grosso, S., Craigen, W. J., et al. (2005). Mutations in the D-2-hydroxyglutarate dehydrogenase gene cause D-2-hydroxyglutaric aciduria. *Am. J. Hum. Genet.* 76, 358–360. doi: 10.1086/427890

Su, R., Dong, L., Li, C., Nachtergaele, S., Wunderlich, M., Qing, Y., et al. (2018). R-2HG exhibits anti-tumor activity by targeting FTO/m(6)A/MYC/CEBPA signaling. *Cell* 172, 90–105.e123. doi: 10.1016/j.cell.2017.11.031

Su, R., Dong, L., Li, Y., Gao, M., Han, L., Wunderlich, M., et al. (2020). Targeting FTO suppresses cancer stem cell maintenance and immune evasion. *Cancer Cell* 38, 79–96 e11. doi: 10.1016/j.ccell.2020.04.017

Sulkowski, P. L., Corso, C. D., Robinson, N. D., Scanlon, S. E., Purshouse, K. R., Bai, H., et al. (2017). 2-Hydroxyglutarate produced by neomorphic IDH mutations

suppresses homologous recombination and induces PARP inhibitor sensitivity. *Sci. Transl. Med.* 9:eaal2463. doi: 10.1126/scitranslmed.aal2463

Sulkowski, P. L., Oeck, S., Dow, J., Economos, N. G., Mirfakhraie, L., Liu, Y., et al. (2020). Oncometabolites suppress DNA repair by disrupting local chromatin signalling. *Nature* 582, 586–591. doi: 10.1038/s41586-020-2363-0

Sun, L., Fu, J., Lin, S. H., Sun, J. L., Xia, L., Lin, C. H., et al. (2020). Particulate matter of 2.5 mum or less in diameter disturbs the balance of TH17/regulatory T cells by targeting glutamate oxaloacetate transaminase 1 and hypoxia-inducible factor 1alpha in an asthma model. *J. Allergy Clin. Immunol.* 145, 402–414. doi: 10.1016/j.jaci.2019.10.008

Tarhonskaya, H., Rydzik, A. M., Leung, I. K., Loik, N. D., Chan, M. C., Kawamura, A., et al. (2014). Non-enzymatic chemistry enables 2-hydroxyglutarate-mediated activation of 2-oxoglutarate oxygenases. *Nat. Commun.* 5:3423. doi: 10.1038/ncomms4423

Tateishi, K., Wakimoto, H., Iafrate, A. J., Tanaka, S., Loebel, F., Lelic, N., et al. (2015). Extreme vulnerability of IDH1 mutant cancers to NAD+ depletion. *Cancer Cell* 28, 773–784. doi: 10.1016/j.ccell.2015.11.006

Trewick, S. C., Henshaw, T. F., Hausinger, R. P., Lindahl, T., and Sedgwick, B. (2002). Oxidative demethylation by *Escherichia coli* AlkB directly reverts DNA base damage. *Nature* 419, 174–178. doi: 10.1038/nature00908

Turcan, S., Rohle, D., Goenka, A., Walsh, L. A., Fang, F., Yilmaz, E., et al. (2012). IDH1 mutation is sufficient to establish the glioma hypermethylator phenotype. *Nature* 483, 479–483. doi: 10.1038/nature10866

Tyrakis, P. A., Palazon, A., Macias, D., Lee, K. L., Phan, A. T., Velica, P., et al. (2016). S-2-hydroxyglutarate regulates CD8(+) T-lymphocyte fate. *Nature* 540, 236–241. doi: 10.1038/nature20165

Viswanath, P., Radoul, M., Izquierdo-Garcia, J. L., Luchman, H. A., Gregory Cairncross, J., Pieper, R. O., et al. (2018a). Mutant IDH1 gliomas downregulate phosphocholine and phosphoethanolamine synthesis in a 2-hydroxyglutarate-dependent manner. *Cancer Metab.* 6:3. doi: 10.1186/s40170-018-0178-3

Viswanath, P., Radoul, M., Izquierdo-Garcia, J. L., Ong, W. Q., Luchman, H. A., Cairncross, J. G., et al. (2018b). 2-hydroxyglutarate-mediated autophagy of the endoplasmic reticulum leads to an unusual downregulation of phospholipid biosynthesis in mutant IDH1 gliomas. *Cancer Res.* 78, 2290–2304. doi: 10.1158/0008-5472.Can-17-2926

Waitkus, M. S., Diplas, B. H., and Yan, H. (2018). Biological role and therapeutic potential of IDH mutations in cancer. *Cancer Cell* 34, 186–195. doi: 10.1016/j.ccell.2018.04.011

Wang, H., Wang, L., Zheng, Q., Lu, Z., Chen, Y., Shen, D., et al. (2020). Oncometabolite L-2-hydroxyglurate directly induces vasculogenic mimicry through PHLDB2 in renal cell carcinoma. *Int. J. Cancer* 148, 1743–1755. doi: 10.1002/ijc.33435

Wang, P., Wu, J., Ma, S., Zhang, L., Yao, J., Hoadley, K. A., et al. (2015). Oncometabolite D-2-hydroxyglutarate inhibits ALKBH DNA repair enzymes and sensitizes IDH mutant cells to alkylating agents. *Cell Rep.* 13, 2353–2361. doi: 10.1016/j.celrep.2015.11.029

Wang, Z., Zhang, C., Liu, X., Wang, Z., Sun, L., Li, G., et al. (2016). Molecular and clinical characterization of PD-L1 expression at transcriptional level via 976 samples of brain glioma. *Oncoimmunology* 5:e1196310. doi: 10.1080/2162402X.2016.1196310

Ward, P. S., Patel, J., Wise, D. R., Abdel-Wahab, O., Bennett, B. D., Coller, H. A., et al. (2010). The common feature of leukemia-associated IDH1 and IDH2 mutations is a neomorphic enzyme activity converting alpha-ketoglutarate to 2-hydroxyglutarate. *Cancer Cell* 17, 225–234. doi: 10.1016/j.ccr.2010.01.020

Watanabe, T., Nobusawa, S., Kleihues, P., and Ohgaki, H. (2009). IDH1 mutations are early events in the development of astrocytomas and oligodendrogliomas. *Am. J. Pathol.* 174, 1149–1153. doi: 10.2353/ajpath.2009.080958

Wise, D. R., Ward, P. S., Shay, J. E., Cross, J. R., Gruber, J. J., Sachdeva, U. M., et al. (2011). Hypoxia promotes isocitrate dehydrogenase-dependent carboxylation of alpha-ketoglutarate to citrate to support cell growth and viability. *Proc. Natl. Acad. Sci. U.S.A.* 108, 19611–19616. doi: 10.1073/pnas.1117773108

Xiao, W., and Loscalzo, J. (2020). Metabolic responses to reductive stress. *Antioxid. Redox Signal.* 32, 1330–1347. doi: 10.1089/ars.2019.7803

Xu, T., Stewart, K. M., Wang, X., Liu, K., Xie, M., Ryu, J. K., et al. (2017). Metabolic control of TH17 and induced Treg cell balance by an epigenetic mechanism. *Nature* 548, 228–233. doi: 10.1038/nature23475

Xu, W., Yang, H., Liu, Y., Yang, Y., Wang, P., Kim, S. H., et al. (2011). Oncometabolite 2-hydroxyglutarate is a competitive inhibitor of alpha-ketoglutarate-dependent dioxygenases. *Cancer Cell* 19, 17–30. doi: 10.1016/j.ccr.2010.12.014

Yamada, T., Nabe, S., Toriyama, K., Suzuki, J., Inoue, K., Imai, Y., et al. (2019). Histone H3K27 demethylase negatively controls the memory formation of antigen-stimulated CD8(+) T cells. *J. Immunol.* 202, 1088–1098. doi: 10.4049/jimmunol.1801083

Yan, H., Parsons, D. W., Jin, G., McLendon, R., Rasheed, B. A., Yuan, W., et al. (2009). IDH1 and IDH2 mutations in gliomas. *N. Engl. J. Med.* 360, 765–773. doi: 10.1056/NEJMoa0808710

Yang, M., and Kahn, A. M. (2006). Insulin-stimulated NADH/NAD+ redox state increases NAD(P)H oxidase activity in cultured rat vascular smooth muscle cells. *Am. J. Hypertens.* 19, 587–592. doi: 10.1016/j.amjhyper.2005.11.017

Ye, D., Guan, K. L., and Xiong, Y. (2018). Metabolism, activity, and targeting of D- and L-2-hydroxyglutarates. *Trends Cancer* 4, 151–165. doi: 10.1016/j.trecan.2017.12.005

Yerinde, C., Siegmund, B., Glauben, R., and Weidinger, C. (2019). Metabolic control of epigenetics and its role in CD8(+) T cell differentiation and function. *Front. Immunol.* 10:2718. doi: 10.3389/fimmu.2019.02718

Yu, D., Liu, Y., Zhou, Y., Ruiz-Rodado, V., Larion, M., Xu, G., et al. (2020). Triptolide suppresses IDH1-mutated malignancy via Nrf2-driven glutathione metabolism. *Proc. Natl. Acad. Sci. U.S.A.* 117, 9964–9972. doi: 10.1073/pnas.1913633117

Zhang, L., and Romero, P. (2018). Metabolic control of CD8(+) T cell fate decisions and antitumor immunity. *Trends Mol. Med.* 24, 30–48. doi: 10.1016/j.molmed.2017.11.005

Zhang, L., Sorensen, M. D., Kristensen, B. W., Reifenberger, G., McIntyre, T. M., and Lin, F. (2018). D-2-hydroxyglutarate is an intercellular mediator in IDH-mutant gliomas inhibiting complement and T cells. *Clin. Cancer Res.* 24, 5381–5391. doi: 10.1158/1078-0432.CCR-17-3855

Zhang, X., Rao, A., Sette, P., Deibert, C., Pomerantz, A., Kim, W. J., et al. (2016). IDH mutant gliomas escape natural killer cell immune surveillance by downregulation of NKG2D ligand expression. *Neuro-Oncology* 18, 1402–1412. doi: 10.1093/neuonc/now061

Zhao, G., and Winkler, M. E. (1996). A novel alpha-ketoglutarate reductase activity of the serA-encoded 3-phosphoglycerate dehydrogenase of *Escherichia coli* K-12 and its possible implications for human 2-hydroxyglutaric aciduria. *J. Bacteriol.* 178, 232–239. doi: 10.1128/jb.178.1.232-239.1996

Zhao, S., Lin, Y., Xu, W., Jiang, W., Zha, Z., Wang, P., et al. (2009). Glioma-derived mutations in IDH1 dominantly inhibit IDH1 catalytic activity and induce HIF-1alpha. *Science* 324, 261–265. doi: 10.1126/science.1170944

Conflict of Interest: The authors declare that the research was conducted in the absence of any commercial or financial relationships that could be construed as a potential conflict of interest.

frontiers in Cell and Developmental Biology

ORIGINAL RESEARCH
published: 16 April 2021
doi: 10.3389/fcell.2021.673827

Expression of Lipid-Metabolism Genes Is Correlated With Immune Microenvironment and Predicts Prognosis in Osteosarcoma

Hu Qian[1†], Ting Lei[1†], Yihe Hu[1,2,3] and Pengfei Lei[1,2*]*

[1] Department of Orthopeadic Surgery, Xiangya Hospital Central South University, Changsha, China, [2] Hunan Engineering Research Center of Biomedical Metal and Ceramic Implants, Changsha, China, [3] Department of Sports Medicine, Xiangya Hospital Central South University, Changsha, China

OPEN ACCESS

Edited by:
Yongbin Chen,
Kunming Institute of Zoology (CAS), China

Reviewed by:
Zongqiang Huang,
First Affiliated Hospital of Zhengzhou University, China
Jianhua Zhou,
Central South University, China
Qianjin Liao,
Central South University, China

***Correspondence:**
Yihe Hu
csuhuyihe@163.com
Pengfei Lei
pengfeilei@csu.edu.cn

[†] These authors have contributed equally to this work and share first authorship

Specialty section:
This article was submitted to Molecular and Cellular Oncology, a section of the journal Frontiers in Cell and Developmental Biology

Received: 28 February 2021
Accepted: 30 March 2021
Published: 16 April 2021

Citation:
Qian H, Lei T, Hu Y and Lei P (2021) Expression of Lipid-Metabolism Genes Is Correlated With Immune Microenvironment and Predicts Prognosis in Osteosarcoma. Front. Cell Dev. Biol. 9:673827. doi: 10.3389/fcell.2021.673827

Objectives: Osteosarcoma was the most popular primary malignant tumor in children and adolescent, and the 5-year survival of osteosarcoma patients gained no substantial improvement over the past 35 years. This study aims to explore the role of lipid metabolism in the development and diagnosis of osteosarcoma.

Methods: Clinical information and corresponding RNA data of osteosarcoma patients were downloaded from TRGET and GEO databases. Consensus clustering was performed to identify new molecular subgroups. ESTIMATE, TIMER and ssGSEA analyses were applied to determinate the tumor immune microenvironment (TIME) and immune status of the identified subgroups. Functional analyses including GO, KEGG, GSVA and GSEA analyses were conducted to elucidate the underlying mechanisms. Prognostic risk model was constructed using LASSO algorithm and multivariate Cox regression analysis.

Results: Two molecular subgroups with significantly different survival were identified. Better prognosis was associated with high immune score, low tumor purity, high abundance of immune infiltrating cells and relatively high immune status. GO and KEGG analyses revealed that the DEGs between the two subgroups were mainly enriched in immune- and bone remodeling-associated pathways. GSVA and GSEA analyses indicated that, lipid catabolism downregulation and lipid hydroxylation upregulation may impede the bone remodeling and development of immune system. Risk model based on lipid metabolism related genes (LMRGs) showed potent potential for survival prediction in osteosarcoma. Nomogram integrating risk model and clinical characteristics could predict the prognosis of osteosarcoma patients accurately.

Conclusion: Expression of lipid-metabolism genes is correlated with immune microenvironment of osteosarcoma patients and could be applied to predict the prognosis of in osteosarcoma accurately.

Keywords: osteosarcoma, lipid metabolism, immune microenvironment, prognosis, individualized therapy

BACKGROUND

Osteosarcoma is the most common primary malignant bone tumor in children and adolescent, which is characterized by poor prognosis and high metastasis rate (Niu et al., 2020; Song et al., 2020). The incidence of osteosarcoma is related with the age of patients, which is about 0.0004% in individuals younger than 25 years old or older than 59 years old, while 0.0001% in individuals aged 25–59 years old (Whelan and Davis, 2018). It is worth noting that 15–20% patients had lung metastasis when they were first diagnosed with osteosarcoma (Miller et al., 2013). The 5-year survival rate of osteosarcoma patients with or without lung metastasis is 60–70%, and 20%, respectively, which has remained stagnant over the past 35 years and is far from satisfaction (Kansara et al., 2014; Negri et al., 2019).

Tracing back to the source, the main reason for the poor prognosis in osteosarcoma is the high extent of tumor heterogeneity caused by significant genomic instability (Whelan and Davis, 2018; Wang et al., 2019). Thus, it is necessary to develop a risk stratification method and identify prognostic genes for personalized targeted therapy of osteosarcoma patients.

Recently, lipid metabolism reprogramming has been regarded as a novel hallmark of tumor malignancy (Cheng et al., 2018), and increasing evidences from clinical and laboratory studies have revealed that lipid metabolism disorder plays a pivotal role in tumorigenesis, tumor progression and treatment (Corbet and Feron, 2017; Luo et al., 2017; Cao, 2019). Niemi et al. (2018) demonstrated that aberrant lipid metabolism in ovarian cancer intensified with increasing stage. Su et al. (2020) reported that enhanced lipid metabolism was necessary for the initiation and differentiation of tumor-associated macrophages. Hilvo et al. (2011) demonstrated that the lipids in the breast cancer tissue were correlated with tumor progression and patient survival. Moreover, previous studies have demonstrated that lipid metabolism related genes (LMRGs) had potent prognostic potential in multiple types of tumors, including ovarian carcinomas (Zheng et al., 2020), lung adenocarcinoma (LAUD) (Li et al., 2020), pancreatic cancer (Ye et al., 2021), hepatocellular carcinoma (HCC) (Hu et al., 2020), renal cell carcinoma (RCC) (Bao et al., 2019) and diffuse gliomas (Wu et al., 2019). As such, targeting lipid metabolism has been regarded as a novel therapeutic strategy for tumor treatment (Visweswaran et al., 2020). Construction of prognostic risk model was an applicable strategy to evaluate the prognostic performance. Up to now, several risk models have been constructed to explore the prognostic value of genes associated with tumor microenvironment, immune cell infiltrating and energy metabolism (Chen Y. et al., 2020; Wen et al., 2020; Zhang et al., 2020; Zhu et al., 2020) in osteosarcoma, whereas the role of LMRGs in osteosarcoma has remained poorly understood.

Tumor immune microenvironment (TIME), which reflexed the immune landscape in the tumor microenvironment, was essential for the initiation and development of tumors (Binnewies et al., 2018). Immune cells take part in the cell reprogramming critically, during which the microenvironment of the tumor cells was modified meticulously by themselves through secreting various kinds of biological factors, thereby endowing surrounding cells with powers to determine the survival and progression of tumors (Hinshaw and Shevde, 2019). In tumor microenvironment, tumor infiltrating immune cells account for the primary non-tumor constituents, which have been demonstrated to play an important role in prognostic prediction of OS patients (Zhang et al., 2020). Thus, TIME takes crucial significance in the development and progression of tumor, and accumulated evidence revealed that TIME was closely associated with pathogenesis of osteosarcoma (Heymann et al., 2019; Luo et al., 2020). Assessing the TIME of osteosarcoma helps to understand the immune status of tumor cells, is conducive to promote the development of immunotherapy and improve the prognosis of osteosarcoma patients.

In the present study, we comprehensively analyzed LMRGs to explore the effect of lipid metabolism on the TIME and survival of osteosarcoma patients. Moreover, we constructed a LMRGs-based risk score model to evaluate the prognostic value of LMRGs in osteosarcoma. Our work may provide a new clue for exploring the underlying molecular mechanisms of osteosarcoma, shed a novel light on the targeting therapy strategy of osteosarcoma and promote the individual-based treatment of osteosarcoma patients.

MATERIALS AND METHODS

Data Collection

Clinical information and sequencing RNA data were downloaded from the Therapeutically Applicable Research To Generate Effective Treatments (TARGET[1]) and Gene Expression Omnibus (GEO[2]) databases. The inclusion criteria were as follows: (a) samples diagnosed as osteosarcoma; (b) samples with mapped clinical information and gene expression matrix; (c) samples with complete clinical information including survival time, survival status, age and sex at least; (d) only one was included if there were paired samples. The exclusion criteria were as follows: (a) normal tissue samples; (b) samples without complete clinical information; (c) samples with no expression value in over half of the genes; (d) samples with bias in expressional value. Ninety three samples acquired from the TARGET database were defined as the training cohort. Seventy samples acquired from GEO databases (GSE21257 and GSE39058) were included and defined as verification cohort after integrating. The demographic data and clinical features of the training cohort and validation cohort were listed in **Table 1**. Datasets of 776 LMRGs were obtained from the Reactome and KEGG databases.

Identification of Molecular Subgroups and TIME Evaluation

Firstly, 74 genes were found to be associated with the prognosis of osteosarcoma through the univariate Cox regression

[1]https://ocg.cancer.gov/programs/target

[2]https://www.ncbi.nlm.nih.gov/geo/

TABLE 1 | Characteristics of patients in the training and validation cohort.

	Training cohort (*n* = 93)	Validation cohort (*n* = 70)	*P*-value
	n/%	n/%	
Age			0.6115
<18 years	71/76.3	51/72.9	
>=18 years	22/30.1	19//27.1	
Sex			0.6649
Female	39/41.9	27/38.6	
Male	54/58.1	43/61.4	
Survival status			0.4311
Alive	55	47	
Dead	35	23	
Histologic response			0.0850
Stage 1/2	16	23	
Stage 3/4	27	16	
NA	47	31	
Race			
White	55	NA	
Asian	6	NA	
Black or African American	9	NA	
NA	20	NA	

NA, not available.

analysis. Consensus clustering was performed according to the expression matric of the 74 genes using the R package "ConsensusClusterPlus." Stromal score, immune score, and tumor purity were calculated using the Estimation of Stromal and Immune cells in Malignant Tumor tissues using Expression data (ESTIMATE) algorithm (Yoshihara et al., 2013).

Immune Analyses

TIMER immune infiltrating analysis[3] was performed to calculate the abundance of six immune infiltrating cells (B cell, Macrophage cell, Dendritic cell, Neutrophil cell, CD4 T cell and CD8 T cell). Datasets including 28 types of immune infiltrating cells and related 782 genes were obtained from molecular signature database[4], and the enrichment of the 28 immune infiltrating cells in the tumor samples were assessed using single sample gene set enrichment analysis (ssGSEA).

Functional Analyses

Differentially expressed genes (DEGs) between the two clusters were identified using R package "Limma." Gene Ontology (GO) analysis and Kyoto Encyclopedia of Genes and Genomes (KEGG) analysis were performed using "clusterProfiler" R package to enrich associated pathways, which was visualized in Metascape[5]. Based on "GO biological process" gene set downloaded from molecular signature database (see text footnote 5), Gene set variation analysis (GSVA) was performed to demonstrate the signaling pathways alteration between the two clusters using the "GSVA" R package. Meanwhile, according to the same dataset, Gene Set Enrichment Analysis (GSEA) was conducted to analyze the difference between clusters.

Establishment and Validation of Risk Model

Least absolute shrinkage and selection operator (LASSO) analysis was conducted to downsize the prognostic genes previously filtrated using "glmnet" R package. The minimum lambda was defined as the optimal value. The genes used for establishment of risk model was determined by multivariate Cox regression analysis. Risk score of each patient in the training and verification cohorts was calculated as: risk score = 1.7063 × expression value of *ALOX15B* + 0.7626 × expression value of *ME1* + 0.6200 × expression value of *GPD1*, and patients were divided into high risk and low risk groups according to the medium value. ROC and Martingale residuals method were performed to assess the predictive efficiency of the model. The whole process of data analysis was depicted in **Figure 1**.

Statistical Analyses

Statistical analyses were performed via R (version 3.6.1) and GraphPad Prism (version 8.0.1), and visualization was conducted via TBtools (Chen C. et al., 2020). Survival analysis was completed using Kaplan–Meier method, and the prediction performance of the risk model was evaluated using time-dependent receiver operating characteristic (ROC) via "survivalROC" R package. Subgroup analysis was carried out when the patients were regrouped according to age, sex, lesion site and metastasis. Discontinuous data was presented as number/percentages while continuous data was shown in the form of mean ± standard deviation (SD). Student's *t*-test was used for statistical analysis between two groups, and one-way ANOVA analysis was selected flexibly when there were three or more groups. A $P < 0.05$ was defined as statistically significant difference.

RESULTS

Identification of Two Molecular Subtypes Based on LMRGs

The consensus clustering approach was conducted to divide the osteosarcoma patients in the training cohort into subgroups based on 74 prognostic genes generated from univariable Cox analysis (**Supplementary Table 1**). The optimal clustering stability was identified when K = 2 (**Figures 2A–C** and **Supplementary Figure 1**). 51 patients were clustered into cluster 1 and 42 patients were clustered into cluster 2. The expression level of the LMRGs in the two subtypes was visualized through the heatmap (**Figure 2D**), and obvious expression difference was found between cluster 1 and cluster 2. Moreover, patients in the cluster 2 enjoyed better overall survival than patients in the cluster 1 ($P = 0.0069$; **Figure 2E**). These results demonstrated that the LMRGs classify the osteosarcoma patients into two molecular subtypes with different overall survival.

[3]https://cistrome.shinyapps.io/timer/

[4]https://www.gseamsigdb.org/gsea/msigdb/index.jsp

[5]https://metascape.org

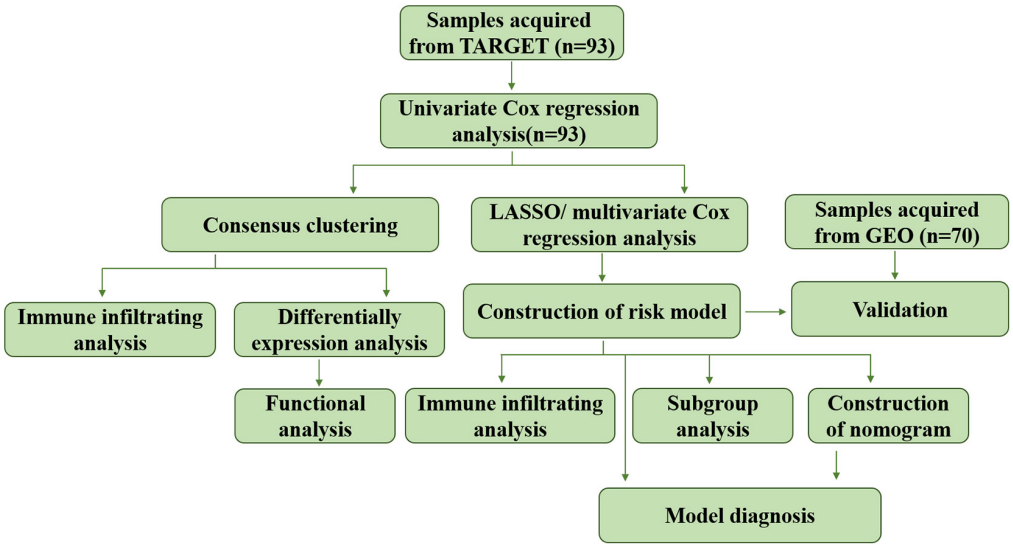

FIGURE 1 | Flow chart of the data analyzing process.

Patients in the Two Molecular Subtypes Exhibited Different TIME and Immune Status

Next, we performed immune analyses to explore the immune difference between the two molecular subtypes. ESTIMATE algorithm revealed that osteosarcoma patients in the cluster 2 had significantly higher immune score ($P < 0.0001$), ESTIMATE score ($P = 0.0008$) and lower tumor purity ($P = 0.0013$) compared with cluster 1, with no significant difference found in stromal score ($P = 0.1916$; **Figures 3A–D**). In addition, TIMER algorithm indicated that the abundance of B cell ($P = 0.0010$), macrophage ($P = 0.0036$), dendritic cell ($P < 0.0001$) and T cell.CD4 ($P = 0.0022$) in cluster 2 was significantly higher than cluster 1, while the abundance of neutrophil was significantly higher in cluster 1 ($P = 0.0004$), and no statistical significance was detected with respect to T cell.CD8 ($P = 0.6407$; **Figure 3E**). Moreover, as illustrated in the heatmap (**Figure 3F**), immune landscape made by ssGSEA algorithm differed significantly between cluster 1 and cluster 2, with a relatively low immune status in cluster 1. Besides, statistical analysis demonstrated that except for eosinophils, mast cell, neutrophil and memory B cell, the other 24 types of cells were significantly higher in cluster 2 than those in cluster 1 (**Figure 3G**). These results demonstrated that the TIME and immune status of the two molecular subtypes differed significantly.

DEG and Functional Analyses

DEGs between the two clusters were identified and functional analyses were performed to explore the underlying signaling mechanisms. A total of 198 DEGs were detected, of which 58 genes were downregulated and 140 genes were upregulated in cluster 2, as compared with cluster 1 (**Figure 4A**). GO enrichment analysis revealed that the DEGs were enriched in bone remodeling- and immune-related biological processes, including bone remodeling, bone resorption, antigen processing and presentation, immune cell differentiation and activation (**Figures 4B,C**). Meanwhile, some crucial molecular functions and cellular components were also enriched (**Supplementary Figure 2**). Similarly, KEGG enrichment analysis also identified some signaling pathways associated with bone remodeling and immune, including osteoclast differentiation, natural killer cell mediated cytotoxicity, and complement and coagulation cascade (**Figure 4D**). PPI analysis identified four sub- models, all of which were closely associated with tumor development and immunity, indicating that immune may be associated with the contribution of lipid metabolism to osteosarcoma (**Figure 4E**). To further explore the relationship between the enriched pathways and the prognosis of osteosarcoma patients, we performed GSVA and GSEA analyses to evaluate the relative expression difference of the pathways in the two clusters. GSVA analysis enriched a lot of differentially expressed pathways, which was visualized by the heatmap (**Figure 4F**). In comparison to cluster 2, the expression of pathways associated with immune, bone remodeling and lipid catabolic process were significantly lower in the cluster 1, whereas the expression of lipid hydroxylation associated pathways were significantly higher. Consistently, GSEA analysis revealed that leukocyte differentiation, myeloid leukocyte differentiation and osteoclast differentiation expressed lowly in cluster 1 (**Figures 4G–I**). All these results demonstrated that expression of LMRG was correlated with dysregulation of immune and bone remodeling, which may be involved in the poor prognosis of osteosarcoma patients.

Development of Risk Model Based on LMRG in the Training Cohort

Then, a risk signature model was constructed to assess the prognostic prediction value of LMRGs in osteosarcoma. LASSO analysis was conducted to screen potential genes for establishing

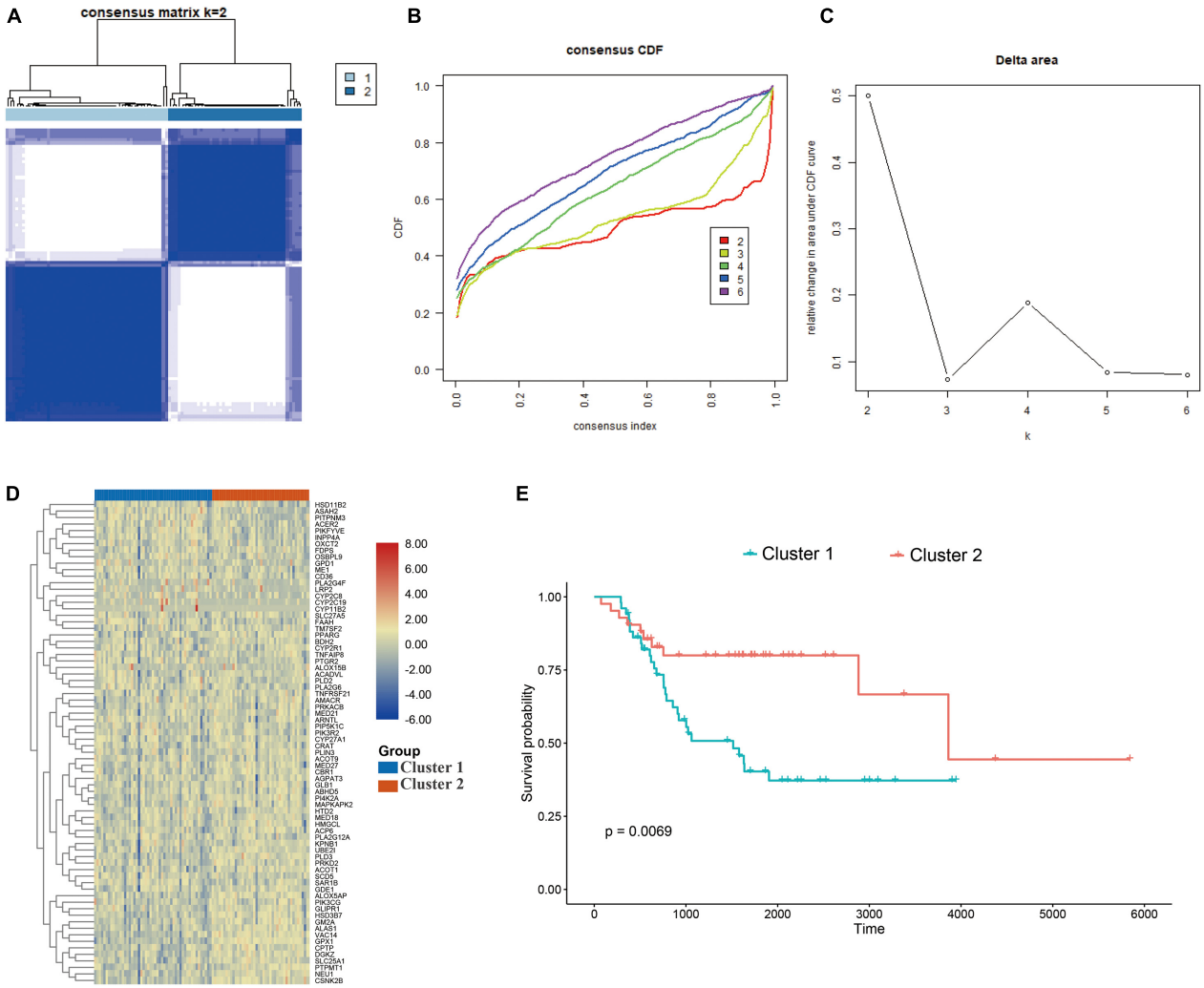

FIGURE 2 | Consensus cluster. **(A–C)** *K* = 2 was identified the optimal value for consensus clustering, **(D)** heatmap visualizing the expression of lipid metabolism gens in the two subgroups, **(E)** survival curve of the patients in the two subgroups.

risk model, and 24 genes were filtered with optimal lambda value (**Figure 5A**). Based on the genes generated from LASSO analysis, multivariate Cox analysis identified three genes, *ME1*, *GPD1,* and *ALOX15B*, to construct the risk model. All of the three genes were risk genes with a hazard ratio of over 1, and Kaplan–Meier analysis demonstrated that all of these genes were independently prognostic marker of osteosarcoma patients (**Supplementary Figure 3**). The established risk model successfully classified the osteosarcoma patients into high risk and low risk groups (**Figure 5B**). As shown in **Figure 5C**, patients in the high risk group trended to expressed the three candidate genes higher than those in the low risk group. Patients in the low risk group had a better overall survival than those in the high risk group (**Figure 5D**). Regarding the model diagnosis of the risk model, ROC curve (**Figure 5E**) and residual plot (**Supplementary Figure 4**) showed acceptable assessment result. Time dependent ROC analysis indicated that the constructed risk model exhibited precise predictive capacity over a period of 5 years, and the area under curve (AUC) of the ROC curve for 1, 3, and 5 years was 0.701, 0.707, and 0.719, respectively (**Figure 5E**). Finally, ESTIMATE algorithm was performed to evaluate the TIME of the two groups, and the result revealed that compared with the high risk group, the stromal score (P = 0.0298), immune score (0.0156), ESTIMATE score (P = 0.0101) were significantly higher in the low risk group (**Figures 5F–H**), while the tumor purity was significantly lower (**Figure 5I**). These results suggested that the constructed risk model possessed potent potential for prognosis prediction of osteosarcoma patients, and it was significantly correlated with TIME in osteosarcoma.

Independence of the Constructed Risk Model

Furthermore, we explored the association between the risk score and clinical features, and evaluated the independence of the constructed risk model via subgroup analysis and regression

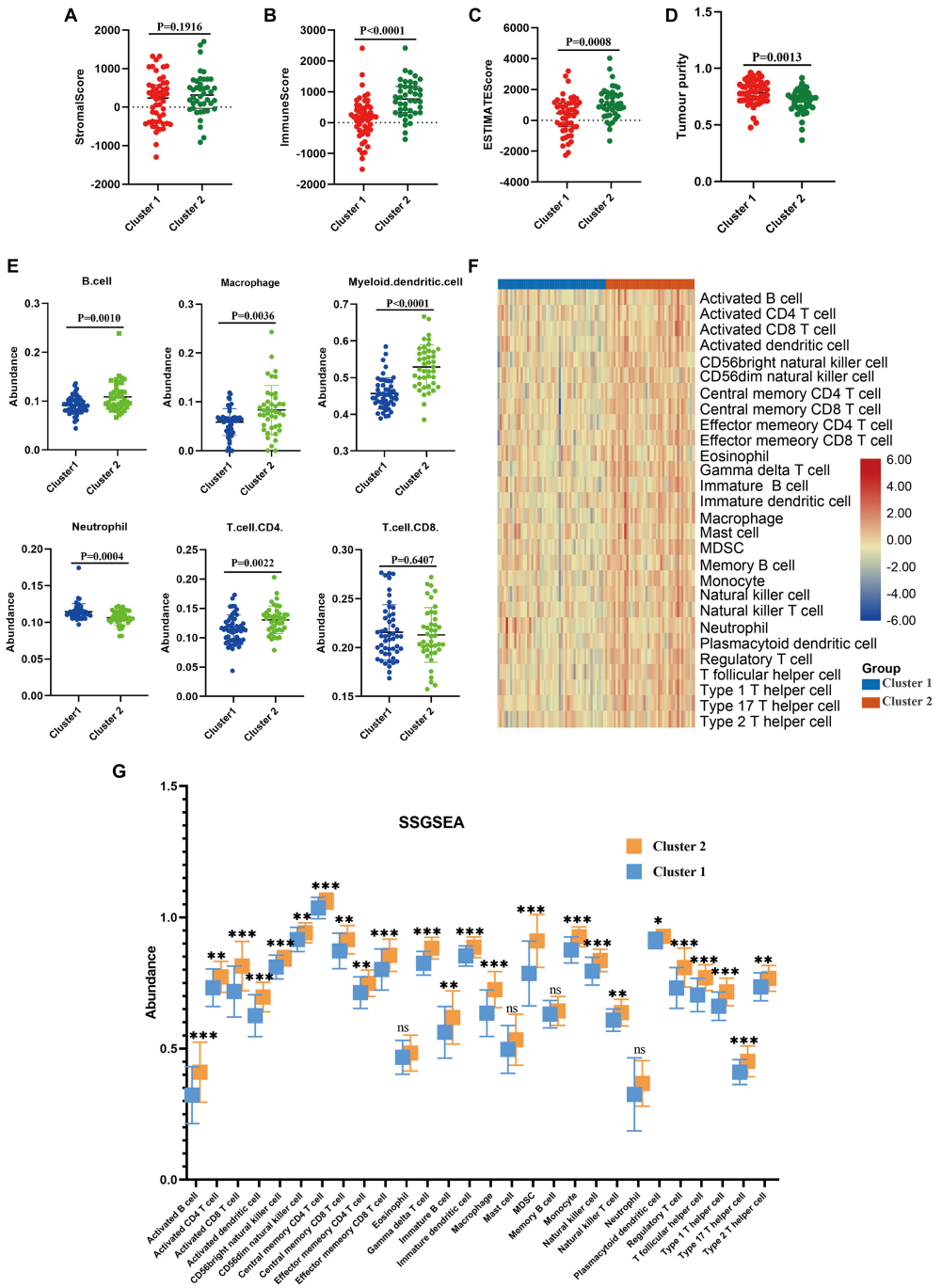

FIGURE 3 | Immune analyses in the two clustered subgroups. **(A)** stromal score, **(B)** immune score, **(C)** ESTIMATE score and **(D)** tumor purity calculated by ESTIMATE algorithm, **(E)** abundance of six immune filtrating cells evaluated by TIMER, **(F)** heatmap depicting the enriching level of 29 immune related cells evaluated by ssGSEA algorithm, **(G)** statistical analysis of ssGSEA. *$p < 0.05$; **$p < 0.01$; ***$p < 0.001$.

analyses. No significant difference was detected between patients with different age (**Figure 6A**), sex (**Figure 6B**), lesion site (**Figure 6C**) and metastasis status (**Figure 6D**) regarding risk score, indicating that there was no association between risk score and clinical characteristics (**Figures 6A–D**). Besides, when the patients were regrouped according to age (**Figure 6E**), sex (**Figure 6F**), and metastasis status (**Figure 6G**), the risk model still exhibited potent predictive performance and those patients with lower risk score enjoyed better prognosis. Moreover, univariate/multivariate Cox regression analyses revealed that the constructed risk model was independent predictive marker of the prognosis of osteosarcoma patients (**Tables 2**, **3**). These results

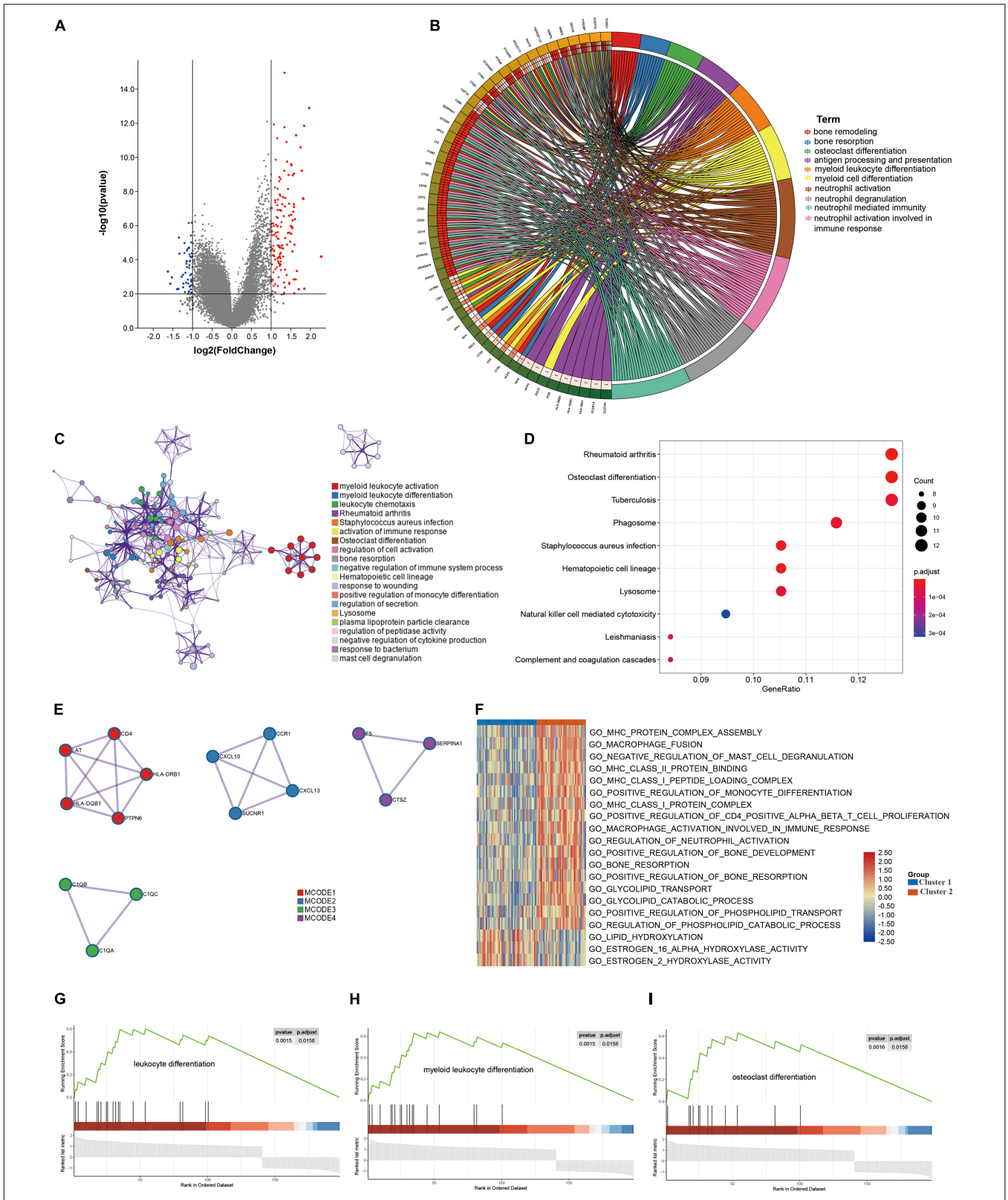

FIGURE 4 | Differentially expressed genes (DEGs) analysis and functional analyses. **(A)** Volcano plot showing the DEGs between the two subgroups, **(B,C)** circle plot and network visualizing the biological processes enriched by gene ontology (GO) analysis, **(D)** bubble diagram showing the signaling pathways enriched by Kyoto Encyclopedia of Genes and Genomes (KEGG) analysis, **(E)** PPI analysis of DEGs, **(F)** heatmap illustrating the result of GSVA analysis, **(G–I)** GSEA plots visualizing the result of GSEA analysis.

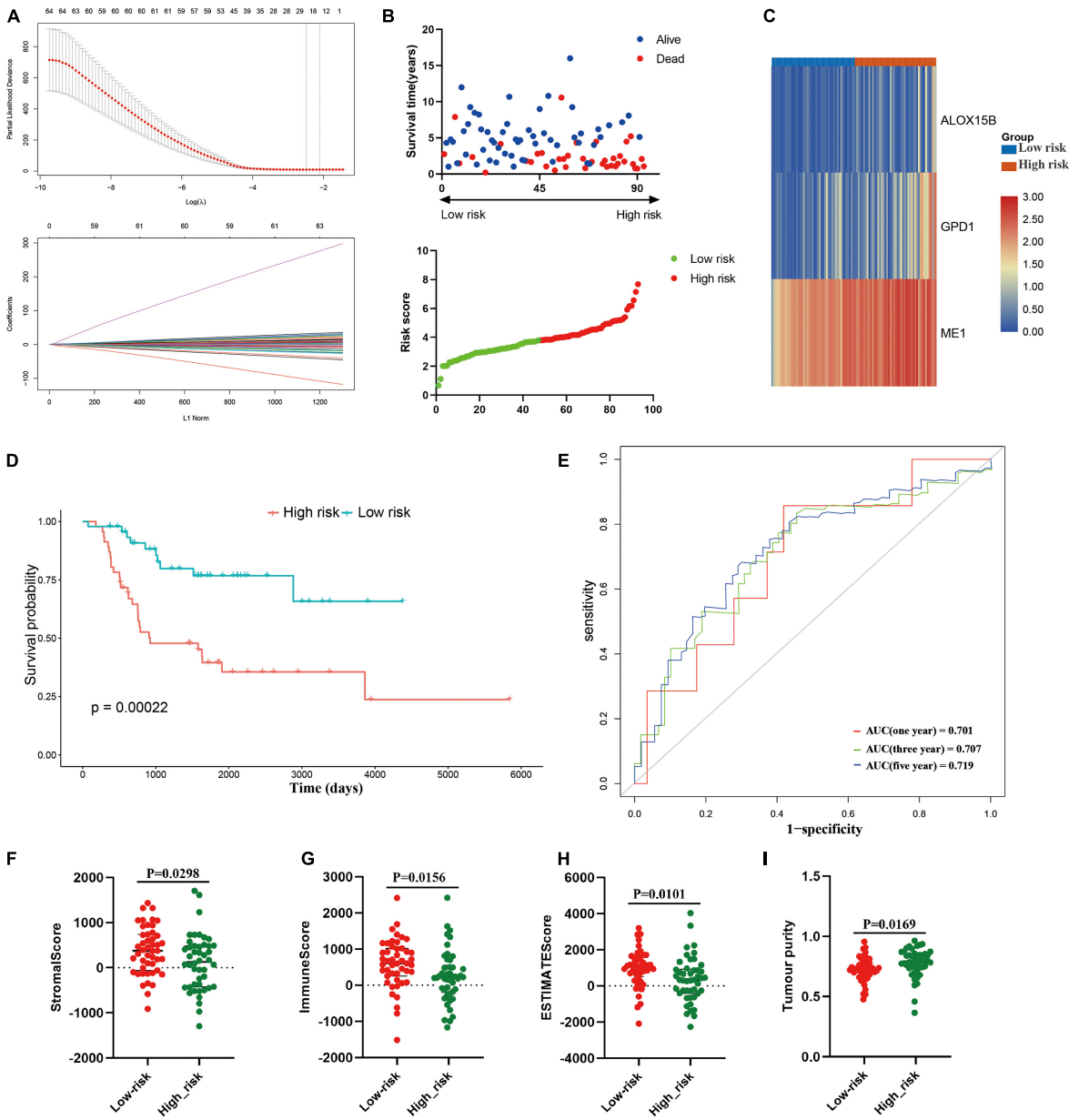

FIGURE 5 | Construction of risk model in the training cohort. **(A)** LASSO analysis with minimal lambda, **(B)** distribution of survival status and risk score of osteosarcoma patients in the high and low risk groups, **(C)** heatmap illustrating the expression of the three candidate genes in the two groups, **(D)** survival curve of the osteosarcoma patients in the two groups, **(E)** time-dependent ROC curve of the risk model, **(F–I)** stomal score, immune score, ESTIMATE score and tumor purity calculated by ESTIMATE algorithm.

demonstrated that the constructed risk model had excellent independence in predicting the prognosis in osteosarcoma.

Risk Model Was Correlated With TIME and Prognosis in Osteosarcoma in the Verification Cohort

Thereafter, we further validate the established prognostic risk score model in the verification cohort. According to above-mentioned formula, the osteosarcoma patients in the verification cohort were stratified into high risk or low risk groups (**Figure 7A**). The expression of the three candidate genes were shown via the heatmap (**Figure 7B**). Survival analysis revealed that patients in the high risk group had poorer prognosis (P = 0.021; **Figure 7C**). ROC analysis indicated that the risk model exhibited the best prediction accuracy in predicting 3-year survival (**Figure 7D**). We also explore the association between the risk model and TIME. Same to the training cohort, in comparison to the high risk group, the stromal score ($P < 0.05$), immune score ($P < 0.001$), ESTIMATE score ($P < 0.05$) were significantly

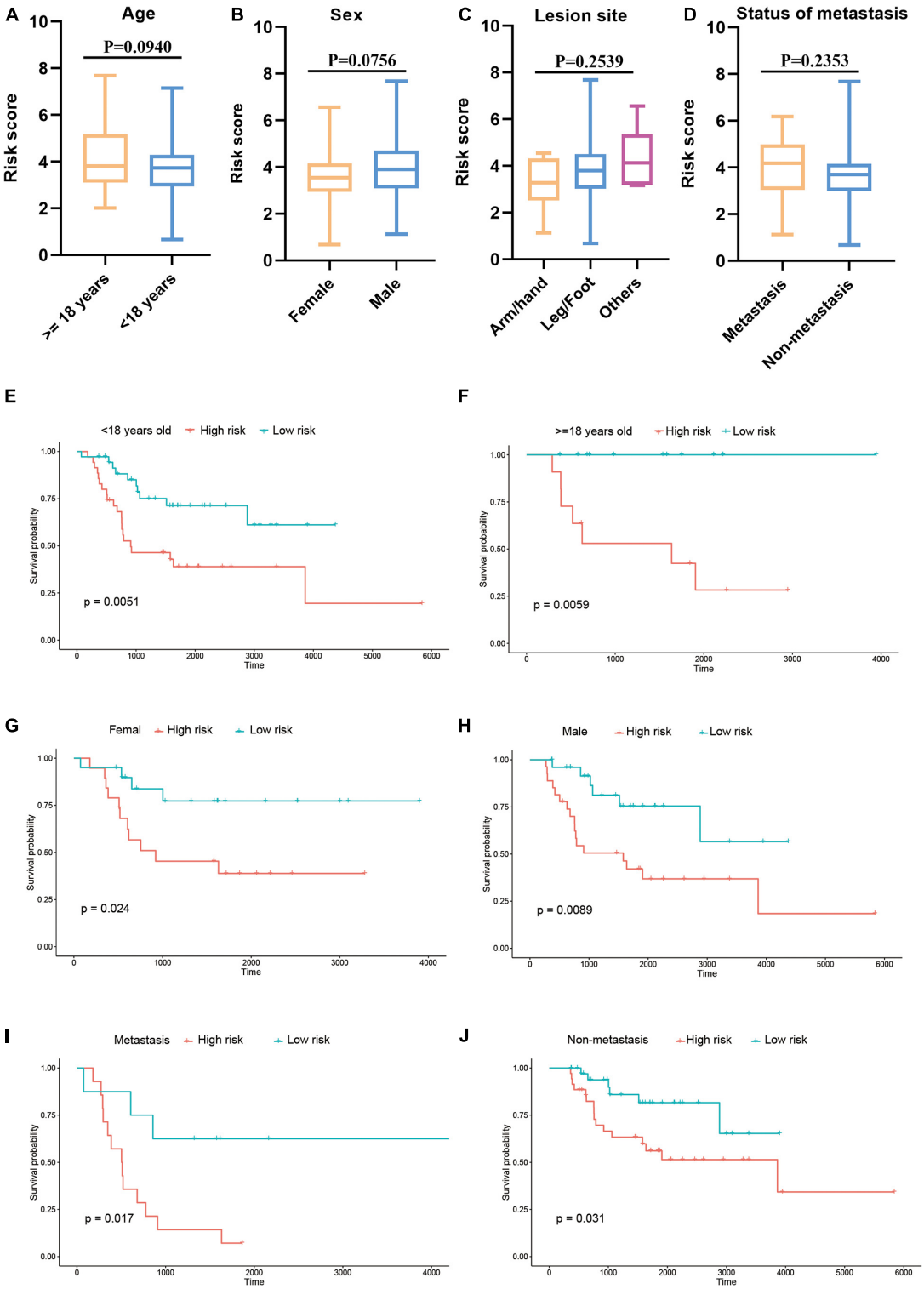

FIGURE 6 | Association of risk score and clinical characteristics **(A–D)**. No significant difference was identified in patients with different age **(A)**, sex **(B)**, lesion site **(C)** and metastasis status **(D)**. Independence analysis of the risk model **(E–J)**. Survival curve of patients regrouped according to age **(E,F)**, sex **(G,H)**, and metastasis **(I,J)**.

TABLE 2 | Univariate analysis of risk score and characteristics in training cohort.

Variates	Coefficient	HR	HR 95%CI (lower)	HR 95%CI (upper)	*p*-value
Risk score	0.52465566	1.68987686	1.309302499	2.1810726	5.58E−05
Sex	−0.0203184	0.97988661	0.510247494	1.8817883	0.951337
Age	−0.0233226	0.97694732	0.914836448	1.0432751	0.486496
Metastasis	1.33251557	3.79056685	1.978018385	7.2640361	5.94E−05
lesion site	1.36256868	3.90621424	1.225603012	12.449798	0.021226

HR, hazard ratio; CI, confidence interval.

TABLE 3 | Multivariate analysis of risk score and characteristics in training cohort.

Variates	Coefficient	HR	HR 95%CI (lower)	HR 95%CI (upper)	*p*-value
Risk score	0.554978	1.741903	1.324072765	2.29158578	7.31E−05
Sex	−0.16642	0.846691	0.426467921	1.680985208	0.63435
Age	−0.01876	0.981413	0.910831832	1.057463256	0.622222
Metastasis	1.4284	4.17202	2.090665046	8.325459388	5.08E−05
Lesion site	0.877566	2.405038	0.902139129	6.411659127	0.079412

higher in the low risk group (**Figures 7E–G**), while the tumor purity was significantly lower ($P < 0.01$; **Figure 7H**). These results demonstrated that the established risk model was correlated with TIME and prognosis in osteosarcoma in the verification cohort.

Construction and Calibration of an Integrated Monogram

Finally, a nomogram integrating the risk model and clinical features were constructed to predict the prognosis of the osteosarcoma patients more precisely. The constructed nomogram was shown in **Figure 8A**, risk score and pathological characteristics were endowed a specific score basing on their contribution on the prognosis in osteosarcoma. Then we validated the nomogram in the training and verification cohort. In terms of the model diagnosis of the nomogram, C-index, the calibration curve (**Figures 8B–D**) and decision curve analysis (**Supplementary Figure 5**) suggested the acceptable accuracy. The C-index for the nomogram in the training cohort reached 0.7520 (95%CI: 0.7078–0.7962). The observed overall survival matched well with the actual survival at 3 and 5 years in the training cohort (**Figures 8B,C**), and similar result was also observed in the verification cohort (**Figures 8D,E**). These results demonstrated that the integrated nomogram could predict the prognosis of osteosarcoma patients accurately.

All of these findings revealed that lipid metabolism dysregulation may lead to disorder of TIME and bone remodeling, resulting in poor prognosis. The constructed risk model based on LMRGs could predict the prognosis of osteosarcoma patients reliably and accurately.

DISCUSSION

Osteosarcoma was the most common primary malignant tumor of bone in children and adolescent (Niu et al., 2020). Despite of the booming development of multiple treatment strategy, the 5-year survival of osteosarcoma patients has remained stagnant over the past 35 years, and it is urgent to develop effective risk stratification approach and individualized targeting treatment strategy (Kansara et al., 2014; Negri et al., 2019). In the present study, we identified two molecular subtypes, which exhibited significantly different lipid metabolism landscapes. Immune analyses indicated that patients with poor prognosis were in relatively low immune status, and possessed lower immune score and ESTIMATE score whereas higher tumor purity, as compared with patients with better prognosis. Further functional analyses revealed that upregulation of lipid hydroxylation was implicated with poor immunity and bone remodeling. Moreover, we established a prognostic risk model based on LMRGs, which predicted the prognosis of osteosarcoma patients precisely. Our results may facilitate the development of targeting therapy for osteosarcoma and help the clinicians to make more rational treatment decisions.

Consensus clustering was a reliable approach to classified samples into different subgroups based on the gene expression matrix. According to the LMRGs expression matrix of osteosarcoma patients, firstly, we identified two molecular subgroups via consensus clustering, which also had significantly different overall survival. Then immune and function analyses were performed to explore the role of lipid metabolism in osteosarcoma successively.

As mentioned previously, TIME plays a crucial role in the prognosis of patients, since tumor progression is associated with the modification of the surrounding stroma, with immune cells being the pivotal components of tumor stroma (Hinshaw and Shevde, 2019). In addition, aberrant metabolism status of tumor cells would result in metabolic variation of TIME. ESTIMATE algorithm was an innovative method to infer the tumor purity, as well as the fraction of immune and stromal cells in tumor according to gene expression value (Yoshihara et al., 2013). Immune scores generated from ESTIMATE algorithm displayed immune components in tumor samples quantitatively, reflecting the TIME. Tumor purity was defined as the proportion of malignant cells in tumor tissue, which was closely correlated

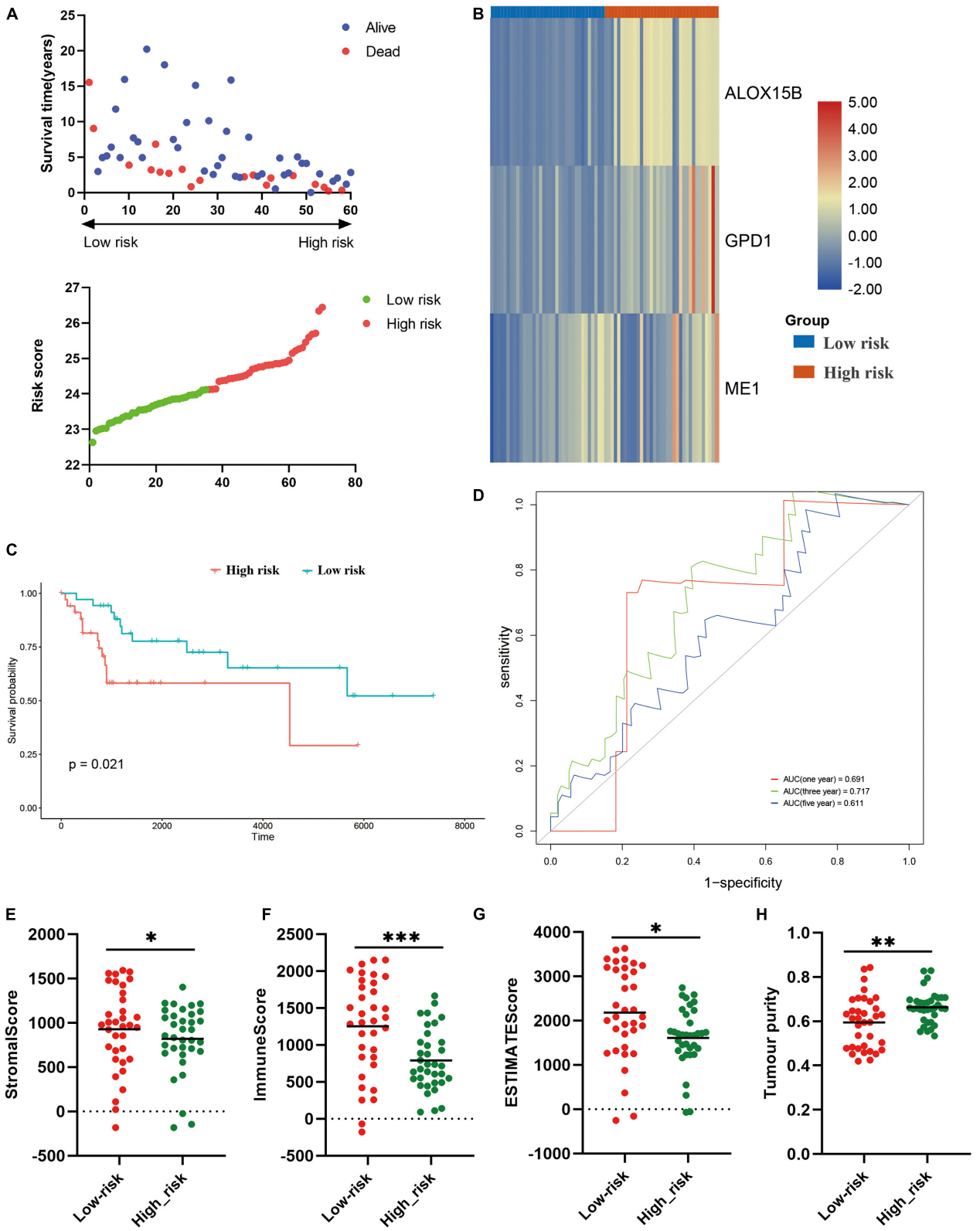

FIGURE 7 | Validation of the constructed risk model in the verification cohort. **(A)** distribution of survival status and risk score, **(B)** heatmap illustrating the expression of three candidate genes in the verification cohort, **(C)** survival curve of the patients in the high and low risk groups in the verification cohort, **(D)** ROC curve of the risk model in the verification cohort, **(E–H)** stromal score, immune score, ESTIMATE score and tumor purity calculated by ESTIMATE algorithm. $^{*}p < 0.05$; $^{**}p < 0.01$; $^{***}p < 0.001$.

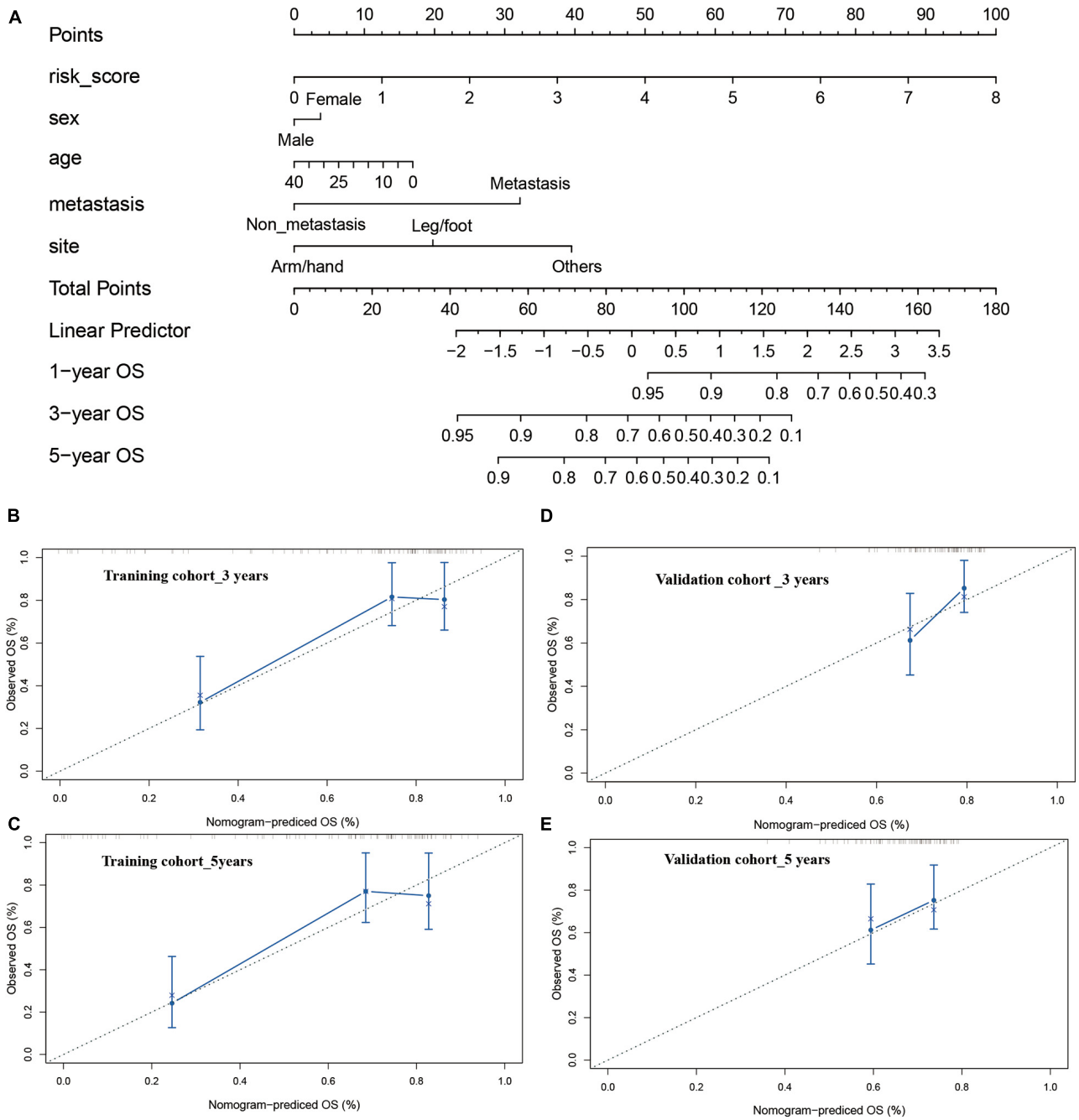

FIGURE 8 | Construction and calibration of nomogram. **(A)** nomogram integrating risk score and clinical features, **(B,C)** calibration of the nomogram at 3 and 5 years in the training cohort, **(D,E)** calibration of the nomogram at 3 and 5 years in the verification cohort.

with prognosis (Yoshihara et al., 2013; Aran et al., 2015; Li et al., 2017). Previously, Hong et al. (2020) and Zhang et al. (2020) have demonstrated that high immune score and low tumor purity were linked with poor prognosis in osteosarcoma. Therefore, we applied ESTIMATE to determinate the TIME of the two subgroups. Our result indicated that these patients with better prognosis had higher immune score and lower purity, which was consistent with previous reports. Furthermore, we applied another two methods, TIMER and ssGSEA, to assess the immune status of the two molecular subgroups. TIMER was a web tool which facilitated the quantification of six tumor-infiltrating immune subsets (Li et al., 2017). TIMER analysis revealed that the abundance of five out of six immune cells was significantly lower in the cluster 1, which was in concert with the result of ESTIMATE and indicated that the immune landscape was downregulated in cluster 1. The ssGSEA analysis outlined the

abundance of 29 immune-related cells, and the result suggested that patients in cluster 1 were in relatively low immune status, further confirming the result of ESTIMATE and TIMER. Taken together, we could assume that low immune score and immune status were implicated with unfavorable prognosis reasonably.

Next, functional analyses between the two subgroups were conducted to explore the underlying biological mechanisms. Based on the identified DEGs, GO analysis, KEGG analysis and PPI analysis synergistically suggested that dysregulation of immunity and bone remodeling may mediate the role of lipid metabolism on the tumorigenesis and progression of osteosarcoma. However, the detailed relationship between lipid metabolism and aberrant immunity and bone remodeling remained unclear. Therefore, we performed GSVA and GSEA analyses to further elucidate the underlying mechanisms. Through GSVA, the activity of signaling pathways in each sample was calculated according to the gene expression level, and the variation over different groups could be estimated (Hänzelmann et al., 2013). The GSVA heatmap result revealed that the activity of lipid catabolism, bone remodeling, immune system development and activation was impeded in cluster 1, whereas lipid hydroxylation was enhanced. GSEA analysis was a canonical method for integrating gene expression information, through which the expression tendency of gene sets in different groups were clarified directly (Subramanian et al., 2005). In this study, GSEA result revealed relatively low expression of immune cells differentiation and osteoclast differentiation in cluster 1. These results indicated that downregulated lipid catabolism and upregulated lipid hydroxylation were implicated with low immune status and poor bone remodeling.

Synthesizing above findings, we could deduce reasonably that dysregulation of lipid metabolism, including hydroxylation upregulation and catabolism downregulation, resulted in the impairment of TIME and bone remodeling, thereby leading to the poor prognosis in osteosarcoma. As mentioned above, lipid metabolism reprogramming was recognized as new hallmark of tumor malignancy. Over the past years, lipid metabolic abnormalities of tumor have gained increasing attention (Maan et al., 2018). Targeting aberrant pathways of lipid metabolism is a promising strategy for antitumor therapy. For example, anti-tumor drugs based on the hydroxylated lipid has been widely used for tumor treatment clinically (Király et al., 2013). In this study, upregulated lipid hydroxylation was found to be associated with poor survival. Among the multiple modification of lipids, hydroxylation was a specific approach during which oxygens were added onto the lipids in the manner of hydroxyl through radical oxygen species (ROS) or non-radical oxidants (Spickett, 2020). As one of the activated radicals of biological systems, hydroxyl radical was prone to induced lipid peroxidation (Spickett, 2020). Because lipids were critical components of multiple membranes and distributed widely (Cheng et al., 2018), lipid peroxidation usually occurred when polyunsaturated fatty acids (PUFAs) were attacked by ROS, which would impair the structure and/or function of membranes subsequently (Yoshida et al., 2013). Lipid peroxidation resulted in the formation of aldehydes with high reactivity (Erejuwa et al., 2013), which further attack the components of cellular membrane, such as lipids and proteins (Höhn and Grune, 2013). Meanwhile, some other products of lipid peroxidation, including malondialdehyde, 4-hydroxynonenal and acrolein, also bound to the amino acid residues of protein covalently via Michael addition, damaging the structure and function of the residues (Fukuda et al., 2009). All of these could explain the contribution of upregulated hydroxylation to the poor prognosis of cancer patients in a certain extent. On the other hand, catabolism downregulation reduced the consumption of lipids, and as a result, accumulative lipids were stored in tumor cells and surrounding cells. The influence of accumulated lipid due to lipid metabolism abnormalities on the tumor-microenvironment dendritic cells may also account for the poor prognosis partly. Because previous studies reported that lipid-laden dendritic cells were unable to present tumor-associated antigens (Herber et al., 2010). And abnormal lipid accumulation inhibited the capacity of dendritic cells to facilitate anti-tumor T cells (Cubillos-Ruiz et al., 2015). This also expounded why the downregulated lipid metabolism led to lower immune score and immune status. Besides, the accumulative lipid may result in poor prognosis via facilitating metastasis which was a critical factor for tumor progression, since the metastatic potential of tumor cells was positively correlated with intracellular lipid storage (Maan et al., 2018).

To further validate the effect of lipid metabolism disorder on the TIME in osteosarcoma and explore the prognostic value of LMRGs in osteosarcoma patients, we constructed a prognostic risk model based on LMRGs and verified it in the validation cohort. The three genes used for establishing risk model in this study have been demonstrated to be closely associated with development and progression of tumors. *ME1* encodes malic enzyme 1 (ME1), which catalyzes the transformation of malate to pyruvate and promotes the formation of NADPH concomitantly. Prior studies reported that ME1 mediated the lipid metabolism through participating in lipid biosynthesis basically (Simmen et al., 2020). Numerous researches have provided the evidence of the pro-oncogenic role of ME1 in multiple tumors (Simmen et al., 2020). *ALOX15B* (Arachidonate 15-Lipoxygenase Type B) has been demonstrated as risk genes in colorectal cancer and lung squamous cell carcinoma (Yuan et al., 2020; Kim et al., 2021). *GPD1* encodes glycerol-3-phosphate dehydrogenase 1 (GPD1), which played a pivotal role in lipid metabolism through catalyzing the transformation of NADH and dihydroxyacetone phosphate to NAD+ and glycerol-3-phosphate reversibly (Yoneten et al., 2019). Studies suggested that *GPD1* was closely related to prognosis of gastrointestinal cancer, breast cancer, and glioblastoma (Xie et al., 2020; Xia et al., 2021). Survival analysis revealed that no matter in the training cohort or the verification cohort, the established risk model exhibited potent predictive performance for the survival of osteosarcoma patients. And significantly lower stromal score, immune score and higher tumor purity were accompanied with poor survival. Moreover, independence analysis and subgroup analysis suggested that the LMRGs-based risk model could predict the prognosis independently in osteosarcoma, regardless of their age, sex and metastasis condition. Finally, a nomogram integrating the risk score

and clinical features was also established and calibrated, and it showed considerable property for predicting the survival. All these results confirmed the prognostic prediction role of LMRGs in osteosarcoma and correlation between aberrant lipid metabolism and TMIE disorder.

Over the recent decades, radiotherapy and chemotherapy for tumors have grew boomingly. However, the 5-year survival of osteosarcoma remained unsatisfactory (Ritter and Bielack, 2010; Kansara et al., 2014; Heng et al., 2020). It is imperative to develop effective methods to classify the patients according their risk score, and conduct reasonable individualized and targeted therapy. Bioinformatic analysis based on sequencing RNA data was a feasible approach for risk stratification and targeted-gene identification. Although researchers have constructed risk model based on tumor microenvironment, immune cell infiltrating and energy metabolism (Chen Y. et al., 2020; Wen et al., 2020; Zhang et al., 2020; Zhu et al., 2020) in osteosarcoma, our study exhibited unique merits compared with previous studies. Firstly, our work focused on the lipid metabolism of osteosarcoma patients, and identified two molecular subgroups with significantly different prognosis and immune status via consensus clustering. Secondly, we explored the biological mechanisms according to the result of clustering and elucidated the underlying mechanism partly. Thirdly, we clarified the influence of lipid metabolism on TIME and prognosis. Last but not least, this work integrated two GEO datasets as a verification cohort, which containing much more samples than previous studies. Our work would provide excellent theoretical instruction for further studies of osteosarcoma. Additionally, result of this study could promote the development of targeted therapy for osteosarcoma and help the clinicians make treatment strategy more rationally.

In general, in this study, we identified two molecular subtypes, cluster 1 and 2. In cluster 1, patients with poor prognosis showed TIME disorder including low immune score and high tumor purity, and the dysregulation of lipid catabolism was implicated with low immune status and aberrant bone remodeling. Risk model based on LMRGs could predicted the prognosis in osteosarcoma precisely, meanwhile, those patients with unfavorable survival in the high risk showed low immune score and high tumor purity. These results indicated that lipid metabolism landscape was correlated with TIME, and deserved considerable attention in determining treatment strategy for osteosarcoma patients, which was a potential target for individualized treatment.

There were some drawbacks in our study which should be notified when generalizing the conclusion. Firstly, due to the absence of information about the progression of the osteosarcoma patients, such as tumor stages, we could not demonstrate the role of LMRG in the development of osteosarcoma. Secondly, our results generated from bioinformatics analysis, which was not further validated by experiments. Thirdly, the data used in this study was downloaded from open database instead of our cohort. The nature of low evidence level of retrospective research still remained, and more prospective studies are needed to be conducted to further confirm the prognostic value of LMRGs in osteosarcoma.

CONCLUSION

In conclusion, in the present study, two molecular subtypes were identified based on LMRGs in osteosarcoma via consensus clustering. Immune analysis and functional analyses revealed that dysregulation of lipid metabolism would impede the immune system and bone remodeling, thereby resulting in poor prognosis. Our work could shed a novel light on the development of new targeting drugs, provide theoretical support for individualized therapy, and facilitate the risk stratification of osteosarcoma patients.

DATA AVAILABILITY STATEMENT

The datasets presented in this study can be found in online repositories. The names of the repository/repositories and accession number(s) can be found in the article/ **Supplementary Material**.

AUTHOR CONTRIBUTIONS

YH and PL conceived the original ideas of this manuscript and reviewed the finished manuscript and executed supervision throughout the process. HQ executed the data collection and data analysis. HQ and TL prepared the manuscript, tables, and figures. All authors have read and approved the manuscript.

FUNDING

This study was supported by the Scientific Research Project of Health and Family Planning Commission of Hunan Province, China (Grant No. B2019188), the Science and Technology Innovation Leading Project for High-tech Industry of Hunan Province (Grant No. 2020SK2008), and the Natural Science Foundation of China (Grant Nos. 82002277 and 81672656).

ACKNOWLEDGMENTS

We thank Shengchao Xu for technology supporting and composition instruction.

SUPPLEMENTARY MATERIAL

The Supplementary Material for this article can be found online at: https://www.frontiersin.org/articles/10.3389/fcell.2021.673827/full#supplementary-material

REFERENCES

Aran, D., Sirota, M., and Butte, A. J. (2015). Systematic pan-cancer analysis of tumour purity. *Nat. Commun.* 6:8971. doi: 10.1038/ncomms9971

Bao, M., Shi, R., Zhang, K., Zhao, Y., Wang, Y., and Bao, X. (2019). Development of a membrane lipid metabolism-based signature to predict overall survival for personalized medicine in ccRCC patients. *EPMA J.* 10, 383–393. doi: 10.1007/s13167-019-00189-8

Binnewies, M., Roberts, E. W., Kersten, K., Chan, V., Fearon, D. F., Merad, M., et al. (2018). Understanding the tumor immune microenvironment (TIME) for effective therapy. *Nat. Med.* 24, 541–550. doi: 10.1038/s41591-018-0014-x

Cao, Y. (2019). Adipocyte and lipid metabolism in cancer drug resistance. *J. Clin. Invest.* 129, 3006–3017. doi: 10.1172/JCI127201

Chen, C., Chen, H., Zhang, Y., Thomas, H. R., Frank, M. H., He, Y., et al. (2020). TBtools: an integrative toolkit developed for interactive analyses of big biological data. *Mol. Plant* 13, 1194–1202. doi: 10.1016/j.molp.2020.06.009

Chen, Y., Zhao, B., and Wang, X. (2020). Tumor infiltrating immune cells (TIICs) as a biomarker for prognosis benefits in patients with osteosarcoma. *BMC Cancer* 20:1022. doi: 10.1186/s12885-020-07536-3

Cheng, C., Geng, F., Cheng, X., and Guo, D. (2018). Lipid metabolism reprogramming and its potential targets in cancer. *Cancer Commun.* 38:27. doi: 10.1186/s40880-018-0301-4

Corbet, C., and Feron, O. (2017). Emerging roles of lipid metabolism in cancer progression. *Curr. Opin. Clin. Nutr. Metab. Care* 20, 254–260. doi: 10.1097/MCO.0000000000000381

Cubillos-Ruiz, J. R., Silberman, P. C., Rutkowski, M. R., Chopra, S., Perales-Puchalt, A., Song, M., et al. (2015). ER stress sensor XBP1 controls anti-tumor immunity by disrupting dendritic cell homeostasis. *Cell* 161, 1527–1538. doi: 10.1016/j.cell.2015.05.025

Erejuwa, O. O., Sulaiman, S. A., and Ab Wahab, M. S. (2013). Evidence in support of potential applications of lipid peroxidation products in cancer treatment. *Oxid. Med. Cell. Longev.* 2013:931251. doi: 10.1155/2013/931251

Fukuda, M., Kanou, F., Shimada, N., Sawabe, M., Saito, Y., Murayama, S., et al. (2009). Elevated levels of 4-hydroxynonenal-histidine Michael adduct in the hippocampi of patients with Alzheimer's disease. *Biomed. Res.* 30, 227–233. doi: 10.2220/biomedres.30.227

Hänzelmann, S., Castelo, R., and Guinney, J. (2013). GSVA: gene set variation analysis for microarray and RNA-seq data. *BMC Bioinform.* 14:7. doi: 10.1186/1471-2105-14-7

Heng, M., Gupta, A., Chung, P. W., Healey, J. H., Vaynrub, M., Rose, P. S., et al. (2020). The role of chemotherapy and radiotherapy in localized extraskeletal osteosarcoma. *Eur. J. Cancer* 125, 130–141. doi: 10.1016/j.ejca.2019.07.029

Herber, D. L., Cao, W., Nefedova, Y., Novitskiy, S. V., Nagaraj, S., Tyurin, V. A., et al. (2010). Lipid accumulation and dendritic cell dysfunction in cancer. *Nat. Med.* 16, 880–886. doi: 10.1038/nm.2172

Heymann, M. F., Lézot, F., and Heymann, D. (2019). The contribution of immune infiltrates and the local microenvironment in the pathogenesis of osteosarcoma. *Cell Immunol.* 343:103711. doi: 10.1016/j.cellimm.2017.10.011

Hilvo, M., Denkert, C., Lehtinen, L., Müller, B., Brockmöller, S., Seppänen-Laakso, T., et al. (2011). Novel theranostic opportunities offered by characterization of altered membrane lipid metabolism in breast cancer progression. *Cancer Res.* 71, 3236–3245. doi: 10.1158/0008-5472.CAN-10-3894

Hinshaw, D. C., and Shevde, L. A. (2019). The tumor microenvironment innately modulates cancer progression. *Cancer Res.* 79, 4557–4566. doi: 10.1158/0008-5472.CAN-18-3962

Höhn, A., and Grune, T. (2013). Lipofuscin: formation, effects and role of macroautophagy. *Redox Biol.* 1, 140–144. doi: 10.1016/j.redox.2013.01.006

Hong, W., Yuan, H., Gu, Y., Liu, M., Ji, Y., Huang, Z., et al. (2020). Immune-related prognosis biomarkers associated with osteosarcoma microenvironment. *Cancer Cell Int.* 20:83. doi: 10.1186/s12935-020-01271-2

Hu, B., Yang, X. B., and Sang, X. T. (2020). Construction of a lipid metabolism-related and immune-associated prognostic signature for hepatocellular carcinoma. *Cancer Med.* 9, 7646–7662. doi: 10.1002/cam4.3353

Kansara, M., Teng, M. W., Smyth, M. J., and Thomas, D. M. (2014). Translational biology of osteosarcoma. *Nat. Rev. Cancer* 14, 722–735. doi: 10.1038/nrc3838

Kim, A., Lim, S. M., Kim, J. H., and Seo, J. S. (2021). Integrative genomic and transcriptomic analyses of tumor suppressor genes and their role on tumor microenvironment and immunity in lung squamous cell carcinoma. *Front. Immunol.* 12:598671. doi: 10.3389/fimmu.2021.598671

Király, A., Váradi, T., Hajdu, T., Rühl, R., Galmarini, C. M., Szöllösi, J., et al. (2013). Hypoxia reduces the efficiency of elisidepsin by inhibiting hydroxylation and altering the structure of lipid rafts. *Mar. Drugs* 11, 4858–4875. doi: 10.3390/md11124858

Li, J., Li, Q., Su, Z., Sun, Q., Zhao, Y., Feng, T., et al. (2020). Lipid metabolism gene-wide profile and survival signature of lung adenocarcinoma. *Lipids Health Dis.* 19:222. doi: 10.1186/s12944-020-01390-9

Li, T., Fan, J., Wang, B., Traugh, N., Chen, Q., Liu, J. S., et al. (2017). TIMER: a web server for comprehensive analysis of tumor-infiltrating immune cells. *Cancer Res.* 77, e108–e110. doi: 10.1158/0008-5472.CAN-17-0307

Luo, X., Cheng, C., Tan, Z., Li, N., Tang, M., Yang, L., et al. (2017). Emerging roles of lipid metabolism in cancer metastasis. *Mol. Cancer* 16:76. doi: 10.1186/s12943-017-0646-3

Luo, Z. W., Liu, P. P., Wang, Z. X., Chen, C. Y., and Xie, H. (2020). Macrophages in osteosarcoma immune microenvironment: implications for immunotherapy. *Front. Oncol.* 10:586580. doi: 10.3389/fonc.2020.586580

Maan, M., Peters, J. M., Dutta, M., and Patterson, A. D. (2018). Lipid metabolism and lipophagy in cancer. *Biochem. Biophys. Res. Commun.* 504, 582–589. doi: 10.1016/j.bbrc.2018.02.097

Miller, B. J., Cram, P., Lynch, C. F., and Buckwalter, J. A. (2013). Risk factors for metastatic disease at presentation with osteosarcoma: an analysis of the SEER database. *J. Bone Joint Surg. Am.* 95:e89. doi: 10.2106/JBJS.L.01189

Negri, G. L., Grande, B. M., Delaidelli, A., El-Naggar, A., Cochrane, D., Lau, C. C., et al. (2019). Integrative genomic analysis of matched primary and metastatic pediatric osteosarcoma. *J. Pathol.* 249, 319–331. doi: 10.1002/path.5319

Niemi, R. J., Braicu, E. I., Kulbe, H., Koistinen, K. M., Sehouli, J., Puistola, U., et al. (2018). Ovarian tumours of different histologic type and clinical stage induce similar changes in lipid metabolism. *Br. J. Cancer* 119, 847–854. doi: 10.1038/s41416-018-0270-z

Niu, J., Yan, T., Guo, W., Wang, W., Zhao, Z., Ren, T., et al. (2020). Identification of potential therapeutic targets and immune cell infiltration characteristics in osteosarcoma using bioinformatics strategy. *Front. Oncol.* 10:1628. doi: 10.3389/fonc.2020.01628

Ritter, J., and Bielack, S. S. (2010). Osteosarcoma. *Ann. Oncol.* 21(Suppl. 7), vii320–vii325. doi: 10.1093/annonc/mdq276

Simmen, F. A., Alhallak, I., and Simmen, R. C. M. (2020). Malic enzyme 1 (ME1) in the biology of cancer: it is not just intermediary metabolism. *J. Mol. Endocrinol.* 65, R77–R90. doi: 10.1530/JME-20-0176

Song, Y. J., Xu, Y., Zhu, X., Fu, J., Deng, C., Chen, H., et al. (2020). Immune landscape of the tumor microenvironment identifies prognostic gene signature CD4/CD68/CSF1R in osteosarcoma. *Front. Oncol.* 10:1198. doi: 10.3389/fonc.2020.01198

Spickett, C. M. (2020). Formation of oxidatively modified lipids as the basis for a cellular epilipidome. *Front. Endocrinol.* 11:602771. doi: 10.3389/fendo.2020.602771

Su, P., Wang, Q., Bi, E., Ma, X., Liu, L., Yang, M., et al. (2020). Enhanced lipid accumulation and metabolism are required for the differentiation and activation of tumor-associated macrophages. *Cancer Res.* 80, 1438–1450. doi: 10.1158/0008-5472.CAN-19-2994

Subramanian, A., Tamayo, P., Mootha, V. K., Mukherjee, S., Ebert, B. L., Gillette, M. A., et al. (2005). Gene set enrichment analysis: a knowledge-based approach for interpreting genome-wide expression profiles. *Proc. Natl. Acad. Sci. U.S.A.* 102, 15545–15550. doi: 10.1073/pnas.0506580102

Visweswaran, M., Arfuso, F., Warrier, S., and Dharmarajan, A. (2020). Aberrant lipid metabolism as an emerging therapeutic strategy to target cancer stem cells. *Stem Cells* 38, 6–14. doi: 10.1002/stem.3101

Wang, D., Niu, X., Wang, Z., Song, C. L., Huang, Z., Chen, K. N., et al. (2019). Multiregion sequencing reveals the genetic heterogeneity and evolutionary history of osteosarcoma and matched pulmonary metastases. *Cancer Res.* 79, 7–20. doi: 10.1158/0008-5472.CAN-18-1086

Wen, C., Wang, H., Wang, H., Mo, H., Zhong, W., Tang, J., et al. (2020). A three-gene signature based on tumour microenvironment predicts overall survival of osteosarcoma in adolescents and young adults. *Aging* 12, 619–645. doi: 10.18632/aging.202170

Whelan, J. S., and Davis, L. E. (2018). osteosarcoma, chondrosarcoma, and chordoma. *J. Clin. Oncol.* 36, 188–193. doi: 10.1200/JCO.2017.75.1743

Wu, F., Zhao, Z., Chai, R. C., Liu, Y. Q., Li, G. Z., Jiang, H. Y., et al. (2019). Prognostic power of a lipid metabolism gene panel for diffuse gliomas. *J. Cell Mol. Med.* 23, 7741–7748. doi: 10.1111/jcmm.14647

Xia, R., Tang, H., Shen, J., Xu, S., Liang, Y., Zhang, Y., et al. (2021). Prognostic value of a novel glycolysis-related gene expression signature for gastrointestinal cancer in the Asian population. *Cancer Cell Int.* 21:154. doi: 10.1186/s12935-021-01857-4

Xie, J., Ye, J., Cai, Z., Luo, Y., Zhu, X., Deng, Y., et al. (2020). GPD1 enhances the anticancer effects of metformin by synergistically increasing total cellular glycerol-3-phosphate. *Cancer Res.* 80, 2150–2162. doi: 10.1158/0008-5472.CAN-19-2852

Ye, Y., Chen, Z., Shen, Y., Qin, Y., and Wang, H. (2021). Development and validation of a four-lipid metabolism gene signature for diagnosis of pancreatic cancer. *FEBS Open Biol.* [Epub ahead of print]. doi: 10.1002/2211-5463.13074

Yoneten, K. K., Kasap, M., Akpinar, G., Gunes, A., Gurel, B., and Utkan, N. Z. (2019). Comparative proteome analysis of breast cancer tissues highlights the importance of glycerol-3-phosphate dehydrogenase 1 and monoacylglycerol lipase in breast cancer metabolism. *Cancer Genom. Proteom.* 16, 377–397. doi: 10.21873/cgp.20143

Yoshida, Y., Umeno, A., and Shichiri, M. (2013). Lipid peroxidation biomarkers for evaluating oxidative stress and assessing antioxidant capacity in vivo. *J. Clin. Biochem. Nutr.* 52, 9–16. doi: 10.3164/jcbn.12-112

Yoshihara, K., Shahmoradgoli, M., Martínez, E., Vegesna, R., Kim, H., Torres-Garcia, W., et al. (2013). Inferring tumour purity and stromal and immune cell admixture from expression data. *Nat. Commun.* 4:2612. doi: 10.1038/ncomms3612

Yuan, Y., Chen, J., Wang, J., Xu, M., Zhang, Y., Sun, P., et al. (2020). Development and clinical validation of a novel 4-gene prognostic signature predicting survival in colorectal cancer. *Front. Oncol.* 10:595. doi: 10.3389/fonc.2020.00595

Zhang, C., Zheng, J. H., Lin, Z. H., Lv, H. Y., Ye, Z. M., Chen, Y. P., et al. (2020). Profiles of immune cell infiltration and immune-related genes in the tumor microenvironment of osteosarcoma. *Aging* 12, 3486–3501. doi: 10.18632/aging.102824

Zheng, M., Mullikin, H., Hester, A., Czogalla, B., Heidegger, H., Vilsmaier, T., et al. (2020). Development and validation of a novel 11-gene prognostic model for serous ovarian carcinomas based on lipid metabolism expression profile. *Int. J. Mol. Sci.* 21:9169. doi: 10.3390/ijms21239169

Zhu, N., Hou, J., Ma, G., Guo, S., Zhao, C., and Chen, B. (2020). Co-expression network analysis identifies a gene signature as a predictive biomarker for energy metabolism in osteosarcoma. *Cancer Cell Int.* 20:259. doi: 10.1186/s12935-020-01352-2

Conflict of Interest: The authors declare that the research was conducted in the absence of any commercial or financial relationships that could be construed as a potential conflict of interest.

The reviewer JZ declared a shared affiliation with all authors to the handling editor at the time of review.

frontiers in Cell and Developmental Biology

SYSTEMATIC REVIEW
published: 27 April 2021
doi: 10.3389/fcell.2021.654337

Interplay Between Glucose Metabolism and Chromatin Modifications in Cancer

Rui Ma[1†], *Yinsheng Wu*[1†], *Shanshan Li*[1,2*] *and Xilan Yu*[1*]

[1] State Key Laboratory of Biocatalysis and Enzyme Engineering, Environmental Microbial Technology Center of Hubei, School of Life Sciences, Hubei University, Wuhan, China, [2] College of Biomedicine and Health, Huazhong Agricultural University, Wuhan, China

Cancer cells reprogram glucose metabolism to meet their malignant proliferation needs and survival under a variety of stress conditions. The prominent metabolic reprogram is aerobic glycolysis, which can help cells accumulate precursors for biosynthesis of macromolecules. In addition to glycolysis, recent studies show that gluconeogenesis and TCA cycle play important roles in tumorigenesis. Here, we provide a comprehensive review about the role of glycolysis, gluconeogenesis, and TCA cycle in tumorigenesis with an emphasis on revealing the novel functions of the relevant enzymes and metabolites. These functions include regulation of cell metabolism, gene expression, cell apoptosis and autophagy. We also summarize the effect of glucose metabolism on chromatin modifications and how this relationship leads to cancer development. Understanding the link between cancer cell metabolism and chromatin modifications will help develop more effective cancer treatments.

Keywords: metabolism, epigenetic modifications, gene transcription, tumorigenesis, histone modifications

OPEN ACCESS

Edited by:
Yongguang Tao,
Central South University, China

Reviewed by:
Estela Jacinto,
University of Medicine and Dentistry of New Jersey, United States
Valentina Tosato,
University of Trieste, Italy

****Correspondence:***
Xilan Yu
yuxilan@hubu.edu.cn
Shanshan Li
shanshanyxl@hotmail.com

[†]These authors have contributed equally to this work

Specialty section:
This article was submitted to Molecular and Cellular Oncology, a section of the journal Frontiers in Cell and Developmental Biology

Received: *15 January 2021*
Accepted: *19 March 2021*
Published: *27 April 2021*

Citation:
Ma R, Wu Y, Li S and Yu X (2021) Interplay Between Glucose Metabolism and Chromatin Modifications in Cancer. Front. Cell Dev. Biol. 9:654337. doi: 10.3389/fcell.2021.654337

INTRODUCTION

Tumor cells need to change their metabolism to support their demands for rapid growth and proliferation, so called metabolism reprogram (Pavlova and Thompson, 2016). This metabolic reprogram enables cells to synthesize a large amount of precursors for biomacromolecule synthesis (Pavlova and Thompson, 2016). The extensive studied metabolic reprogram is aerobic glycolysis, also known as the "Warburg effect." That is, cancer cells preferentially convert pyruvate, the end product of glycolysis into lactate instead of transporting pyruvate into the mitochondria for oxidative phosphorylation. Although aerobic glycolysis is a less efficient way to produce energy (2 ATP/glucose), it helps accumulate a large amount of metabolite precursors for biosynthesis of macromolecules, i.e., nucleic acids, fatty acids, and amino acids (Hanahan and Weinberg, 2011). Initially, the mitochondria in tumor cells was thought to have defects, which makes them unable to perform oxidative phosphorylation and highly dependent on glycolysis (Dang and Semenza, 1999). However, the function of mitochondria in most tumor cells is intact. Recent studies show that tumor cells mainly use the tricarboxylic acid (TCA) cycle in the G1 phase and prefer glycolysis in the S phase (Liu et al., 2021), suggesting that both TCA cycle and glycolysis are important for tumor cells.

Many metabolic enzymes and metabolites have non-metabolic functions in tumorigenesis, including regulation of chromatin modifications, gene transcription, DNA damage, etc. (Yu and Li, 2017). These non-metabolic functions provide useful clues to develop more efficient anti-cancer therapy. In this review, we described the functions of metabolic enzymes and

metabolites from glycolysis, gluconeogenesis, and TCA cycle in tumorigenesis with an emphasis on their non-metabolic functions. We also described how they are regulated and their effects on chromatin modifications.

METABOLIC REGULATION OF TUMOR CELL PROLIFERATION

The Role of Glycolytic Enzymes in Tumorigenesis

Hexokinase

Hexokinase (HK2) is the first rate-limiting enzyme in glycolysis, which is highly expressed in tumor cells and acts as a potential target for cancer treatment (Chen J. et al., 2014). HK2 binds to the mitochondrial membrane *via* its interaction with the outer membrane porin protein, voltage-dependent anion channel (VDAC) (**Figure 1**). VDAC is a critical channel that regulates the release rate of mitochondrial intermembrane pro-apoptotic proteins, such as cytochrome *c* (Linden et al., 1982). The interaction between HK2 and VDAC inhibits the release of intermembrane pro-apoptotic proteins, thereby protecting tumor cells from apoptosis (**Figure 1**) (Linden et al., 1982). HK2 has also been reported to interact with the mammalian target of rapamycin complex 1 (mTORC1) by binding to its subunit, regulatory-associated protein of mTOR (Raptor) (**Figure 1**) (Roberts et al., 2014). Upon glucose deprivation, HK2 directly binds to mTORC1 to inhibit its function and activate the protective autophagy pathway (Roberts et al., 2014).

The expression of HK2 is closely correlated to the occurrence of cancers such as laryngeal cancer and breast cancer, metastasis of breast cancer cells and poor prognosis of patients (Palmieri et al., 2009; Kwee et al., 2012; Min et al., 2013). HK2 expression is regulated by microRNAs, long non-coding RNA and various transcript factors. The expression of miR-143 is negatively correlated with the HK2 expression level in a variety of cancers, including prostate cancer, breast cancer, and head and neck squamous cell carcinoma (HNSCC) (Zhang et al., 2017). miR-143 directly targets the 3′UTR (3′ untranslated region) of HK2 to repress its expression (Peschiaroli et al., 2013). miR-155 down-regulates the transcription of miR-143 by targeting its transcription activator C/EBP β, which then affects HK2 expression (Jiang et al., 2012). The long non-coding RNA UCA1 up-regulates HK2 transcription by repressing miR-203 and upregulated UCA1 enhances the malignant phenotype of esophageal cancer (Liu et al., 2020). HK2 is also regulated by transcription factors. For example, hypoxia-inducible factor 1α (HIF-1α) binds the promoter of HK2 to activate HK2 transcription, which accelerates glycolysis and facilitates cutaneous squamous cell carcinoma (cSCC) development (Zhou et al., 2018). In addition, the expression of HK2 is activated by transforming growth factor-β (TGF-β) and this activation requires transcription factors like Smad2, Smad3, and c-Myc (Yin et al., 2019).

Phosphoglucose Isomerase

Phosphoglucose isomerase (PGI) is the second glycolytic enzyme, which is highly expressed in a variety of tumor cells, including human breast carcinoma BT-549 cells,human colon cancer cell HCT116, human bladder cancer cell J82 (Tsutsumi et al., 2004, 2009; Funasaka et al., 2009). In lung cancer patients, high PGI expression is associated with poor prognosis and reduced survival rate (Funasaka et al., 2005). The activity of PGI1 can be inhibited by small molecules, i.e., the glucose analog, 2-deoxy-D-glucose (2-DG) (**Figure 1**) (Pusapati et al., 2016). The small molecule inhibitor, Esculetin can directly bind PGI and repress its activity, which triggers apoptosis and inhibits tumor growth (Wu S. T. et al., 2020).

PGI also acts as an autocrine motility factor (AMF) in tumor progression and metastasis (Funasaka et al., 2005). Its receptor, AMFR/gp78 is overexpressed in multiple tumors and correlated with poor prognosis (Pusapati et al., 2016). It is known that PGI/AMF can function as an anti-apoptotic factor. PGI/AMF down-regulates the expression of apoptotic protease activating factor-1 (Apaf-1) and caspase-9 genes to reduce apoptosis (Haga et al., 2003). In addition, PGI/AMF can reduce apoptosis by activating the PI3K/Akt signaling pathway (**Figure 1**) (Fruman and Rommel, 2014).

Phosphofructokinase 1

Phosphofructokinase 1 (PFK1) catalyzes the conversion of fructose-6-phosphate into fructose-1,6-bisphosphate. PFK1 has 3 isoforms: platelet (PFKP), muscle (PFKM) and liver (PFKL), among which PFKP is the major PFK1 isoform and overexpressed in human glioblastoma cells (Mor et al., 2011). PFK1 facilitates tumor growth as knockdown of PFK1 inhibits the migration and proliferation of colorectal cancer (Lang et al., 2019).

The activity of PFK1 is regulated by different covalent modifications. For example, PFPKP can be acetylated by lysine acetyltransferase 5 (KAT5) at lysine 395 (K395) upon activation of the epidermal growth factor receptor (EGFR) (Lee et al., 2018). Acetylated PFPKP then translocates into the plasma membrane, where it is phosphorylated by EGFR at tyrosine 64 (Y64) to enhance its activity (Lee et al., 2018). PFKP can also been phosphorylated by AKT at serine 386 (S386), which protects PFKP from degradation and facilitates tumor growth (Lee et al., 2017). Under anaerobic conditions, PFK1 is modified by O-linked β-N-acetylglucosamine (O-GlcNAc) at serine 529 (S529) (Yi et al., 2012). Glycosylation of PFK1 reduces its activity and diverts the glucose flux into the pentose phosphate pathway (PPP), resulting in a significant increase in NADPH, which promotes the proliferation and tumorigenicity of lung cancer cells (Yi et al., 2012).

Aldolase

Aldolase catalyzes the conversion of fructose 1-6-diphosphate to glyceraldehyde 3-phosphate and dihydroxy-acetone phosphate. Aldolase has three tissue-specific isozymes: ALDOA (muscles), ALDOB (liver) and ALDOC (neuronal tissue) (Lincet and Icard, 2015). Among these isozymes, ALDOA is overexpressed in a series of cancers, including colorectal cancer, hepatocellular carcinoma, lung cancer, and pancreatic cancer and promotes tumor growth, invasion, and migration (Du et al., 2014; Shimizu et al., 2014; Ji et al., 2016; Kawai et al., 2017). Mechanistically, ALDOA activates the EGFR/MAPK pathway to

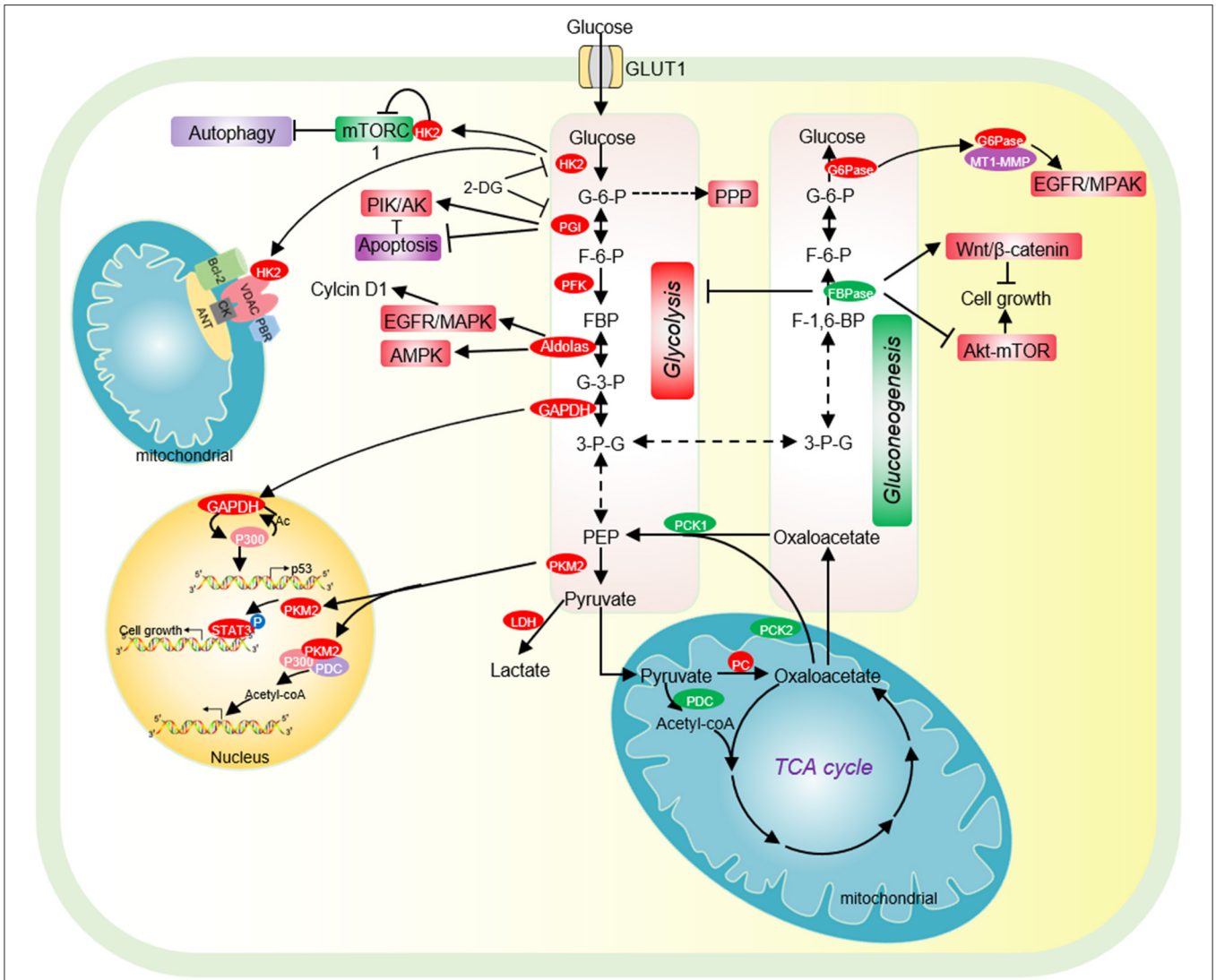

FIGURE 1 | The effect of glycolysis and gluconeogenesis on tumor cell proliferation. Cancer cells have increased glucose uptake, leading to accelerated glycolysis and biomass accumulation. The high expression of GLUT1, HK2, PGI, PFK, Aldolase, GAPDH, and PKM2 significantly accelerates aerobic glycolysis. Increased lactate dehydrogenase (LDH) activity and decreased pyruvate dehydrogenase (PDC) activity result in increased lactate export, attenuated TCA cycle and diversion of glycolysis to pentose phosphate pathway (PPP). HK2 not only directly binds to mTORC1 to activate autophagy, but also interacts with VDAC to protect tumor cells from apoptosis. PGI inhibits cell apoptosis by inhibiting the expression of Apaf-1 and caspase-9 and activating the PI3K/Akt signaling pathway. Acetylated nuclear GAPDH promotes tumorigenesis by activating p300 and promoting p53 expression. Aldolase promotes cell cycle progression through the EGFR/MAPK signaling pathway, and activates AMPK to maintain tumor cell survival in glucose deficiency. Nuclear PKM2 performs a variety of non-metabolic functions to promote cell cycle progression. Low expression of pyruvate carboxylase (PC), the key enzyme of gluconeogenesis, is essential for the proliferation of some cancer cells. PC is essential for the synthesis of fatty acid and glycerol in cancer cells. The low expression of the key enzyme PEPCK of gluconeogenesis is beneficial for the proliferation of cancer cells. FBPase acts as a tumor suppressor and inhibits the proliferation of tumor cells. G6PT promotes the invasion of glioblastoma by interacting with MT1-MMP. HK2, hexokinase 2; G-6-P, glucose-6-phosphate; PGI, phosphoglucose isomerase; F-6-P, fructose-6-phosphate; FBP, fructose-1,6-biphosphate; G-3-P, glyceraldehyde-3-phosphate; 3-P-G, 3-phosphoglycerate; GAPDH, Glyceraldehyde-3-phosphate dehydrogenase; PKM2, Pyruvate kinase M2; LDH, lactate dehydrogenase; PC, Pyruvate carboxylase; PCK1/2, phosphoenolpyruvate carboxykinase 1/2; PDC, pyruvate dehydrogenase complex; PEP, phosphoenolpyruvate; PKM2, pyruvate kinase M2; FBPase, fructose-1,6-bisphosphatase; G6Pase, glucose-6-phosphatase.

up-regulate the expression of cell cycle protein D1 (cyclin D1) (Fu H. et al., 2018). In lung cancer, ALDOA stabilizes HIF-1α to activate its downstream target MMP9, which enhances lung cancer invasion and migration (Chang et al., 2017). ALDOA also interacts with γ-actin to promote metastasis of non-small cell lung cancer (NSCLC) and blocking this interaction decreases metastasis (**Figure 1**) (Chang et al., 2019).

Unlike ALDOA, ALDOB is significantly reduced in metastasis-inclined HCC (MIH) and its role in tumorigenesis is ambiguous (Tao et al., 2015). Overexpression of ALDOB inhibits the metastasis of liver cancer cells by inducing Ten-Eleven

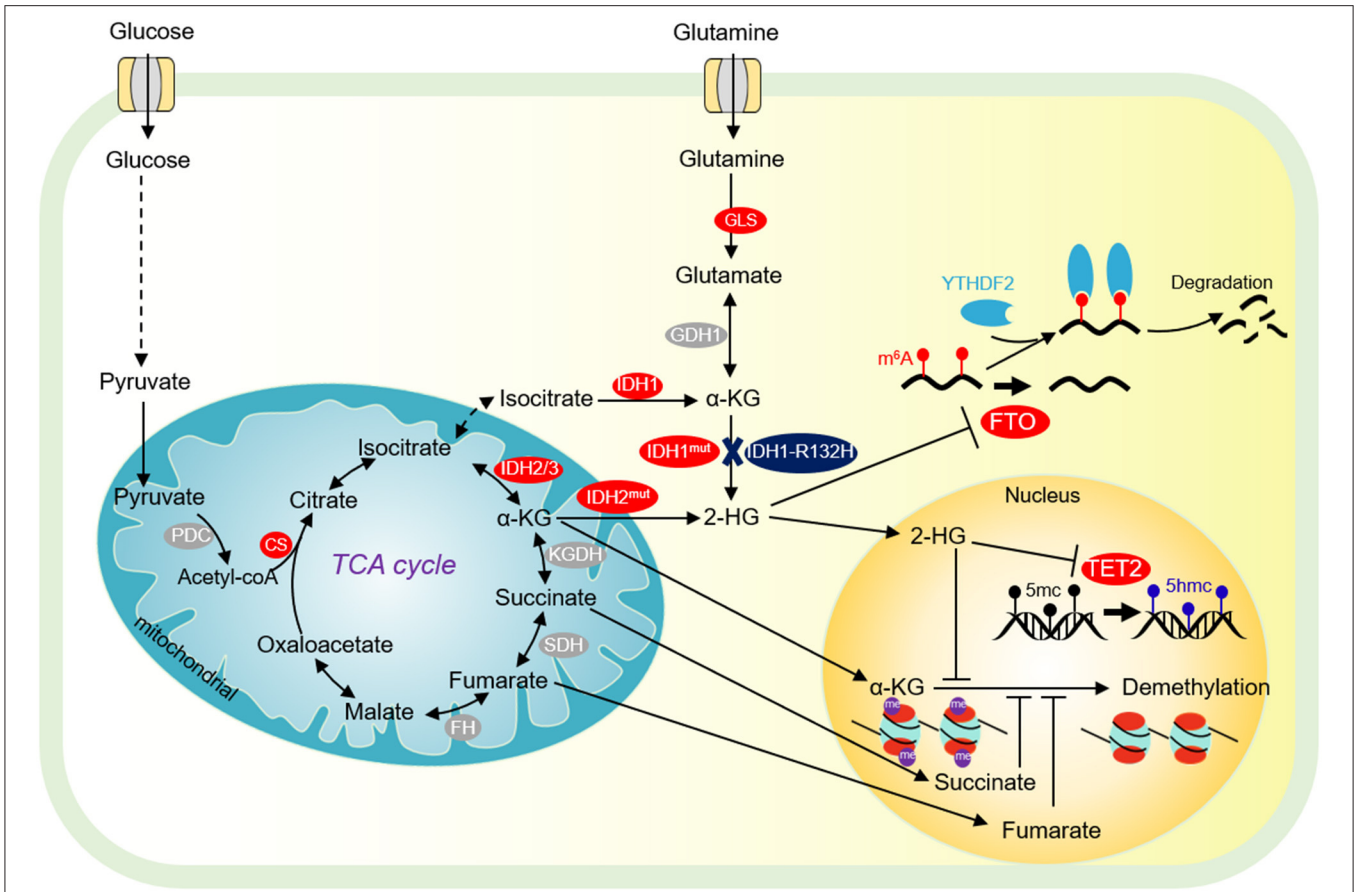

FIGURE 2 | Tricarboxylic acid (TCA) cycle and chromatin demethylation in cancer cells. Although the TCA cycle is repressed in tumor cells, it is also essential for tumor growth. α-KG derived from glucose metabolism or glutamine is essential for tumor cell proliferation and chromatin demethylation. α-KG can be metabolized to succinate and fumarate by FH and SDH in the TCA cycle, respectively. Succinate and fumarate are competitive inhibitors of α-KG dependent demethylases. α-KG can also be converted to 2-HG by mutated isocitrate dehydrogenase 1/2 (IDH1/2). 2-HG is a competitive inhibitor of α-KG-dependent demethylase, which can inhibit DNA methylation mediated by TET2 and JMJD2D, and FTO-mediated m^6A-dependent mRNA degradation. PDC, pyruvate dehydrogenase complex; CS, citrate synthase; FH, fumarate dehydrogenase; SDH, succinate dehydrogenase; IDH1/2/3, isocitrate dehydrogenase 1 and 2 and 3; Mut IDH1/2, mutated isocitrate dehydrogenase 1 and 2; α-KG, α-ketoglutarate; FTO, fat mass- and obesity-associated; YTHDF2, YTH domain-containing family protein 2.

Translocation 1 (TET1) (Tao et al., 2015). However, another study found that ALDOB is significantly up-regulated by GATA6 in metastatic liver cancer cell HCT116 to accelerate fructose metabolism, which is beneficial to tumor cell proliferation and metastasis (Li et al., 2017). Further efforts are required to elucidate the precise function of ALDOB in tumorigenesis.

Glyceraldehyde-3-Phosphate Dehydrogenase

Glyceraldehyde-3-phosphate dehydrogenase (GAPDH) catalyzes the reversible conversion of glyceraldehyde-3-phosphate to 1,3-bisphosphoglycerate. Although GAPDH is a known glycolytic enzyme, it has some non-metabolic functions in tumorigenesis. GAPDH has been reported to increase glycolysis and autophagy to protect cells from caspase-independent cell death (CICD) (Colell et al., 2007). GAPDH accelerates glycolysis to increase ATP production, which is associated with its protective effect from apoptosis in the absence of caspase activation (Colell et al., 2007). Under the same conditions, GAPDH facilitates the expression of Atg12 and increases the autophagic flow, which further preserves cell survival (Colell et al., 2007). Under starvation conditions, GAPDH can inhibit multiple transport pathways including Coat Protein I (COPI) transport by targeting the GTPase-activating protein (GAP) against ADP-Ribosylation Factor 1 (ARF1) (Yang et al., 2018). Consequently, GAPDH reduces energy consumption and maintains energy homeostasis (Yang et al., 2018).

The biological function of GAPDH is closely related to its subcellular location (Tristan et al., 2011). When GAPDH is localized in the cytoplasm, GAPDH can interact with the GTPase Rheb to regulate mTOR and autophagy. During glucose starvation, the interaction between GAPDH and Rheb is enhanced, which dissociates Rheb from mTORC1 to reduce its activity and induce autophagy (Lee et al., 2009). Under high glucose conditions, the glycolytic metabolite glyceraldhyde-3-phosphate interferes with the interaction between GAPDH and Rheb, which promotes mTORC1 activity (Lee et al., 2009).

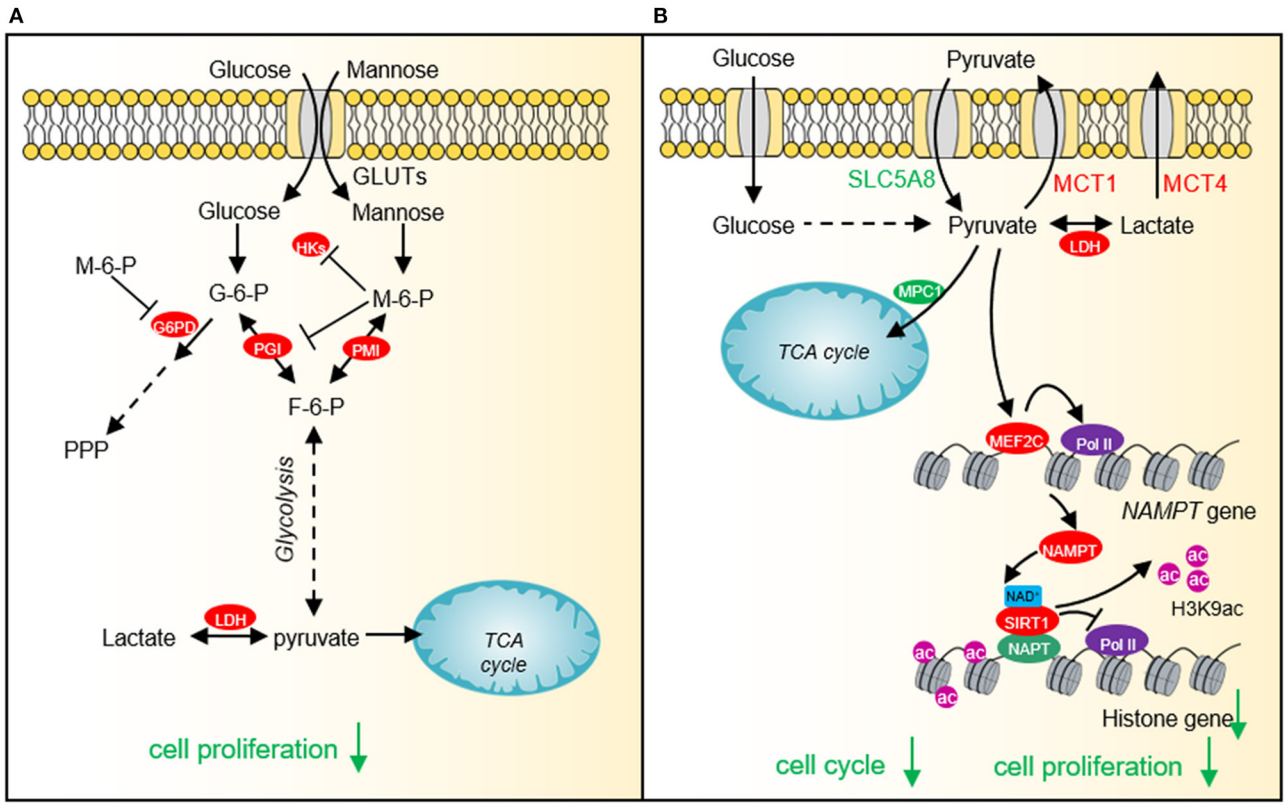

FIGURE 3 | The effect of mannose and pyruvate on cancer cell proliferation. **(A)** Exogenous mannose generates mannose-6-phosphate under the catalysis of hexokinase. High levels of mannose-6-phosphate significantly inhibit aerobic glycolysis and pentose phosphate pathway (PPP) by inhibiting the activities of hexokinase, PGI and G6PD, which affects lactate production and TCA cycle, resulting in cell growth arrest and chemotherapeutic sensitivity. **(B)** Pyruvate represses histone gene expression by inducing the expression of NAD^+ biosynthesis enzyme, nicotinamide phosphoribosyltransferase (NAMPT) *via* myocyte enhancer factor 2C (MEF2C), which then increases NAD^+ levels and activates the histone deacetylase activity of SIRT1. Downregulated histone gene expression leads to cell cycle arrest and tumor cell growth defects. HKs, hexokinases; G-6-P, glucose-6-phosphate; M-6-P, Mannose-6-phosphate; PMI, Mannose-6-phosphate isomerase; PGI, phosphoglucose isomerase; F-6-P, fructose-6-phosphate; LDH, lactate dehydrogenase; SLC5A8, Sodium-coupled monocarboxylate transporter 1; MCT1, Monocarboxylate transporter 1; MCT4, Monocarboxylate transporter 4; MEF2C, myocyte enhancer factor 2C; NAMPT, nicotinamide phosphoribosyltransferase; SIRT1, Silent mating type information regulation 2 homolog-1; NPAT, Nuclear protein of the ataxia telangiectasia mutated locus.

When GAPDH is localized in the mitochondria, GAPDH binds to voltage-dependent anion channels (VDAC) to promote the release of cytochrome *c* and apoptosis-inducing factor (AIF) to induce apoptosis under stress conditions (Tristan et al., 2011). GAPDH has also been reported to translocate into the nucleus when it is S-nitrosated (Kornberg et al., 2010). In the nucleus, GAPDH can interact with the E3 ubiquitin ligase Siah and enhance its activity, leading to Siah-dependent degradation of nuclear proteins and cell death (Hara et al., 2005). The nucleus nitrosylated GAPDH can also interact with the histone deacetylase SIRT1, HDAC2, and DNA-activated protein kinase (DNA-PK) to inhibit their catalytic activity (Kornberg et al., 2010).

GAPDH undergoes various types of covalent modifications, which regulate its localization and/or activity. GAPDH has been reported to be phosphorylated at serine 122 (S122) by AMP-activated protein kinase (AMPK), which promotes its localization in the nucleus (Chang et al., 2015). In the nucleus, the AMPK-phosphorylated GAPDH can competitively bind to SIRT1 and displace SIRT1 repressor DBC1 to activate SIRT1 (Chang et al., 2015). As SIRT1 can stimulate autophagy by deacetylating autophagy protein LC3, the nucleus GAPDH increases autophagy to facilitate cell survival in the absence of glucose (Chang et al., 2015). In addition, GAPDH can be acetylated by histone acetyltransferase p300 and CREB-binding protein CBP, which then enhances the catalytic activity of p300/CBP in a positive feedback manner (**Figure 1**) (Sen et al., 2008). The nitrosylated GAPDH is translocated to the nucleus and interacts with p300/CBP. Upon acetylation, the nitrosylated GAPDH can deliver the N-Nitroso group to p300/CBP to promote their self-acetylation and enhance their activity (Sen et al., 2008). Activated p300/CBP up-regulates the transcription of their downstream targets, i.e., P53 to inhibit tumor cell proliferation (Tristan et al., 2011).

Pyruvate Kinase

Pyruvate kinase (PK) is the last rate limiting enzyme in glycolysis, which catalyzes the production of pyruvate from

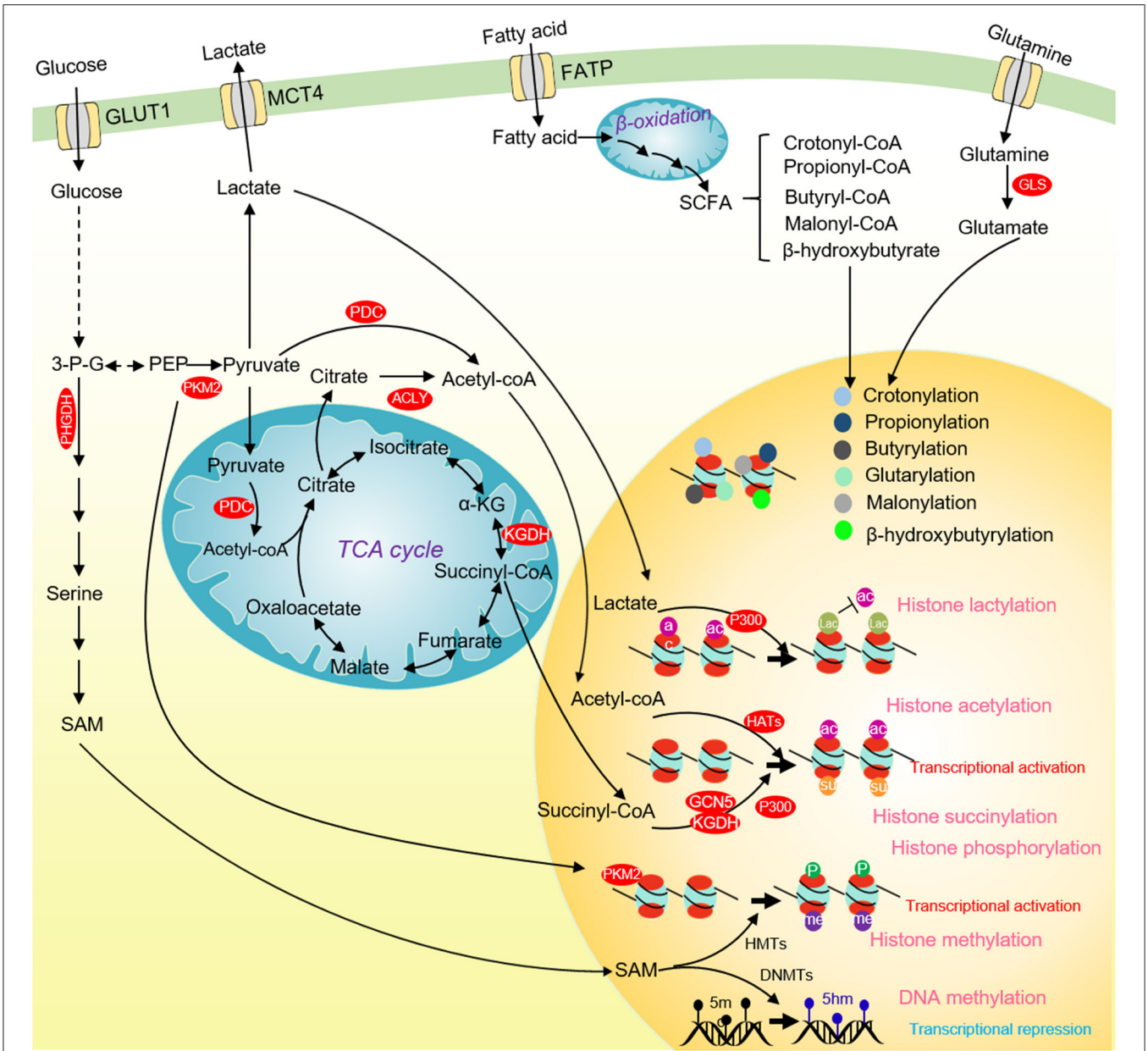

FIGURE 4 | Glucose metabolism and chromatin modifications in cancer cells. ACLY and PDC contribute to nuclear acetyl-CoA production and subsequent histone acetylation and gene activation. Glucose-derived serine and one-carbon metabolism are accelerated in cancer cells to produce SAM. SAM not only enhances DNA methylation to repress the transcription of tumor suppressor genes, but also activates the transcription of tumor-promoting genes by methylating histones. Nuclear PKM2 phosphorylates STAT3 to activate CCND1 transcription and promote cell cycle progression. The TCA cycle intermediate succinate-CoA is fueled to histone succinylation by succinyltransferase (α-KGDH, GCN5, and p300) to activate gene transcription. p300 uses lactate as a substrate to catalyze the lactylation of multiple histone lysine residues to inhibit histone acetylation. Some short-chain fatty acids produced by β-oxidation of fatty acids can provide substrates for histone crotonylation, propionylation, butyrylation, β-hydroxyisobutyrylation, glutarylation and malonylation. ACLY, ATP-citrate lyase; PKM2, pyruvate kinase M2; α-KG, α-ketoglutarate; SCFAs, short-chain fatty acids; 3-P-G, 3-phosphoglycerate; SAM, S-adenosyl methionine; HMTs, Histone methyltransferases; DNMTs, DNA methyltransferases; GCN5, general control non-derepressible 5; p300, histone acetyltransferase p300.

phosphoenolpyruvate (PEP). PK has four different subtypes L, R, M1, M2 that are encoded by two different genes *PKLR* and *PKM*. The L-type and R-type isozymes are encoded by the gene *PKLR* with differential splicing of RNA. While L-type isoenzyme is mainly expressed in liver, kidney, and intestine, R-type isoenzyme is mainly expressed in erythrocytes (Mazurek, 2011). *PKM* gene can undergo alternative splicing to form PKM1 containing exon 9 or PKM2 containing of exon 10. Although PKM1 can activate glucose catabolism, stimulate autophagy, and promote the proliferation of malignant tumors, including

pulmonary neuroendocrine tumors (NETs) and small cell lung cancer (SCLC) (Morita et al., 2018), PKM2 is considered as a specific pyruvate kinase in tumor cells (Israelsen and Vander Heiden, 2015; Morita et al., 2018). PKM2 exists in two states: a dimeric form and a tetrameric form with different PK activities. When PKM2 is in a tetrameric state, it has high PK activity to participate in glycolysis; PKM2 has low PK activity in a dimeric state (Israelsen and Vander Heiden, 2015). Compared with constitutive active PKM1, the activity of PKM2 is low and activated only in the presence of allosteric activators (Chaneton and Gottlieb, 2012). The low PK activity of PKM2 contributes to the "Warburg effect" and metabolic reprogramming in cancer cells. For example, PKM2 diverts glucose metabolism to anabolic metabolism, including the pentose phosphate pathway (PPP), uronic acid pathway (UAP), and polyol pathway (PYP) in a variety of tumor cells and clinical cancer patients, which allows cells to synthesize biological macromolecules (Zhang Z. et al., 2019). The work in yeast revealed that the low PK activity facilitates the diversion of glycolysis to pentose phosphate pathway, which enables cells to accumulate NADPH to maintain the redox balance (Tosato et al., 2012). This implies an important role of PKM2 in tumorigenesis by regulating the antioxidant defense of tumor cells as the strong deregulation of the oxidative stress network has been described in yeast cells with chromosome translocation, which serves as model to study the formation of neoplastic mammalian cells (Sims et al., 2016). In fact, in human lung cancer cells, increased intracellular reactive oxygen species (ROS) concentrations inhibits the glycolytic enzyme pyruvate kinase M2 (PKM2) by oxidating PKM2 at Cys358, which is required to divert glucose flux into the pentose phosphate pathway to combat ROS (Anastasiou et al., 2011).

Due to its important role in tumorigenesis, PKM2 is regulated at both transcriptional and post-transcriptional levels. Three splicing factors, hnRNPL (PTB), hnRNPAI, hnRNPA2 can directly bind exon 9 of *PKM* mRNA, which releases exon 10 and promotes PKM2 expression (Chen et al., 2012). Once activated by epidermal cell growth factor (EGF), the epidermal cell growth factor receptor (EGFR) upregulates the expression of PKM2 by activating the PLCγ1-PKCε-IKKβ-RelA signaling cascade (Yang et al., 2011). PKM2 also undergoes some posttranslational modifications to regulate its activity (Zhang Z. et al., 2019). The acetylation of PKM2 at lysine 305 (K305) reduces its kinase activity by reducing its binding affinity to PEP (Lv et al., 2011). Meanwhile, the acetylation of PKM2 at K305 increases its interaction with heat shock cognate protein 70 (HSC70), which then promotes its degradation by chaperone-mediated autophagy (Lv et al., 2011). The acetylation of KM2 at lysine 433 (K433) inhibits its PK activity by interfering with its binding to allosteric activator FBP (Lv et al., 2013). PKM2 is phosphorylated by fibroblast growth factor receptor type 1 (FGFR1) at tyrosine 105 (Y105), which inhibits its binding to FBP, resulting in a decrease of its activity (Hitosugi et al., 2009).

PKM2 has been reported to function as a transcription cofactor to regulate gene expression. PKM2 can directly interact with the HIF-1α and facilitate the recruitment of HIF-1α and p300 to hypoxia response elements to activate the transcription of HIF-1α target genes (Luo et al., 2011). Nuclear PKM2 binds to β-catenin/TCF/LEF, thereby activating the expression of β-catenin downstream genes, i.e., CCND1 and MYC to promote cell proliferation (Yang et al., 2011). PKM2 forms a complex with pyruvate dehydrogenase (PDC) and p300, which promotes histone acetylation and activates the transcription of aromatic hydrocarbon receptor genes (**Figure 1**) (Zhang Z. et al., 2019).

Notably, PKM2 has been reported to function as a protein kinase to perform a variety of biological functions. PKM2 phosphorylates the mTORC1 inhibitor AKT1S1 to activate mTORC1 signaling pathway, inhibit autophagy in cancer cells and accelerates oncogenic growth (He et al., 2016). PKM2 inhibits oxidative stress-induced apoptosis by phosphorylating BCL2 to increase its protein stability (Liang et al., 2017). PKM2 phosphorylates the signal transducer and activator of transcription 3 (STAT3) to activate the expression of genes required for tumor cell proliferation (Li et al., 2015) (**Figure 1**). Nuclear PKM2 phosphorylates β-catenin at tyrosine 333 (Y333) to enhance β-catenin recruitment and dissociate histone deacetylase HDAC3 at the CCND1 promoter region, which eventually promotes CCND1 transcription and cell cycle progress (Yang et al., 2011). PKM2 has also been reported to modulate histone modifications, which will be discussed later.

Lactate Dehydrogenase

The LDH family has three isoenzymes: LDHA, LDHB, and LDHC. Among them, LDHA catalyzes the conversion of pyruvate to lactate (Feng et al., 2018); LDHB catalyzes the conversion of lactate to pyruvate (Brisson et al., 2016); LDHC is only expressed in the testis (Hua et al., 2017). LDHA is highly expressed in a variety of tumor cells, includes hepatocellular carcinoma, breast cancer, pancreatic cancer, sophageal squamous cell carcinoma (Sheng et al., 2012; Zhao et al., 2013; Hua et al., 2017; Mohammad et al., 2019; Zhou et al., 2019). Knockout or inhibition of LDHA significantly retards tumor cell proliferation, metastasis, and induces cell apoptosis (Zhuang et al., 2010; Miao et al., 2013), indicating that LDHA plays an important role in tumorigenesis and metastasis.

Under both normal and hypoxic conditions, tumor cells rely heavily on LDHA for energy production (Fantin et al., 2006). LDHA may increase the carcinogenicity of intestinal-type gastric cancer (ITGC) by indirectly regulating the expression of octamer-binding transcription factor 4 (Oct-4) (Zhang et al., 2012). LDHA also protects tumor cells from ROS and apoptosis (Le et al., 2010).

The activity of LDHA can be regulated by post-translational modifications. LDHA is phosphorylated at tyrosine 10 (Y10) by oncogenic receptor tyrosine kinase FGFR1, which facilitates the formation of active LDHA tetramers (Fan et al., 2011). FGFR1-catalyzed LDHA phosphorylation can be enhanced by adenylate kinase hCINAP to augment the catalytic activity of LDHA (Ji et al., 2017). LDHA can also be acetylated and recognized by HSC70, which then delivers LDHA to lysosome to be degraded (Zhao et al., 2013).

LDHB is also essential for tumorigenesis and tumor cell survival, which is associated with its regulatory role in autophagy. Protons generated by LDHB is necessary to promote lysosomal acidification and maintain basal autophagy in cancer cells (Brisson et al., 2016). LDHB can be phosphorylated by Aurora-A

to promote glycolysis and tumor progression (Cheng et al., 2019). In addition, LDHB is acetylated at lysine 329 (K329), which can be deacetylated by SIRT5 to enhance its activity (Shi et al., 2019). SIRT5-mediated LDHB deacetylation promotes autophagy and tumorigenesis (Shi et al., 2019).

Gluconeogenesis Enzymes and Tumorigenesis

The glucose concentration in the central area of solid tumors is low (Butler et al., 1975). In the absence of glucose, tumor cells need to use smaller carbon substrates such as lactate and amino acids to synthesize glucose and precursors required for tumor cell growth by gluconeogenesis (Hu et al., 2017). Therefore, the key enzymes in the process of gluconeogenesis are also critical to cancer occurrence and development.

Pyruvate Carboxylase

Pyruvate carboxylase (PC) not only provides oxaloacetate for gluconeogenesis, but also participates in the *de novo* synthesis of fatty acids and the synthesis of glycerol (Jitrapakdee et al., 2006). PC catalyzes the conversion of pyruvate to oxaloacetate, which is then condensed with acetyl-CoA to form citrate. The PC-mediated pyruvate/citrate cycle is necessary for *de novo* fatty acid synthesis (Ballard and Hanson, 1967; Kajimoto et al., 2005). Glycerol is also derived from oxaloacetate with the coordinated action of PC and phosphoenolpyruvate carboxykinase (PEPCK). PEPCK converts oxaloacetate to phosphoenolpyruvate (PEP), which is subsequently converted to glycerol (Reshef et al., 2003).

PC is overexpressed in human breast cancer tissues and correlated with the late stage of tumor progression (Phannasil et al., 2015). PC is important to support the growth and invasion of breast cancer (Phannasil et al., 2015). In addition to anaplerosis, PC affects pyruvate cycling and biosynthesis of metabolites such as the serine, glycine, 5-carbon sugar, and fatty acids (Phannasil et al., 2017).

Phosphoenolpyruvate Carboxykinase

Phosphoenolpyruvate carboxykinase (PEPCK) decarboxylates and phosphorylates oxaloacetate to form PEP in the second step of gluconeogenesis. PEPCK has two isozymes: PEPCK1 (encoded by *PCK1*), PEPCK2 (encoded by *PCK2*), which are distributed in the mitochondria and cytoplasm, respectively (**Figure 1**). PEPCK1 is overexpressed in colorectal cancer and melanoma (Li Y. et al., 2015), whereas PEPCK2 is highly expressed in lung cancer (Vincent et al., 2015), prostate cancer (Zhao et al., 2017), and breast cancer (Mendez-Lucas et al., 2014).

The effect of PEPCK on tumorigenesis is tissue-specific. Overexpression of PEPCK1 activates mTORC1 to promote glycolysis and facilitate colorectal cancer proliferation (Vincent et al., 2015). Under the conditions of glucose deficiency, amino acid limitation, and endoplasmic reticulum (ER) stress, the transcription of PEPCK2 is up-regulated, thereby increasing the adaptability of breast cancer cells to stress conditions (Morita et al., 2018). However, PEPCK1 has been reported to be down-regulated and function as a tumor suppressor in clear cell renal cell carcinoma (ccRCC), liver cancer and hepatocellular carcinoma (HCC) (Tuo et al., 2018, 2019; Shi et al., 2020). Overexpression of PEPCK1 in liver cancer cells significantly reduces the level of cellular ATP to activate AMPK and promote the expression of p27, which causes cell cycle arrest at G1 phase (Tuo et al., 2019). Knockdown of PEPCK1 in ccRCC cells increases the stability of LDHA to enhance the "Warburg effect" and promote cell proliferation and metastasis (Shi et al., 2020). Overexpression of PCK1 can inhibit proliferation of hepatoma cells by reducing the production of ROS and repressing the expression of thioredoxin reductase 1 (TXNRD1) (Tuo et al., 2018).

Fructose-1,6-Bisphosphatase

Fructose-1,6-bisphosphatase (FBPase) catalyzes the second rate-limiting reaction of gluconeogenesis. There are two isoforms of FBPase in mammals: FBP1 (liver) and FBP2 (muscle). Both FBP1 and FBP2 function as tumor suppressors to inhibit the proliferation of tumor cells. Depletion of FBP1/2 contributes to the initiation, promotion and progression of a variety of tumors, including pancreatic ductal adenocarcinoma (PDAC) (Moore et al., 2012), ccRCC (Hirata et al., 2016), colon cancer (Zhang et al., 2016), gastric cancer (Bigl et al., 2008), lung cancer (Gutteridge et al., 2017), and cervical carcinoma (Zhang Y. P. et al., 2019). The FBP1 promoter region in tumor cells is hypermethylated to silent its expression, which is beneficial to tumor cell survival and proliferation (Gutteridge et al., 2017). Knockdown of FBP1 can promote the epithelial-mesenchymal transition, invasion, and metastasis of prostate cancer cells by activating the MAPK signaling pathway, while overexpression of FBP1 can inhibit the proliferation and metastasis of cholangiocarcinoma cells through the Wnt/β-catenin pathway (**Figure 1**) (Zhao et al., 2018). FBP2 has also been reported to activate the AMPK signal transduction, inhibit the Akt-mTOR pathway, attenuate glucose metabolism, enhance cell apoptosis, and inhibit tumor cell proliferation (**Figure 1**) (Li et al., 2013).

Glucose-6-Phosphatase

Glucose-6-phosphatase (G6Pase) catalyzes the last step of gluconeogenesis, which consists of glucose-6-phosphatase catalytic subunit (G6PC) and glucose-6-phosphate translocase (G6PT). G6PT transports glucose-6-phosphate (G-6-P) from the cytoplasm into the endoplasmic reticulum (ER) lumen, where G-6-P is hydrolyzed by G6PC. G6Pase is overexpressed in non-gluconeogenic tumors such as ovarian cancer and glioblastoma (Wang and Dong, 2019). In G6PC-rich ovarian cancer and glioblastoma, G6PC facilitates tumor growth by promoting glycogenolysis. Knockdown of G6PC activates the expression of glycogen synthase and reduces the expression of glycogen phosphorylase, leading to accumulation of glycogen and cell cycle arrest, thereby inhibiting tumor cell proliferation and triggering cell death (Wang and Dong, 2019). In addition, G6PC positively regulates cell cycle progression by modulating cyclin dependent kinase inhibitor 1B (CDKN1B) (Guo et al., 2015). Inhibition of G6PC can enhance the phosphorylation of CDKN1B, thereby reducing the expression of CDK2 and cyclin D1, leading to cell cycle arrest (Guo et al., 2015). G6PT can also promote the invasion of glioblastoma in combined with membrane type 1 matrix metalloproteinase (MT1-MMP)

(Fortier et al., 2008). Inhibition of G6PT and MT1-MMP blocks the MAPK pathway and prevents brain tumor invasion (**Figure 1**) (Fortier et al., 2008). Under hypoxia conditions, knockout of G6PT induces necrosis of glioblastoma cells (Lord-Dufour et al., 2009). However, in glycemic-rich tissues such as liver, G6PC mainly acts on gluconeogenesis and glycogen accumulation, which is not beneficial for tumorigenesis. Thus, G6PC is often expressed at low levels in liver cancer tissues to accumulate a large amount of G-6-P, which could be used for nucleotide synthesis (Wang et al., 2012).

TCA Cycle and Tumorigenesis

TCA cycle is the central hub of energy metabolism, macromolecule synthesis, and redox balance. Enzymes in the TCA cycles play important roles in cancer metabolism and tumorigenesis (Anderson et al., 2018). In this section, we will describe the following TCA enzymes: citrate synthase (CS), isocitrate dehydrogenase (IDH), α-ketoglutarate dehydrogenase complex (α-KGDHC), and succinate dehydrogenase (SDH).

Citrate Synthase

Citrate synthase (CS) is the first rate-limiting enzyme in the TCA cycle, catalyzing the formation of citrate from acetyl-CoA and oxaloacetate (**Figure 2**). Growing evidence indicates that CS plays an important role in regulating cancer cell growth and tumorigenesis (Chen L. et al., 2014). Knockdown of CS inhibits tumor cell proliferation, cell colony formation, cell migration, cell invasion, and cell cycle progression (Cai et al., 2020).

The expression of CS is regulated by STAT3. Inhibition of STAT3 down-regulates the expression of CS and thus inhibits cell growth and proliferation (MacPherson et al., 2017). Exogenous addition of sodium citrate attenuates this inhibitory effect (MacPherson et al., 2017).

Isocitrate Dehydrogenase

Isocitrate dehydrogenase (IDH) is the second rate-limiting enzyme in the TCA cycle. IDH is composed of three isoenzymes: the cytoplasmic IDH1 and the mitochondrial IDH2/3 (**Figure 2**). IDH is mutated in a variety of tumor cells (Sajnani et al., 2017). IDH mutations stimulate the occurrence of cancer in a variety of biological processes. Tumor cells with IDH1R132H mutations can increase the level of HIF-1α, thereby promoting tumor cell growth (**Figure 2**) (Zhao et al., 2009). The IDH1 R132H mutant catalyzes the conversion of α-KG to oncometabolite 2-hydroxyglutamate (2-HG) (**Figure 2**). The mutations of R172 and R140 in IDH2 lead to accumulation of 2-HG at extremely high levels (Dang et al., 2016). High levels of 2-HG competitively inhibit the activities of α-KG-dependent histone demethylase and TET2 DNA demethylase, leading to global chromatin methylation disorders, which is beneficial to tumorigenesis (Chowdhury et al., 2011; Xu et al., 2011). Interestingly, 2-HG has also been reported to repress tumor cell proliferation by targeting FTO/m^{6}A/MYC/CEBPA signals (**Figure 2**) (Su et al., 2018). R-2HG targets Fat mass and obesity-associated (FTO) and inhibits its RNA demethylase activity, which significantly increases the abundance of m^{6}A in cancer cells, leading to degradation of myc/CEBPA mRNAs in an m^{6}A-dependent manner (Su et al., 2018). As a consequence, tumor cell proliferation is impaired (Su et al., 2018). Inhibition of FTO by R-2-HG also ameliorates aerobic glycolysis by increasing m^{6}A levels in the mRNA of phosphofructokinase (PFKP) and LDHB, which reduces the expression of PFKP and LDHB (Qing et al., 2021).

α- Etoglutarate Dehydrogenase Complex

α-ketoglutarate dehydrogenase complex (α-KGDHC) is the third rate-limiting enzyme in the TCA cycle, which is composed of α-KG dehydrogenase (OGDH), dihydrolipidamide S-succinyltransferase (DLST) and dihydrolipidamide dehydrogenase (DLD). The expression of OGDH is low in many cancers due to DNA hypermethylation at its promoter and the low expression of DLD is related to the poor prognosis of some cancer patients (Zhang et al., 2015; Shin et al., 2020). Recent studies have shown that the α-KGDH complex enters into the nucleus and acts with lysine acetyltransferase 2A (KAT2A) to catalyze histone succinylation, which is beneficial for cell proliferation and tumor development (**Figure 2**) (Wang et al., 2017).

Succinate Dehydrogenase

Succinate dehydrogenase (SDH) converts succinate to fumarate. Mutations or loss of function of SDH can lead to hereditary paraganglioma, pheochromocytoma, and other genetic syndrome (Sajnani et al., 2017). The single-base substitution of SDH that causes a 33-amino acid C terminal truncation of SDHC protein, increases the intracellular ROS, which leads to metabolic stress, genome instability, and promote tumorigenesis (Slane et al., 2006). Meanwhile, SDH mutation can lead to the accumulation of succinate, which can activate succinate receptor 1 (SUCNR1), also known as regulatory G protein coupled metabolic receptor 91 (GPR91), and stimulate the release of vascular endothelial growth factor (VEGF), which then activates various kinase signal transduction pathways involved in tumorigenesis, angiogenesis, and other biological processes (Sajnani et al., 2017).

IMPACT OF GLUCOSE METABOLITES ON TUMORIGENESIS

In order to fulfill the needs of tumor cell growth and proliferation, tumor cells must increase the uptake of nutrients. Glucose and glutamine are the two main nutrients used for cell proliferation and biomacromolecule synthesis in tumor cells (Pavlova and Thompson, 2016). Lactate has recently been shown to serve as an energy source to help tumor cells survive in the absence of glucose (Rabinowitz and Enerback, 2020). Therefore, glucose-derived intermediate metabolites have become the targets of cancer treatment. Limiting the glucose uptake or repressing the expression and activity of glucose transporter GLUT1 can significantly inhibit the proliferation and survival of a variety of tumor cells (Gras et al., 2014). Mannose, as a monosaccharide, shares the same transporter with glucose, which significantly inhibits the growth of various tumor cells and the proliferation of xenogeneic tumors in nude mice (**Figure 3A**) (Gonzalez et al., 2018). 2-DG is a glucose analog, which is also transported by

GLUT into cells and then phosphorylated by hexokinase to form 2-deoxy-D-glucose-6-phosphate (2DG-6-P) (Zhang et al., 2014). The accumulation of 2DG-6-P attenuates glycolysis by non-competitively inhibiting HK and competitively inhibiting PGI, which in turn leads to reduced ATP production, cell cycle arrest, and cell death (**Figure 1**) (Zhang et al., 2014).

Pyruvate

Our recent study shows that cancer cells prefer low intracellular pyruvate as the intracellular pyruvate concentration is lower in cervical cancer and lung cancer than adjacent normal tissues (Ma et al., 2019). Exogenous supplied pyruvate inhibits the proliferation of various types of cancer cells, including human cervical cancer cells, liver carcinoma cells, and breast adenocarcinoma cells pyruvate as well as xenografted tumor, implying that pyruvate can function as a potential anti-cancer compound (Ma et al., 2019). Further study indicates that pyruvate reduces the expression of core histone genes to decompact chromatin structure and cause cell cycle arrest (**Figure 3B**) (Ma et al., 2019). Mechanistically, pyruvate induces the expression of NAD^+ biosynthetic enzyme nicotinamide phosphoribosyl transferase (NAMPT) by activating myocyte enhancer factor 2C (MEF2C). The up-regulated NAMPT significantly promotes the biosynthesis of NAD^+, thereby enhancing the activity of the NAD^+-dependent histone deacetylase SIRT1. The activated SIRT1 reduces H3K9ac in the promoter region of histone genes and represses histone gene transcription (Ma et al., 2019).

The pyruvate analogs have also been reported to have anti-cancer effects. 3-bromopyruvate not only effectively attenuates aerobic glycolysis of tumor cells, but also inhibits mitochondrial oxidative phosphorylation (Fan et al., 2019; Linke et al., 2020). Ethyl pyruvate, another derivative of pyruvate, has recently been reported to inhibit tumor cell invasion, migration, and apoptosis (Liu Q. et al., 2019; Zhang T. et al., 2019). Specifically, ethyl pyruvate inhibits the growth of non-small cell lung cancer (NSCLC) by blocking the high mobility group box 1 (HMGB1)-RAGE axis and NF-κB/STAT3 pathway (Liu Q. et al., 2019). Ethyl pyruvate down-regulates the expression of HMGB1 and RAGE, induces the accumulation of cell cycle inhibitor p27, which leads to blockage of cell cycle progression (Liu Q. et al., 2019; Zhang T. et al., 2019).

Lactate

Increased lactate production has been considered as an important marker of the "Warburg effect." Lactate not only acts as an energy source and gluconeogenic precursor to protect cancer cells from glucose deprivation, but also functions as a signaling molecule to mediate a variety of biological processes (Hu et al., 2017; Brooks, 2020). As a shuttle molecule, lactate plays an important role in converting oxidative cells to glycolytic cells. Lactate inhibits prolylhydroxylase 2 activity and activates HIF-1α in normoxic oxidative tumor cells. HIF-1α then up-regulates the transcription of glycolytic enzymes, which accelerates glycolysis and promotes tumor growth (De Saedeleer et al., 2012). In addition to HIF-1α, lactate also affects the transcription of key oncogenes (MYC, RAS, PI3KCA), transcription factors (E2F1), tumor suppressors (BRCA1, BRCA2) and genes involved in cell cycle and proliferation (San-Millan et al., 2019). Lactate can also stabilize HIF-2α and activate MYC to induce glutamine transporter ASCT2 and glutaminase 1 (GLS1). The high expression of GLS1 promotes the uptake and catabolism of glutamine, which is beneficial for the survival and proliferation of oxidative cancer cells (Brooks, 2020). Another important mechanism by which lactate regulates gene expression is causing lactylation of lysine residues on histones, which will be discussed later. Therefore, targeting lactate metabolism or inhibiting lactate uptake has become an effective strategy for tumor treatment (Brooks, 2020).

Citrate

Citrate has potential anti-tumor functions in different types of cancer cells, including acute monocytic leukemia (U937), breast cancer (MCF-7), pancreatic cancer (BxPC3), lung cancer (A549), Glioma (G6), neuroblastoma (Tet21N), pleural mesothelioma (MSTO-211H), gastric cancer BGC-823 and SGC-790 (Huang et al., 2020). Sodium citrate can attenuate glycolysis and cause cell cycle arrest by inhibiting the activity of PFK1 (Huang et al., 2020). Citrate can also reduce the expression of anti-apoptotic proteins B-cell lymphoma-2 (Bcl-2) and Myeloid cell leukemia-1 (Mcl-1) to trigger cell apoptosis (Chen L. et al., 2014).

METABOLIC REGULATION OF CHROMATIN MODIFICATIONS

Most chromatin modifying enzymes use metabolites as cofactors or substrates, so their activity is directly or indirectly regulated by these metabolites, such as acetyl coenzyme A (acetyl-CoA), S-adenosylmethionine (SAM). In addition, α-ketoglutarate, lactate, succinate, and some short chain fatty acids have recently been found to be involved in chromatin modifications. In this section, we will discuss the effects of glucose-derived metabolites and metabolic enzymes on chromatin modifications.

Contribution of Metabolism to Chromatin Modification in Cancer

Histone Glcnacylation

Acetylglucosamine glycosylation (GlcNAcylation) is one of the most common protein post-translational modifications. It is an advanced glycation formed by a series of condensation, oxidation, and rearrangement of monosaccharides in the form of aldose (such as glucose and fructose) or glycolysis by-products (Dall'olio and Trinchera, 2017). GlcNAcylation can directly affect chromatin structure and gene expression by modifying histone residues or epigenetic regulatory factors (histone methyltransferases, protein kinases, and acetyltransferases) (Slawson et al., 2008; Sakabe and Hart, 2010; Dehennaut et al., 2014). Glycosylated histones H3 and H4 disrupt the assembly of nucleosomes and reduce histone acetylation, leading to disassembly of chromatin structure and deregulated gene expression (Chen et al., 2013). Breast cancer cells have a high level of histone H3 glycosylation; however, when the deglycase DJ-1 is knocked down, the overall level of histone glycosylation is significantly increased and the cell viability is

decreased (Zheng et al., 2019). This result indicates that when histones have excessive glycosylation, it greatly affects histone acetylation and ubiquitination and causes damage to tumor cells. DNA demethylase TET2 interacts with glycosyltransferase OGT and forms a complex at the transcription start site (TSS) to induce histone H2B S112 GlcNAcylation and promote gene transcription (Chen et al., 2013). In addition, multiple amino acid residues of histone demethylase EZH2 can be glycosylated by OGT to enhance its protein stability and enzymatic activity to promote tumor progression (Lo et al., 2018).

Histone Phosphorylation

The direct evidence to link glucose metabolism and histone phosphorylation is the finding that PKM2 phosphorylates H3 on threonine 11 (H3T11) (Yang et al., 2012). PKM2 interacts with β-catenin and binds at the CCND1 promoter region to phosphorylate histone H3T11, which causes the dissociation of histone deacetylase HDAC3 from chromatin and an increase of H3K9 acetylation (H3K9ac) at CCND1 promoter to activate CCND1 transcription (**Figure 4**) (Yang et al., 2012). Our group also showed that the yeast pyruvate kinase Pyk1 can form a complex called SESAME to phosphorylate histone H3T11 (H3pT11) to repress gene expression in response to glucose and serine availability (Li S. et al., 2015; Yu et al., 2017). We also find that SESAME phosphorylates H3T11 at telomeres to maintain the integrity of telomere heterochromatin during chronological aging (Zhang et al., 2021). H3pT11 can contribute to tumorigenesis by recruiting chromatin modifying factors. For example, H3pT11 can be bound by WDR5, a subunit of MLL complex to promote H3K4 methylation (Kim et al., 2014). In addition, the E3 ubiquitin ligase RNF8 can bind H3pT11 to mediate H3K4 ubiquitination and facilitate the expression of MYC and CCND1 (Xia et al., 2017).

Histone Acetylation

Acetyl-coenzyme A (acetyl-CoA) is an important substrate for histone acetylation. Acetyl-CoA is produced from pyruvate, citrate, and acetate by pyruvate dehydrogenase complex (PDC), ATP citrate synthase (ACLY), and acetyl-CoA synthetase short-chain family member (ACSS), respectively. Acetyl-CoA can also be generated from fatty acid β-oxidation as well as the metabolism of amino acids and ketone bodies (Sivanand et al., 2018). In cancer cells, deprivation of glucose, glutamine or pyruvate reduces the overall level of histone acetylation (Mcbrian et al., 2013). The glycolysis inhibitor 2-DG or knockdown of hexokinase, pyruvate dehydrogenase, and pyruvate kinase significantly reduces most histone acetylation, leading to compacted chromatin structure, repressed gene expression and reduced tumor cell proliferation (Liu et al., 2015; Yucel et al., 2019). These studies indicate that glucose metabolism can directly regulate histone acetylation.

In addition to modulating the intracellular acetyl-CoA level, glucose metabolism can affect histone acetylation by regulating the activity of histone deacetylase enzyme HDAC. The glucose-derived pyruvate can inhibit tumor cell proliferation by activating the HDAC activity of SIRT1 to reduce H3K9ac (Ma et al., 2019). The catalytic activity of class III histone deacetylases (Sirtuins) depends on NAD^+, a cofactor of glucose metabolism, which makes it sensitizes to NAD^+ and glucose metabolism changes. Moreover, the activity of Sirtuins is regulated by some NAD^+ producing enzymes. The nuclear LDH interacts with SIRT1 and enhances its activity by producing localized NAD^+, which helps cells adapt to oxidative stress (Castonguay et al., 2014). GAPDH interacts with Sir2, the yeast homolog of SIRT1, and enhances its activity by elevating nuclear NAD^+ (Ringel et al., 2013).

Histone Lactylation

Recent studies revealed that histones can undergo a new type of histone modification, histone lactylation (**Figure 4**) (Zhang et al., 2019). As a product of glucose metabolism, lactate serves as the substrate for histone lactylation, which can modify at ∼28 residues on human and mouse core histones (Zhang et al., 2019). Like histone acetylation, the lactylated histones can directly promote gene transcription (Zhang et al., 2019). The discovery of histone lactylation provides a new insight into studying the role of lactate in tumorigenesis and metabolic diseases.

Chromatin Methylation

Chromatin methylation consists of three major types: DNA, RNA, and histone methylation. Chromatin methylation is catalyzed by methyltransferases using SAM as a methyl donor, which is mainly produced from glucose-derived serine metabolism (Yu et al., 2018). We and others have reported that the intracellular SAM concentration can specifically regulate the level of histone H3K4 trimethylation (H3K4me3) in both yeast and mouse embryonic stem cells (mESCs) (**Figure 4**) (Shyh-Chang et al., 2013; Wu et al., 2019). As a methyl donor, the intracellular SAM also regulates the global DNA methylation. The *de novo* DNA methylation by DNA methyltransferase 3a (DNMT3a) is sensitive to SAM changes, and SAM can effectively induce DNA methylation and reduce the expression of Vascular endothelial growth factor C (VEGF-C), thus inhibiting tumor growth (Nishikawa et al., 2015).

Chromatin Demethylation

It has been reported that α-ketoglutarate (α-KG) acts as a cofactor for several chromatin-modifying enzymes, including histone demethylase, Ten-eleven-translocation (TET) family of enzymes involved in DNA and RNA demethylation (**Figure 2**) (Tran et al., 2019). α-KG is an important metabolic intermediate produced in the TCA cycle, and is a key point linking carbon and nitrogen metabolism. Recent studies show that inhibition of glucose metabolism reduces α-KG level and inhibits the activity of the Jumonji family demethylase JMJD2B (Fu L. N. et al., 2018). JMJD2B can demethylate H3K9/K36 at autophagy associated gene (*ATG*) promoter to regulate autophagy (Fu L. N. et al., 2018). The glucose-derived α-KG maintains H3K27me3 at low levels to regulate chromatin accessibility and glioma cell survival (Chung et al., 2020). The TET proteins are α-KG-dependent dioxygenases that oxidize 5-methylcytosine (5mC) to 5-hydroxymethylcytosine (5hmC) to mediate DNA demethylation (Xiao et al., 2012). α-KG can regulate genome-wide DNA methylation and tumorigenesis by targeting TET (Xiao et al., 2012). In addition, the RNA demethylase, Fat mass

and obesity-associated protein (FTO) is also α-KG-dependent (Jia et al., 2011). Therefore, emerging researches for cancer therapy are aimed at manipulating the α-KG level.

As described earlier, α-KG can be converted to 2-HG by the IDH1/2 mutant. 2-HG is also a competitive inhibitor of multiple dioxygenases (Wang P. et al., 2015). R-2HG can inhibit the RNA demethylase activity of FTO, increase m^6A at *MYC* and *CEBPA* mRNAs and reduce their stability, which ultimately inhibits tumor growth (Su et al., 2018). Thus, α-KG plays an important role in regulating chromatin (de)methylation by targeting the activity of chromatin demethylases. In addition, glycolysis can also indirectly inhibit the activity of histone demethylase Jhd2 by promoting H3K14ac, thus mediating a crosstalk between H3K14ac and H3K4me3 (Wu et al., 2019).

Histone Acylation

Histone acylation is an important chromatin modification for transcription regulation (**Figure 4**). There are various types of histone acylation, including crotonylation, 2-hydroxyisobutyrylation, butyrylation, propionylation, glutarylation, malonylation, and succinylation (Yu et al., 2018). These modifications are regulated by short-chain acyl-CoA species, which are produced during cellular metabolism. Histone acylation is associated with transcriptionally active genes and functions in a variety of physiological processes, including signal-dependent gene activation, spermatogenesis, tissue injury, and metabolic stress (Sabari et al., 2017). The histone acetyltransferase, p300 has crotonyltransferase activity and catalyzes H3K18 crotonylation depending on the intracellular crotonyl-CoA concentrations (Kollenstart et al., 2019). Chromodomain Y-like corepressor CDYL acts as a crotonyl-CoA hydratase to convert crotonyl-CoA to β-hydroxybutyryl, which negatively regulates histone crotonylation during spermatogenesis (Liu et al., 2017). Under chronic social defeat stress, CDYL is upregulated to reduce histone crotonylation and increase H3K27 trimethylation (H3K27me3), leading to repressed transcription of neuropeptide VGF (Liu Y. et al., 2019). The class I histone deacetylases (HDACs) have been demonstrated to function as the major histone decrotonylases and are regulated by microbiota derived short chain fatty acids (Wei et al., 2017).

Histone propionylation is an active chromatin marker. Propionyl-CoA stimulates gene transcription by promoting the enrichment of H3K14 propionylation at promoters of active genes (Kebede et al., 2017). The MYST family of lysine acetyltransferases (KATs) MOF directly binds propionyl-CoA and possesses strong propionyltransferase activity both *in vitro* and *in vivo* (Han et al., 2018). Histone acetyltransferase p300 can also catalyze H3K23 propionylation and histone deacetylase SIRT2 can remove this modification in presence of NAD^+, which mediates the crosstalk between histone acetylation and propionylation (Liu et al., 2009).

Similarly, histone butyrylation is catalyzed by p300/CBP and regulated by intracellular butyryl-CoA level (Chen et al., 2007). Histone K5 and K8 butyrylation is enriched at meiotic gene promoter and mediates spermatogenesis (Du et al., 2011).

Histone glutarylation and malonylation are recently identified histone modifications despite little is known about their biological functions. H4K91 can be glutarylated by lysine acetyltransferase 2A (KAT2A) and deglutarylated by SIRT7, which has been served as a new regulatory mechanism for chromatin dynamics (Bao et al., 2019). Molonylation of histone H2AK119 can inhibit H2A phosphorylation and influence chromosome segregation (Ishiguro et al., 2018). Histone malonylation also provides a new insight into neural tube defects (NTDs) caused by high glucose-induced diabetes (Zhang et al., 2020).

Histone β-hydroxybutyrylation is induced by ketogenesis under prolonged fasting (Xie et al., 2016). Ketone bodies including acetoacetic acid, β-hydroxybutyric acid and acetone are intermediate products of liver fatty acid oxidation during starvation, strenuous exercise and diabetes. SIRT3 acts as the de-β-hydroxybutyrylase and selectively catalyzes de-β-hydroxybutyrylation of histones due to its Zn-dependent domain (Zhang X. et al., 2019). Exogenous β-hydroxybutyrate treatment increases H3K9 β-hydroxybutyrylation and activates the expression of MMP-2 and VEGF in diabetic rats (Wu X. et al., 2020). Nevertheless, the role of β-hydroxybutyrylation in tumorigenesis and metastasis remains to be explored.

DEVELOPMENT OF ANTI-CANCER THERAPY BY TARGETING CANCER METABOLISM

Metabolic abnormalities in tumor cells also become the potential targets for the development of anti-cancer drugs. As previously mentioned, some metabolites have anti-cancer activity, including pyruvate, 2DG-6-P, mannose-6-phosphate, and citrate. Most metabolic enzymes that regulate epigenetic modifications are upregulated in tumors and some metabolic enzymes have become targets for cancer treatment (Yu and Li, 2017). There are some drugs targeting glycolysis of tumor cells in preclinical or clinical studies, such as inhibitors for glucose transporters (GLUTs): Phloretin, Fasentin, and lonidamine (LN) (Oudard et al., 2003; Palmieri et al., 2009; Dando et al., 2017), and gossypol, an inhibitor for LDH (Doherty and Cleveland, 2013). In addition, some anti-cancer drugs that target gluconeogenesis have been used in clinical trials. The inhibitor of PEPCK, 3-Mercaptopicolinic acid (MPA) induces tumor cell apoptosis by causing glucose starvation (Wang and Dong, 2019). CM-272 can reverse the Snail-mediated FBP1 expression defects under hypoxic conditions and inhibit the proliferation of hepatocellular carcinoma (HCC) (Barcena-Varela et al., 2019). Dexamethasone promotes gluconeogenesis by enhancing the expression of G6PC and PEPCK, thereby inhibiting the growth of HCC (Wang and Dong, 2019). As we understand more about the role of TCA cycle in tumorigenesis, targeting the TCA cycle to treat cancer has begun to emerge. For example, the IDH2 mutant has become a target for clinical cancer treatment and two drugs have been developed, Enasidenib (AG-221, inhibitors mutant IDH2) and AG-881 (inhibitors of mutant IDH1/2) (Yen et al., 2010). AG-221 is used as a single drug treatment of acute myelogenous

leukemia (AML) and solid tumors by reducing intracellular 2-HG (Yen et al., 2010). AG-881 is currently undergoing clinical trials for AML patients with IDH1/2 mutations (Yen et al., 2010). These drugs not only affect cancer metabolism, but also control chromatin modifications. Understanding the relationship between cancer cell metabolism and chromatin modifications not only helps elucidate the mechanism of tumorigenesis, but also facilitates the development of more efficient, accurate, and specific treatment strategies for cancer treatment.

DISCUSSION

Cancer cells have their specific metabolic pathways and epigenetic modifications that are distinct from normal cells, which contribute to the occurrence and development of tumors. Metabolic reprogram and the concurrent changes in chromatin modifications help tumor cells survive and proliferate in the nutrient-poor environment. Although there is significant progress toward understanding the relationship between cancer metabolism and chromatin modifications, there are still many problems that need to be resolved. First, we and others noticed that some metabolic enzymes and metabolites have both positive and negative effects on cell growth. We have previously reported that pyruvate can inhibit tumor growth by inhibiting histone gene expression (Ma et al., 2019). Pyruvate can also inhibit the activity of HDAC1/3 to trigger apoptosis of colon cancer cells (Thangaraju et al., 2009). However, pyruvate has also been reported to protect cancer cells from DNA damage and oxidative stress under certain circumstance (Tauffenberger et al., 2019). Some metabolic enzymes regulate tumorigenesis in a tissue-dependent manner. PEPCK1 facilitates colorectal cancer proliferation (Yamaguchi et al., 2019); however, it functions as a tumor suppressor in clear cell renal cell carcinoma (ccRCC), liver cancer and hepatocellular carcinoma (HCC) (Liu et al., 2018). Therefore, the anti-tumor drugs developed to target cancer metabolism may also have cell and/or tissue specificity. Secondly, as more metabolic enzymes and metabolites are found to be translocated into the nucleus, elucidating the functions of these metabolic enzymes and metabolites in the nucleus is important for development of anti-cancer therapy.

DATA AVAILABILITY STATEMENT

The original contributions presented in the study are included in the article/supplementary material, further inquiries can be directed to the corresponding authors.

AUTHOR CONTRIBUTIONS

RM, YW, SL, and XY wrote and revised the manuscript. All authors contributed to the article and approved the submitted version.

FUNDING

This project was supported by funding from National Natural Science Foundation of China (31970578 to SL, 31872812 to XY) and Natural Science Foundation of Hubei Province (2019CFA077 to XY).

ACKNOWLEDGMENTS

We apologize to colleagues whose work cannot be cited here due to space limitation.

REFERENCES

Anastasiou, D., Poulogiannis, G., Asara, J. M., Boxer, M. B., Jiang, J. K., Shen, M., et al. (2011). Inhibition of pyruvate kinase M2 by reactive oxygen species contributes to cellular antioxidant responses. *Science* 334, 1278–1283. doi: 10.1126/science.1211485

Anderson, N. M., Mucka, P., Kern, J. G., and Feng, H. (2018). The emerging role and targetability of the TCA cycle in cancer metabolism. *Protein Cell* 9, 216–237. doi: 10.1007/s13238-017-0451-1

Ballard, F. J., and Hanson, R. W. (1967). The citrate cleavage pathway and lipogenesis in rat adipose tissue: replenishment of oxaloacetate. *J. Lipid Res.* 8, 73–79. doi: 10.1016/S0022-2275(20)38917-3

Bao, X., Liu, Z., Zhang, W., Gladysz, K., Fung, Y. M. E., Tian, G., et al. (2019). Glutarylation of histone H4 lysine 91 regulates chromatin dynamics. *Mol. Cell* 76, 660–675 e669. doi: 10.1016/j.molcel.2019.08.018

Barcena-Varela, M., Caruso, S., Llerena, S., Alvarez-Sola, G., Uriarte, I., Latasa, M. U., et al. (2019). Dual targeting of histone methyltransferase G9a and DNA-methyltransferase 1 for the treatment of experimental hepatocellular carcinoma. *Hepatology* 69, 587–603. doi: 10.1002/hep.30168

Bigl, M., Jandrig, B., Horn, L. C., and Eschrich, K. (2008). Aberrant methylation of human L- and M-fructose 1,6-bisphosphatase genes in cancer. *Biochem. Biophys. Res. Commun.* 377, 720–724. doi: 10.1016/j.bbrc.2008.10.045

Brisson, L., Banski, P., Sboarina, M., Dethier, C., Danhier, P., Fontenille, M. J., et al. (2016). Lactate dehydrogenase B controls lysosome activity and autophagy in cancer. *Cancer Cell* 30, 418–431. doi: 10.1016/j.ccell.2016.08.005

Brooks, G. A. (2020). Lactate as a fulcrum of metabolism. *Redox Biol.* 35:101454. doi: 10.1016/j.redox.2020.101454

Butler, T. P., Grantham, F. H., and Gullino, P. M. (1975). Bulk transfer of fluid in the interstitial compartment of mammary tumors. *Cancer Res.* 35(11 Pt 1), 3084–3088.

Cai, Z., Deng, Y., Ye, J., Zhuo, Y., Liu, Z., Liang, Y., et al. (2020). Aberrant expression of citrate synthase is linked to disease progression and clinical outcome in prostate cancer. *Cancer Manag. Res.* 12, 6149–6163. doi: 10.2147/CMAR.S255817

Castonguay, Z., Auger, C., Thomas, S. C., Chahma, M., and Appanna, V. D. (2014). Nuclear lactate dehydrogenase modulates histone modification in human hepatocytes. *Biochem. Biophys. Res. Commun.* 454, 172–177. doi: 10.1016/j.bbrc.2014.10.071

Chaneton, B., and Gottlieb, E. (2012). Rocking cell metabolism: revised functions of the key glycolytic regulator PKM2 in cancer. *Trends Biochem. Sci.* 37, 309–316. doi: 10.1016/j.tibs.2012.04.003

Chang, C., Su, H., Zhang, D., Wang, Y., Shen, Q., Liu, B., et al. (2015). AMPK-dependent phosphorylation of GAPDH triggers Sirt1 activation and is necessary for autophagy upon glucose starvation. *Mol. Cell* 60, 930–940. doi: 10.1016/j.molcel.2015.10.037

Chang, Y. C., Chan, Y. C., Chang, W. M., Lin, Y. F., Yang, C. J., Su, C. Y., et al. (2017). Feedback regulation of ALDOA activates the HIF-1alpha/MMP9 axis to promote lung cancer progression. *Cancer Lett.* 403, 28–36. doi: 10.1016/j.canlet.2017.06.001

Chang, Y. C., Chiou, J., Yang, Y. F., Su, C. Y., Lin, Y. F., Yang, C. N., et al. (2019). Therapeutic targeting of aldolase a interactions inhibits

lung cancer metastasis and prolongs survival. *Cancer Res.* 79, 4754–4766. doi: 10.1158/0008-5472.CAN-18-4080

Chen, J., Zhang, S., Li, Y., Tang, Z., and Kong, W. (2014). Hexokinase 2 overexpression promotes the proliferation and survival of laryngeal squamous cell carcinoma. *Tumour Biol.* 35, 3743–3753. doi: 10.1007/s13277-013-1496-2

Chen, L., Liu, T., Zhou, J., Wang, Y., Wang, X., Di, W., et al. (2014). Citrate synthase expression affects tumor phenotype and drug resistance in human ovarian carcinoma. *PLoS ONE* 9:e115708. doi: 10.1371/journal.pone.0115708

Chen, M., David, C. J., and Manley, J. L. (2012). Concentration-dependent control of pyruvate kinase M mutually exclusive splicing by hnRNP proteins. *Nat. Struct. Mol. Biol.* 19, 346–354. doi: 10.1038/nsmb.2219

Chen, Q., Chen, Y., Bian, C., Fujiki, R., and Yu, X. (2013). TET2 promotes histone O-GlcNAcylation during gene transcription. *Nature* 493, 561–564. doi: 10.1038/nature11742

Chen, Y., Sprung, R., Tang, Y., Ball, H., Sangras, B., Kim, S. C., et al. (2007). Lysine propionylation and butyrylation are novel post-translational modifications in histones. *Mol. Cell. Proteomics* 6, 812–819. doi: 10.1074/mcp.M700021-MCP200

Cheng, A., Zhang, P., Wang, B., Yang, D., Duan, X., Jiang, Y., et al. (2019). Aurora-A mediated phosphorylation of LDHB promotes glycolysis and tumor progression by relieving the substrate-inhibition effect. *Nat. Commun.* 10:5566. doi: 10.1038/s41467-019-13485-8

Chowdhury, R., Yeoh, K. K., Tian, Y. M., Hillringhaus, L., Bagg, E. A., Rose, N. R., et al. (2011). The oncometabolite 2-hydroxyglutarate inhibits histone lysine demethylases. *EMBO Rep.* 12, 463–469. doi: 10.1038/embor.2011.43

Chung, C., Sweha, S. R., Pratt, D., Tamrazi, B., Panwalkar, P., Banda, A., et al. (2020). Integrated metabolic and epigenomic reprograming by H3K27M mutations in diffuse intrinsic pontine gliomas. *Cancer Cell* 38, 334–349 e339. doi: 10.1016/j.ccell.2020.07.008

Colell, A., Ricci, J. E., Tait, S., Milasta, S., Maurer, U., Bouchier-Hayes, L., et al. (2007). GAPDH and autophagy preserve survival after apoptotic cytochrome c release in the absence of caspase activation. *Cell* 129, 983–997. doi: 10.1016/j.cell.2007.03.045

Dall'olio, F., and Trinchera, M. (2017). Epigenetic bases of aberrant glycosylation in cancer. *Int. J. Mol. Sci.* 18:998. doi: 10.3390/ijms18050998

Dando, I., Pacchiana, R., Pozza, E. D., Cataldo, I., Bruno, S., Conti, P., et al. (2017). UCP2 inhibition induces ROS/Akt/mTOR axis: role of GAPDH nuclear translocation in genipin/everolimus anticancer synergism. *Free Radic. Biol. Med.* 113, 176–189. doi: 10.1016/j.freeradbiomed.2017.09.022

Dang, C. V., and Semenza, G. L. (1999). Oncogenic alterations of metabolism. *Trends Biochem. Sci.* 24, 68–72. doi: 10.1016/S0968-0004(98)01344-9

Dang, L., Yen, K., and Attar, E. C. (2016). IDH mutations in cancer and progress toward development of targeted therapeutics. *Ann. Oncol.* 27, 599–608. doi: 10.1093/annonc/mdw013

De Saedeleer, C. J., Copetti, T., Porporato, P. E., Verrax, J., Feron, O., and Sonveaux, P. (2012). Lactate activates HIF-1 in oxidative but not in Warburg-phenotype human tumor cells. *PLoS ONE* 7:e46571. doi: 10.1371/journal.pone.0046571

Dehennaut, V., Leprince, D., and Lefebvre, T. (2014). O-GlcNAcylation, an epigenetic mark. Focus on the histone code, TET family proteins, and polycomb group proteins. *Front. Endocrinol.* 5:155. doi: 10.3389/fendo.2014.00155

Doherty, J. R., and Cleveland, J. L. (2013). Targeting lactate metabolism for cancer therapeutics. *J. Clin. Invest.* 123, 3685–3692. doi: 10.1172/JCI69741

Du, J., Zhou, Y., Su, X., Yu, J. J., Khan, S., Jiang, H., et al. (2011). Sirt5 is a NAD-dependent protein lysine demalonylase and desuccinylase. *Science* 334, 806–809. doi: 10.1126/science.1207861

Du, S., Guan, Z., Hao, L., Song, Y., Wang, L., Gong, L., et al. (2014). Fructose-bisphosphate aldolase a is a potential metastasis-associated marker of lung squamous cell carcinoma and promotes lung cell tumorigenesis and migration. *PLoS ONE* 9:e85804. doi: 10.1371/journal.pone.0085804

Fan, J., Hitosugi, T., Chung, T. W., Xie, J., Ge, Q., Gu, T. L., et al. (2011). Tyrosine phosphorylation of lactate dehydrogenase A is important for NADH/NAD(+) redox homeostasis in cancer cells. *Mol. Cell. Biol.* 31, 4938–4950. doi: 10.1128/MCB.06120-11

Fan, T., Sun, G., Sun, X., Zhao, L., Zhong, R., and Peng, Y. (2019). Tumor energy metabolism and potential of 3-bromopyruvate as an inhibitor of aerobic glycolysis: implications in tumor treatment. *Cancers* 11:317. doi: 10.3390/cancers11030317

Fantin, V. R., St-Pierre, J., and Leder, P. (2006). Attenuation of LDH-A expression uncovers a link between glycolysis, mitochondrial physiology, and tumor maintenance. *Cancer Cell* 9, 425–434. doi: 10.1016/j.ccr.2006.04.023

Feng, Y., Xiong, Y., Qiao, T., Li, X., Jia, L., and Han, Y. (2018). Lactate dehydrogenase A: a key player in carcinogenesis and potential target in cancer therapy. *Cancer Med.* 7, 6124–6136. doi: 10.1002/cam4.1820

Fortier, S., Labelle, D., Sina, A., Moreau, R., and Annabi, B. (2008). Silencing of the MT1-MMP/ G6PT axis suppresses calcium mobilization by sphingosine-1-phosphate in glioblastoma cells. *FEBS Lett.* 582, 799–804. doi: 10.1016/j.febslet.2008.01.061

Fruman, D. A., and Rommel, C. (2014). PI3K and cancer: lessons, challenges and opportunities. *Nat. Rev. Drug Discov.* 13, 140–156. doi: 10.1038/nrd4204

Fu, H., Gao, H., Qi, X., Zhao, L., Wu, D., Bai, Y., et al. (2018). Aldolase A promotes proliferation and G1/S transition via the EGFR/MAPK pathway in non-small cell lung cancer. *Cancer Commun.* 38:18. doi: 10.1186/s40880-018-0290-3

Fu, L. N., Wang, Y. Q., Tan, J., Xu, J., Gao, Q. Y., Chen, Y. X., et al. (2018). Role of JMJD2B in colon cancer cell survival under glucose-deprived conditions and the underlying mechanisms. *Oncogene* 37, 389–402. doi: 10.1038/onc.2017.345

Funasaka, T., Hogan, V., and Raz, A. (2009). Phosphoglucose isomerase/autocrine motility factor mediates epithelial and mesenchymal phenotype conversions in breast cancer. *Cancer Res.* 69, 5349–5356. doi: 10.1158/0008-5472.CAN-09-0488

Funasaka, T., Yanagawa, T., Hogan, V., and Raz, A. (2005). Regulation of phosphoglucose isomerase/autocrine motility factor expression by hypoxia. *FASEB J.* 19, 1422–1430. doi: 10.1096/fj.05-3699com

Gonzalez, P. S., O'prey, J., Cardaci, S., Barthet, V. J.A., Sakamaki, J. I., Beaumatin, F., et al. (2018). Mannose impairs tumour growth and enhances chemotherapy. *Nature* 563, 719–723. doi: 10.1038/s41586-018-0729-3

Gras, D., Roze, E., Caillet, S., Meneret, A., Doummar, D., Billette De Villemeur, T., et al. (2014). GLUT1 deficiency syndrome: an update. *Rev. Neurol.* 170, 91–99. doi: 10.1016/j.neurol.2013.09.005

Guo, T., Chen, T., Gu, C., Li, B., and Xu, C. (2015). Genetic and molecular analyses reveal G6PC as a key element connecting glucose metabolism and cell cycle control in ovarian cancer. *Tumour Biol.* 36, 7649–7658. doi: 10.1007/s13277-015-3463-6

Gutteridge, R. E., Singh, C. K., Ndiaye, M. A., and Ahmad, N. (2017). Targeted knockdown of polo-like kinase 1 alters metabolic regulation in melanoma. *Cancer Lett.* 394, 13–21. doi: 10.1016/j.canlet.2017.02.013

Haga, A., Funasaka, T., Niinaka, Y., Raz, A., and Nagase, H. (2003). Autocrine motility factor signaling induces tumor apoptotic resistance by regulations Apaf-1 and Caspase-9 apoptosome expression. *Int. J. Cancer* 107, 707–714. doi: 10.1002/ijc.11449

Han, Z., Wu, H., Kim, S., Yang, X., Li, Q., Huang, H., et al. (2018). Revealing the protein propionylation activity of the histone acetyltransferase MOF (males absent on the first). *J. Biol. Chem.* 293, 3410–3420. doi: 10.1074/jbc.RA117.000529

Hanahan, D., and Weinberg, R. A. (2011). Hallmarks of cancer: the next generation. *Cell* 144, 646–674. doi: 10.1016/j.cell.2011.02.013

Hara, M. R., Agrawal, N., Kim, S. F., Cascio, M. B., Fujimuro, M., Ozeki, Y., et al. (2005). S-nitrosylated GAPDH initiates apoptotic cell death by nuclear translocation following Siah1 binding. *Nat. Cell Biol.* 7, 665–674. doi: 10.1038/ncb1268

He, C. L., Bian, Y. Y., Xue, Y., Liu, Z. X., Zhou, K. Q., Yao, C. F., et al. (2016). Pyruvate Kinase M2 Activates mTORC1 by Phosphorylating AKT1S1. *Sci. Rep.* 6:21524. doi: 10.1038/srep21524

Hirata, H., Sugimachi, K., Komatsu, H., Ueda, M., Masuda, T., Uchi, R., et al. (2016). Decreased expression of fructose-1,6-bisphosphatase associates with glucose metabolism and tumor progression in hepatocellular carcinoma. *Cancer Res.* 76, 3265–3276. doi: 10.1158/0008-5472.CAN-15-2601

Hitosugi, T., Kang, S., Vander Heiden, M. G., Chung, T. W., Elf, S., Lythgoe, K., et al. (2009). Tyrosine phosphorylation inhibits PKM2 to promote the Warburg effect and tumor growth. *Sci. Signal.* 2:ra73. doi: 10.1126/scisignal.2000431

Hu, X., Chao, M., and Wu, H. (2017). Central role of lactate and proton in cancer cell resistance to glucose deprivation and its clinical translation. *Signal. Transduct. Target Ther.* 2:16047. doi: 10.1038/sigtrans.2016.47

Hua, Y., Liang, C., Zhu, J., Miao, C., Yu, Y., Xu, A., et al. (2017). Expression of lactate dehydrogenase C correlates with poor prognosis in renal cell carcinoma. *Tumour Biol.* 39:1010428317695968. doi: 10.1177/1010428317695968

Huang, L., Wang, C., Xu, H., and Peng, G. (2020). Targeting citrate as a novel therapeutic strategy in cancer treatment. *Biochim. Biophys. Acta Rev. Cancer* 1873:188332. doi: 10.1016/j.bbcan.2019.188332

Ishiguro, T., Tanabe, K., Kobayashi, Y., Mizumoto, S., Kanai, M., and Kawashima, S. A. (2018). Malonylation of histone H2A at lysine 119 inhibits Bub1-dependent H2A phosphorylation and chromosomal localization of shugoshin proteins. *Sci. Rep.* 8:7671. doi: 10.1038/s41598-018-26114-z

Israelsen, W. J., and Vander Heiden, M. G. (2015). Pyruvate kinase: function, regulation and role in cancer. *Semin. Cell Dev. Biol.* 43, 43–51. doi: 10.1016/j.semcdb.2015.08.004

Ji, S., Zhang, B., Liu, J., Qin, Y., Liang, C., Shi, S., et al. (2016). ALDOA functions as an oncogene in the highly metastatic pancreatic cancer. *Cancer Lett.* 374, 127–135. doi: 10.1016/j.canlet.2016.01.054

Ji, Y., Yang, C., Tang, Z., Yang, Y., Tian, Y., Yao, H., et al. (2017). Adenylate kinase hCINAP determines self-renewal of colorectal cancer stem cells by facilitating LDHA phosphorylation. *Nat. Commun.* 8:15308. doi: 10.1038/ncomms16000

Jia, G., Fu, Y., Zhao, X., Dai, Q., Zheng, G., Yang, Y., et al. (2011). N6-methyladenosine in nuclear RNA is a major substrate of the obesity-associated FTO. *Nat. Chem. Biol.* 7, 885–887. doi: 10.1038/nchembio.687

Jiang, S., Zhang, L. F., Zhang, H. W., Hu, S., Lu, M. H., Liang, S., et al. (2012). A novel miR-155/miR-143 cascade controls glycolysis by regulating hexokinase 2 in breast cancer cells. *EMBO J.* 31, 1985–1998. doi: 10.1038/emboj.2012.45

Jitrapakdee, S., Vidal-Puig, A., and Wallace, J. C. (2006). Anaplerotic roles of pyruvate carboxylase in mammalian tissues. *Cell. Mol. Life Sci.* 63, 843–854. doi: 10.1007/s00018-005-5410-y

Kajimoto, K., Terada, H., Baba, Y., and Shinohara, Y. (2005). Essential role of citrate export from mitochondria at early differentiation stage of 3T3-L1 cells for their effective differentiation into fat cells, as revealed by studies using specific inhibitors of mitochondrial di- and tricarboxylate carriers. *Mol. Genet. Metab.* 85, 46–53. doi: 10.1016/j.ymgme.2005.01.006

Kawai, K., Uemura, M., Munakata, K., Takahashi, H., Haraguchi, N., Nishimura, J., et al. (2017). Fructose-bisphosphate aldolase A is a key regulator of hypoxic adaptation in colorectal cancer cells and involved in treatment resistance and poor prognosis. *Int. J. Oncol.* 50, 525–534. doi: 10.3892/ijo.2016.3814

Kebede, A. F., Nieborak, A., Shahidian, L. Z., Le Gras, S., Richter, F., Gomez, D. A., et al. (2017). Histone propionylation is a mark of active chromatin. *Nat. Struct. Mol. Biol.* 24, 1048–1056. doi: 10.1038/nsmb.3490

Kim, J. Y., Banerjee, T., Vinckevicius, A., Luo, Q., Parker, J. B., Baker, M. R., et al. (2014). A role for WDR5 in integrating threonine 11 phosphorylation to lysine 4 methylation on histone H3 during androgen signaling and in prostate cancer. *Mol. Cell* 54, 613–625. doi: 10.1016/j.molcel.2014.03.043

Kollenstart, L., De Groot, A. J.L., Janssen, G. M.C., Cheng, X., Vreeken, K., Martino, F., et al. (2019). Gcn5 and Esa1 function as histone crotonyltransferases to regulate crotonylation-dependent transcription. *J. Biol. Chem.* 294, 20122–20134. doi: 10.1074/jbc.RA119.010302

Kornberg, M. D., Sen, N., Hara, M. R., Juluri, K. R., Nguyen, J. V., Snowman, A. M., et al. (2010). GAPDH mediates nitrosylation of nuclear proteins. *Nat. Cell Biol.* 12, 1094–1100. doi: 10.1038/ncb2114

Kwee, S. A., Hernandez, B., Chan, O., and Wong, L. (2012). Choline kinase alpha and hexokinase-2 protein expression in hepatocellular carcinoma: association with survival. *PLoS ONE* 7:e46591. doi: 10.1371/journal.pone.0046591

Lang, L., Chemmalakuzhy, R., Shay, C., and Teng, Y. (2019). PFKP signaling at a glance: an emerging mediator of cancer cell metabolism. *Adv. Exp. Med. Biol.* 1134, 243–258. doi: 10.1007/978-3-030-12668-1_13

Le, A., Cooper, C. R., Gouw, A. M., Dinavahi, R., Maitra, A., Deck, L. M., et al. (2010). Inhibition of lactate dehydrogenase A induces oxidative stress and inhibits tumor progression. *Proc. Natl. Acad. Sci. U.S.A.* 107, 2037–2042. doi: 10.1073/pnas.0914433107

Lee, J. H., Liu, R., Li, J., Wang, Y., Tan, L., Li, X. J., et al. (2018). EGFR-phosphorylated platelet isoform of phosphofructokinase 1 promotes PI3K activation. *Mol. Cell* 70, 197–210 e197. doi: 10.1016/j.molcel.2018.03.018

Lee, J. H., Liu, R., Li, J., Zhang, C., Wang, Y., Cai, Q., et al. (2017). Stabilization of phosphofructokinase 1 platelet isoform by AKT promotes tumorigenesis. *Nat. Commun.* 8:949. doi: 10.1038/s41467-017-00906-9

Lee, M. N., Ha, S. H., Kim, J., Koh, A., Lee, C. S., Kim, J. H., et al. (2009). Glycolytic flux signals to mTOR through glyceraldehyde-3-phosphate dehydrogenase-mediated regulation of Rheb. *Mol. Cell. Biol.* 29, 3991–4001. doi: 10.1128/MCB.00165-09

Li, H., Wang, J., Xu, H., Xing, R., Pan, Y., Li, W., et al. (2013). Decreased fructose-1,6-bisphosphatase-2 expression promotes glycolysis and growth in gastric cancer cells. *Mol. Cancer* 12:110. doi: 10.1186/1476-4598-12-110

Li, Q., Li, Y., Xu, J., Wang, S., Xu, Y., Li, X., et al. (2017). Aldolase B overexpression is associated with poor prognosis and promotes tumor progression by epithelial-mesenchymal transition in colorectal adenocarcinoma. *Cell. Physiol. Biochem.* 42, 397–406. doi: 10.1159/000477484

Li, Q., Zhang, D., Chen, X., He, L., Li, T., Xu, X., et al. (2015). Nuclear PKM2 contributes to gefitinib resistance via upregulation of STAT3 activation in colorectal cancer. *Sci. Rep* 5, 16082. doi: 10.1038/srep16082

Li, S., Swanson, S. K., Gogol, M., Florens, L., Washburn, M. P., Workman, J. L., et al. (2015). Serine and SAM responsive complex SESAME regulates histone modification crosstalk by sensing cellular metabolism. *Mol. Cell* 60, 408–421. doi: 10.1016/j.molcel.2015.09.024

Li, Y., Luo, S., Ma, R., Liu, J., Xu, P., Zhang, H., et al. (2015). Upregulation of cytosolic phosphoenolpyruvate carboxykinase is a critical metabolic event in melanoma cells that repopulate tumors. *Cancer Res.* 75, 1191–1196. doi: 10.1158/0008-5472.CAN-14-2615

Liang, J., Cao, R., Wang, X., Zhang, Y., Wang, P., Gao, H., et al. (2017). Mitochondrial PKM2 regulates oxidative stress-induced apoptosis by stabilizing Bcl2. *Cell Res.* 27, 329–351. doi: 10.1038/cr.2016.159

Lincet, H., and Icard, P. (2015). How do glycolytic enzymes favour cancer cell proliferation by nonmetabolic functions? *Oncogene* 34, 3751–3759. doi: 10.1038/onc.2014.320

Linden, M., Gellerfors, P., and Nelson, B. D. (1982). Pore protein and the hexokinase-binding protein from the outer membrane of rat liver mitochondria are identical. *FEBS Lett.* 141, 189–192. doi: 10.1016/0014-5793(82)80044-6

Linke, C., Wosle, M., and Harder, A. (2020). Anti-cancer agent 3-bromopyruvate reduces growth of MPNST and inhibits metabolic pathways in a representative *in-vitro* model. *BMC Cancer* 20:896. doi: 10.1186/s12885-020-07397-w

Liu, B., Lin, Y., Darwanto, A., Song, X., Xu, G., and Zhang, K. (2009). Identification and characterization of propionylation at histone H3 lysine 23 in mammalian cells. *J. Biol. Chem.* 284, 32288–32295. doi: 10.1074/jbc.M109.045856

Liu, H. E., Shi, H. H., and Luo, X. J. (2020). Upregulated long noncoding RNA UCA1 enhances warburg effect via miR-203/HK2 axis in esophagal cancer. *J. Oncol.* 2020:8847687. doi: 10.1155/2020/8847687

Liu, J., Peng, Y., Shi, L., Wan, L., Inuzuka, H., Long, J., et al. (2021). Skp2 dictates cell cycle-dependent metabolic oscillation between glycolysis and TCA cycle. *Cell Res.* 31, 80–93. doi: 10.1038/s41422-020-0372-z

Liu, M. X., Jin, L., Sun, S. J., Liu, P., Feng, X., Cheng, Z. L., et al. (2018). Metabolic reprogramming by PCK1 promotes TCA cataplerosis, oxidative stress and apoptosis in liver cancer cells and suppresses hepatocellular carcinoma. *Oncogene* 37, 1637–1653. doi: 10.1038/s41388-017-0070-6

Liu, Q., Huo, Y., Zheng, H., Zhao, J., Jia, L., and Wang, P. (2019). Ethyl pyruvate suppresses the growth, invasion and migration and induces the apoptosis of nonsmall cell lung cancer cells via the HMGB1/RAGE axis and the NFkappaB/STAT3 pathway. *Oncol. Rep.* 42, 817–825. doi: 10.3892/or.2019.7176

Liu, S., Yu, H., Liu, Y., Liu, X., Zhang, Y., Bu, C., et al. (2017). Chromodomain protein CDYL acts as a crotonyl-CoA hydratase to regulate histone crotonylation and spermatogenesis. *Mol. Cell* 67, 853–866 e855. doi: 10.1016/j.molcel.2017.07.011

Liu, X. S., Little, J. B., and Yuan, Z. M. (2015). Glycolytic metabolism influences global chromatin structure. *Oncotarget* 6, 4214–4225. doi: 10.18632/oncotarget.2929

Liu, Y., Li, M., Fan, M., Song, Y., Yu, H., Zhi, X., et al. (2019). Chromodomain Y-like protein-mediated histone crotonylation regulates stress-induced depressive behaviors. *Biol. Psychiatry* 85, 635–649. doi: 10.1016/j.biopsych.2018.11.025

Lo, P. W., Shie, J. J., Chen, C. H., Wu, C. Y., Hsu, T. L., and Wong, C. H. (2018). O-GlcNAcylation regulates the stability and enzymatic activity of the

histone methyltransferase EZH2. *Proc. Natl. Acad. Sci. U.S.A.* 115, 7302–7307. doi: 10.1073/pnas.1801850115

Lord-Dufour, S., Copland, I. B., Levros, L. C. Jr., Post, M., Das, A., Khosla, C., et al. (2009). Evidence for transcriptional regulation of the glucose-6-phosphate transporter by HIF-1alpha: targeting G6PT with mumbaistatin analogs in hypoxic mesenchymal stromal cells. *Stem Cells* 27, 489–497. doi: 10.1634/stemcells.2008-0855

Luo, W., Hu, H., Chang, R., Zhong, J., Knabel, M., O'meally, R., et al. (2011). Pyruvate kinase M2 is a PHD3-stimulated coactivator for hypoxia-inducible factor 1. *Cell* 145, 732–744. doi: 10.1016/j.cell.2011.03.054

Lv, L., Li, D., Zhao, D., Lin, R., Chu, Y., Zhang, H., et al. (2011). Acetylation targets the M2 isoform of pyruvate kinase for degradation through chaperone-mediated autophagy and promotes tumor growth. *Mol. Cell* 42, 719–730. doi: 10.1016/j.molcel.2011.04.025

Lv, L., Xu, Y. P., Zhao, D., Li, F. L., Wang, W., Sasaki, N., et al. (2013). Mitogenic and oncogenic stimulation of K433 acetylation promotes PKM2 protein kinase activity and nuclear localization. *Mol. Cell* 52, 340–352. doi: 10.1016/j.molcel.2013.09.004

Ma, R., Wu, Y., Zhai, Y., Hu, B., Ma, W., Yang, W., et al. (2019). Exogenous pyruvate represses histone gene expression and inhibits cancer cell proliferation via the NAMPT-NAD+-SIRT1 pathway. *Nucleic Acids Res.* 47, 11132–11150. doi: 10.1093/nar/gkz864

MacPherson, S., Horkoff, M., Gravel, C., Hoffmann, T., Zuber, J., and Lum, J. J. (2017). STAT3 regulation of citrate synthase is essential during the initiation of lymphocyte cell growth. *Cell Rep.* 19, 910–918. doi: 10.1016/j.celrep.2017.04.012

Mazurek, S. (2011). Pyruvate kinase type M2: a key regulator of the metabolic budget system in tumor cells. *Int. J. Biochem. Cell Biol.* 43, 969–980. doi: 10.1016/j.biocel.2010.02.005

Mcbrian, M. A., Behbahan, I. S., Ferrari, R., Su, T., Huang, T. W., Li, K., et al. (2013). Histone acetylation regulates intracellular pH. *Mol. Cell* 49, 310–321. doi: 10.1016/j.molcel.2012.10.025

Mendez-Lucas, A., Hyrossova, P., Novellasdemunt, L., Vinals, F., and Perales, J. C. (2014). Mitochondrial phosphoenolpyruvate carboxykinase (PEPCK-M) is a pro-survival, endoplasmic reticulum (ER) stress response gene involved in tumor cell adaptation to nutrient availability. *J. Biol. Chem.* 289, 22090–22102. doi: 10.1074/jbc.M114.566927

Miao, P., Sheng, S., Sun, X., Liu, J., and Huang, G. (2013). Lactate dehydrogenase A in cancer: a promising target for diagnosis and therapy. *IUBMB Life* 65, 904–910. doi: 10.1002/iub.1216

Min, J. W., Kim, K. I., Kim, H. A., Kim, E. K., Noh, W. C., Jeon, H. B., et al. (2013). INPP4B-mediated tumor resistance is associated with modulation of glucose metabolism via hexokinase 2 regulation in laryngeal cancer cells. *Biochem. Biophys. Res. Commun.* 440, 137–142. doi: 10.1016/j.bbrc.2013.09.041

Mohammad, G. H., Vassileva, V., Acedo, P., Olde Damink, S. W.M., Malago, M., Dhar, D. K., et al. (2019). Targeting pyruvate kinase M2 and lactate dehydrogenase a is an effective combination strategy for the treatment of pancreatic cancer. *Cancers* 11:1372. doi: 10.3390/cancers11091372

Moore, L. E., Jaeger, E., Nickerson, M. L., Brennan, P., De Vries, S., Roy, R., et al. (2012). Genomic copy number alterations in clear cell renal carcinoma: associations with case characteristics and mechanisms of VHL gene inactivation. *Oncogenesis* 1:e14. doi: 10.1038/oncsis.2012.14

Mor, I., Cheung, E. C., and Vousden, K. H. (2011). Control of glycolysis through regulation of PFK1: old friends and recent additions. *Cold Spring Harb. Symp. Quant. Biol.* 76, 211–216. doi: 10.1101/sqb.2011.76.010868

Morita, M., Sato, T., Nomura, M., Sakamoto, Y., Inoue, Y., Tanaka, R., et al. (2018). PKM1 confers metabolic advantages and promotes cell-autonomous tumor cell growth. *Cancer Cell* 33, 355–367 e357. doi: 10.1016/j.ccell.2018.02.004

Nishikawa, K., Iwamoto, Y., Kobayashi, Y., Katsuoka, F., Kawaguchi, S., Tsujita, T., et al. (2015). DNA methyltransferase 3a regulates osteoclast differentiation by coupling to an S-adenosylmethionine-producing metabolic pathway. *Nat. Med.* 21, 281–287. doi: 10.1038/nm.3774

Oudard, S., Carpentier, A., Banu, E., Fauchon, F., Celerier, D., Poupon, M. F., et al. (2003). Phase II study of lonidamine and diazepam in the treatment of recurrent glioblastoma multiforme. *J. Neurooncol.* 63, 81–86. doi: 10.1023/A:1023756707900

Palmieri, D., Fitzgerald, D., Shreeve, S. M., Hua, E., Bronder, J. L., Weil, R. J., et al. (2009). Analyses of resected human brain metastases of breast cancer reveal the association between up-regulation of hexokinase 2 and poor prognosis. *Mol. Cancer Res.* 7, 1438–1445. doi: 10.1158/1541-7786.MCR-09-0234

Pavlova, N. N., and Thompson, C. B. (2016). The emerging hallmarks of cancer metabolism. *Cell Metab.* 23, 27–47. doi: 10.1016/j.cmet.2015.12.006

Peschiaroli, A., Giacobbe, A., Formosa, A., Markert, E. K., Bongiorno-Borbone, L., Levine, A. J., et al. (2013). miR-143 regulates hexokinase 2 expression in cancer cells. *Oncogene* 32, 797–802. doi: 10.1038/onc.2012.100

Phannasil, P., Ansari, I. H., El Azzouny, M., Longacre, M. J., Rattanapornsompong, K., Burant, C. F., et al. (2017). Mass spectrometry analysis shows the biosynthetic pathways supported by pyruvate carboxylase in highly invasive breast cancer cells. *Biochim. Biophys. Acta Mol. Basis Dis.* 1863, 537–551. doi: 10.1016/j.bbadis.2016.11.021

Phannasil, P., Thuwajit, C., Warnnissorn, M., Wallace, J. C., Macdonald, M. J., and Jitrapakdee, S. (2015). Pyruvate carboxylase is up-regulated in breast cancer and essential to support growth and invasion of MDA-MB-231 cells. *PLoS ONE* 10:e0129848. doi: 10.1371/journal.pone.0129848

Pusapati, R. V., Daemen, A., Wilson, C., Sandoval, W., Gao, M., Haley, B., et al. (2016). mTORC1-dependent metabolic reprogramming underlies escape from glycolysis addiction in cancer cells. *Cancer Cell* 29, 548–562. doi: 10.1016/j.ccell.2016.02.018

Qing, Y., Dong, L., Gao, L., Li, C., Li, Y., Han, L., et al. (2021). R-2-hydroxyglutarate attenuates aerobic glycolysis in leukemia by targeting the FTO/m(6)A/PFKP/LDHB axis. *Mol Cell.* 81, 922–939.e9. doi: 10.1016/j.molcel.2020.12.026

Rabinowitz, J. D., and Enerback, S. (2020). Lactate: the ugly duckling of energy metabolism. *Nat. Metab.* 2, 566–571. doi: 10.1038/s42255-020-0243-4

Reshef, L., Olswang, Y., Cassuto, H., Blum, B., Croniger, C. M., Kalhan, S. C., et al. (2003). Glyceroneogenesis and the triglyceride/fatty acid cycle. *J. Biol. Chem.* 278, 30413–30416. doi: 10.1074/jbc.R300017200

Ringel, A. E., Ryznar, R., Picariello, H., Huang, K. L., Lazarus, A. G., and Holmes, S. G. (2013). Yeast Tdh3 (glyceraldehyde 3-phosphate dehydrogenase) is a Sir2-interacting factor that regulates transcriptional silencing and rDNA recombination. *PLoS Genet.* 9:e1003871. doi: 10.1371/journal.pgen.1003871

Roberts, D. J., Tan-Sah, V. P., Ding, E. Y., Smith, J. M., and Miyamoto, S. (2014). Hexokinase-II positively regulates glucose starvation-induced autophagy through TORC1 inhibition. *Mol. Cell* 53, 521–533. doi: 10.1016/j.molcel.2013.12.019

Sabari, B. R., Zhang, D., Allis, C. D., and Zhao, Y. (2017). Metabolic regulation of gene expression through histone acylations. *Nat. Rev. Mol. Cell Biol.* 18, 90–101. doi: 10.1038/nrm.2016.140

Sajnani, K., Islam, F., Smith, R. A., Gopalan, V., and Lam, A. K. (2017). Genetic alterations in Krebs cycle and its impact on cancer pathogenesis. *Biochimie* 135, 164–172. doi: 10.1016/j.biochi.2017.02.008

Sakabe, K., and Hart, G. W. (2010). O-GlcNAc transferase regulates mitotic chromatin dynamics. *J. Biol. Chem.* 285, 34460–34468. doi: 10.1074/jbc.M110.158170

San-Millan, I., Julian, C. G., Matarazzo, C., Martinez, J., and Brooks, G. A. (2019). Is lactate an oncometabolite? Evidence supporting a role for lactate in the regulation of transcriptional activity of cancer-related genes in MCF7 breast cancer cells. *Front. Oncol.* 9:1536. doi: 10.3389/fonc.2019.01536

Sen, N., Hara, M. R., Kornberg, M. D., Cascio, M. B., Bae, B. I., Shahani, N., et al. (2008). Nitric oxide-induced nuclear GAPDH activates p300/CBP and mediates apoptosis. *Nat. Cell Biol.* 10, 866–873. doi: 10.1038/ncb1747

Sheng, S. L., Liu, J. J., Dai, Y. H., Sun, X. G., Xiong, X. P., and Huang, G. (2012). Knockdown of lactate dehydrogenase A suppresses tumor growth and metastasis of human hepatocellular carcinoma. *FEBS J.* 279, 3898–3910. doi: 10.1111/j.1742-4658.2012.08748.x

Shi, L., An, S., Liu, Y., Liu, J., and Wang, F. (2020). PCK1 regulates glycolysis and tumor progression in clear cell renal cell carcinoma through LDHA. *Onco. Targets Ther.* 13, 2613–2627. doi: 10.2147/OTT.S241717

Shi, L., Yan, H., An, S., Shen, M., Jia, W., Zhang, R., et al. (2019). SIRT5-mediated deacetylation of LDHB promotes autophagy and tumorigenesis in colorectal cancer. *Mol. Oncol.* 13, 358–375. doi: 10.1002/1878-0261.12408

Shimizu, T., Inoue, K., Hachiya, H., Shibuya, N., Shimoda, M., and Kubota, K. (2014). Frequent alteration of the protein synthesis of enzymes for glucose metabolism in hepatocellular carcinomas. *J. Gastroenterol.* 49, 1324–1332. doi: 10.1007/s00535-013-0895-x

Shin, D., Lee, J., You, J. H., Kim, D., and Roh, J. L. (2020). Dihydrolipoamide dehydrogenase regulates cystine deprivation-induced ferroptosis in head and neck cancer. *Redox Biol.* 30:101418. doi: 10.1016/j.redox.2019.101418

Shyh-Chang, N., Locasale, J. W., Lyssiotis, C. A., Zheng, Y., Teo, R. Y., Ratanasirintrawoot, S., et al. (2013). Influence of threonine metabolism on S-adenosylmethionine and histone methylation. *Science* 339, 222–226. doi: 10.1126/science.1226603

Sims, J., Bruschi, C. V., Bertin, C., West, N., Breitenbach, M., Schroeder, S., et al. (2016). High reactive oxygen species levels are detected at the end of the chronological life span of translocant yeast cells. *Mol. Genet. Genomics* 291, 423–435. doi: 10.1007/s00438-015-1120-9

Sivanand, S., Viney, I., and Wellen, K. E. (2018). Spatiotemporal control of acetyl-CoA metabolism in chromatin regulation. *Trends Biochem. Sci.* 43, 61–74. doi: 10.1016/j.tibs.2017.11.004

Slane, B. G., Aykin-Burns, N., Smith, B. J., Kalen, A. L., Goswami, P. C., Domann, F. E., et al. (2006). Mutation of succinate dehydrogenase subunit C results in increased O2.-, oxidative stress, and genomic instability. *Cancer Res.* 66, 7615–7620. doi: 10.1158/0008-5472.CAN-06-0833

Slawson, C., Lakshmanan, T., Knapp, S., and Hart, G. W. (2008). A mitotic GlcNAcylation/phosphorylation signaling complex alters the posttranslational state of the cytoskeletal protein vimentin. *Mol. Biol. Cell* 19, 4130–4140. doi: 10.1091/mbc.e07-11-1146

Su, R., Dong, L., Li, C., Nachtergaele, S., Wunderlich, M., Qing, Y., et al. (2018). R-2HG exhibits anti-tumor activity by targeting FTO/m(6)A/MYC/CEBPA signaling. *Cell* 172, 90–105 e123. doi: 10.1016/j.cell.2017.11.031

Tao, Q. F., Yuan, S. X., Yang, F., Yang, S., Yang, Y., Yuan, J. H., et al. (2015). Aldolase B inhibits metastasis through Ten-Eleven Translocation 1 and serves as a prognostic biomarker in hepatocellular carcinoma. *Mol. Cancer* 14:170. doi: 10.1186/s12943-015-0437-7

Tauffenberger, A., Fiumelli, H., Almustafa, S., and Magistretti, P. J. (2019). Lactate and pyruvate promote oxidative stress resistance through hormetic ROS signaling. *Cell Death Dis.* 10:653. doi: 10.1038/s41419-019-1877-6

Thangaraju, M., Carswell, K. N., Prasad, P. D., and Ganapathy, V. (2009). Colon cancer cells maintain low levels of pyruvate to avoid cell death caused by inhibition of HDAC1/HDAC3. *Biochem. J.* 417, 379–389. doi: 10.1042/BJ20081132

Tosato, V., Gruning, N. M., Breitenbach, M., Arnak, R., Ralser, M., and Bruschi, C. V. (2012). Warburg effect and translocation-induced genomic instability: two yeast models for cancer cells. *Front. Oncol.* 2:212. doi: 10.3389/fonc.2012.00212

Tran, K. A., Dillingham, C. M., and Sridharan, R. (2019). The role of alpha-ketoglutarate-dependent proteins in pluripotency acquisition and maintenance. *J. Biol. Chem.* 294, 5408–5419. doi: 10.1074/jbc.TM118.000831

Tristan, C., Shahani, N., Sedlak, T. W., and Sawa, A. (2011). The diverse functions of GAPDH: views from different subcellular compartments. *Cell. Signal.* 23, 317–323. doi: 10.1016/j.cellsig.2010.08.003

Tsutsumi, S., Fukasawa, T., Yamauchi, H., Kato, T., Kigure, W., Morita, H., et al. (2009). Phosphoglucose isomerase enhances colorectal cancer metastasis. *Int. J. Oncol.* 35, 1117–1121. doi: 10.3892/ijo_00000427

Tsutsumi, S., Yanagawa, T., Shimura, T., Kuwano, H., and Raz, A. (2004). Autocrine motility factor signaling enhances pancreatic cancer metastasis. *Clin. Cancer Res.* 10, 7775–7784. doi: 10.1158/1078-0432.CCR-04-1015

Tuo, L., Xiang, J., Pan, X., Gao, Q., Zhang, G., Yang, Y., et al. (2018). PCK1 Downregulation promotes TXNRD1 expression and hepatoma cell growth via the Nrf2/Keap1 pathway. *Front. Oncol.* 8:611. doi: 10.3389/fonc.2018.00611

Tuo, L., Xiang, J., Pan, X., Hu, J., Tang, H., Liang, L., et al. (2019). PCK1 negatively regulates cell cycle progression and hepatoma cell proliferation via the AMPK/p27(Kip1) axis. *J. Exp. Clin. Cancer Res.* 38:50. doi: 10.1186/s13046-019-1029-y

Vincent, E. E., Sergushichev, A., Griss, T., Gingras, M. C., Samborska, B., Ntimbane, T., et al. (2015). Mitochondrial phosphoenolpyruvate carboxykinase regulates metabolic adaptation and enables glucose-independent tumor growth. *Mol. Cell* 60, 195–207. doi: 10.1016/j.molcel.2015.08.013

Wang, B., Hsu, S. H., Frankel, W., Ghoshal, K., and Jacob, S. T. (2012). Stat3-mediated activation of microRNA-23a suppresses gluconeogenesis in hepatocellular carcinoma by down-regulating glucose-6-phosphatase and peroxisome proliferator-activated receptor gamma, coactivator 1 alpha. *Hepatology* 56, 186–197. doi: 10.1002/hep.25632

Wang, P., Wu, J., Ma, S., Zhang, L., Yao, J., Hoadley, K. A., et al. (2015). Oncometabolite D-2-hydroxyglutarate inhibits ALKBH DNA repair enzymes and sensitizes IDH mutant cells to alkylating agents. *Cell Rep.* 13, 2353–2361. doi: 10.1016/j.celrep.2015.11.029

Wang, Y., Guo, Y. R., Liu, K., Yin, Z., Liu, R., Xia, Y., et al. (2017). KAT2A coupled with the alpha-KGDH complex acts as a histone H3 succinyltransferase. *Nature* 552, 273–277. doi: 10.1038/nature25003

Wang, Z., and Dong, C. (2019). Gluconeogenesis in cancer: function and regulation of PEPCK, FBPase, and G6Pase. *Trends Cancer* 5, 30–45. doi: 10.1016/j.trecan.2018.11.003

Wei, W., Liu, X., Chen, J., Gao, S., Lu, L., Zhang, H., et al. (2017). Class I histone deacetylases are major histone decrotonylases: evidence for critical and broad function of histone crotonylation in transcription. *Cell Res.* 27, 898–915. doi: 10.1038/cr.2017.68

Wu, S. T., Liu, B., Ai, Z. Z., Hong, Z. C., You, P. T., Wu, H. Z., et al. (2020). Esculetin inhibits cancer cell glycolysis by binding tumor PGK2, GPD2, and GPI. *Front. Pharmacol.* 11:379. doi: 10.3389/fphar.2020.00379

Wu, X., Miao, D., Liu, Z., Liu, K., Zhang, B., Li, J., et al. (2020). beta-hydroxybutyrate antagonizes aortic endothelial injury by promoting generation of VEGF in diabetic rats. *Tissue Cell* 64:101345. doi: 10.1016/j.tice.2020.101345

Wu, Y., Zhang, S., Gong, X., Yu, Q., Zhang, Y., Luo, M., et al. (2019). Glycolysis regulates gene expression by promoting the crosstalk between H3K4me3 and H3K14ac in *Saccharomyces cerevisiae*. *J. Genet. Genomics* 46, 561–574. doi: 10.1016/j.jgg.2019.11.007

Xia, Y., Yang, W., Fa, M., Li, X., Wang, Y., Jiang, Y., et al. (2017). RNF8 mediates histone H3 ubiquitylation and promotes glycolysis and tumorigenesis. *J. Exp. Med.* 214, 1843–1855. doi: 10.1084/jem.20170015

Xiao, M., Yang, H., Xu, W., Ma, S., Lin, H., Zhu, H., et al. (2012). Inhibition of alpha-KG-dependent histone and DNA demethylases by fumarate and succinate that are accumulated in mutations of FH and SDH tumor suppressors. *Genes Dev.* 26, 1326–1338. doi: 10.1101/gad.191056.112

Xie, Z., Zhang, D., Chung, D., Tang, Z., Huang, H., Dai, L., et al. (2016). Metabolic regulation of gene expression by histone lysine beta-hydroxybutyrylation. *Mol. Cell* 62, 194–206. doi: 10.1016/j.molcel.2016.03.036

Xu, W., Yang, H., Liu, Y., Yang, Y., Wang, P., Kim, S. H., et al. (2011). Oncometabolite 2-hydroxyglutarate is a competitive inhibitor of alpha-ketoglutarate-dependent dioxygenases. *Cancer Cell* 19, 17–30. doi: 10.1016/j.ccr.2010.12.014

Yamaguchi, N., Weinberg, E. M., Nguyen, A., Liberti, M. V., Goodarzi, H., Janjigian, Y. Y., et al. (2019). PCK1 and DHODH drive colorectal cancer liver metastatic colonization and hypoxic growth by promoting nucleotide synthesis. *Elife* 8:e52135. doi: 10.7554/eLife.52135.sa2

Yang, J. S., Hsu, J. W., Park, S. Y., Li, J., Oldham, W. M., Beznoussenko, G. V., et al. (2018). GAPDH inhibits intracellular pathways during starvation for cellular energy homeostasis. *Nature* 561, 263–267. doi: 10.1038/s41586-018-0475-6

Yang, W., Xia, Y., Hawke, D., Li, X., Liang, J., Xing, D., et al. (2012). PKM2 phosphorylates histone H3 and promotes gene transcription and tumorigenesis. *Cell* 150, 685–696. doi: 10.1016/j.cell.2012.07.018

Yang, W., Xia, Y., Ji, H., Zheng, Y., Liang, J., Huang, W., et al. (2011). Nuclear PKM2 regulates beta-catenin transactivation upon EGFR activation. *Nature* 480, 118–122. doi: 10.1038/nature10598

Yen, K. E., Bittinger, M. A., Su, S. M., and Fantin, V. R. (2010). Cancer-associated IDH mutations: biomarker and therapeutic opportunities. *Oncogene* 29, 6409–6417. doi: 10.1038/onc.2010.444

Yi, W., Clark, P. M., Mason, D. E., Keenan, M. C., Hill, C., Goddard, W. A. 3rd, et al. (2012). Phosphofructokinase 1 glycosylation regulates cell growth and metabolism. *Science* 337, 975–980. doi: 10.1126/science.1222278

Yin, X., Choudhury, M., Kang, J. H., Schaefbauer, K. J., Jung, M. Y., Andrianifahanana, M., et al. (2019). Hexokinase 2 couples glycolysis with the profibrotic actions of TGF-beta. *Sci. Signal.* 12:eaax4067. doi: 10.1126/scisignal.aax4067

Yu, Q., Tong, C., Luo, M., Xue, X., Mei, Q., Ma, L., et al. (2017). Regulation of SESAME-mediated H3T11 phosphorylation by glycolytic enzymes and metabolites. *PLoS ONE* 12:e0175576. doi: 10.1371/journal.pone.0175576

Yu, X., and Li, S. (2017). Non-metabolic functions of glycolytic enzymes in tumorigenesis. *Oncogene* 36, 2629–2636. doi: 10.1038/onc.2016.410

Yu, X., Ma, R., Wu, Y., Zhai, Y., and Li, S. (2018). Reciprocal regulation of metabolic reprogramming and epigenetic modifications in cancer. *Front. Genet.* 9:394. doi: 10.3389/fgene.2018.00394

Yucel, N., Wang, Y. X., Mai, T., Porpiglia, E., Lund, P. J., Markov, G., et al. (2019). Glucose metabolism drives histone acetylation landscape transitions that dictate muscle stem cell function. *Cell Rep.* 27, 3939–3955 e3936. doi: 10.1016/j.celrep.2019.05.092

Zhang, D., Li, J., Wang, F., Hu, J., Wang, S., and Sun, Y. (2014). 2-Deoxy-D-glucose targeting of glucose metabolism in cancer cells as a potential therapy. *Cancer Lett.* 355, 176–183. doi: 10.1016/j.canlet.2014.09.003

Zhang, D., Tang, Z., Huang, H., Zhou, G., Cui, C., Weng, Y., et al. (2019). Metabolic regulation of gene expression by histone lactylation. *Nature* 574, 575–580.

Zhang, J., Wang, J., Xing, H., Li, Q., Zhao, Q., and Li, J. (2016). Down-regulation of FBP1 by ZEB1-mediated repression confers to growth and invasion in lung cancer cells. *Mol. Cell. Biochem.* 411, 331–340. doi: 10.1007/s11010-015-2595-8

Zhang, J. Y., Zhang, F., Hong, C. Q., Giuliano, A. E., Cui, X. J., Zhou, G. J., et al. (2015). Critical protein GAPDH and its regulatory mechanisms in cancer cells. *Cancer Biol. Med.* 12, 10–22. doi: 10.7497/j.issn.2095-3941.2014.0019

Zhang, L. F., Jiang, S., and Liu, M. F. (2017). MicroRNA regulation and analytical methods in cancer cell metabolism. *Cell. Mol. Life Sci.* 74, 2929–2941. doi: 10.1007/s00018-017-2508-y

Zhang, Q., Cai, T., Xiao, Z., Li, D., Wan, C., Cui, X., et al. (2020). Identification of histone malonylation in the human fetal brain and implications for diabetes-induced neural tube defects. *Mol. Genet. Genomic Med.* 8:e1403. doi: 10.1002/mgg3.1403

Zhang, S., Yu, X., Zhang, Y., Xue, X., Yu, Q., Zha, Z., et al. (2021). Metabolic regulation of telomere silencing by SESAME complex-catalyzed H3T11 phosphorylation. *Nat. Commun.* 12:594. doi: 10.1038/s41467-020-20711-1

Zhang, T., Guan, X. W., Gribben, J. G., Liu, F. T., and Jia, L. (2019). Blockade of HMGB1 signaling pathway by ethyl pyruvate inhibits tumor growth in diffuse large B-cell lymphoma. *Cell Death Dis.* 10:330. doi: 10.1038/s41419-019-1563-8

Zhang, X., Cao, R., Niu, J., Yang, S., Ma, H., Zhao, S., et al. (2019). Molecular basis for hierarchical histone de-beta-hydroxybutyrylation by SIRT3. *Cell Discov.* 5:35. doi: 10.1038/s41421-019-0103-0

Zhang, Y., Zhang, X., Wang, X., Gan, L., Yu, G., Chen, Y., et al. (2012). Inhibition of LDH-A by lentivirus-mediated small interfering RNA suppresses intestinal-type gastric cancer tumorigenicity through the downregulation of Oct4. *Cancer Lett.* 321, 45–54. doi: 10.1016/j.canlet.2012.03.013

Zhang, Y. P., Liu, K. L., Yang, Z., Lu, B. S., Qi, J. C., Han, Z. W., et al. (2019). The involvement of FBP1 in prostate cancer cell epithelial mesenchymal transition, invasion and metastasis by regulating the MAPK signaling pathway. *Cell Cycle* 18, 2432–2446. doi: 10.1080/15384101.2019.1648956

Zhang, Z., Deng, X., Liu, Y., Liu, Y., Sun, L., and Chen, F. (2019). PKM2, function and expression and regulation. *Cell Biosci.* 9:52. doi: 10.1186/s13578-019-0317-8

Zhao, D., Zou, S. W., Liu, Y., Zhou, X., Mo, Y., Wang, P., et al. (2013). Lysine-5 acetylation negatively regulates lactate dehydrogenase A and is decreased in pancreatic cancer. *Cancer Cell* 23, 464–476. doi: 10.1016/j.ccr.2013.02.005

Zhao, J., Li, J., Fan, T. W.M., and Hou, S. X. (2017). Glycolytic reprogramming through PCK2 regulates tumor initiation of prostate cancer cells. *Oncotarget* 8, 83602–83618. doi: 10.18632/oncotarget.18787

Zhao, S., Lin, Y., Xu, W., Jiang, W., Zha, Z., Wang, P., et al. (2009). Glioma-derived mutations in IDH1 dominantly inhibit IDH1 catalytic activity and induce HIF-1alpha. *Science* 324, 261–265. doi: 10.1126/science.1170944

Zhao, W., Yang, S., Chen, J., Zhao, J., and Dong, J. (2018). Forced overexpression of FBP1 inhibits proliferation and metastasis in cholangiocarcinoma cells via Wnt/beta-catenin pathway. *Life Sci.* 210, 224–234. doi: 10.1016/j.lfs.2018.09.009

Zheng, Q., Omans, N. D., Leicher, R., Osunsade, A., Agustinus, A. S., Finkin-Groner, E., et al. (2019). Reversible histone glycation is associated with disease-related changes in chromatin architecture. *Nat. Commun.* 10:1289. doi: 10.1038/s41467-019-09192-z

Zhou, L., Wang, Y., Zhou, M., Zhang, Y., Wang, P., Li, X., et al. (2018). HOXA9 inhibits HIF-1alpha-mediated glycolysis through interacting with CRIP2 to repress cutaneous squamous cell carcinoma development. *Nat. Commun.* 9:1480. doi: 10.1038/s41467-018-03914-5

Zhou, Y., Niu, W., Luo, Y., Li, H., Xie, Y., Wang, H., et al. (2019). p53/Lactate dehydrogenase A axis negatively regulates aerobic glycolysis and tumor progression in breast cancer expressing wild-type p53. *Cancer Sci.* 110, 939–949. doi: 10.1111/cas.1s3928

Zhuang, L., Scolyer, R. A., Murali, R., Mccarthy, S. W., Zhang, X. D., Thompson, J. F., et al. (2010). Lactate dehydrogenase 5 expression in melanoma increases with disease progression and is associated with expression of Bcl-XL and Mcl-1, but not Bcl-2 proteins. *Mod. Pathol.* 23, 45–53. doi: 10.1038/modpathol.2009.129

Conflict of Interest: The authors declare that the research was conducted in the absence of any commercial or financial relationships that could be construed as a potential conflict of interest.

frontiers in Cell and Developmental Biology

ORIGINAL RESEARCH
published: 11 May 2021
doi: 10.3389/fcell.2021.678209

Ivacaftor Inhibits Glioblastoma Stem Cell Maintenance and Tumor Progression

Kun Liu[1,2†], Jun Pu[3†], Zhi Nie[1,2†], Yulin Shi[1,2], Liping Jiang[1], Qisheng Wu[1], Yongbin Chen[1,2,4] and Cuiping Yang[1,2]*

[1] Key Laboratory of Animal Models and Human Disease Mechanisms of Chinese Academy of Sciences and Yunnan Province, Kunming Institute of Zoology, Kunming, China, [2] Kunming College of Life Science, University of Chinese Academy of Sciences, Beijing, China, [3] Department of Neurosurgery, The Second Affiliated Hospital, Kunming Medical University, Kunming, China, [4] Center for Excellence in Animal Evolution and Genetics, Chinese Academy of Sciences, Kunming, China

OPEN ACCESS

Edited by:
Zexian Liu,
Sun Yat-sen University Cancer Center (SYSUCC), China

Reviewed by:
Hai Hu,
Sun Yat-sen Memorial Hospital, China
Yong Peng,
Sichuan University, China
Xianghuo He,
Fudan University, China

***Correspondence:**
Cuiping Yang
cuipingyang@mail.kiz.ac.cn

[†] These authors have contributed equally to this work

Specialty section:
This article was submitted to Molecular and Cellular Oncology, a section of the journal Frontiers in Cell and Developmental Biology

Received: 09 March 2021
Accepted: 07 April 2021
Published: 11 May 2021

Citation:
Liu K, Pu J, Nie Z, Shi Y, Jiang L, Wu Q, Chen Y and Yang C (2021) Ivacaftor Inhibits Glioblastoma Stem Cell Maintenance and Tumor Progression. Front. Cell Dev. Biol. 9:678209. doi: 10.3389/fcell.2021.678209

Glioblastoma (GBM) is the most common and malignant primary brain tumor. Glioblastoma stem cells (GSCs) not only initiate and sustain uncontrolled cell proliferation but also resistant to conventional clinical therapies including temozolomide (TMZ) dependent chemotherapy and radiotherapy, implying that there is an urgent need to identify new therapeutic strategies especially specific targeting GSCs. Here, we provide evidence showing that ivacaftor commonly applied in cystic fibrosis therapy acts as a potent inhibitor for GSCs maintenance. We found that ivacaftor promotes cellular apoptosis *in vitro* and represses patient-derived xenograft (PDX) tumor growth *in vivo*. In addition, we demonstrate that ivacaftor decreases stemness marker gene expressions of GSCs, including CD133, CD44, and Sox2. In summary, our findings reveal that ivacaftor inhibits glioblastoma progression via specifically eliminating GSCs, which opens a new avenue for GBM clinical therapy in the future.

Keywords: ivacaftor, glioblastoma, glioblastoma stem cell, apoptosis, stemness

INTRODUCTION

Glioblastoma (GBM) is the most aggressive primary tumor in the central nervous system (Stupp et al., 2005; Wen and Kesari, 2008; Strickland and Stoll, 2017). Despite conventional clinical therapies including surgery, radiotherapy, chemotherapy, and immunotherapy, the median survival of GBM patients remains less than 15 months after diagnosis (Wen and Kesari, 2008). It has been well recognized that GBM was initiated by a subpopulation of cells termed as glioblastoma stem cells (GSCs), which are characterized by sustaining abilities of self-renewal, multilineage differentiation and resistance to current therapeutic strategies (Chen et al., 2012; Parada et al., 2017). Radiotherapy and chemotherapy are cytotoxic to highly proliferative tumor cells, but fail to eliminate the relatively quiescent GSCs, which is the major cause leads to GBM recurrence (Das et al., 2008; Lathia et al., 2015). Temozolomide (TMZ) is an orally alkylating agent that commonly used for the standard glioma clinical treatment via triggering DNA damage (Stevens et al., 1987; Ochs and Kaina, 2000). However, more than 50% of glioma patients received TMZ treatment show resistance to TMZ therapy (Lee, 2016). This is attributed to GSCs recalcitrance to TMZ

therapy due to their enhanced DNA repair ability or/and high methyl guanine methyl transferase expression (Hu et al., 2019; Gao et al., 2021). Small molecule compounds, including clofoctol (Hu et al., 2019), LLP-3 (Guvenc et al., 2013), gboxin (Shi Y. F. et al., 2019), inhibitor of dopamine receptor D4 (Dolma et al., 2016), and inhibitor of STAT3 (Shi et al., 2018), have been documented to inhibit GSCs self-renewal ability. However, so far, none of an optimal drug was used for selectively targeting GSCs approved for GBM clinical therapy. Therefore, there is an urgent need to identify new drugs synergizing with TMZ to effectively eliminate GSCs and translate them into clinical application for GBM patients.

Ivacaftor was approved by U.S. Food and Drug Administration in 2019 for use in cystic fibrosis (Hoy, 2019). The clinical safety of ivacaftor was confirmed by a phase III trial study (Rowe et al., 2017). In this study, we identified ivacaftor as a promising anti-glioblastoma drug via specifically and effectively repressing GSCs. Mechanistically, we provide evidence showing that ivacaftor inhibits GSCs stemness marker genes expressions including CD133, CD44, and Sox2. In summary, our findings reveal that ivacaftor inhibits glioblastoma progression via specifically eliminating GSCs, which opens a new avenue for GBM clinical therapy in the future.

RESULTS

Ivacaftor Inhibits GSCs Proliferation and Induces Cellular Apoptosis

Ivacaftor was generally used for cystic fibrosis therapy, however, its potential activities in anti-cancer have not been characterized. As shown in **Figure 1A**, the chemical structure of ivacaftor was depicted. To explore the drug repurposing effect of ivacaftor, we examined the potential inhibitory effect of ivacaftor in GSCs, normal human astrocyte cells (NHA) and two GSCs including GSC11 (Bhat et al., 2013) and GBM1 (Zhou et al., 2018) cells, were treated with indicated concentrations of ivacaftor. As shown in **Figure 1B**, ivacaftor significantly inhibits GSCs cell viability, compared with less inhibitory effect in NHA cells, implying that ivacaftor specifically blocks GSCs survival. The cell proliferation of GSCs was also attenuated following ivacaftor treatment (**Figure 1C**). To verify whether the cell cycle of GSCs was disrupted by ivacaftor, we performed BrdU incorporation assay. As shown in **Figures 1D,E**, the cell proliferation was substantially impaired after ivacaftor treatment compared to control group, as indicated by decreased BrdU positive-cell ratio after ivacaftor treatment. Furthermore, the cellular apoptosis of GSC11 cells treated with ivacaftor was determined by flow cytometry experiment, which was gradually induced with increased amount of ivacaftor treatment (**Figures 1F,G**). In addition, immunoblot results confirmed that apoptotic related factors, including Bax and cleaved PARP, were remarkably increased, while the anti-apoptosis marker, Bcl-2 was decreased, following ivacaftor treatment in a dosage or time-dependent manner (**Figure 1H**). These findings strongly indicate that ivacaftor inhibits GBM via inducing GSCs cellular apoptosis and attenuating GSCs self-renewal ability.

Ivacaftor Attenuates GSCs Self-Renewal

To further investigate the inhibitory effects of ivacaftor on GSCs, we took advantages of tumor sphere formation approach to examine the GSCs self-renewal ability. We found that ivacaftor caused a dose-dependent suppression of tumor spheres formation ability of GSCs. As shown in **Figures 2A–C**, ivacaftor treatment decreased tumor sphere formation especially larger tumor spheres (diameter larger than 50 μm). Consistently, GSC11 cells were treated with or without 5 μM ivacaftor followed by staining with CD133 antibody to validate the membrane accumulated CD133 expression, our results showed that CD133 positive cells were markedly decreased by ivacaftor treatment compared with control (**Figures 2D,E**). Consistently, the *in vitro* tumor sphere limiting dilution assay showed that the tumor spheres were dramatically decreased after ivacaftor treatment (**Figure 2F**). Furthermore, the expressions of key regulators involved in GSCs stemness maintenance, including CD133, CD44, and Sox2, were significantly decreased following ivacaftor treatment (**Figure 2G**). The above results strongly support that ivacaftor specifically and effectively impairs GSCs self-renewal ability *in vitro*.

Ivacaftor Synergizes With TMZ to Induce Cellular Apoptosis of GSCs

Given that temozolomide was first-hand chemotherapy drug for GBM patients, and there are emerging references documenting that multiple compounds, including tideglusib (Zhou et al., 2016), clofoctol (Hu et al., 2019), could sensitize responses of GSCs to TMZ. We next sought to examine whether ivacaftor has similar effect. GSCs were treated with 5 μM ivacaftor, 200 μM TMZ, and 5 μM ivacaftor plus 200 μM TMZ, respectively. The tumor sphere formation ability was examined. As expected, TMZ or ivacaftor treatment significantly suppressed GSCs tumor sphere formation ability (**Figures 3A,B**). Importantly, ivacaftor in combination with TMZ treatment almost abrogated tumor spheres (**Figures 3A,B**), which was further confirmed by *in vitro* limiting dilution assay (**Figure 3C**).

To further validate the *in vivo* effect of ivacaftor in combination with TMZ, subcutaneous xenograft tumor model was performed. Male nude mice were randomly divided into different drug treatment groups, 1×10^6 GSC11 cells were injected into nude mice subcutaneously. The mice were intraperitoneally injected with phosphate buffered saline (PBS) vehicle, ivacaftor (3 mg/kg), TMZ (60 mg/kg) and ivacaftor (3 mg/kg) plus TMZ (60 mg/kg), respectively, twice a week for 5 weeks when the xenograft tumor volume reached approximately 50 mm^3 (**Figure 3D**). We found that TMZ had a modest effect on inhibiting xenograft tumor growth, whereas ivacaftor had a better inhibitory effect compared with TMZ treatment group (**Figures 3E–G**). As expected, TMZ combined with ivacaftor markedly suppressed xenograft tumor growth *in vivo* compared with other groups (**Figures 3E–G**). In line with this finding, immunohistochemistry staining showed that ivacaftor, TMZ and TMZ plus ivacaftor treatment, respectively, unanimously increased cleaved caspase 3 (CC3) positive cell staining, and decreased Ki67 positive cells staining,

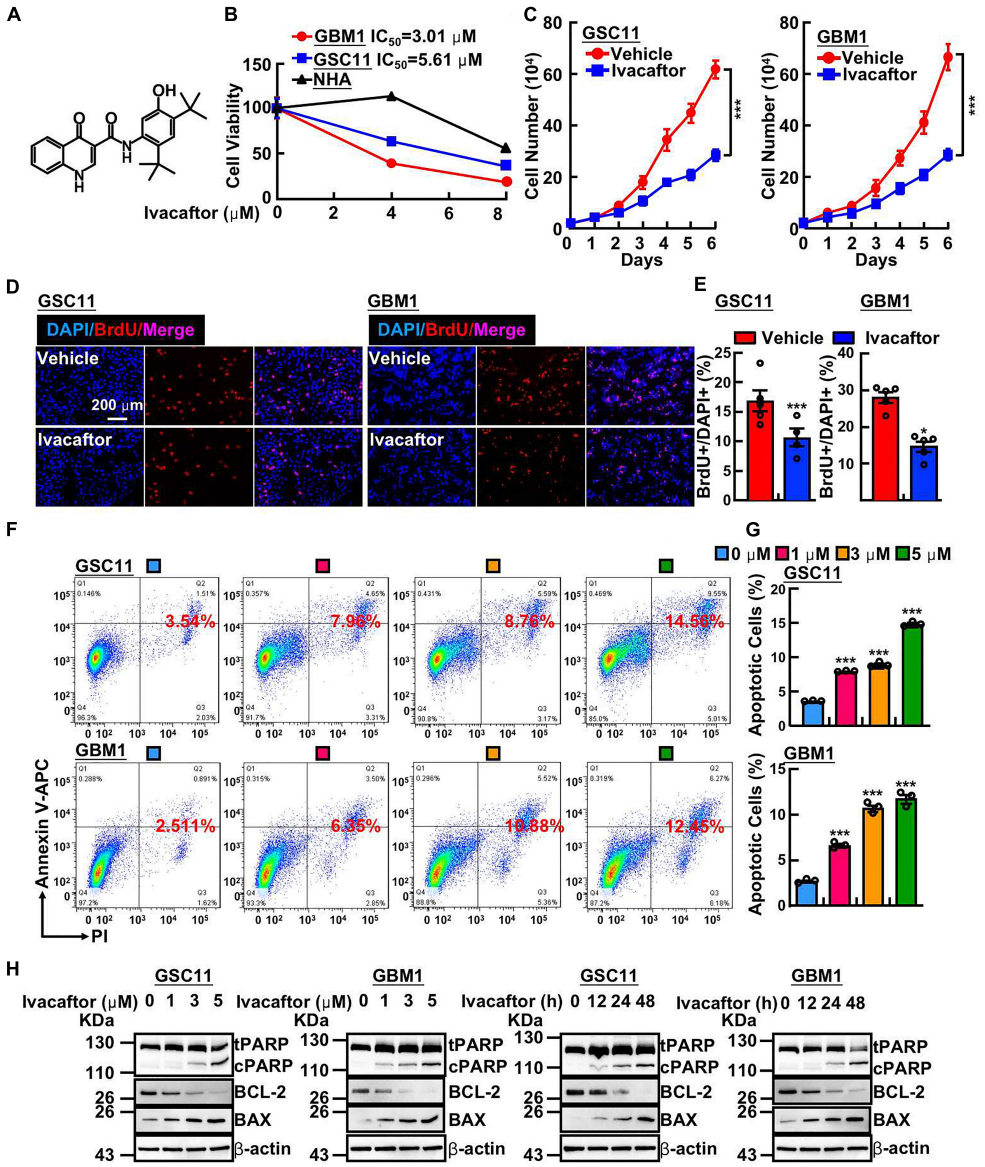

FIGURE 1 | Ivacaftor inhibits GSCs proliferation and induces cellular apoptosis. **(A)** The chemical structure of FDA-approved drug ivacaftor. **(B)** Cell viability of indicated cells treated with various concentrations of ivacaftor. **(C)** The cells proliferation of GSC11 (left panel) and GBM1 (right panel) treated by 5 mM ivacaftor. **(D,E)** Representative images of BrdU incorporation assay in GSC11 (left panel) and GBM1 (right panel) treated with or without ivacaftor. Scale bar: 200 mm. **(E)** Quantification data for **(D)**. **(F,G)** Ivacaftor treatment significantly increases cellular apoptosis in GSC11 and GBM1 cells determined by flow cytometry assay. **(G)** Quantification data for **(F)**. **(H)** Apoptotic cell markers were dramatically increased following treatment with indicated concentrations of ivacaftor. tPARP, total PARP; cPARP, cleaved PARP. Data are shown as means ± SEM, $^{*}P < 0.05$; $^{***}P < 0.001$; *t*-test.

with the most effective phenotype in TMZ plus ivacaftor group compared to other groups (**Figures 3H,I**). These results prompted us to hypothesize that ivacaftor could be used as novel clinical chemotherapy strategy to cure TMZ resistant GBM patients in the future.

Ivacaftor Suppresses Patient-Derived Xenograft Tumor Growth *in vivo*

To corroborate the clinical application of ivacaftor, patient-derived xenograft (PDX) mouse model was performed. Three clinical specimens of GBM patients were subcutaneously transplanted into nude mice and treated with ivacaftor (3 mg/kg) by intraperitoneal injection twice a week for 5 weeks. Five weeks later, the nude mice were sacrificed and the tumors were collected. As shown in **Figures 4A,B**, ivacaftor treatment dramatically retarded PDX tumor growth *in vivo* compared to PBS vehicle group (**Figure 4B**). In addition, PDX tumor sections were subject to immunohistochemical staining. The results showed that ivacaftor-treated PDX tumors exhibited more cellular apoptotic signals with increased cleaved

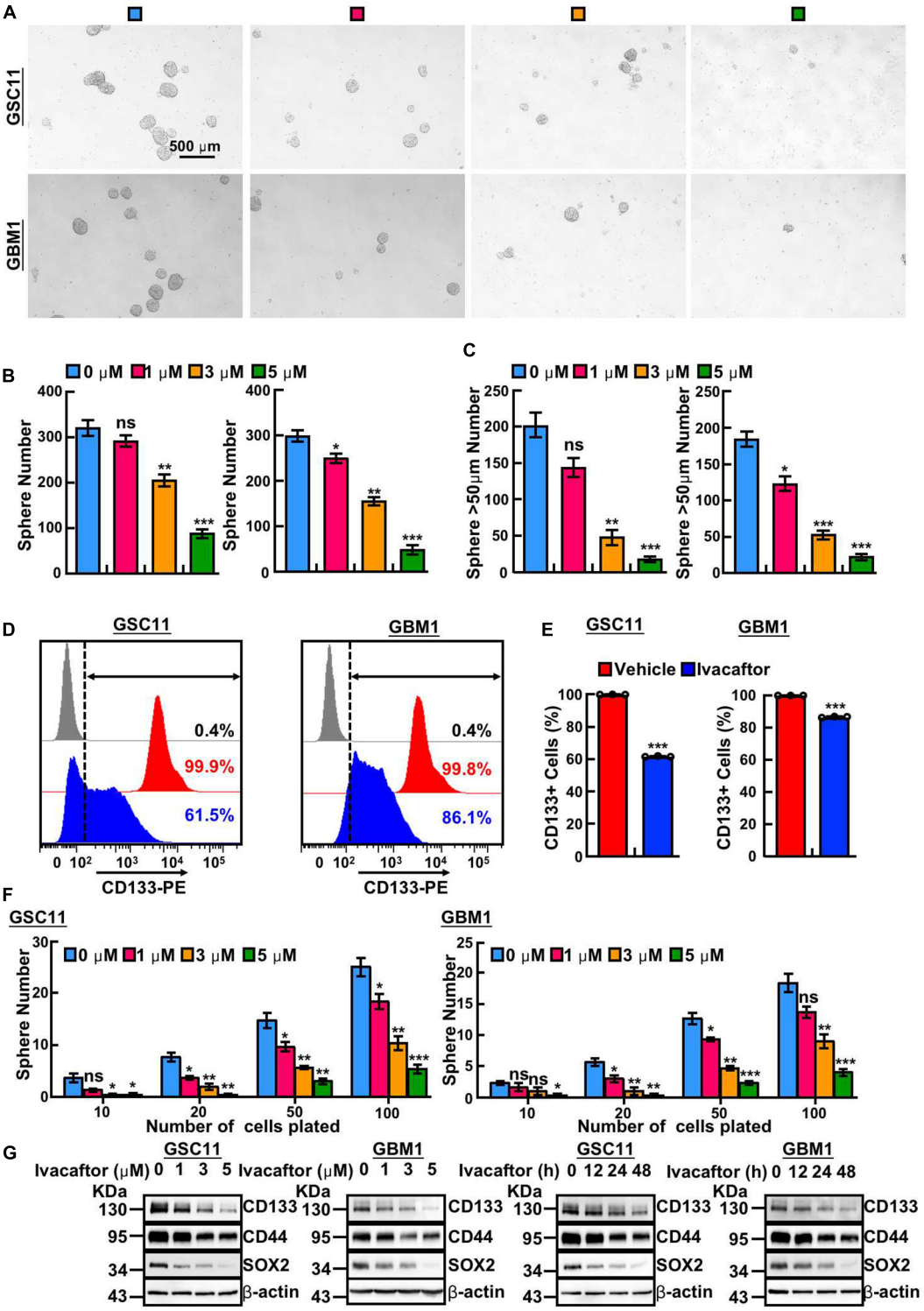

FIGURE 2 | Ivacaftor inhibits GSCs self-renewal ability. **(A)** Representative images of tumor sphere derived from GSC11 (top panel) and GBM1 (down panel) treated with indicated concentrations of ivacaftor. Scale bar: 500 μm. **(B)** Tumor sphere formation ability was significantly attenuated by treating GSC11 (left panel) and GBM1 (right panel) cells with different concentrations of ivacaftor. **(C)** Ivacaftor treatment significantly decreased GSC11 (left panel) and GBM1 (right panel) larger tumor sphere (diameter larger than 50 μm) formation ability. **(D,E)** CD133 membrane accumulated positive cells in GSC11 and GBM1 were decreased after treatment with 5 μM ivacaftor for 48 h determined by flow cytometry assay. **(E)** Quantification data for **(D)**. **(F)** Effects of ivacaftor in indicated cells evaluated by *in vitro* limiting dilution assay. **(G)** GSC11 and GBM1 cells self-renewal ability and stemness marker gene expressions were inhibited by ivacaftor via time- or dosage-dependent manner. Data are shown as means ± SEM, $^{*}P < 0.05$; $^{**}P < 0.01$; $^{***}P < 0.001$; *t*-test.

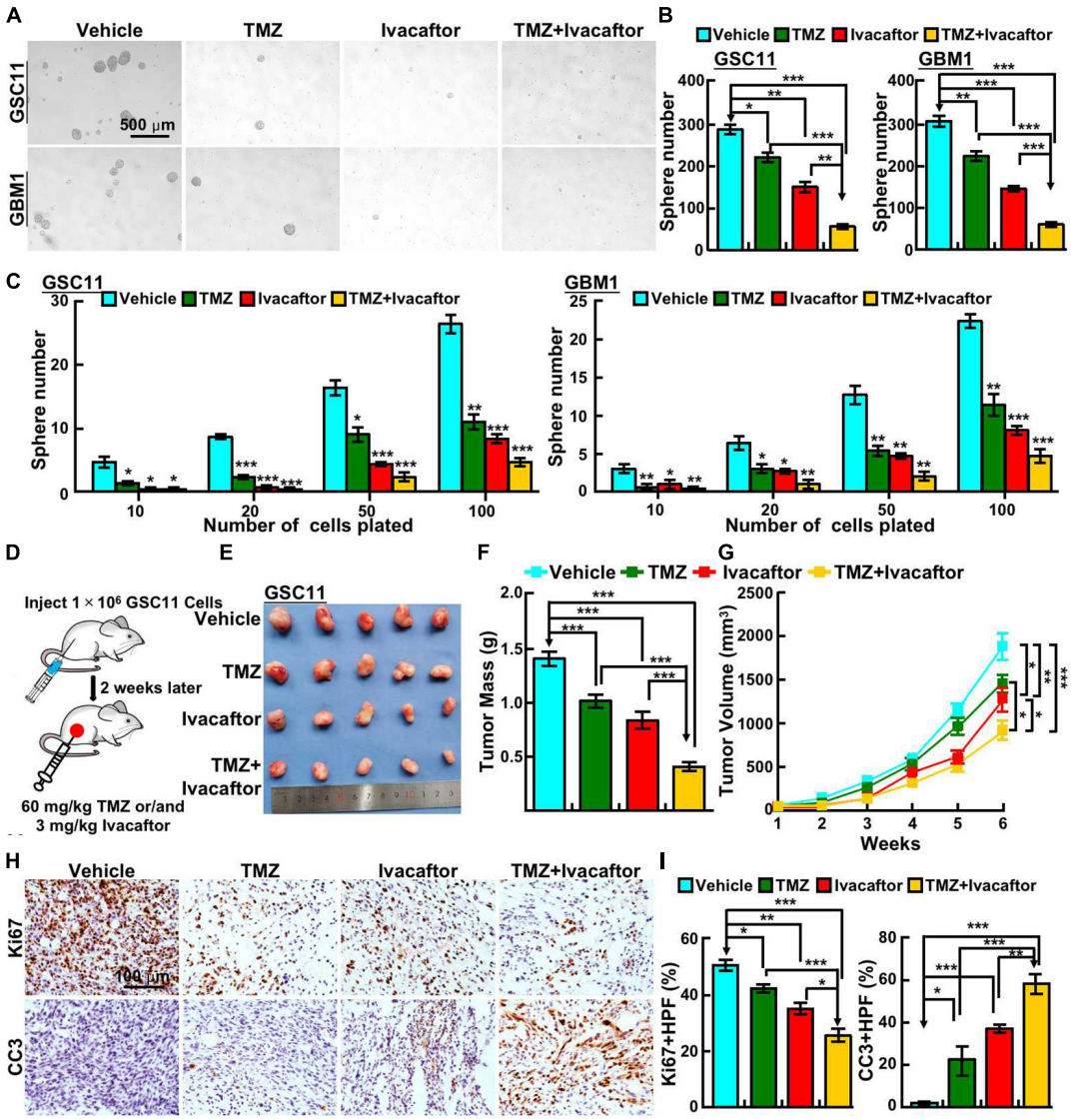

FIGURE 3 | Ivacaftor sensitizes GSCs response to TMZ. **(A,B)** Ivacaftor plus TMZ decreased GSC11 (top panel) and GBM1 (bottom panel) cells tumor sphere formation ability. Scale bar: 500 μm. **(B)** Quantification result of **(A)**. **(C)** Tumor sphere derived from GSC11 (left panel) and GBM1 (right panel) cells were counted after treating indicated cells with 200 μM TMZ, 5 μM ivacaftor, or 5 μM ivacaftor combined with 200 μM TMZ. **(D)** Flow chart of xenograft tumor formation assay in nude mouse. **(E)** Representative images of tumors treated with 3 mg/kg ivacaftor alone or combined with 60 mg/kg TMZ. **(F)** Tumor masses of xenograft tumors treated with indicated drugs were shown. **(G)** Tumor volumes of xenograft tumors treated with indicated drugs were shown. **(H,I)** Representative images of immunohistochemical staining of Ki67 and CC3 in xenograft tumor sections. CC3 means cleaved caspase 3. **(I)** Quantification data for panel **(H)**. Data are shown as means ± SEM, $^{*}P < 0.05$; $^{**}P < 0.01$; $^{***}P < 0.001$; *t*-test.

caspase 3 staining and deceased proliferative cell markers Ki67 staining compared with the PBS vehicle treatment group (**Figures 4C,D**).

DISCUSSION

Glioblastoma is the most aggressive brain tumor in adults and characterized by high heterogeneity containing a small subpopulation of GSCs responsible for conventional therapeutic resistance and tumor recurrence (Stupp et al., 2005; Wen and Kesari, 2008). Until now, valuable and effective GSC-targeting drugs are still not available in clinical practice. It is highly notable that clinical therapies that specifically blocks crucial regulators involved in GSCs maintenance may cause better clinical outcome.

In this study, we provided the first evidence showing that ivacaftor suppresses GSCs cell proliferation, self-renewal and xenograft tumor growth, and induces cellular apoptosis. Previous study reported that FDA-approved drug ivacaftor targets cystic fibrosis transmembrane conductance regulator (CFTR) to treat cystic fibrosis, and CFTR has been indicated

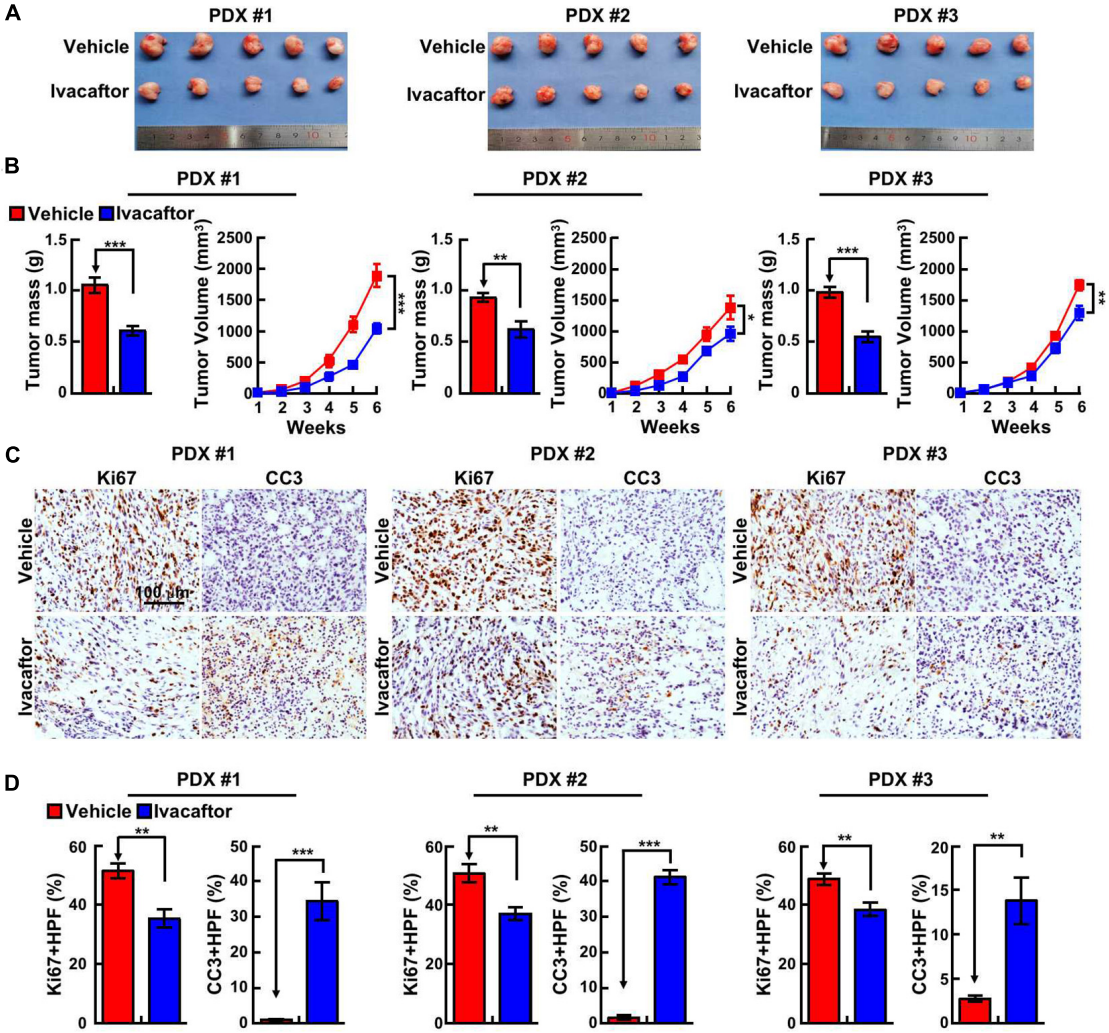

FIGURE 4 | Ivacaftor inhibits PDX tumor growth *in vivo*. **(A)** Representative images of PDX tumors derived from three independent GBM clinical specimens treated with ivacaftor or vehicle. **(B)** Tumor mass and volume of three xenograft tumors treated with 3 mg/kg ivacaftor or vehicle. **(C,D)** Representative images of immunohistochemical staining of Ki67 and CC3 in three PDX tumors. **(D)** Quantification data for **(C)**. Data are shown as means ± SEM, $^{*}P < 0.05$; $^{**}P < 0.01$; $^{***}P < 0.001$; *t*-test.

to facilitate glioma progression (Zhao et al., 2020). However, another finding demonstrates that CFTR activation inhibits GBM cell proliferation and migration (Zhong et al., 2019), indicating that CFTR functions as a tumor suppressor in GBM. The controversial findings of CFTR in glioma suggest that the direct target of ivacaftor in GSCs maintenance might be different. In addition, Hisert et al. (2020a,b)) provided evidence showing that ivacaftor dampens monocyte sensitivity to interferon-γ in cystic fibrosis patients. In line with this finding, ivacaftor has also been shown to improve the aberrant pathophysiology and microenvironment of the cystic fibrosis gut to favor a more healthy microbiota, which leads to reduced intestinal inflammation process (Ooi et al., 2018). Based on the fact that interferon-γ plays pivotal roles in tumor immunity (Ni and Lu, 2018), interferon-γ/JAK/STAT signaling might also mediate the inhibitory role of ivacaftor in GBM. Therefore, defining the novel target(s) of ivacaftor in GSCs using proteomic or transcriptome analysis might help us to decipher the underlying mechanism of suppressive roles of ivacaftor in GBM in the future.

A growing body of evidence indicates that CD133, CD44, and Sox2 were involved in sustaining GSCs self-renewal, which facilitates GBM tumorigenesis (Bao et al., 2006; Yin et al., 2007; Wei et al., 2013; Zhu et al., 2020). Thus, identifying leading compounds inhibit their expressions will be promising to be translated into clinical therapies for GBM patients. In this study, we showed that ivacaftor represses GSCs by directly attenuating CD133, CD44, and Sox2 expression., although the hub-gene controlling the stemness marker gene expression are not yet uncovered. However, the functional effects of ivacaftor *in vivo*

using conventional xenograft tumor and PDX mouse models strongly support that the drug repurposing of ivacaftor could benefit TMZ resistant GBM patients in the future.

MATERIALS AND METHODS

Cell Culture and Reagents

GBM1 cells were a kind gift from Dr. Yu Shi at Institute of Pathology and Southwest Cancer Center, Southwest Hospital and were characterized previously (Zhou et al., 2018). GBM1 cells were cultured in Neurobasal A medium (Gibco, 2585380) containing B27 supplement (1:50, Invitrogen, Cat#2175161), GlutaMAX (1:100, Gibco, Cat#35-50-061), Sodium pyruvate (1:100, Gibco Cat#R25-0000-Cl), MEM NEAA (1:100, Gibco, Cat#11140-050), 20 ng/mL bFGF (Gibco, Cat#PHG0266) and 1% penicillin/streptomycin. The GSC11 cells were cultured in DMEM/F12, supplemented with B27, 20 ng/mL EGF (Gibco, Cat#PHG0311L), 20 ng/mL bFGF, 4 μg/mL heparin (Sigma, H3149-500KU-9) and 1% penicillin/streptomycin. Normal human astrocyte cells (NHA) were a kind gift from Dr. Xiaozhong Peng at Institute of Medical Biology, Chinese Academy of Medical Sciences (Hu et al., 2019). NHA cells were cultured in commercial astrocyte medium (Cat#1801, ScienCell) supplemented with 1% astrocyte growth factor (ScienCell) and 2% FBS (ScienCell). All cells were cultured at 37°C in a 5% CO_2 humidified environment. Ivacaftor and temozolomide were purchased from MedChemExpress (Ivacaftor, Cat#HY-13017), (Temozolomide, Cat#HY-17364/CS-0943).

Cell Proliferation and BrdU Incorporation Assay

A total of 2×10^4 single GSC11 and GBM1 cells were plated into laminin-precoated 12-wells plates. Exact cell numbers for each day were assessed by an automatic cell analyzer countstar (Shanghai Ruiyu Biotech Co., China, IC 1000). BrdU incorporation assay was performed as our previous indicated (Yin et al., 2017). Briefly, GSC11 and GBM1 cells were pre-treated with 10 μM BrdU (Abcam, Cat# ab142567, dilution 1:100) for 20 min, followed by fixing with 4% PFA and incubated with BrdU primary antibody (Cell Signaling Technology, Cat# 5292s, dilution 1:1000) at 4°C overnight, the cells were then gently washed with PBS and incubated with anti-mouse Alexa 594 antibody (Abclonal, Cat# 61303, dilution 1:500). DAPI was used for DNA staining. Images were examined by Nikon Ti fluorescence microscope.

In vitro Limiting Dilution and Tumor Sphere Formation Assay

For *in vitro* limiting dilution assay, GSC11 and GBM1 cells were dissociated into a single-cell suspension and plated in 96-well plates (Corning, Cat#3474) in 100 μL serum-free medium. After 14 days, the numbers of tumor spheres derived from GSC11 and GBM1 cells were recorded. For tumor sphere formation assay, GSC11 and GBM1 cells were dissociated into single cells and a total of 30,000 per 2 mL serum-free medium, and then plated into ultra-low attachment 6-well plates (Corning, Cat#3471). The numbers of spheres were counted under Nikon Ti microscope.

Flow Cytometry

Apoptotic cells in early and late stages were detected using an annexin V-APC Apoptosis Detection Kit from BioLegend (Cat#640932, PharMingen) (Xu et al., 2020). In brief, GSC11 cells were treated with indicated concentrations of ivacaftor or DMSO control. Cells were collected and washed, then resuspended by annexin V binding buffer followed by adding 5 μL annexin V-APC and 5 μL propidium iodide. Indicated cells were incubated with the staining buffer for 30 min at room temperature and analyzed by flow cytometry (BD Bioscience). More than 30,000 events were recorded for each experiment and analyzed by FlowJo software. For CD133 membrane accumulated form analysis, GSC11 cells were incubated with phycoerythrin conjugated anti-CD133 or corresponding negative control antibodies for 30 min in dark at the room temperature at 4°C, and $CD133^+$ cells were then examined using flow cytometry (BD Bioscience).

Immunoblot

Immunoblot assay was performed as documented (Jiang et al., 2018). The detail information of antibodies used in this study are as follows: β-actin (Proteintech, Cat#60008-1-1g), Bcl-2 (Cell signaling technology, Cat#15071S), PARP (Cell signaling technology, Cat#9542S), Cleaved Caspase 3 (Cell signaling technology, Cat#9661S), Bax (Abcam, Cat#ab77566), and CD133 (Miltenyi, Cat#130092395).

In vivo Xenograft Tumor Model

All animal studies were approved by the Ethics Committee of Kunming Institute of Zoology. 5∼6 weeks old male BALB/c nude (GemPharmatech Co., Ltd., Nanjing, China) mice were used. For subcutaneous xenograft models, GSC11 cells (1×10^6 cells per mouse) were subcutaneously injected into the nude mice. Ivacaftor (3 mg/kg) in PBS was intraperitoneally injected twice a week for 5 weeks after tumors grew to 50 mm^3. For PDX model, three independent GBM specimens were transplanted into nude mice. Eight weeks later, the mice were sacrificed and the xenografts were cut out and transplanted subcutaneously into nude mice, mice were treated by PBS alone, TMZ alone (60 mg/kg), Ivacaftor (3 mg/kg) or TMZ plus Ivacaftor (3 mg/kg) twice a week for 5 weeks. Xenograft tumor volume were measured using Vernier calipers (Suzhou, China) by indicated time. Tumor volume was calculated by the formula length X $(width)^2/2$.

Immunohistochemistry Assay

Immunohistochemistry assay was performed as previously described (Shi Y. et al., 2019). Briefly, Immunohistochemistry was carried out in 3 μm paraffin sections (Dako, Cat#DK-2600, Glostrup, Denmark). The slides were then incubated in graded ethanol, incubated in 3% hydrogen peroxide for 20 min, and were pretreated with sodium

citrate buffer for 25 min at 121°C for antigen retrieval. After washing with PBS, the tissues were immune-stained with primary antibodies against Ki67 and cleaved caspase 3 at 4°C overnight. After being washed with PBS buffer, the tissues were covered by an anti-mouse/rabbit polymer horseradish peroxidase-label for 60 min at the room temperature. The slides were treated with the prepared diaminobenzidine solution and incubated for approximate 1 min to achieve proper brown color.

Statistics

All data are presented as the mean ± SEM. All experiments were performed at least three times. All analyses were performed using GraphPad Prism 5 (GraphPad Software). Two-tailed Student's *t*-test was used for statistical analysis for experiments with two comparisons. *P*-values less than 0.05 was considered statistically significant. For all figures, *, **, *** indicate $P < 0.05$, $P < 0.01$, $P < 0.001$, respectively.

DATA AVAILABILITY STATEMENT

The raw data supporting the conclusions of this article will be made available by the authors, without undue reservation.

ETHICS STATEMENT

The animal study was reviewed and approved by the Ethics Committee of Kunming Institute of Zoology.

AUTHOR CONTRIBUTIONS

CY supervised the whole study. CY and YC wrote the manuscript. KL, JP, and ZN performed the tumor sphere and xenograft tumor model assays. YS, LJ, and QW helped the real-time PCR and immunoblot assays. All authors contributed to the article and approved the submitted version.

FUNDING

This study was supported by the National Natural Science Foundation of China (U1902216 and 81772996) and Yunnan Applied Basic Research Projects (2019FJ009, 202001AS070037, 2019FB111, 2019HB076, and AMHD-2020-3). CY was also supported by Youth Innovation Promotion Association, CAS, Yunnan Ten Thousand Talents Plan Young and Elite Talents Project, and Project of Innovative Research Team of Yunnan Province (2019HC005).

REFERENCES

Bao, S., Wu, Q., Sathornsumetee, S., Hao, Y., Li, Z., Hjelmeland, A. B., et al. (2006). Stem cell-like glioma cells promote tumor angiogenesis through vascular endothelial growth factor. *Cancer Res.* 66, 7843–7848. doi: 10.1158/0008-5472.can-06-1010

Bhat, K. P. L., Balasubramaniyan, V., Vaillant, B., Ezhilarasan, R., Hummelink, K., Hollingsworth, F., et al. (2013). Mesenchymal differentiation mediated by NF-kappaB promotes radiation resistance in glioblastoma. *Cancer Cell* 24, 331–346.

Chen, J., Li, Y. J., Yu, T. S., McKay, R. M., Burns, D. K., Kernie, S. G., et al. (2012). A restricted cell population propagates glioblastoma growth after chemotherapy. *Nature* 488, 522–526. doi: 10.1038/nature11287

Das, S., Srikanth, M., and Kessler, J. A. (2008). Cancer stem cells and glioma. *Nat. Clin. Pract. Neurol.* 4, 427–435.

Dolma, S., Selvadurai, H. J., Lan, X. Y., Lee, L., Kushida, M., Voisin, V., et al. (2016). Inhibition of dopamine receptor D4 impedes autophagic flux, proliferation, and survival of glioblastoma stem cells. *Cancer Cell.* 29, 859–873. doi: 10.1016/j.ccell.2016.05.002

Gao, X. Y., Zang, J., Zheng, M. H., Zhang, Y. F., Yue, K. Y., Cao, X. L., et al. (2021). Temozolomide treatment induces HMGB1 to promote the formation of glioma stem cells via the TLR2/NEAT1/Wnt Pathway in Glioblastoma. *Front. Cell. Dev. Biol.* 9:620883. doi: 10.3389/fcell.2021.620883

Guvenc, H., Pavlyukov, M. S., Joshi, K., Kurt, H., Banasavadi-Siddegowda, Y. K., Mao, P., et al. (2013). Impairment of glioma stem cell survival and growth by a novel inhibitor for survivin-ran protein complex. *Clin. Cancer Res.* 19, 631–642. doi: 10.1158/1078-0432.ccr-12-0647

Hisert, K. B., Birkland, T. P., Schoenfelt, K. Q., Long, M. E., Grogan, B., Carter, S., et al. (2020b). Ivacaftor decreases monocyte sensitivity to interferon-gamma in people with cystic fibrosis. *ERJ Open Res.* 6, 00318–2019. doi: 10.1183/23120541.00318-2019

Hisert, K. B., Birkland, T. P., Schoenfelt, K. Q., Long, M. E., Grogan, B., Carter, S., et al. (2020a). CFTR modulator therapy enhances peripheral blood monocyte contributions to immune responses in people with cystic fibrosis. *Front. Pharmacol.* 11:1219. doi: 10.3389/fphar.2020.01219

Hoy, S. M. (2019). Elexacaftor/ivacaftor/tezacaftor: first approval. *Drugs* 79, 2001–2007. doi: 10.1007/s40265-019-01233-7

Hu, Y., Zhang, M. L., Tian, N. Y., Li, D. K., Wu, F., Hu, P. S., et al. (2019). The antibiotic clofoctol suppresses glioma stem cell proliferation by activating KLF13. *J. Clin. Invest.* 129, 3072–3085. doi: 10.1172/jci124979

Jiang, L. P., Fan, S. Q., Xiong, Q. X., Zhou, Y. C., Yang, Z. Z., Li, G. F., et al. (2018). GRK5 functions as an oncogenic factor in non-small-cell lung cancer. *Cell Death Dis.* 9:295.

Lathia, J. D., Mack, S. C., Mulkearns-Hubert, E. E., Valentim, C. L. L., and Rich, J. N. (2015). Cancer stem cells in glioblastoma. *Gene Dev.* 29, 1203–1217.

Lee, S. Y. (2016). Temozolomide resistance in glioblastoma multiforme. *Genes Dis.* 3, 198–210. doi: 10.1016/j.gendis.2016.04.007

Ni, L., and Lu, J. (2018). Interferon gamma in cancer immunotherapy. *Cancer Med.* 7, 4509–4516. doi: 10.1002/cam4.1700

Ochs, K., and Kaina, B. (2000). Apoptosis induced by DNA damage O6-methylguanine is Bcl-2 and caspase-9/3 regulated and Fas/caspase-8 independent. *Cancer Res.* 60, 5815–5824.

Ooi, C. Y., Syed, S. A., Rossi, L., Garg, M., Needham, B., Avolio, J., et al. (2018). Impact of CFTR modulation with ivacaftor on gut microbiota and intestinal inflammation. *Sci. Rep.* 8:17834.

Parada, L. F., Dirks, P. B., and Wechsler-Reya, R. J. (2017). Brain tumor stem cells remain in play. *J. Clin. Oncol.* 35, 2428–2431. doi: 10.1200/jco.2017.73.9540

Rowe, S. M., Daines, C., Ringshausen, F. C., Kerem, E., Wilson, J., Tullis, E., et al. (2017). Tezacaftor-ivacaftor in residual-function heterozygotes with cystic fibrosis. *N. Engl. J. Med.* 377, 2024–2035. doi: 10.1056/nejmoa1709847

Shi, Y., Fan, S., Wu, M., Zuo, Z., Li, X., Jiang, L., et al. (2019). YTHDF1 links hypoxia adaptation and non-small cell lung cancer progression. *Nat. Commun.* 10:4892.

Shi, Y., Guryanova, O. A., Zhou, W. C., Liu, C., Huang, Z., Fang, X. G., et al. (2018). Ibrutinib inactivates BMX-STAT3 in glioma stem cells to impair malignant growth and radioresistance. *Sci. Transl. Med.* 10:eaah6816. doi: 10.1126/scitranslmed.aah6816

Shi, Y. F., Lim, S. K., Liang, Q. R., Iyer, S. V., Wang, H. Y., Wang, Z. L., et al. (2019). Gboxin is an oxidative phosphorylation inhibitor that targets glioblastoma. *Nature* 567, 341–346. doi: 10.1038/s41586-019-0993-x

Stevens, M. F. G., Hickman, J. A., Langdon, S. P., Chubb, D., Vickers, L., Stone, R., et al. (1987). Antitumor imidazotetrazines .13. Antitumor-activity and

pharmacokinetics in mice of 8-Carbamoyl-3-Methyl-Imidazo[5,1-D]-1,2,3,5-Tetrazin-4(3h)-One (Ccrg 81045-M-and-B-39831), a novel drug with potential as an alternative to dacarbazine. *Cancer Res.* 47, 5846–5852.

Strickland, M., and Stoll, E. A. (2017). Metabolic reprogramming in Glioma. *Front. Cell. Dev. Biol.* 5:43. doi: 10.3389/fcell.2017.00043

Stupp, R., Mason, W. P., van den Bent, M. J., Weller, M., Fisher, B., Taphoorn, M. J. B., et al. (2005). Radiotherapy plus concomitant and adjuvant temozolomide for glioblastoma. *New Engl. J. Med.* 352, 987–996.

Wei, Y., Jiang, Y., Zou, F., Liu, Y., Wang, S., Xu, N., et al. (2013). Activation of PI3K/Akt pathway by CD133-p85 interaction promotes tumorigenic capacity of glioma stem cells. *Proc. Natl. Acad. Sci. U.S.A.* 110, 6829–6834. doi: 10.1073/pnas.1217002110

Wen, P. Y., and Kesari, S. (2008). Malignant gliomas in adults. *New. Engl. J. Med.* 359, 492–507. doi: 10.1056/nejmra0708126

Xu, P., Jiang, L., Yang, Y., Wu, M., Liu, B., Shi, Y., et al. (2020). PAQR4 promotes chemoresistance in non-small cell lung cancer through inhibiting Nrf2 protein degradation. *Theranostics* 10, 3767–3778. doi: 10.7150/thno.43142

Yin, L., Jiang, L. P., Shen, Q. S., Xiong, Q. X., Zhuo, X., Zhang, L. L., et al. (2017). NCAPH plays important roles in human colon cancer. *Cell Death Dis.* 8:e2680. doi: 10.1038/cddis.2017.88

Yin, S., Li, J., Hu, C., Chen, X., Yao, M., Yan, M., et al. (2007). CD133 positive hepatocellular carcinoma cells possess high capacity for tumorigenicity. *Int. J. Cancer* 120, 1444–1450. doi: 10.1002/ijc.22476

Zhao, M., Zhang, J., Huang, W., Dong, J., and Guo, J. (2020). CFTR promotes malignant glioma development via up-regulation of Akt/Bcl2-mediated anti-apoptosis pathway. *J. Cell. Mol. Med.* 24, 7301–7312. doi: 10.1111/jcmm.15300

Zhong, X., Chen, H. Q., Yang, X. L., Wang, Q., Chen, W., and Li, C. (2019). CFTR activation suppresses glioblastoma cell proliferation, migration and invasion. *Biochem. Biophys. Res. Commun.* 508, 1279–1285. doi: 10.1016/j.bbrc.2018.12.080

Zhou, A., Lin, K., Zhang, S., Chen, Y., Zhang, N., Xue, J., et al. (2016). Nuclear GSK3beta promotes tumorigenesis by phosphorylating KDM1A and inducing its deubiquitylation by USP22. *Nat. Cell Biol.* 18, 954–966. doi: 10.1038/ncb3396

Zhou, K., Yao, Y. L., He, Z. C., Chen, C., Zhang, X. N., Yang, K. D., et al. (2018). VDAC2 interacts with PFKP to regulate glucose metabolism and phenotypic reprogramming of glioma stem cells. *Cell Death Dis.* 9:988.

Zhu, Z., Mesci, P., Bernatchez, J. A., Gimple, R. C., Wang, X., Schafer, S. T., et al. (2020). Zika virus targets glioblastoma stem cells through a SOX2-Integrin alphavbeta5 Axis. *Cell Stem Cell 26* 18:e10.

Conflict of Interest: The authors declare that the research was conducted in the absence of any commercial or financial relationships that could be construed as a potential conflict of interest.

frontiers in Cell and Developmental Biology

ORIGINAL RESEARCH
published: 14 June 2021
doi: 10.3389/fcell.2021.691676

A Novel Risk Model Based on Lipid Metabolism-Associated Genes Predicts Prognosis and Indicates Immune Microenvironment in Breast Cancer

*Zhimin Ye[1,2], Shengmei Zou[3], Zhiyuan Niu[1,2], Zhijie Xu[2] and Yongbin Hu[1,2]**

[1] Department of Pathology, School of Basic Medical Sciences, Central South University, Changsha, China, [2] Department of Pathology, Xiangya Hospital, Central South University, Changsha, China, [3] Department of Neurology and Research Center of Neurology in Second Affiliated Hospital, Key Laboratory of Medical Neurobiology of Zhejiang Province, Zhejiang University School of Medicine, Hangzhou, China

OPEN ACCESS

Edited by:
Yongbin Chen, Kunming Institute of Zoology (CAS), China

Reviewed by:
Liang Wang, China Medical University, China
Larry Wang, University of Southern California, United States
Ceshi Chen, Kunming Institute of Zoology, China

***Correspondence:**
Yongbin Hu
yongbinhu@csu.edu.cn

Specialty section:
This article was submitted to Molecular and Cellular Oncology, a section of the journal Frontiers in Cell and Developmental Biology

Received: *06 April 2021*
Accepted: *07 May 2021*
Published: *14 June 2021*

Citation:
Ye Z, Zou S, Niu Z, Xu Z and Hu Y (2021) A Novel Risk Model Based on Lipid Metabolism-Associated Genes Predicts Prognosis and Indicates Immune Microenvironment in Breast Cancer. Front. Cell Dev. Biol. 9:691676. doi: 10.3389/fcell.2021.691676

Background: Breast cancer (BRCA) is the most common tumor in women, and lipid metabolism involvement has been demonstrated in its tumorigenesis and development. However, the role of lipid metabolism-associated genes (LMAGs) in the immune microenvironment and prognosis of BRCA remains unclear.

Methods: A total of 1076 patients with BRCA were extracted from The Cancer Genome Atlas database and randomly assigned to the training cohort (n = 760) or validation cohort (n = 316). Kaplan–Meier analysis was used to assess differences in survival. Consensus clustering was performed to categorize the patients with BRCA into subtypes. Using multivariate Cox regression analysis, an LMAG-based prognostic risk model was constructed from the training cohort and validated using the validation cohort. The immune microenvironment was evaluated using the ESTIMATE and tumor immune estimation resource algorithms, CIBERSORT, and single sample gene set enrichment analyses.

Results: Consensus clustering classified the patients with BRCA into two subgroups with significantly different overall survival rates and immune microenvironments. Better prognosis was associated with high immune infiltration. The prognostic risk model, based on four LMAGs (*MED10*, *PLA2G2D*, *CYP4F11*, and *GPS2*), successfully stratified the patients into high- and low-risk groups in both the training and validation sets. High risk scores predicted poor prognosis and indicated low immune status. Subgroup analysis suggested that the risk model was an independent predictor of prognosis in BRCA.

Conclusion: This study demonstrated, for the first time, that LMAG expression plays a crucial role in BRCA. The LMAG-based risk model successfully predicted the prognosis and indicated the immune microenvironment of patients with BRCA. Our study may provide inspiration for further research on BRCA pathomechanisms.

Keywords: breast cancer, lipid metabolism, tumor immune microenvironment, risk model, prognosis

INTRODUCTION

Breast cancer (BRCA) is the most common malignancy and the second leading cause of cancer-related death among women globally (DeSantis et al., 2019). Epidemiological studies have revealed that at least 268,000 patients are newly diagnosed with BRCA each year and 41,760 patients die. The incidence of BRCA has been steadily increasing (Siegel et al., 2019; Britt et al., 2020; Zhao et al., 2020). Currently, the therapeutic strategies for BRCA mainly include surgical resection, endocrine therapy, and combining surgery with various types of adjuvant therapies, including radiotherapy, chemotherapy, and immunotherapy (Waks and Winer, 2019; Zhao et al., 2020). The therapeutic objective is to improve the long-term survival and quality of life of patients with BRCA. The 5-year overall survival rate for early diagnosis of BRCA is >90%, which declines to 27% in stage IV patients (DeSantis et al., 2019). BRCA mainly includes three subtypes: ERBB2+, hormone receptor positive/ERBB2 negative (HR+/ERBB2-), and triple-negative. As the tumors are remarkably heterogeneous, fixed-treatment modes are not effective for all patients. Considering the significant tumor heterogeneity of BRCA, multivariable indicators are more significant than single biomarkers for prognosis prediction (Zhang et al., 2020), and risk models based on gene expression are a promising option (Yu et al., 2019).

The dysregulation of lipid metabolism plays a pivotal role in tumorigenesis and development, and increasing evidence indicates that lipid metabolism is essentially reprogrammed in tumors. This is regarded as a new hallmark of malignant tumors (Cheng et al., 2018; Maan et al., 2018; Visweswaran et al., 2020; Matsushita et al., 2021). Growing data suggest that lipid-metabolic reprogramming also plays an important role in the invasion and metastasis of malignant tumors (Luo et al., 2017). Targeting the lipid metabolism of tumor cells has been recognized as an attractive tumor treatment strategy (Liu et al., 2017; Visweswaran et al., 2020). Emerging evidence also indicates that aberrant lipid metabolism is involved in drug resistance during cancer treatment (Iwamoto et al., 2018; Cao, 2019). Previous studies have reported that risk signatures derived from lipid metabolism-associated genes (LMAGs) exhibit potent capability in predicting the prognosis of various tumors, including serous ovarian carcinomas (Zheng et al., 2020), clear cell renal cell carcinomas (Zheng et al., 2020), pancreatic cancer (Ye et al., 2021), lung adenocarcinomas (Li et al., 2020), and diffuse gliomas (Li et al., 2020). However, the prognostic value of LMAGs in patients with BRCA remains largely unknown.

The tumor microenvironment (TM) is a crucial regulator of malignancy (Wu et al., 2021). In particular, the tumor immune microenvironment, which reflects the immune status of the tumor tissues, performs critical functions, and has attracted increasing attention (Pitt et al., 2016; Locy et al., 2018; Lei et al., 2020). Immune cells in the immune microenvironment possess effective regulatory and destructive effects on tumor cells, and may have dual tumor-promoting and tumor-antagonizing roles (Lei et al., 2020). Recently, various studies have demonstrated that the immune microenvironment is crucial for the development and therapeutic efficacy of tumors (Lei et al., 2020). Meanwhile, increasing evidence indicates that dysregulation of the lipid metabolism greatly influences the immune microenvironment (Hao et al., 2019). However, the association between LMAGs and the tumor immune microenvironment remains obscure in BRCA.

Therefore, in this study, we explore the role of lipid metabolism in the oncogenesis and development of BRCA, using multiple bioinformatics methods. A novel prognostic risk model was constructed, based on LMAG expression levels, to evaluate the prognostic value of LMAGs in patients with BRCA. We also comprehensively analyzed differences in the immune microenvironments of patients with BRCA. In addition, we preliminarily elucidated the potential signaling pathways involved.

To the best of our knowledge, this is the first study to report the prognostic role of LMAGs in BRCA. The results of this study should provide inspiration for elucidating the molecular mechanisms of BRCA tumorigenesis and progression, promoting the development of personalized targeted therapy, and improving the prognosis of patients with BRCA.

MATERIALS AND METHODS

Data Collection

The clinical data and gene expression matrices of enrolled patients were obtained from The Cancer Genome Atlas database[1]. In this study, 1076 BRCA samples were included, of which 760 samples were assigned to the training cohort and 316 to the validation cohort. The baseline data of all the samples are summarized in **Table 1**. A total of 776 LMAGs were collected from the Kyoto Encyclopedia of Genes and Genomes (KEGG) and Reactome databases, and 78 of these were identified as prognostic for BRCA, using univariable Cox regression analysis. And the process of data analysis is shown in **Figure 1**.

Consensus Clustering

According to the expression matrix of the 78 LMAGs, consensus clustering was performed using the R package "ConsensusClusterPlus" to divide the patients with BRCA in the training cohort into subgroups. Clustering was implemented on the grounds of partitioning around medoids, with Euclidean distances.

Immune Analysis

The estimation of stromal and immune cells in malignant tumor tissues using expression data (ESTIMATE) method was applied to calculate the immune score, ESTIMATE score, and tumor purity of the patients, via the R package "estimate" (Yoshihara et al., 2013). Tumor immune estimation resource (TIMER) analysis[2] was conducted

[1]https://portal.gdc.cancer.gov/

[2]https://cistrome.shinyapps.io/timer/

TABLE 1 | Clinical characteristics of samples.

Variable	Training cohort (*N* = 760)	Validation cohort (*N* = 316)
	N (%)	*N* (%)
Age		
<58 years old	377 (49.6)	145 (45.9)
≥58 years old	383 (50.4)	171 (54.1)
Metastasis		
Yes	24 (3.2)	10 (3.2)
No	736 (96.8)	306 (96.8)
Tumor stage		
Stage 1	137 (18.0)	51 (16.1)
Stage 2	430 (56.6)	183 (57.9)
Stage 3	167 (22.0)	74 (23.4)
Stage 4	26 (3.4)	8 (2.5)
Race		
Asian	37 (4.9)	19 (6.0)
Black or African American	124 (16.3)	39 (12.3)
White	546 (71.8)	227 (71.8)
Unknown	53 (7.0)	31 (9.8)
Radiotherapy		
Yes	389 (51.2)	157 (49.7)
No	286 (37.6)	133 (42.1)
Unknown	85 (11.2)	26 (8.2)

to evaluate the abundance of six types of immune cells (neutrophils, CD4 T cells, macrophages, CD8 T cells, dendritic cells, and B cells) (Li et al., 2017). The CIBERSORT algorithm was employed to estimate the ratio of 22 types of infiltrating immune cells. Single sample gene set enrichment analysis (ssGSEA) was performed to assess the infiltration level of 28 types of immune cells using the "GSVA" R package.

Construction and Validation of Risk Model Based on LMAGs

Based on univariable regression analysis, the least absolute shrinkage and selection operator algorithm was applied using the R package "glmnet" to select candidate genes for constructing the risk model. The genes included in the risk model were determined using multivariate regression analysis. Which were listed in **Table 2**. Each patient in both the training and validation cohorts was assigned a risk score, according to the following formula: risk score = (−0.2141 × *PLA2G2D* expression) + (0.52944 × *MED10* expression) + (−0.1887 × *CYP4F11* expression) + (−0.4069 × *GPS2* expression). The patients were categorized into low- and high-risk groups, with the median of the risk score regarded as the cutoff. Kaplan–Meier analysis was employed to estimate the difference in overall survival between the categorized patients via the R package "survival." The prognostic capability of the risk model was validated using time-dependent receiver operating characteristic (ROC) analysis with the R package "survivalROC."

Evaluation of Risk Model Independence

Univariate and multivariate Cox regression analyses were performed to estimate whether the risk score was an independent predictor of BRCA prognosis. A subgroup analysis was conducted to confirm the independence of the risk model. The patients with BRCA in the training cohort were regrouped into new subgroups based on different clinical characteristics, and the patients in each subgroup were stratified into high- and low-risk groups, based on the median risk score.

Functional Analysis

Differential expression analysis was conducted using the "limma" R package to identify differentially expressed genes (DEGs) for subsequent analyses. Gene ontology (GO) and KEGG analyses were performed to enrich the DEGs into associated pathways using the "clusterProfiler" R package. Enrichment analysis was also performed using the web tool "metascape"[3]. Moreover, the activity of each GO term in each patient with BRCA was evaluated via gene set variation analysis (GSVA) using the "GSVA" R package.

[3]https://metascape.org

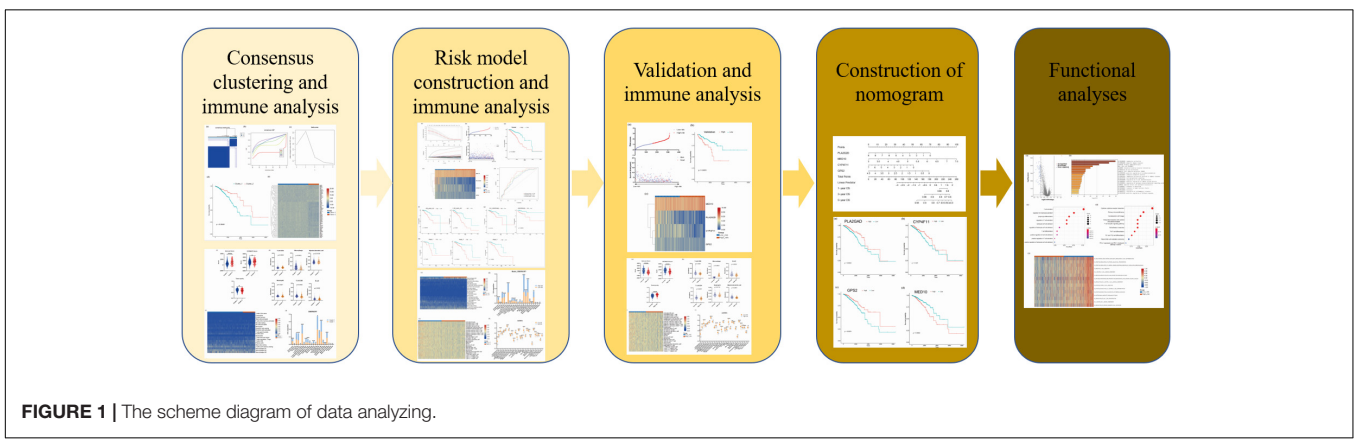

FIGURE 1 | The scheme diagram of data analyzing.

TABLE 2 | Features of the genes used for constructing the risk model.

Gene name	Full name	Category	Function
MED10	Mediator Complex Subunit 10	Protein Coding	Component of the Mediator complex, a coactivator involved in regulating the transcription of nearly all RNA polymerase II-dependent genes
PLA2G2D	Phospholipase A2 Group IID	Protein Coding	Secretory calcium-dependent phospholipase A2 that primarily targets extracellular lipids, exerting anti-inflammatory, and immunosuppressive effects
CYP4F11	Cytochrome P450 Family 4 Subfamily F Member 11	Protein Coding	A cytochrome P450 monooxygenase involved in the metabolism of various endogenous substrates, including fatty acids and their oxygenated derivatives
GPS2	G Protein Pathway Suppressor 2	Protein Coding	Key regulator of inflammation, lipid metabolism, and mitochondrion homeostasis that acts by inhibiting the activity of the ubiquitin-conjugating enzyme UBE2N/Ubc13, thereby inhibiting 'Lys-63'-linked ubiquitination

Statistical Analysis

Data analyses were mainly completed using R (version 4.0) and GraphPad Prism (version 8.0), and visualization also employed TBtools (Chen et al., 2020). Discontinuous data are presented as number (percentage), and continuous data are displayed as mean ± standard deviation. Differences between two groups were calculated using Student's *t*-tests, while those among more than two groups were calculated using one-way ANOVA. Statistical significance was defined as $p < 0.05$.

RESULTS

Consensus Clustering for LMAGs Correlated With Prognosis and Immune Microenvironment in BRCA

Consensus clustering was conducted to cluster the patients with BRCA in the training cohort into subgroups. The results showed that consensus clustering was the most stable when $K = 2$ (**Figures 2A–C** and **Supplementary Figure 1**). Therefore, the patients with BRCA were divided into two groups, with 564 patients in Cluster 1 and 196 patients in Cluster 2. Survival analysis indicated that the overall survival of the two clusters differed, and that patients in Cluster 2 had a significantly better prognosis (**Figure 2D**). Heatmap visualization showed that the prognostic LMAG expression of the patients with BRCA also differed significantly between the two clusters (**Figure 2E**). The ESTIMATE assessment suggested that the patients in Cluster 2 had higher immune scores and ESTIMATE scores and lower tumor purity (**Figure 3A**). In addition, TIMER analysis demonstrated a statistical difference between the two clusters regarding the abundance of infiltrating immune cells. The abundance of CD4 T cells and myeloid dendritic cells was lower in Cluster 1 than in Cluster 2, whereas the opposite trend was observed in macrophage cells and CD8 T cells (**Figure 3B**). Meanwhile, the CIBERSORT algorithm was used to calculate the infiltration level of the immune cells (**Figure 3C**), and quantitative analysis suggested a significant difference between the two clusters (**Figure 3D**). Finally, ssGSEA was performed to assess the immune status of the patients with BRCA, and the results are illustrated in a heatmap (**Figure 3E**), which shows that the patients in Cluster 2 had a relatively high immune status compared with those in Cluster 1. Statistical analysis confirmed the ssGSEA results (**Figure 3F**). These findings indicate that LMAG expression is associated with the prognosis and immune microenvironment of patients with BRCA.

Construction of an LMAG-Based Risk Model Using the Training Cohort

A risk model based on LMAGs was established to evaluate the prognostic value of LMAGs in BRCA. Based on univariate Cox analysis, least absolute shrinkage and selection operator analysis screened out 15 genes for subsequent analysis (**Figure 4A**). Of these, multivariate Cox analysis identified four genes to include in the constructed risk model, *MED10*, *PLA2G2D*, *CYP4F11*, and *GPS2*, all of which can independently predict the prognosis of patients with BRCA (**Supplementary Figure 2**). According to the median risk score, the patients were categorized into high- and low-risk groups. The risk score and survival status distributions of the patients are depicted in **Figure 4B**. A heatmap visualizing the expression pattern of the genes used in the risk model suggested that patients in the high-risk group tended to express risk genes with a hazard ratio > 1, including *MED10*, while patients in the low-risk group tended to express protective genes with a hazard ratio < 1, including *PLA2G2D*, *CYP4F11*, and *GPS2* (**Figure 4C**). The Kaplan–Meier survival curve indicated that the patients in the low-risk group had significantly better overall survival (**Figure 4D**). With respect to model diagnosis, the areas under the curve of the time-dependent ROC curves were 0.744 for one-year survival, 0.700 for three-year survival, and 0.678 for five-year survival, respectively, suggesting the acceptable stability of the risk model (**Figure 4E**). These results indicate that the LMAG-based risk model could accurately predict the prognosis of patients with BRCA.

The Risk Model Is an Independent Indicator for BRCA Prognosis

Univariable/multivariable Cox regression and subgroup analyses were conducted to verify the independence of the LMAG-based risk model. Univariate Cox regression analysis revealed that the risk score could predict the prognosis of patients with BRCA independently ($p = 2.47E{-}10$) (**Supplementary Table 1**). In the multivariable regression analysis, the risk score remained statistically significant for BRCA survival ($p = 1.42E{-}06$) (**Supplementary Table 2**). Additionally, the patients with BRCA in the training cohort were regrouped into subgroups based on

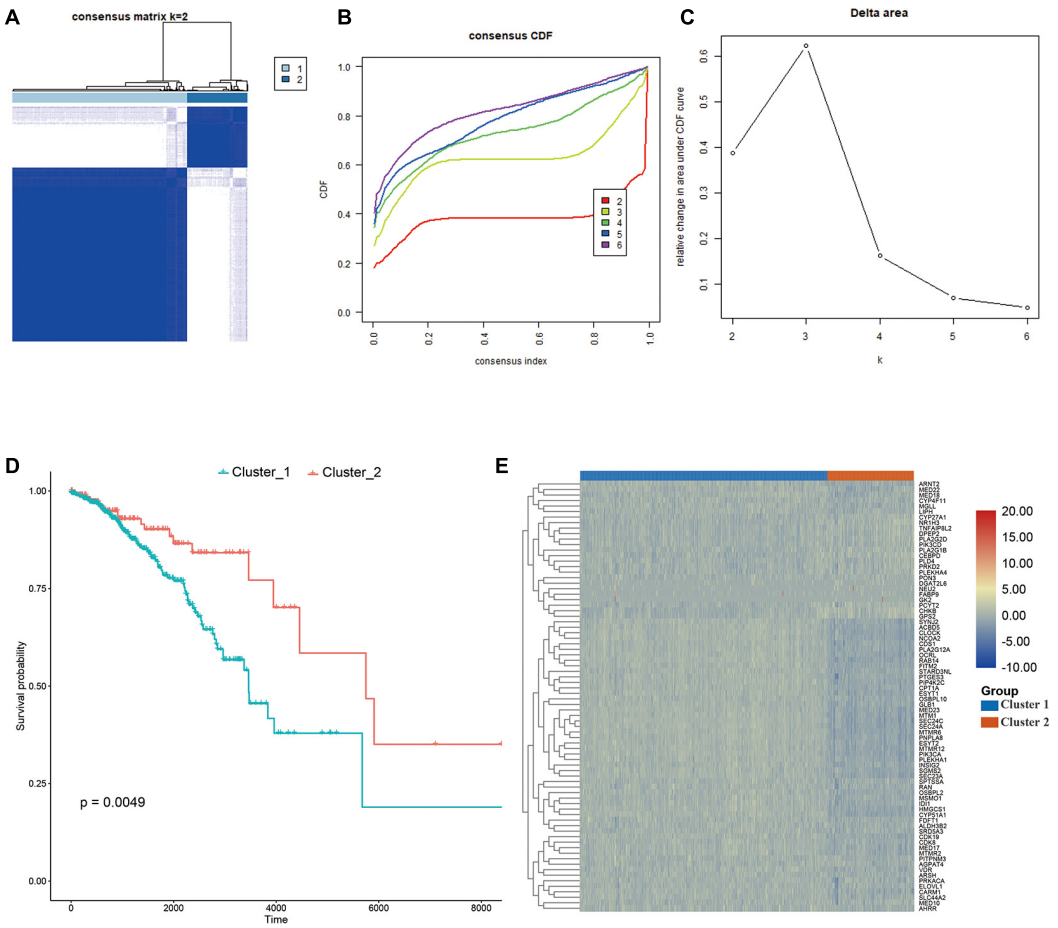

FIGURE 2 | Consensus clustering. **(A–C)** The clustering demonstrating the best stability with $K = 2$, **(D)** Kaplan–Meier analysis curve, **(E)** heatmap illustrating the different expressional pattern of the prognostic lipid metabolism associated genes in the two clusters.

age (<58 and ≥58 years old), tumor stage (stage 1, stage 2, and stage 3), and radiotherapy application. Regardless of the subgroups, the LMAG-based risk model stratified the patients with BRCA into the high- and low-risk groups, and the patients in the low-risk group still showed significantly longer survival (**Figures 4F–H**).These results indicate the excellent independence of the risk model.

The Risk Model Was Associated With Immune Microenvironment in the Training Cohort

The association between the risk model and the immune microenvironment in BRCA was assessed using multiple immune analyses. The ESTIMATE results revealed that the patients with BRCA in the high-risk group had significantly lower immune scores and ESTIMATE scores, and higher tumor purity, than those in the low-risk group (**Figure 5A**). The TIMER algorithm indicated that the abundances of B cells ($p < 0.0001$), neutrophils ($p = 0.0086$), CD4 T cells ($p < 0.0001$), myeloid dendritic cells ($p < 0.0001$), and CD8 T cells ($p < 0.0001$) in the low-risk group were statistically higher than those in the high-risk group, while the opposite was observed for macrophages (**Figure 5B**). The results of the CIBERSORT immune-infiltration analysis are depicted in a heatmap (**Figure 5C**), and the corresponding statistical analysis suggested significant differences in most immune-infiltrating cells (**Figure 5D**). Moreover, ssGSEA revealed that the patients with BRCA in the low-risk group had a relatively high immune status compared with those in the high-risk group (**Figure 5E**). Meanwhile, quantitative analysis confirmed higher ssGSEA scores in the low-risk group than in the high-risk group (**Figure 5F**). The above findings demonstrate that the LMAG-based risk model was related to the immune microenvironment in BRCA.

The Risk Model Correlated With Prognosis and Immune Microenvironment in the Validation Cohort

To further confirm the practicability and reliability of the LMAG-based risk model, it was verified using the validation cohort. According to the median risk score, the patients in

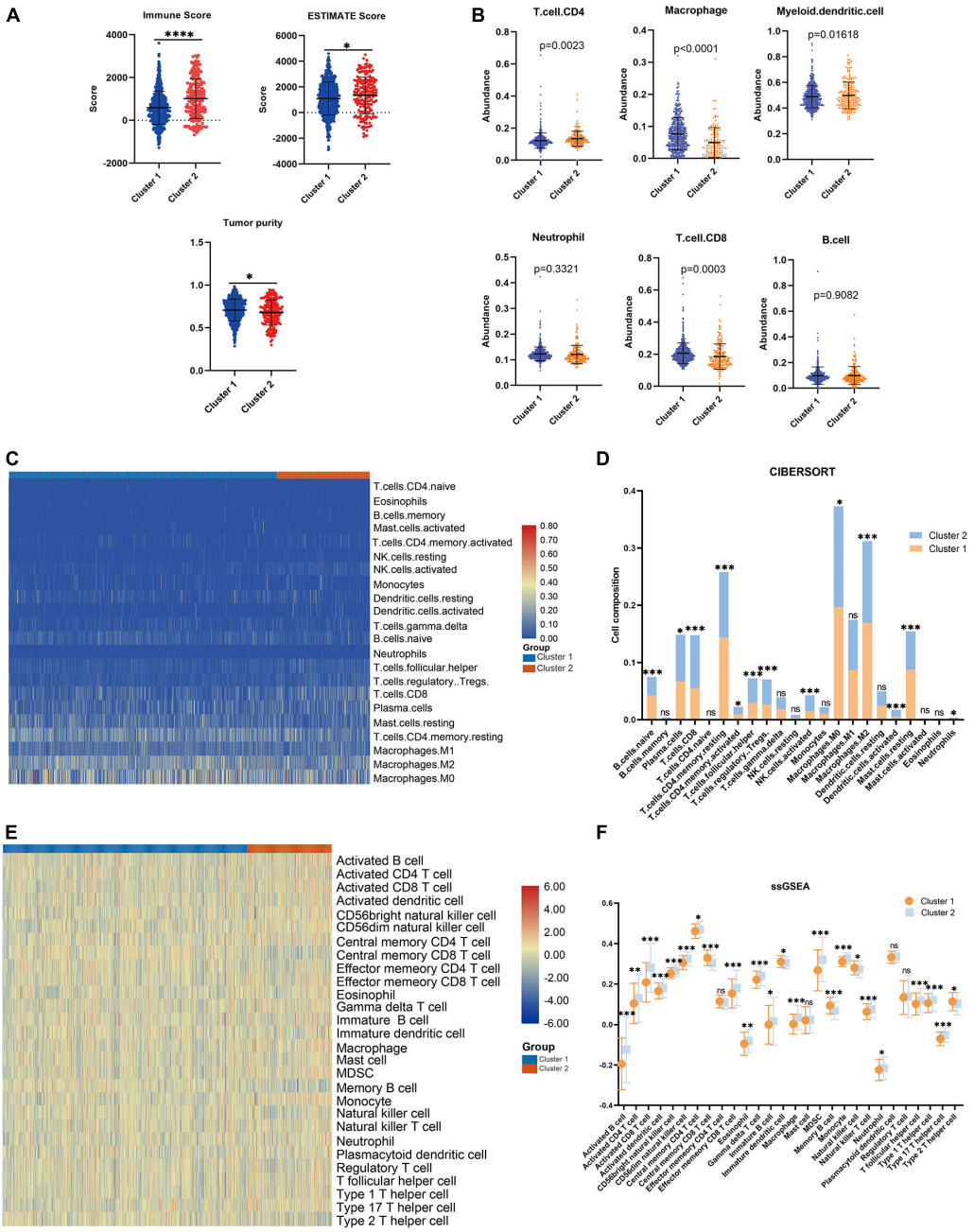

FIGURE 3 | Immune analyses in the clustered subgroups. **(A)** ESTIMATE algorithm, **(B)** TIMER algorithm, **(C,D)** CIBERSORT analysis, and ssGSEA analysis **(E,F)**. $^{*}p < 0.05$, $^{**}p < 0.01$, $^{***}p < 0.001$, $^{****}p < 0.0001$.

the validation cohort were stratified into high- and low-risk groups. The survival status and risk score distributions are illustrated in **Figure 6A**. As expected, the overall prognosis of the two groups differed significantly, and the patients in the low-risk group showed longer survival ($p = 0.001$) (**Figure 6B**). The expressions of the four genes included in the risk model are shown in a heatmap (**Figure 6C**). Patients in the low-risk group showed a tendency to express protective genes (*PLA2G2D*, *CYP4F11*, and *GPS2*), whereas patients in the high-risk group tended to express the risk gene *MED10*. Furthermore, the relationship between the risk score and the BRCA immune microenvironment was confirmed in the validation cohort. In the ESTIMATE analysis, a low risk score was significantly associated with high immune and ESTIMATE scores, and low tumor purity (**Figure 7A**). Regarding the TIMER analysis, the abundance of all six immune cells was statistically different between the two groups (**Figure 7B**). Except for macrophages ($p < 0.0001$), the abundances of all the immune cells were

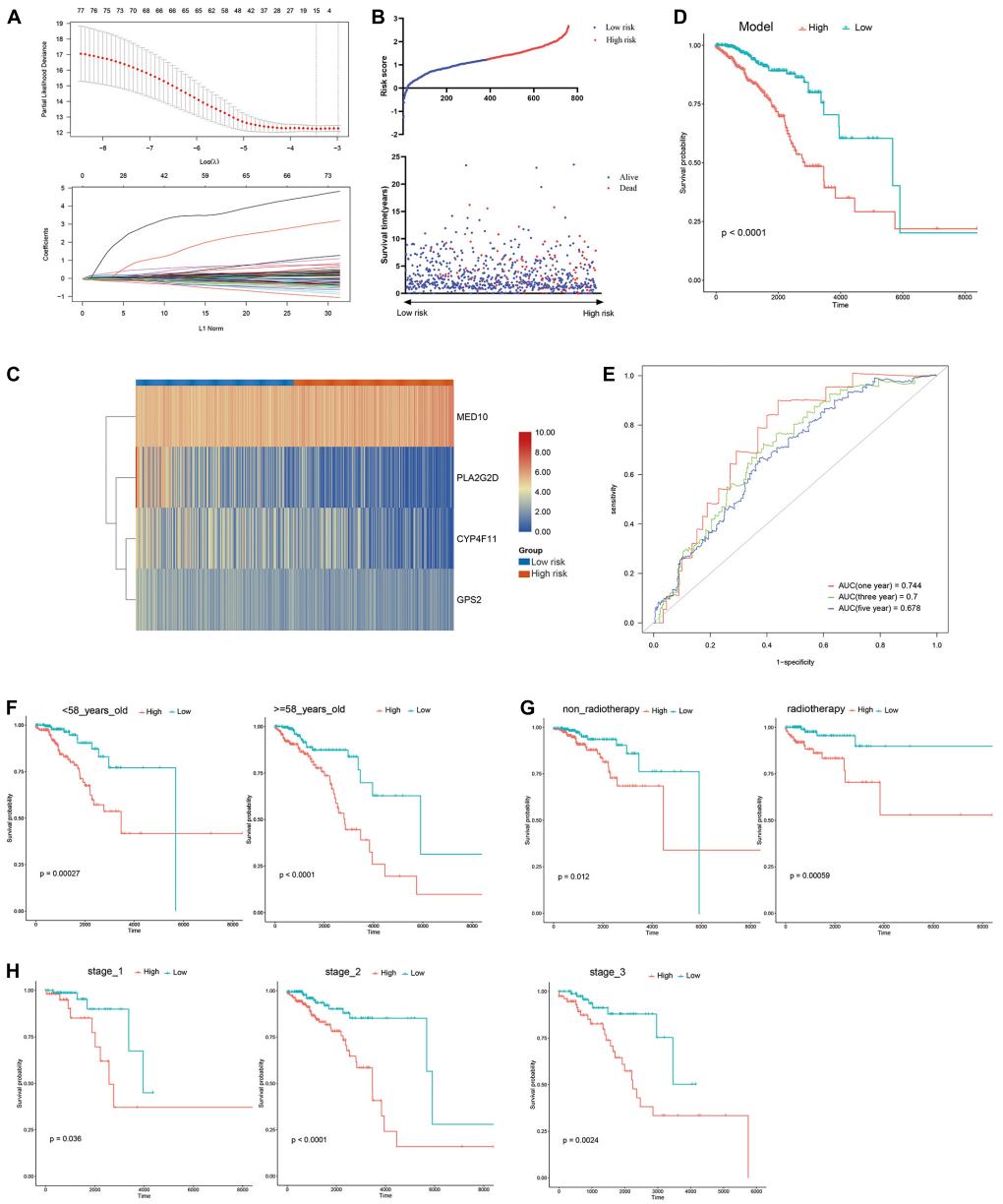

FIGURE 4 | Construction of risk model. **(A)** LASSO analysis revealing the minimal lambda, **(B)** survival status and risk score, **(C)** heatmap visualizing the expression pattern of the four candidate LMAGs, **(D)** survival curve illustrating the overall survival of the BRCA patients, **(E)** time-dependent ROC curve, **(F–H)** subgroup analyses suggesting the independence of the risk model regarding age, radiotherapy, and tumor stage.

significantly higher in the low-risk group than in the high-risk group. The heatmap visualization and corresponding statistical analysis of the CIBERSORT algorithm are depicted in **Figures 7C,D**, respectively. In the ssGSEA, relatively high immune status was observed in the low-risk group compared to the high-risk group (**Figure 7E**), and quantitative analysis identified statistical differences in most immune cells between the two groups (**Figure 7F**). These results suggest that the LMAG-based risk model is related to prognosis and the immune microenvironment in BRCA.

Establishment of a Risk Model-Based Nomogram in the Training Cohort

To develop a strategy to quantitatively predict the probability of survival in BRCA, a prognostic nomogram was constructed, based on the four genes from the risk model, via Cox proportional hazards analysis (**Figure 8**). As depicted in the nomogram, each prognostic gene in the risk model was endowed with a specific score and a corresponding expression value, and the total score was obtained by summing the scores of all the variables. Correspondingly, the survival probability of patients with BRCA

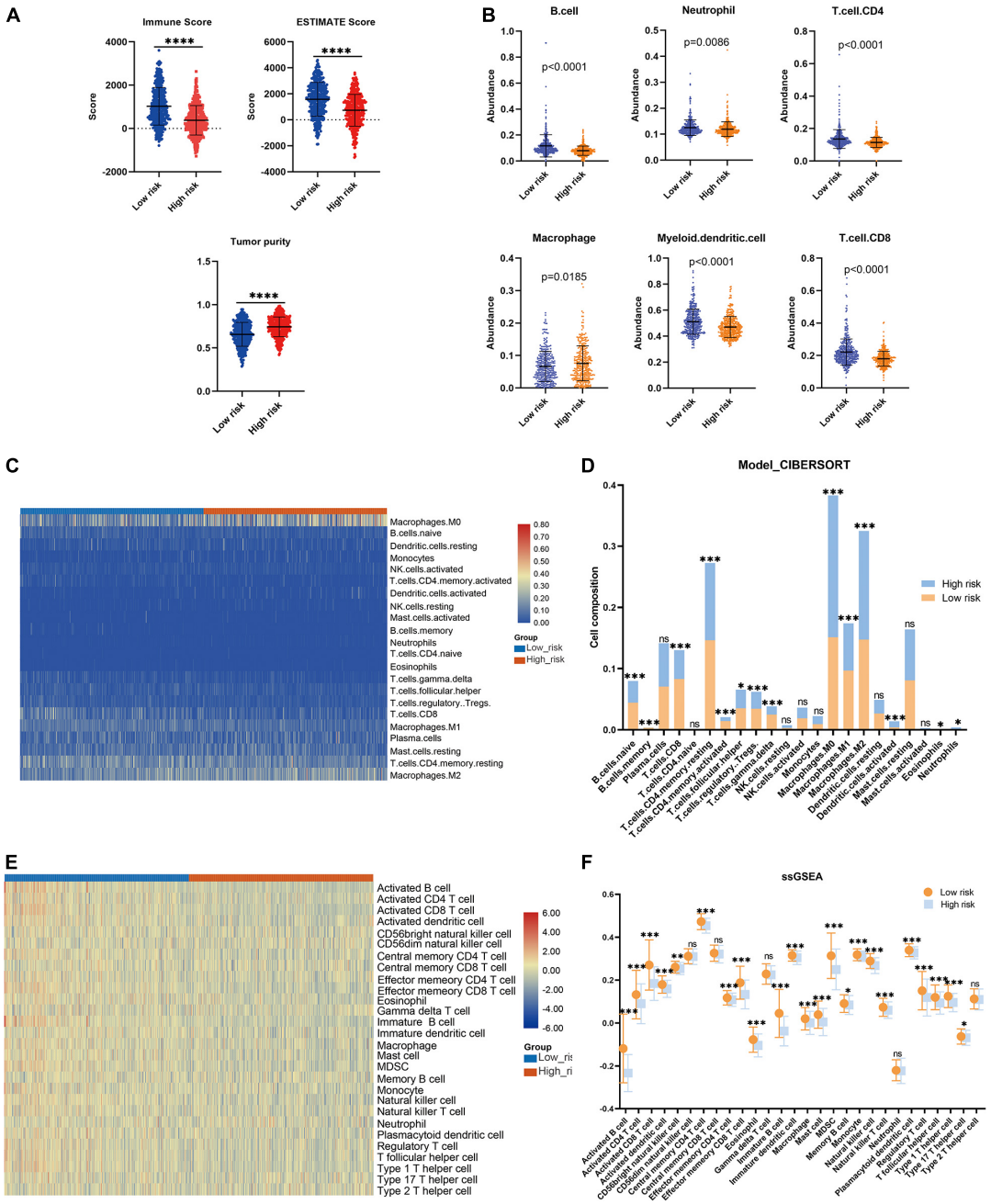

FIGURE 5 | Immune microenvironment landscape in the training cohort. **(A)** ESTIMATE algorithm, **(B)** TIMER algorithm, **(C,D)** CIBERSORT analysis, and ssGSEA analysis **(E,F)**. *$p < 0.05$, **$p < 0.01$, ***$p < 0.001$, ****$p < 0.0001$.

can be calculated according to the total score. The one-year, three-year, and overall survival rates of the patients with BRCA were predicted using the nomogram.

Immune-Related Signaling Pathways May Mediate the Role of LMAGs in BRCA

Finally, to further explore the molecular mechanisms associated with the roles of LMAGs in BRCA, functional analyses were conducted. Eighty DEGs were identified between the high-risk and low-risk groups; the volcano plot is shown in **Figure 9A**. It is worth noting that all of the DEGs were downregulated in the high-risk group compared with the low-risk group. Enrichment analyses revealed that the DEGs were mainly enriched in immune-related signaling pathways (**Figures 9B–D**), suggesting that immunity may mediate the significance of LMAGs in the prognosis of patients with BRCA. GO analysis indicated that the DEGs were mainly

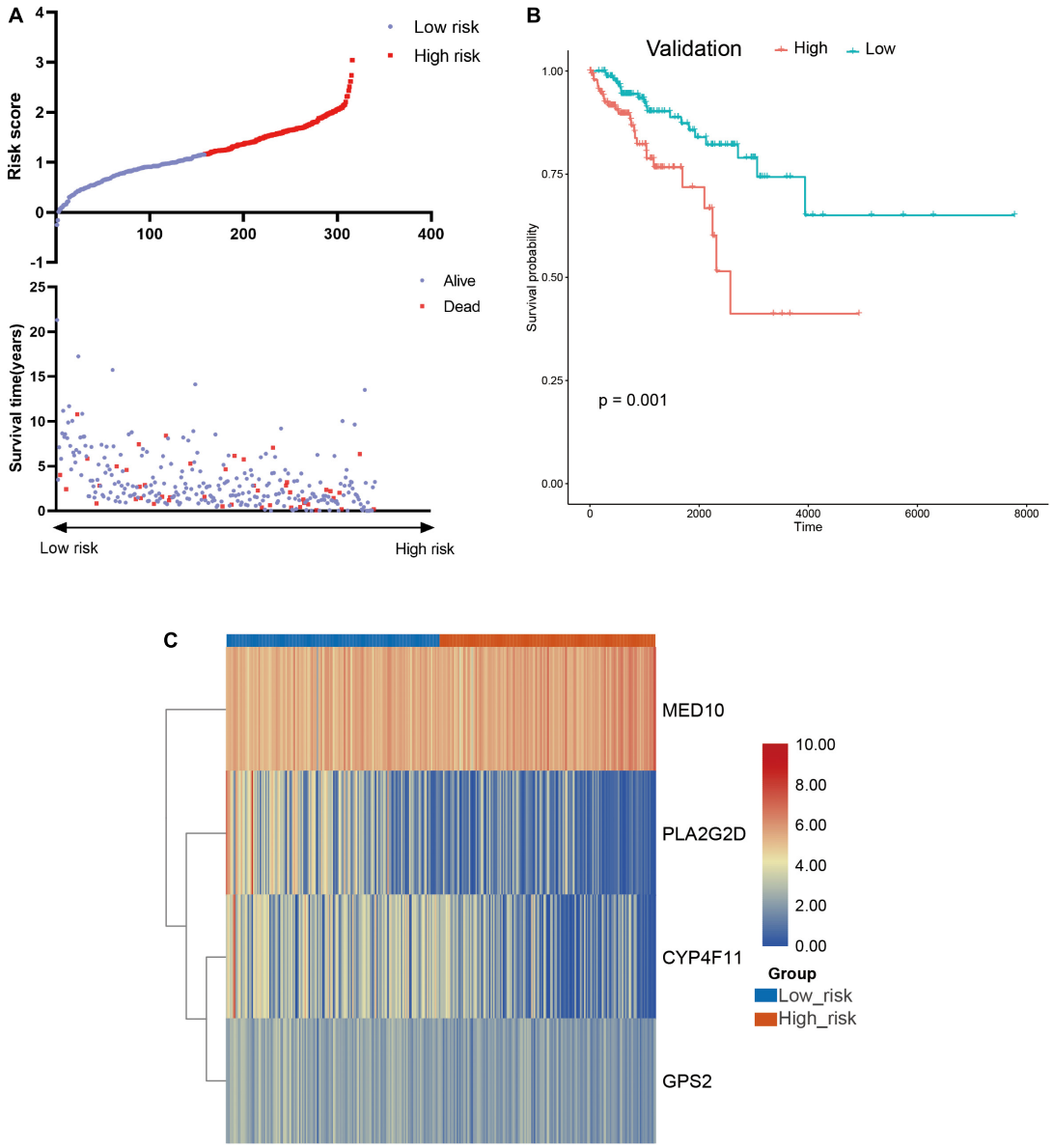

FIGURE 6 | Verification of the risk model in the validation cohort. **(A)** Survival status and risk score in the validation set, **(B)** survival curve showing the survival of the patients in the validation cohort, **(C)** heatmap illustrating the expression of candidate LMAGs in the validation cohort.

enriched in biological processes associated with immune cell activation, differentiation, and adhesion (**Figure 9C**), although they were also enriched in some crucial molecular functions and cellular components (**Supplementary Figure 3**). KEGG analysis demonstrated that the DEGs were enriched in signaling pathways related to immune cell differentiation (**Figure 9D**). Furthermore, GSVA was performed to calculate the activity of the GO terms in each patient with BRCA and the results, visualized in a heatmap (**Figure 9E**), suggest that the activities of immune-related pathways were relatively downregulated in the high-risk group. These findings indicate that immune-related signaling pathways may mediate the role of LMAGs in BRCA.

DISCUSSION

As one of the deadliest malignancies in women, BRCA has always been a serious public health issue and imposes a huge burden on humankind worldwide (Harbeck and Gnant, 2017; Batalha et al., 2021). Although the prognosis has improved significantly with the development of medical technology, the 5-year overall survival of patients with advanced BRCA is still far from satisfactory (Harbeck and Gnant, 2017; Tian et al., 2020). Constructing a risk model is an innovative and applicable way to predict a patient's prognosis, and it provides a valuable supplement for the TNM stage system in patient risk stratification. Considering the significance of lipid metabolism

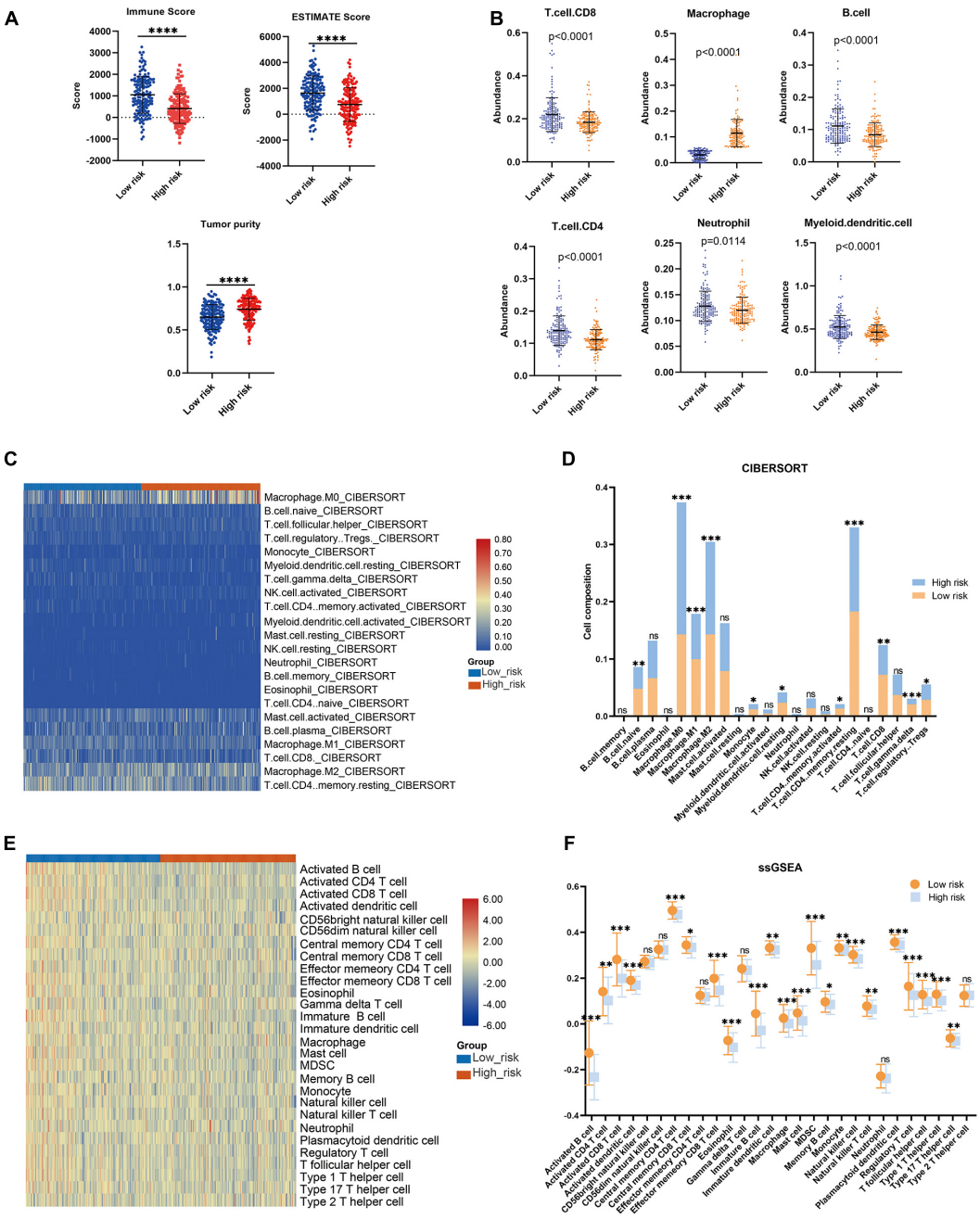

FIGURE 7 | Association between the risk model and immune microenvironment in the validation cohort. **(A)** ESTIMATE algorithm, **(B)** TIMER algorithm, **(C,D)** CIBERSORT analysis, and ssGSEA analysis **(E,F)**. *$p < 0.05$, **$p < 0.01$, ***$p < 0.001$, ****$p < 0.0001$.

in BRCA biology, we developed a prognostic model based on four LMAGs and estimated the effect of LMAGs on the immune microenvironment of patients with BRCA. The results suggest that the LMAG-based risk model possesses potent predictive capacity in the prognosis of patients with BRCA and can indicate the tumor immune microenvironment. Additionally, functional analyses showed that immune-associated signaling pathways mediated the role of LMAGs in BRCA. The results of this work could provide a novel perspective for future BRCA research, optimize risk stratification, promote the development of targeted therapy, and help to improve the prognosis of patients with BRCA.

It has been previously reported that the lipid metabolite 27OHC was a potential risk biomarker for BRCA and can act as a mitogen (Nazih and Bard, 2020). This means that abnormal lipid metabolism plays a pivotal role in the pathogenesis of BRCA. Immune abnormality is also an important risk factor for BRCA. The crosstalk between the immune system and cancer cells will

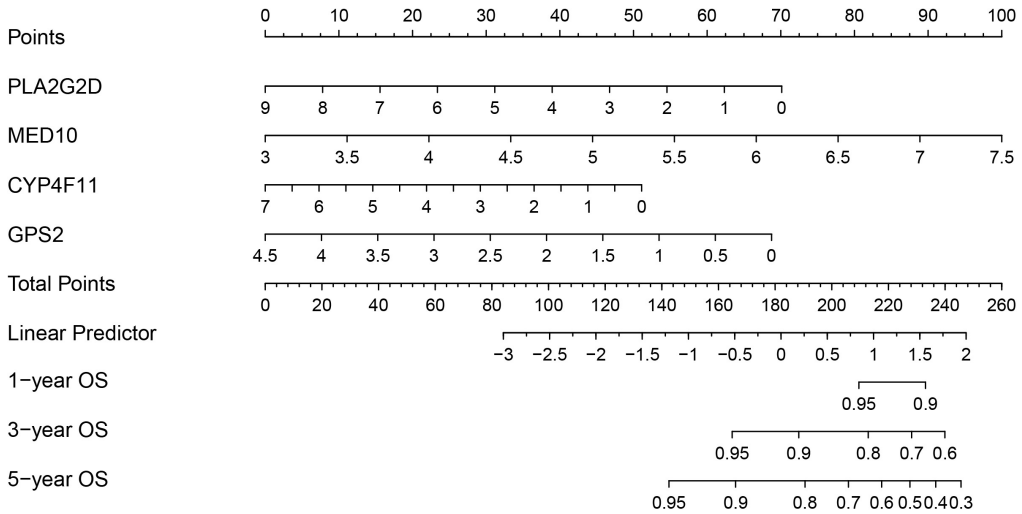

FIGURE 8 | Nomogram based on the prognosis-associated lipid metabolism-associated genes.

change dynamically during the development and treatment of cancer (King et al., 2017).

LMAGs expression predicted the prognosis and was associated with the immune microenvironment of patients with BRCA. Consensus clustering is an acknowledged unsupervised clustering method that can identify new molecular subtypes according to different omics datasets (Wilkerson and Hayes, 2010). In this study, consensus clustering successfully classified the patients with BRCA into two clusters, according to the expression level of prognostic LMAGs. The patients in Cluster 2 had a favorable prognosis, suggesting that LMAG expression is valuable in the prediction of BRCA prognosis. Although further functional analyses were not performed to clarify the inherent associations and molecular cascades of the two newly identified molecular subgroups, the consensus clustering results provide a novel perspective for further research on BRCA.

As the two molecular subtypes are an innovative classification of BRCA, they provide a supplement or substitution for the existing categorization system. It should be noted that the ratio between the two groups was approximately three to one, which was not equal, but is acceptable. In addition, we found statistically significant differences in immune microenvironment between the two subgroups. In particular, better overall survival was correlated with higher immune scores, lower tumor purity, and relatively high immune status, which is consistent with a previous study (Qi et al., 2020). High tumor purity implies shorter survival time and such tumors are more likely to be diagnosed as malignant. Considering that the clustering was conducted based on an LMAG expression matrix, we could reasonably infer that LMAG expression was correlated with the immune microenvironment of patients with BRCA.

Immune cell infiltration into the TM reflects the immune landscape in tumors (Ho et al., 2020). Suppressing anti-tumor immune response is the main mechanism through which cancer cells evade supervision and destruction by the immune system (De Cicco et al., 2020). The functional roles of the various immune cells differ. Usually, CD8 T cells, CD4 T cells, dendritic cells, B cells, and NK cells exert anti-tumor functions, regulatory T cells play a pro-tumor role, and macrophages and monocytes play equivocal roles in the progression of tumor progression (Chimal-Ramírez et al., 2013; Zhang and Zhang, 2020; Batalha et al., 2021). Results of TIMER in clustered and risk model-stratified subgroups are not completely consistent in this study, especially CD8 T cell, which is worth further investigation. We constructed a risk model to estimate and validate the role of LMAGs in the immune microenvironment of BRCA. The established LMAG-based risk model stratified the patients into groups with different prognoses that were correlated with immune infiltration in both the training and validation cohorts. Moreover, model diagnosis using ROC analysis indicated that the risk model is a reliable indicator of prognosis. Overall, these results reveal that the LMAG-based risk model is a well-developed reference for predicting the prognosis of patients with BRCA, and that it is closely related to the tumor immune microenvironment in BRCA.

The constructed risk model in this study was not influenced by other clinical parameters, such as age. In addition to stability, independence is a critical index for an effective prognostic risk model. In this study, the prognosis was correlated with the risk score, and univariable and multivariate regression analyses indicated that the risk model was an independent indicator of BRCA prognosis. To further explore the possibility of interference resulting from other indexes, subgroup analysis was performed to confirm the prognosis-predicting power of the risk model. The results suggest that the risk score remains effective in predicting BRCA prognosis even when the patients are regrouped according to clinical parameters. Unfortunately, subgroup analysis of metastasis could not be conducted, as this factor was limited by sample size. The LMAG-based risk model was independently predictive of prognosis in BRCA.

All the genes in our constructed risk model were related to tumors prognosis. Risk models are an applicable method

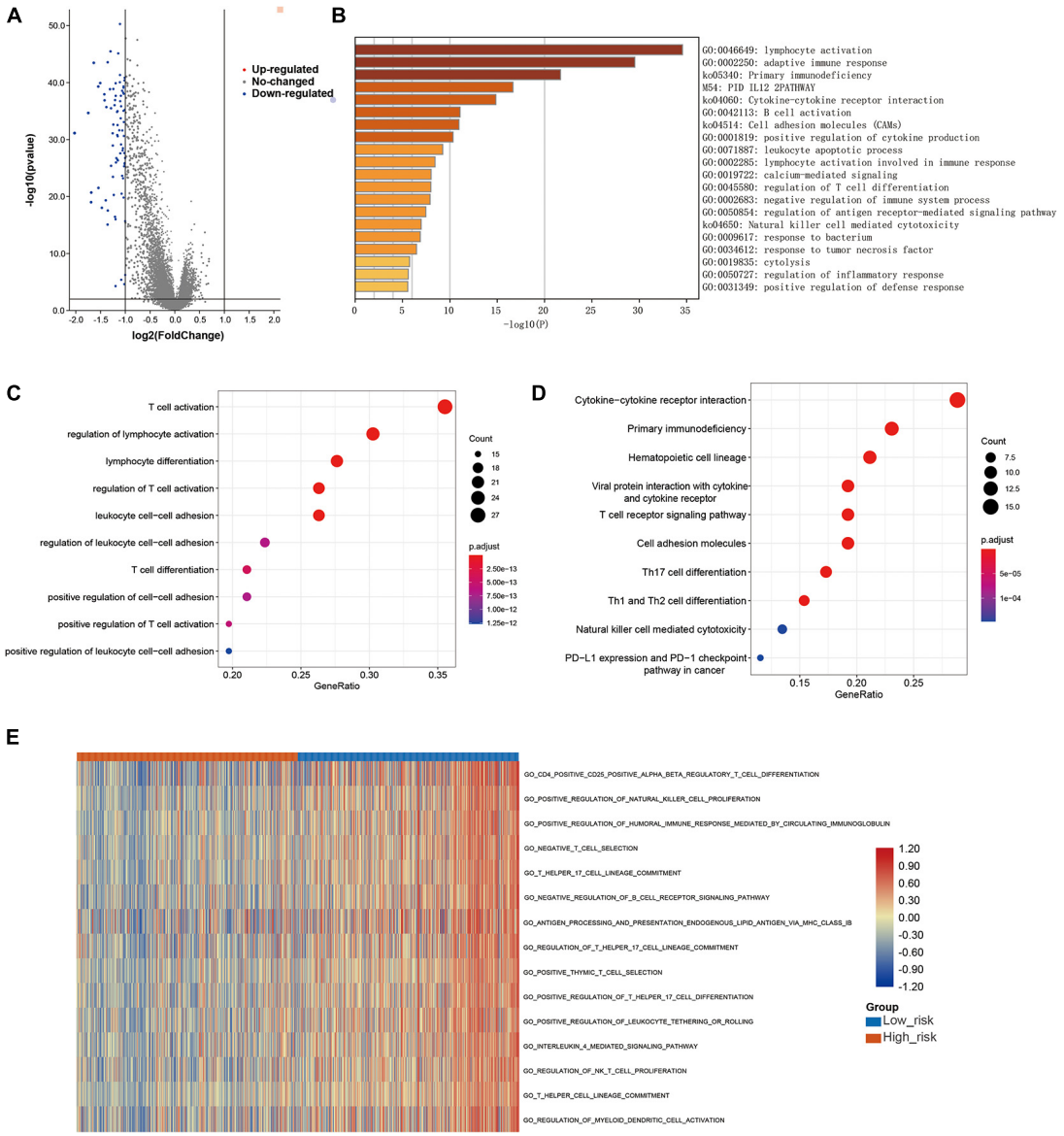

FIGURE 9 | Functional analyses. **(A)** Volcano plot depicting the differentially expressed genes (DEGs) between the two groups, **(B,C)** bubble plot derived from gene ontology (GO) analysis suggesting that the DEGs were mainly enriched in immune-associated biological processes, **(D)** bubble diagram derived from Kyoto Encyclopedia of Genes and Genomes (KEGG) analysis showing that the DEGs were enriched in immune-associated signaling pathways, **(E)** GSVA plots visualizing the result of GSVA analysis.

for developing prognostic molecular biomarkers and have been constructed for a variety of tumors, showing powerful predictive ability (Chen et al., 2021; Lv et al., 2021). Generally, the patients were scored according to candidate-gene expression values and coefficients, and lower scores indicated a favorable prognosis. In the present study, four candidate LMAGs, including one risk gene and three protective genes that have all been demonstrated to be involved in the progression and prognosis of tumors, were selected for the construction of the risk model.

MED10 encodes the mediator of RNA polymerase II transcription subunit 10 (MED10), and previous studies have suggested that *MED10* expression is a risk factor for multiple types of tumors (Xu et al., 2018; Sahar et al., 2019; Wang et al., 2021). Xu et al. (2018) and Wang et al. (2021) demonstrated that *MED10* is a critical prognostic gene in glioblastoma and hepatocellular carcinoma, respectively. The protein level of *MED10* has also been shown to be upregulated in uterine leiomyoma compared to that in the adjacent myometrium (Sahar et al., 2019). In line with the above reports, *MED10* was shown to be detrimental for the prognosis of patients with BRCA, and tended to be expressed in the high-risk group in this study. Phospholipase A2 group IID (PLA2G2D), encoded by *PLA2G2D*, is an immunosuppressor involved in the conversion of lipid balance to an anti-inflammation status,

which can play a detrimental or beneficial role, depending on inflammatory and tumorous context (Miki et al., 2016). A previous study revealed that the expression of *PLA2G2D* was reduced 23-fold in colorectal adenocarcinomas compared to normal tissue (Mounier et al., 2008; Xiong et al., 2021). Xiong et al. (2021) reported that *PLA2G2D* is a prognosis-predicting gene in head and neck squamous cell carcinoma. The cytochrome P450 (CYP) superfamily are the most important microsomal mixed functional oxidases. *CYP4F11* encodes a member of this superfamily, cytochrome P450, family 4, subfamily F, polypeptide 11 (CYP4F11), which catalyzes the formation of stearoyl CoA desaturase inhibitors (Theodoropoulos et al., 2016). The expression of *CYP4F11* has been significantly and independently correlated with survival in esophageal squamous cell carcinoma and colorectal cancer (Alnabulsi et al., 2017; Wu et al., 2018). It is especially worth noting that the gene expression level of *CYP4F11* in BRCA is significantly higher than that in adjacent tissues (Bandala et al., 2012). Finally, *GPS2* encodes G protein suppressor 2 (GPS2), which was identified as a constituent of the silencing mediator of retinoic acid and thyroid hormone receptor corepressor complexes (Cheng and Kao, 2009). *GPS2* has been shown to play a tumor-suppressive role in liposarcoma (Huang et al., 2016) and BRCA (Cheng and Kao, 2009; Chan et al., 2020), and the loss of GPS2 facilitated tumor growth and the proliferation of cancer cells (Chan et al., 2020). These findings indicate that the aberrant expression of the candidate LMAGs is involved in the progression and prognosis of multiple types of tumors, including BRCA; therefore, it was reasonable to integrate them to establish a risk model for risk stratification and prognosis prediction in BRCA.

Immune-associated signaling cascades mediate the significance of LMAGs in BRCA. The GO and KEGG analyses suggested that the DEGs between the high- and low-risk groups were mainly enriched in immune-associated pathways. More specifically, GSVA revealed that patients in the low-risk group had a relatively high immune status. Considering the overall survival of the patients, it was reasonable to deduce that a favorable prognosis correlated with high immune cell infiltration. The patients were classified based on their LMAG expression values; thus, we concluded that the risk model predicted prognosis and indicated the immune microenvironment.

In recent years, increasing numbers of pre-clinical and clinical studies have highlighted the crucial role of metabolism in the clinical and immune responses of patients with cancer (Bleve et al., 2020). Emerging evidence has revealed an intricate interplay between lipid metabolism and immune cell responses in tumors (Chen and Sui, 2021; Xiang and Miao, 2021). The detailed mechanisms can be interpreted in multiple dimensions. As mentioned previously, lipid-metabolic reprogramming is a new hallmark of malignant cancers. It is mostly altered to meet the requirements of nutrients for cellular proliferation, and could impact the state and functions of infiltrating immune cells (Liu W. et al., 2021; Qin and Chen, 2021; Xiang and Miao, 2021). Macrophages can be reprogrammed to promote tumor progression via increased cholesterol efflux (Goossens et al., 2019; Matsushita et al., 2021). Exogenous and endogenous lipid metabolism exerts different functions on T cells (Matsushita et al., 2021). The anti-tumor role of T cells may be enhanced by cholesterol; however, its role is negatively regulated by liver X receptors in the oxysterol-abundant TM (Matsushita et al., 2021). A recent study demonstrated that lipid metabolism reprograming, triggered by the unbalanced lipid metabolism in senescent T cells, prevented the senescence of effector T cells (Liu X. et al., 2021) and enhanced the functional specialization of regulatory T cells in cancers (Lim et al., 2021). Lipid accumulation in the dendritic cells damaged their anti-tumor functions, as the affected cells could not effectively present tumor-associated antigens (Herber et al., 2010). High levels of lipids in the TM can stimulate the generation of myeloid-derived suppressor cells, resulting in significant metabolic and functional rewiring (Al-Khami et al., 2017). Moreover, lipid metabolism is one of the most essential energy sources for various cells in the TM. Competition for lipid-metabolic nutrients between proliferative tumor cells and immune-infiltrating cells greatly influences their metabolic status and drastically modifies their functional phenotypes (Chang et al., 2015; O'Neill et al., 2016; Bleve et al., 2020). Thus, it was not surprising that LMAG expression was associated with the immune microenvironment in BRCA, or that a better prognosis was associated with high immune scores and a high abundance of immune cells. Additionally, some LMAGs are also responsible for immune regulation, exerting immune-suppressing or immune-promoting functions. In particular, *PLA2G2D*, one of the genes used to construct the risk model in this study, is abundantly expressed in the dendritic cells of lymphoid tissues and has anti-inflammatory and immunosuppressive functions (Miki et al., 2016). The expression of these dual-role LMAGs modifies the activity of immune-related pathways, leading to alterations in immune cell function and infiltration. These findings suggest that immune-related pathways mediate the effects of LMAG expression on the immune microenvironment and prognosis of BRCA.

The results of this study demonstrate that the LMAG-based risk model was connected with the tumor immune microenvironment and with prognosis in BRCA. To the best of our knowledge, this is the first study to report the function of LMAGs in the TM and prognosis of BRCA. Our findings provide innovative insights and could be used as a reference for targeted therapy in patients with BRCA.

Strengths and Shortcomings

Several risk-stratification models have been constructed to predict the prognosis of patients with BRCA. However, our study has some unique assets. Above all, this study constructed a prognostic model based on lipid metabolism, which fills the gap of a LMAG-related risk model for predicting BRCA prognosis. Moreover, we not only focused on the predictive performance of LMAGs but also explored the effect of LMAG expression on the tumor immune microenvironment of patients with BRCA. In addition, the molecular mechanisms accounting for the prognostic role of LMAGs in BRCA were preliminarily elucidated and we constructed a nomogram to quantify the influence of each candidate LMAG on the survival of patients with BRCA.

We acknowledge that there are some inevitable limitations to this work. First, our conclusion was drawn based on open datasets, but not on the sequenced data of our cohorts. Second, the results of this study were not further validated using clinical samples or laboratory experiments.

CONCLUSION

In summary, this study comprehensively evaluates the role of LMAGs in the prognosis and immune microenvironment of patients with BRCA and explores the molecular mechanisms involved. The LMAG-based risk model that we constructed successfully predicted the overall survival of patients and indicated the tumor immune microenvironment in BRCA. In addition, our results suggest that immune-associated signaling pathways might mediate the functions of LMAGs in BRCA. Our work provides an innovative perspective for future BRCA research and the development of targeted therapy strategies for patients with BRCA. Further studies are needed to validate the clinical prognostic value of the LMAG-based risk model and to explore the underlying mechanisms.

DATA AVAILABILITY STATEMENT

The datasets presented in this study can be found in online repositories. The names of the repository/repositories and accession number(s) can be found in the article/**Supplementary Material**.

AUTHOR CONTRIBUTIONS

YH conceived the original ideas of this manuscript, reviewed the finished manuscript, and executed supervision throughout the process. ZY and SZ executed the data collection and data analysis. ZY, SZ, ZN, and ZX prepared the manuscript. ZY prepared the tables and figures. All authors contributed to the article and approved the submitted version.

SUPPLEMENTARY MATERIAL

The Supplementary Material for this article can be found online at: https://www.frontiersin.org/articles/10.3389/fcell.2021.691676/full#supplementary-material

REFERENCES

Al-Khami, A. A., Zheng, L., Del Valle, L., Hossain, F., Wyczechowska, D., Zabaleta, J., et al. (2017). Exogenous lipid uptake induces metabolic and functional reprogramming of tumor-associated myeloid-derived suppressor cells. *Oncoimmunology* 6:e1344804.

Alnabulsi, A., Swan, R., Cash, B., Alnabulsi, A., and Murray, G. I. (2017). The differential expression of omega-3 and omega-6 fatty acid metabolising enzymes in colorectal cancer and its prognostic significance. *Br. J. Cancer* 116, 1612–1620.

Bandala, C., Floriano-Sánchez, E., Cárdenas-Rodríguez, N., López-Cruz, J., and Lara-Padilla, E. (2012). RNA expression of cytochrome P450 in Mexican women with breast cancer. *Asian Pacific J. Cancer Prev. APJCP* 13, 2647–2653.

Batalha, S., Ferreira, S., and Brito, C. (2021). The peripheral immune landscape of breast cancer: clinical findings and in vitro models for biomarker discovery. *Cancers* 13:1305. doi: 10.3390/cancers13061305

Bleve, A., Durante, B., Sica, A., and Consonni, F. M. (2020). Lipid metabolism and cancer immunotherapy: immunosuppressive myeloid cells at the crossroad. *Int. J. Mol. Sci.* 21:5845. doi: 10.3390/ijms21165845

Britt, K. L., Cuzick, J., and Phillips, K. A. (2020). Key steps for effective breast cancer prevention. *Nat. Rev. Cancer* 20, 417–436. doi: 10.1038/s41568-020-0266-x

Cao, Y. (2019). Adipocyte and lipid metabolism in cancer drug resistance. *J. Clin. Invest.* 129, 3006–3017. doi: 10.1172/jci127201

Chan, S., Smith, E., Gao, Y., Kwan, J., Blum, B. C., Tilston-Lunel, A. M., et al. (2020). Loss of G-protein pathway suppressor 2 promotes tumor growth through activation of AKT signaling. *Front. Cell Dev. Biol.* 8:608044. doi: 10.3389/fcell.2020.608044

Chang, C. H., Qiu, J., O'Sullivan, D., Buck, M. D., Noguchi, T., Curtis, J. D., et al. (2015). Metabolic competition in the tumor microenvironment is a driver of cancer progression. *Cell* 162, 1229–1241. doi: 10.1016/j.cell.2015.08.016

Chen, C., Chen, H., Zhang, Y., Thomas, H. R., Frank, M. H., He, Y., et al. (2020). TBtools: an integrative toolkit developed for interactive analyses of big biological data. *Mol. Plant* 13, 1194–1202. doi: 10.1016/j.molp.2020.06.009

Chen, L., Zhou, X., Kong, X., Su, Z., Wang, X., Li, S., et al. (2021). The prognostic significance of anisomycin-activated phospho-c-Jun NH2-terminal kinase (p-JNK) in predicting breast cancer patients' survival time. *Front. Cell Dev. Biol.* 9:656693. doi: 10.3389/fcell.2021.656693

Chen, Y., and Sui, M. (2021). Lipid metabolism in tumor-associated natural killer cells. *Adv. Exp. Med. Biol.* 1316, 71–85. doi: 10.1007/978-981-33-6785-2_5

Cheng, C., Geng, F., Cheng, X., and Guo, D. (2018). Lipid metabolism reprogramming and its potential targets in cancer. *Cancer Commun. (Lond. Engl.)* 38:27. doi: 10.1186/s40880-018-0301-4

Cheng, X., and Kao, H. Y. (2009). G protein pathway suppressor 2 (GPS2) is a transcriptional corepressor important for estrogen receptor alpha-mediated transcriptional regulation. *J. Biol. Chem.* 284, 36395–36404. doi: 10.1074/jbc.m109.062109

Chimal-Ramírez, G. K., Espinoza-Sánchez, N. A., and Fuentes-Pananá, E. M. (2013). Protumor activities of the immune response: insights in the mechanisms of immunological shift, oncotraining, and oncopromotion. *J. Oncol.* 2013:835956.

De Cicco, P., Ercolano, G., and Ianaro, A. (2020). The new era of cancer immunotherapy: targeting myeloid-derived suppressor cells to overcome immune evasion. *Front. Immunol.* 11:1680. doi: 10.3389/fimmu.2020.01680

DeSantis, C. E., Ma, J., Gaudet, M. M., Newman, L. A., Miller, K. D., Goding Sauer, A., et al. (2019). Breast cancer statistics, 2019. *CA A Cancer J. Clin.* 69, 438–451.

Goossens, P., Rodriguez-Vita, J., Etzerodt, A., Masse, M., Rastoin, O., Gouirand, V., et al. (2019). Membrane cholesterol efflux drives tumor-associated macrophage reprogramming and tumor progression. *Cell Metab.* 29, 1376–1389.e1374.

Hao, Y., Li, D., Xu, Y., Ouyang, J., Wang, Y., Zhang, Y., et al. (2019). Investigation of lipid metabolism dysregulation and the effects on immune microenvironments in pan-cancer using multiple omics data. *BMC Bioinformatics* 20:195. doi: 10.1186/s12859-019-2734-4

Harbeck, N., and Gnant, M. (2017). Breast cancer. *Lancet (Lond. Engl.)* 389, 1134–1150.

Herber, D. L., Cao, W., Nefedova, Y., Novitskiy, S. V., Nagaraj, S., Tyurin, V. A., et al. (2010). Lipid accumulation and dendritic cell dysfunction in cancer. *Nat. Med.* 16, 880–886.

Ho, W. J., Jaffee, E. M., and Zheng, L. (2020). The tumour microenvironment in pancreatic cancer - clinical challenges and opportunities. *Nat. Rev. Clin. Oncol.* 17, 527–540. doi: 10.1038/s41571-020-0363-5

Huang, X. D., Xiao, F. J., Wang, S. X., Yin, R. H., Lu, C. R., Li, Q. F., et al. (2016). G protein pathway suppressor 2 (GPS2) acts as a tumor suppressor in liposarcoma. *Tumour Biol.* 37, 13333–13343. doi: 10.1007/s13277-016-5220-x

Iwamoto, H., Abe, M., Yang, Y., Cui, D., Seki, T., Nakamura, M., et al. (2018). Cancer lipid metabolism confers antiangiogenic drug resistance. *Cell Metab.* 28, 104–117.e105.

King, J., Mir, H., and Singh, S. (2017). Association of cytokines and chemokines in pathogenesis of breast cancer. *Prog. Mol. Biol. Transl. Sci.* 151, 113–136. doi: 10.1016/bs.pmbts.2017.07.003

Lei, X., Lei, Y., Li, J. K., Du, W. X., Li, R. G., Yang, J., et al. (2020). Immune cells within the tumor microenvironment: biological functions and roles in cancer immunotherapy. *Cancer Lett.* 470, 126–133. doi: 10.1016/j.canlet.2019.11.009

Li, J., Li, Q., Su, Z., Sun, Q., Zhao, Y., Feng, T., et al. (2020). Lipid metabolism gene-wide profile and survival signature of lung adenocarcinoma. *Lipids Health Dis.* 19:222.

Li, T., Fan, J., Wang, B., Traugh, N., Chen, Q., Liu, J. S., et al. (2017). TIMER: a web server for comprehensive analysis of tumor-infiltrating immune cells. *Cancer Res.* 77, e108–e110.

Lim, S. A., Wei, J., Nguyen, T. M., Shi, H., Su, W., Palacios, G., et al. (2021). Lipid signalling enforces functional specialization of T(reg) cells in tumours. *Nature* 591, 306–311. doi: 10.1038/s41586-021-03235-6

Liu, Q., Luo, Q., Halim, A., and Song, G. (2017). Targeting lipid metabolism of cancer cells: a promising therapeutic strategy for cancer. *Cancer Lett.* 401, 39–45. doi: 10.1016/j.canlet.2017.05.002

Liu, W., Song, H., Li, X., Ren, D., Ding, S., and Li, Y. (2021). Lipid metabolism in tumor-associated myeloid-derived suppressor cells. *Adv. Exp. Med. Biol.* 1316, 103–115. doi: 10.1007/978-981-33-6785-2_7

Liu, X., Hartman, C. L., Li, L., Albert, C. J., Si, F., Gao, A., et al. (2021). Reprogramming lipid metabolism prevents effector T cell senescence and enhances tumor immunotherapy. *Sci. Transl. Med.* 13:eaaz6314. doi: 10.1126/scitranslmed.aaz6314

Locy, H., de Mey, S., de Mey, W., De Ridder, M., Thielemans, K., and Maenhout, S. K. (2018). Immunomodulation of the tumor microenvironment: turn foe into friend. *Front. Immunol.* 9:2909. doi: 10.3389/fimmu.2018.02909

Luo, X., Cheng, C., Tan, Z., Li, N., Tang, M., Yang, L., et al. (2017). Emerging roles of lipid metabolism in cancer metastasis. *Mol. Cancer* 16:76.

Lv, D., Wu, X., Wang, M., Chen, W., Yang, S., Liu, Y., et al. (2021). Functional assessment of four novel immune-related biomarkers in the pathogenesis of clear cell renal cell carcinoma. *Front. Cell Dev. Biol.* 9:621618. doi: 10.3389/fcell.2021.621618

Maan, M., Peters, J. M., Dutta, M., and Patterson, A. D. (2018). Lipid metabolism and lipophagy in cancer. *Biochem. Biophys. Res. Commun.* 504, 582–589. doi: 10.1016/j.bbrc.2018.02.097

Matsushita, Y., Nakagawa, H., and Koike, K. (2021). Lipid metabolism in oncology: why it matters, how to research, and how to treat. *Cancers* 13:474. doi: 10.3390/cancers13030474

Miki, Y., Kidoguchi, Y., Sato, M., Taketomi, Y., Taya, C., Muramatsu, K., et al. (2016). Dual roles of group IID phospholipase A2 in inflammation and cancer. *J. Biol. Chem.* 291, 15588–15601. doi: 10.1074/jbc.m116.734624

Mounier, C. M., Wendum, D., Greenspan, E., Fléjou, J. F., Rosenberg, D. W., and Lambeau, G. (2008). Distinct expression pattern of the full set of secreted phospholipases A2 in human colorectal adenocarcinomas: sPLA2-III as a biomarker candidate. *Br. J. Cancer* 98, 587–595. doi: 10.1038/sj.bjc.6604184

Nazih, H., and Bard, J. M. (2020). Cholesterol, oxysterols and LXRs in breast cancer pathophysiology. *Int. J. Mol. Sci.* 21:1356. doi: 10.3390/ijms21041356

O'Neill, L. A., Kishton, R. J., and Rathmell, J. (2016). A guide to immunometabolism for immunologists. *Nat. Rev. Immunol.* 16, 553–565. doi: 10.1038/nri.2016.70

Pitt, J. M., Marabelle, A., Eggermont, A., Soria, J. C., Kroemer, G., and Zitvogel, L. (2016). Targeting the tumor microenvironment: removing obstruction to anticancer immune responses and immunotherapy. *Ann. Oncol.* 27, 1482–1492. doi: 10.1093/annonc/mdw168

Qi, J., Liu, Y., Hu, J., Lu, L., Dou, Z., Dai, H., et al. (2020). Identification of FPR3 as a unique biomarker for targeted therapy in the immune microenvironment of breast cancer. *Front. Pharmacol.* 11:593247. doi: 10.3389/fphar.2020.593247

Qin, H., and Chen, Y. (2021). Lipid metabolism and tumor antigen presentation. *Adv. Exp. Med. Biol.* 1316, 169–189. doi: 10.1007/978-981-33-6785-2_11

Sahar, T., Nigam, A., Anjum, S., Waziri, F., Biswas, S., Jain, S. K., et al. (2019). Interactome analysis of the differentially expressed proteins in uterine leiomyoma. *Anticancer Agents Med. Chem.* 19, 1293–1312. doi: 10.2174/1871520619666190206143523

Siegel, R. L., Miller, K. D., and Jemal, A. (2019). Cancer statistics, 2019. *CA A Cancer J. Clin.* 69, 7–34.

Theodoropoulos, P. C., Gonzales, S. S., Winterton, S. E., Rodriguez-Navas, C., McKnight, J. S., Morlock, L. K., et al. (2016). Discovery of tumor-specific irreversible inhibitors of stearoyl CoA desaturase. *Nat. Chem. Biol.* 12, 218–225.

Tian, Z., Tang, J., Liao, X., Yang, Q., Wu, Y., and Wu, G. (2020). Identification of a 9-gene prognostic signature for breast cancer. *Cancer Med.* 9, 9471–9484. doi: 10.1002/cam4.3523

Visweswaran, M., Arfuso, F., Warrier, S., and Dharmarajan, A. (2020). Aberrant lipid metabolism as an emerging therapeutic strategy to target cancer stem cells. *Stem Cells (Dayton, Ohio)* 38, 6–14. doi: 10.1002/stem.3101

Waks, A. G., and Winer, E. P. (2019). Breast cancer treatment: a review. *JAMA* 321, 288–300.

Wang, W., Zhang, C., Yu, Q., Zheng, X., Yin, C., Yan, X., et al. (2021). Development of a novel lipid metabolism-based risk score model in hepatocellular carcinoma patients. *BMC Gastroenterol.* 21:68. doi: 10.1186/s12876-021-01638-3

Wilkerson, M. D., and Hayes, D. N. (2010). ConsensusClusterPlus: a class discovery tool with confidence assessments and item tracking. *Bioinformatics (Oxf. Engl.)* 26, 1572–1573. doi: 10.1093/bioinformatics/btq170

Wu, B., Bai, C., Du, Z., Zou, H., Wu, J., Xie, W., et al. (2018). The arachidonic acid metabolism protein-protein interaction network and its expression pattern in esophageal diseases. *Am. J. Transl. Res.* 10, 907–924.

Wu, P., Gao, W., Su, M., Nice, E. C., Zhang, W., Lin, J., et al. (2021). Adaptive mechanisms of tumor therapy resistance driven by tumor microenvironment. *Front. Cell Dev. Biol.* 9:641469. doi: 10.3389/fcell.2021.641469

Xiang, Y., and Miao, H. (2021). Lipid metabolism in tumor-associated macrophages. *Adv. Exp. Med. Biol.* 1316, 87–101. doi: 10.1007/978-981-33-6785-2_6

Xiong, Y., Si, Y., Feng, Y., Zhuo, S., Cui, B., and Zhang, Z. (2021). Prognostic value of lipid metabolism-related genes in head and neck squamous cell carcinoma. *Immun. Inflamm. Dis.* 9, 196–209. doi: 10.1002/iid3.379

Xu, P., Yang, J., Liu, J., Yang, X., Liao, J., Yuan, F., et al. (2018). Identification of glioblastoma gene prognosis modules based on weighted gene co-expression network analysis. *BMC Med. Genomics* 11:96. doi: 10.1186/s12920-018-0407-1

Ye, Y., Chen, Z., Shen, Y., Qin, Y., and Wang, H. (2021). Development and validation of a four-lipid metabolism gene signature for diagnosis of pancreatic cancer. *FEBS Open Bio* doi: 10.1002/2211-5463.13074

Yoshihara, K., Shahmoradgoli, M., Martínez, E., Vegesna, R., Kim, H., Torres-Garcia, W., et al. (2013). Inferring tumour purity and stromal and immune cell admixture from expression data. *Nat. Commun.* 4, 2612.

Yu, F., Quan, F., Xu, J., Zhang, Y., Xie, Y., Zhang, J., et al. (2019). Breast cancer prognosis signature: linking risk stratification to disease subtypes. *Brief. Bioinform.* 20, 2130–2140. doi: 10.1093/bib/bby073

Zhang, M., Wang, Y., Wang, Y., Jiang, L., Li, X., Gao, H., et al. (2020). Integrative analysis of DNA methylation and gene expression to determine specific diagnostic biomarkers and prognostic biomarkers of breast cancer. *Front. Cell Dev. Biol.* 8:529386. doi: 10.3389/fcell.2020.529386

Zhang, Y., and Zhang, Z. (2020). The history and advances in cancer immunotherapy: understanding the characteristics of tumor-infiltrating immune cells and their therapeutic implications. *Cell. Mol. Immunol.* 17, 807–821. doi: 10.1038/s41423-020-0488-6

Zhao, E., Lan, Y., Quan, F., Zhu, X., Suru, A., Wan, L., et al. (2020). Identification of a Six-lncRNA signature with prognostic value for breast cancer patients. *Front. Genet.* 11:673. doi: 10.3389/fgene.2020.00673

Zheng, M., Mullikin, H., Hester, A., Czogalla, B., Heidegger, H., Vilsmaier, T., et al. (2020). Development and validation of a Novel 11-gene prognostic model for serous ovarian carcinomas based on lipid metabolism expression profile. *Int. J. Mol. Sci.* 21:9169. doi: 10.3390/ijms21239169

Conflict of Interest: The authors declare that the research was conducted in the absence of any commercial or financial relationships that could be construed as a potential conflict of interest.

frontiers in Cell and Developmental Biology

ORIGINAL RESEARCH
published: 25 June 2021
doi: 10.3389/fcell.2021.678967

SMARCC1 Suppresses Tumor Progression by Inhibiting the PI3K/AKT Signaling Pathway in Prostate Cancer

Zhao-Ming Xiao[1†], Dao-Jun Lv[2†], Yu-zhong Yu[1], Chong Wang[1], Tao Xie[1], Tao Wang[1], Xian-Lu Song[3] and Shan-Chao Zhao[1,4]*

[1] Department of Urology, Nanfang Hospital, Southern Medical University, Guangzhou, China, [2] Guangdong Key Laboratory of Urology, Department of Urology, Minimally Invasive Surgery Center, The First Affiliated Hospital of Guangzhou Medical University, Guangzhou, China, [3] Department of Radiotherapy, Affiliated Cancer Hospital and Institute of Guangzhou Medical University, Guangzhou, China, [4] Department of Urology, The Third Affiliated Hospital, Southern Medical University, Guangzhou, China

Background: SWI/SNF-related, matrix-associated, actin-dependent regulator of chromatin subfamily C member 1 (*SMARCC1*) protein is a potential tumor suppressor in various cancers. However, its role in prostate cancer (PCa) remains controversial. The aim of this study was to determine the biological function of *SMARCC1* in PCa and explore the underlying regulatory mechanisms.

Methods: The expression of *SMARCC1* was validated in PCa tissues by immunohistochemistry. Meanwhile, function experiments were used to evaluate the regulatory role on cell proliferation and metastasis in PCa cells with *SMARCC1* depletion both *in vitro* and *in vivo*. The expression levels of relevant proteins were detected by Western blotting.

Results: Our finding showed that *SMARCC1* was significantly downregulated in prostate adenocarcinoma, with a higher Gleason score (GS) than that in low GS. The decreased expression of *SMARCC1* was significantly correlated with a higher GS and poor prognosis. Additionally, we found that silencing of *SMARCC1* dramatically accelerated cell proliferation by promoting cell cycle progression and enhancing cell migration by inducing epithelial mesenchymal transition (EMT). Furthermore, depletion of *SMARCC1* facilitated PCa xenograft growth and lung metastasis in murine models. Mechanistically, the loss of *SMARCC1* activated the *PI3K/AKT* pathway in PCa cells.

Conclusion: *SMARCC1* suppresses PCa cell proliferation and metastasis *via* the *PI3K/AKT* signaling pathway and is a novel therapeutic target.

Keywords: *SMARCC1*, prostate cancer, proliferation, epithelial-mesenchymal-transition, *PI3K/AKT* pathway

OPEN ACCESS

Edited by:
Yongbin Chen,
Kunming Institute of Zoology (CAS), China

Reviewed by:
Huiqing Wang,
Second Military Medical University, China
Zhifeng Liu,
General Hospital of Guangzhou Military Command, China
Zhijie Li,
Jinan University, China

****Correspondence:***
Shan-Chao Zhao
lulululu@smu.edu.cn

[†] These authors have contributed equally to this work and share first authorship

Specialty section:
This article was submitted to Molecular and Cellular Oncology, a section of the journal Frontiers in Cell and Developmental Biology

Received: *10 March 2021*
Accepted: *16 April 2021*
Published: *25 June 2021*

Citation:
Xiao Z-M, Lv D-J, Yu Y-z, Wang C, Xie T, Wang T, Song X-L and Zhao S-C (2021) SMARCC1 Suppresses Tumor Progression by Inhibiting the PI3K/AKT Signaling Pathway in Prostate Cancer. Front. Cell Dev. Biol. 9:678967. doi: 10.3389/fcell.2021.678967

INTRODUCTION

Prostate cancer (PCa) is a common malignancy afflicting elderly males, with over 1.6 million men diagnosed every year (Pernar et al., 2018; Siegel et al., 2021). In America, the morbidity rate of PCa has ranked first in all cancer-related deaths (Siegel et al., 2021). Globally, it is estimated that 366,000 men die of PCa annually, making it the fifth most common cause of cancer-related deaths worldwide (Pernar et al., 2018; Siegel et al., 2021). Multiple mutations in several key epigenetic factors, including Rb1 and BRCA, drive the progression of PCa to aggressive phenotype at terminal stage, characterized by limited survival, revealing an important role of epigenetic dysregulation on PCa progression (Crea et al., 2011; Liu, 2016; Chan et al., 2018; Sheahan and Ellis, 2018; Oh et al., 2019; Wu et al., 2019; Ge et al., 2020; Liang et al., 2020). However, the specific function and profound mechanisms of various epigenetic factors involved in PCa progression are still uncertain. Thus, it is extremely urgent and worthwhile to further explore the role and mechanisms of epigenetic regulators in PCa progression.

The *SWI/SNF*-related, matrix-associated, actin-dependent regulator of chromatin subfamily C member 1 (*SMARCC1*) is one of the core subunits of the SWI/SNF complex involved in epigenetic regulation on genome transcription (Reisman et al., 2009; Shain and Pollack, 2013; Hohmann and Vakoc, 2014; Alver et al., 2017; Lu and Allis, 2017; Savas and Skardasi, 2018). It is regarded as a tumor suppressor in several cancers, including renal, colon, and pancreatic carcinoma (Andersen et al., 2009; Iwagami et al., 2013; Wang et al., 2021). However, its role in PCa remains ambiguous and controversial. Previous studies have shown that *SMARCC1* is upregulated in PCa tissue and may promote the initiation and progression in PCa *via* the transactivating androgen receptor (Hong et al., 2005; Heebøll et al., 2008), whereas a retrospective study on patients with local PCa indicated that *SMARCC1* positive staining in the prostate biopsy samples correlated with prolonged survival, which is indicative of a tumor-suppressive role in PCa (Hansen et al., 2011). These discrepancies may be partly attributed to different cancer models and expression systems.

In this study, we aimed to explore the role of *SMARCC1* in the proliferation and metastasis of PCa by using a series of *in vitro* functional assays and *in vivo* mouse model due to lack of conclusive research on the mechanism of SMRCC1 during PCa progression. Moreover, the potential mechanism by which *SMARCC1* mediates the development and progression of PCa was also investigated.

Abbreviations: PCa, prostate cancer; *SMARCC1*, SWI/SNF-related, matrix-associated, actin-dependent regulator of chromatin subfamily C member 1; BPH, benign prostatic hyperplasia; GS, Gleason score; SWI/SNF complex, Switch/sucrose non-fermentable complex; H&E staining, hematoxylin and eosin staining; PSB, phosphate buffer solution; siRNA, small interference RNA; shRNA, short hairpin RNA; MOI, multiplicity of infection, qRT-PCR, quantitative real-time polymerase chain reaction; cDNA, complementary DNA; GAPDH, glyceraldehyde-3 phosphate dehydrogenase; RIPA, radio-immunoprecipitation assays; PMSF, phenylmethylsulfonyl fluoride solution; SDS-PAGE, sodium dodecyl sulfate polyacrylamide gel electrophoresis; PVDF, polyvinylidene fluoride; HRP, horseradish peroxidase; DMSO, dimethyl sulfoxide; SEM, standard error of mean; CDK, cyclin-dependent kinase; CKI, cyclin-dependent kinase inhibitor; EMT, epithelial to mesenchymal transition; MMP2, matrix metalloproteinase 2; PBST, PBS-tween solution; PI3K/AKT, phosphatidylinositol 3 kinase/protein kinase B; Rb1, retinoblastoma-associated protein 1; BRCA, breast cancer susceptibility gene; ATPase, adenosine triphosphatase.

MATERIALS AND METHODS

Prostate Cancer Tissues

Tumor and matched benign prostatic hyperplasia tissue samples were collected from 100 PCa patients who received radical prostatectomy for prostate cancer at Nanfang Hospital, Southern Medical University (Guangzhou, China). The PCa patients were enrolled in our research project according to the following standards: (1) the patients were diagnosed with PCa before surgery, in accordance with biopsy pathological diagnosis, (2) post-operation pathological examination confirmed the diagnosis of PCa, and (3) the patients were informed and consented to the collection of specimens. Meanwhile, some PCa patients were excluded from our research cohort due to the following criteria: (1) patients with other malignant diseases or a second primary tumor, (2) PCa patients who received preoperative androgen deprivation therapy, chemotherapy, or radiotherapy before surgery, and (3) HIV- or syphilis-positive patients. The relevant clinicopathological data of the patients was also obtained. All patients signed the informed consent, and sample collection was approved by the ethical protocols of the Ethics Committee of Nanfang Hospital, Southern Medical University.

Immunohistochemistry

The paraffin sections were dewaxed in xylene, rehydrated through an ethanol gradient, and washed in phosphate buffer saline (PBS). After boiling in 10 mM citrate buffer (pH 6) for 10 min for antigen retrieval, the sections were immersed in 3% H_2O_2 for 10 min to inhibit endogenous peroxidase. The sections were then blocked with 1% goat serum and incubated overnight with primary antibodies against *SMARCC1* (1:800; Abcam, cat. ab126180, United States), E-Cadherin (1:100; CST, cat. 24E10, United States), *Claudin1* (1:100; CST, cat. 13255T, United States), MMP2 (1:50; HuaBio, cat. ER40806, China), *P504S* (1:100; Proteintech, cat. 15918-1-AP, China), and *Ki67* (1:100; Biossci, cat. BA1063, China) at 4°C. After washing thrice with PBS, the sections were then probed with the secondary antibody for 1 h and rinsed three times with PBS. The DAB Kit (Biossci, cat. BP0770, China) was used for immunostaining, and the nucleus was counterstained with hematoxylin. The sections were then dehydrated through an ethanol gradient and sealed with neutral balsam. The stained sections were observed under a light microscope (BX53, Olympus, Japan) fitted with a digital camera (DP72, Olympus, Japan). The *in situ SMARCC1* expression level was analyzed independently by two pathologists blinded to the patients' clinical information. The staining intensity was scored as negative (0), weak (1), medium (2), or strong (3), and the percentage of positively stained area was scored as 0 (0%), 1 (1–25%), 2 (26–50%), 3 (51–75%), and 4 (76–100%). The total staining score was calculated by multiplying the intensity and positivity scores, and the samples were graded as low (0–5), medium (6–8), and high (9–12) expression accordingly. In addition, low staining intensity in tissue was classified as

negative, while both medium and high staining intensity were classified as positive.

Bioinformatics Analyses

The disease-free survival data was extracted from the Gene Expression Profiling Interactive Analysis (GEPIA) database[1] and analyzed using R. The cutoff was set as 30% high vs. 70% low.

Cell Culture

RWPE-1, LNCAP, C4-2, PC3, 22RV1, and DU145 cell lines were obtained from the Cell Bank of Typical Culture Preservation Committee of the Chinese Academy of Sciences (Shanghai, China). The RWPE-1 cells were cultured in primary keratinocyte culture medium (iCell Bioscience Inc., cat. PriMed-iCell-010, China), and the other cell lines were cultured in RPMI 1640 (Gibco, cat. 11875-093, United States) supplemented with 10% fetal bovine serum (FBS; Gibco, cat. 10270-106, United States) and 1% penicillin–streptomycin solution (Gibco, 15140-122, United States) at 37°C under 5% CO_2. As per experimental requirements, the cells were treated with 20 ng/ml LY294002 (Macklin, cat. HY-10108, China) in dimethyl sulfoxide for 24 h (Bao et al., 2015).

SMARCC1 Knockdown

The cells were seeded in six-well plates at a density of 0.5×10^6 cells/well and transfected 24 h later with *SMARCC1* siRNA using Lipofectamine 3000 (Invitrogen, United States). The cells were harvested 48 h after transfection, and *SMARCC1* mRNA and protein levels were analyzed by quantitative real-time polymerase chain reaction (qRT-PCR) and western blotting. The lentivirus vector containing the *SMARCC1* shRNA was synthesized by Vigene Biosciences Inc. (China). Briefly, 0.5×10^6 cells were plated in six-well plates and infected 24 h later with the virus at a multiplicity of infection (MOI) of 30 in serum-free medium. Fresh complete medium containing 2 μg/ml puromycin was added 48 h after transfection, and the cells were cultured for 4 days. The sh-*SMARCC1* cell lines with stable knockdown were detected by qRT-PCR and western blotting. siRNA targeted to *SMARCC1*: 5′-CCUCACAAGACGAUGAAGATT-3′ 5′-UCUUCAUCGUCUUGUGAGGTT-3′ was synthesized in GenePharma Co., Ltd (Suzhou, CHINA) and sh RNA contained in lentivirus vectors was designed according to siRNA sequence.

RNA Extraction and qRT-PCR

RNA was extracted using Trizol reagent (Invitrogen, cat. 15596018, United States) and reverse-transcribed to cDNA using PrimeScript RT Master Mix Kit (Takara, cat. RR036A, Japan) according to the manufacturer's instructions. The cDNA was amplified with the PrimeScript™ RT-PCR Kit (Takara, cat. DRR015A, Japan) on Applied Biosystems™ 7500 fast Dx real-time PCR cycler (Thermofisher, United States) according to the manufacturer's protocol. GAPDH was used as the internal control, and relative expression levels were calculated by the $2^{-\Delta\Delta CT}$ method. Primer sequence was obtained from website primerbank (https://pga.mgh.harvard.edu/primerbank/) and shown as following: *SMARCC1* (Forward sequence: 5′-AGCTGTTTATCGACGGAAGGA-3′; Reverse sequence: 5′-GCATCCGCATGAACATACTTCTT-3′); GAPDH (Forward sequence: 5′-GGAGCGAGATCCCTCCAAAAT-3′; Reverse sequence: 5′-GGCTGTTGTCATACTTCTCATGG-3′).

[1]http://gepia.cancer-pku.cn/

Protein Extraction and Western Blotting

The suitably treated cells were homogenized in radioimmunoprecipitation assay (RIPA) buffer supplemented with phenylmethylsulfonyl fluoride (KGP250, KeyGEN BioTECH, Nanjing, China) at the ratio of 1,000:1, along with protease inhibitor (Mecklin, cat. P885281, China) and phosphatase inhibitor (FDbio, cat. FD7186, China), each at 100:1 ratio. The cells were lysed by ultrasonication for 20 min and centrifuged at 12,000 rpm for 5 min at 4°C. The nuclear and cytoplasmic proteins were fractionated using the nucleus extraction kit (Pythonbio, cat. AAPR285, Guangzhou, China). Briefly, 1×10^7 of cells were lysed using a specific buffer at 4°C for 20 min and centrifuged for 5 min. The cytoplasmic fraction was removed, and the nuclear fraction was washed thrice with PBS. Protein was extracted from both fractions using RIPA buffer as described above. The respective supernatants were aspirated, mixed with × 5 loading buffer (FDbio, cat. FD0006, China) at a ratio of 1:4, and denatured by boiling. An equal amount of protein per sample was separated by 10% sodium dodecyl sulfate polyacrylamide gel electrophoresis and transferred to polyvinylidene fluoride membrane (Millpore, cat. MB0323, United States). After blocking with 10% milk or bovine serum (for phosphorylated proteins), the membranes were incubated overnight with primary antibodies specific for *SMARCC1* (1:500; CST, cat. D7F83, United States), *Cyclin D1* (1:500; CST, cat. 92G2, United States), *Cyclin E1* (1:500; CST, cat. HE12, United States), *CDK6* (1:500; CST, cat. DSC83, United States), *p21* (1:500; CST, cat. 12D1, United States), *p27* (CST, cat. D96C12, United States), *E-Cadherin* (1:500; CST, cat. 24E10/4A2, United States), *N-Cadherin* (1:500; CST, cat. D4R1H, United States), *Vimentin* (1:500; CST, cat. D21H3, United States), β-*catenin* (1:500; CST, cat. D10A8, United States), *Snail* (1:500; CST, cat. C15D3, United States), *Slug* (1:500; CST, cat. C19G7, United States), *Zeb1* (1:500; CST, cat. D80D3, United States), *Zeb2* (1:500; ABclone, cat. A5705, CHINA), *Akt* (1:500; CST, C67E7, United States), *p-Ak*^{Ser473} (1:500; CST, cat. D9E, United States), *p-Akt*^{Thr308} (1:500; CST, cat. D25E6, United States), *GAPDH* (1:1,000; Proteintech, cat. 104941-AP, China; CST, cat. D4C6R, United States), and *H3* (1:500; Bioss, cat. bs-0349R, China) at 4°C. Total and cytoplasmatic proteins were normalized to GAPDH, and nuclear protein was normalized to histone *H3*. PVDF membranes were washed with PBS-tween solution (PBST) and incubated with horseradish peroxidase-conjugated secondary antibody for 1 h. After washing thrice with PBS, the positive bands were detected by FDbio-Dura enhanced chemiluminescence kit (FDbio, cat. FD8020, China).

Cell Viability Assay

The cells were seeded in 96-well plates at a density of 1,000 cells/well in triplicates, and viability was measured using the Cell Counting Kit 8 (Dojindo, cat. CK04, Japan) according to the manufacturer's instructions. The absorption at

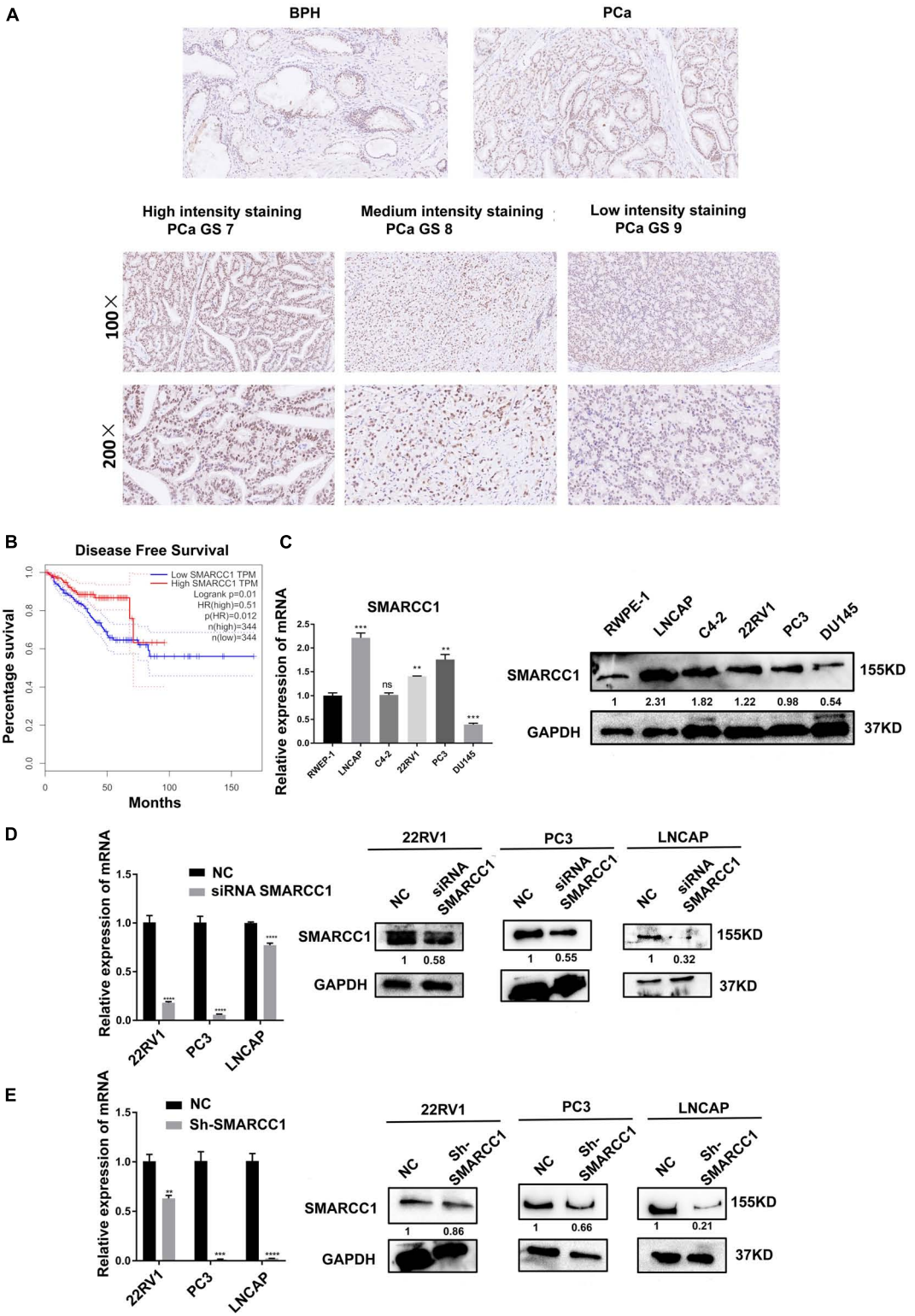

FIGURE 1 | *SMARCC1* is downregulated in PCa tissues and correlates with poor prognosis. **(A)** Representative images of BPH and PCa tissues with Gleason score 7, 8, and 9 showing *in situ SMARCC1* expression (magnification, ×100). **(B)** Disease-free survival of PCa patients with a different *SMARCC1* expression from the GEPIA database. **(C)** Endogenous expression of *SMARCC1* mRNA in immortalized normal prostatic epithelial cells and PCa cell lines. **(D,E)** *SMARCC1* mRNA **(D)** and protein **(E)** levels in PCa cells transduced with *SMARCC1* shRNA lentivirus. Relative mRNA expression levels are shown in the bar graph, and gray density values of proteins are indicated under the corresponding bands. All data are presented as mean ± SEM of at least three independent experiments. $^{***}p < 0.001$; $^{****}p < 0.0001$.

TABLE 1 | *SMARCC1* expression profile in tissue from BPH and PCa.

Origin type of tissue specimens	Immunohistochemical staining intensity		χ^2	*P*-value
	Negative (n, %)	Positive (n, %)		
BPH	37 (74)	13 (26)	2.487	0.115
PCa	61 (61)	39 (39)		

TABLE 2 | Correlation between *SMARCC1* expression and pathological characteristics of PCa.

Pathological characteristics	Immunohistochemical staining intensity			χ^2	*P*-value
	Low (n, %)	Medium (n, %)	Strong (n, %)		
Age					
≤60	4 (100)	–	–	2.664	0.264
>60	57 (59.4)	31 (32.3)	8 (8.3)		
Gleason score					
≤7	27 (50)	23 (42.6)	4 (7.4)	**7.469**	**0.024**
>7	34 (73.9)	8 (17.4)	4 (8.7)		
T stage					
T1–2	7 (46.7)	6 (40)	2 (13.3)	1.547	0.461
T3–4	50 (63.3)	23 (29.1)	6 (7.6)		
Metastasis to lymph nodes					
Yes	17 (73.9)	6 (26.1)	–	3.439	0.179
No	44 (57.1)	25 (32.5)	8 (10.4)		
Invasion to seminal vesicle					
Yes	37 (58.7)	21 (33.4)	5 (7.9)	0.375	0.829
No	21 (63.6)	9 (27.3)	3 (9.1)		
AJCC clinicopathological stage					
I–IIc	6 (50)	4 (33.3)	2 (16.7)	3.348	0.501
IIIa–IIIc	49 (60.5)	26 (32.1)	6 (7.4)		
IVa–IVb	6 (85.7)	1 (14.3)	0		
ERG staining					
Negative	37 (63.8)	15 (25.9)	6 (10.3)	3.477	0.176
Positive	9 (42.9)	10 (47.6)	2 (9.5)		

Bold values illustrate statistical significance.

450 nm was detected using Microplate Reader Synergy Neo2 (Biotek, United States).

Colony Formation Assay

The cells were seeded in six-well plates at a density of 3×10^3 cells/well in complete medium and cultured for 12–14 days till colonies were visible. The colonies were fixed with methanol and stained using the Wright–Giemsa kit (Baso, cat. BA4017, China). Colonies harboring >50 cells were counted under a microscope.

Flow Cytometry Assay

The cell cycle distribution was analyzed using a specific detection kit (KeyGENE BioTECH, cat. KGA512, Nanjing, China). Briefly, the suitably treated cells were harvested and fixed in 75% ethanol for 48 h. After washing with PBS, the cells were incubated with ribonuclease at 37°C for 30 min to remove intracellular RNA. The DNA was stained with propidium iodide (PI), and cells were acquired in the FACS Calibur flow cytometer (Bioscience, United States) to measure the DNA content.

EDU Assay

The cells were incubated with EDU solution (EDU assay kit, cat. C10310-1, RiboBio, China) diluted 1:1,000 in complete medium for 2 h. After washing thrice with PBS, the cells were fixed with 4% paraformaldehyde for 10 min and neutralized by 2 mg/ml glycine. The cells were then permeabilized with 0.5% Triton and incubated with the kit reaction agent for 30 min. After washing thrice with 0.5% Triton and once with methanol, the cells were counterstained with Hoechst 33342 (diluted 1:1,000 with ddH_2O) for 10 min to stain the nucleus and washed thrice with PBS. The EDU-positive cells were counted under an inverted microscope (Olympus, cat. 1X71, Japan) fitted with DP72 camera (Olympus, Japan).

Immunofluorescence Assay

The cells were seeded in a 24-well plate at a density of 0.2×10^6 cells/well and fixed with 4% paraformaldehyde for 10 min following 24 h of incubation. After neutralizing with 2 mg/ml glycine, the fixed cells were permeabilized with 0.5% Triton for

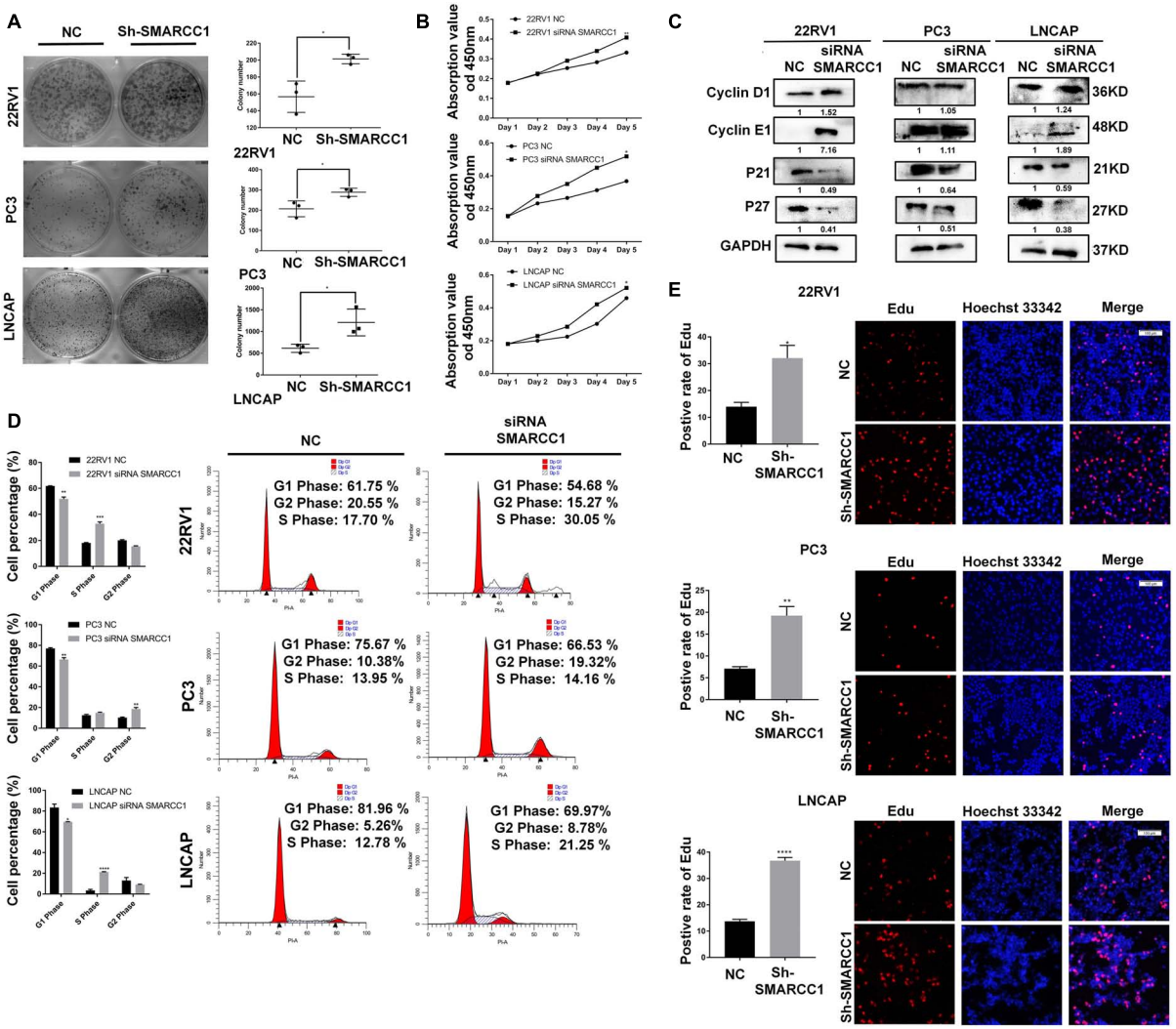

FIGURE 2 | *SMARCC1* knockdown increased PCa cell viability and proliferation. **(A)** Number of colonies formed by control and *SMARCC1* knockdown PCa cells. **(B)** Percentage of viable PCa cells treated as indicated. **(C)** CKI and cyclin mRNA and protein levels in the indicated groups. Relative mRNA expression levels are shown in the bar graph, and gray density values of proteins are indicated under the corresponding bands. **(D)** Bar graph showing the distribution of PCa cell lines in the different cell cycle stages. **(E)** Representative images (right panel, scale bar: 100 μm) of EDU-stained cells and bar graph showing the percentage of EDU-positive cells in the S phase. All data are presented as mean ± SEM of at least three independent experiments. $^{*}p < 0.05$; $^{**}p < 0.01$; $^{***}p < 0.001$; $^{****}p < 0.0001$.

10 min and washed thrice with PBS. The cells were then blocked with 10% BSA for 1 h and incubated with primary antibodies against E-Cadherin (1:100; CST, cat. 24E10, United States), N-Cadherin (1:100; CST, cat. D4R1H, United States), Vimentin (1:100; CST, cat. D21H3, United States), β-catenin (1:200; CST, cat. D10A8, United States), and p-Akt^{Ser473} (1:200; CST, cat. D9E, United States) at 37°C for 2 h. After washing thrice with PBST for 5 min, the cells were incubated with the secondary antibody at 37°C for 1 h. The stained cells were washed thrice with PBST and observed under an inverted microscope (Olympus, cat. 1X71, Japan) fitted with DP72 camera (Olympus, Japan).

Wound Healing Assay

The cells were seeded in a six-well plate at a density of 0.8×10^6 cells/well and cultured for 48 h till 90% confluent. The monolayer was scratched longitudinally with a 10-μl pipette tip, and the debris was removed by washing thrice with PBS. Fresh serum-free medium was added, and the wound region was photographed at 0, 12, and 24 h after scratching under an inverted microscope (Olympus, cat. 1X71, Japan) with DP72 camera (Olympus, Japan). The extent of wound healing was measured using Image J (NIH, United States).

Transwell Assay

The cells were seeded in the upper chambers of 24-well Transwell inserts (Corning, cat. 3422, United States) at a density of 1×10^5 cells/well in serum-free medium, and the lower chambers were filled with complete medium supplemented with 20% FBS. After culturing for 48 h, the unmigrated cells on the upper surface of the membranes were swabbed

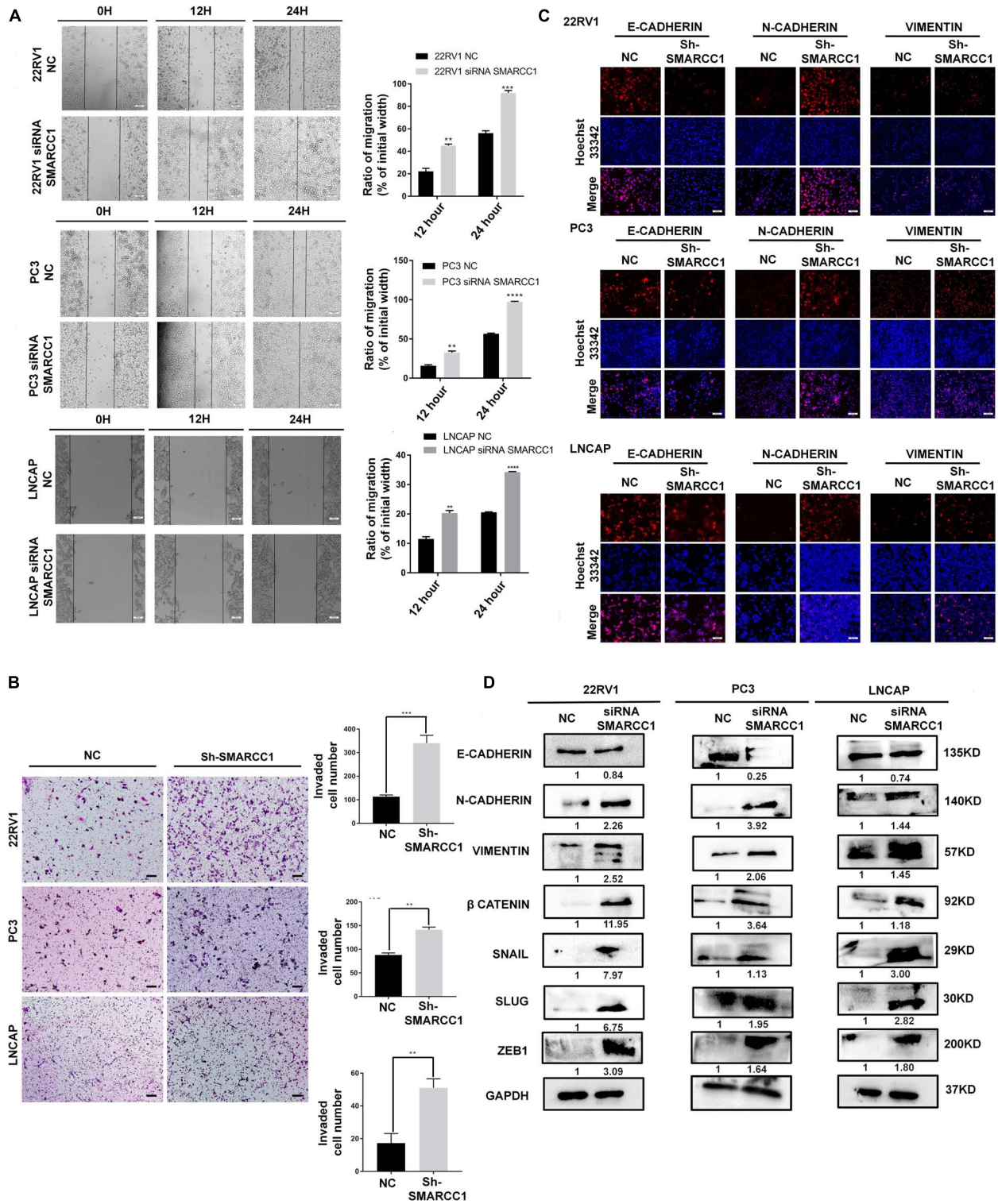

FIGURE 3 | *SMARCC1* knockdown induced EMT, migration and metastasis of PCa. **(A)** Representative images showing *in vitro* wound area coverage by control and *SMARCC1*-knockdown PCa cells (left panel; magnification 100×; Scale bar – 10 μm) and percentage of migration (right panel). **(B)** Representative images showing migration of PCa cells in the Transwell assay (magnification 100×; Scale bar – 50 μm) and percentage of migrating cells. **(C)** Representative immunofluorescence images showing E-cadherin, N-cadherin and vimentin expression in PCa cell lines (Scale bar: 100 μm). **(D)** Expression of EMT markers and transcription factors involved in EMT in the indicated groups. Gray density values of proteins are indicated under the correspondent bands. All data are presented as mean ± SEM of at least three independent experiments. $^{**}p < 0.01$;$^{***}p < 0.001$; $^{****}p < 0.0001$.

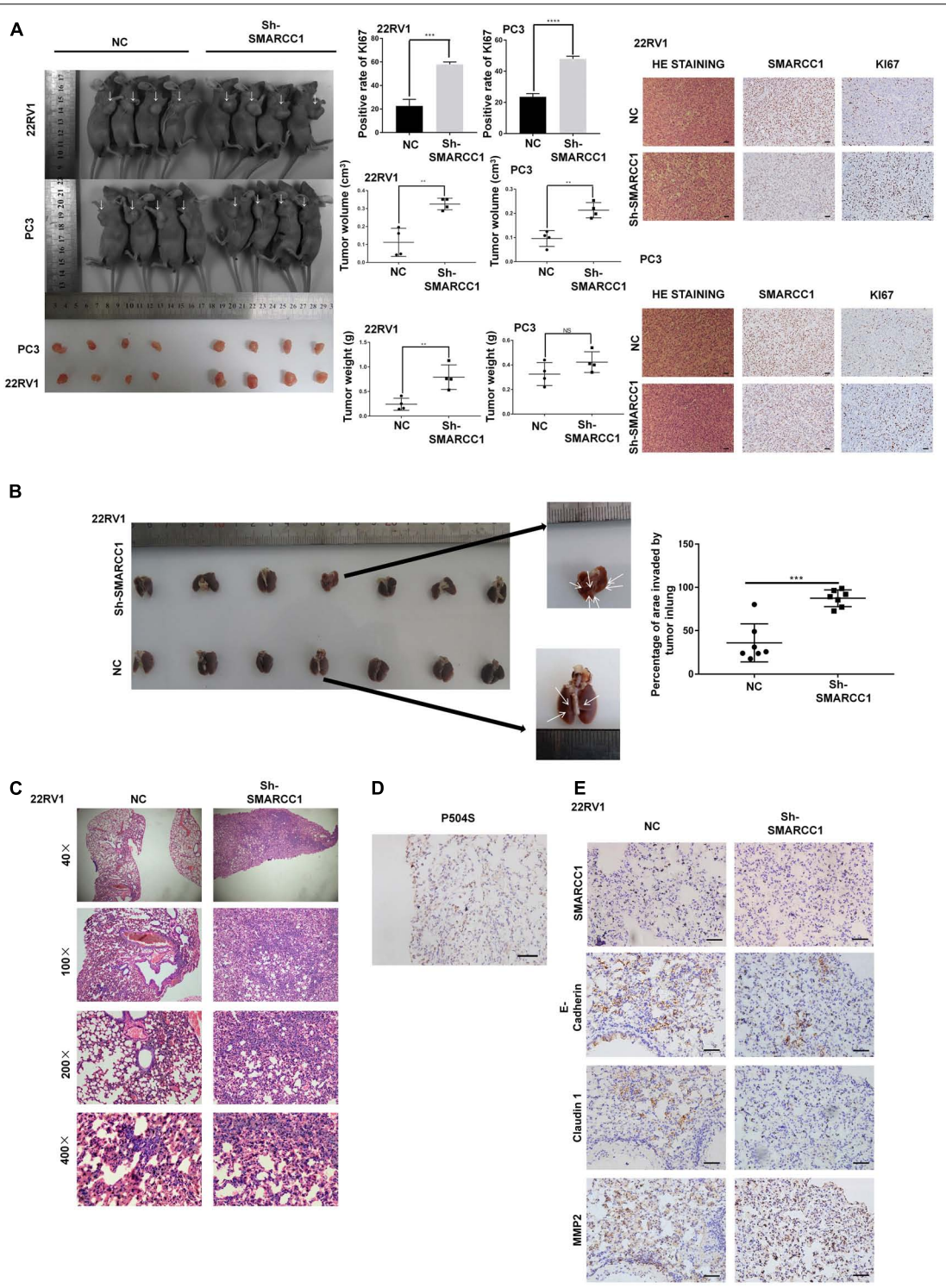

FIGURE 4 | *SMARCC1* knockdown promoted tumor growth and metastasis *in vivo*. **(A)** Left panel: representative images of subcutaneous tumor xenografts in the indicated groups and scatter plots showing tumor volume and weight. Right panel: representative immunohistochemistry (IHC) images showing *SMARCC1* and KI67 expression (magnification, ×200; scale bar, 20 μm) and bar graph showing the percentage of KI67+ cells. **(B,C)** Schematic illustration of lung metastasis model. Representative images of H&E-stained tumor nodules and scatter plots showing the percentage of lung area invaded by PCa cells in the indicated groups. **(D)** Representative IHC images of metastatic nodules showing the positive staining of P504S indicative of prostate origin (magnification, ×400; scale bar, 20 μm). **(E)** Representative IHC images of metastatic nodules showing the *in situ* expression of *SMARCC1*, MMP2, E-cadherin, and claudin1 (magnification, ×400; scale bar, 20 μm). All data were presented as mean ± SEM of at least three independent experiments. $^{**}p < 0.01$; $^{***}p < 0.001$; $^{****}p < 0.0001$.

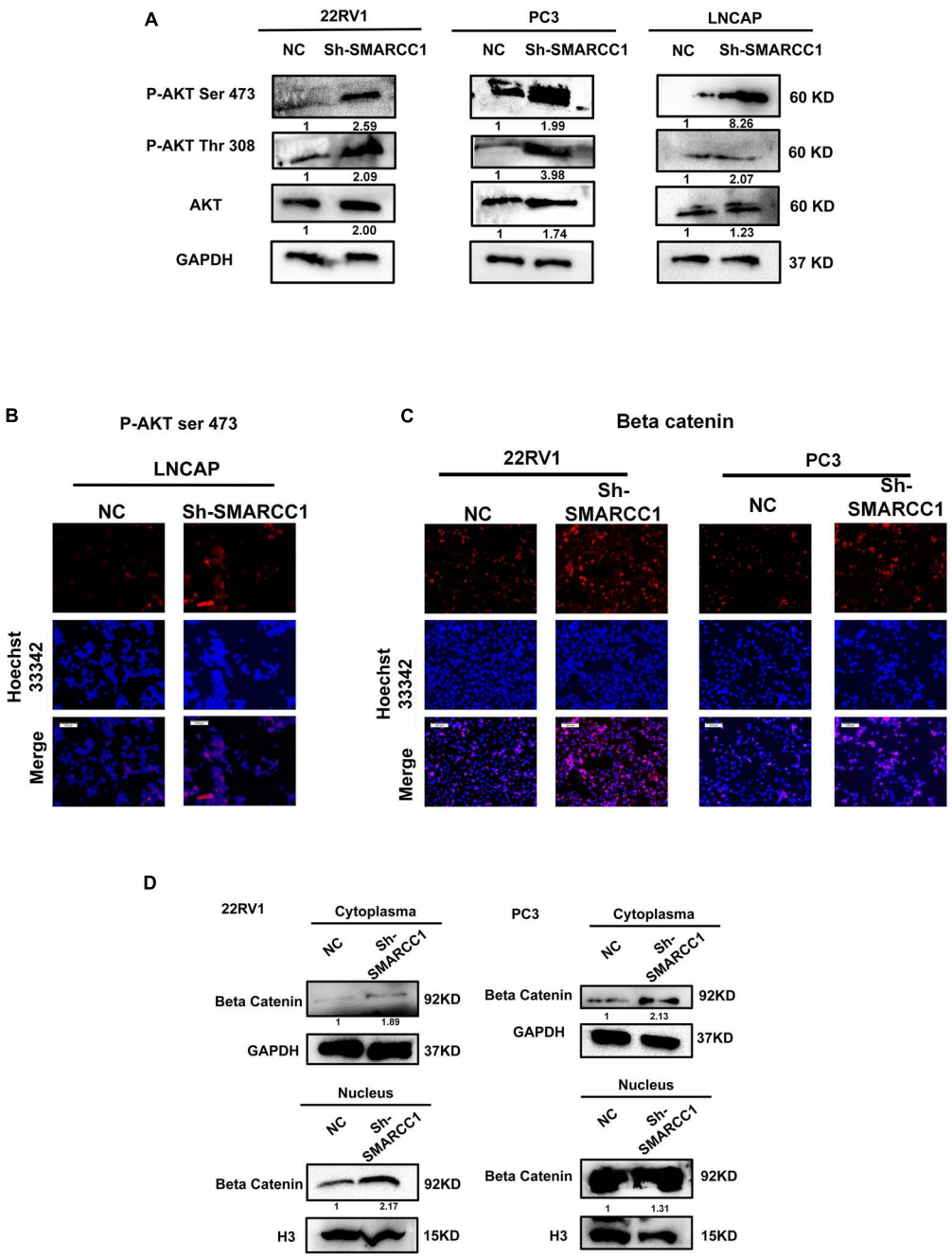

FIGURE 5 | *SMARCC1* knockdown activated the PI3K/AKT pathway in PCa cell lines. **(A)** Immunoblots showing the expression levels of phosphorylated PI3K/AKT mediators. The gray density values are indicated under the corresponding bands. **(B)** Representative immunofluorescence images showing the *in situ* expression of p-AKT$^{ser-473}$ in the LNCAP cell line (scale bar, 100 μm). **(C)** Representative immunofluorescence images showing the expression of β-catenin in the cytoplasm and nucleus of 22RV1 and PC3 cell lines (scale bar, 100 μm). **(D)** Immunoblots showing the expression levels of β-catenin in the cytoplasmic and nuclear fractions. The gray density values are indicated under the corresponding bands.

with a cotton ball, and the migrated cells on the lower surface were fixed with methanol for 10 min and stained with Wright–Giemsa kit (Baso, cat. BA4017, China). The number of migrated cells were counted in three random fields under a BX53 microscope (Olympus, Japan) fitted with DP72 camera (Olympus, Japan).

Mouse Xenograft Models

BALB/c nude mice were obtained from Guangdong Medical Laboratory Animal Center (Guangdong, China). All animal experiments were approved by the Ethical Committee of Southern Medical University and conducted according to the

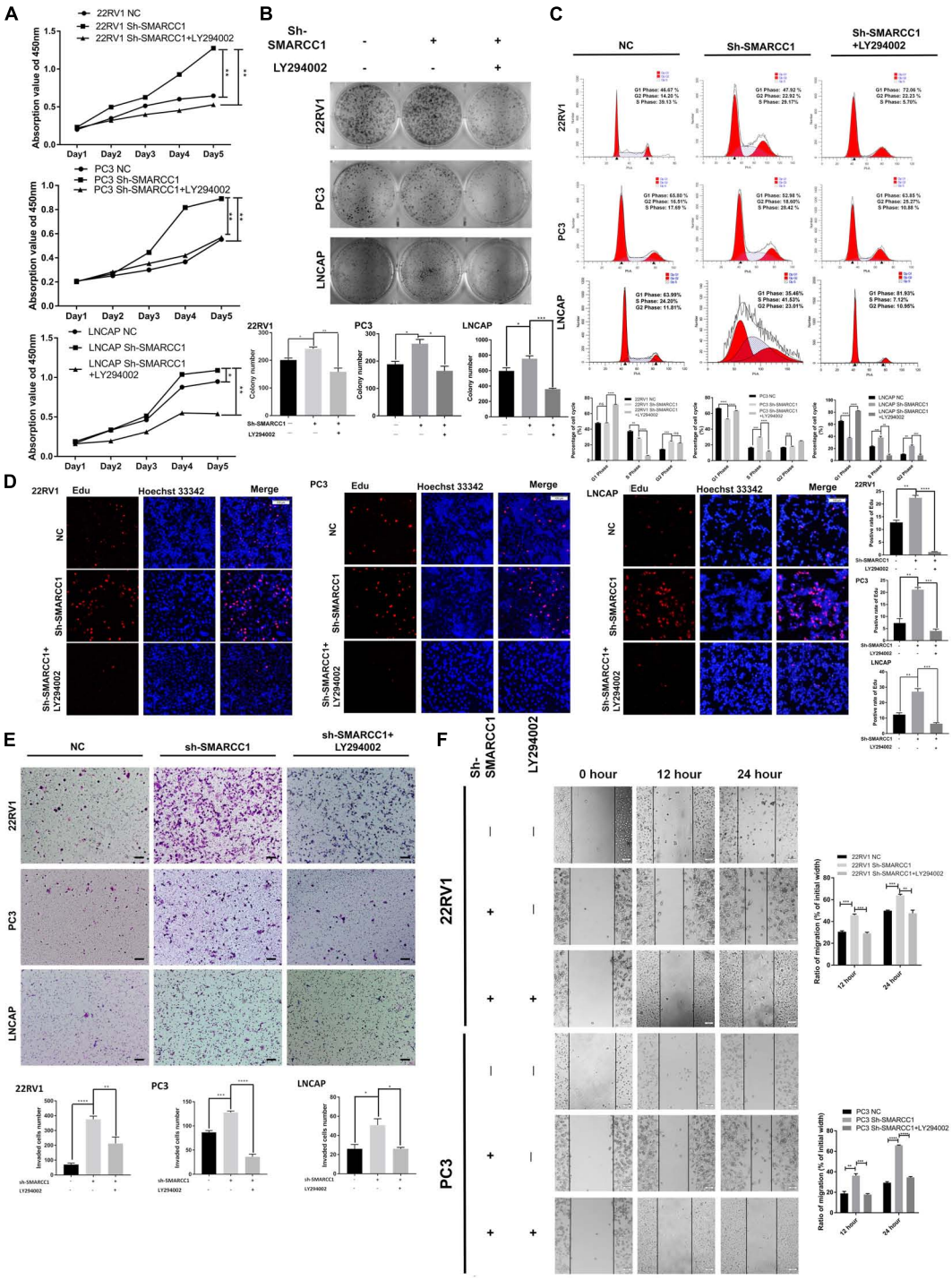

FIGURE 6 | PI3K/AKT pathway blockade reversed the phenotypic effect of *SMARCC1* knockdown. **(A)** Viability rate, **(B)** number of colonies, **(C)** cell cycle distribution, and **(D)** Representative image of EdU for LNCAP with Sh-*SMARCC1* was selected from area presented in **Figure 2E** for LNCAP cell line with Sh-*SMARCC1*. **(E)** Transwell assay on *SMARCC1* knocked-down PCa cell lines treated with ly294002 (scale bar – 100 μm). **(F)** Wound healing assay on migration ability of *SMARCC1* knocked-down PCa cell lines treated with ly294002. All data are presented as mean ± SEM of at least three independent experiments. $^{*}p < 0.05$; $^{**}p < 0.01$; $^{***}p < 0.001$; $^{****}p < 0.0001$.

NIH Guide for the Care and Use of Laboratory Animals. The subcutaneous xenograft was established in 4-week-old mice by subcutaneously injecting 5×10^6 cells into their flanks (four mice per group). The animals were sacrificed 33 days after inoculation, and the tumors were weighed, measured, and photographed with SX720 HS camera (Canon, Japan). For the

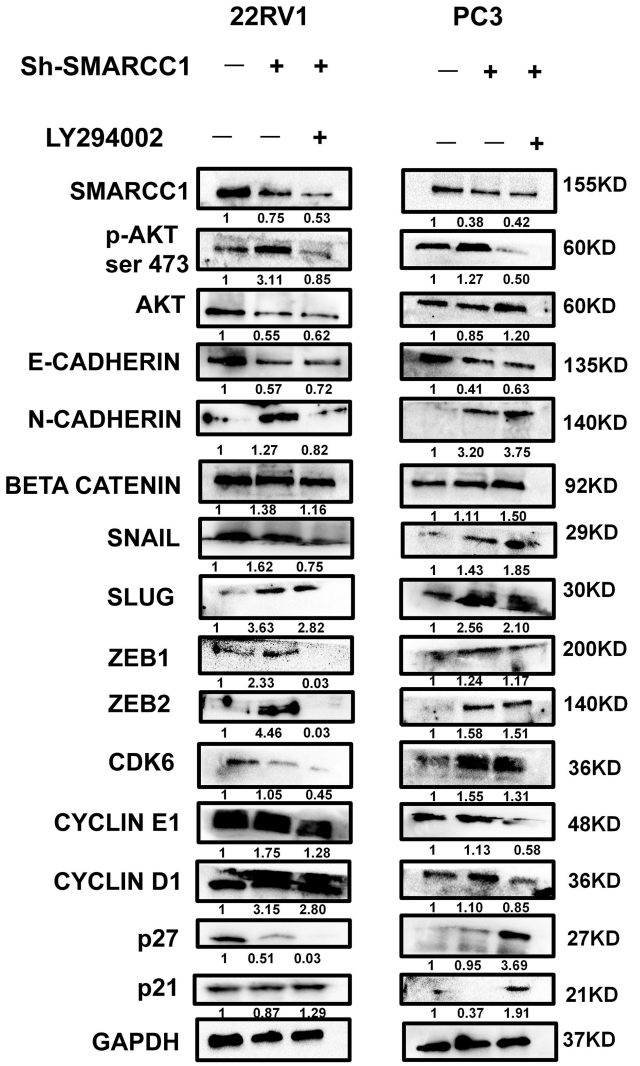

FIGURE 7 | PI3K/AKT pathway blockade with LY294002 partially reversed the protein expression in *SMARCC1* knockdown PCa cells. The gray density values are indicated under the corresponding bands.

lung metastasis model, 0.2×10^6 cells were injected intravenously into 6-week-old mice through the tail vein. The animals were sacrificed 6 weeks later, and the lung tissues were removed and photographed with SX720 HS camera (Canon, Japan). The tissues were fixed in 10% formalin, embedded in paraffin, and cut into sections. Hematoxylin–eosin staining was performed as per standard protocols and photographed under the BX53 microscope (Olympus, Japan) using DP72 camera (Olympus, Japan). IHC was performed to detect the *in situ* expression of proliferation and metastasis markers as described. The area invaded by the tumor was calculated by Image J software (NIH, United States).

Statistical Analysis

All statistical analyses were performed using GraphPad 7.0 (GraphPad Software Inc., United States) or SPSS 22.0 (IBM Corp., United States). Chi-square test or Fisher's exact test was used to determine the correlations between the *in situ* protein abundance and the clinicopathological factors in PCa tissues. Numerical data were expressed as means ± standard error of mean. Differences between variables were confirmed by two-tailed Student's *t*-test or one-way analysis of variance (ANOVA) for continuous variable groups. When ANOVA was significant, *post-hoc* testing of differences between groups was carried out using the least significant difference test. Survival curves were plotted using Kaplan–Meier's method and compared by the log-rank test. A P-value < 0.05 was considered statistically significant.

RESULTS

SMARCC1 Is Downregulated in PCa Tissues With GS More Than 7 and Correlates With Poor Prognosis

Compared with that in matched non-tumorous tissues of BPH, *in situ SMARCC1* expression in PCa tissue was slightly upregulated without statistical significance (**Figure 1A** and **Table 1**). In PCa cases with GS > 7, *in situ SMARCC1* expression was significantly downregulated (**Figure 1A** and **Table 2**). Consistent with this, the GEPIA data showed that the high expression of *SMARCC1* positively correlates with prolonged disease-free survival in PCa patients (**Figure 1B**). Thus, the loss of *SMARCC1* portends poor prognosis and disease progression in PCa. Moreover, endogenous expression of *SMARCC1* in PCa cell lines was validated using western blotting assay and was further knocked down using transient transfection of siRNA or lentivirus vector containing short hairpin RNA (**Figures 1C–E**).

SMARCC1 Inhibits PCa Cell Proliferation *in vitro*

SMARCC1 silencing significantly increased the viability of PCa cells as well as the number of colonies formed *in vitro* (**Figures 2A,B**). Loss of *SMARCC1* upregulated *cyclinD1/E1* and downregulated the *cyclin-dependent kinase inhibitors* (*CKIs*) *p21* and *p27*, which indicated accelerated cell cycle transition (**Figure 2C**). Consistent with this, EDU incorporation and PI staining assays showed that *SMARCC1* knockdown increased the percentage of cells entering S and G2 phases and decreased that of cells remaining in G1 phase (**Figures 2D,E**). In conclusion, *SMARCC1* loss in PCa cells accelerated cell cycle progression and increased their proliferation by downregulating *CKIs* and activating *cyclin D1/E1*.

SMARCC1 Silencing Accelerates the Metastasis of PCa Cells by Inducing EMT

Transwell and wound healing assays showed that loss of *SMARCC1* significantly increased the migration of PCa cells *in vitro* (**Figures 3A,B**). Consistent with this, *SMARCC1* knockdown markedly increased the expression of mesenchymal markers, including vimentin and N-cadherin, and decreased that of *E-cadherin* (**Figures 3C,D**). In addition, EMT-related transcription factors, including *Slug*, *Snail*, and *Zeb1*, were also

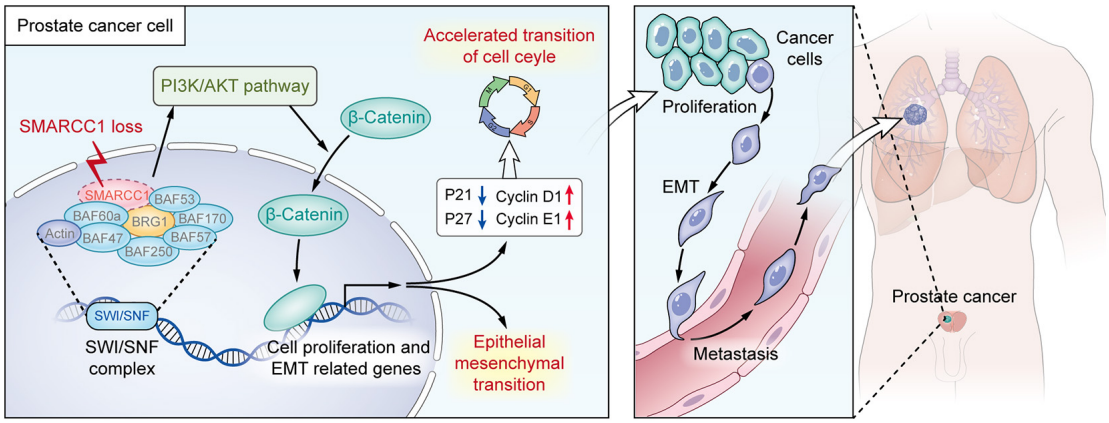

FIGURE 8 | Illustration for the pro-oncogenesis effect of *SMARCC1* loss on PCa. *SMARCC1* loss in PCa activates the PI3K/AKT pathway and induces the translocation of β-catenin to promote proliferation and epithelial mesenchymal transition.

upregulated in the *SMARCC1*-knockdown cells (**Figure 3D**). In conclusion, *SMARCC1* loss promoted the EMT of PCa cells, thereby inducing migration and metastasis.

Knockdown of *SMARCC1* Promotes the Growth and Metastasis of Human PCa Cells *in vivo*

To validate the potential impact of *SMARCC1* depletion on PCa cell proliferation *in vivo*, PC-3/sh-*SMARCC1* cells and PC-3/sh-Ctrl as well as 22Rv1/sh-*SMARCC1* cells and 22Rv1/sh-Ctrl cells were injected subcutaneously in nude mice. Tumors in mice implanted with sh-*SMARCC1* cells grew faster than control cells. *SMARCC1* knockdown cells exhibited significantly larger tumor volume and weight than control cells (**Figure 4A**). H&E staining showed the histopathological features of the tumor tissues. The positive rate of proliferation mark, Ki-67, was dramatically higher in xenografts with sh-*SMARCC1* cells by IHC staining (**Figure 4A**). These results provided evidence that *SMARCC1* may be a remarkable determinant for PCa cell growth. As for tumor metastasis *in vivo*, a tail vein xenograft model was generated. The tumor presence was validated by histological examination. The results demonstrated that mice injected with 22Rv1/*SMARCC1* shRNA cells produced more lung colonization compared to those with that of the control cells (**Figures 4B,C**). As shown in **Figure 4D**, *P540S* was stained to confirm the neoplasms' histologic type and origin of lung colonization. Moreover, we also found that the *SMARCC1*-knockdown pulmonary tumor nodules showed significantly higher levels of the matrix *metalloproteinase* (MMP2) and low levels of epithelial markers including *E-Cadherin* and *Claudin 1* (**Figure 4E**).

Loss of *SMARCC1* Activates the *PI3K/AKT* Pathway in PCa Cells

SMARCC1 knockdown activated the *PI3K/AKT* pathway in PCa cells, as indicated by the elevated phosphorylation of *Akt* at ser-473 and thr-308 (**Figures 5A,B**). Activation of the *PI3K/AKT* pathway stabilizes β-catenin and promotes its nuclear translocation, wherein it regulates the transcription of target genes. Loss of *SMARCC1* significantly increased the accumulation of β-catenin in the nuclear fraction of PCa cells (**Figures 5C,D**). Furthermore, the *PI3K/AKT* pathway blockade with the specific inhibitor LY294002 reversed the pro-proliferative and pro-metastatic effects of *SMARCC1* knockdown (**Figure 6**) without completely altering the expression levels of EMT and proliferation-related factors. This indicates that the *PI3K/AKT* pathway may partly mediate the pro-oncogenic effect induced by *SMARCC1* knockdown in PCa, and other pathways and mechanisms may also be involved (**Figure 7**).

DISCUSSION

High frequent mutations of several key epigenetic factors, including Rb1 and BRCA, have been revealed to induce an aggressive phenotype at the terminal stage of PCa and reflect a promoting effect of epigenetic dysregulation on PCa progression. As one of the core subunits, *SMARCC1* belongs to the SWI/SNF complex, which functions as a key epigenetic complex on genome transcription and consists of 12–14 subunits, including adenosine triphosphatase (ATPase), core, and other accessory subunits (Reisman et al., 2009; Shain and Pollack, 2013; Hohmann and Vakoc, 2014; Alver et al., 2017; Lu and Allis, 2017; Savas and Skardasi, 2018; Lei et al., 2019). A high frequency of mutations with function loss in coding genes of the SWI/SNF complex has been identified by whole genome sequencing in various cancers, especially renal carcinoma and melanoma, implying its important role in tumor suppression (Shain and Pollack, 2013; Stachowiak et al., 2020; Tsuda et al., 2021; Wang et al., 2021; Zhou et al., 2021). Mechanistically, the loss of function of the SWI/SNF complex promotes the transcription of genes related to proliferation and dedifferentiation, impairs DNA repairs, and reduces the antagonistic effect on the PRC complex (Nagl et al., 2005; Wilson et al., 2010; Tolstorukov et al., 2013; Alver et al., 2017; Stanton et al., 2017; Aras et al., 2019; Ribeiro-Silva et al., 2019; Hu et al., 2020).

However, the role of the *SWI/SNF* complex is ambiguous and controversial in PCa (Deocampo et al., 2004; Hong et al., 2005; Link et al., 2005; Heebøll et al., 2008; Hansen et al., 2011; Lee and Roberts, 2013; Prensner et al., 2013). Several studies show that it promotes PCa initiation and progression by transactivating the androgen receptor (Deocampo et al., 2004; Hong et al., 2005; Link et al., 2005), but there are also reports that some subunits function as tumor suppressors (Hansen et al., 2011; Lee and Roberts, 2013; Prensner et al., 2013). For instance, the long non-coding RNA *SChLAP1* promoted an aggressive PCa phenotype by antagonizing the *SNF5* subunit (Lee and Roberts, 2013; Prensner et al., 2013). The effect of *SMARCC1* in PCa is likewise still ambiguous and controversial. One study demonstrated the upregulation of *SMARCC1* in PCa tissues relative to benign prostate tissues (Heebøll et al., 2008), whereas a retrospective study found that the positive staining of *SMARCC1* in PCa tissues correlated with prolonged survival among local PCa patients (Hansen et al., 2011). In this study, we systematically elucidated the expression and role of *SMARCC1* in PCa. Our findings demonstrated that *SMARCC1* was significantly downregulated in PCa tissues with GS > 7, and its low expression correlated with shortened disease-free survival. In addition, silencing of *SMARCC1* in PC-3, 22RV1, and LNCaP cells significantly increased cell proliferation by promoting entry into the S phase of the cell cycle and facilitated cell migration by inducing EMT. The *in vivo* studies using a murine model showed that *SMARCC1* knocking down led to the acceleration of tumor growth and lung metastasis. These observations demonstrated the tumor-suppressive role of *SMARCC1* in PCa.

Infinite proliferation is an important hallmark of tumors (Nagl et al., 2005; Hu et al., 2020). Timing of proliferation depends on the transition speed of cell cycle and is directly associated with the expression of cell cycle-related genes (Nagl et al., 2005; Carrassa, 2013; Hu et al., 2020). Cell cycle transition through different checkpoints is driven by specific cyclins and cyclin-dependent kinases (*CDKs*) and blocked by *CKIs* that inhibit cyclins and *cyclin–CDK* complexes (Nagl et al., 2005; Hu et al., 2020). It has been reported that component loss of the *SWI/SNF* complex downregulates *CKIs* and upregulates cyclins at the transcriptional level (Nagl et al., 2005; Hu et al., 2020). Consistent with previous reports, we found that *SMARCC1* knockdown accelerated cell cycle transition and induced a hyper-proliferative phenotype in PCa cell lines by upregulating G1/S-specific protein *cyclin D1/E1* but downregulating cyclin-dependent kinase inhibitors *p21* and *p27*, implying that *SMARCC1* may be a potential druggable target for cell cycle checkpoint pathway in PCa.

Subunit loss in the SWI/SNF complex induces dedifferentiation phenotype, while EMT results from dedifferentiation in cancer cells (Alver et al., 2017; Wang and Unternaehrer, 2019). Previously, studies have indicated that the subunit loss of the *SWI/SNF* complex may facilitate the metastasis of tumor cells by inducing EMT in colon and gastric carcinoma (Yan et al., 2014; Wang et al., 2019). EMT is triggered by transcription factors like *Snail*, *Slug*, and *Zeb1* that repress the epithelial factor *E-cadherin* and endows the cells with greater metastatic abilities (Yan et al., 2014; Wang and Unternaehrer, 2019; Wang et al., 2019). However, it was uncertain whether the suppression of *SMARCC1* would induce EMT in PCa. We, therefore, analyzed the key proteins of EMT and found that silencing of *SMARCC1* resulted in a remarkably increased expression of vimentin and N-cadherin as well as a reduced expression of E-cadherin, which are considered as characteristic features of EMT.

It has been reported that the component loss in the *SWI/SNF* complex promotes the malignant progression of rhabdomyosarcoma and ovary carcinoma *via* activation of the *PI3K/AKT* pathway (Foster et al., 2009; Bitler et al., 2015). In PCa, activation of the PI3K/AKT pathway promotes the nuclear translocation of β-catenin, which triggers the expression of proliferation and EMT-related genes and specifically promotes tumor progression by transactivating androgen receptor and its downstream pathway (Sharma et al., 2002; Hennessy et al., 2005; Carnero, 2010; Noorolyai et al., 2019). However, the specific role of the PI3K/Akt pathway in PCa with *SMARCC1* loss still needs to be investigated. Previous studies revealed the synergistic effect of the SWI/SNF complex with other epigenetic factors, including histone acetylase and Rb1, on genome transcription (Strobeck et al., 2000; Chatterjee et al., 2018), while *SMARCC1* functions as a scaffold structure in the SWI/SNF complex to undertake coordination with other epigenetic factors (Chatterjee et al., 2018), even though we observed a significant upregulation of β-catenin in the nuclear fraction of PCa cells with *SMARCC1* depletion in our study, indicating that the *PI3K/AKT* pathway mediates the pro-oncogenic effects of *SMARCC1* loss. However, the PI3K/AKT inhibitor LY294002 only partially reversed these pro-oncogenic effects, which indicates the potential involvement of other epigenetic factors. Taken together, *SMARCC1* may function as a tumor suppressor in PCa along with other epigenetic factors, which warrant further investigation.

In summary, the downregulation of *SMARCC1* is correlated with a poor prognosis and an aggressive phenotype of PCa. *SMARCC1* depletion facilitates PCa cell proliferation by promoting cell cycle progression and enhanced cell migration by EMT. In addition, *SMARCC1* loss activates the PI3K/Akt signaling pathway, which plays a key role in the progression of PCa. Therefore, *SMARCC1* may be a promising therapeutic target in PCa, especially for cases with low expression levels (**Figure 8**).

DATA AVAILABILITY STATEMENT

The raw data supporting the conclusions of this article will be made available by the authors, without undue reservation.

ETHICS STATEMENT

The studies involving human participants were reviewed and approved by the Ethics Committee of Nanfang Hospital,

Southern Medical University. The patients/participants provided their written informed consent to participate in this study. The animal study was reviewed and approved by the Ethics Committee of Nanfang Hospital, Southern Medical University.

AUTHOR CONTRIBUTIONS

Z-MX and D-JL performed the material preparation, data collection, and data analysis. Y-ZY, CW, and TW assisted in collecting data. Z-MX wrote the first draft of the manuscript. D-JL revised the manuscript. S-CZ and D-JL executed the funding acquisition. S-CZ supervised the study. All authors contributed to the study conception and design, commented on previous versions of the manuscript, read, and approved the final manuscript.

FUNDING

This study was supported by the National Natural Science Foundation of China (No. 81972394), the Guangdong Basic and Applied Basic Research Foundation (2020A1515010066), the Outstanding Youths Development Scheme of Nanfang Hospital, Southern Medical University (No. 2015J005), the China Postdoctoral Science Foundation funded project (No. 2019M662865), the Guangdong Basic and Applied Basic Research Foundation (No. 2019A1515110033), the Distinguished Young Talents in Higher Education Foundation of Guangdong Province (No. 2019KQNCX115), the Achievement Cultivation and Clinical Transformation Application Cultivation projects of the First Affiliated Hospital of Guangzhou Medical University (No. ZH201908), and the Science and Technology Plan Project of Guangzhou (No. 202102010150).

REFERENCES

Alver, B. H., Kim, K. H., Lu, P., Wang, X., Manchester, H. E., Wang, W., et al. (2017). The SWI/SNF chromatin remodelling complex is required for maintenance of lineage specific enhancers. *Nat. Commun.* 8:14648. doi: 10.1038/ncomms14648

Andersen, C. L., Christensen, L. L., Thorsen, K., Schepeler, T., Sørensen, F. B., Verspaget, H. W., et al. (2009). Dysregulation of the transcription factors SOX4, CBFB and SMARCC1 correlates with outcome of colorectal cancer. *Br. J. Cancer* 100, 511–523. doi: 10.1038/sj.bjc.6604884

Aras, S., Saladi, S. V., Basuroy, T., Marathe, H. G., Lorès, P., and de la Serna, I. L. (2019). BAF60A mediates interactions between the microphthalmia-associated transcription factor and the BRG1-containing SWI/SNF complex during melanocyte differentiation. *J. Cell Physiol.* 234, 11780–11791. doi: 10.1002/jcp.27840

Bao, J. M., He, M. Y., Liu, Y. W., Lu, Y. J., Hong, Y. Q., Luo, H. H., et al. (2015). AGE/RAGE/Akt pathway contributes to prostate cancer cell proliferation by promoting Rb phosphorylation and degradation. *Am. J. Cancer Res.* 5, 1741–1750.

Bitler, B. G., Fatkhutdinov, N., and Zhang, R. (2015). Potential therapeutic targets in ARID1A-mutated cancers. *Expert. Opin. Ther. Targets* 19, 1419–1422. doi: 10.1517/14728222.2015.1062879

Carnero, A. (2010). The PKB/AKT pathway in cancer. *Curr. Pharm. Des.* 16, 34–44. doi: 10.2174/138161210789941865

Carrassa, L. (2013). Cell cycle, checkpoints and cancer. *Atlas Genet. Cytogenet. Oncol. Haematol.* 18, 67–75.

Chan, J. J., Kwok, Z. H., Chew, X. H., Zhang, B., Liu, C., Soong, T. W., et al. (2018). A FTH1 gene:pseudogene:microRNA network regulates tumorigenesis in prostate cancer. *Nucleic Acids Res.* 46, 1998–2011. doi: 10.1093/nar/gkx1248

Chatterjee, S. S., Biswas, M., Boila, L. D., Banerjee, D., and Sengupta, A. (2018). SMARCB1 deficiency integrates epigenetic signals to oncogenic gene expression program maintenance in human acute myeloid leukemia. *Mol. Cancer Res.* 16, 791–804. doi: 10.1158/1541-7786.Mcr-17-0493

Crea, F., Hurt, E. M., Mathews, L. A., Cabarcas, S. M., Sun, L., Marquez, V. E., et al. (2011). Pharmacologic disruption of Polycomb Repressive Complex 2 inhibits tumorigenicity and tumor progression in prostate cancer. *Mol. Cancer* 10, 40. doi: 10.1186/1476-4598-10-40

Deocampo, N. D., Bello-Deocampo, D., and Tindall, D. J. (2004). SWI/SNF as an enhancer of androgen receptor transactivation in prostate cells. *Cancer Res.* 64, 840–840.

Foster, K., Wang, Y., Zhou, D., and Wright, C. (2009). Dependence on PI3K/Akt signaling for malignant rhabdoid tumor cell survival. *Cancer Chemother. Pharmacol.* 63, 783–791. doi: 10.1007/s00280-008-0796-5

Ge, R., Wang, Z., Montironi, R., Jiang, Z., Cheng, M., Santoni, M., et al. (2020). Epigenetic modulations and lineage plasticity in advanced prostate cancer. *Ann. Oncol.* 31, 470–479. doi: 10.1016/j.annonc.2020.02.002

Hansen, R. L., Heeboll, S., Ottosen, P. D., Dyrskjøt, L., and Borre, M. (2011). Smarcc1 expression: a significant predictor of disease-specific survival in patients with clinically localized prostate cancer treated with no intention to cure. *Scand. J. Urol. Nephrol.* 45, 91–96. doi: 10.3109/00365599.2010.530295

Heebøll, S., Borre, M., Ottosen, P. D., Andersen, C. L., Mansilla, F., Dyrskjøt, L., et al. (2008). SMARCC1 expression is upregulated in prostate cancer and positively correlated with tumour recurrence and dedifferentiation. *Histol. Histopathol.* 23, 1069–1076. doi: 10.14670/hh-23.1069

Hennessy, B. T., Smith, D. L., Ram, P. T., Lu, Y., and Mills, G. B. (2005). Exploiting the PI3K/AKT pathway for cancer drug discovery. *Nat. Rev. Drug Discov.* 4, 988–1004. doi: 10.1038/nrd1902

Hohmann, A. F., and Vakoc, C. R. (2014). A rationale to target the SWI/SNF complex for cancer therapy. *Trends Genet.* 30, 356–363. doi: 10.1016/j.tig.2014.05.001

Hong, C. Y., Suh, J. H., Kim, K., Gong, E. Y., Jeon, S. H., Ko, M., et al. (2005). Modulation of androgen receptor transactivation by the SWI3-related gene product (SRG3) in multiple ways. *Mol. Cell Biol.* 25, 4841–4852. doi: 10.1128/mcb.25.12.4841-4852.2005

Hu, B., Lin, J. Z., Yang, X. B., and Sang, X. T. (2020). The roles of mutated SWI/SNF complexes in the initiation and development of hepatocellular carcinoma and its regulatory effect on the immune system: a review. *Cell Prolif.* 53:e12791. doi: 10.1111/cpr.12791

Iwagami, Y., Eguchi, H., Nagano, H., Akita, H., Hama, N., Wada, H., et al. (2013). miR-320c regulates gemcitabine-resistance in pancreatic cancer via SMARCC1. *Br. J. Cancer* 109, 502–511. doi: 10.1038/bjc.2013.320

Lee, R. S., and Roberts, C. W. (2013). Linking the SWI/SNF complex to prostate cancer. *Nat. Genet.* 45, 1268–1269. doi: 10.1038/ng.2805

Lei, I., Tian, S., Chen, V., Zhao, Y., and Wang, Z. (2019). SWI/SNF component BAF250a coordinates OCT4 and WNT signaling pathway to control cardiac lineage differentiation. *Front. Cell Dev. Biol.* 7:358. doi: 10.3389/fcell.2019.00358

Liang, C., Niu, L., Xiao, Z., Zheng, C., Shen, Y., Shi, Y., et al. (2020). Whole-genome sequencing of prostate cancer reveals novel mutation-driven processes and molecular subgroups. *Life Sci.* 254:117218. doi: 10.1016/j.lfs.2019.117218

Link, K. A., Burd, C. J., Williams, E., Marshall, T., Rosson, G., Henry, E., et al. (2005). BAF57 governs androgen receptor action and androgen-dependent proliferation through SWI/SNF. *Mol. Cell Biol.* 25, 2200–2215. doi: 10.1128/mcb.25.6.2200-2215.2005

Liu, W. (2016). DNA alterations in the tumor genome and their associations with clinical outcome in prostate cancer. *Asian J. Androl.* 18, 533–542. doi: 10.4103/1008-682x.177120

Lu, C., and Allis, C. D. (2017). SWI/SNF complex in cancer. *Nat. Genet.* 49, 178–179. doi: 10.1038/ng.3779

Nagl, N. G. Jr., Patsialou, A., Haines, D. S., Dallas, P. B., Beck, G. R. Jr., and Moran, E. (2005). The p270 (ARID1A/SMARCF1) subunit of mammalian SWI/SNF-related complexes is essential for normal cell cycle arrest. *Cancer Res.* 65, 9236–9244. doi: 10.1158/0008-5472.Can-05-1225

Noorolyai, S., Shajari, N., Baghbani, E., Sadreddini, S., and Baradaran, B. (2019). The relation between PI3K/AKT signalling pathway and cancer. *Gene* 698, 120–128. doi: 10.1016/j.gene.2019.02.076

Oh, M., Alkhushaym, N., Fallatah, S., Althagafi, A., Aljadeed, R., Alsowaida, Y., et al. (2019). The association of BRCA1 and BRCA2 mutations with prostate cancer risk, frequency, and mortality: a meta-analysis. *Prostate* 79, 880–895. doi: 10.1002/pros.23795

Pernar, C. H., Ebot, E. M., Wilson, K. M., and Mucci, L. A. (2018). The epidemiology of prostate cancer. *Cold Spring Harb. Perspect. Med.* 8:a030361. doi: 10.1101/cshperspect.a030361

Prensner, J. R., Iyer, M. K., Sahu, A., Asangani, I. A., Cao, Q., Patel, L., et al. (2013). The long noncoding RNA SChLAP1 promotes aggressive prostate cancer and antagonizes the SWI/SNF complex. *Nat. Genet.* 45, 1392–1398. doi: 10.1038/ng.2771

Reisman, D., Glaros, S., and Thompson, E. A. (2009). The SWI/SNF complex and cancer. *Oncogene* 28, 1653–1668. doi: 10.1038/onc.2009.4

Ribeiro-Silva, C., Vermeulen, W., and Lans, H. (2019). SWI/SNF: complex complexes in genome stability and cancer. *DNA Rep. (Amst)* 77, 87–95. doi: 10.1016/j.dnarep.2019.03.007

Savas, S., and Skardasi, G. (2018). The SWI/SNF complex subunit genes: their functions, variations, and links to risk and survival outcomes in human cancers. *Crit. Rev. Oncol. Hematol.* 123, 114–131. doi: 10.1016/j.critrevonc.2018.01.009

Shain, A. H., and Pollack, J. R. (2013). The spectrum of SWI/SNF mutations, ubiquitous in human cancers. *PLoS One* 8:e55119. doi: 10.1371/journal.pone.0055119

Sharma, M., Chuang, W. W., and Sun, Z. (2002). Phosphatidylinositol 3-kinase/Akt stimulates androgen pathway through GSK3beta inhibition and nuclear beta-catenin accumulation. *J. Biol. Chem.* 277, 30935–30941. doi: 10.1074/jbc.M201919200

Sheahan, A. V., and Ellis, L. (2018). Epigenetic reprogramming: a key mechanism driving therapeutic resistance. *Urol. Oncol.* 36, 375–379. doi: 10.1016/j.urolonc.2017.12.021

Siegel, R. L., Miller, K. D., Fuchs, H. E., and Jemal, A. (2021). Cancer statistics, 2021. *CA Cancer J. Clin.* 71, 7–33. doi: 10.3322/caac.21654

Stachowiak, M., Szymanski, M., Ornoch, A., Jancewicz, I., Rusetska, N., Chrzan, A., et al. (2020). SWI/SNF chromatin remodeling complex and glucose metabolism are deregulated in advanced bladder cancer. *IUBMB Life* 72, 1175–1188. doi: 10.1002/iub.2254

Stanton, B. Z., Hodges, C., Calarco, J. P., Braun, S. M., Ku, W. L., Kadoch, C., et al. (2017). Smarca4 ATPase mutations disrupt direct eviction of PRC1 from chromatin. *Nat. Genet.* 49, 282–288. doi: 10.1038/ng.3735

Strobeck, M. W., Knudsen, K. E., Fribourg, A. F., DeCristofaro, M. F., Weissman, B. E., Imbalzano, A. N., et al. (2000). BRG-1 is required for RB-mediated cell cycle arrest. *Proc. Natl. Acad. Sci. U.S.A.* 97, 7748–7753. doi: 10.1073/pnas.97.14.7748

Tolstorukov, M. Y., Sansam, C. G., Lu, P., Koellhoffer, E. C., Helming, K. C., Alver, B. H., et al. (2013). Swi/Snf chromatin remodeling/tumor suppressor complex establishes nucleosome occupancy at target promoters. *Proc. Natl. Acad. Sci. U.S.A.* 110, 10165–10170. doi: 10.1073/pnas.1302209110

Tsuda, M., Fukuda, A., Kawai, M., Araki, O., and Seno, H. (2021). The role of the SWI/SNF chromatin remodeling complex in pancreatic ductal adenocarcinoma. *Cancer Sci.* 112, 490–497. doi: 10.1111/cas.14768

Wang, G., Lv, Q., Ma, C., Zhang, Y., Li, H., and Ding, Q. (2021). SMARCC1 expression is positively correlated with pathological grade and good prognosis in renal cell carcinoma. *Transl. Androl. Urol.* 10, 236–242. doi: 10.21037/tau-20-935

Wang, H., and Unternaehrer, J. J. (2019). Epithelial-mesenchymal transition and cancer stem cells: at the crossroads of differentiation and dedifferentiation. *Dev. Dyn.* 248, 10–20. doi: 10.1002/dvdy.24678

Wang, W., Friedland, S. C., Guo, B., O'Dell, M. R., Alexander, W. B., Whitney-Miller, C. L., et al. (2019). ARID1A, a SWI/SNF subunit, is critical to acinar cell homeostasis and regeneration and is a barrier to transformation and epithelial-mesenchymal transition in the pancreas. *Gut* 68, 1245–1258. doi: 10.1136/gutjnl-2017-315541

Wilson, B. G., Wang, X., Shen, X., McKenna, E. S., Lemieux, M. E., Cho, Y. J., et al. (2010). Epigenetic antagonism between polycomb and SWI/SNF complexes during oncogenic transformation. *Cancer Cell* 18, 316–328. doi: 10.1016/j.ccr.2010.09.006

Wu, G., Sun, Y., Xiang, Z., Wang, K., Liu, B., Xiao, G., et al. (2019). Preclinical study using circular RNA 17 and micro RNA 181c-5p to suppress the enzalutamide-resistant prostate cancer progression. *Cell Death Dis.* 10:37. doi: 10.1038/s41419-018-1048-1

Yan, H. B., Wang, X. F., Zhang, Q., Tang, Z. Q., Jiang, Y. H., Fan, H. Z., et al. (2014). Reduced expression of the chromatin remodeling gene ARID1A enhances gastric cancer cell migration and invasion via downregulation of E-cadherin transcription. *Carcinogenesis* 35, 867–876. doi: 10.1093/carcin/bgt398

Zhou, M., Yuan, J., Deng, Y., Fan, X., and Shen, J. (2021). Emerging role of SWI/SNF complex deficiency as a target of immune checkpoint blockade in human cancers. *Oncogenesis* 10:3. doi: 10.1038/s41389-020-00296-6

Conflict of Interest: The authors declare that the research was conducted in the absence of any commercial or financial relationships that could be construed as a potential conflict of interest.

frontiers in Cell and Developmental Biology

ORIGINAL RESEARCH
published: 08 July 2021
doi: 10.3389/fcell.2021.715674

Decreased m6A Modification of CD34/CD276(B7-H3) Leads to Immune Escape in Colon Cancer

Yiran Zhou[1†], Haodong Zhou[1†], Jianlin Shi[2†], Aoran Guan[1], Yankun Zhu[1], Zongliu Hou[3] and Ruhong Li[1]*

[1] Key Laboratory of Tumor Immunological Prevention and Treatment of Yunnan Province, First Department of General Surgery, Yan'an Affiliated Hospital of Kunming Medical University, Kunming, China, [2] Key Laboratory of Tumor Immunological Prevention and Treatment of Yunnan Province, Department of Thoracic Surgery, Yan'an Affiliated Hospital of Kunming Medical University, Kunming, China, [3] Key Laboratory of Tumor Immunological Prevention and Treatment of Yunnan Province, Kunming, China

OPEN ACCESS

Edited by:
Yongbin Chen,
Key Laboratory of Animal Models and Human Disease Mechanisms, Kunming Institute of Zoology (CAS), China

Reviewed by:
Zhixiang Zuo,
Sun Yat-sen University, China
Qianjin Liao,
Central South University, China
Gang Yin,
Central South University, China

***Correspondence:**
Ruhong Li
lrh212@126.com

† These authors have contributed equally to this work

Specialty section:
This article was submitted to Molecular and Cellular Oncology, a section of the journal Frontiers in Cell and Developmental Biology

Received: *27 May 2021*
Accepted: *21 June 2021*
Published: *08 July 2021*

Citation:
Zhou Y, Zhou H, Shi J, Guan A, Zhu Y, Hou Z and Li R (2021) Decreased m6A Modification of CD34/CD276(B7-H3) Leads to Immune Escape in Colon Cancer. Front. Cell Dev. Biol. 9:715674. doi: 10.3389/fcell.2021.715674

Previous studies have reported that m6a modification promotes tumor immune escape by affecting tumor microenvironment (TME). Due to the complexity of TME, a single biomarker is insufficient to describe the complex biological characteristics of tumor and its microenvironment. Therefore, it is more meaningful to explore a group of effective biomarkers reflecting different characteristics of cancer to evaluate the biological characteristics of solid tumors. Here, the immune gene CD34/CD276 with different m6A peak was obtained by m6A sequencing (MeRIP-seq) of colon cancer (CRC)clinical samples and combined with MsIgDB database, which was used to perform cluster analysis on TCGA-COAD level 3 data. The CD34/CD276 as a molecular marker for CRC prognosis was confirmed by survival analysis and immunohistochemical assay. Further bioinformatics analysis was carried out to analyze the molecular mechanism of CD34/CD276 affecting the TME through m6a-dependent down-regulation and ultimately promoting immune escape of CRC.

Keywords: N6-methyladenosine, colon cancer, CD34, CD276(B7-H3), immune escape

INTRODUCTION

CRC is the second most common cancer in men and the third most common cancer in women worldwide. Immune evasion caused by tumor progression is the most important factor leading to the death of CRC patients (Dekker et al., 2019). While immunotherapy for cancer has been shown to have significant efficacy, only a small number of patients tend to experience clinical benefits, mainly due to the tumor immunosuppressive microenvironment (Yang et al., 2019). The tumor microenvironment (TME), which consists of extracellular matrix, myofibroblasts, cytokines, fibroblasts, neuroendocrine cells, adipocytes, immune-related cells, and blood vessels (Wang et al., 2018), induces phenotypic changes of cancer cells and immune cells through complex molecular mechanisms to promote immune escape (Kaymak et al., 2021). The crosstalk between TME and immune cells is initiated and regulated by receptors on the cell surface (Clara et al., 2020). Because of the complexity of TME, a single biomarker is not enough to describe the complex biological characteristics of a tumor and its microenvironment (Rolff et al., 2016). Therefore, exploring a

group of effective biomarkers reflecting the different characteristics of cancer is more meaningful for evaluating the biological characteristics of solid tumors (Hanahan and Weinberg, 2011).

N6-Methyladenosine (m6A) is considered the most abundant internal chemical modification of human mRNA. It has an important role in tumor progression by participating in RNA processing, nuclear output, translation, degradation, and RNA-protein interaction (Van Laethem et al., 2012; Wang et al., 2014; Liu et al., 2015). Many studies have reported a correlation between TME promoting tumor immune escape and m6A modification. E.g., the low expression of m6A methyltransferase WTAP is related to the high T cell-associated immune response of gastric cancer (Lin et al., 2020; Chong et al., 2021). In the mouse CRC model, the depletion of YTHDF1 strengthens the early initiation of T cells to new tumor antigens (Han et al., 2019), but the role of m6A in cancer immunity has not been extensively explored.

Herein, we obtained the immune gene CD34/CD276 with different m6A peak by m6A sequencing (MeRIP-seq) of CRC clinical samples combined with MsIgDB database. Based on TCGA database bioinformatics analysis combined with immunohistochemical verification, we confirmed that CD34/CD276 could be used as a molecular marker for CRC prognosis and promote CRC immune escape by relying on the down-regulation mechanism of m6A modification.

MATERIALS AND METHODS

Tissue Specimen Collection

A total of 40 patients with CRC who received surgical treatment in the first department of general surgery of Yan'an Hospital Affiliated to Kunming Medical University on January 10, 2019 were selected. CRC tissues and distal paracancerous tissues were collected during the operation and stored in liquid nitrogen.

This study was approved by the Ethics Committee of our hospital. None of the patients received adjuvant chemoradiotherapy or immunotherapy before surgery, and all the tissues were pathologically confirmed as colorectal adenocarcinoma. The CRC tissues and paracancerous tissues of 10 patients were randomly selected for High-Throughput m6A Sequencing, and the CRC tissues of 40 patients were verified by immunohistochemical analysis.

High-Throughput m6A Sequencing

Total RNA was extracted using Trizol reagent (Invitrogen, CA, United States) following the manufacturer's procedure. The total RNA quality and quantity were analyzed using a Bioanalyzer 2100 and RNA 6000 Nano LabChip Kit (Agilent, CA, United States) with RIN number >7.0. Approximately more than 25 μg of total RNA representing a specific adipose type were used to deplete ribosomal RNA according to the instructions of Epicentre Ribo-Zero Gold Kit (Illumina, San Diego, United States). Following purification, the ribosomal-depleted RNA was fragmented into ∼100-nt-long oligonucleotides using divalent cations under elevated temperature. Then, the cleaved RNA fragments were subjected to incubated for 2 h at 4°C with m6A-specific antibody (No. 202003, Synaptic Systems, Germany) in IP buffer (50 mM Tris-HCl, 750?mM NaCl and 0.5% Igepal CA-630) supplemented with BSA (0.5 μg μl^{-1}). The mixture was then incubated with protein-A beads and eluted with elution buffer (1 × IP buffer and 6.7 mM m6A). Eluted RNA was precipitated by 75% ethanol. Eluted m6A-containing fragments (IP) and untreated input control fragments were converted to the final cDNA library in accordance with a strand-specific library preparation by the dUTP method. The average insert size for the paired-end libraries was ∼100 ± 50 bp. Next, we performed the paired-end 2 × 150 bp sequencing on an Illumina Novaseq^{TM} 6000 platform at the LC-BIO Bio-tech Ltd. (Hangzhou, China) following the vendor's recommended protocol.

The Expression of CD276/CD34 in CRC Tissues Was Detected by Immunohistochemistry

The paraffin sections of CRC tissues were prepared, each containing two parts of the same tumor tissue, and were baked at 60°C for 120 min for dewaxing and hydration. Antigen repair was carried out under high temperature and pressure. CD274/CD34 antibody from Abcam was used, and the sections were sealed after staining. The target area of the tissue was selected with the Eclipse CI-L photo microscope for 200-fold imaging. During imaging, the tissue was tried to fill the whole field of vision to ensure the consistent background light of each photo. After imaging, Image-Pro Plus 6.0 analysis software was used to measure the cumulative optical density (IOD) of three field positives in each section with pixel area as the standard unit, as well as the corresponding tissue pixel Area; the AREAL DENSITY = IOD/Area.

Analysis of m6A Features of Differentially Immune Genes Between CRC and Paired PCa Issues

First, Cutadapt and perl scripts in house were used to remove the reads that contained adaptor contamination, low-quality bases, and undetermined bases. Then, sequence quality was verified using Fast QC. We used HISAT2 to map reads to the genome of Homo sapiens (Version: v96) with default parameters. Mapped reads of IP and input libraries were provided for R package exomePeak, which identified m6A peaks with bed or bam format that could be adapted for visualization on the UCSC genome browser or IGV software[1]. MEME and HOME were used for *de novo* and known motif finding followed by localization of the motif with respect to peak summit by perl scripts in house. Called peaks were annotated by intersection with gene architecture using ChIPseeker. Next, StringTie was used to perform expression level for all mRNAs from input libraries by calculating FPKM {FPKM = [total_exon_fragments/mapped_reads (millions) × exon_length (kB)]}. The differentially expressed mRNAs were selected with log2 (fold change) > 1 or < −1 and $P < 0.05$ by R package edgeR.

[1]http://www.igv.org/

Target Genes Were Obtained by Matching MeRIP-Seq Results With MSIgDB Database

MSIgDB database[2] was used to obtain immune genes match MeRIP sequencing results, and get immune genes with m6A differences peak as target genes, eventually resulting in Venn diagram.

The Data Mining of Target Gene Is Based on the TCGA Database

Based on R 4.0.1[3], the TCGA[4] Level 3 RNA sequencing data and relevant clinical information of patients were downloaded. The R package "Consensus Cluster Plus" was used to Cluster all TCGA CRC patients based on the target gene. Cumulative distribution function and consistency matrix were used to determine the optimal clustering. K-M survival curves were used to compare the survival of different clusters. The gene sets of 29 kinds of immune cells were downloaded from the MSIGDB database, and an SSGSEA score was used for 29 kinds of immune cells in each sample. Ciborsort evaluated the infiltration of immune cells in different clusters, and the infiltration of different immune cells in different stages was compared. An estimate algorithm was used to calculate tumor purity in different clusters, and classical immune checkpoint molecular expression in different clusters was compared. GSEA enrichment analysis was performed on cluster samples. Finally, the target gene, GSEA optimally enriched GO, and KEGG entry gene was uploaded to the STRING database to construct a protein-protein interaction (PPI) network. A $P < 0.05$ was considered statistically significant.

RESULTS

Patient Clinical Information

Among 40 patients with CRC included in the study, 18 were female with an average age of 62.39 ± 7.8 years, and 22 were male with an average age of 64.86 ± 9.44 years. There were 2 cases of TNM Stage I, 14 cases of Stage II, 12 cases of Stage II, and 12 cases of Stage IV. The detailed clinical characteristics of the subjects are shown in **Table 1**.

TABLE 1 | Clinical characteristics of the studied patients.

Id	Gender	Age	Stage
Patient 1	Female	55	Stage II
Patient 2	Female	62	Stage IV
Patient 3	Male	71	Stage I
Patient 4	Female	54	Stage III
Patient 5	Male	63	Stage IV
Patient 6	Male	66	Stage II
Patient 7	Male	78	Stage II
Patient 8	Male	67	Stage II
Patient 9	Female	49	Stage III
Patient 10	Female	77	Stage IV
Patient 11	Male	56	Stage III
Patient 12	Male	79	Stage III
Patient 13	Female	67	Stage II
Patient 14	Female	73	Stage II
Patient 15	Male	71	Stage III
Patient 16	Male	73	Stage III
Patient 17	Male	69	Stage IV
Patient 18	Female	63	Stage II
Patient 19	Female	67	Stage IV
Patient 20	Female	66	Stage IV
Patient 21	Male	64	Stage II
Patient 22	Female	71	Stage II
Patient 23	Female	65	Stage III
Patient 24	Male	59	Stage I
Patient 25	Male	67	Stage IV
Patient 26	Female	54	Stage II
Patient 27	Male	70	Stage II
Patient 28	Male	55	Stage III
Patient 29	Male	59	Stage III
Patient 30	Male	76	Stage IV
Patient 31	Male	65	Stage II
Patient 32	Female	67	Stage IV
Patient 33	Female	59	Stage IV
Patient 34	Female	54	Stage III
Patient 35	Male	46	Stage II
Patient 36	Female	54	Stage IV
Patient 37	Male	43	Stage III
Patient 38	Male	72	Stage III
Patient 39	Male	58	Stage IV
Patient 40	Female	66	Stage II

Acquire Target Gene CD34/CD276

Quality control analysis was performed on the sequencing RAW data of CRC samples, and the quality control results were shown in **Supplementary Material 1**. Using the peak-calling software, the R package exomePeak performed a peak scan across the whole genome and calculated the differences between the peak groups. All regions with $P < 0.05$ were considered as a peak, and ChIPseeker was used to annotate these peaks. Finally, 111 genes with m6A differential peaks were obtained. The 330 immune-related genes were obtained from the MSIgDB database, after which the target genes were obtained by the intersection (**Figure 1**).

Correlation Between Expression of CD34/CD276 and m6A Factor

Twenty regulatory factors of m6A RNA methylation were collected from the literature, and the correlation between CD34/CD276 and their expression was analyzed using the TCGA database, test for association between paired genes, using one of Pearson's product moment

[2]http://www.gsea-msigdb.org/gsea/index.jsp

[3]https://cran.r-project.org/

[4]http://cancergenome.nih.gov

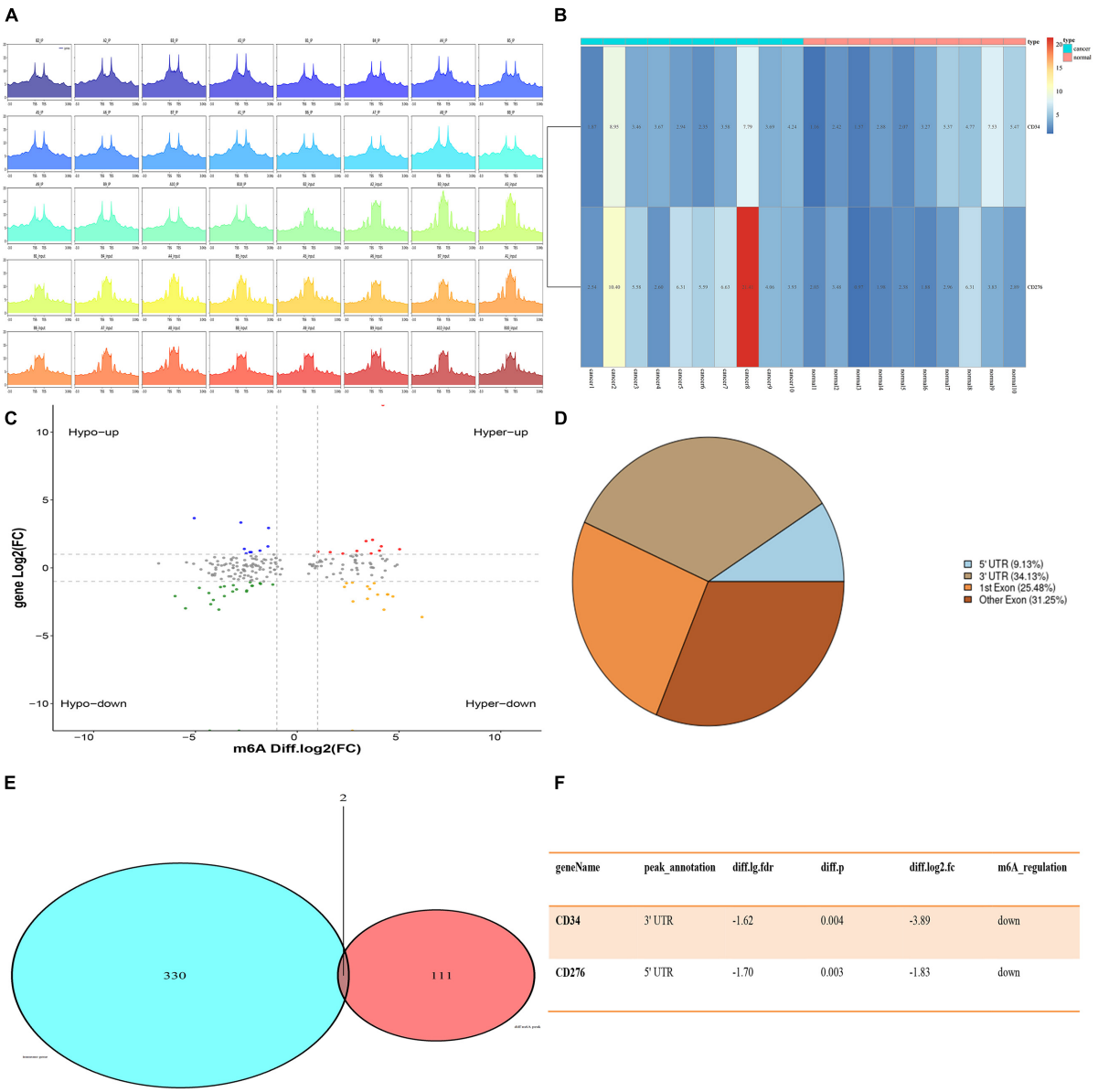

FIGURE 1 | Expression of CD34/CD276 and m6A modification in CRC. **(A)** Peak statistics of clinical sequencing samples. **(B)** Compared with paracancerous tissues, the expression of CD276 was up-regulated in CRC tissue ($P < 0.05$), while the expression of CD34 did not significantly change ($P > 0.05$). **(C)** Difference m6A peak Volcano map. **(D)** Difference m6A peak calling. **(E,F)** CD34/CD276 is down-regulated m6A peak immune genes in CRC.

correlation coefficient, The results were filtered with $P < 0.001$ (**Figure 2**).

Based on CD34/CD276, 472 CRC Samples in TCGA Were Clustered for Survival Analysis

Cluster analysis was performed on 472 patients in TCGA database using R package "ConsensusClusterPlus" according to the expression levels of CD34 and CD276, Consensus Clustering takes a subsample from a set of microarray data and determines a cluster with a specified number of clusters (k). For each k, the paired consensus values are calculated, that is, the proportion of the number of occurrences of two samples in the same subsample in the same cluster, and stored in a symmetric consensus matrix. Consensus matrices are summarized in several graphical presentations to enable users to determine a reasonable number and membership of clusters. Cluster analysis was performed on 472 patients in the TCGA database according to the expression levels of CD34 and CD276 (Consensus Cumulative Distribution Function, CDF) results show that: when $k = 2$, the consistency and clustering confidence reach the maximum, and survival analysis was performed on patients with different cluster samples. Kaplan-Meier method was used to estimate the survival time distribution

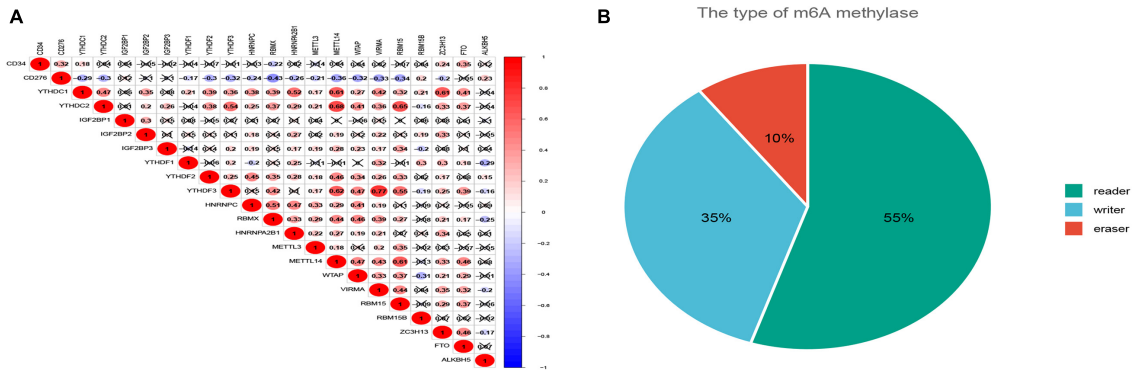

FIGURE 2 | The co-expression of CD34/CD276 and m6A regulator in CRC. **(A)** The expression level of CD34 was positively correlated with the expression of FTO, while the expression level of CD276 was positively correlated with the expression of ALKBH5. **(B)** The regulatory factors of m6A were classified by function.

of different clusters, which was presented in the form of survival curve to analyze the survival characteristics, and the survival curve between the two groups was tested by Log Rank, The results showed that the survival rate of Cluster1 group was higher than that of Cluster2 group ($P < 0.05$) (**Figure 3**).

The Immune Assessment Was Conducted for Different Cluster Samples

Twenty-nine immune-related genes were collected from the MSIgDB database to construct GMT files, and R package "GSVA" was used to evaluate the immunity of each tumor sample and then the enrichment scores were calculated. After normalizing the results, R Package "limma" was used for difference comparison and heat map display. The results showed that the immune score of Cluster1 group was lower than that of Cluster2 group ($P < 0.05$), Cluster1 was the group with low immune score (Immunity_L) and Cluster2 was the group with high immune score (Immunity_H) (**Figure 4**).

Immune Microenvironment Assessment of Different Cluster Samples

The "Estimate" R package (Estimation of Stromal and Immune cells in Malignant Tumor tissues using Expression data) was used to evaluate the tumor immune microenvironment (Gene expression score of Stromal cells) and tumor purity of different groups, The results showed that compared with the Immunity_L group, the purity of tumors in the Immunity_H group was significantly decreased ($P < 0.001$) and the content of stromal cells was increased ($P < 0.05$) (**Figure 5**).

GSEA Enrichment Analysis Was Performed for Different Cluster Samples and Building of PPI Network

GSEA enrichment analysis was performed on tumor samples based on cluster grouping, according the normalized enrichment score (NES) and the estimated probability that the normalized enrichment score represents a false positive finding (FDR), the optimal enrichment KEGG pathway was obtained, and genes contributing to the optimally enriched KEGG signaling pathway were selected for protein-protein interaction analysis with CD34/CD276 through STRING online database, Maximal Clique Centrality (MCC) method was used to calculate the top 10 key proteins in the PPI network (using CytoHubba plug-in of Cytoscape software) (**Figure 6**).

Immunohistochemistry Was Used to Evaluate the Correlation Between CD34/CD276 Expression and CRC

The expression of CD34/CD276 in 40 CRC samples was measured by using the immunochemical test. The results showed that the expression of CD34/CD276 was detected in all samples, and the level of CD34/CD276 was significantly reduced in stage I and II compared with that in stage III and IV ($P < 0.001$) (**Figure 7**).

DISCUSSION

In this paper, we revealed that the immune gene CD34/CD276 could be combined as a group of molecular markers for the prognosis of CRC. We also analyzed the signal pathway and molecular mechanism of immune escape of CRC by down-regulation of m6A modification.

Many studies have reported a close relationship between the dynamic changes of M6A modification and tumor immune escape. Our results showed that in CRC, the immune gene CD34/CD276m6A modification was significantly down-regulated, the expression of CD276mRNA was up-regulated, while the expression of CD34mRNA showed no significant change. Further bioinformatics analysis based on the TCGA database revealed that cluster analysis of tumor samples based on CD34/CD276 mRNA expression could well predict the survival status of patients. CD34 antigen is a kind of cell surface glycoprotein belonging to the one-way transmembrane protein family, which is usually regarded as a marker of hematopoietic progenitor cells and has been previously used in cell therapy of various blood diseases (Hsieh et al., 2020).

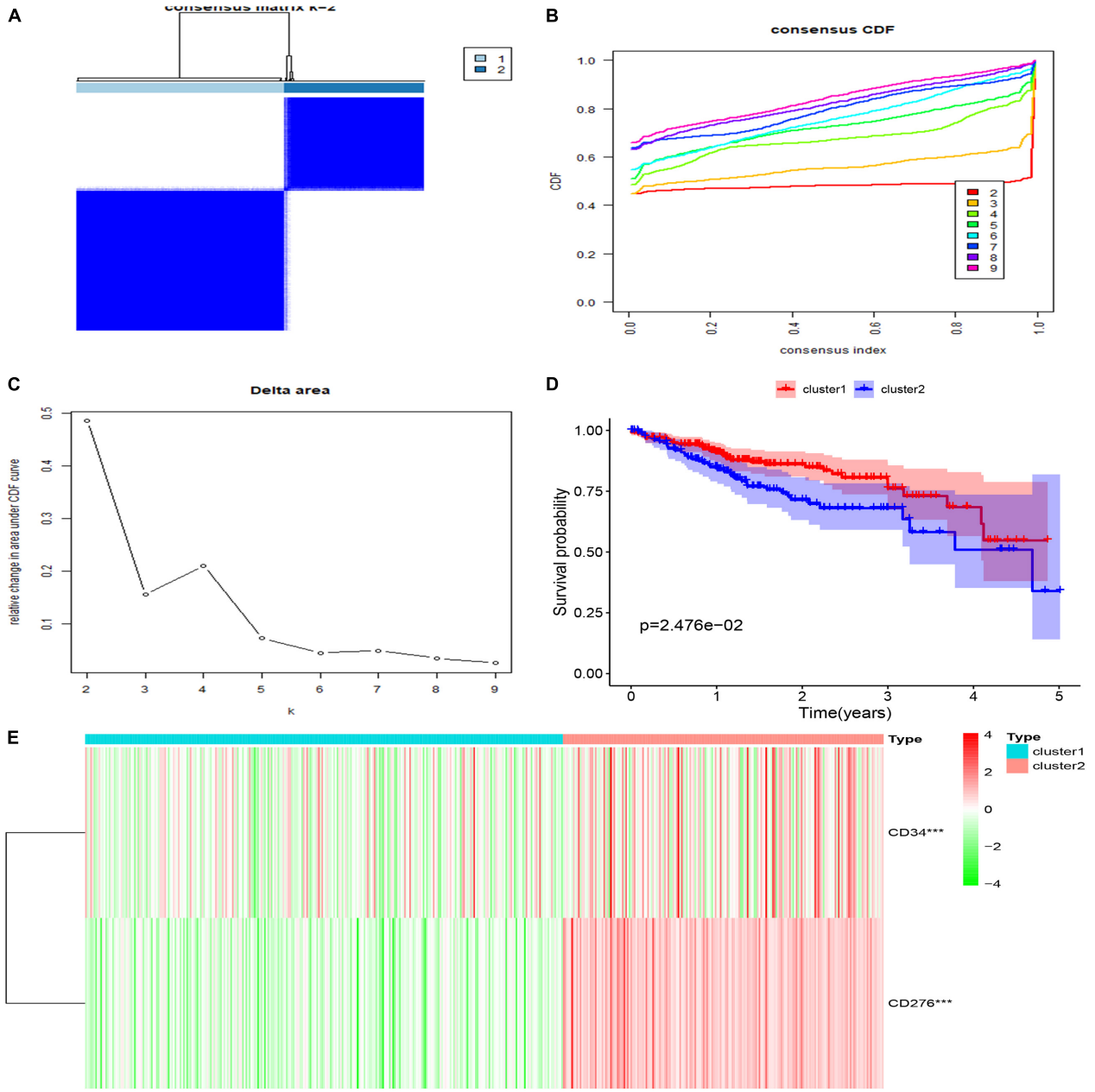

FIGURE 3 | Clustering and survival analysis based on TCGA database. **(A–C)** The results of consistent cluster matrix, cumulative distribution function curve, and relative change of area under the curve showed that the expression of CD34/CD276 could be divided into two types of CRC samples. **(D)** K-M survival curve showed that patients with Cluster1 showed higher survival ability than those with Cluster2 ($P < 0.05$). **(E)** Compared with Cluster1, the expression of CD34/CD276 was up-regulated in Cluster2 (***$P < 0.001$).

The evolutionary conservation of its gene sequence and protein structure in many species highlights the relevance. So far, this molecule has an important role in various cellular processes, including cell adhesion, signal transduction, and maintenance of progenitor phenotype (Inda et al., 2007; Sidney et al., 2014). However, understanding the origin of molecular development, immune regulation, and other related functions is far from complete (Díaz-Flores et al., 2020). CD276 is a new member of the B7 family of costimulatory molecules (Sun et al., 2013). It is considered as an immune costimulatory/inhibitory factor regulating the interaction between tumor and immune system (Arigami et al., 2010). The ligand of CD276 and its immunomodulatory effect have not been fully determined (Stodden et al., 2008). Although CD34/CD276 is widely expressed in mRNA in CRC, the expression of the protein is limited in steady-state, which indicates that there is an important

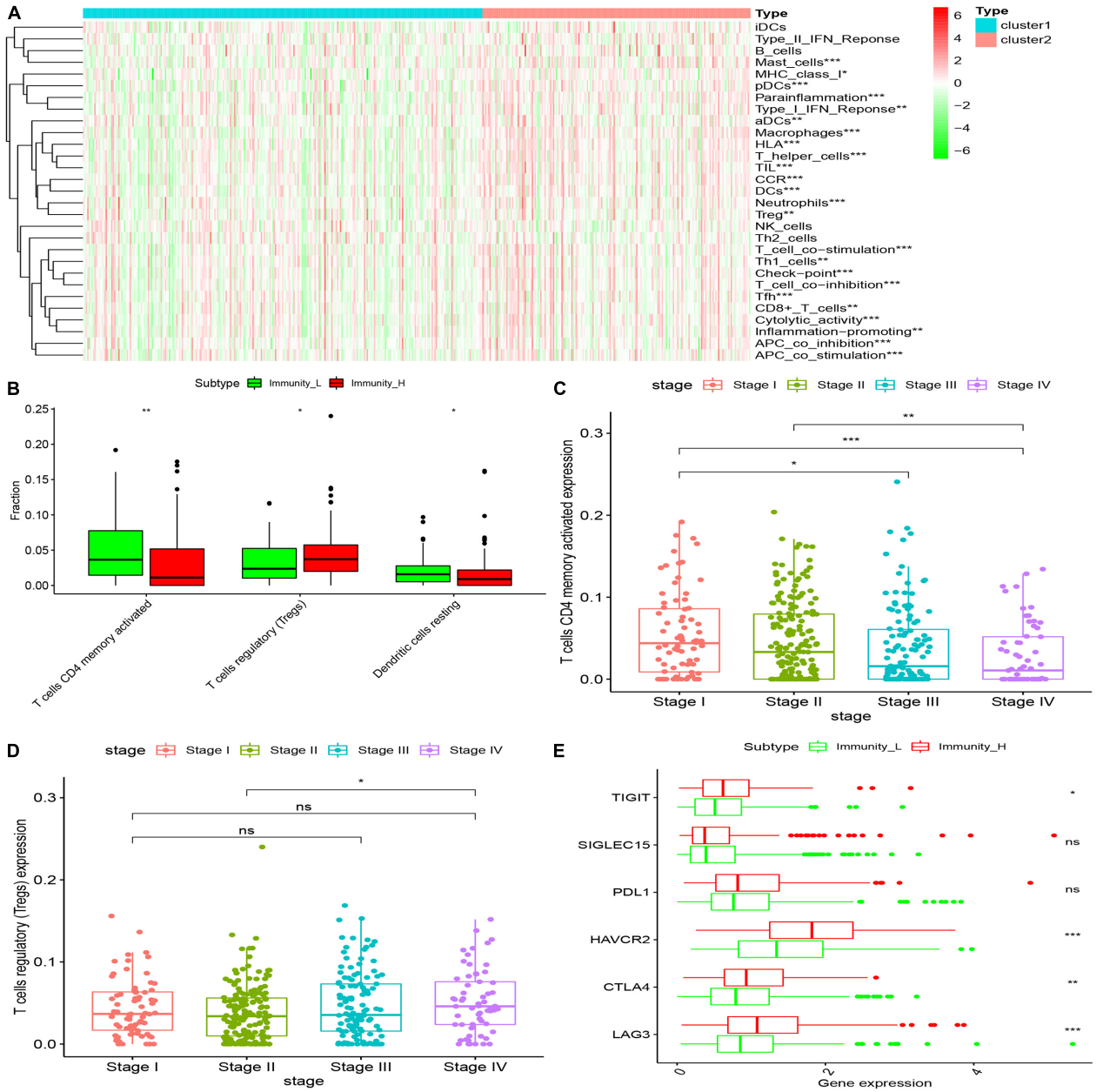

FIGURE 4 | The immune components of different clusters were evaluated. **(A)** The results of SSGSEA showed that the low expression of CD34 and CD276 in the Cluster1 group was the low immune score group, while the high expression of CD34 and CD276 in the Cluster2 group was the high immune score group (*$P < 0.05$, **$P < 0.01$, ***$P < 0.001$). **(B)** The immune cell composition of Cluster1 and Cluster2 was further analyzed using the Ciborsort R package. The results showed that in Cluster2, the ratio of activated memory T cellsCD4 and dendritic resting cells was lower than that in Cluster1 (*$P < 0.05$, **$P < 0.01$), while the ratio of regulatory T cells was relatively higher in Cluster1 (*$P < 0.05$, **$P < 0.01$, ***$P < 0.001$). **(C,D)** The infiltration level of activated memory T cellsCD4 was negatively correlated with CRC TNM stage, the infiltration level of T cells (Tregs) was positively correlated with tumor TNM stage (*$P < 0.05$). **(E)** There was no significant difference in the expression of immune checkpoint PDL1 and SiGLEC15 between the groups with high and low immune scores ($P > 0.05$); the expression levels of TIGIT and CTLA4 were up-regulated in the group with high immune scores, and the expression levels of HAVCR2 and LAG3 were significantly up-regulated in the group with high immune scores (*$P < 0.05$, **$P < 0.01$, ***$P < 0.001$).

post-transcriptional or post-translational regulatory mechanism (Kraan et al., 2014; Picarda et al., 2016; Kapoor et al., 2020). Our study confirmed that the expression of CD34 was positively correlated with FTO expression, while the expression of CD276 was positively correlated with the expression of ALKBH5. FTO/ALKBH5 was confirmed as the key "eraser" of m6A (Huang et al., 2020). The m6A modification site of CD34 is located at 3UTR, which may be related to its stability, translation, nuclear

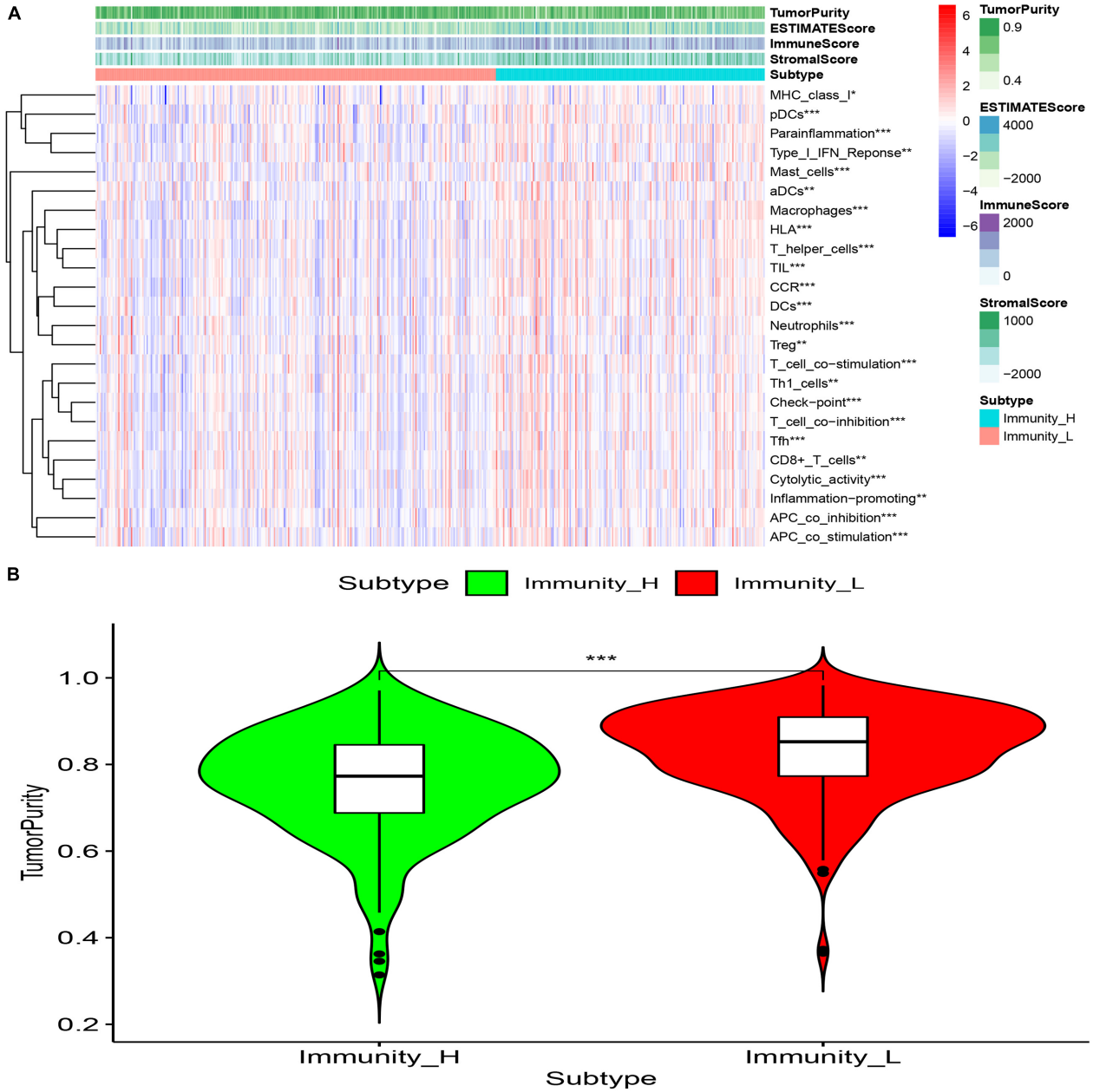

FIGURE 5 | (A) Compared with the low immune score group, high immune array Stromal Score, Immune Score, ESTIMATE Score were higher (*$p < 0.05$; **$p < 0.01$; ***$p < 0.001$). **(B)** Compared with the low immune score group, the tumor purity of the high immune array was significantly reduced (***$P < 0.001$).

output, and cellular localization (Ke et al., 2015; Yue et al., 2018), while the m6A modification site of CD276 is located at 5UTR. It is possible that the down-regulation of m6A modification affects its ability to translate or bind to a specific RBA binding protein (RBP) (Bugaut and Balasubramanian, 2012).

The ssGSEA analysis of tumor samples with high and low expression of CD34/CD276 showed that the tumor samples with high expression of CD34/CD276 had a higher immune score, and ssGSEA was a single sample GSEA algorithm. For each sample, the immune score based on ssGSEA was obtained using immune-related gene signature and expression data. Nonetheless, the high immune score could not inhibit tumor growth, but it promoted tumor immune escape. This partly explains the lower viability of patients with high immune scores. CIBERSORT is a widely used method for high-throughput characterization of tumor-infiltrating immune cells from complex tissues (Chen et al., 2018). The temporal and spatial distribution of immune cells in the stroma around the tumor strongly affects the prognosis and treatment response. Nevertheless, this is related to the type of infiltrating immune

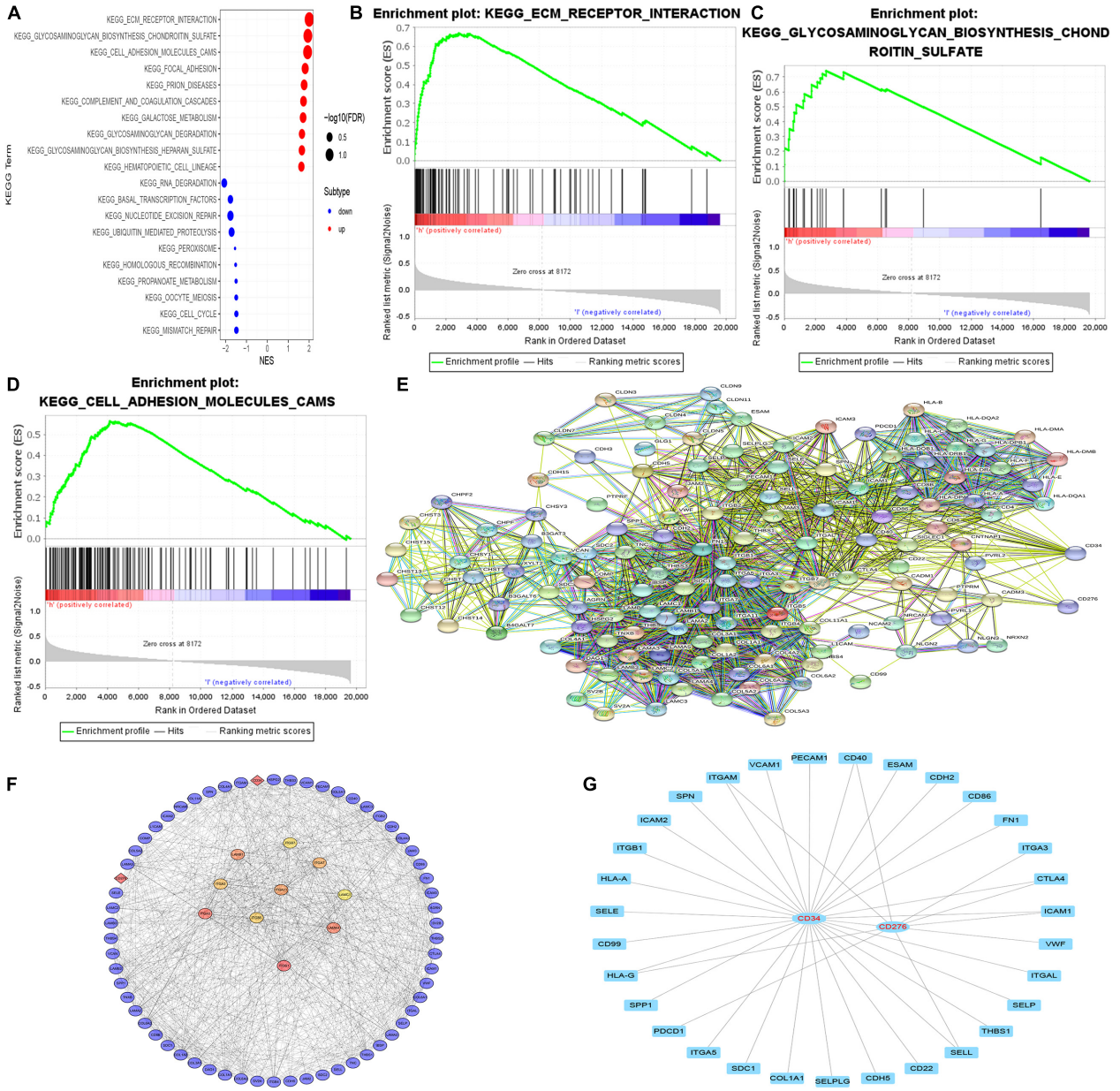

FIGURE 6 | GSEA enrichment analysis and PPI network. **(A–D)** According to both FDR and NES as screening conditions, ECM receptor interaction, glycosaminoglycan biosynthesis chondroitin sulfate, and Cell adhesion molecules (CAMS) are the best KEGG enrichment items. **(E)** The string online database was used to construct a PPI network for all genes in the optimally enriched KEGG signaling pathway (high confidence = 0.7). **(F)** MCC method was used to calculate the top 10 key proteins in the PPI network. **(G)** The molecule that acts directly with CD34/CD276.

cells because it is regulated by the unique immune editing mode of the tumor (Dunn et al., 2002). The infiltration level of regulatory T cells (Tregs) was up-regulated in the group with high expression of CD34/CD276. In TME, Tregs can be induced and differentiated by traditional T cells with a strong immunosuppressive function and promote the occurrence and development of tumors, which is the key factor of tumor immune escape (Li et al., 2020). On the other hand, the infiltration of activated memory Tcells CD4 (CD4+T cells), which promote tumor immunity, is down-regulated. CD4+T cells themselves are not the main immune subtypes of treatment, but the participation of CD4+T cells is also related to the production of effective anti-tumor response (Tay et al., 2021). Previous studies in mouse models have shown that effective response of CD8+T cells to MHCII-negative tumors requires the "helper function" of CD4+T cells. CD4+ helper T cells can inhibit the expression of inhibitory receptors in CD8+T cells and are essential for the formation of functional CD8+ memory T cells (Zhai et al., 2020). We also

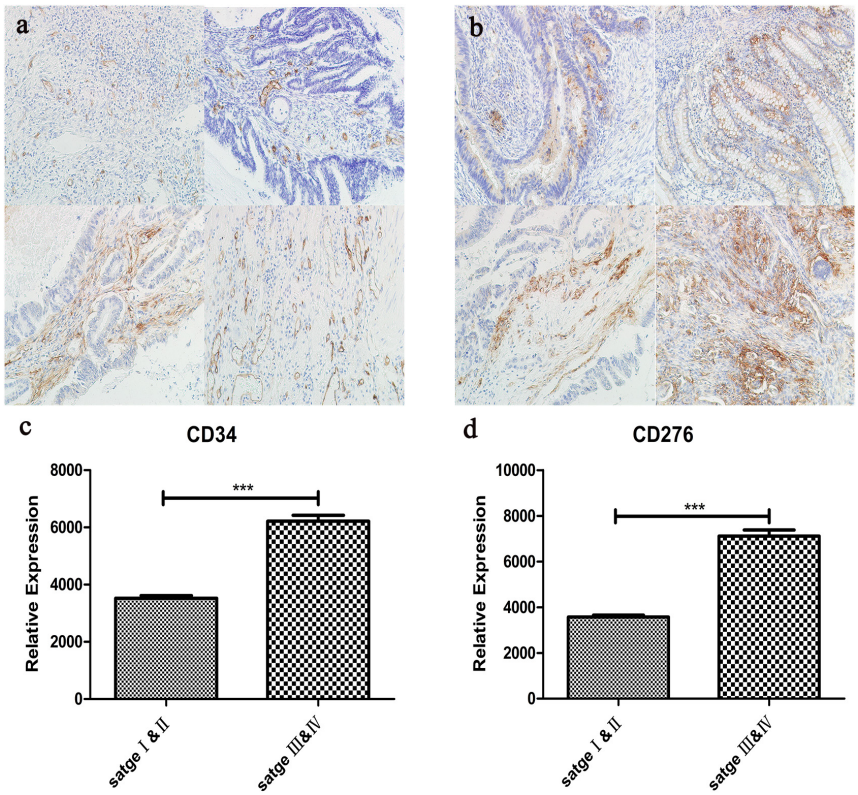

FIGURE 7 | (a) The expression of CD34 in CRC tissues was detected by immunohistochemistry, upper left:stage I, upper right:stage II, left lower:stage III, lower right:stage IV. **(b)** The expression of CD276 in CRC tissues was detected by immunohistochemistry, upper left:stage I, upper right:stage II, left lower:stage III, lower right:stage IV. **(c)** Compared with stage I and II, CD34 expression was significantly up-regulated in stage III and IV (***$P < 0.001$). **(d)** Compared with stage I and II, CD276 expression was significantly up-regulated in stage III and IV (***$P < 0.001$).

confirmed that the invasion of activated memory T cellsCD4 was negatively correlated with the TNM stage of CRC, while Tregs was positively correlated, which indicated that the dynamic changes of activated memory Tcells CD4 and Tregs are the key factors affecting the immune escape of CRC. In addition, we also evaluated the expression of immune checkpoints in both groups, where LAG3, HAVCR2, CTLA4, and TICIT were up-regulated in the group with high expression of CD34/CD276 (Wilky, 2019; He and Xu, 2020), which further confirmed that the high expression of CD34/CD276 drives immune escape in CRC.

The high content of unknown mixtures still limits the practicability of evaluating tumor-infiltrating immune cells. Estimate, also known as "estimating stroma and immune cells of malignant tumors using expression data," is an algorithm for describing TME. The algorithm infers the infiltration of stromal cells and immune cells and evaluates tumor purity (Yoshihara et al., 2013). We found that the microenvironment score, matrix score, and immune score were higher, the tumor purity was significantly decreased, and the matrix content was increased in the group with high expression of CD34/CD276. This suggests that the high expression of CD34/CD276 may promote a more complex tumor extracellular microenvironment, thus promoting the immune escape of CRC, which is consistent with the best KEGG pathway for GSEA enrichment analysis. ECM receptor interaction, glycosaminoglycan biosynthesis chondroitin sulfate, and cell adhesion molecules (CAMs) signaling pathways may be the potential mechanisms of CD34/CD276 promoting immune escape of CRC. Tumor progression is characterized by dense collagen matrix accumulation and dynamic reorganization necessary to adapt to the growing invasive mass (Yamauchi et al., 2020).

In TME, T cells need to compress their nuclei in order to migrate to the sclerotic matrix, affecting gene expression, and cell mobility. In addition, nuclear compression caused by matrix stiffness leads to multiple damages to the nucleus and cell membrane during a forced passage, which eventually leads to T cell death. Intact extracellular matrix (ECM) structure and interstitial components are powerful tools for predicting the efficacy of cancer treatment (Hallmann et al., 2015; Meurette and Mehlen, 2018). ECM is a collection of interacting molecules, which is mainly composed of collagen, fibronectin, and elastin that form a matrix fiber network, and are also composed of hyaluronic acid (HA), tendon proteins, and glycoproteins containing glycosaminoglycan (GAG), thus affecting cell behavior and biomechanical and biochemical properties of the matrix (Pudełko et al., 2019; Le et al., 2020). Because cell adhesion receptors are connected to signal transduction pathways, these cell-cell interactions with ECM

regulate cell phenotype, proliferation, differentiation, survival, and migration. Therefore, the changes in the expression of cell adhesion molecules and their ligands directly affect immune escape and metastasis. The abnormal expression of adhesion molecules can prevent the immune system from touching the whole tumor, a process known asendothelial anergy. This is an effective mechanism used by tumors to prevent immune cells from metastasizing to the tumor site (Darby et al., 2014; Nadanaka et al., 2018; Harjunpää et al., 2019; Läubli and Borsig, 2019; Druzhkova et al., 2020). Chondroitin sulfate (CS), as a representative sulfated glycosaminoglycan (GAG), participates in tumor immune regulation by binding to various cytokines and growth factors, cell surface receptors, adhesion molecules, enzymes, or fibrous glycoproteins in ECM, such as direct interaction with Toll-like receptors in the TME, and mediated macrophage activation. Binding to IL-8 can protect chemokines from proteolysis to stimulate angiogenesis while binding to various types of collagen can promote participation in immune cell adhesion and chemotaxis (Jalkanen and Jalkanen, 1992; Tazzyman et al., 2013; Silver and Silver, 2014; Wu et al., 2018).

We also used an online string database to construct a PPI network for genes in the optimal enrichment pathway and label 40 genes of core nodes for further exploration. While constructing the PPI network, we added CD34/CD276 gene to further evaluate its synergism. Our results showed a direct interaction between CD34/CD276 and ITGAM, CD40, IGTA3, CTLA4, ICAM1, VWF, SELL, HLA-G, and PDCD1. As an important immune checkpoint, CTLA4 has been confirmed to be significantly up-regulated in the group with high expression of CD34/CD276. This also suggests that CD34/CD276 has a synergistic effect on promoting immune escape of CRC. Finally, we further confirmed the clinical relationship between CD34/CD276 protein and CRC by IHC.

CONCLUSION

In conclusion, through the clinical sample MeRIP-seq combined with MsigDB database and TGCA database data mining, we determined that CD34/CD276 can be combined as a molecular marker for predicting the viability inpatients with CRC, which may promote the immune microenvironment remodeling of CRC and ultimately promote immune escape by relying on the down-regulation of m6A modification. Although the molecular mechanism still needs to be verified by additional experiments, our findings provide a new insight into m6A modification for promoting the immune escape of CRC. Our results can provide new clues for the mechanism of CRC progression.

DATA AVAILABILITY STATEMENT

The raw data used in this study are available in the GEO database, accession no. GSE179042 (https://www.ncbi.nlm.nih.gov/geo/query/acc.cgi?acc=GSE179042, token uzahsmakzvqrxqt).

ETHICS STATEMENT

The studies involving human participants were reviewed and approved by the Yan'an Hospital Affiliated of Kunming Medical University. The patients/participants provided their written informed consent to participate in this study.

AUTHOR CONTRIBUTIONS

YRZ, HZ, and JS carried out the studies, participated in collecting the data, and drafted the manuscript. AG and YKZ performed the statistical analysis and participated in its design. ZH and RL participated in the acquisition, analysis, or interpretation of the data and draft the manuscript. All authors read and approved the final manuscript.

FUNDING

This study was supported by the Joint Fund of Yunnan Provincial Department of Science and Technology and Kunming Medical University [2018FE001 (-095)].

ACKNOWLEDGMENTS

We would like to thank all study participants who were enrolled in this study.

SUPPLEMENTARY MATERIAL

The Supplementary Material for this article can be found online at: https://www.frontiersin.org/articles/10.3389/fcell.2021.715674/full#supplementary-material

REFERENCES

Arigami, T., Narita, N., Mizuno, R., Nguyen, L., Ye, X., Chung, A., et al. (2010). B7-h3 ligand expression by primary breast cancer and associated with regional nodal metastasis. *Ann. Surg.* 252, 1044–1051. doi: 10.1097/SLA.0b013e3181f1939d

Bugaut, A., and Balasubramanian, S. (2012). 5'-UTR RNA G-quadruplexes: translation regulation and targeting. *Nucleic Acids Res.* 40, 4727–4741. doi: 10.1093/nar/gks068

Chen, B., Khodadoust, M. S., Liu, C. L., Newman, A. M., and Alizadeh, A. A. (2018). Profiling tumor infiltrating immune cells with CIBERSORT. *Methods Mol. Biol.* 1711, 243–259. doi: 10.1007/978-1-4939-7493-1_12

Chong, W., Shang, L., Liu, J., Fang, Z., Du, F., Wu, H., et al. (2021). m(6)A regulator-based methylation modification patterns characterized by distinct tumor microenvironment immune profiles in colon cancer. *Theranostics* 11, 2201–2217. doi: 10.7150/thno.52717

Clara, J. A., Monge, C., Yang, Y., and Takebe, N. (2020). Targeting signalling pathways and the immune microenvironment of cancer stem cells - a clinical update. *Nat. Rev. Clin. Oncol.* 17, 204–232. doi: 10.1038/s41571-019-0293-2

Darby, I. A., Laverdet, B., Bonté, F., and Desmoulière, A. (2014). Fibroblasts and myofibroblasts in wound healing. *Clin. Cosmet. Investig. Dermatol.* 7, 301–311. doi: 10.2147/ccid.s50046

Dekker, E., Tanis, P. J., Vleugels, J. L. A., Kasi, P. M., and Wallace, M. B. (2019). Colorectal cancer. *Lancet* 394, 1467–1480. doi: 10.1016/s0140-6736(19)32319-0

Díaz-Flores, L., Gutiérrez, R., García, M. P., González-Gómez, M., Díaz-Flores, L. Jr., Álvarez-Argüelles, H., et al. (2020). Presence/absence and specific location of resident CD34+ stromal cells/telocytes condition stromal cell development in repair and tumors. *Front. Cell. Dev. Biol.* 8:544845. doi: 10.3389/fcell.2020.544845

Druzhkova, I., Shirmanova, M., Ignatova, N., Dudenkova, V., Lukina, M., Zagaynova, E., et al. (2020). Expression of EMT-Related genes in hybrid E/M colorectal cancer cells determines fibroblast activation and collagen remodeling. *Int. J. Mol. Sci.* 21:8119. doi: 10.3390/ijms21218119

Dunn, G. P., Bruce, A. T., Ikeda, H., Old, L. J., and Schreiber, R. D. (2002). Cancer immunoediting: from immunosurveillance to tumor escape. *Nat. Immunol.* 3, 991–998. doi: 10.1038/ni1102-991

Hallmann, R., Zhang, X., Di Russo, J., Li, L., Song, J., Hannocks, M. J., et al. (2015). The regulation of immune cell trafficking by the extracellular matrix. *Curr. Opin. Cell. Biol.* 36, 54–61. doi: 10.1016/j.ceb.2015.06.006

Han, D., Liu, J., Chen, C., Dong, L., Liu, Y., Chang, R., et al. (2019). Anti-tumour immunity controlled through mRNA m(6)A methylation and YTHDF1 in dendritic cells. *Nature* 566, 270–274. doi: 10.1038/s41586-019-0916-x

Hanahan, D., and Weinberg, R. A. (2011). Hallmarks of cancer: the next generation. *Cell* 144, 646–674. doi: 10.1016/j.cell.2011.02.013

Harjunpää, H., Llort Asens, M., Guenther, C., and Fagerholm, S. C. (2019). Cell adhesion molecules and their roles and regulation in the immune and tumor microenvironment. *Front. Immunol.* 10:1078. doi: 10.3389/fimmu.2019.01078

He, X., and Xu, C. (2020). Immune checkpoint signaling and cancer immunotherapy. *Cell Res.* 30, 660–669. doi: 10.1038/s41422-020-0343-4

Hsieh, M. J., Chiu, T. J., Lin, Y. C., Weng, C. C., Weng, Y. T., Hsiao, C. C., et al. (2020). Inactivation of APC induces CD34 upregulation to promote epithelial-mesenchymal transition and cancer stem cell traits in pancreatic cancer. *Int. J. Mol. Sci.* 21:4473. doi: 10.3390/ijms21124473

Huang, H., Weng, H., and Chen, J. (2020). m(6)A modification in coding and non-coding RNAs: roles and therapeutic implications in cancer. *Cancer Cell* 37, 270–288. doi: 10.1016/j.ccell.2020.02.004

Inda, A. M., Andrini, L. B., García, M. N., García, A. L., Fernández Blanco, A., Furnus, C. C., et al. (2007). Evaluation of angiogenesis with the expression of VEGF and CD34 in human non-small cell lung cancer. *J. Exp. Clin. Cancer Res.* 26, 375–378.

Jalkanen, S., and Jalkanen, M. (1992). Lymphocyte CD44 binds the COOH-terminal heparin-binding domain of fibronectin. *J. Cell. Biol.* 116, 817–825. doi: 10.1083/jcb.116.3.817

Kapoor, S., Shenoy, S. P., and Bose, B. (2020). CD34 cells in somatic, regenerative and cancer stem cells: developmental biology, cell therapy, and omics big data perspective. *J. Cell. Biochem.* 121, 3058–3069. doi: 10.1002/jcb.29571

Kaymak, I., Williams, K. S., Cantor, J. R., and Jones, R. G. (2021). Immunometabolic interplay in the tumor microenvironment. *Cancer Cell* 39, 28–37. doi: 10.1016/j.ccell.2020.09.004

Ke, S., Alemu, E. A., Mertens, C., Gantman, E. C., Fak, J. J., Mele, A., et al. (2015). A majority of m6A residues are in the last exons, allowing the potential for 3' UTR regulation. *Genes Dev.* 29, 2037–2053. doi: 10.1101/gad.269415.115

Kraan, J., van den Broek, P., Verhoef, C., Grunhagen, D. J., Taal, W., Gratama, J. W., et al. (2014). Endothelial CD276 (B7-H3) expression is increased in human malignancies and distinguishes between normal and tumour-derived circulating endothelial cells. *Br. J. Cancer* 111, 149–156. doi: 10.1038/bjc.2014.286

Läubli, H., and Borsig, L. (2019). Altered cell adhesion and glycosylation promote cancer immune suppression and metastasis. *Front. Immunol.* 10:2120. doi: 10.3389/fimmu.2019.02120

Le, C. C., Bennasroune, A., Langlois, B., Salesse, S., Boulagnon-Rombi, C., Morjani, H., et al. (2020). Functional interplay between collagen network and cell behavior within tumor microenvironment in colorectal cancer. *Front. Oncol.* 10:527. doi: 10.3389/fonc.2020.00527

Li, C., Jiang, P., Wei, S., Xu, X., and Wang, J. (2020). Regulatory T cells in tumor microenvironment: new mechanisms, potential therapeutic strategies and future prospects. *Mol. Cancer* 19:116. doi: 10.1186/s12943-020-01234-1

Lin, S., Xu, H., Zhang, A., Ni, Y., Xu, Y., Meng, T., et al. (2020). Prognosis analysis and validation of m(6)A signature and tumor immune microenvironment in Glioma. *Front. Oncol.* 10:541401. doi: 10.3389/fonc.2020.541401

Liu, N., Dai, Q., Zheng, G., He, C., Parisien, M., and Pan, T. (2015). N(6)-methyladenosine-dependent RNA structural switches regulate RNA-protein interactions. *Nature* 518, 560–564. doi: 10.1038/nature14234

Meurette, O., and Mehlen, P. (2018). Notch signaling in the tumor microenvironment. *Cancer Cell* 34, 536–548. doi: 10.1016/j.ccell.2018.07.009

Nadanaka, S., Kinouchi, H., and Kitagawa, H. (2018). Chondroitin sulfate-mediated N-cadherin/β-catenin signaling is associated with basal-like breast cancer cell invasion. *J. Biol. Chem.* 293, 444–465. doi: 10.1074/jbc.M117.814509

Picarda, E., Ohaegbulam, K. C., and Zang, X. (2016). Molecular pathways: targeting B7-H3 (CD276) for human cancer immunotherapy. *Clin. Cancer Res.* 22, 3425–3431. doi: 10.1158/1078-0432.ccr-15-2428

Pudełko, A., Wisowski, G., Olczyk, K., and Koźma, E. M. (2019). The dual role of the glycosaminoglycan chondroitin-6-sulfate in the development, progression and metastasis of cancer. *Febs J.* 286, 1815–1837. doi: 10.1111/febs.14748

Rolff, H., Christensen, I., and Vainer, B. (2016). The prognostic and predictive value of soluble Type IV collagen in colorectal cancer: a retrospective multicenter study. *Clin. Cancer Res.* 22, 2427–2434.

Sidney, L. E., Branch, M. J., Dunphy, S. E., Dua, H. S., and Hopkinson, A. (2014). Concise review: evidence for CD34 as a common marker for diverse progenitors. *Stem Cells* 32, 1380–1389. doi: 10.1002/stem.1661

Silver, D. J., and Silver, J. (2014). Contributions of chondroitin sulfate proteoglycans to neurodevelopment, injury, and cancer. *Curr. Opin. Neurobiol.* 27, 171–178. doi: 10.1016/j.conb.2014.03.016

Stodden, D. F., Goodway, J. D., Langendorfer, S. J., Roberton, M. A., Rudisill, M. E., Garcia, C., et al. (2008). A developmental perspective on the role of motor skill competence in physical activity: an emergent relationship. *Quest* 60, 290–306.

Sun, J., Mao, Y., Zhang, Y. Q., Guo, Y. D., Mu, C. Y., Fu, F. Q., et al. (2013). Clinical significance of the induction of macrophage differentiation by the costimulatory molecule B7-H3 in human non-small cell lung cancer. *Oncol. Lett.* 6, 1253–1260. doi: 10.3892/ol.2013.1586

Tay, R. E., Richardson, E. K., and Toh, H. C. (2021). Revisiting the role of CD4(+) T cells in cancer immunotherapy-new insights into old paradigms. *Cancer Gene Ther.* 28, 5–17. doi: 10.1038/s41417-020-0183-x

Tazzyman, S., Niaz, H., and Murdoch, C. (2013). Neutrophil-mediated tumour angiogenesis: subversion of immune responses to promote tumour growth. *Semin. Cancer Biol.* 23, 149–158. doi: 10.1016/j.semcancer.2013.02.003

Van Laethem, J. L., Verslype, C., Iovanna, J. L., Michl, P., Conroy, T., Louvet, C., et al. (2012). New strategies and designs in pancreatic cancer research: consensus guidelines report from a European expert panel. *Ann. Oncol.* 23, 570–576. doi: 10.1093/annonc/mdr351

Wang, X., Lu, Z., Gomez, A., Hon, G. C., Yue, Y., Han, D., et al. (2014). N6-methyladenosine-dependent regulation of messenger RNA stability. *Nature* 505, 117–120. doi: 10.1038/nature12730

Wang, Y. A., Li, X. L., Mo, Y. Z., Fan, C. M., Tang, L., Xiong, F., et al. (2018). Effects of tumor metabolic microenvironment on regulatory T cells. *Mol. Cancer* 17:168. doi: 10.1186/s12943-018-0913-y

Wilky, B. A. (2019). Immune checkpoint inhibitors: the linchpins of modern immunotherapy. *Immunol. Rev.* 290, 6–23. doi: 10.1111/imr.12766

Wu, F., Zhou, C., Zhou, D., Ou, S., Liu, Z., and Huang, H. (2018). Immune-enhancing activities of chondroitin sulfate in murine macrophage RAW 264.7 cells. *Carbohydr. Polym.* 198, 611–619. doi: 10.1016/j.carbpol.2018.06.071

Yamauchi, M., Gibbons, D. L., Zong, C., Fradette, J. J., Bota-Rabassedas, N., and Kurie, J. M. (2020). Fibroblast heterogeneity and its impact on extracellular

matrix and immune landscape remodeling in cancer. *Matrix Biol.* 9, 8–18. doi: 10.1016/j.matbio.2020.05.001

Yang, L., Li, A., Lei, Q., and Zhang, Y. (2019). Tumor-intrinsic signaling pathways: key roles in the regulation of the immunosuppressive tumor microenvironment. *J. Hematol. Oncol.* 12:125. doi: 10.1186/s13045-019-0804-8

Yoshihara, K., Shahmoradgoli, M., Martínez, E., Vegesna, R., Kim, H., Torres-Garcia, W., et al. (2013). Inferring tumour purity and stromal and immune cell admixture from expression data. *Nat. Commun.* 4:2612. doi: 10.1038/ncomms3612

Yue, Y., Liu, J., Cui, X., Cao, J., Luo, G., Zhang, Z., et al. (2018). VIRMA mediates preferential m(6)A mRNA methylation in 3'UTR and near stop codon and associates with alternative polyadenylation. *Cell Discov.* 4:10. doi: 10.1038/s41421-018-0019-0

Zhai, W., Zhou, X., Wang, H., Li, W., Chen, G., Sui, X., et al. (2020). A novel cyclic peptide targeting LAG-3 for cancer immunotherapy by activating antigen-specific CD8(+) T cell responses. *Acta Pharm. Sin. B* 10, 1047–1060. doi: 10.1016/j.apsb.2020.01.005

Conflict of Interest: The authors declare that the research was conducted in the absence of any commercial or financial relationships that could be construed as a potential conflict of interest.

frontiers in Cell and Developmental Biology

ORIGINAL RESEARCH
published: 09 July 2021
doi: 10.3389/fcell.2021.679176

Long Non-coding RNA ASNR Targeting miR-519e-5p Promotes Gastric Cancer Development by Regulating FGFR2

Zihao Chen[1,2], Yong Li[2], Bibo Tan[2], Fang Li[3], Qun Zhao[2], Liqiao Fan[2], Zhidong Zhang[2], Xuefeng Zhao[2], Yu Liu[2] and Dong Wang[2]*

[1] Graduate School of Hebei Medical University, Shijiazhuang, China, [2] The Third Department of Surgery, The Fourth Hospital of Hebei Medical University, Shijiazhuang, China, [3] Department of Pathology, The Fourth Hospital of Hebei Medical University, Shijiazhuang, China

Gastric cancer (GC), as a common gastrointestinal tumor, is an important cause of death from cancer all around the world. Long non-coding RNAs (lncRNAs), a novel class of transcripts, have attracted great attention of researchers. However, the mechanisms of the clinical significance of most lncRNAs in human cancer are mainly undocumented. This research desires to explore the clinical significance, biological function, and mechanism of Lnc_ASNR (apoptosis suppressing-non-coding RNA) in GC. Cell proliferation, cell cycle, cell migration, and invasion abilities were respectively determined by 3-(4,5)-dimethylthiahiazo (-z-y1)-3,5-di-phenytetrazoliumromide (MTT), flow cytometry, wound healing, and Transwell assay (Sigma-Aldrich, St. Louis, MO, United States). The association of Lnc_ASNR, miR-519e-5p, and fibroblast growth factor receptor 2 (FGFR2) was evaluated *via* luciferase reporter experiments. The tumor xenograft assay was conducted to confirm the results of cell experiments. High expressed Lnc_ASNR was detected in both GC cells and tissues using qRT-PCR. Downregulated Lnc_ASNR could reduce proliferation, migration, and invasion in GC cells, while upregulated Lnc_ASNR could promote the cell proliferation, migration, and invasion. Moreover, the effect of Lnc_ASNR on migration and invasion ability is closely related to epithelial-mesenchymal transition (EMT). The bioinformatics analysis, luciferase assay, and Western blot demonstrated that Lnc_ASNR inhibited miR-519e-5p expression but increased FGFR2 expression. Lnc_ASNR and FGFR2 were both targeted to miR-519e-5p, and they were negatively correlated with the expression of miR-519e-5p. All investigations indicated that Lnc_ASNR functioned as a ceRNA targeting miR-519e-5p and facilitated GC development by regulating the pathway of miR-519e-5p/FGFR2.

Keywords: gastric cancer, long non-coding RNA, Lnc_ASNR, proliferation, invasion, migration

OPEN ACCESS

Edited by:
Yongbin Chen, Kunming Institute of Zoology (CAS), China

Reviewed by:
Chaohong Liu, Huazhong University of Science and Technology, China
Shuang Liu, Central South University, China
Shengtao Zhou, Sichuan University, China

***Correspondence:**
Yong Li
li_yong_hbth@126.com

Specialty section:
This article was submitted to Molecular and Cellular Oncology, a section of the journal Frontiers in Cell and Developmental Biology

Received: *11 March 2021*
Accepted: *10 June 2021*
Published: *09 July 2021*

Citation:
Chen Z, Li Y, Tan B, Li F, Zhao Q, Fan L, Zhang Z, Zhao X, Liu Y and Wang D (2021) Long Non-coding RNA ASNR Targeting miR-519e-5p Promotes Gastric Cancer Development by Regulating FGFR2. Front. Cell Dev. Biol. 9:679176. doi: 10.3389/fcell.2021.679176

Abbreviations: GC, gastric cancer; lncRNAs, long non-coding RNAs; qRT-PCR, quantitative real-time PCR; MTT, 3-(4,5)-dimethylthiahiazo (-z-y1)-3,5-di-phenytetrazoliumromide; EMT, epithelial-mesenchymal transition; FGFR, fibroblast growth factor receptor; nt, nucleotides; ceRNA, competitive endogenous RNA; TNM, tumor-node-metastasis; si-NC, negative control siRNA; GFP, green fluorescent protein; RIPA, radio immunoprecipitation assay; OS, overall survival; CIC, cancer-initiating cells.

INTRODUCTION

Gastric cancer (GC) is a prevalent malignant tumor around the world with the sixth incidence rate and second mortality rate, which seriously affects human health (Bray et al., 2018). The advanced diagnosis and therapy of GC has achieved development in recent years. However, many limitations existed that hinder the effectiveness of GC treatment. The early symptoms of most GC patients are not obvious, and diagnosis delay becomes the main obstacle of GC treatment and prognosis. The combination of gastroscopy and biopsy is the universally recognized gold standard for GC diagnosis (Virgilio et al., 2017; den Hollander et al., 2019). However, its application in GC screening is still limited because it is not easy to be accepted by patients due to the invasiveness and high cost. At present, the most commonly used tumor biomarkers in clinical are insufficient to completely replace biopsy, so it is of great significance to explore more specific and sensitive biomarkers for early diagnosis of GC to improve the clinical treatment effect.

Long non-coding RNA (lncRNA) is an RNA molecule with a length between 200 and 100,000 nucleotides (nt), which can be transcribed independently. lncRNA is molecularly similar to mRNA, but there is no identifiable potential to encode functional proteins (Ulitsky, 2016). Researchers confirmed that lncRNA contains a significant biological function among several diseases (Montes et al., 2021; Zhang F. et al., 2021; Zhang Y. et al., 2021; Zhu et al., 2021). It is related to tumor development, chemotherapy sensitivity, and prognosis and especially plays a vital role in the resistance of multiple tumor chemotherapy drugs, especially in GC (Zhang and Wang, 2021), prostate cancer (Shang et al., 2019), and pancreatic cancer (Zhou et al., 2020). The expression of lncRNA is abnormal in a wide range of cancers. lncRNA demonstrates an essential influence in facilitating and inhibiting cancer occurrence and development, which proves its clinical potential as a biomarker and therapeutic target (Kim et al., 2018; Ramnarine et al., 2019; Wang Y. L. et al., 2019; Olivero et al., 2020). Recent findings indicated that lncRNA can interact with proteins, RNA, and lipids, thereby producing cancer signal transduction (Lin and Yang, 2018). In addition, lncRNAs, as competing endogenous RNAs (ceRNAs) or microRNA sponge, can regulate expression by competitively binding to microRNA (Song et al., 2017; Sun et al., 2017; Huang et al., 2019). Researchers have found that most lncRNAs are upregulated or downregulated expressly in tissues and serum plasma of patients with GC (Zhang et al., 2018; Wang C. J. et al., 2019; Guo et al., 2020; Yuan et al., 2020). Therefore, lncRNA can be used as a potential tumor marker for GC diagnosis.

Lnc_ASNR (non-coding RNA that inhibits apoptosis) is a nuclear-reserved lncRNA. Lnc_ASNR located in the chr14-q22.2 region is a newly discovered lncRNA associated with cancer and other diseases. Compared with normal tissues, Lnc_ASNR expression is significantly increased in four tumor tissues. Chen's group (Chen et al., 2016) has found that Lnc_ASNR promotes the reduction of cytoplasmic AUF1 levels and inhibits AUF1-mediated degradation of Bcl-2 mRNA in colon cancer RKO cells, which leads to high expression of Bcl-2 and significantly inhibits cell apoptosis. However, the role and mechanism of Lnc_ASNR in tumorigenesis and development are unclear, which suggested that the study of the impact of Lnc_ASNR on tumors remains to be explored. Herein, we first evaluated whether Lnc_ASNR changes in the expression of lncRNA in GC and further clarified the biological function of Lnc_ASNR and the molecular mechanism that regulates the occurrence and development of GC. The research results help to identify important molecules that effectively regulate the occurrence and development of GC, which will provide a theoretical basis for clinical molecular diagnosis of GC and the development of targeted drugs. Our results exhibit important scientific significance and potential clinical application value for improving patient prognosis and enhancing survival rate.

MATERIALS AND METHODS

Clinical and Histologic Evaluation of Human Tissues

In this study, 76 paired tumor tissues and adjacent non-tumor tissues were collected from GC patients at the Fourth Hospital of Hebei Medical University from 2017 to 2020. The GC diagnosis was histopathologically confirmed. Clinical pathological features, including gender, age, tumor-node-metastasis (TNM) staging, and tumor size, were summarized. None of them received preoperative treatment, including chemotherapy or radiotherapy. After obtaining the tissues, the samples were immediately placed in liquid nitrogen and then stored at −80°C. The research was approved by the Research Ethics Committee at the Fourth Hospital of Hebei Medical University (Shijiazhuang, China). All patients were informed and gave their consent.

Cell Culture

Four GC cell lines (MKN45, MKN28, AGS, and HGC27) and gastric mucosal epithelial cell (GES-1) were purchased from the Cell Bank of the Chinese Academy of Sciences (Shanghai, China). All cells were cultured in Roswell Park Memorial Institute (RPMI) 1640 medium (GIBCO, Thermo Fisher Scientific, Waltham, MA, United States) containing 10% fetal bovine serum (FBS) (BI), 100 U/ml penicillin, and 100 mg/ml streptomycin (Invitrogen, Thermo Fisher Scientific) at 37°C with 5% CO_2.

RNA Extraction and Quantitative Real-Time PCR

RNAiso Plus (TaKaRa, Tokyo, Japan) was utilized to extract total RNA from cells and tissue samples according to manufacturer's information. The OD260/OD280 ratio ranging from 1.9 to 2.1 tested by UV spectrophotometer is qualified. Reverse transcription polymerase chain reaction was performed by LnRctue lncRNA First-Strand cDNA kit (TIANGEN, Beijing, China) and LnRctue lncRNA qPCR kit (SYBR Green) (TIANGEN) for quantitative real-time PCR (qRT-PCR) according to manufacturer's information. ABI 7500 real-time PCR system (Applied Biosystems, Waltham, MA, United States) was utilized to conduct qRT-PCR and collect data. GAPDH was used as a loading control. Our qRT-PCR results were analyzed

and expressed relative to threshold cycle (C_t) values, and then converted to fold changes. The specific primer sequences used in our study are provided in the **Supplementary Table 1**.

Vector Construction and Transfection and siRNA Transfection

Based on manufacturer's information, Lipofectamine 2000 (Invitrogen) was used to transfect plasmid vectors and siRNAs into GC cells. The plasmid vector pcDNA3.1 used for Lnc_ASNR overexpression in MKN28, the siRNA (three individual ASNR siRNAs) used for Lnc_ASNR knockdown in MKN45 cells, miR-519e-5p inhibitor, and miR-519e-5p mimics, and the negative control (vector or NC) were obtained from Invitrogen. To upregulate ASNR, the coding sequence was increased based on the manufacturer's instructions and subcloned into the pcDNA3.1 (+) vector (Invitrogen). Then Lipofectamine 2000 (Invitrogen) was used to transfect MKN28 cells with a negative control vector or a ASNR-expressed plasmid. In order to downregulate ASNR, Lipofectamine 2000 (Invitrogen) was utilized to transfect MKN28 cells with the target sequence of negative control siRNA. After being transfected for 48 h, cells were obtained for qRT-PCR and Western blot experiments. The siRNA sequences used in our study are provided in the **Supplementary Table 2**.

Lentiviral Infection

The MKN45 cell suspension was seeded onto a six-well plate at concentration of 3×10^4 cells/well, and the cells were grown to a density of 20%. We have created two different groups, sh-ASNR transfected with shASNR green fluorescent protein (GFP) lentivirus and shNC (GENECHEM) transfected with empty GFP lentivirus, respectively. An appropriate amount of lentivirus was added according to the differences in infection (MOI = 20). After 3 days of transfection, a fluorescence microscope was used to observe GFP-tagged gene expression. Cells with transfection efficiency > 80% were selected for further analyses.

Cell Proliferation Assays

The cell viability of MKN45 cells transfected with si-ASNR and MKN28 cells transfected with pcDNA3.1-ASNR was evaluated *via* MTT Cell Proliferation and Cytotoxicity Assay Kit (Solarbio, Beijing, China) based on the manufacturer's guidance. Transfected MKN-45 cells and MKN28 cells (5×10^4/well) were incubated with MTT (20 μl/well) at 37°C for 4 h. Next, DMSO was added and mixed for 10 min to ensure the crystals were dissolved. The optical density value was measured at the absorbance 570 nm under Thermo Scientific Microplate Reader Multiskan MK3 (Thermo Fisher Scientific).

Flow Cytometry for Cell Cycle Analysis

si-ASNR- or si-NC-transfected MKN45 cells and pcDNA3.1-ASNR- or blank vector–transfected MKN28 cells were obtained after 48 h of transfection by Lipofectamine 2000 (Invitrogen). Next, the cells were dyed with propidium iodide (PI) utilizing the DNA content quantitative measurement method (cell cycle) (Solarbio) and detected *via* FACScan. Calculate and compare the percentage of cells in G0/G1, S, and G2/M phases.

Wound-Healing Assay

To conduct the wound healing experiment, 3×10^5 cells were seeded into six-well plates and cultured overnight. Cells were transfected with pcDNA3.1-ASNR, si-ASNR, and si-NC, respectively. When the cultured cells reached a density of 90%, a sterile 10-ml disposable pipette tip was used to produce uniform scratches. The cells were then grown in a medium containing 1% FBS for 48 h. At indicated time points, a microscope was used to obtain images of the plate (Olympus, Tokyo, Japan). Meanwhile, scratch area and wound-healing percentage were calculated. The experiment was repeated three times in parallel.

Cell Migration and Invasion Assays

si-ASNR- or si-NC transfected MKN45 cells and pcDNA3.1-ASNR-transfected MKN28 cells were harvested after 48 h of transfection and then collected. Twenty-four-well Transwell plates (8 μm pore size) (Corning Inc, Corning, NY, United States) were applied for cell migration and invasion assays. Briefly, 50 μl of Matrigel was placed into the Transwell upper chambers (Sigma-Aldrich). Cells (1×10^5) suspended in 100 μl of serum-free culture medium were seeded into the upper chambers. Added RPMI 1640 culture medium supplemented with 10% FBS into the wells under the chamber. The cells were cultured in the medium for 48 h at 37°C with 5% CO_2. Then, a cotton swab was utilized to wipe away the remaining cells on the membrane. Cells migrated or invaded through the membrane were stained with methanol and 0.1% crystal violet. Cells were then imaged and counted using an IX71 inverted microscope (Olympus). Five random fields were counted in each well. The experiment was repeated three times in parallel.

Western Blot Assay and Antibodies

Radio immunoprecipitation assay (RIPA) protein lysis buffer (Solarbio) supplemented with protease inhibitor cocktail (Roche, Basel, Switzerland) and phenylmethylsulfonyl fluoride (Roche) was applied for protein extraction. The proteins concentration was evaluated through a BCA Protein Assay Kit (Solarbio). Ten percent sodium dodecyl sulfate–polyacrylamide gel electrophoresis (SDS-PAGE) was used to detach protein extracts (50 μg). The protein extracts were transferred to 0.22 mm polyvinylidene fluoride membranes (Sigma), then incubated with specific antibodies. ECL chromogenic substrate was applied to evaluate the specific bands. The specific bands were then quantified by densitometry (Quantity One software, Bio-Rad) with β-actin used as a control. All antibodies (1:2,000 dilutions) were purchased from Abcam (Cambridge, United Kingdom).

Luciferase Reporter Assay

The 3′-UTR of human FGFR2 or Lnc_ASNR was amplified from human genomic DNA and individually inserted into a pGL3-basic vector (Promega, Madison, WI, United States). The fragment of FGFR2 or lncRNA-ASNR 3′-UTR mutant was then inserted into the pGL3-basic vector (Promega) control vector

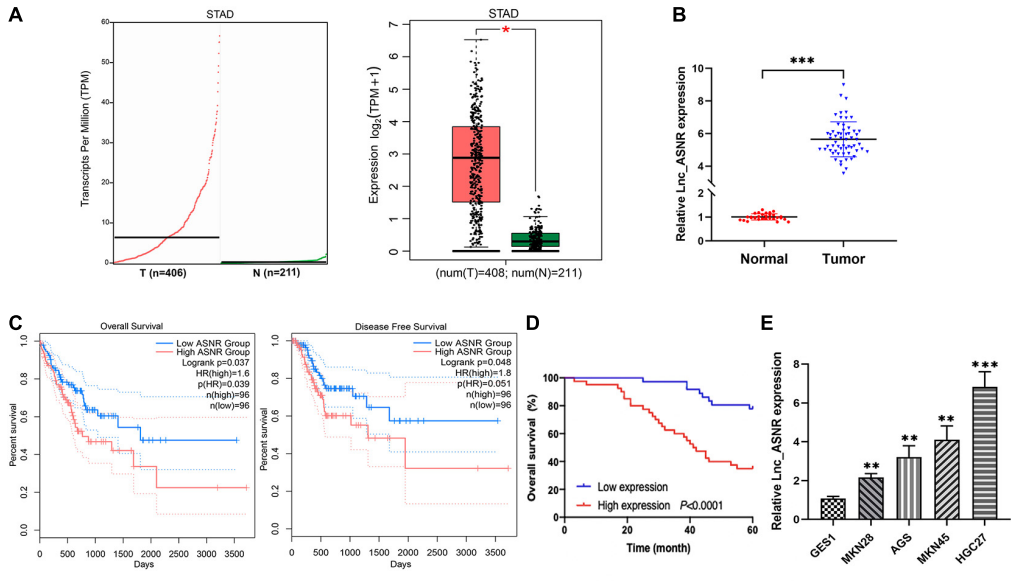

FIGURE 1 | High expression of Lnc_ASNR in GC tissue samples and cell lines. **(A)** Lnc_ASNR expression was analyzed by using GEPIA2 in GC tissues and normal tissues. **(B)** qRT-PCR was applied to indicate the expression of Lnc_ASNR in GC tissue samples and adjacent non-tumor tissue samples (n = 76). **(C)** Overall survival and disease-free survival were analyzed using GEPIA2. **(D)** Kaplan–Meier analysis showed the relationship between Lnc_ASNR expression and overall survival time of GC patients. **(E)** qRT-PCR showed the expression of Lnc_ASNR in the normal cell line and GC cell lines. Error bars, mean ± SEM. $^{*}P < 0.05$; $^{**}P < 0.01$; $^{***}P < 0.001$.

at the same position. To perform the reporter experiments, transfect MKN45 cells with wild-type or mutant reporter plasmid and miR-519e-5p mimic by Lipofectamine 2000 (Invitrogen). After 36 h of transfection, the luciferase activities and the firefly luciferase vitalities were detected under Dual-Luciferase® Reporter Assay System (Promega). They were normalized based on Renilla luciferase activity.

Immunohistochemistry

Formalin and paraffin were used to fix and embed the isolated tumor tissues, respectively. The tissue examples were then cut into 5 mm thick. Immunochemical staining was performed following the standard protocol. Tumors from mice were immunostained for H&E, Ki67. Inverted microscope (Nikon, Tokyo, Japan) was applied to capture the staining intensities of Ki67, and ImageJ software was used to analyze the data. Anti-Ki67 (1:50) was purchased from Roche.

Xenograft Study

All experiments were approved by the Committee on the Ethics of Animal Experiments of Hebei Medical University. The investigations were conducted strictly on the basis of the recommendations in the *Guide for the Care and Use of Laboratory Animals of the National Institutes of Health*. MKN45 cells were stably infected with control shRNA or sh-ASNR using lentiviruses. GC cells were injected into either side of the armpit regions of the male BALB/c nude mice. The mice (4–5 weeks old) were randomly divided into two groups (n = 6/group). Tumor volumes and weights were measured every 3 days, and tumor volumes were measured regularly. Calculate as the equation: $V = 0.5 \times D \times d^2$ (V, volume; D, longest diameter; d, diameter perpendicular to the longest diameter). After 16 days of treatment, mice were killed and tumors were excised. As mentioned earlier, H&E and IHC staining were performed on tumor tissues. The shRNA sequences used in our study were provided in the **Supplementary Table 3**.

Statistical Analysis

All experimental data analyses were carried out using Student's t-test and one-way ANOVA (GraphPad Prism 8). All data were presented as mean ± SD. The clinical correlations between two genes were analyzed by linear regression. The interrelation between the expression of ASNR and the clinical features in GC was confirmed by Fisher's exact test. Impact of variables on survival was evaluated by univariate and multivariate Cox proportional hazard models. Overall survival (OS) rates were determined *via* Kaplan–Meier method. $P < 0.05$ was regarded as statistical significance.

RESULTS

Lnc_ASNR Is Highly Expressed in GC and High Level of Lnc_ASNR Predicts Poor Prognosis

Lnc_ASNR was highly expressed in the GC tissues by analyzing their expression level in the TCGA datasets and GTEx datasets through using GEPIA2 online web tool[1](**Figure 1A**). To

[1]http://gepia2.cancer-pku.cn/

determine Lnc_ASNR expression in GC tissues, real-time PCR was carried out in GC tissues and adjacent normal tissues. The result exhibited that Lnc_ASNR expression was obviously increased in GC tissue (**Figure 1B**). Those results together indicated that Lnc_ASNR was highly expressed in GC tissue. In addition, we also measured Lnc_ASNR expression in GES-1, MKN28, AGS, MKN45, and HGC27 cells. As shown in **Figure 1E**, Lnc_ASNR expression in the GC cell lines was obviously higher than that in the GES-1 cell. Compared with the highly differentiated cell line MKN28, the Lnc_ASNR expression was higher in the lowly differentiated cell line MKN45 (**Figure 1E**).

To evaluate the clinical significance of Lnc_ASNR overexpression in GC, we explored the expression of Lnc_ASNR in 76 patients with GC and evaluated their relationship with clinicopathological features. Median expression level was considered to be the key value. Tissues were grouped into low expression group with 36 samples and high expression group with 40 samples. As indicated in **Table 1**, high Lnc_ASNR levels was significantly associated with larger tumor size ($p = 0.012$), depth of invasion ($p = 0.008$), lymph node metastasis ($p = 0.001$), and TNM stage ($p = 0.018$). In contrast, no obvious association was found between Lnc_ASNR expression and other features including gender ($p = 0.921$) and age ($p = 0.235$). Correlation between Lnc_ASNR expression level and prognosis of GC patients was evaluated. According to the upper and lower quartiles of Lnc_ASNR expression, patients are divided into high-expression and low-expression groups. It was found that the expression of Lnc_ASNR affected the survival rate of the patient using GEPIA2 web tool. The overall survival (OS) and disease-free survival (DFS) of the low ASNR group were better than the high ASNR group (**Figure 1C**). It could be confirmed from Kaplan–Meier survival analysis that Lnc_ASNR highly expressed patients exhibited shorter OS, compared with Lnc_ASNR lowly expressed patients (**Figure 1D**). In addition, univariate survival analysis showed OS of patients were significantly correlated with that tumor size, infiltrating depth, Lauren classification, tissue differentiation, TNM stage, and Lnc_ASNR expression levels (**Table 2**). These factors were further evaluated by multifactor Cox regression analysis, indicating that Lnc_ASNR expression level and tissue differentiation are independent prognostic factors for patients (**Table 3**).

Knockdown of Lnc_ASNR Inhibits While ASNR Overexpression Promotes GC Cell Proliferation, Migration, and Invasion

We hypothesized that Lnc_ASNR may act as an oncogene, based on the increased expression of Lnc_ASNR in GC. Therefore, siRNA was used to downregulate the expression of Lnc_ASNR in MKN45 cells. qRT-PCR was used to verify knockdown efficiency of siRNA, and siRNA3 was chosen for subsequent experiments because of the highest knockdown efficiency (**Figure 2A**). Cell proliferation assay (MTT) results showed that silencing Lnc_ASNR inhibited the proliferation of GC cells (**Figure 2B**). It could be seen from the flow cytometry analysis that when Lnc_ASNR was silenced, the percentage of cells in G0/G1 phase would increase, while the percentage of cells in S phase would decrease (**Figure 2D**). The wound-healing assay and Transwell assay data suggested that compared with the control group, the si-Lnc_ASNR group significantly reduced the number of cells that migrated and invaded (**Figure 2E**).

To deeply verify whether Lnc_ASNR is related to GC, the expression of related mRNA and protein was evaluated by performing qRT-PCR and Western blot experiments. We found that both the mRNA and protein expression of PCNA, cell proliferation marker gene, was decreased (**Figure 2C**). Both mRNA and protein expression levels of cyclin A, cyclin D1, and cyclin E were decreased, while P21 and P27 expression levels were increased in the cells transfected with siRNA (**Figure 2F**). Furthermore, the mRNA and protein expression levels of MMP2, MMP9, and ICAM1, cell invasion- and migration-related gene, were decreased, while TIMP1, TIMP2, and NM23 were increased (**Figure 2F**).

Contrary to the results of silencing Lnc_ASNR, overexpression of Lnc_ASNR facilitated the proliferation, migration, and invasion of MKN28 cells (**Figures 3A–F**).

Lnc_ASNR Influences GC Cell EMT

We found that cell migration and invasion are closely related to Lnc_ASNR levels. Since epithelial-mesenchymal transition (EMT) is a key step that contributes to tumor metastasis, we evaluated the effect of Lnc_ASNR on EMT. In order to further verify the abovementioned results, qRT-PCR and Western blot assay were conducted to evaluate the EMT-induced marker expression in cells downregulating or upregulating Lnc_ASNR. As shown in **Figure 2F**, high expressed epithelial markers E-cadherin, low expressed interstitial markers *N*-cadherin and vimentin were detected in the cells downregulated by Lnc_ASNR, indicating that the inhibition of Lnc_ASNR promoted the change of EMT to MET. Moreover, EMT transcription factor expression, including Snail, Twist, and ZEB1, was significantly downregulated (**Figure 2F**) in si-Lnc_ASNR-transfected cells. However, the results observed in the cells transfected with pcDNA3.1-Lnc_ASNR were just the opposite (**Figure 3F**). These results are consistent with our hypothesis that Lnc_ASNR affects the malignant phenotype by regulating EMT.

Lnc_ASNR Promotes GC Cell Tumorigenesis *in vivo*

In order to provide further evidence for the above findings, stably expressed sh-Lnc_ASNR or sh-NC AGS cells were constructed by infecting cells with shRNA vectors. Then, in order to determine the correlation between Lnc_ASNR and tumorigenesis of GC cells *in vivo*, AGS cells with stable knockdown of Lnc_ASNR were injected into nude mice. In contrary to the tumor formed by the control cells, the tumor formed by the Lnc_ASNR-silenced cells has taken significantly slower time (**Figure 4A**). In addition, compared with the control group, tumor volume of the sh-Lnc_ASNR group was significantly decreased (**Figures 4B,C**). We also found that the protein expression of cell proliferation marker gene, PCNA, and cell invasion and migration-related gene, MMP2, MMP9, and ICAM1, were decreased, while NM23 was increased

TABLE 1 | Association of Lnc_ASNR expression with clinicopathological features of gastric cancer.

Features	Number	Lnc_ASNR expression levels		X^2	*p*-Value
		High	Low		
Gender					
Male	46	24	22	0.010	0.921
Female	30	16	14		
Age (years)					
≤59	35	21	14	1.413	0.235
>59	41	19	22		
Tumor size (cm)					
≤4.8	48	20	28	6.283	0.012
>4.8	28	20	8		
Lauren classification					
Intestinal	21	7	14	11.689	0.003
Diffuse	30	23	7		
Mixed	25	10	15		
Tissue differentiation					
Well	5	0	5	12.110	0.001
Moderate	36	15	21		
Poor	35	25	10		
Infiltrating depth					
T1	3	0	3	10.717	0.008
T2	26	9	17		
T3	40	25	15		
T4	7	6	1		
Nodal status					
N0	18	3	15	16.223	0.001
N1	16	8	8		
N2	18	10	8		
N3	25	19	5		
Distant metastasis					
M0	74	38	36	1.849	0.495
M1	2	2	0		
TNM stage					
I	6	1	5	8.756	0.018
II	28	11	17		
III	40	26	14		
IV	2	2	0		

in the sh-Lnc_ASNR group (**Figure 4D**). The above results demonstrated that the downregulated Lnc_ASNR could suppress tumor development *in vivo*. Furthermore, the results of H&E staining indicated that the sh-Lnc_ASNR group significantly suppressed tumorigenesis. Additionally, immunohistochemical staining of tumor tissues demonstrated that contrary to the sh-NC group, a decrease in Ki-67 was detected in the sh-Lnc_ASNR group (**Figure 4E**).

In vivo investigations above complement the evidence of *in vitro* functional studies involving Lnc_ASNR.

Lnc_ASNR Functions as ceRNA and Sponges miR-519e-5p in GC Cells

In addition to regulating the target in epigenetics, some lncRNAs can also act as competing endogenous RNA (ceRNA) of specific miRNA to affect the target gene expression. We predicted the potential target of Lnc_ASNR by searching the biological information database miRDB. We examined the Lnc_ASNR sequence and found the miR-519e-5p-binding site and identified miR-519e-5p as a candidate binding miRNA (**Figure 5A**). In order to detect the miR-519e-5p expression in GC tissues, real-time PCR was performed in GC tissues and matched adjacent normal tissues. It was clearly indicated that the expression of miR-519e-5p was markedly downregulated in GC samples (**Figure 5B**). Besides, Lnc_ASNR expression was negatively correlated with that of miR-519e-5p in GC samples (**Figure 5C**). We attempted to analyze the regulation of miR-519e-5p by Lnc_ASNR. Highly differentiated MKN28 cells were transfected pcDNA3.1(+) vector carrying the coding sequence of Lnc_ASNR to overexpress Lnc_ASNR, and downregulation of miR-519e-5p

TABLE 2 | Univariate analysis of prognostic factors in 76 patients with gastric cancer.

Characteristics	All cases	5-year survival rate	X^2	*p*-Value
Gender				
Male	46	54.35% (25/46)	0.039	0.842
Female	30	56.67% (17/30)		
Age (years)				
<60	35	54.29% (19/35)	0.025	0.874
≥60	41	56.10% (23/41)		
Tumor size (cm)				
≤4.8	48	66.67% (32/48)	6.853	0.009
>4.8	28	35.71% (10/28)		
Lauren classification				
Intestinal	21	76.19% (16/21)	8.143	0.017
Diffuse	30	36.67% (11/30)		
Mixed	25	60.00% (15/25)		
Tissue differentiation				
Well	5	100.00% (5/5)	6.521	0.037
Moderate	36	61.11% (22/36)		
Poor	35	42.86% (15/35)		
Infiltrating depth				
T1	3	100.00% (3/3)	9.041	0.019
T2	26	69.23% (18/26)		
T3	40	50.00% (20/40)		
T4	7	14.29% (1/7)		
Nodal status				
N0	18	72.22% (13/18)	3.208	0.361
N1	16	50.00% (8/16)		
N2	18	44.44% (8/18)		
N3	25	52.00% (13/25)		
Distant metastasis				
M0	74	56.76% (42/74)	2.537	0.197
M1	2	0.00% (0/2)		
TNM stage				
I	6	83.33% (5/6)	7.253	0.041
II	28	67.86% (19/28)		
III	40	45.00% (18/40)		
IV	2	0.00% (0/2)		
ASNR expression				
Low	36	75.00% (27/36)	10.777	0.001
High	40	37.50% (15/40)		

TABLE 3 | Multivariate analysis of prognostic factors in 76 patients with gastric cancer.

Clinicopathological features	*B*	*SE*	Wald	*p*-Value	95% CI
Tumor size (cm)	0.350	0.515	0.462	0.497	0.257∼1.934
Lauren classification	1.974	1.185	2.775	0.096	0.706∼73.446
Tissue differentiation	3.301	1.228	7.228	0.007	2.446∼300.984
Infiltrating depth	0.104	0.739	0.020	0.888	0.261∼4.724
TNM stage	1.789	1.246	2.062	0.151	0.520∼68.760
ASNR expression	2.772	0.821	11.400	0.001	0.013∼0.313

expression was detected by qPCR (**Figure 5D**). Whereas, lowly differentiated MKN45 cells were transfected with si-Lnc_ASNR to silence Lnc_ASNR and upregulated miR-519e-5p expression was detected by qPCR (**Figure 5E**). To further verify the targeting relationships between miR-519e-5p and Lnc_ASNR, luciferase reporter experiment was performed in MKN45 cells.

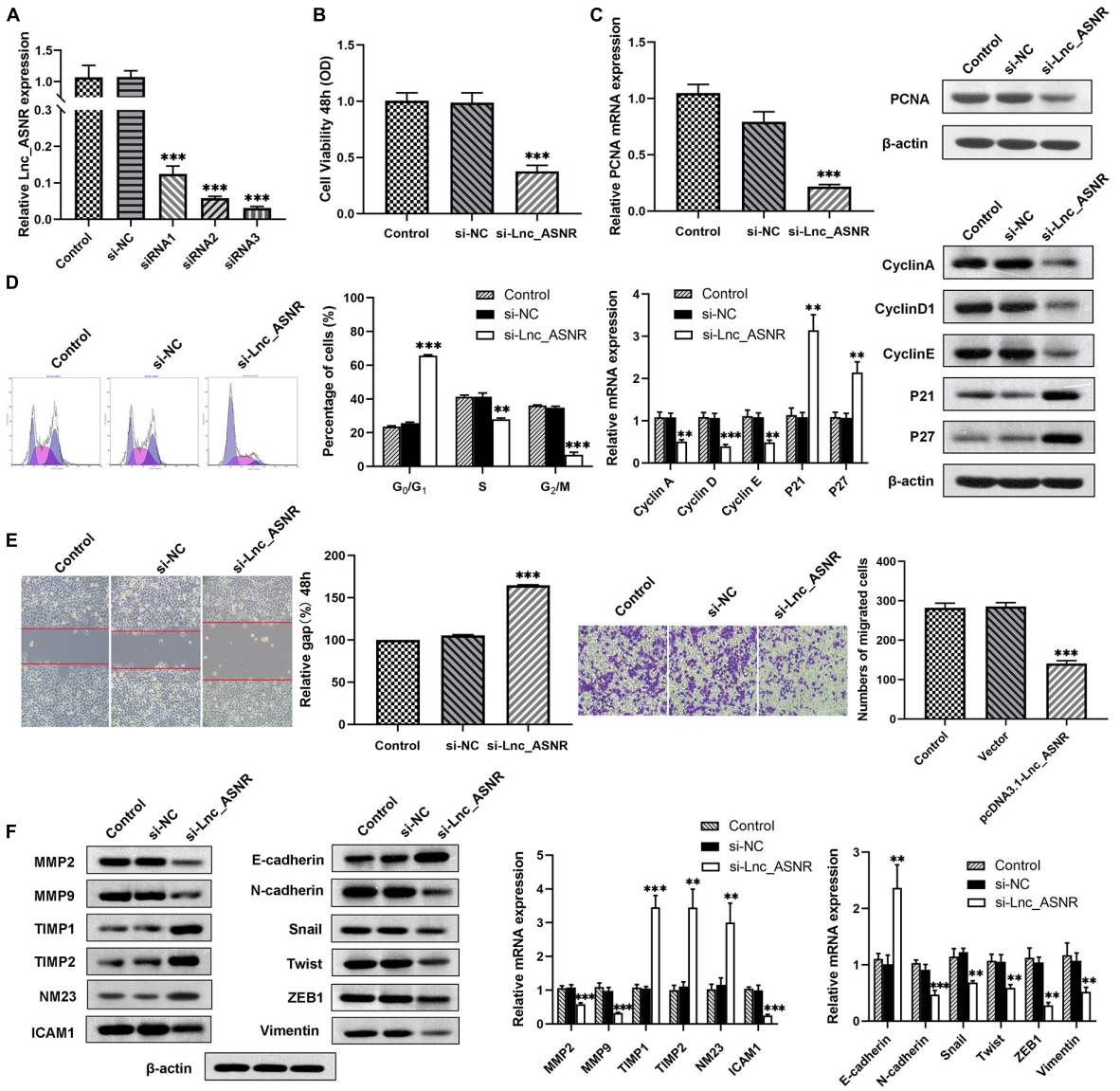

FIGURE 2 | Silenced Lnc_ASNR inhibits GC cell proliferation, migration, and invasion. **(A)** qPCR showed the silence efficiency of Lnc_ASNR siRNAs. **(B)** MTT experiments detected the cell viability of MKN45 cells after treatment with Lnc_ASNR siRNA or control siRNAs. **(C)** qPCR and western blot assays showed PCNA mRNA and protein levels in si-Lnc_ASNR transfected MKN45 cells. **(D)** Flow cytometry was applied to verify cell cycle in MKN45 cell lines and qPCR and western blot assays were conducted to evaluate the cycle-related mRNA and protein levels. **(E)** The migration ability with Lnc_ASNR-silenced MKN45 cells was detected by wound-healing assay. The invasion ability was detected by invasion assay with Lnc_ASNR-silenced MKN45 cells. **(F)** The expression of metastasis-related mRNA and proteins with Lnc_ASNR-silenced MKN45 cells were investigated by performing qPCR and western blot assays. Error bars, mean ± SEM. $^{*}P < 0.05$; $^{**}P < 0.01$; $^{***}P < 0.001$.

As represented in **Figure 5F**, miR-519e-5p mimic apparently decreased the activity of luciferase in Lnc_ASNR-wild, while no significant change was detected in Lnc_ASNR-mut.

Therefore, these data suggested that Lnc_ASNR acts as a miR-519e-5p sponge in GC.

FGFR2 Is a Downstream Target of miR-519e-5p

Online miRNA target prediction databases (including Targetscan and miRDB) were applied to predict potential target genes of miR-519e-5p, and FGFR2 was determined as a potential downstream gene of miR-519e-5p (**Figure 6A**). Real-time PCR was carried out in GC tissues and matched adjacent normal tissues to evaluate the FGFR2 expression. An obvious upregulation of FGFR2 expression was detected in GC tissue samples (**Figure 6B**). Besides, FGFR2 expression was positively correlated with the expression of Lnc_ASNR (**Figure 6C**) and negatively related to miR-519e-5p expression in GC tissue samples (**Figure 6D**). In addition, FGFR2 expression in GES-1, MKN28, AGS, MKN45, and HGC27 cells was also detected. It

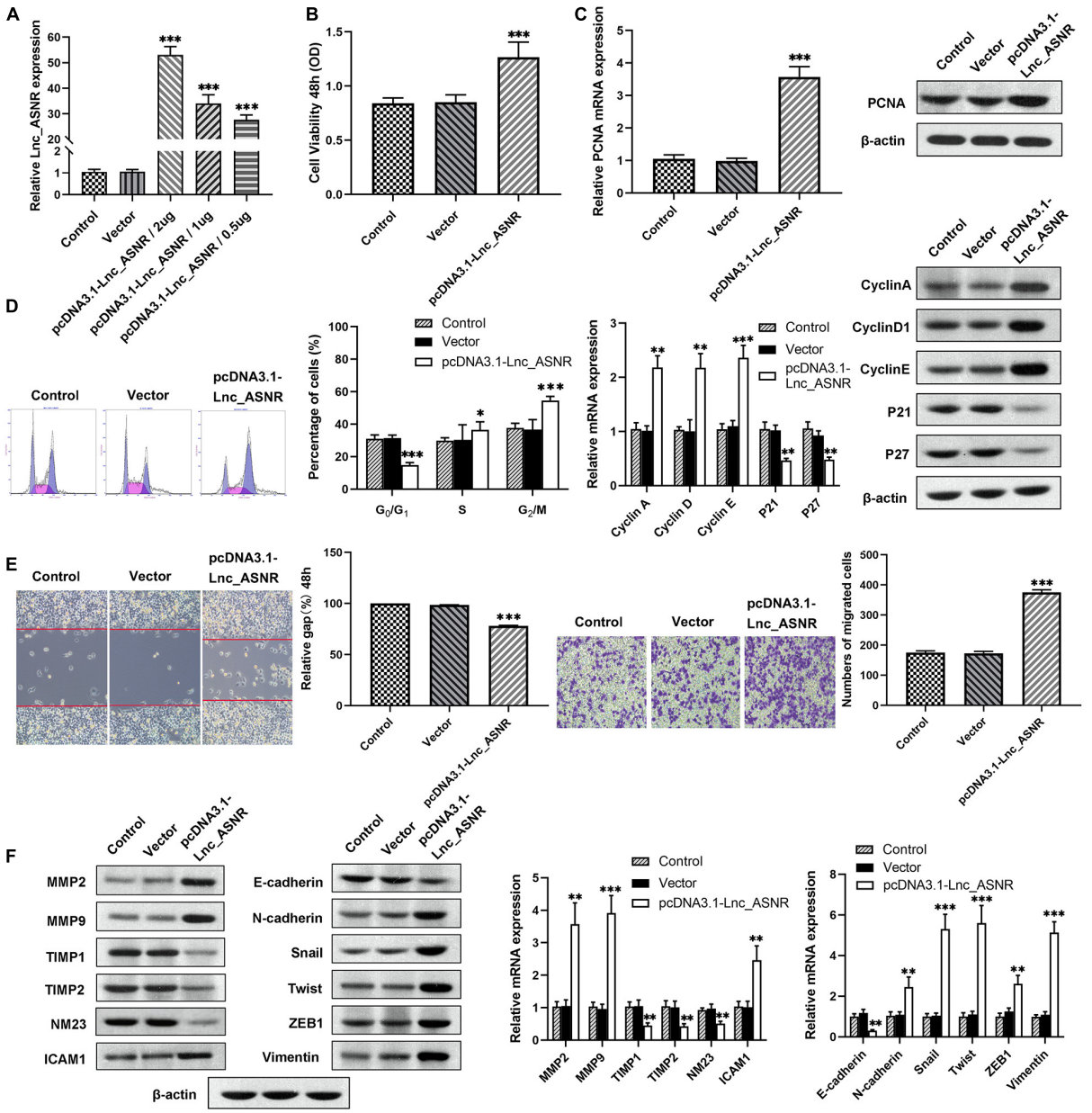

FIGURE 3 | Lnc_ASNR overexpression promotes GC cell proliferation, migration, and invasion. **(A)** qPCR detected overexpress efficiency of pcDNA3.1-Lnc_ASNR. **(B)** MTT assays examined the cell viability of MKN28 cells after treatment with pcDNA3.1-Lnc_ASNR or vector. **(C)** PCNA mRNA and protein level in pcDNA3.1-Lnc_ASNR-transfected MKN28 cells were evaluated by carrying out qPCR and western blot assays. **(D)** Cell cycle was verified by using flow cytometry in MKN28 cell lines and cycle-related mRNA and protein level were evaluated by qPCR and western blot assays. **(E)** The migration ability with Lnc_ASNR-overexpressed MKN28 cells was detected by wound-healing assay. The invasion ability was detected by invasion assay with Lnc_ASNR-overexpressed MKN28 cells. **(F)** The expression of metastasis-related mRNA and proteins with Lnc_ASNR overexpressed MKN28 cells were investigated by performing qPCR and western blot assays. Error bars, mean ± SEM. $^{*}P < 0.05$; $^{**}P < 0.01$; $^{***}P < 0.001$.

was clearly indicated from **Figure 6E** that FGFR2 expression was markedly higher in GC cell lines than that of control cells.

Next, low differentiated MKN45 cells were transfected with miR-519e-5p mimic, and qRT-PCR was used to verify that miR-519e-5p expression was markedly increased (**Figure 6F**). In addition, the FGFR2 expression level was evaluated by qRT-PCR and Western blot experiments, and the data demonstrated that the FGFR2 expression level was markedly downregulated (**Figure 6G**). On the contrary, miR-519e-5p inhibitor was used to transfect highly differentiated MKN28 cells, and corresponding results demonstrated that the expression of miR-519e-5p was markedly decreased (**Figure 6H**). Moreover, FGFR2 expression was investigated by conducting qRT-PCR and Western blot experiments, and the results suggested that FGFR2 expression

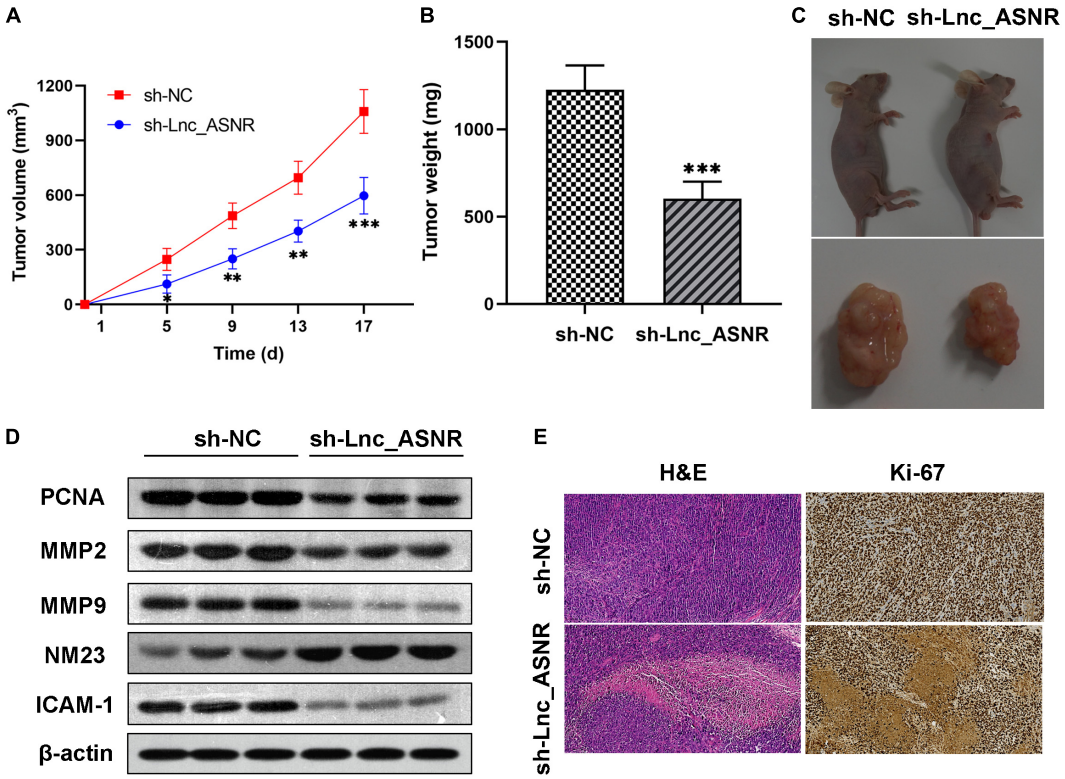

FIGURE 4 | Silenced Lnc_ASNR suppresses the tumorigenesis ability *in vivo*. **(A)** The sizes of tumors were measured, and the volume was calculated every 4 days. **(B)** Tumor weights in different groups were shown. **(C)** Images of tumors formed from AGS cells in different groups were represented. **(D)** Related protein expression levels in tumor tissues were investigated *via* western blot assays. **(E)** Images of H&E staining and Ki67 immunostaining for nude mice tumor tissues in different groups. Error bars, mean ± SEM. $^{*}P < 0.05$; $^{**}P < 0.01$; $^{***}P < 0.001$.

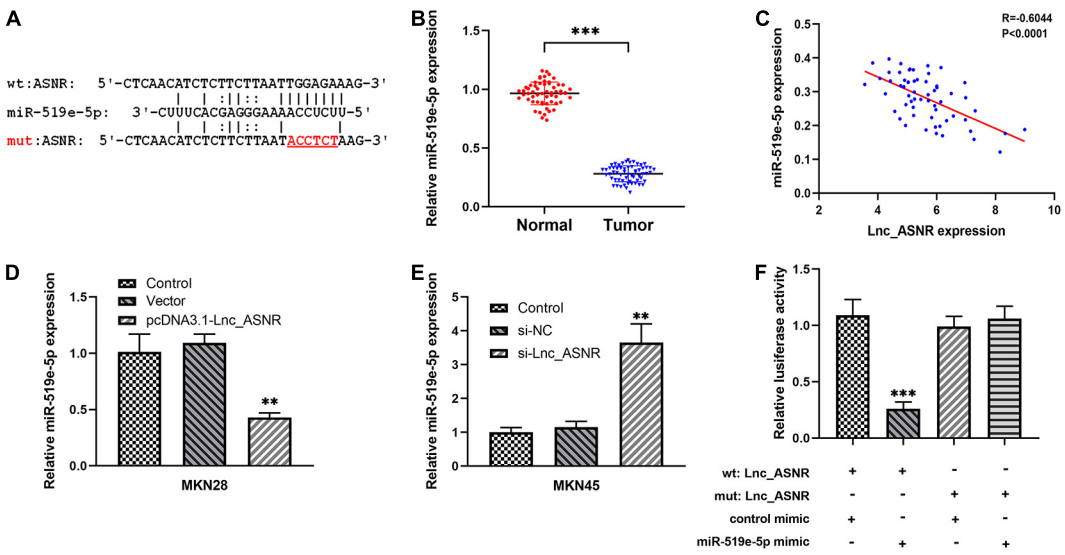

FIGURE 5 | The relationship between Lnc_ASNR and miR-519e-5p. **(A)** The predicted combining positions between Lnc_ASNR and miR-519e-5p were predicted by using "miRDB" website (http://mirdb.org/). **(B)** qRT-PCR was applied to indicate the expression of miR-519e-5p in GC tissue samples and adjacent non-tumor tissue samples. **(C)** Correlation analysis was used to evaluate the relationship between miR-519e-5p expression and Lnc_ASNR expression. **(D)** qPCR detected the levels of miR-519e-5p in GC cells after Lnc_ASNR was overexpressed. **(E)** qPCR detected the levels of miR-519e-5p in GC cells after Lnc_ASNR was silenced. **(F)** Luciferase activity detection. Error bars, mean ± SEM. $^{*}P < 0.05$; $^{**}P < 0.01$; $^{***}P < 0.001$.

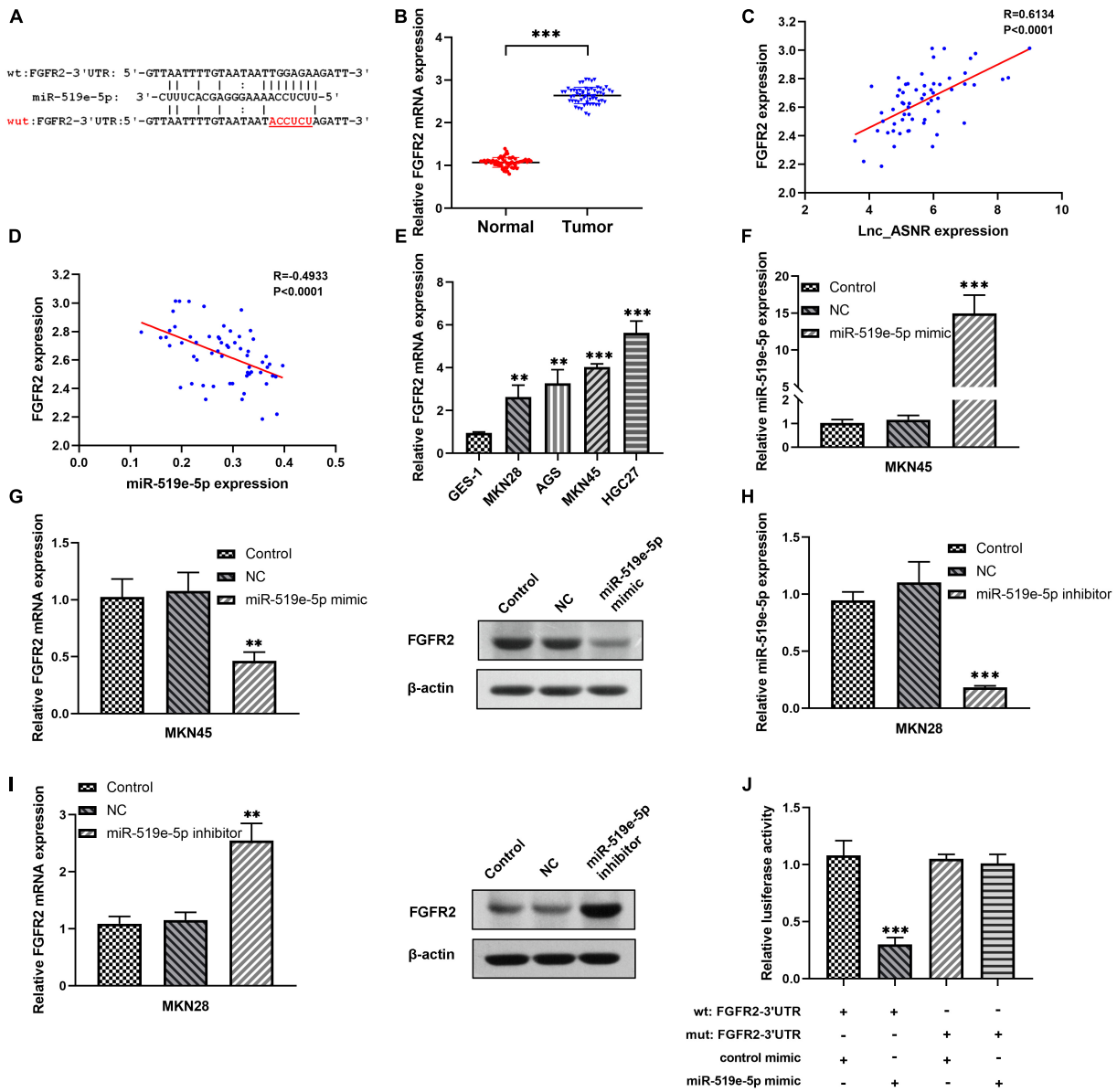

FIGURE 6 | The relationship between FGFR2 and miR-519e-5p in GC cells. **(A)** The potential binding sites between miR-519e-5p and FGFR2 were predicted from "Targetscan" website (http://www.targetscan.org/) and "miRDB" website (http://mirdb.org/). **(B)** qRT-PCR was applied to indicate the expression of FGFR2 in GC tissue samples and adjacent non-tumor tissue samples. **(C)** Correlation analysis was used to evaluate the relationship between FGFR2 expression and Lnc_ASNR expression. **(D)** Correlation analysis was used to evaluate the relationship between FGFR2 expression and miR-519e-5p expression. **(E)** qRT-PCR showed the expression of FGFR2 in the normal cell line and GC cell lines. **(F)** qPCR detected the overexpress efficiency of miR-519e-5p mimic. **(G)** Relative FGFR2 expression and protein levels in GC cells after miR-519e-5p was overexpressed. **(H)** qPCR detected the silence efficiency of miR-519e-5p inhibitor. **(I)** Relative FGFR2 expression and protein levels in GC cells after miR-519e-5p was silence. **(J)** Luciferase activity examination. Error bars, mean ± SEM. $^{*}P < 0.05$; $^{**}P < 0.01$; $^{***}P < 0.001$.

was obviously increased (**Figure 6I**). To further evaluate the targeting correlation between miR-519e-5p and FGFR2, luciferase reporter experiment was performed in the MKN45 cells. As exhibited in **Figure 6J**, miR-519e-5p mimic markedly suppressed the vitality of luciferase in FGFR2-wild, while no significant change was detected in FGFR2-mut.

Therefore, these data indicated that FGFR2 is an important downstream target of miR-519e-5p.

The Lnc_ASNR/miR-519e-5p/FGFR2 Axis Promotes Proliferation, Invasion, and Migration of GC

Mechanism research was conducted to clarify the relationship between Lnc_ASNR and FGFR2. Lnc_ASNR was silenced in lowly differentiated MKN45 cells. qRT-PCR and western blot assay inhibited that decreased Lnc_ASNR reduced the level

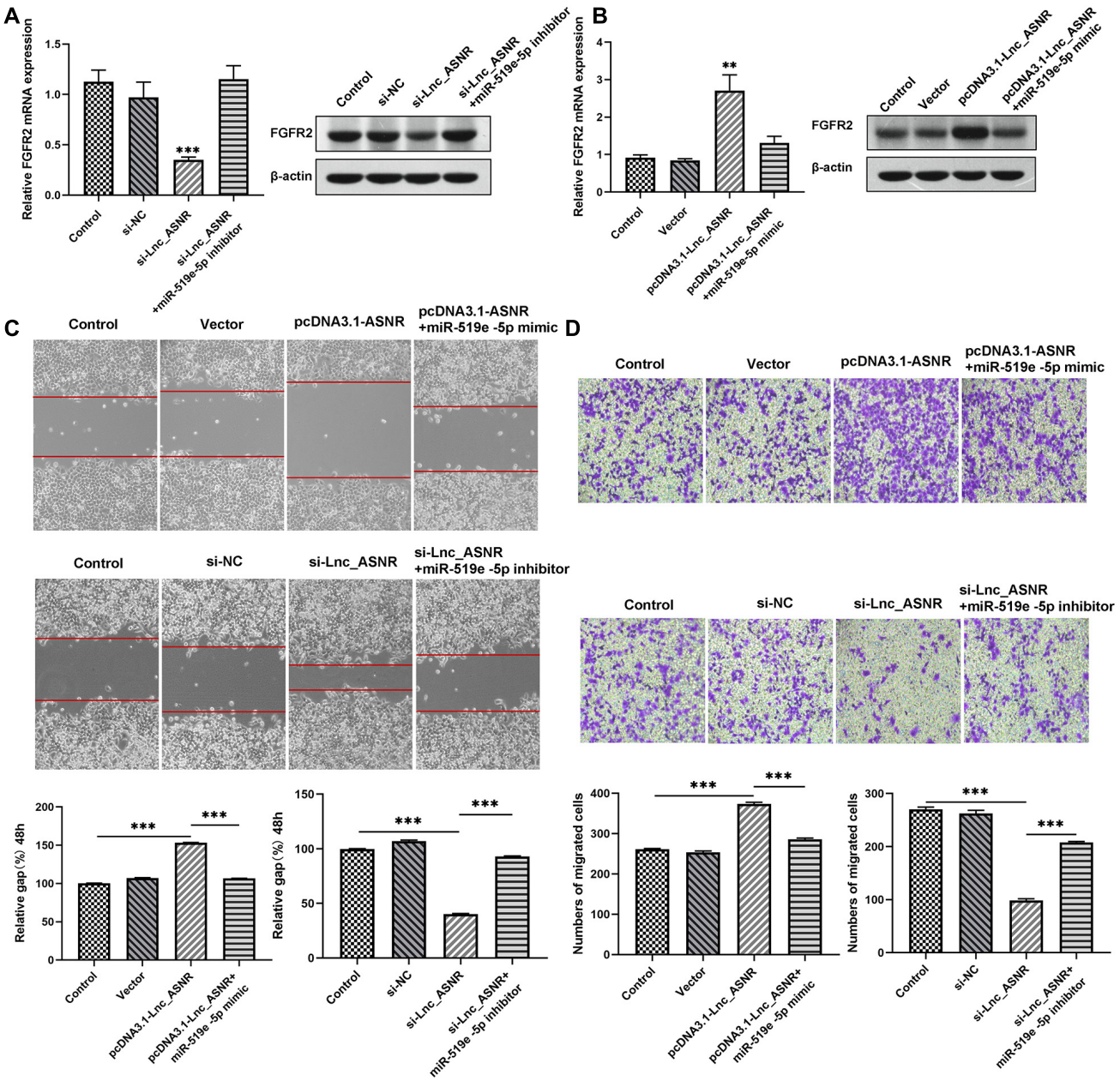

FIGURE 7 | Lnc_ASNR/miR-519e-5p axis regulates GC progression. **(A)** The effects of Lnc_ASNR inhibition on the expression of FGFR2. **(B)** The effects of Lnc_ASNR overexpression on the expression of FGFR2. **(C)** The rescue experiments about si-Lnc_ASNR and pcDNA3.1-ASNR for cell migration. **(D)** The rescue experiments about si-Lnc_ASNR and pcDNA3.1-ASNR for cell invasion. Error bars, mean ± SEM. $^{*}P < 0.05$; $^{**}P < 0.01$; $^{***}P < 0.001$.

of FGFR2 protein, which is consistent with the miR-519e-5p-induced FGFR2 protein downregulation. When transfected with si-ANSR + miR-519e-5p inhibitor in MKN45 cells, it was found that FGFR2 expression was restored (**Figure 7A**). In contrast, upregulated FGFR2 was detected in highly differentiated MKN28 cells who overexpressed Lnc_ASNR. When pcDNA3.1-ASNR + miR-519e-5p mimic was transfected in MKN45 cells, it was found that FGFR2 expression was reversed (**Figure 7B**). The effect of Lnc_ASNR/miR-519e-5p axis on GC was then evaluated. MKN28 cells were transfected with vectors, pcDNA3.1-ASNR, and pcDNA3.1-ASNR + miR-519e-5p minic, respectively. MKN45 cells were transfected with si-NC, si-ASNR, and si-ASNR + miR-519e-5p inhibitors, respectively. As shown in **Figures 7C,D**, miR-519e-5p mimics could counteract the enhancement effect of overexpression of Lnc_ASNR on cell migration and invasion ability, while miR-519e-5p inhibitor could reverse the inhibitory effect of knockdown of Lnc_ASNR on cell migration and invasion ability.

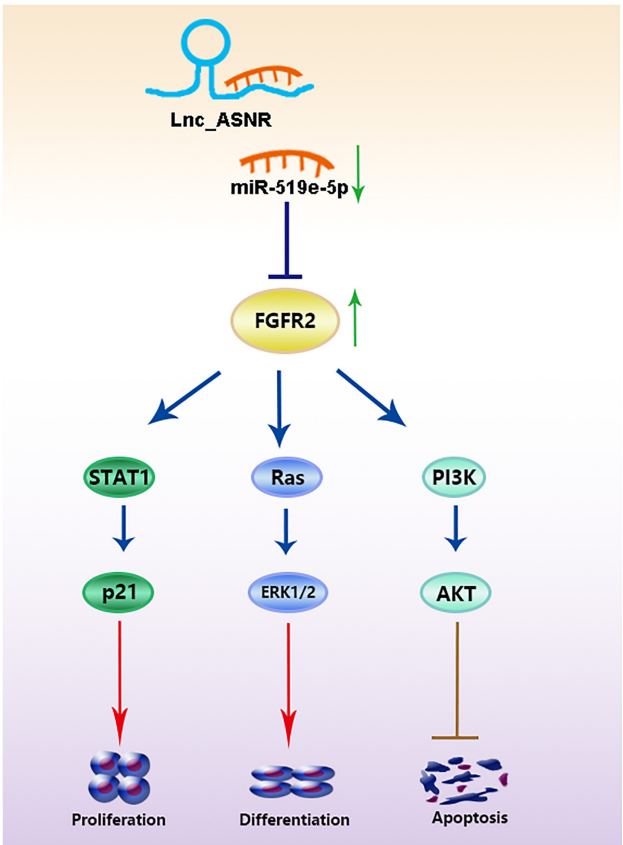

FIGURE 8 | Lnc_ASNR acted as a ceRNA for miR-519e-5p promoting GC development by regulating FGFR2.

Ultimately, correlation analysis in GC showed that Lnc_ASNR expression and miR-519e-5p expression was negatively related, while Lnc_ASNR expression and FGFR2 expression was positively related. Overall, the above results demonstrated that Lnc_ASNR acted as a ceRNA for miR-519e-5p, thereby reducing FGFR2 expression and imposing posttranscriptional regulatory levels (**Figure 8**).

DISCUSSION

Generally, explorations for cancer drivers are focused on protein-coding genes in cancer genomes before the discovery of non-coding RNAs. However, increasing research results verified that lncRNAs are crucial in cellular progression and diseases development (Han et al., 2019; Pradas-Juni et al., 2020), especially in cancer (Papaioannou et al., 2019; Schulte et al., 2020; Silva-Fisher et al., 2020). Abnormal expression of lncRNAs may lead to accelerated tumor growth (Geng et al., 2018; Lin and Yang, 2018; Sallam et al., 2018). The therapeutic methods available to advanced GC patients are limited, and there remains potential to improve the treatment effect. It is essential to investigate thoroughly the internal mechanisms of GC occurrence and development and explore novel prognostic markers. Large amounts of lncRNAs are verified to play crucial roles in GC development. Increasing researchers pay more attention to investigate the functions and regulation of lncRNAs to explore novel predictors for the diagnosis and therapeutics of GC (Fu et al., 2020; Qin et al., 2020; Ren et al., 2020). Herein, a GC-associated lncRNA ASNR was identified, which was markedly increased in GC cells and tissues. High Lnc_ASNR expression was related to advanced TNM staging, larger tumor size, and positive lymph node metastasis. In addition, the upregulated expression of Lnc_ASNR was related to the shortening of OS and DFS in GC patients. The above investigations showed that knocking down Lnc_ASNR suppressed cell proliferation, declined tumor growth, and facilitated cell apoptosis, while upregulated Lnc_ASNR accelerated cell proliferation, invasion, and metastasis. These functional evidences indicate that Lnc_ASNR plays a carcinogenic role in the occurrence of GC, which can be used as a potential prognostic indicator.

Increasing evidences indicate that there is a novel and extensive interaction network involving ceRNA. It was reported that ncRNAs could regulate target RNA through combining their linking position of protein coding messengers (Wang P. et al., 2020; Wang W. et al., 2020; Zhao et al., 2020). Emerging researches confirm the ceRNA hypothesis and indicate that ceRNA regulation is related to the carcinogenic effects of GC. For example, LncRNA MT1JP can suppress cell growth, migration, and invasion, promote cell apoptosis *in vitro*, and inhibit tumor growth and metastasis *in vivo* (Zhang et al., 2018). In our previous investigations, we suggested that lncRNA PWRN1 acts as a ceRNA-targeting miR-425-5p and inhibits the growth of GC by intervening p53 signaling pathway (Chen et al., 2018). Thus, we assumed that lncRNA may play the role of ceRNA and participate in occurrence of GC. It was confirmed by bioinformatics analysis and luciferase reporter gene analysis that miR-519e-5p was targeted by Lnc_ASNR. Recently, miR-519e-5p has only been reported in acute myocardial infarction (Wang F. et al., 2014) and pregnancy-related complications (Hromadnikova et al., 2015; Zhang et al., 2016), while few investigations on the relationship between miR-519e-5p and GC were reported. In our research, we confirmed that the endogenous level of Lnc_ASNR could influence the miR-519e-5p expression. The miR-519e-5p expression was increased in GC cells when Lnc_ASNR was silenced. Contrary to the results of silencing Lnc_ASNR, miR-519e-5p expression was decreased upon Lnc_ASNR overexpression, which confirmed our hypothesis. Above investigations revealed the importance of the correlation between Lnc_ASNR with miR-519e-5p in GC, which was contributed to that Lnc_ASNR exhibited a carcinogenic effect through causing miR-519e-5p to produce sponges in GC cells.

In general, lncRNAs exhibit function by relying on ceRNA to inhibit miRNA targets (Shen et al., 2018; Chen et al., 2019; Yang et al., 2019). Therefore, miRNA targets are important

parts of ceRNA network. It is worth to note that FGFR2 is a potential miR-519e-5p target site which has never been reported *via* online-predicting database. In order to verify that miR-519e-5p was directly targeted by FGFR2, we carried out luciferase reporter experiments and confirmed that FGFR2 was targeted by miR-519e-5p at 3′-UTR. In addition, transfection of miR-519e-5p mimic inhibits FGFR2 mRNA and protein expression, while transfection of miR-519e-5p inhibitor promotes FGFR2 mRNA and protein expression. The protein encoded by the FGFR2 gene is one of the members of the fibroblast growth factor receptor (FGFR) family (Wu et al., 2013). At present, four types of FGFRs have been identified, namely FGFR1, FGFR2, FGFR3, and FGFR4. The main function of FGFR, a receptor for FGF, is to transduce FGF signal to RAS-ERK and PI3K-AKT signal cascade amplification. The missense mutations of the FGFR2 gene occur in endometrial cancer, cervical cancer, breast cancer, lung cancer, and GC. The amplified FGFR2 induces the activation of FGFR2 signaling. FGFR2 has been proposed as a target for targeted therapy of GC (Pearson et al., 2016; Kuboki et al., 2018; Kim et al., 2019). Yu et al. (2018) revealed that overexpressed FGFR2 accelerated the production of cancer-initiating cells (CIC) and enhanced the resistance to lapatinib in HER2-positive GC cells. We further determined that miR-519e-5p could reverse the effect of Lnc_ASNR on FGFR2 expression level, indicating that Lnc_ANSR acts on miR-519e-5p through sponge adsorption, which further affects the expression of downstream target gene FGFR2, thereby affecting cell proliferation, invasion, and migration activity.

In summary, our findings validated a novel lncRNA, called Lnc_ASNR, and found that Lnc_ASNR expression was related to poor prognosis in GC. The study found that Lnc_ASNR was a carcinogenic lncRNA exhibiting a targeting relationship with miR-519e-5p. GC patients with higher expression of Lnc_ASNR promoted tumor growth by regulating the miR-519e-5p/FGFR2 pathway. The current study reveals a further insight into the function of lncRNA–miRNA–mRNA–ceRNA network in GC progression. The promoter function of Lnc_ASNR in the GC progress was first reported. The potential molecular mechanism involved in the Lnc_ASNR/miR-519e-5p/FGFR2 axis could be a potentially useful approach for GC diagnosis and therapies.

DATA AVAILABILITY STATEMENT

The original contributions presented in the study are included in the article/**Supplementary Material**, further inquiries can be directed to the corresponding author/s.

ETHICS STATEMENT

The animal study was reviewed and approved by Research Ethics Committee at the Fourth Hospital of Hebei Medical University. Written informed consent was obtained from the individual(s) for the publication of any potentially identifiable images or data included in this article.

AUTHOR CONTRIBUTIONS

ZC and YLo planned, designed, and coordinated this research and drafted the manuscript. BT and QZ participated in the conception and design of the manuscript and revised it critically for important intellectual content. FL and LF contributed to the conception and design and helped in drafting the manuscript. ZZ, XZ, and YLu contributed to analyzing and interpreting data and improved the crucial parts. DW helped in writing a part of the manuscript and analyzed the data. All the authors read and approved the final manuscript.

ACKNOWLEDGMENTS

We thank all the members in our laboratory and department and all the patients and their families involved in the current study.

SUPPLEMENTARY MATERIAL

The Supplementary Material for this article can be found online at: https://www.frontiersin.org/articles/10.3389/fcell.2021.679176/full#supplementary-material

REFERENCES

Bray, F., Ferlay, J., Soerjomataram, I., Siegel, R. L., Torre, L. A., and Jemal, A. (2018). Global cancer statistics 2018: GLOBOCAN estimates of incidence and mortality worldwide for 36 cancers in 185 countries. *CA Cancer J. Clin.* 68, 394–424. doi: 10.3322/caac.21492

Chen, J., Liu, L., Wei, G., Wu, W., Luo, H., Yuan, J., et al. (2016). The long noncoding RNA ASNR regulates degradation of Bcl-2 mRNA through its interaction with AUF1. *Sci. Rep.* 6:32189. doi: 10.1038/srep32189

Chen, J., Yu, Y., Li, H., Hu, Q., Chen, X., He, Y., et al. (2019). Long non-coding RNA PVT1 promotes tumor progression by regulating the miR-143/HK2 axis in gallbladder cancer. *Mol. Cancer* 18:33. doi: 10.1186/s12943-019-0947-9

Chen, Z., Ju, H., Yu, S., Zhao, T., Jing, X., Li, P., et al. (2018). Prader-Willi region non-protein coding RNA 1 suppressed gastric cancer growth as a competing endogenous RNA of miR-425-5p. *Clin. Sci.* 132, 1003–1019. doi: 10.1042/CS20171588

den Hollander, W. J., Holster, I. L., den Hoed, C. M., Capelle, L. G., Tang, T. J., Anten, M. P., et al. (2019). Surveillance of premalignant gastric lesions: a multicentre prospective cohort study from low incidence regions. *Gut* 68, 585–593. doi: 10.1136/gutjnl-2017-314498

Fu, T., Ji, K., Jin, L., Zhang, J., Wu, X., Ji, X., et al. (2020). ASB16-AS1 up-regulated and phosphorylated TRIM37 to activate NF-kappaB pathway and promote proliferation, stemness, and cisplatin resistance of gastric cancer. *Gastric Cancer* 24, 45–59. doi: 10.1007/s10120-020-01096-y

Geng, H., Bu, H. F., Liu, F., Wu, L., Pfeifer, K., Chou, P. M., et al. (2018). In inflamed intestinal tissues and epithelial cells, interleukin 22 signaling increases expression of H19 long noncoding RNA, which promotes mucosal regeneration. *Gastroenterology* 155, 144–155. doi: 10.1053/j.gastro.2018.03.058

Guo, X., Lv, X., Ru, Y., Zhou, F., Wang, N., Xi, H., et al. (2020). Circulating exosomal gastric cancer-associated long noncoding RNA1 as a biomarker for early detection and monitoring progression of gastric cancer: a multiphase study. *JAMA Surg.* 155, 572–579. doi: 10.1001/jamasurg.2020.1133

Han, X., Huang, S., Xue, P., Fu, J., Liu, L., Zhang, C., et al. (2019). LncRNA PTPRE-AS1 modulates M2 macrophage activation and inflammatory diseases by epigenetic promotion of PTPRE. *Sci. Adv.* 5:eaax9230. doi: 10.1126/sciadv.aax9230

Hromadnikova, I., Kotlabova, K., Ondrackova, M., Pirkova, P., Kestlerova, A., Novotna, V., et al. (2015). Expression profile of C19MC microRNAs in placental tissue in pregnancy-related complications. *DNA Cell Biol.* 34, 437–457. doi: 10.1089/dna.2014.2687

Huang, Y., Xu, Y., Lu, Y., Zhu, S., Guo, Y., Sun, C., et al. (2019). lncRNA Gm10451 regulates PTIP to facilitate iPSCs-derived beta-like cell differentiation by targeting miR-338-3p as a ceRNA. *Biomaterials* 216:119266. doi: 10.1016/j.biomaterials.2019.119266

Kim, H. S., Kim, J. H., and Jang, H. J. (2019). Pathologic and prognostic impacts of FGFR2 amplification in gastric cancer: a meta-analysis and systemic review. *J. Cancer* 10, 2560–2567. doi: 10.7150/jca.29184

Kim, J., Piao, H. L., Kim, B. J., Yao, F., Han, Z., Wang, Y., et al. (2018). Long noncoding RNA MALAT1 suppresses breast cancer metastasis. *Nat. Genet.* 50, 1705–1715. doi: 10.1038/s41588-018-0252-3

Kuboki, Y., Schatz, C. A., Koechert, K., Schubert, S., Feng, J., Wittemer-Rump, S., et al. (2018). In situ analysis of FGFR2 mRNA and comparison with FGFR2 gene copy number by dual-color in situ hybridization in a large cohort of gastric cancer patients. *Gastric Cancer* 21, 401–412. doi: 10.1007/s10120-017-0758-x

Lin, C., and Yang, L. (2018). Long noncoding RNA in cancer: wiring signaling circuitry. *Trends Cell Biol.* 28, 287–301. doi: 10.1016/j.tcb.2017.11.008

Montes, M., Lubas, M., Arendrup, F. S., Mentz, B., Rohatgi, N., Tumas, S., et al. (2021). The long non-coding RNA MIR31HG regulates the senescence associated secretory phenotype. *Nat. Commun.* 12:2459. doi: 10.1038/s41467-021-22746-4

Olivero, C. E., Martinez-Terroba, E., Zimmer, J., Liao, C., Tesfaye, E., Hooshdaran, N., et al. (2020). p53 activates the long noncoding RNA Pvt1b to inhibit Myc and suppress tumorigenesis. *Mol. Cell* 77, 761–774.e8. doi: 10.1016/j.molcel.2019.12.014

Papaioannou, D., Petri, A., Dovey, O. M., Terreri, S., Wang, E., Collins, F. A., et al. (2019). The long non-coding RNA HOXB-AS3 regulates ribosomal RNA transcription in NPM1-mutated acute myeloid leukemia. *Nat. Commun.* 10:5351. doi: 10.1038/s41467-019-13259-2

Pearson, A., Smyth, E., Babina, I. S., Herrera-Abreu, M. T., Tarazona, N., Peckitt, C., et al. (2016). High-level clonal FGFR amplification and response to FGFR inhibition in a translational clinical trial. *Cancer Discov.* 6, 838–851. doi: 10.1158/2159-8290.CD-15-1246

Pradas-Juni, M., Hansmeier, N. R., Link, J. C., Schmidt, E., Larsen, B. D., Klemm, P., et al. (2020). A MAFG-lncRNA axis links systemic nutrient abundance to hepatic glucose metabolism. *Nat. Commun.* 11:644. doi: 10.1038/s41467-020-14323-y

Qin, C., Jin, L., Li, J., Zha, W., Ding, H., Liu, X., et al. (2020). Long non-coding RNA LINC02163 accelerates malignant tumor behaviors in breast cancer by regulating the microRNA-511-3p/HMGA2 axis. *Oncol. Res.* 28, 483–495. doi: 10.3727/096504020X15928179818438

Ramnarine, V. R., Kobelev, M., Gibb, E. A., Nouri, M., Lin, D., Wang, Y., et al. (2019). The evolution of long noncoding RNA acceptance in prostate cancer initiation, progression, and its clinical utility in disease management. *Eur. Urol.* 76, 546–559. doi: 10.1016/j.eururo.2019.07.040

Ren, Z., Liu, X., Si, Y., and Yang, D. (2020). Long non-coding RNA DDX11-AS1 facilitates gastric cancer progression by regulating miR-873-5p/SPC18 axis. *Artif. Cells Nanomed. Biotechnol.* 48, 572–583. doi: 10.1080/21691401.2020.1726937

Sallam, T., Sandhu, J., and Tontonoz, P. (2018). Long noncoding RNA discovery in cardiovascular disease: decoding form to function. *Circ. Res.* 122, 155–166. doi: 10.1161/CIRCRESAHA.117.311802

Schulte, C., Barwari, T., Joshi, A., Zeller, T., and Mayr, M. (2020). Noncoding RNAs versus protein biomarkers in cardiovascular disease. *Trends Mol. Med.* 26, 583–596. doi: 10.1016/j.molmed.2020.02.001

Shang, Z., Yu, J., Sun, L., Tian, J., Zhu, S., Zhang, B., et al. (2019). LncRNA PCAT1 activates AKT and NF-kappaB signaling in castration-resistant prostate cancer by regulating the PHLPP/FKBP51/IKKalpha complex. *Nucleic Acids Res.* 47, 4211–4225. doi: 10.1093/nar/gkz108

Shen, L., Wang, Q., Liu, R., Chen, Z., Zhang, X., Zhou, P., et al. (2018). LncRNA lnc-RI regulates homologous recombination repair of DNA double-strand breaks by stabilizing RAD51 mRNA as a competitive endogenous RNA. *Nucleic Acids Res.* 46, 717–729. doi: 10.1093/nar/gkx1224

Silva-Fisher, J. M., Dang, H. X., White, N. M., Strand, M. S., Krasnick, B. A., Rozycki, E. B., et al. (2020). Long non-coding RNA RAMS11 promotes metastatic colorectal cancer progression. *Nat. Commun.* 11:2156. doi: 10.1038/s41467-020-15547-8

Song, Y. X., Sun, J. X., Zhao, J. H., Yang, Y. C., Shi, J. X., Wu, Z. H., et al. (2017). Non-coding RNAs participate in the regulatory network of CLDN4 via ceRNA mediated miRNA evasion. *Nat. Commun.* 8:289. doi: 10.1038/s41467-017-00304-1

Sun, Y., Zhou, Y., Bai, Y., Wang, Q., Bao, J., Luo, Y., et al. (2017). A long non-coding RNA HOTTIP expression is associated with disease progression and predicts outcome in small cell lung cancer patients. *Mol. Cancer* 16:162. doi: 10.1186/s12943-017-0729-1

Ulitsky, I. (2016). Evolution to the rescue: using comparative genomics to understand long non-coding RNAs. *Nat. Rev. Genet.* 17, 601–614. doi: 10.1038/nrg.2016.85

Virgilio, E., Proietti, A., D'Urso, R., Cardelli, P., Giarnieri, E., Montagnini, M., et al. (2017). Measuring intragastric tumor markers in gastric cancer patients: a systematic literature review on significance and reliability. *Anticancer Res.* 37, 2817–2821. doi: 10.21873/anticanres.11632

Wang, C. J., Zhu, C. C., Xu, J., Wang, M., Zhao, W. Y., Liu, Q., et al. (2019). The lncRNA UCA1 promotes proliferation, migration, immune escape and inhibits apoptosis in gastric cancer by sponging anti-tumor miRNAs. *Mol. Cancer* 18:115. doi: 10.1186/s12943-019-1032-0

Wang, F., Long, G., Zhao, C., Li, H., Chaugai, S., Wang, Y., et al. (2014). Atherosclerosis-related circulating miRNAs as novel and sensitive predictors for acute myocardial infarction. *PLoS One* 9:e105734. doi: 10.1371/journal.pone.0105734

Wang, P., Li, X., Gao, Y., Guo, Q., Ning, S., Zhang, Y., et al. (2020). LnCeVar: a comprehensive database of genomic variations that disturb ceRNA network regulation. *Nucleic Acids Res.* 48, D111–D117. doi: 10.1093/nar/gkz887

Wang, W., Hu, W., Wang, Y., An, Y., Song, L., Shang, P., et al. (2020). Long non-coding RNA UCA1 promotes malignant phenotypes of renal cancer cells by modulating the miR-182-5p/DLL4 axis as a ceRNA. *Mol. Cancer* 19:18. doi: 10.1186/s12943-020-1132-x

Wang, Y. L., Liu, J. Y., Yang, J. E., Yu, X. M., Chen, Z. L., Chen, Y. J., et al. (2019). Lnc-UCID promotes G1/S transition and hepatoma growth by preventing DHX9-mediated CDK6 down-regulation. *Hepatology* 70, 259–275. doi: 10.1002/hep.30613

Wu, Y. M., Su, F., Kalyana-Sundaram, S., Khazanov, N., Ateeq, B., Cao, X., et al. (2013). Identification of targetable FGFR gene fusions in diverse cancers. *Cancer Discov.* 3, 636–647. doi: 10.1158/2159-8290.CD-13-0050

Yang, J., Qiu, Q., Qian, X., Yi, J., Jiao, Y., Yu, M., et al. (2019). Long noncoding RNA LCAT1 functions as a ceRNA to regulate RAC1 function by sponging miR-4715-5p in lung cancer. *Mol. Cancer* 18:171. doi: 10.1186/s12943-019-1107-y

Yu, Y., Yu, X., Liu, H., Song, Q., and Yang, Y. (2018). miR494 inhibits cancerinitiating cell phenotypes and reverses resistance to lapatinib by downregulating FGFR2 in HER2positive gastric cancer. *Int. J. Mol. Med.* 42, 998–1007. doi: 10.3892/ijmm.2018.3680

Yuan, L., Xu, Z. Y., Ruan, S. M., Mo, S., Qin, J. J., and Cheng, X. D. (2020). Long non-coding RNAs towards precision medicine in gastric cancer: early diagnosis, treatment, and drug resistance. *Mol. Cancer* 19:96. doi: 10.1186/s12943-020-01219-0

Zhang, F., Wang, H., Yu, J., Yao, X., Yang, S., Li, W., et al. (2021). LncRNA CRNDE attenuates chemoresistance in gastric cancer via SRSF6-regulated alternative splicing of PICALM. *Mol. Cancer* 20:6. doi: 10.1186/s12943-020-01299-y

Zhang, G., Li, S., Lu, J., Ge, Y., Wang, Q., Ma, G., et al. (2018). LncRNA MT1JP functions as a ceRNA in regulating FBXW7 through competitively binding to miR-92a-3p in gastric cancer. *Mol. Cancer* 17:87. doi: 10.1186/s12943-018-0829-6

Zhang, M., Muralimanoharan, S., Wortman, A. C., and Mendelson, C. R. (2016). Primate-specific miR-515 family members inhibit key genes in human trophoblast differentiation and are upregulated in preeclampsia. *Proc. Natl. Acad. Sci. U.S.A.* 113, E7069–E7076. doi: 10.1073/pnas.1607849113

Zhang, Y., Zhang, X., Cai, B., Li, Y., Jiang, Y., Fu, X., et al. (2021). The long noncoding RNA lncCIRBIL disrupts the nuclear translocation of Bclaf1 alleviating cardiac ischemia-reperfusion injury. *Nat. Commun.* 12:522. doi: 10.1038/s41467-020-20844-3

Zhang, Z., and Wang, H. (2021). HCP5 promotes proliferation and contributes to cisplatin resistance in gastric cancer through miR-519d/HMGA1 axis. *Cancer Manag. Res.* 13, 787–794. doi: 10.2147/CMAR.S289997

Zhao, X., Su, L., He, X., Zhao, B., and Miao, J. (2020). Long noncoding RNA CA7-4 promotes autophagy and apoptosis via sponging MIR877-3P and MIR5680 in high glucose-induced vascular endothelial cells. *Autophagy* 16, 70–85. doi: 10.1080/15548627.2019.1598750

Zhou, C., Yi, C., Yi, Y., Qin, W., Yan, Y., Dong, X., et al. (2020). LncRNA PVT1 promotes gemcitabine resistance of pancreatic cancer via activating Wnt/beta-catenin and autophagy pathway through modulating the miR-619-5p/Pygo2 and miR-619-5p/ATG14 axes. *Mol. Cancer* 19:118. doi: 10.1186/s12943-020-01237-y

Zhu, G., Luo, H., Feng, Y., Guryanova, O. A., Xu, J., Chen, S., et al. (2021). HOXBLINC long non-coding RNA activation promotes leukemogenesis in NPM1-mutant acute myeloid leukemia. *Nat. Commun.* 12:1956. doi: 10.1038/s41467-021-22095-2

Conflict of Interest: The authors declare that the research was conducted in the absence of any commercial or financial relationships that could be construed as a potential conflict of interest.

frontiers in Cell and Developmental Biology

ORIGINAL RESEARCH
published: 12 July 2021
doi: 10.3389/fcell.2021.690542

Predicting Panel of Metabolism and Immune-Related Genes for the Prognosis of Human Ovarian Cancer

Lingyun Zhang[1,2†], Wenwen Sun[3†], Weimin Ren[4†], Jinguo Zhang[5,6] and Guoxiong Xu[5,6*]*

[1] Department of Medical Oncology, Zhongshan Hospital, Fudan University, Shanghai, China, [2] Cancer Center, Zhongshan Hospital, Fudan University, Shanghai, China, [3] Department of Pathology, Shanghai First Maternity and Infant Hospital, Tongji University, Shanghai, China, [4] Department of Pathology, Shanghai 9th People's Hospital, Shanghai Jiao Tong University School of Medicine, Shanghai, China, [5] Research Center for Clinical Medicine, Jinshan Hospital, Fudan University, Shanghai, China, [6] Department of Oncology, Shanghai Medical College, Fudan University, Shanghai, China

OPEN ACCESS

Edited by:
Guillermo Barreto,
Biopôle de l'Université de Lorraine, France

Reviewed by:
Chang Zou,
Jinan University, China
José Cesar Rosa Neto,
University of São Paulo, Brazil

***Correspondence:**
Guoxiong Xu
guoxiong.xu@fudan.edu.cn
orcid.org/0000-0002-9074-8754
Lingyun Zhang
lingyunzhang15@fudan.edu.cn
orcid.org/0000-0002-1928-1055

† These authors have contributed equally to this work

Specialty section:
This article was submitted to Molecular and Cellular Oncology, a section of the journal Frontiers in Cell and Developmental Biology

Received: 03 April 2021
Accepted: 21 June 2021
Published: 12 July 2021

Citation:
Zhang L, Sun W, Ren W, Zhang J and Xu G (2021) Predicting Panel of Metabolism and Immune-Related Genes for the Prognosis of Human Ovarian Cancer. Front. Cell Dev. Biol. 9:690542. doi: 10.3389/fcell.2021.690542

Objective: Ovarian cancer (OC) is a high deadly gynecologic cancer with a poor prognosis. The identification of genomic aberrations could predict the clinical prognosis of OC patients and may eventually develop new therapeutic strategies in the future. The purpose of this study is to create comprehensive co-expressed gene networks correlated with metabolism and the immune process of OC.

Methods: The transcriptome profiles of TCGA OC datasets and GSE26193 datasets were analyzed. The mRNA expression level, hub genomic alteration, patient's survival status, and tumor cell immune microenvironment of metabolism-related genes were analyzed from TCGA, GTEX, Oncomine, Kaplan-Meier Plotter, cBioPortal, TIMER, ESTIMATE, and CIBERSORT databases. We further validated the mRNA and protein expression levels of these hub genes in OC cell lines and tissues using qRT-PCR and immunohistochemistry.

Results: The LASSO-Cox regression analyses unveiled seven differently expressed metabolism-related genes, including *GFPT2, DGKD, ACACB, ACSM3, IDO1, TPMT*, and *PGP*. The Cox regression risk model could be served as an independent marker to predict the overall clinical survival of OC patients. The expression of GFPT2, DGKD, ACACB, and ACSM3 were downregulated in OC tissues, while IDO1, TPMT, and PGP were upregulated in OC tissues than in control. Moreover, DGKD and IDO1 were significantly associated with the human immune system.

Conclusion: The differently expressed metabolism-related genes were identified to be a risk model in the prediction of the prognosis of OC. The identified hub genes related to OC prognosis may play important roles in influencing both human metabolism and the immune system.

Keywords: ovarian cancer, risk model, prognosis, metabolism, immune

INTRODUCTION

Human ovarian cancer (OC) is one of the most deadly gynecologic malignancies in the world (Siegel et al., 2020). Epithelial OC, the main type in histological, is regarded as originating from human epithelial cells of the ovary or the fallopian tube (Zhang et al., 2017). OC patients are usually diagnosed at the advanced clinic stage owing to the absence of symptoms at an early stage and the lack of an effective diagnostic marker. Although advances in surgery, chemotherapy, radiotherapy, immune and targeted therapy have been achieved great progress in OC treatment, the 5-year overall survival rate is still very low. One of the major reasons is the lack of effective markers to predict the prognosis which could give OC patients an early opportunity to change the treatment project. Thus, the exploration of new prognostic markers to distinguish and predict OC patients' outcomes have a high clinical value.

Metabolic reprogramming is recently regarded as one of the new hallmarks of cancer (Hanahan and Weinberg, 2011). The previous work showed that one of the key enzymes of vitamin metabolism plays an important role in the process of OC and could be treated as a potential molecular biomarker of OC (Zhang et al., 2017). Recently, the dysfunction of oncogenes and tumor suppressors promotes metabolic reprogramming and enhances nutrient uptake to sustain energy supply and biomass synthesis (Boroughs and DeBerardinis, 2015). The difference in metabolism biology between tumor cells and normal cells makes drugs targeted metabolic pathways, which becomes a hot topic in cancer treatment. New agents focusing on metabolic genes were reported could eliminate tumor cells. The disorder of cell metabolisms such as accumulation of glycogen, fatty acid metabolism, and unsaturated lipids was found to take effect on the development of cancer (Iida et al., 2012). Even though the therapy targeted metabolism system in cancer treatment has proved to be effective, the molecular mechanism is poorly exploited (Khadirnaikar et al., 2020).

Besides, the other important hallmark of cancer is reported as immune infiltration (Hanahan and Weinberg, 2011). The human immune system plays a role in the beginning and process of tumors (Galon et al., 2013; Khadirnaikar et al., 2020). Since the metabolism and immune system are both the vital hallmarks of cancer, they may take part in the development of OC to a certain extent together. Immunotherapy which increases tumor-infiltrating T cells in tumors helps to clear tumor cells effectively because of the immune-active nature of tumors (Baert et al., 2017). The research showed that there was a significant correlation between high lymphocyte infiltration and the survival time in OC patients (Ovarian Tumor Tissue Analysis (OTTA) Consortium, Goode et al., 2017; Khadirnaikar et al., 2020). While the potential processes of the human immune system in some cancer types have been clarified, the mechanism of immune-related genes in OC is still not very clear. And to our knowledge, until now there is no research focusing on the genes of OC from both the metabolism system and immune system simultaneously.

The study was aimed to identify the differently expressed metabolism-related genes and try to further declare their association with the human immune system. We analyzed the correlation between the expression levels of these genes with clinical characteristics. The underlying molecular regulatory mechanisms were also further elucidated through bioinformatics analyses.

MATERIALS AND METHODS

Public Data Mining

The Cancer Genome Atlas database (TCGA[1]) and Genotype-Tissue Expression database (GTEX[2]), which contains 379 OC surgical specimens and 88 normal ovarian tissue for conducting the primary analysis. The transcriptome data of GSE26193 containing 107 OC samples with clinical characteristics (Mateescu et al., 2011) were further retrieved from the Gene Expression Omnibus database (GEO[3]). Patients who received chemotherapy, radiotherapy and treatment before surgery were excluded. Probes were included only with gene annotation and matched with one gene symbol.

Detection of Differently Metabolism-Related Genes

$|\log FC| > 1$ and P-value < 0.05 was set as the cut-off criteria. We screened 91 differently expressed metabolism-related genes by the "limma" R package in TCGA-OV dataset compare to GTEX normal tissues. The mRNA expression was validated by the Gene Expression Profiling Interactive Analysis database (GEPIA[4]) and the Oncomine database[5] (Wen et al., 2020).

Functional Enrichment Analysis and PPI Network Construction

Gene ontology (GO) (Ashburner et al., 2000) and Kyoto Encyclopedia of Genes and Genomes (KEGG) pathway enrichment analyses (Kanehisa et al., 2017) were used to investigate the biological functions of the differently expressed metabolism-related genes by the R package (Ritchie et al., 2015). The Protein-Protein Interaction (PPI) network with high confidence was established from the Search Tool for the Retrieval of Interacting Genes (STRING) database[6] (Szklarczyk et al., 2019).

Establishment of Prognostic Risk Model

TCGA-OV dataset was treated as a training cohort. GSE26193 dataset was adjusted as the external validation cohort. The expression data of the differently metabolism-related genes from the TCGA-OV dataset were employed to establish a risk score model. The impact of each differently expressed metabolism-related gene on OS of OC patients was further to be valued via the univariate Cox proportional risk regression model. Log-rank $P < 0.05$ was considered statistically significant. LASSO-Cox

[1]https://portal.gdc.cancer.gov/
[2]https://www.gtexportal.org
[3]https://www.ncbi.nlm.nih.gov/geo/
[4]http://gepia.cancer-pku.cn/
[5]https://www.oncomine.org/resource/main.html
[6]https://string-db.org/

regression was used to minus the scope of genes (Tibshirani, 1997). Internal and external validation cohorts were then used to verify the robustness of the risk model. Moreover, the clinical indexes and risk scores were included in univariate and multivariate Cox regression analyses to validate the independence of the risk model. A cutoff value by the Gordon index was used to divide the high-risk and low-risk groups (Wen et al., 2020). A log-rank test was used in comparing the survival difference between the two groups. The OS of each group was performed using the Kaplan–Meier (KM) survival curve.

Survival Analysis of Metabolism-Related Genes in Kaplan-Meier Plotter

The OS, PFS, and clinical stage of OC patients were performed from the Kaplan–Meier Plotter[7]. The 95% confidence intervals (CIs) of hazard ratio (HR) and log-rank *P*-value were counted.

Oncomine Analysis

The mRNA levels of the seven differently expressed metabolism-related genes in OC and normal control tissues were analyzed from the Oncomine database[8]. Fold-change = 1.5, $P = 0.05$, mRNA data type were determined as the thresholds.

cBioPortal Database Analysis

The cBioPortal[9] was applied for estimating the genetic alterations of the differently expressed metabolism-related genes. The mRNA expression z scores (RNA Seq V2 RSEM) were got with a z score threshold of ± 2.0 (Zhang et al., 2020). An overview of genetic alterations is presented by OncoPrint.

Correlation of Differently Metabolism-Related Genes With Immune Cells

Further research of the correlation of seven differently expressed metabolism-related genes with immune cells was analyzed in The Tumor IMmune Estimation Resource (TIMER[10]). ESTIMATE (Estimation of STromal and Immune cells in MAlignant Tumors using Expression data) was used to measure the fraction of immune cells in tumor samples using gene expression profile. CIBERSORT (Cell-type Identification By Estimating Relative Subsets Of RNA Transcripts) is a deconvolution algorithm that characterizes the cell composition of complex tissues from gene expression profiles. In the present study, TCGA OC samples were analyzed via the CIBERSORT algorithm to describe 22 immune cells by $P < 0.05$. The violin plot of associations between DGKD, IDO1 expression, and 22 immune cells was produced with "vioplot" and "limma" packages in R 4.02 (Zhang et al., 2021). Scatter plots of the correlation of tumor-infiltrating immune cells proportion with the PNPO expression were plotted with "ggplot2," "ggpubr," and "gridExtra" R packages.

[7]www.kmplot.com

[8]www.oncomine.org

[9]www.cbioportal.org

[10]https://cistrome.shinyapps.io/timer/

qRT-PCR

Total RNA was collected and extracted from human non-tumorous human ovarian surface epithelial cells (HOSEpiC), human OC cell lines SK-OV-3 (adenocarcinoma), OVCAR-3 (adenocarcinoma), ES-2 (clear cell carcinoma), and A2780 (human ovarian carcinoma) by the RNA-Quick Purification Kit (Yishan Biotechnology Co., Ltd., Shanghai, China). The primer sequences were shown in **Supplementary Table 1**.

Immunohistochemistry

The study of the human subject was approved by the Ethics Committee of Shanghai First Maternity and Infant Hospital, Tongji University. Human OC tissues and control tissues were got from Shanghai First Maternity and Infant Hospital. Five ovarian tissue samples were obtained from patients with OC. Five control ovarian tissue samples and five control fallopian tube tissue samples were obtained from patients with non-tumorous ovaries and fallopian tubes, respectively. The following antibodies anti-ACSM3 (#10168-2-AP), anti-TPMT (#10682-1-AP), anti-IDO1 (#13268-1-AP), anti-ACACA (#21923-1-AP), and anti-PGP (#25081-1-AP) were obtained from ProteinTech Group (Chicago, IL, United States). Anti-DGKD (#abs111548) and anti-GFPT2 (#abs111910) were obtained from Absin Bioscience Inc. (Shanghai, China).

Statistical Analysis

Statistical analyses of bioinformatics results were used by R software version 3.6.1[11] and performed by GraphPad Prism 8.0 (GraphPad Software Inc., San Diego, CA, United States). A log-rank test was used to compare the high-risk with the low-risk group in the Kaplan-Meier curve. Different expression of seven hub genes between two groups of experimental results was compared by a two-tailed Student's *t*-test. Data were shown as mean ± the standard deviation. $P < 0.05$ was considered as statistical significance.

RESULTS

Identification of Differently Expressed Genes in OC

The flowchart of the analysis process is displayed in **Supplementary Figure 1**. The gene expression profiles were got from the dataset TCGA and GTEX database, which contains 379 OC surgical specimens and 88 normal ovarian specimens. The heat map of differently expressed genes between human OC tissue and ovarian normal tissue was shown in **Supplementary Figure 2**. Function annotation analyses were then executed. GO enrichment suggested that the differently expressed genes were major consisted of extracellular structure organization, extracellular matrix, and cell adhesion molecular binding (**Supplementary Figure 3A**). KEGG enrichment indicated that the hub genes were mainly related to the cell cycle, Ras signaling pathway, and Platinum drug resistance (**Supplementary Figure 3B**).

[11]https://www.r-project.org/

Identification and Bioinformatics of Hub Genes in OC

The heatmap of total differently expressed metabolism-related genes between OC surgical tissues and control normal ovarian tissues were extracted (**Supplementary Figure 4A**). The PPI network of the differently expressed metabolism-related genes was constructed by the STRING database (**Supplementary Figure 4B**). GO analysis enlightened that the differently metabolism-related genes were mainly related to small molecular catabolic processes, mitochondrial matrix, and coenzyme binding (**Supplementary Figure 4C**). KEGG analysis indicated that the genes were mainly associated with drug metabolism, glycerophospholipid metabolism, and glutathione metabolism (**Supplementary Figure 4D**).

Validation of the Prognostic Risk Model

To determine the correlation with the prognosis, seven differently expressed metabolism-related genes (four low-risk genes and three high-risk genes) were screened as hub genes to be analyzed with overall survival (OS) of OC patients in TCGA (**Figure 1A**). OC patients were separated into a high-risk group (n = 187) and a low-risk group (n = 188) by the median risk score in the training cohort (TCGA dataset). We identified the prognostic outcome was worse in the high-risk group than the low-risk group ($P < 0.01$) (**Figure 1B**). The results of the verification cohort (GSE26193) were similar to the training group (**Figure 1C**). The risk score has a significant correlation with the OS by univariate (**Figure 1D**) and multivariate (**Supplementary Figure 5**) Cox regression analysis. Thus, the results suggested that the risk score was a better factor to predict the prognosis of OC than other clinical indices, such as age and stage. The mRNA expression level of each differently metabolism-related gene was extracted from the GEPIA database. The mRNA expression of GFPT2, DGKD, ACACB, and ACSM3 were downregulated in OC patients, while IDO1, TPMT, and PGP were upregulated in OC patients (**Figure 1E**). It was shown that most genes in the risk model had different expressions in OC mRNA level compared with normal ovarian tissues ($P < 0.05$).

Prognostic Value of the Risk Model

The risk score of patients was ranked (**Figure 2A**) and the survival state of patients was shown by dot chart (**Figure 2B**) in the training cohort. The hub genes were separated into a high-risk and low-risk group which were shown in the heat map (**Figure 2C**). It was suggested that patients in a high-risk score group had worse OS than in a low-risk group. Similarly, the risk score, dot chart, and heat map were similar to the training group (**Figures 2D–F**). The results concluded that the risk model could be served as a prognostic factor of OC patients.

Analysis of Hub Genes and Clinical Data

To investigate the association between metabolism and OC patients' clinical data, we analyze the seven metabolism-related genes with OS, progression-free survival (PFS), and clinical stage. The analysis results indicated that the expression of GFPT2, ACACB, ACSM3, IDO1, TPMT, and PGP had a remarkable association with patient OS (**Figure 3A**), while the expression of GFPT2, DGKD, ACACB, ACSM3, IDO1, and PGP were remarkably associated with patient PFS (**Figure 3B**). For OS analysis, higher expression of GFPT2 and ACACB indicated poorer OS, while higher expression of ACSM3, IDO1, TPMT, and PGP indicated better patient OS ($P < 0.05$). For PFS analysis, higher expression of GFPT2, DGKD, and ACACB indicated poorer PFS, while higher expression of ACSM3, IDO1, and PGP indicated better patient PFS ($P < 0.05$). Exploration of the differently metabolism-related genes during the clinic progression of OC showed that the levels of DGKD, ACACB, TPMT, and PGP were significant correlated with the clinical stage (**Figure 3C**). Thus, these results showed that these genes contribute to the evolution of OC ($P < 0.05$).

Genetic Alterations in OC Patients

ACSM3 and IDO1 were significantly overexpressed in OC, while GFPT2, DGKD, and ACACB were significantly decreased in the Oncomine database (**Supplementary Figure 6A**). The relevant mRNA expression data of TPMT and PGP in OC were absent in the Oncomine database, but they were found to be upregulated in OC in the TCGA database. The analysis of genetic alterations of the hub genes was analyzed from cBioPortal. Amplification, mRNA high, deep deletion, and mutation were found in the high-risk group, while amplification, mRNA high, and deep deletion appeared in the low-risk group. TPMT had the most frequent genetic alterations (15%), while amplification was its most popular genetic alteration (**Supplementary Figures 6B**, 7).

Expression of the Hub Genes in Human OC Cell Lines and Tissues

To further assess the seven metabolism-related gene expression levels in OC, we perform qRT-PCR to search the mRNA expression of the hub genes in human OC cell lines (**Figure 4**). The mRNA expression of GFPT2 was decreased in SK-OV-3, ES-2, and A2780 cell lines than in the control non-tumorous HOSEpiC cell line. DGKD mRNA expression was decreased in OVCAR-3 than HOSEpiC cell line. ACACB mRNA level was lower expressed in all OC cell lines we tested. ACSM3 mRNA expression was decreased in SK-OV-3, OVCAR-3, ES-2, A2780 cell lines than the control cell line. The mRNA expression of IDO1 was higher in SK-OV-3, A2780 than in the HOSEpiC cell line, while PGP mRNA expression was higher in A2780 cells than in control. We also tested the mRNA expression of TPMT, but there was no significant value so we did not show it here. Interestingly, we found the hub genes expression level maybe not very consistent among different cell lines, but the general expression level trend was the same as the results that we extracted from the online database. The protein expression levels of GFPT2, DGKD, ACACB, and ACSM3 were lower in OC tissues than normal ovarian and fallopian tube tissues. While the protein levels of IDO1,

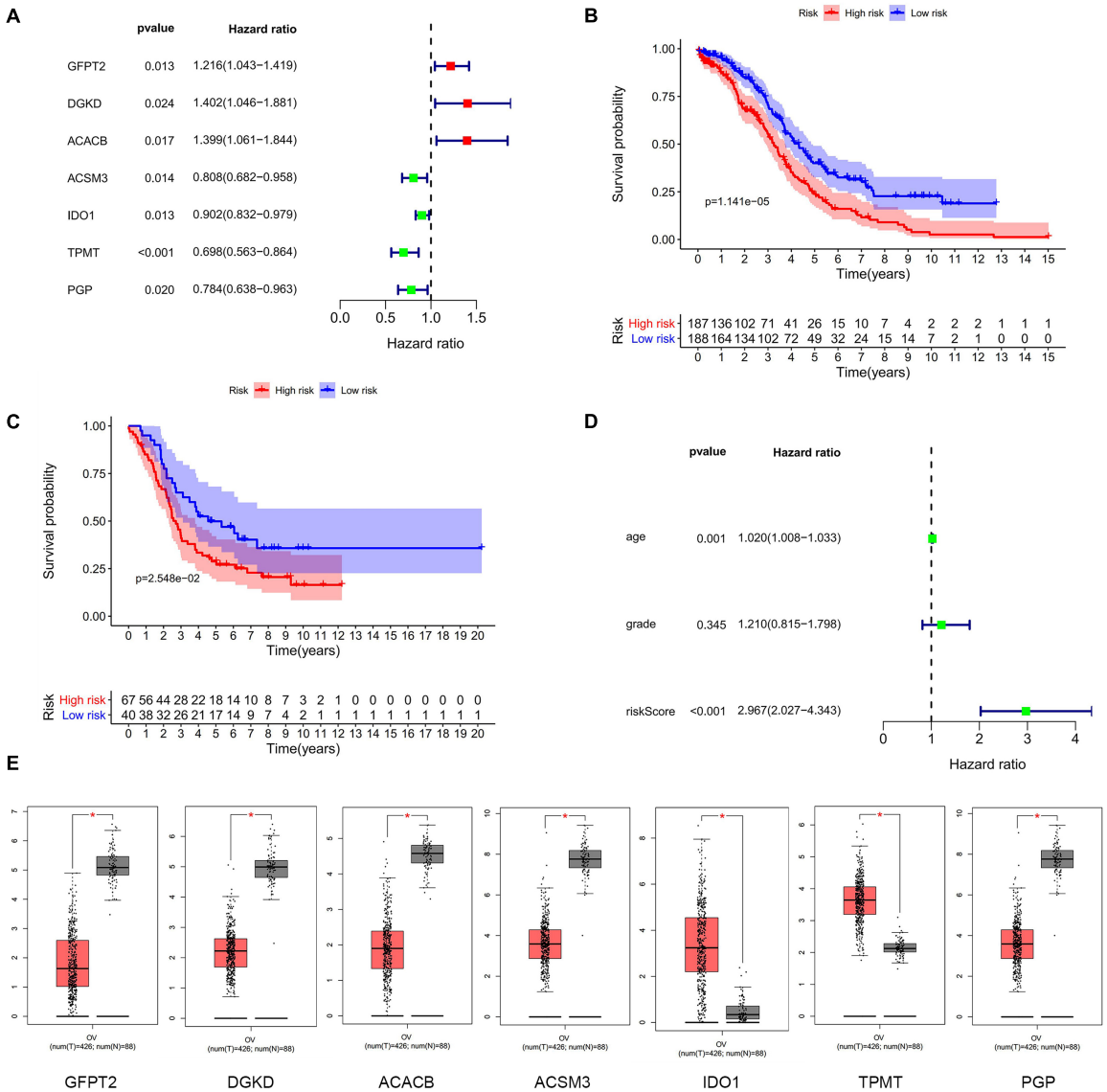

FIGURE 1 | The differently expressed metabolism-related genes panel. **(A)** Establishment of the seven metabolism-related genes' panel correlated to OC patients outcomes. Red, high-risk genes; Green, low-risk genes. **(B)** Kaplan-Meier curve analysis of seven metabolism-related genes with OS in the training dataset of TCGA. Red, high-risk group; Blue, low-risk group. **(C)** Kaplan-Meier curve analysis of seven metabolism-related genes with OS in validation dataset of GEO. Red, high-risk group; Blue, low-risk group. **(D)** Forrest plots in the training cohort. **(E)** The transcription level of seven metabolism-related genes between human OC and normal tissues in TCGA. Red, tumor group; Gray, normal group.

TPMT, and PGP were overexpressed in OC tissues than in control (**Figure 5**).

Correlation With Immune Cell Infiltration in OC Patients

Metabolism and immune disorder were both the important hallmarks of cancer, and they could cross-talk in some content during the process of cancer. We further investigate the correlation in the TIMER database. Two of the hub genes, DGKD and IDO1 have the most significantly association with the infiltration of immune cells. Obviously, a negative correlation between DGKD and the infiltration of B cells (Cor = −0.148, P = 1.19e−03), CD8 + T cells (Cor = −0.199, P = 1.18e−05), macrophages (Cor = −0.149, P = 1.04e−03), neutrophils (Cor = −0.254, P = 1.58e−08), and dendritic cells (Cor = −0.217, P = 1.55e−06) were found, when DGKD was positively associated with the purity (Cor = 0.172, P = 1.42e−04; **Figure 6A**). On the contrary, a positive interrelation between IDO1 expression and the infiltration of B cells (Cor = 0.251, P = 7.34e−05), CD8 + T cells (Cor = 0.472, P = 5.71e−15), CD4 + T cells (Cor = 0.185, P = 3.68e−03), neutrophils (Cor = 0.502, P = 5.91e−17), and dendritic cells (Cor = 0.425, P = 3.79e−12) were showed, while IDO1 was negatively related with the purity (Cor = −0.241,

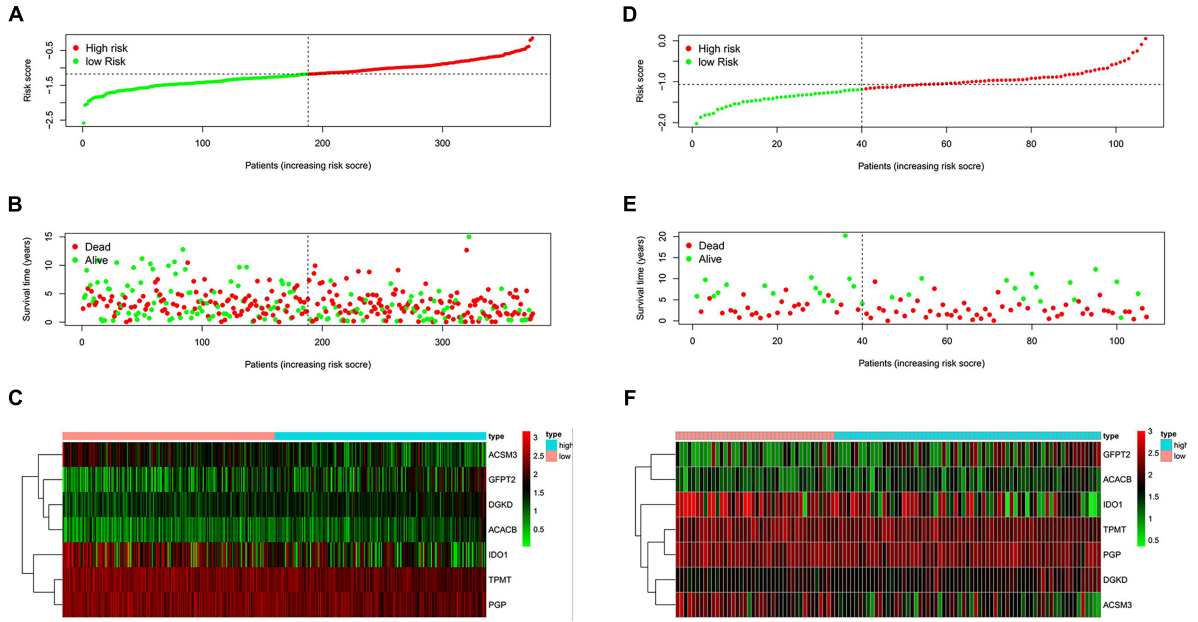

FIGURE 2 | Evaluation of the performance of the risk model. **(A,D)** Distribution of risk score in patients. **(B,E)** Survival status scatter plots of patients (red dots represent death, blue dots represent alive). **(C,F)** The seven-gene expression patterns in the training cohort. **(A–C)** from TCGA database. **(D–F)** from GEO database.

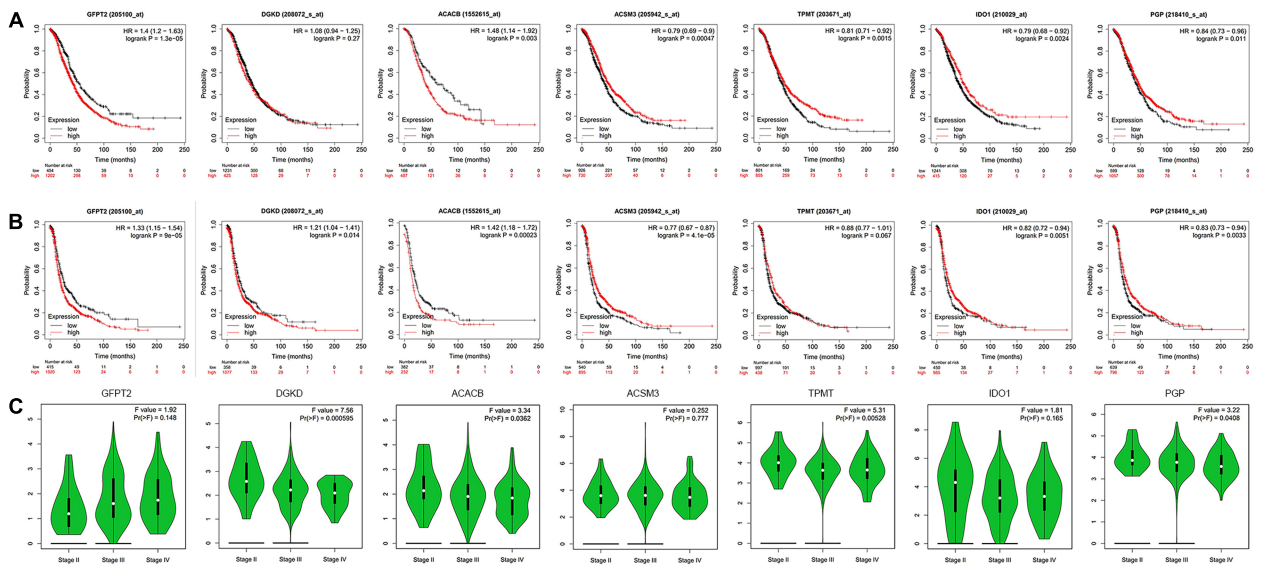

FIGURE 3 | Analysis of hub genes with clinical data. **(A)** Kaplan-Meier curve analysis of OS comparing the high and low levels of seven metabolism-related genes. **(B)** Kaplan-Meier curve analysis of PFS comparing the high and low expression levels of seven metabolism-related genes. **(C)** The violin pot shows the correlations with the clinical stage. Red, high expression; Blue, low expression.

$P = 1.16e{-}04$; **Figure 6B**). Moreover, we also found GFPT2 expression was positively associated with macrophages and neutrophils (**Figure 6C**), while ACACB expression was negatively correlated with neutrophils and dendritic cells (**Figure 6D**). However, there is no significant correlation of the expression of ACSM3, TPMT, and PGP with infiltrating levels of immune cells infiltration (**Figures 6E,F,G**).

To further exam the relationship of DGKD and IDO1 with the organic immune system, tumor-infiltrating immune cells were searched through CIBERSORT and ESTIMATE. It showed a negative relationship between DGKD and immune cells infiltration ($R = -0.25$, $P = 7.4e{-}07$, **Figure 7A**), while a positive association was found between IDO1 expression and immune cells infiltration ($R = 0.54$, $P < 2.2e{-}15$, **Figure 7B**)

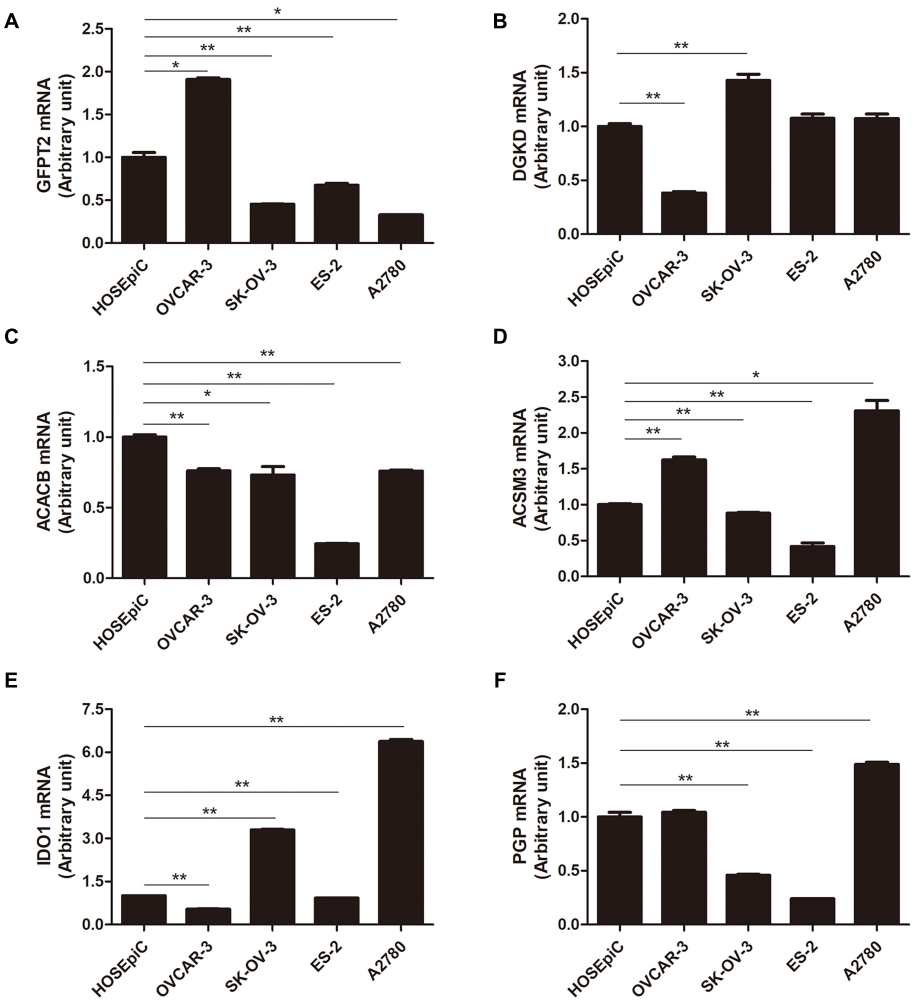

FIGURE 4 | The mRNA level of six hub genes in normal ovarian cell line and OC cell lines by qRT-PCR. **(A)** GFPT2, **(B)** DGKD, **(C)** ACACB, **(D)** ACSM3, **(E)** IDO1, and **(F)** PGP. *$P < 0.05$, **$P < 0.01$.

in CIBERSORT database. The data showed that five types of tumor-infiltrating immune cells were significantly correlated with DGKD expression, including macrophages M0, monocytes, and dendritic cells activated were positive with DGKD, while macrophages M1 and neutrophils were negative with DGKD expression ($P < 0.05$, **Figure 7C**). And six kinds of tumor-infiltrating immune cells have a significant correlation with IDO1, including T cells gamma delta, macrophage M1, T cells follicular helper, and dendritic cells activated were positive with IDO1 expression, while macrophages M0 and macrophages M2 were negative with IDO1 expression ($P < 0.05$, **Figure 7D**). Similarly, we found the infiltration of B cells memory, T cell follicular helper, T cells gamma delta, dendritic cells activated, macrophages M1, NK cell activated, and eosinophils were negatively correlated with the expression of DGKD while macrophages M0 and NK cells resisting were positively correlated with the expression of DGKD in ESTIMATE database (**Supplementary Figure 8A**). The T cells gamma delta, T cells follicular helper, T cells CD4 memory activated, dendritic cells activated, and macrophages M1 were positively related with IDO1 while macrophages M0 and macrophages M2 were negatively associated with IDO1 in the ESTIMATE database (**Supplementary Figure 8B**). These results further proved the expression levels of DGKD and IDO1 could affect the immune system of OC patients.

Correlation of PNPO With Hub Genes in OC Patients

We found PNPO took an essential effect on the progress of OC from our previous work. PNPO was one key enzyme of vitamin B6 and participated in human many physical metabolism processes. The present study showed that the seven hub genes were anticipating the metabolism process of human OC and were associated with immune cell infiltration. We deduced PNPO may have crosstalk with these genes from metabolism and immune process. Then we examined the correlation of PNPO with seven hub genes via TCGA ovarian cancer datasets. It showed a positive correlation between PNPO and IDO1expression (**Figure 8A**), while there was no

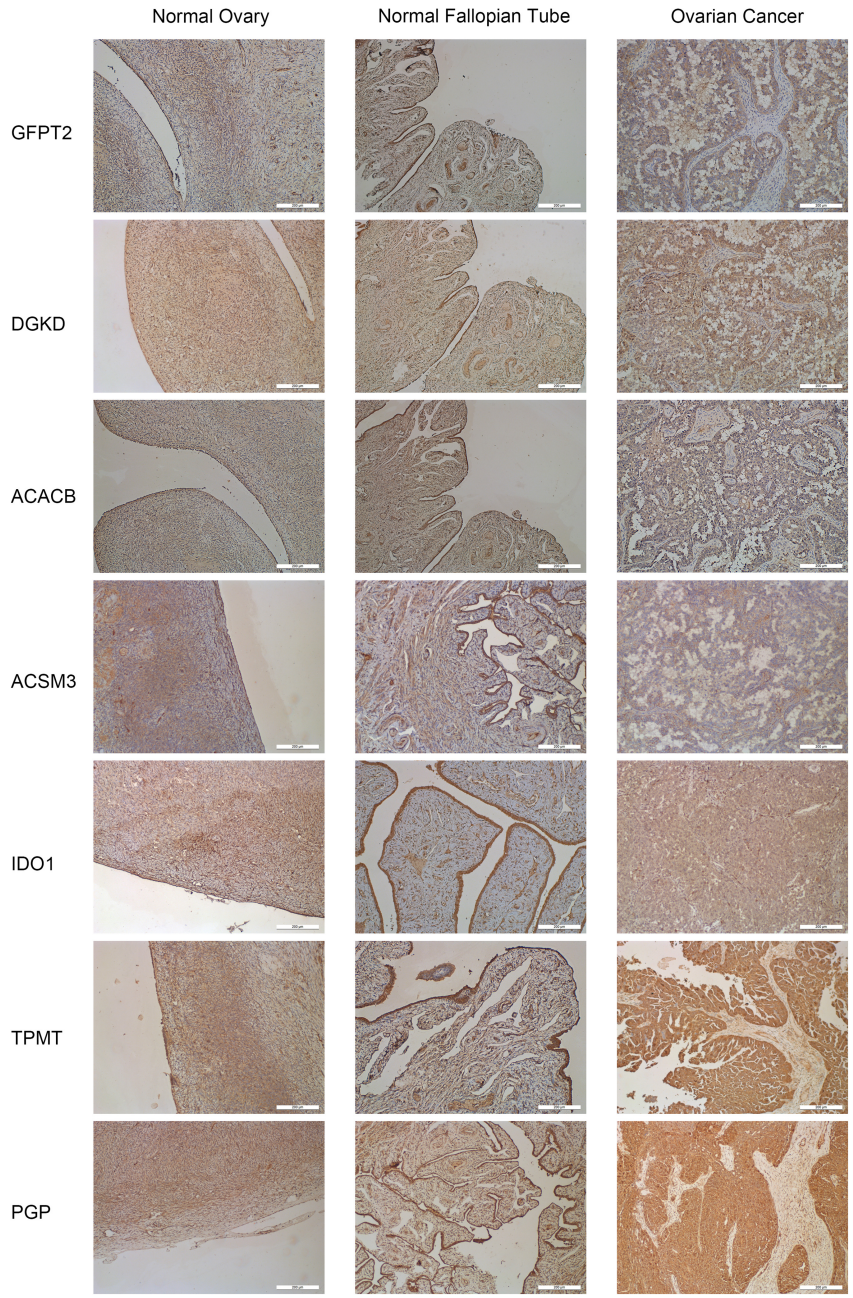

FIGURE 5 | Representative immunohistochemistry staining for seven hub genes in normal ovarian tissues, normal fallopian tube tissues, and OC tissues. The staining of IDO1, TPMT, and PGP was strong in OC tissues. Magnification × 200.

correlation between the expression of PNPO and the other six hub genes (**Figure 8B**). We further found the infiltration of NK cells resisting, macrophages M1 and eosinophils were positively related with the expression of PNPO in the ESTIMATE database (**Supplementary Figure 9A**), although there was no significant correlation in the TIMER database (**Supplementary Figure 9B**). The data indicate that PNPO may take part in the regulation of metabolism and the immune system in OC patients.

DISCUSSION

Many Human OC patients were usually diagnosed in an advanced stage in the world. The OC patients generally have a good response to therapy but in turn to recurrence very soon. Until now, there is no excellent molecular biomarker to assess the prognosis of OC. Therefore, it is urgent to explore novel biomarkers to accurately assess OC patient outcomes. As we knew, cancer is a comprehensive process that depending on the

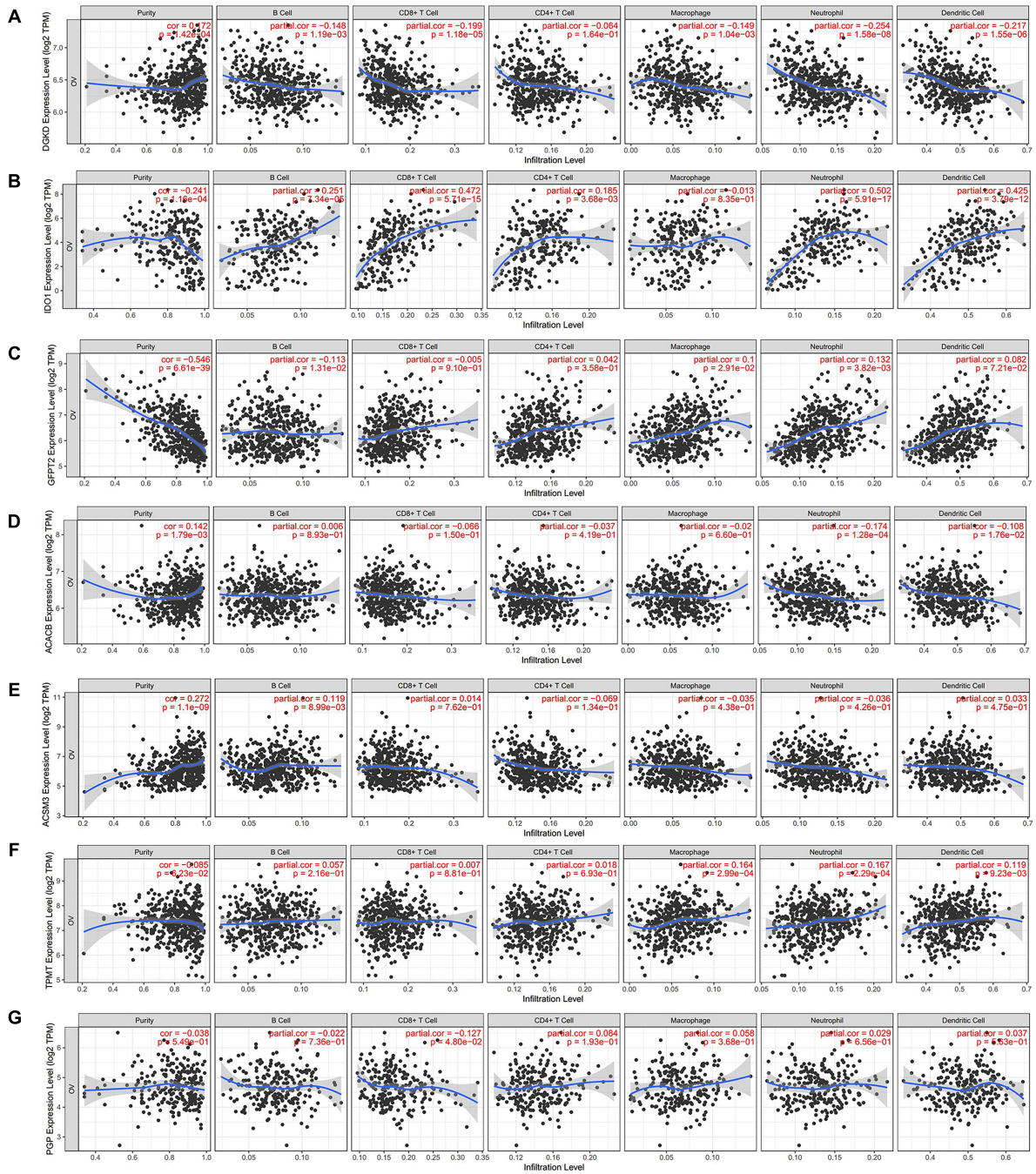

FIGURE 6 | Analysis of immune cells infiltration with seven hub genes expression in TIMER database. The correlation between the infiltration of immune cells and the expression of DGKD **(A)**, IDO1 **(B)**, GFPT2 **(C)**, ACACB **(D)**, ACSM3 **(E)**, TPMT **(F)**, and PGP **(G)**.

interaction among cancer cells, the microenvironment, and the physical immune system. Increasing evidence revealed that the dysfunction of metabolism and immune response could affect the development of cancer.

The current study used TCGA to analyze the mRNA transcriptome of OC patients. We identified the differently expressed metabolism-related genes from a training cohort and perform a firm risk model to predict the survival rate of OC patients. We found a panel of different metabolism-related genes, concluding GFPT2, DGKD, ACACB, ACSM3, IDO1, TPMT, and PGP were correlated with OC patients' survival. Furthermore, comprehensive analyses of the seven differently metabolism-related genes at mRNA and protein levels, genetic alterations were carried out. Besides, we further

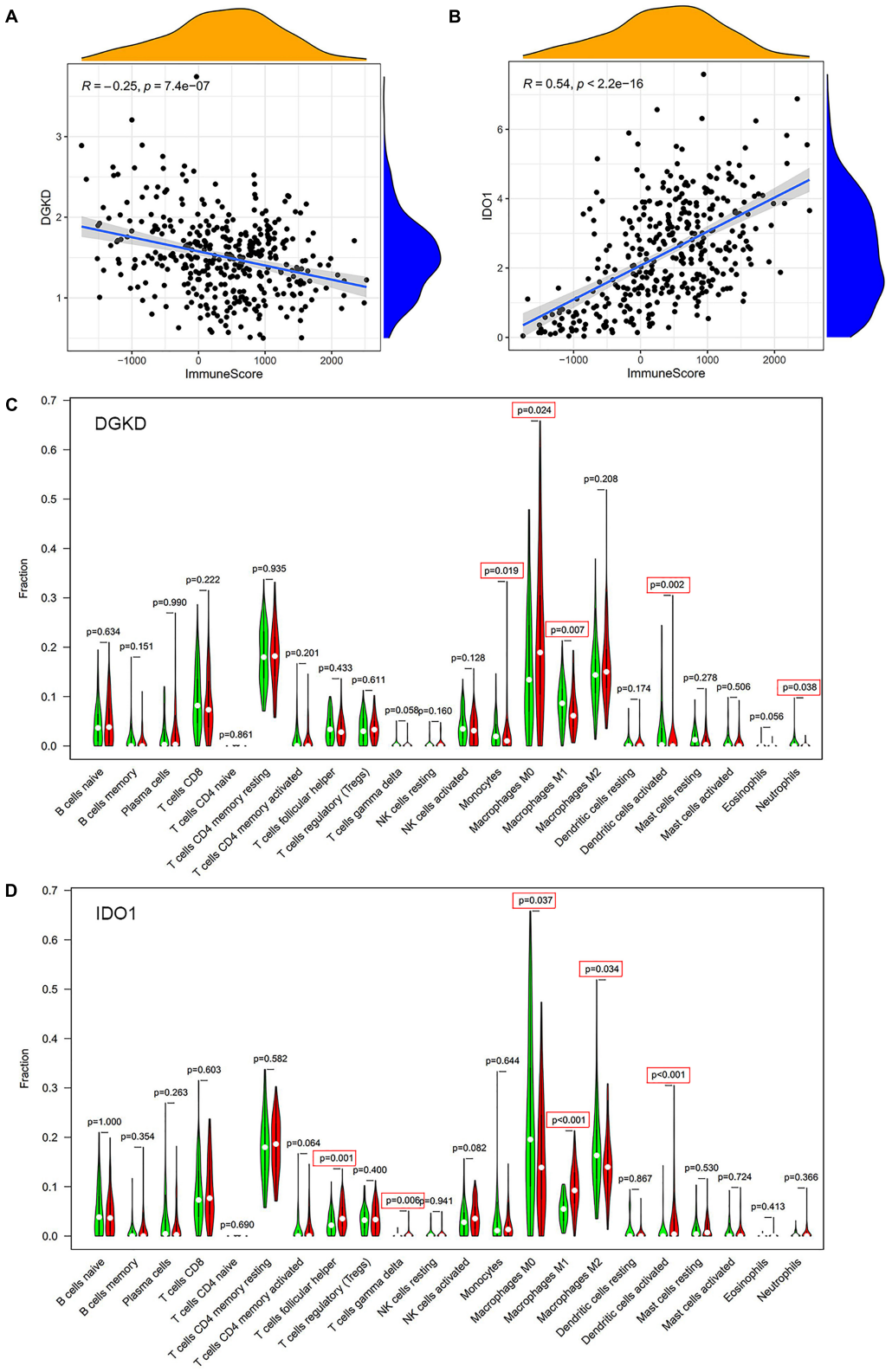

FIGURE 7 | Analysis of immune cells infiltration with DGKD and IDO1 expression in CIBERSORT database. The negative correlation of DGKD expression with immune cells **(A)** and the positive correlation of IDO1 expression with immune cells **(B)**. The Violin plot of immune cells between OC tumor samples with the low or high expression level of DGKD **(C)** and IDO1 **(D)** relative to its median expression level, respectively. Red, high expression; Green, low expression.

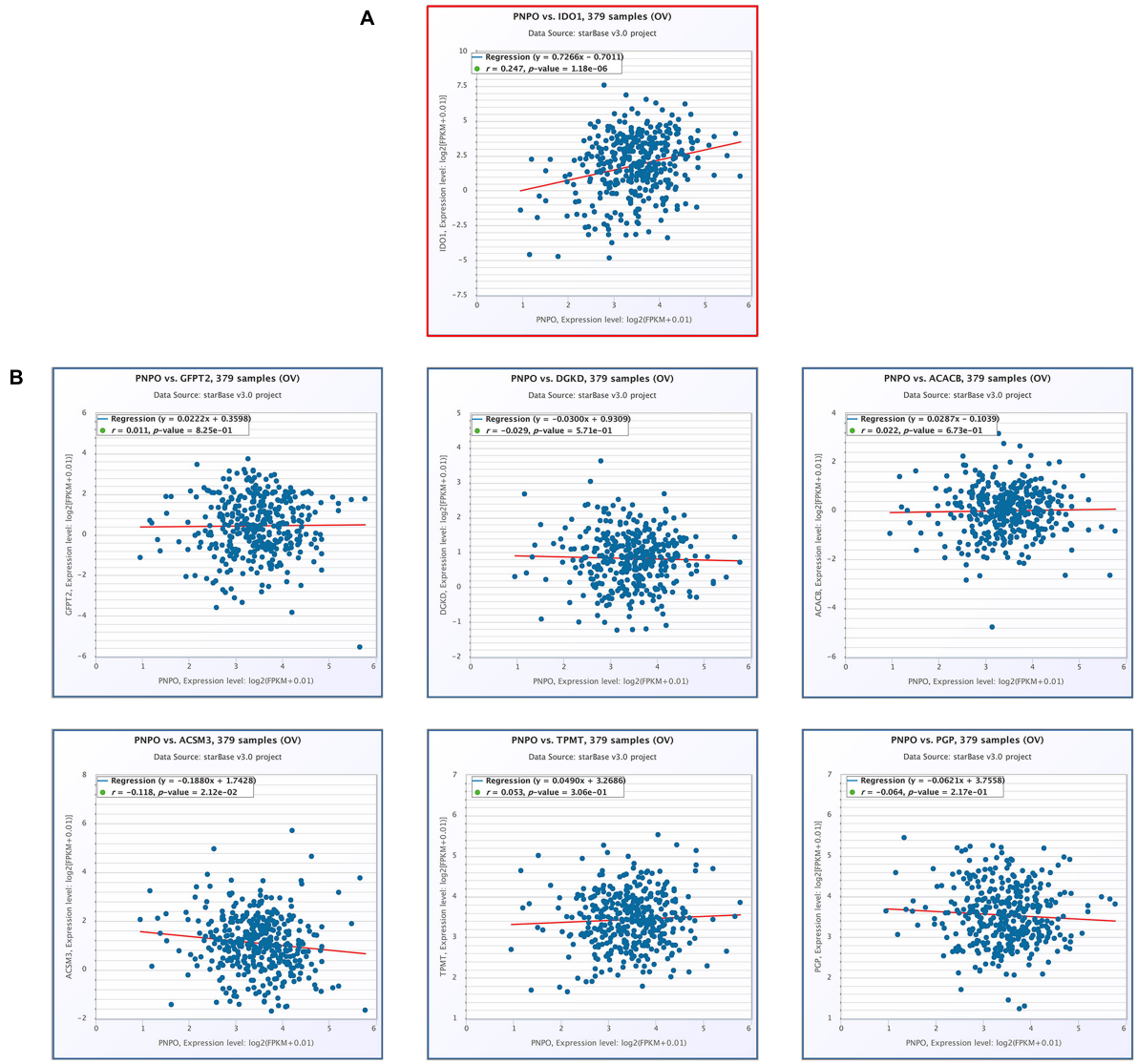

FIGURE 8 | The correlation of seven hub genes with the expression of PNPO in the TCGA-OC cohort (starBase). **(A)** The positive correlation between PNPO and IDO1. **(B)** The correlation between the expression of PNPO and the other six hub genes.

investigate the correlation of the candidate hub genes with the body immune microenvironment from the TIMER, CIBERSORT, and ESTIMATE databases. At last, the genes both associated with human metabolism and immune system were screened.

From our previous work, we found pyridoxine 5′-phosphate oxidase (PNPO) is overexpressed in human OC tissues and could be served as a potential therapeutic target (Zhang et al., 2017). PNPO works as one key enzyme in vitamin B6 metabolism, converting pyridoxine 5′-phosphate and pyridoxamine 5′-phosphate into pyridoxal 5′-phosphate, which serves as a co-factor for more than 150 enzymes constituting about 4% of human enzyme activities (Ueland et al., 2017). Although we did not find PNPO as one of the candidate hub genes of the penal predicting OC patients of prognosis from an online network, we found PNPO plays an essential role in the human metabolism process. The results of PNPO had a positive correlation with IDO1 suggesting that the interaction of different metabolism processes may exist on the development of OC. We further found PNPO has a positive relationship with the infiltration of NK cells resisting, macrophages M1, and eosinophils. These data indicated that PNPO took part in the development of OC not only by affecting the organic metabolism but also by influencing the human physical immune system.

IDO1 is a rate-limiting oxidoreductase that catalyzes tryptophan to kynurenine (Takikawa, 2005). Tryptophan is an essential amino acid needed by the physical metabolism to construct proteins for cellular growth and immune function. IDO1 might restrict the inflow of tryptophan from blood to tumor and produce tumor-toxic metabolites in endothelial

cells, thus decreasing tumor growth (Riesenberg et al., 2007; Feng et al., 2020). We found IDO1 was a low-risk gene and the overexpression of IDO1 may predict a good prognosis for OC patients. It is suggested that the higher expression level of IDO1 has a positive correlation with OS and PFS in OC, which was consistent with our results (Feng et al., 2020). A positive correlation was found between IDO1 and dendritic cells, macrophages, and T cells infiltration (Li et al., 2018; Feng et al., 2020). It was shown that IDO1 is an essential factor in the innate immune system and could be induced by IFN-γ which is mainly produced by activated infiltrating CD8 + and CD4 + T cells (Takikawa et al., 1988; Feng et al., 2020). However, IDO1 was also reported to be related to poor prognosis in some cancer and used as a checkpoint by tumors to escape immune surveillance (Ino, 2011; Tsai et al., 2019; Zhang et al., 2019; Steeneck et al., 2020). It was viewed as a mediator of the immune system in some cancer (Cesario et al., 2011; Kristeleit et al., 2017). The expression of IDO1 seems to decrease tumor infiltration of B cells and to increase the infiltration of regulatory T lymphocytes (Carvajal-Hausdorf et al., 2017). The complexity of this phenomenon may be partly because IDO1 is expressed in two compartments, including tumor cells and tumor-infiltrating lymphocytes. The tumor microenvironment could be influenced by their interaction, result in variant outcomes of tumor prognosis (Feng et al., 2020). These data suggesting us physical energy metabolism genes may take effect by regulating the immune environment in the development of OC. Our results also showed that IDO1 and PNPO have a positive correlation, indicating both tryptophan and vitamin metabolism were involved in the development of OC. How the way of the crosstalk between these two metabolic pathways needs further research.

DGKD, a lipid kinase that terminates diacylglycerol signaling, catalyzes diacylglycerol phosphorylation to produce phosphatidic acid (Kanoh et al., 1990; Murakami et al., 2020). Diacylglycerol was important in lipid metabolism (Chibalin et al., 2008). Intracellular diacylglycerol and phosphatidic acid levels are usually under dynamic equilibrium, and disturbances of this balance may lead to the disorder of cellular metabolism (Chibalin et al., 2008). DGKD is one key enzyme involved in cellular signal transduction (Imai et al., 2002). It was discovered that DGKD overexpression could protect and improve glucose homeostasis in diabetes by AMPK-related signal transduction and lipid metabolism (Jiang et al., 2016; Wada et al., 2016). DGKD regulated the de-ubiquitination of EGFR through targeting Akt and USP8 or by modulating PKC signaling (Crotty et al., 2006; Cai et al., 2010) and decreased the expression of cyclin D1 (Sakai et al., 2018). We found DGKD was a high-risk gene that predicting a poor prognosis of OC patients. We also found DGKD was low expressed in OC patients, and DGKD has a negative correlation with B cells, CD8 + T cells, macrophages, neutrophils, dendritic cells, and NK cells infiltration. To our knowledge, there was no relative report of DGKD in human OC until we prepare this article. The data indicated that DGKD could act as a candidate prognosis indicator gene in OC by affecting physical metabolism and the immune system.

GFPT2 was a key enzyme of the hexosamine biosynthesis pathway that was investigated to anticipate the biology of colorectal cancer cells via enhancing the glycosylation of p65 and activating the NF-κB pathway (Zhang et al., 2018). GFPT2 was discovered to be overexpressed in mesenchymal cell lines (Simpson et al., 2012). The data showed that GFPT2 had a positive association with the clinical stage, which was overexpressed in OC tissues. The down-regulated expression of GFPT2 in OC cells could reduce β-catenin nuclear location and the expression level of Slug and Zeb1 (Zhou et al., 2019). Our data also suggest the GFPT2 was a high-risk gene in OC and is related to poor prognosis in OC.

ACACB is one isoform of acetyl-CoA carboxylase which controls fatty acid β-oxidation (McGarry et al., 1978; Hunkeler et al., 2018). The inhibition of fatty acid oxidation through ACACB could perturb tumor cells absorbing energy (Gonzalez-Angulo et al., 2012; Lu et al., 2019). ACACB has studied metabolic syndrome, obesity, colorectal cancer, diabetes diseases, lung cancer, and hepatocellular carcinoma (Svensson et al., 2016; Yu et al., 2018; Lally et al., 2019). Meanwhile, ACACB was served as a prognostic indicator in breast cancer patients receiving neoadjuvant chemotherapy (Klintman et al., 2016; Lu et al., 2019). ACACB is overexpressed in liver cancer and is highly associated with the prognosis (Ye et al., 2019). We found ACACB was a high-risk gene in OC and is related to poor survival.

The expression of ACSM3 was decreased in hepatocellular carcinoma tissues. And ACSM3 was found to be correlated with poor survival in advanced hepatocellular carcinoma (Gopal et al., 2017; Ruan et al., 2017). Loss of ACSM3 expression was suggested with the activation of the TGFβ, MYC, and WNT signaling pathways (Ruan et al., 2017). There was a positive association between ACSM3 and CD8 + T cells, macrophages, T regulatory cells, and dendritic cells in melanoma (Zhu et al., 2020). In our present study, ACSM3 was decreased in OC and the downregulation of ACSM3 was found to be correlated with poor survival time of OC patients. But there was no correlation between ACSM3 and the immune microenvironment in OC.

TPMT is an enzyme that took an important effect in the metabolism of immunosuppressant azathioprine and mercaptopurine drugs mainly in rheumatoid arthritis, pediatric leukemia, and inflammatory bowel disease (Booth et al., 2011).Several studies have shown that the absence of TPMT activity may be associated with increased risk for drug-related toxicity of patients, including myelosuppression, hepatotoxicity, and pancreatitis (Meggitt and Reynolds, 2001; Gisbert and Gomollon, 2008). TPMT deficiency is associated with severe bone marrow toxicity and the heterozygote of TPMT is an increased risk factor of myelosuppression (Lennard, 2014). PGP has been described as a phosphatase. PGP targets phosphoglycolate, which resulted largely from a side activity of pyruvate kinase (Segerer et al., 2016). PGP was a metabolic repair enzyme that could regulate central carbon metabolism (Linster et al., 2013; Dumont et al., 2019). Until now there is no research on TPMT and PGP of OC. We found that TPMT and PGP were overexpressed in OC patients and had a significant correlation with OS and clinical

stage. Combined with the other five genes, the seven genes panel could be the candidate prognosis biomarkers of OC.

CONCLUSION

We used the seven hub genes panel as a molecular signature to build a risk model which could accurately predict the prognosis in OC patients. High-risk and low-risk of OC patients can be screened by this panel that may help oncologists to provide a more proper therapeutic strategy for patients with OC. Besides, *DGKD* and *IDO1*, two genes of the panel, were significantly correlated with the physical immune system, suggesting that metabolism and immune microenvironment may play crosstalk efforts in the development of OC.

DATA AVAILABILITY STATEMENT

The datasets presented in this study can be found in online repositories. The names of the repository/repositories and accession number(s) can be found in the article/ **Supplementary Material**.

ETHICS STATEMENT

The studies involving human participants were reviewed and approved by the Ethics Committee of Shanghai First Maternity and Infant Hospital, Tongji University (Ethical committee No. KS21161). The patients/participants provided their written informed consent to participate in this study. Written informed consent was obtained from the individual(s) for the publication of any potentially identifiable images or data included in this article.

AUTHOR CONTRIBUTIONS

LZ and WR developed the idea and designed the research. LZ, WS, and JZ analyzed the data. LZ and JZ performed cell culture and PCR. WS performed the IHC. LZ, WS, and WR wrote the draft of the manuscript. GX supervised the study and edited the manuscript. All authors read and approved the final version of the manuscript.

FUNDING

This study was supported by grants from the National Natural Science Foundation of China (grants nos. 81902624 and 81872121).

SUPPLEMENTARY MATERIAL

The Supplementary Material for this article can be found online at: https://www.frontiersin.org/articles/10.3389/fcell.2021.690542/full#supplementary-material

Supplementary Figure 1 | The analysis flow chat of this study in finding hub genes of human ovarian cancer.

Supplementary Figure 2 | Heatmap of differently expressed genes between human ovarian cancer and normal ovarian tissue.

Supplementary Figure 3 | GO and KEGG analysis of differently expressed genes between ovarian cancer and normal ovarian tissue. **(A)** Go enrichment analysis. **(B)** KEGG analysis.

Supplementary Figure 4 | Identification of the differentially expressed metabolism-related genes. **(A)** Heatmap of the differentially expressed metabolism-related genes between OC and normal tissue in TCGA. Red, high expression; Green, low expression. **(B)** PPI network of the hub genes based on the STRING database. **(C)** GO enrichment analysis results. **(D)** KEGG pathway enrichment analysis results.

Supplementary Figure 5 | Forrest plots of multivariate Cox regression analysis in the training cohort.

Supplementary Figure 6 | The expression of seven metabolism-related hub-genes in OC patients. **(A)** The mRNA levels of seven metabolism-related genes in OC (Oncomine). Red, high expression; Blue, low expression. **(B)** OncoPrint summary of genetic alterations of the hub genes.

Supplementary Figure 7 | Summary of alteration frequency with high expression **(A)** and low expression **(B)** of seven genes, respectively.

Supplementary Figure 8 | Association of immune cells with DGKD **(A)** and IDO1 **(B)** expression in ESTIMATE.

Supplementary Figure 9 | Association of immune cells with PNPO expression in ESTIMATE database **(A)** and TIMER database **(B)**.

REFERENCES

Ashburner, M., Ball, C. A., Blake, J. A., Botstein, D., Butler, H., Cherry, J. M., et al. (2000). Gene ontology: tool for the unification of biology. The gene ontology consortium. *Nat. Genet.* 25, 25–29. doi: 10.1038/75556

Baert, T., Vergote, I., and Coosemans, A. (2017). Ovarian cancer and the immune system. *Gynecol. Oncol. Rep.* 19, 57–58. doi: 10.1016/j.gore.2017.01.002

Booth, R. A., Ansari, M. T., Loit, E., Tricco, A. C., Weeks, L., Doucette, S., et al. (2011). Assessment of thiopurine S-methyltransferase activity in patients prescribed thiopurines: a systematic review. *Ann. Intern. Med.* 154, 814–823. doi: 10.7326/0003-4819-154-12-201106210-00009

Boroughs, L. K., and DeBerardinis, R. J. (2015). Metabolic pathways promoting cancer cell survival and growth. *Nat. Cell Biol.* 17, 351–359. doi: 10.1038/ncb3124

Cai, J., Crotty, T. M., Reichert, E., Carraway, K. L. 3rd, Stafforini, D. M., and Topham, M. K. (2010). Diacylglycerol kinase delta and protein kinase C(alpha) modulate epidermal growth factor receptor abundance and degradation through ubiquitin-specific protease 8. *J. Biol. Chem.* 285, 6952–6959. doi: 10.1074/jbc.M109.055731

Carvajal-Hausdorf, D. E., Mani, N., Velcheti, V., Schalper, K. A., and Rimm, D. L. (2017). Objective measurement and clinical significance of IDO1 protein in hormone receptor-positive breast cancer. *J. Immunother. Cancer* 5:81. doi: 10.1186/s40425-017-0285-7

Cesario, A., Rocca, B., and Rutella, S. (2011). The interplay between indoleamine 2,3-dioxygenase 1 (IDO1) and cyclooxygenase (COX)-2 in chronic inflammation and cancer. *Curr. Med. Chem.* 18, 2263–2271. doi: 10.2174/092986711795656063

Chibalin, A. V., Leng, Y., Vieira, E., Krook, A., Bjornholm, M., Long, Y. C., et al. (2008). Downregulation of diacylglycerol kinase delta contributes to hyperglycemia-induced insulin resistance. *Cell* 132, 375–386. doi: 10.1016/j.cell.2007.12.035

Crotty, T., Cai, J., Sakane, F., Taketomi, A., Prescott, S. M., and Topham, M. K. (2006). Diacylglycerol kinase delta regulates protein kinase C and epidermal growth factor receptor signaling. *Proc. Natl. Acad. Sci. U.S.A.* 103, 15485–15490. doi: 10.1073/pnas.0604104103

Dumont, L., Richardson, M. B., van der Peet, P., Marapana, D. S., Triglia, T., Dixon, M. W. A., et al. (2019). The metabolite repair enzyme phosphoglycolate phosphatase regulates central carbon metabolism and fosmidomycin sensitivity in plasmodium falciparum. *mBio* 10, e2060–e2019. doi: 10.1128/mBio.02060-19

Feng, X., Tang, R., Zhang, R., Wang, H., Ji, Z., Shao, Y., et al. (2020). A comprehensive analysis of IDO1 expression with tumour-infiltrating immune cells and mutation burden in gynaecologic and breast cancers. *J. Cell Mol. Med.* 24, 5238–5248. doi: 10.1111/jcmm.15176

Galon, J., Angell, H. K., Bedognetti, D., and Marincola, F. M. (2013). The continuum of cancer immunosurveillance: prognostic, predictive, and mechanistic signatures. *Immunity* 39, 11–26. doi: 10.1016/j.immuni.2013.07.008

Gisbert, J. P., and Gomollon, F. (2008). Thiopurine-induced myelotoxicity in patients with inflammatory bowel disease: a review. *Am. J. Gastroenterol.* 103, 1783–1800. doi: 10.1111/j.1572-0241.2008.01848.x

Gonzalez-Angulo, A. M., Iwamoto, T., Liu, S., Chen, H., Do, K. A., Hortobagyi, G. N., et al. (2012). Gene expression, molecular class changes, and pathway analysis after neoadjuvant systemic therapy for breast cancer. *Clin. Cancer Res.* 18, 1109–1119. doi: 10.1158/1078-0432.CCR-11-2762

Gopal, R., Selvarasu, K., Pandian, P. P., and Ganesan, K. (2017). Integrative transcriptome analysis of liver cancer profiles identifies upstream regulators and clinical significance of ACSM3 gene expression. *Cell Oncol. (Dordr.)* 40, 219–233. doi: 10.1007/s13402-017-0321-0

Hanahan, D., and Weinberg, R. A. (2011). Hallmarks of cancer: the next generation. *Cell* 144, 646–674. doi: 10.1016/j.cell.2011.02.013

Hunkeler, M., Hagmann, A., Stuttfeld, E., Chami, M., Guri, Y., Stahlberg, H., et al. (2018). Structural basis for regulation of human acetyl-CoA carboxylase. *Nature* 558, 470–474. doi: 10.1038/s41586-018-0201-4

Iida, Y., Aoki, K., Asakura, T., Ueda, K., Yanaihara, N., Takakura, S., et al. (2012). Hypoxia promotes glycogen synthesis and accumulation in human ovarian clear cell carcinoma. *Int. J. Oncol.* 40, 2122–2130. doi: 10.3892/ijo.2012.1406

Imai, S., Sakane, F., and Kanoh, H. (2002). Phorbol ester-regulated oligomerization of diacylglycerol kinase delta linked to its phosphorylation and translocation. *J. Biol. Chem.* 277, 35323–35332. doi: 10.1074/jbc.M202035200

Ino, K. (2011). Indoleamine 2,3-dioxygenase and immune tolerance in ovarian cancer. *Curr. Opin. Obstet. Gynecol.* 23, 13–18. doi: 10.1097/GCO.0b013e3283409c79

Jiang, L. Q., de Castro Barbosa, T., Massart, J., Deshmukh, A. S., Lofgren, L., Duque-Guimaraes, D. E., et al. (2016). Diacylglycerol kinase-delta regulates AMPK signaling, lipid metabolism, and skeletal muscle energetics. *Am. J. Physiol. Endocrinol. Metab.* 310, E51–E60. doi: 10.1152/ajpendo.00209.2015

Kanehisa, M., Furumichi, M., Tanabe, M., Sato, Y., and Morishima, K. (2017). KEGG: new perspectives on genomes, pathways, diseases and drugs. *Nucleic Acids Res.* 45, D353–D361. doi: 10.1093/nar/gkw1092

Kanoh, H., Yamada, K., and Sakane, F. (1990). Diacylglycerol kinase: a key modulator of signal transduction? *Trends Biochem. Sci.* 15, 47–50. doi: 10.1016/0968-0004(90)90172-8

Khadirnaikar, S., Kumar, P., and Shukla, S. K. (2020). Development and validation of an immune prognostic signature for ovarian carcinoma. *Cancer Rep. (Hoboken)* 3:e1166. doi: 10.1002/cnr2.1166

Klintman, M., Buus, R., Cheang, M. C., Sheri, A., Smith, I. E., and Dowsett, M. (2016). Changes in expression of genes representing key biologic processes after neoadjuvant chemotherapy in breast cancer, and prognostic implications in residual disease. *Clin. Cancer Res.* 22, 2405–2416. doi: 10.1158/1078-0432.CCR-15-1488

Kristeleit, R., Davidenko, I., Shirinkin, V., El-Khouly, F., Bondarenko, I., Goodheart, M. J., et al. (2017). A randomised, open-label, phase 2 study of the IDO1 inhibitor epacadostat (INCB024360) versus tamoxifen as therapy for biochemically recurrent (CA-125 relapse)-only epithelial ovarian cancer, primary peritoneal carcinoma, or fallopian tube cancer. *Gynecol. Oncol.* 146, 484–490. doi: 10.1016/j.ygyno.2017.07.005

Lally, J. S. V., Ghoshal, S., DePeralta, D. K., Moaven, O., Wei, L., Masia, R., et al. (2019). Inhibition of Acetyl-CoA carboxylase by phosphorylation or the inhibitor ND-654 suppresses lipogenesis and hepatocellular carcinoma. *Cell Metab.* 29, 174.e5–182.e5. doi: 10.1016/j.cmet.2018.08.020

Lennard, L. (2014). Implementation of TPMT testing. *Br. J. Clin. Pharmacol.* 77, 704–714. doi: 10.1111/bcp.12226

Li, S., Han, X., Lyu, N., Xie, Q., Deng, H., Mu, L., et al. (2018). Mechanism and prognostic value of indoleamine 2,3-dioxygenase 1 expressed in hepatocellular carcinoma. *Cancer Sci.* 109, 3726–3736. doi: 10.1111/cas.13811

Linster, C. L., Van Schaftingen, E., and Hanson, A. D. (2013). Metabolite damage and its repair or pre-emption. *Nat. Chem. Biol.* 9, 72–80. doi: 10.1038/nchembio.1141

Lu, X., Gao, C., Liu, C., Zhuang, J., Su, P., Li, H., et al. (2019). Identification of the key pathways and genes involved in HER2-positive breast cancer with brain metastasis. *Pathol. Res. Pract.* 215:152475. doi: 10.1016/j.prp.2019.152475

Mateescu, B., Batista, L., Cardon, M., Gruosso, T., de Feraudy, Y., Mariani, O., et al. (2011). miR-141 and miR-200a act on ovarian tumorigenesis by controlling oxidative stress response. *Nat. Med.* 17, 1627–1635. doi: 10.1038/nm.2512

McGarry, J. D., Leatherman, G. F., and Foster, D. W. (1978). Carnitine palmitoyltransferase I. The site of inhibition of hepatic fatty acid oxidation by malonyl-CoA. *J. Biol. Chem.* 253, 4128–4136. doi: 10.1016/s0021-9258(17)34693-8

Meggitt, S. J., and Reynolds, N. J. (2001). Azathioprine for atopic dermatitis. *Clin. Exp. Dermatol.* 26, 369–375. doi: 10.1046/j.1365-2230.2001.00837.x

Murakami, C., Hoshino, F., Sakai, H., Hayashi, Y., Yamashita, A., and Sakane, F. (2020). Diacylglycerol kinase delta and sphingomyelin synthase-related protein functionally interact via their sterile alpha motif domains. *J. Biol. Chem.* 295, 2932–2947. doi: 10.1074/jbc.RA119.012369

Ovarian Tumor Tissue Analysis (OTTA) Consortium, Goode, E. L., Block, M. S., Kalli, K. R., Vierkant, R. A., Chen, W., et al. (2017). Dose-response association of CD8+ tumor-infiltrating lymphocytes and survival time in high-grade serous ovarian cancer. *JAMA Oncol.* 3:e173290. doi: 10.1001/jamaoncol.2017.3290

Riesenberg, R., Weiler, C., Spring, O., Eder, M., Buchner, A., Popp, T., et al. (2007). Expression of indoleamine 2,3-dioxygenase in tumor endothelial cells correlates with long-term survival of patients with renal cell carcinoma. *Clin. Cancer Res.* 13, 6993–7002. doi: 10.1158/1078-0432.CCR-07-0942

Ritchie, M. E., Phipson, B., Wu, D., Hu, Y., Law, C. W., Shi, W., et al. (2015). limma powers differential expression analyses for RNA-sequencing and microarray studies. *Nucleic Acids Res.* 43:e47. doi: 10.1093/nar/gkv007

Ruan, H. Y., Yang, C., Tao, X. M., He, J., Wang, T., Wang, H., et al. (2017). Downregulation of ACSM3 promotes metastasis and predicts poor prognosis in hepatocellular carcinoma. *Am. J. Cancer Res.* 7, 543–553.

Sakai, H., Murakami, C., Matsumoto, K. I., Urano, T., and Sakane, F. (2018). Diacylglycerol kinase delta controls down-regulation of cyclin D1 for C2C12 myogenic differentiation. *Biochimie* 151, 45–53. doi: 10.1016/j.biochi.2018.05.017

Segerer, G., Hadamek, K., Zundler, M., Fekete, A., Seifried, A., Mueller, M. J., et al. (2016). An essential developmental function for murine phosphoglycolate phosphatase in safeguarding cell proliferation. *Sci. Rep.* 6:35160. doi: 10.1038/srep35160

Siegel, R. L., Miller, K. D., and Jemal, A. (2020). Cancer statistics, 2020. *CA Cancer J. Clin.* 70, 7–30. doi: 10.3322/caac.21590

Simpson, N. E., Tryndyak, V. P., Beland, F. A., and Pogribny, I. P. (2012). An in vitro investigation of metabolically sensitive biomarkers in breast cancer progression. *Breast Cancer Res. Treat.* 133, 959–968. doi: 10.1007/s10549-011-1871-x

Steeneck, C., Kinzel, O., Anderhub, S., Hornberger, M., Pinto, S., Morschhaeuser, B., et al. (2020). Discovery of Hydroxyamidine based inhibitors of IDO1 for cancer immunotherapy with reduced potential for glucuronidation. *ACS Med. Chem. Lett.* 11, 179–187. doi: 10.1021/acsmedchemlett.9b00572

Svensson, R. U., Parker, S. J., Eichner, L. J., Kolar, M. J., Wallace, M., Brun, S. N., et al. (2016). Inhibition of acetyl-CoA carboxylase suppresses fatty acid synthesis and tumor growth of non-small-cell lung cancer in preclinical models. *Nat. Med.* 22, 1108–1119. doi: 10.1038/nm.4181

Szklarczyk, D., Gable, A. L., Lyon, D., Junge, A., Wyder, S., Huerta-Cepas, J., et al. (2019). STRING v11: protein-protein association networks with increased coverage, supporting functional discovery in genome-wide experimental datasets. *Nucleic Acids Res.* 47, D607–D613. doi: 10.1093/nar/gky1131

Takikawa, O. (2005). Biochemical and medical aspects of the indoleamine 2,3-dioxygenase-initiated L-tryptophan metabolism. *Biochem. Biophys. Res. Commun.* 338, 12–19. doi: 10.1016/j.bbrc.2005.09.032

Takikawa, O., Kuroiwa, T., Yamazaki, F., and Kido, R. (1988). Mechanism of interferon-gamma action. Characterization of indoleamine 2,3-dioxygenase in cultured human cells induced by interferon-gamma and evaluation of the enzyme-mediated tryptophan degradation in its anticellular activity. *J. Biol. Chem.* 263, 2041–2048. doi: 10.1016/s0021-9258(19)77982-4

Tibshirani, R. (1997). The lasso method for variable selection in the Cox model. *Stat. Med.* 16, 385–395. doi: 10.1002/(sici)1097-0258(19970228)16:4<385::aid-sim380>3.0.co;2-3

Tsai, Y. S., Jou, Y. C., Tsai, H. T., Cheong, I. S., and Tzai, T. S. (2019). Indoleamine-2,3-dioxygenase-1 expression predicts poorer survival and up-regulates ZEB2 expression in human early stage bladder cancer. *Urol. Oncol.* 37, 810.e17–810.e27. doi: 10.1016/j.urolonc.2019.05.005

Ueland, P. M., McCann, A., Midttun, O., and Ulvik, A. (2017). Inflammation, vitamin B6 and related pathways. *Mol. Aspects Med.* 53, 10–27. doi: 10.1016/j.mam.2016.08.001

Wada, Y., Sakiyama, S., Sakai, H., and Sakane, F. (2016). Myristic acid enhances diacylglycerol kinase delta-dependent glucose uptake in myotubes. *Lipids* 51, 897–903. doi: 10.1007/s11745-016-4162-9

Wen, F., Huang, J., Lu, X., Huang, W., Wang, Y., Bai, Y., et al. (2020). Identification and prognostic value of metabolism-related genes in gastric cancer. *Aging (Albany NY)* 12, 17647–17661. doi: 10.18632/aging.103838

Ye, B., Yin, L., Wang, Q., and Xu, C. (2019). ACC1 is overexpressed in liver cancers and contributes to the proliferation of human hepatoma Hep G2 cells and the rat liver cell line BRL 3A. *Mol. Med. Rep.* 19, 3431–3440. doi: 10.3892/mmr.2019.9994

Yu, C., Hong, H., Lu, J., Zhao, X., Hu, W., Zhang, S., et al. (2018). Prediction of target genes and pathways associated with cetuximab insensitivity in colorectal cancer. *Technol. Cancer Res. Treat.* 17:1533033818806905. doi: 10.1177/1533033818806905

Zhang, J., Pang, Y., Xie, T., and Zhu, L. (2019). CXCR4 antagonism in combination with IDO1 inhibition weakens immune suppression and inhibits tumor growth in mouse breast cancer bone metastases. *Onco Targets Ther.* 12, 4985–4992. doi: 10.2147/OTT.S200643

Zhang, J., Wang, L., Xu, X., Li, X., Guan, W., Meng, T., et al. (2020). Transcriptome-based network analysis unveils eight immune-related genes as molecular signatures in the immunomodulatory subtype of triple-negative breast cancer. *Front. Oncol.* 10:1787. doi: 10.3389/fonc.2020.01787

Zhang, J., Zhang, J., Wang, F., Xu, X., Li, X., Guan, W., et al. (2021). Overexpressed COL5A1 is correlated with tumor progression, paclitaxel resistance, and tumor-infiltrating immune cells in ovarian cancer. *J. Cell Physiol.* 1–13. doi: 10.1002/jcp.30350

Zhang, L., Zhou, D., Guan, W., Ren, W., Sun, W., Shi, J., et al. (2017). Pyridoxine 5'-phosphate oxidase is a novel therapeutic target and regulated by the TGF-beta signalling pathway in epithelial ovarian cancer. *Cell Death Dis.* 8:3214. doi: 10.1038/s41419-017-0050-3

Zhang, W., Bouchard, G., Yu, A., Shafiq, M., Jamali, M., Shrager, J. B., et al. (2018). GFPT2-expressing cancer-associated fibroblasts mediate metabolic reprogramming in human lung adenocarcinoma. *Cancer Res.* 78, 3445–3457. doi: 10.1158/0008-5472.CAN-17-2928

Zhou, L., Luo, M., Cheng, L. J., Li, R. N., Liu, B., and Linghu, H. (2019). Glutamine-fructose-6-phosphate transaminase 2 (GFPT2) promotes the EMT of serous ovarian cancer by activating the hexosamine biosynthetic pathway to increase the nuclear location of beta-catenin. *Pathol. Res. Pract.* 215:152681. doi: 10.1016/j.prp.2019.152681

Zhu, Z., Wang, D., and Shen, Y. (2020). Loss of ACSM3 confers worsened prognosis and immune exclusion to cutaneous melanoma. *J. Cancer* 11, 6582–6590. doi: 10.7150/jca.48354

Conflict of Interest: The authors declare that the research was conducted in the absence of any commercial or financial relationships that could be construed as a potential conflict of interest.

frontiers in Cell and Developmental Biology

ORIGINAL RESEARCH
published: 07 September 2021
doi: 10.3389/fcell.2021.731790

Identification and Validation of a Nine-Gene Amino Acid Metabolism-Related Risk Signature in HCC

*Yajuan Zhao†, Junli Zhang†, Shuhan Wang, Qianqian Jiang and Keshu Xu**

Division of Gastroenterology, Union Hospital, Tongji Medical College, Huazhong University of Science and Technology, Wuhan, China

OPEN ACCESS

Edited by:
Guillermo Barreto, UMR 7365 CNRS-Université de Lorraine, Biopôle de l'Université de Lorraine, France

Reviewed by:
Indrabahadur Singh, German Cancer Research Center (DKFZ), Germany
Miguel Angel Olmedo Suarez, Consejo de Ciencia y Tecnología del Estado de Puebla (CONCYTEP), Mexico

***Correspondence:**
Keshu Xu
xl2017@hust.edu.cn

†These authors have contributed equally to this work and share first authorship

Specialty section:
This article was submitted to Molecular and Cellular Oncology, a section of the journal Frontiers in Cell and Developmental Biology

Received: *28 June 2021*
Accepted: *12 August 2021*
Published: *07 September 2021*

Citation:
Zhao Y, Zhang J, Wang S, Jiang Q and Xu K (2021) Identification and Validation of a Nine-Gene Amino Acid Metabolism-Related Risk Signature in HCC. Front. Cell Dev. Biol. 9:731790. doi: 10.3389/fcell.2021.731790

Background: Hepatocellular carcinoma (HCC) is the world's second most deadly cancer, and metabolic reprogramming is its distinguishing feature. Among metabolite profiling, variation in amino acid metabolism supports tumor proliferation and metastasis to the most extent, yet a systematic study on the role of amino acid metabolism-related genes in HCC is still lacking. An effective amino acid metabolism-related prediction signature is urgently needed to assess the prognosis of HCC patients for individualized treatment.

Materials and Methods: RNA-seq data of HCC from the TCGA-LIHC and GSE14520 (GPL3921) datasets were defined as the training set and validation set, respectively. Amino acid metabolic genes were extracted from the Molecular Signature Database. Univariate Cox and LASSO regression analyses were performed to build a predictive risk signature. K-M curves, ROC curves, and univariate and multivariate Cox regression were conducted to evaluate the predictive value of this risk signature. Functional enrichment was analyzed by GSEA and CIBERSORTx software.

Results: A nine-gene amino acid metabolism-related risk signature including B3GAT3, B4GALT2, CYB5R3, GNPDA1, GOT2, HEXB, HMGCS2, PLOD2, and SEPHS1 was constructed to predict the overall survival (OS) of HCC patients. Patients were separated into high-risk and low-risk groups based on risk scores and low-risk patients had lower risk scores and longer survival time. Univariate and multivariate Cox regression verified that this signature was an independent risk factor for HCC. ROC curves showed that this risk signature can effectively predict the 1-, 2-, 3- and 5-year survival times of patients with HCC. Additionally, prognostic nomograms were established based on the training set and validation set. These genes were closely correlated with the immune regulation.

Conclusion: Our study identified a nine-gene amino acid metabolism-related risk signature and built predictive nomograms for OS in HCC. These findings will help us to personalize the treatment of liver cancer patients.

Keywords: amino acid metabolism, gene, prognosis, immune infiltration, nomogram, hepatocellular carcinoma

INTRODUCTION

A series of biochemical changes during cancer development can promote infinite tumor cell proliferation, activate tissue invasion and metastasis, and prevent tumor cell growth from being inhibited. Metabolic reprogramming is one of the most critical biochemical variations observed in cancer (Boroughs and DeBerardinis, 2015). Amino acids are essential nutrients and energy sources for tumor cells. Amino acids associate with the metabolism of glucose, lipids and nucleotides, which are crucial for tumor proliferation, invasion and metastasis (Li and Zhang, 2016; Vettore et al., 2020). Many cancers require exogenous supplementation with glutamine to maintain tumor cell proliferation, in a process called "glutamine dependence"(Lukey et al., 2017). Serine, glycine and threonine metabolism and the one-carbon unit product derived from these processes properly satisfy tumor cell proliferation and maintain the redox, genetic and epigenetic state (Locasale, 2013).

Increasing studies have supported that amino acid metabolic genes are vitally important in tumor development. Glutaminase 2 (GLS2) encodes glutaminase, which can induce tumor cells to resist ROS-related apoptosis and enhance drug resistance through p53 mediated transcription (Matés et al., 2020). Serine hydroxymethyltransferase 2 (SHMT2) can be induced by both c-Myc and HIF1α to enhance the ability to resist hypoxia-induced tumor cell death and promote the invasion of various cancers (Ye et al., 2014). Solute carrier family 7 member 8 (SLC7A8) is an important branched-chain amino acid (BCAA) transporter. SLC7A8 regulates the activation of glutamine-dependent mTOR and enhances the resistance of pancreatic cancer to gemcitabine, which promotes tumor proliferation and inhibits apoptosis (Feng et al., 2018).

Globally, liver cancer is the second most deadly tumor, with a 5-year survival rate of 18% (Villanueva, 2019). Hepatocellular carcinoma is the most common type of liver cancer, accounting for 90% (Forner et al., 2018). Current treatments such as surgical therapy, chemotherapy, and radiotherapy have significantly suppressed cancer proliferation and improved the survival of HCC patients. However, HCC displays a high degree of molecular heterogeneity among patients, at different locations within a patient, and even within a single tumor, which is closely correlated with the common occurrence of drug resistance and relapse after surgical resection and comprehensive treatment, consequently leading to a poor prognosis (Li and Wang, 2016; Xu et al., 2019). It is urgent that more effective biomarkers be identified to provide individual treatment for HCC patients. The liver is the central organ for amino acid metabolism and the importance of amino acid metabolism in HCC has been noticed in recent years. Aberrant amino acid and protein metabolism provided active biosynthesis support for HCC. For example, branched-chain amino acid (BCAA) metabolism disorders are common in HCC, such as upregulation of isoleucine and downregulation of glutamate (Di Poto et al., 2017). Moreover, an increasing proportion of BCAAs restrains the proliferation of HepG2 liver tumor cells and helps to recover liver functions and prevent early recrudescence after surgical resection (Tajiri and Shimizu, 2013). A recent study revealed that BCAA reduction is an independent risk factor for sarcopenia in the course of HCC recurrence, worsening the prognosis of HCC patients (Sano et al., 2021). Research on amino acid metabolism is of great significance for the prevention and treatment of HCC. HCC tumor cell can active immune reaction and provide appropriate tumor microenvironment for cancer development (Long et al., 2019). B and T cells played a vital role in the HCC tumor microenvironment. NK cell decreasing enrolled in HBV or HCV infection and promote the progression of liver cancer (Sun et al., 2015). However, whether amino acid metabolism-related genes are involved in immune regulation of HCC remains unclear. Moreover, effective amino acid metabolic genes to predict the overall survival (OS) of patients with HCC are still lacking.

In this study, we obtained HCC RNA sequencing data from the TCGA database and the GEO database, mined amino acid metabolism-related genes closely related to the OS of HCC patients, and then established an effective signature of amino acid metabolism-related biomarkers to extend the knowledge of molecular mechanisms and clinical prognosis of HCC.

MATERIALS AND METHODS

Data Collection

We downloaded the RNA-seq (HTseq-FPKM) data and clinical data of HCC from the TCGA database.[1] The TCGA barcode was used to match different patients, and 370 HCC and 50 normal samples were selected as the training set. The clinical information included age, gender, histological grade, stage, TNM classification, survival time and survival status.

The GSE14520 (GPL3921) dataset was obtained from the GEO database, which contained gene expression and clinical data of HCC, paired non-tumor tissues, and healthy liver tissues analyzed by Affymetrix microarray profiling. Finally, 221 tumor samples were selected as the validation set. The clinical information included age, gender, main tumor size, number of tumors, TNM staging, BCLC staging and CLIP staging. Clinical data of the two cohorts are listed in **Table 1**.

Screening Metabolism-Related Differentially Expressed Genes

We downloaded the KEGG gene sets (c2.cp.kegg.v7.0.symbols.gmt) from the Molecular Signature Database (MSigDB) and extracted genes in amino acid metabolism pathways to find amino acid metabolic genes from the training set. Next, the intersecting amino acid metabolic genes in the validation set and the training set were selected, and their expression was corrected by the "sva" package (R software version 4.0.2) for further differential analysis. The "limma" package was employed to obtain differentially expressed genes (DEGs) between normal liver tissues and HCC from the training set. FDR < 0.05 and $|\log FC| \geq 0.5$ were the criteria used to define DEGs.

[1] https://portal.gdc.cancer.gov/

TABLE 1 | The clinicopathological characteristics of HCC patients in the training set and validation set.

Parameter		Total (%)
TCGA		***n* = 370**
Survival status	Alive	244 (65.9)
	Dead	126 (34.1)
Age	≤65 years	231 (62.4)
	>65 years	138 (37.3)
Gender	Male	249 (67.3)
	Female	121 (32.7)
Histological grade	G1	55 (14.9)
	G2	177 (47.8)
	G3	121 (32.7)
	G4	12 (3.2)
Stage	I	170 (45.9)
	II	86 (23.2)
	III	85 (23.0)
	IV	5 (1.4)
T	T1	180 (48.6)
	T2	94 (25.4)
	T3	80 (21.6)
	T4	13 (3.5)
N	N0	251 (67.8)
	N1	4 (1.1)
	NA	115 (31.1)
M	M0	265 (71.6)
	M1	4 (1.1)
	NA	101 (27.3)
GSE14520 in GEO		***n* = 221**
Survival status	Alive	136 (61.5)
	Dead	85 (38.5)
Gender	Male	191 (86.4)
	Female	30 (13.6)
Age	≤65 years	200 (90.5)
	>65 years	21 (9.5)
Main tumor size	>5 cm	80 (36.2)
	≤5 cm	140 (63.3)
MultiNodular	No	176 (79.6)
	Yes	45 (20.4)
TNM staging	I	93 (42.1)
	II	77 (34.8)
	III	49 (22.2)
BCLC staging	0	20 (9.0)
	A	148 (67.0)
	B	22 (10.0)
	C	22 (10.0)
CLIP staging score	0	97 (43.9)
	1	94 (42.5)
	2	35 (15.8)
	3	9 (4.1)
	4	3 (1.4)
	5	1 (0.5)

Building and Validating the Amino Acid Metabolism-Related Prognostic Signature

To select genes significantly related to patient overall survival (OS) in the training set, a univariate Cox proportional hazard regression analysis was carried out. To ensure accurate results, patients with a survival time of less than 30 days were excluded. To prevent overfitting of the model, LASSO regression was carried out by "glmnet" R package. Genes with independent prognostic values were selected and the risk score formula was as follows:

$$\begin{aligned} Risk\ score\ =\ &(Coefficient\ mRNA1\ \times\ expression\ of\ mRNA1)\\ &+(Coefficient\ mRNA2\ \times\ expression\ of\ mRNA2)\\ &+\cdots+(Coefficient\ mRNAn\ \times\ expression\ mRNAn). \end{aligned}$$

According to the median risk scores, HCC patients were divided into high-risk and low-risk groups in both the training set and the validation set. Univariate and multivariate Cox proportional hazard regression analyses of risk scores and clinicopathological items were conducted to validate the performance of the prognostic signature. We generated Kaplan-Meier(K-M) curves using the "survival" and "survminer" R packages. To evaluate the predictive performance of the risk score for the 1-, 3-, and 5- year survival of HCC patients, we plotted a time-dependent receiver operating characteristic (ROC) curve with the "timeROC" and "survival" R packages.

Establishing Predictive Nomograms

The results of the multivariate analysis were used to build nomograms for predicting 1-, 2-, 3-, and 5- year survival. The "rms" R package was employed to establish and visualize the results. The discrimination performance and predicting value of nomograms were assessed by Harrell's C-index and calibration curve.

Functional Enrichment Analysis

Gene set enrichment analyses (GSEA) were analyzed according to the Molecular Signatures Database (MSigDB, version 7.2) to reveal the molecular mechanism of the prognostic gene signature. The "c2 KEGG gene set," and "c5 all GO gene sets" were chosen for analysis. GSEA software (version 4.1.0) was employed and the parameters were as follows: number of permutations = 1,000, min size = 15 and max size = 500. Pathways with NOM p-value < 0.05 and FDR q-value < 0.25 were defined as significantly enriched. The results were visualized by the "ggplot2" R package. The infiltration scores of 22 immune cells in the training set and validation set were analyzed with the CIBERSORTx web tool. The algorithm was run using the LM22 signature matrix at 1,000 permutations.

Cell Culture and Treatment

The human hepatocyte LO2 cell line, human hepatoma HepG2 and Hep3B cell lines were obtained from the America Type

Culture Collection (ATCC, Manassas, VA, United States). The cells were incubated at 37℃ in a humid atmosphere containing 5% CO_2. The cells were cultured in dulbecco's modified eagle's medium (DMEM) supplemented with 10% fetal bovine serum (FBS) (GIBCO-BRL, Thermo Fisher Scientific, Waltham, MA, United States). Cells were inoculated in 12-well plates and 6-well plates at densities of $1*10^5$/well and $2*10^5$/well, respectively.

Quantitative Real-Time PCR

Total RNA from the cells were extracted by RNA isolater Total RNA Extraction Reagent (Vazyme, Nanjing, China) and were used to synthesis cDNA by HiScript II Q RT SuperMix for qPCR (Vazyme, Nanjing, China). To measure the abundance of mRNA, the cDNA template, primers (**Supplementary Table 1**) and AceQ qPCR SYBR Green Master Mix (Vazyme, Nanjing, China) were mixed and run in a Light-Cycler 480 Software (Roche Diagnostics GmbH, Mannheim, Germany). Glyceraldehyde-3-phosphate dehydrogenase (GAPDH) was used as an internal control. The $2^{-\Delta\Delta Ct}$ method was used to calculate mRNA expression.

Western Blot Analyses

Total protein from the cells was extracted and concentrations were quantitated. Protein samples were mixed with 1 × SDS-polyacrylamide gel electrophoresis(SDS-PAGE) loading buffer and boiled for 10 min. Denatured proteins were separated by 10% polyacrylamide gels (EpiZyme, Shanghai, China). The separated proteins were transferred to polyvinylidene fluoride (PVDF) membranes (Millipore Corp., Billerica, MA, United States). The membranes were blocked with 8% non-fat milk prepared with TBST containing 0.1% Tween20 for 1 h, and incubated in the diluted specific antibodies (**Supplementary Table 2**) at 4℃ overnight with gentle shaking, and the next day were incubated with the secondary antibody for 1 h. The immunoreactive bands were detected with enhanced chemiluminescence (ECL) kit (Vazyme, Nanjing, China) and quantified with ImageJ software (V1.8.0, National Institutes of Health).

Immunohistochemistry Analysis

A total of three pairs of HCC and paired adjacent tissues were obtained from three patients of Union Hospital, Tongji Medical College, Huazhong University of Science and Technology. This clinical trial is registered in the Chinese Clinical Trial Registry (ChiCTR2100049106). The histologic grades of all HCC tissues were identified by the pathology department. Liver tissues were fixed with 4% paraformaldehyde, embedded in paraffin and made into 4 μm slices. Slices were dewaxed and incubated with diluted specific primary antibodies at 4℃ overnight (**Supplementary Table 3**) and were subsequently incubated with biotinylated secondary antibody (Proteintech, Wuhan, China) at room temperature for 1 h. DAB chromogenic reagent was used to detect positive staining, and each section was counterstained with hematoxylin. An optical microscope (Olympus, BX-51, Tokyo, Japan) was used to take 40 × immunohistochemical images. For semi-quantitative immunostaining analysis, 5 random fields per slice were used to calculate average optical density, and ImageJ software (V1.8.0, National Institutes of Health) was used for analysis.

Statistical Analysis

All statistical analyses were conducted by R software v4.0.2 and Graphpad Prism software v8.0.2. "Wilcox test" was used to compare gene expression and immune scores between different groups. Univariate Cox and LASSO regression analyses were adopted to identify the prognostic signature. The OS and recurrence-free survival (RFS) were analyzed by Kaplan-Meier analysis with a log-rank test. Gene expression at different stages was compared with one-way ANOVA. Immunohistochemical statistical analysis and gene and protein expression in different cells were analyzed by unpaired *t*-test. $P < 0.05$ was considered statistically significant.

RESULTS

Building a Nine-Gene Amino Acid Metabolism-Related Risk Signature

There were 393 amino acid metabolic genes in the training set, and 327 amino acid metabolism-related genes were obtained after intersecting with the validation set. Further differential expression analysis showed that there were 140 differentially expressed genes (DEGs) in the training set (82 upregulated and 58 downregulated, **Supplementary Table 4**). The heatmap and volcano plot of 140 DEGs are drawn in **Figures 1A,B**. Next, we adopted the univariate Cox proportional hazard regression analysis to identify mRNAs related to OS. The 41 genes with prognostic value ($p < 0.01$) in univariate Cox regression were further analyzed by LASSO regression (**Supplementary Table 5** and **Figures 1C–E**). The model was constructed by using the "glmnet" and "survival" R packages. Finally, 9 amino acid metabolism-related genes were chosen to establish a prognostic model, including B3GAT3, B4GALT2, CYB5R3, GNPDA1, GOT2, HEXB, HMGCS2, PLOD2, and SEPHS1. Detailed information on nine genes is listed in **Table 2**. The risk score formula was as follows: Risk score = (0.0068*expression$_{B3GAT3}$) + (0.0123* expression$_{B4GALT2}$) + (0.0001*expression$_{CYB5R3}$) + (0.0072* expression$_{GNPDA1}$)—(0.0006* expression$_{GOT2}$) + (0.0071* expression$_{HEXB}$)—(2.5286e-05* expression$_{HMGCS2}$) + (0.0181* expression$_{PLOD2}$) + (0.0601* expression$_{SEPHS1}$).

Validating the Amino Acid Metabolism-Related Risk Signature

According to the formula, we calculated the risk scores of patients in the training set and validation set. Then we separated patients into high-risk and low-risk groups according to the median risk score. The K-M curves showed worse OS in the high-risk group than in the low-risk group in both the training set and validation set (p = 1.437e−08, and p = 1.35e−02, respectively) (**Figures 2A,B**). In **Figure 3**, we plotted heatmaps of gene expression and displayed the impact of risk scores on risk ranking, survival time and survival status. The results verified that the signature had significant prognostic value for HCC patients. The independent prognostic analysis of the univariate and multivariate Cox proportional hazard regression also verified the

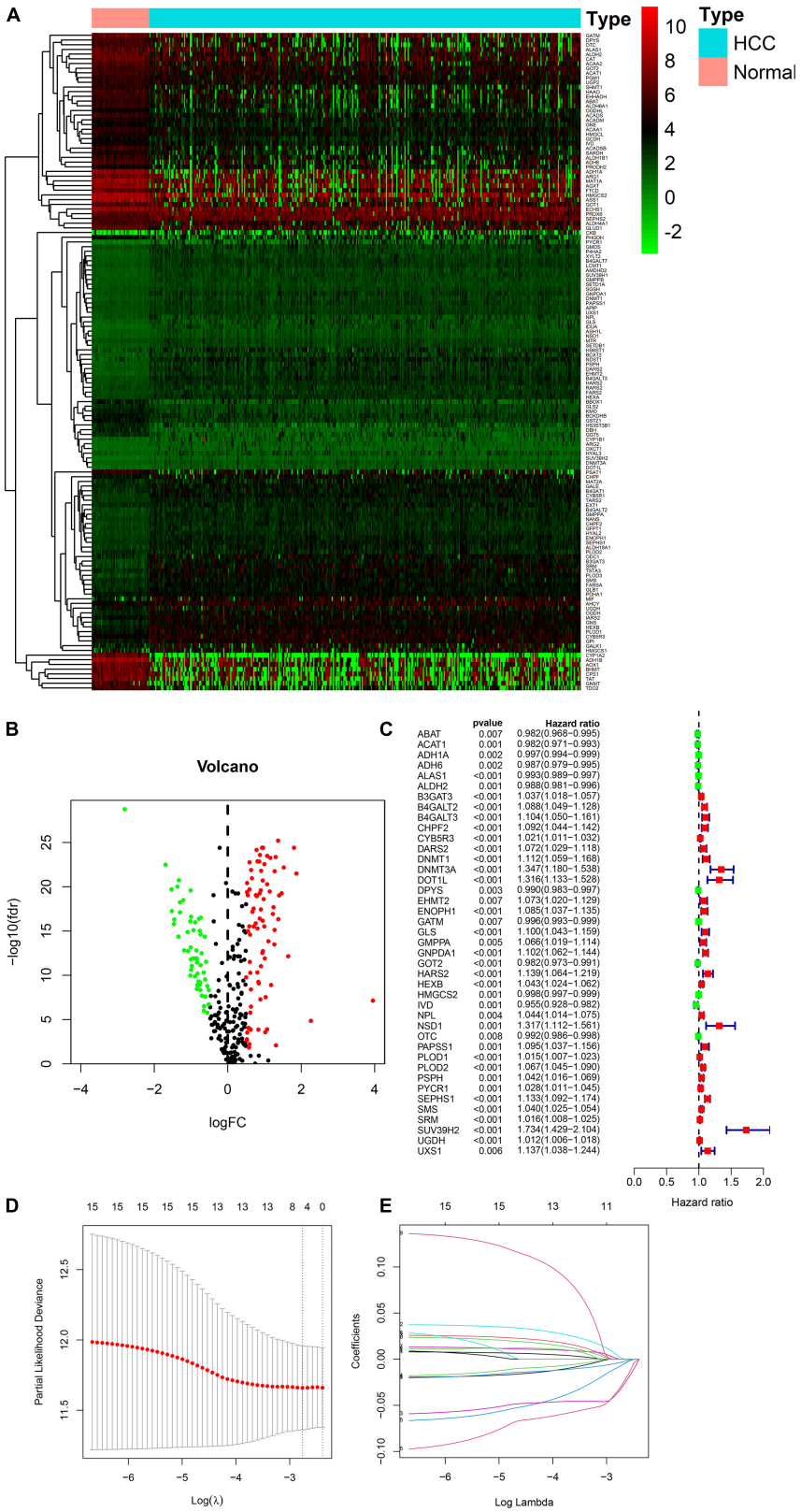

FIGURE 1 | Visualization of differential amino acid metabolism-related genes. **(A)** The heatmap of differential amino acid metabolism-related genes. **(B)** The volcano plot of differential amino acid metabolism-related genes. **(C)** The forest plot of univariate Cox regression of OS related amino acid metabolism-related genes. **(D,E)** LASSO regression analysis.

TABLE 2 | Detail information of nine genes in the risk signature.

Gene symbol	Full name	Function of the encoded protein
B3GAT3	Beta-1, 3-glucuronyltransferase 3	B3GAT3 is a glycosyltransferase that plays an important role in proteoglycan (PG) biosynthesis
B4GALT2	Beta-1, 4-galactosyltransferase 2	B4GALT2 is a beta-1, 4-galactosyltransferase (beta4GalT) and synthesizes N-acetyllactosamine in glycolipids and glycoproteins
CYB5R3	Cytochrome b5 reductase 3	CYB5R3 encodes cytochrome b5 reductase, functions in desaturation and elongation of fatty acids, in cholesterol biosynthesis, and in drug metabolism
GNPDA1	Glucosamine-6-phosphate deaminase 1	GNPDA1 links the hexosamine system with the glycolytic pathway and promotes the catabolism of hexosamines derived from glycoproteins, glycolipids, and sialic acids into phosphate sugars to provide energy sources
GOT2	Glutamic-oxaloacetic transaminase 2	GOT plays a role in amino acid metabolism and the urea and tricarboxylic acid cycles
HEXB	Hexosaminidase subunit beta	HEXB catalyzes the degradation of the ganglioside GM2, and other molecules containing terminal N-acetyl hexosamines
HMGCS2	3-hydroxy-3-methylglutaryl-CoA synthase 2	HMGCS2 is a mitochondrial enzyme that catalyzes the first reaction of ketogenesis, a metabolic pathway that provides lipid-derived energy for various organs during times of carbohydrate deprivation
PLOD2	Procollagen-lysine	PLOD2 catalyzes the hydroxylation of lysyl residues in collagen-like peptides
SEPHS1	Selenophosphate synthetase 1	SEPHS1 is an enzyme that synthesizes selenophosphate from selenide and ATP

effective prognostic value (**Figure 4**). Furthermore, ROC curves were drawn to assess the efficiency of risk scores in predicting 1-, 2-, 3-, and 5- year survival. In the training set, the AUCs for 1-, 2-, 3-, and 5- year survival was 0.813 ($P < 0.001$, 95%CI:0.748–0.878), 0.770 ($P < 0.001$, 95%CI:0.705–0.835), 0.744 ($P < 0.001$, 95%CI:0.6690.820) and 0.702 ($P < 0.001$, 95%CI:0.611–0.793), respectively. In the validation set, the AUCs for 1-, 2-, 3-, and 5- year survival was 0.643 ($P = 0.013$, 95%CI:0.530–0.757), 0.696 ($P < 0.001$, 95%CI:0.615–0.777), 0.686 ($P < 0.001$, 95%CI:0.606–0.765) and 0.634 ($P = 0.027$, 95%CI:0.515—0.752), respectively (**Figures 2C,D**).

Validating the Nine Genes in External Databases

We analyzed the expression of nine genes in twenty types of cancers in the Oncomine database. The thresholds were as follows: *p*-value = 1E-4, fold change = 2, gene rank = Top 10%, and data type = mRNA. Nine genes were altered in different cancers (**Figure 5A**). GOT2 and HMGCS2 were downregulated in HCC, while PLOD2 and SEPHS1 were upregulated in HCC. The HCCDB database curated 15 public HCC expression datasets, among which the HCCDB18 dataset contained RNA-seq of 212 tumor and 177 adjacent normal tissues obtained from the ICGC-LIR-JP cohort. As shown in **Figure 5B**, B3GAT3, B4GALT2, CYB5R3, GNPDA1, HEXB, and SEPHS1 were significantly upregulated in HCC samples, while GOT2 and HMGCS2 were downregulated.

We compared the protein expression encoded by the nine genes between HCC and normal liver tissues in the Human Protein Atlas (HPA) database. Consistent with the mRNA expression levels, GOT2 and HMGCS2 decreased in HCC tissues, and B4GALT2, CYB5R3, GNPDA1, HEXB, and SEPHS1 increased in HCC tissues. B3GAT3 and PLOD2 had no differential expression (**Figure 6**).

To verify the clinical performance of these nine genes, we discussed the relationship between mRNA levels and pathological stages according to the Gene Expression Profiling Interactive Analysis (GEPIA) database. GOT2 and HMGCS2 were gradually downregulated from stage I to stage IV, while B4GALT2, GNPDA1, PLOD2 and SEPHS1 were gradually upregulated from stage I to stage III (**Figure 7A**). We also explored the influence of each gene on OS and recurrence-free survival (RFS) of HCC patients. High expression of GOT2, HMGCS2 and low expression of B3GAT3, B4GALT2, CYB5R3, GNPDA1, HEXB, PLOD2, SEPHS1 correlated with favorable OS (**Figure 7B**). In addition, low expression of B3GAT3 and GNPDA1 and high expression of GOT2 correlated with favorable RFS (**Figure 7C**).

Cholangiocarcinoma (CHOL) is the second most common subtype of liver cancer. To identify whether the prognostic signature is specific for HCC, we compared the expression of nine genes between CHOL and normal liver tissues based on the GEPIA database. B3GAT3, B4GALT2, CYB5R3, GNPDA1, HEXB, SEPHS1 were upregulated and GOT2 was downregulated in CHOL, which was consistent with expression in HCC (**Figure 7D**). However, PLOD2 and HMGCS2 had no difference between CHOL and normal liver tissues. These results may indicate that the risk signature is specific for HCC rather than other subtypes of liver cancer.

Creating Predictive Nomograms

Based on the final regression analysis, a nomogram was created that incorporated a 9-gene risk signature and clinicopathological parameters. In the training set, age, gender, grade, stage and risk score were chosen in the final model (**Figure 8A**). In the validation set, age, gender, main tumor size, multinodular status, TNM staging, BCLC staging, CLIP staging and risk score were chosen in the final model (**Figure 8B**). Both of the nomograms displayed good discrimination performance. The C-index were 0.786 (95%CI: 0.734–0.838) and 0.722 (95%CI: 0.665–0.779) in the training set and validation set, respectively. Besides, calibration plots showed that nomograms of both the training set and validation set had good agreements between the prediction

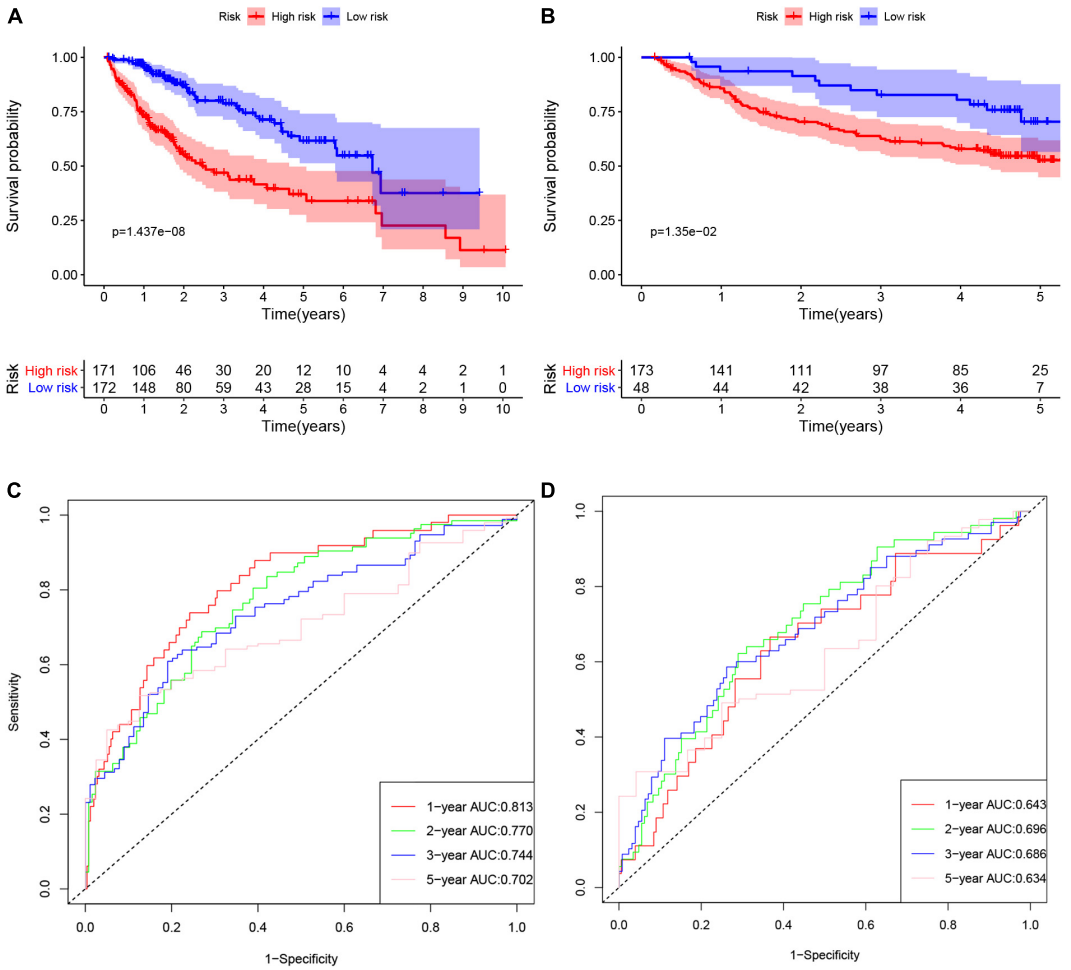

FIGURE 2 | The K-M curves of high-risk and low-risk groups in the training set **(A)** and validation set **(B)**. The ROC curves of risk signature's predicting performance in 1-, 2-, 3-, and 5-year survival for HCC patients in the training set **(C)** and validation set **(D)**.

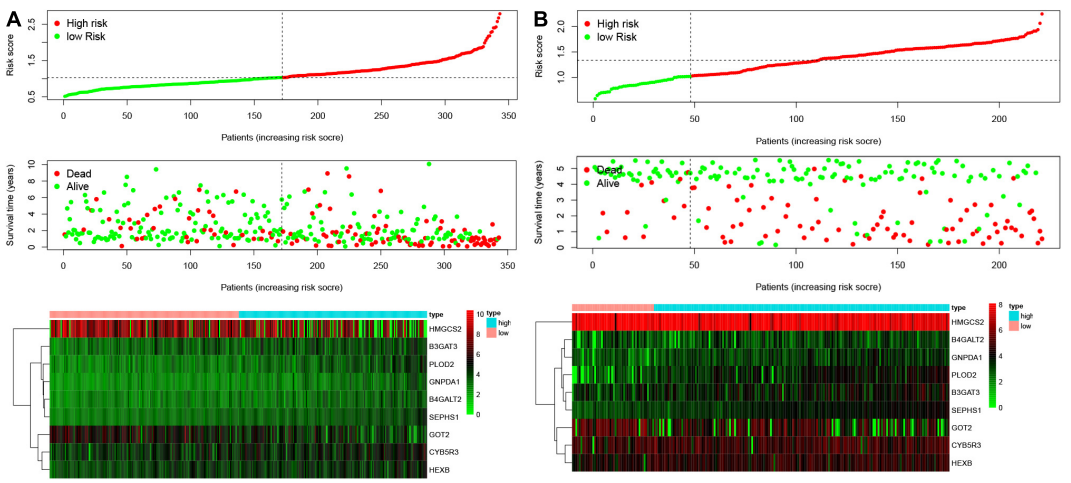

FIGURE 3 | Characteristics of risk scores and heatmaps of the amino acid metabolism-related gene signature. **(A)** The risk score, survival time, and status of patients in the training set. **(B)** The risk score, survival time, and status of patients in the validation set.

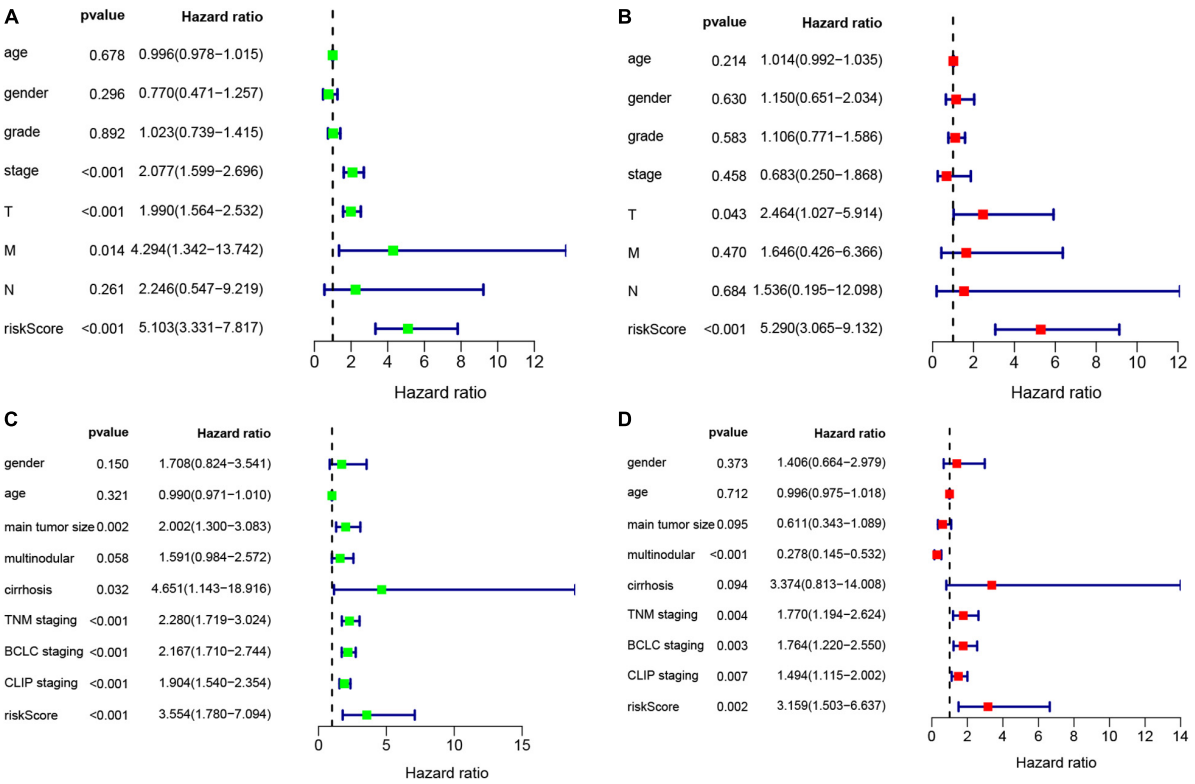

FIGURE 4 | Univariate and multivariate Cox analysis to evaluate independent prognostic value of the risk signature. **(A)** Univariate Cox analysis in the training set. **(B)** Multivariate Cox analysis in the training set. **(C)** Univariate Cox analysis in the validation set. **(D)** Multivariate Cox analysis in the validation set.

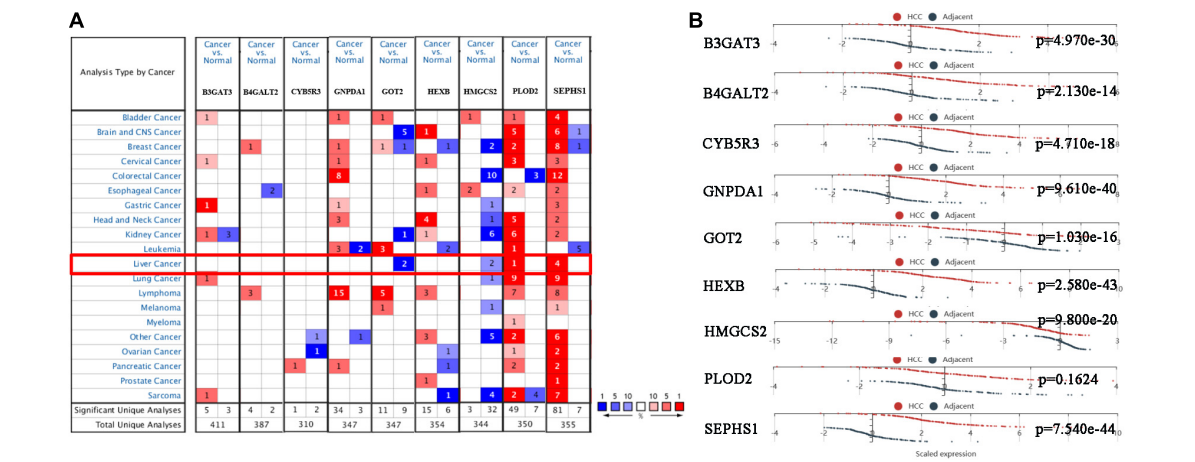

FIGURE 5 | The mRNA expression of the prognostic genes in HCC patients. **(A)** mRNA expression of the prognostic genes in 20 cancers from the Oncomine database. **(B)** mRNA expression of the prognostic genes between HCC and normal tissues in the HCCDB database.

and actual clinical survival outcomes (**Figures 8C,D**). A total score could be calculated to measure the 1-, 2-, 3-, and 5-year survival rates of HCC patients.

Functional Enrichment Analysis

We performed GSEA to clarify the enrichment pathways of the low-risk and high-risk groups in the training set. In the high-risk group, KEGG pathways were mainly enriched in the cell cycle, nucleotide metabolism, and immune-related pathways, including RIG-I like receptor signaling pathway, Toll-like receptor signaling pathway, and cytokine-cytokine receptor interaction. In the low-risk group, KEGG pathways mainly enriched in drug metabolism-cytochrome P450, amino acid metabolism and fatty acid metabolism (**Figure 9A**). In the high-risk group,

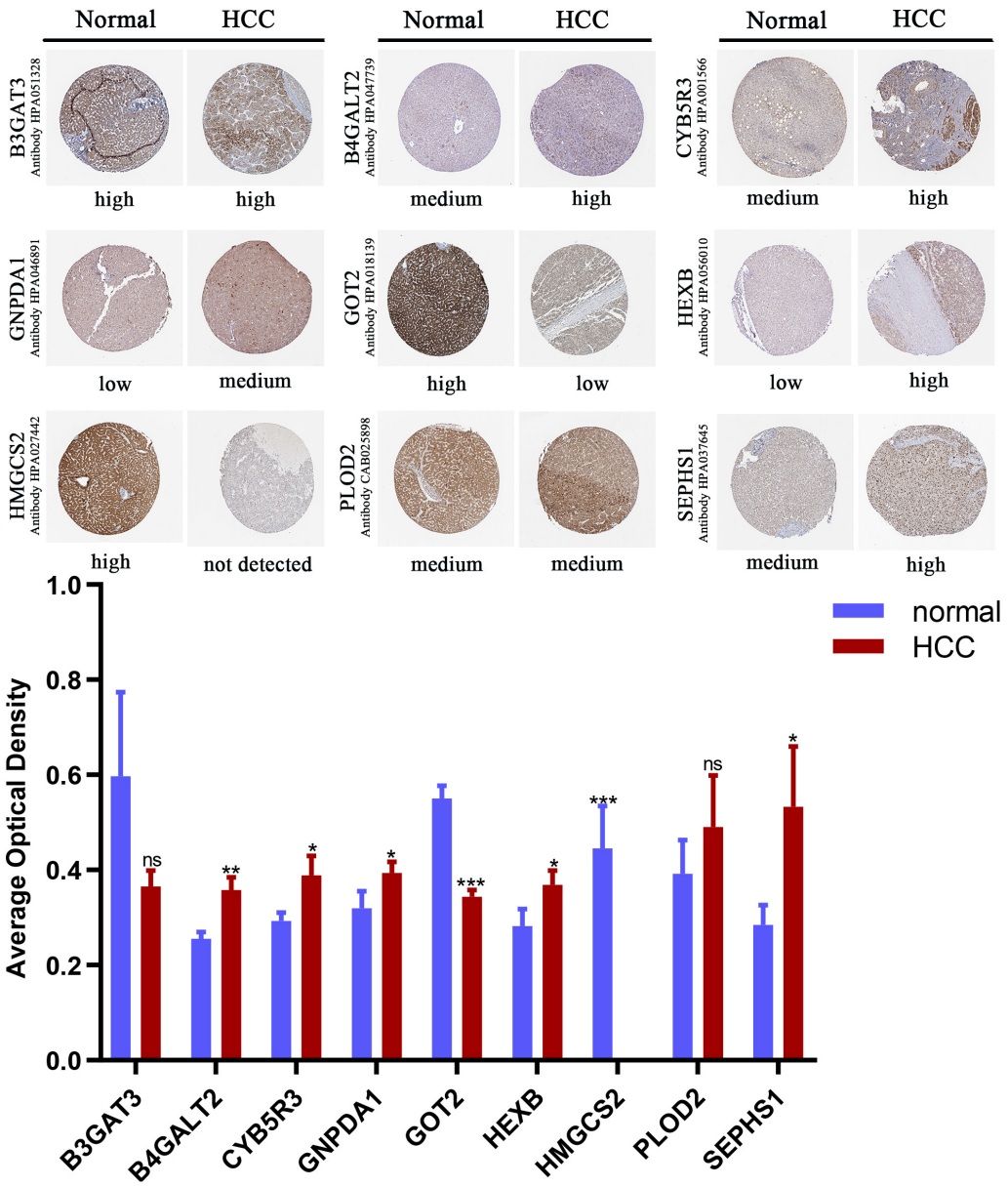

FIGURE 6 | Immunohistochemistry staining of the prognostic genes in HCC and normal liver tissues (the HPA database). Data are shown as mean ± SD, $*p < 0.05$, $**p < 0.01$, $***p < 0.001$ vs normal liver tissues.

biological processes were mostly enriched in the cell cycle, nuclear transport, P53 signaling, and diversification of immune molecules, and in the low-risk group, biological processes were mainly enriched in amino acid and fatty acid catabolic processes, toxin and drug metabolic processes (**Figure 9B**).

We subsequently explored the connection between the risk score and immune status. According to the CIBERSORTx database, we compared the infiltration scores of 22 immune cells in the low-risk group and the high-risk group. In the training set, the high-risk group had significantly higher infiltration of memory B cells, activated memory $CD4^+$ T cells, T follicular helper (Tfh) cells, M0 macrophages, and neutrophils, while the low-risk group had significantly higher infiltration of naive B cells, resting memory $CD4^+$ T cells, resting natural killer (NK) cells, activated NK cells, monocytes and activated mast cells (**Figure 9C**). In the validation set, the high-risk group had significantly higher scores of naive $CD4^+$ T cells and M0 macrophages, and a lower score of Tfh cells (**Figure 9D**).

Validating the Nine Genes in Cells and Human Liver Tissues

We compared the mRNA levels of nine genes between the LO2 cell line and HCC cell lines (HepG2 and Hep3B) by qRT-PCR analysis. As shown in **Figure 10A**, expression of B3GAT3,

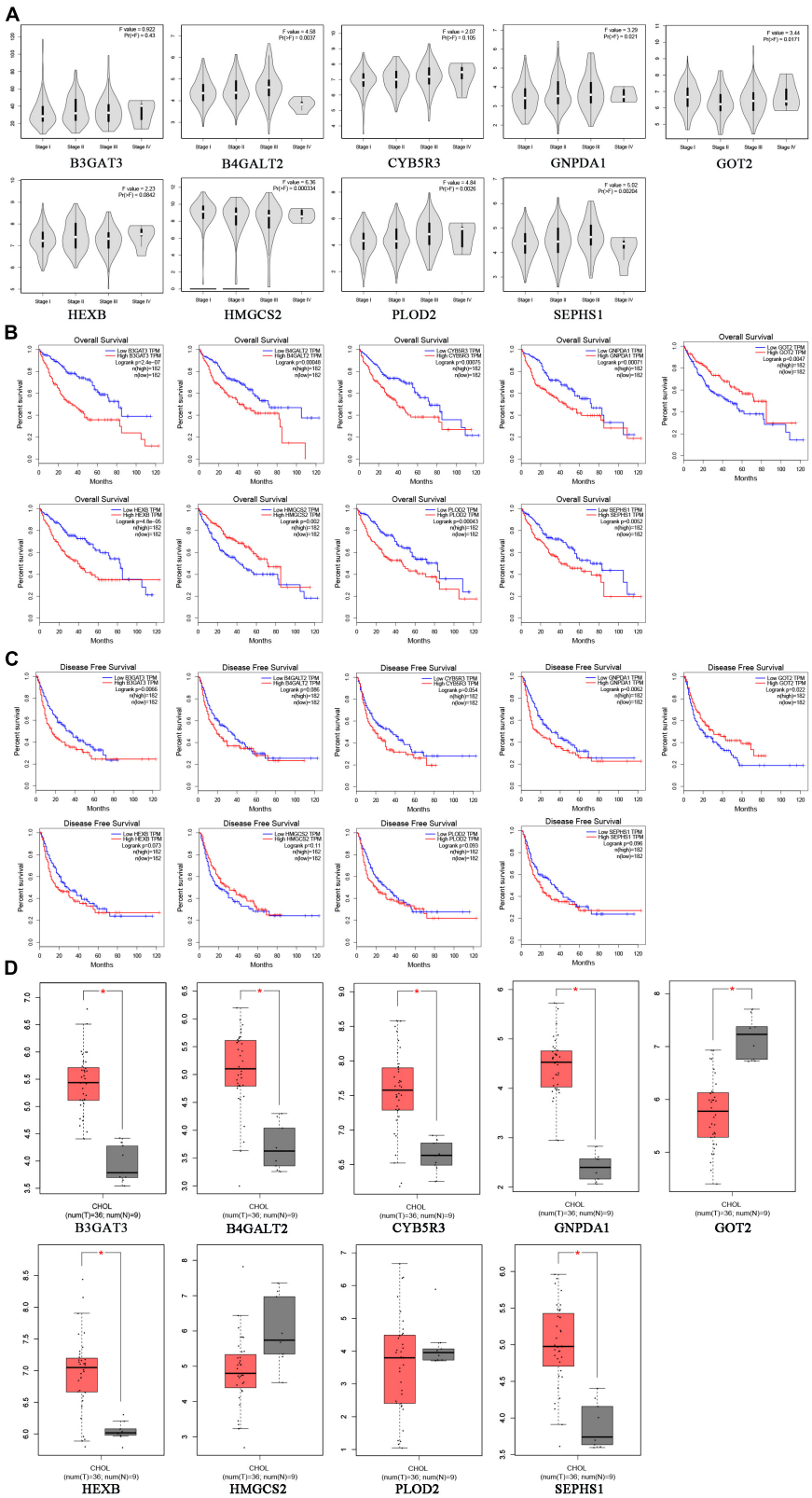

FIGURE 7 | The expression of prognostic genes in HCC and CHOL analyzed based on the GEPIA database. **(A)** The mRNA expression from stage I to stage IV in HCC patients. **(B)** The prognostic value of OS in HCC patients. **(C)** The prognostic value of RFS in HCC patients. **(D)** The mRNA expression in 9 normal liver tissues and 36 CHOL tissues.

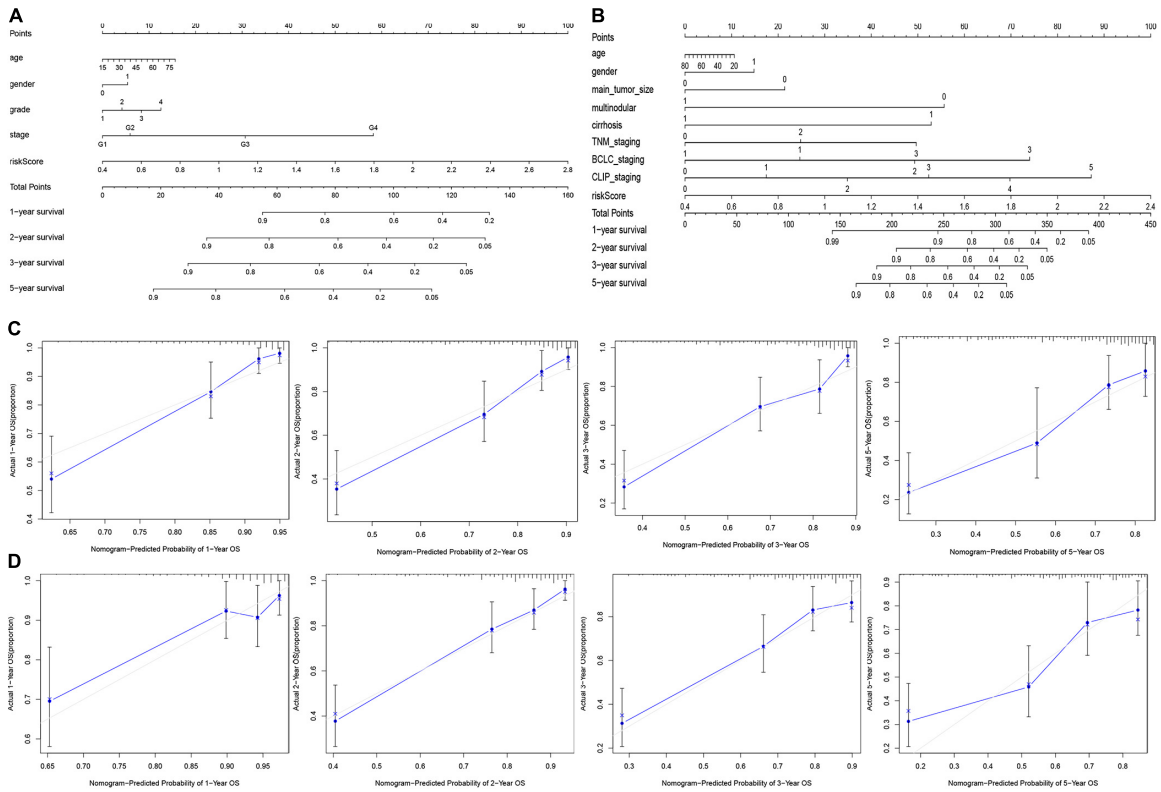

FIGURE 8 | Nomograms for predicting the OS of 1-, 2-, 3-, and 5-years in the training set **(A)** and validation set **(B)**. Calibration plot of nomograms in the training set **(C)** and the validation set **(D)**.

CYB5R3, and PLOD2 were significantly higher in HepG2 cells than in LO2 cells, expression of B4GALT2 was significantly higher in Hep3B cells than in LO2 cells, and expression of GNPDA1, HEXB, SEPHS1 were significantly higher in both HepG2 and Hep3B cells compared with LO2 cells.

Protein expression analyzed by western blot showed that PLOD2 was significantly upregulated in HepG2 and Hep3B cells compared with LO2 cells, HEXB was significantly upregulated in HepG2 cells compared with LO2 cells, and HMGCS2 was significantly downregulated in Hep3B cells compared with LO2 cells (**Figure 10B**). Besides, immunohistochemistry analysis revealed that B4GALT2, CYB5R3, HEXB, PLOD2, and SEPHS1 were significantly upregulated while GOT2 was significantly downregulated in HCC tissues compared with adjacent normal tissues (**Figure 11**).

DISCUSSION

Metabolism has been revealed to be closely correlated with epigenetics in cancer in recent years (Vander and DeBerardinis, 2017; Thakur and Chen, 2019). Aberrant metabolism promotes tumor proliferation and metastasis. Many metabolism-related genes have proven to be effective prognostic biomarkers. HCC has active metabolic reprogramming and amino acid metabolism is an important metabolic variation. Several studies have explored the energy metabolism-related risk signatures of HCC through bioinformatic methods (Zou et al., 2019; Liu et al., 2020; Tang et al., 2020). However, there is still a lack of bioinformatic research on amino acid metabolism-related genes in HCC. In this study, for the first time, we analyzed the characteristics of amino acid metabolism-related genes in HCC and built a risk signature correlated with OS. First, we identified 140 amino acid metabolism-related DEGs between HCC and normal liver tissues based on RNA-seq data. Next, we built an effective prognostic signature based on univariate Cox and LASSO regression. Nine genes are contained in this signature (B3GAT3, B4GALT2, CYB5R3, GNPDA1, GOT2, HEXB, HMGCS2, PLOD2, and SEPHS1).

Patients can be divided into high-risk and low-risk groups according to risk scores. K-M curves showed that low-risk patients had a longer survival time than high-risk patients. Furthermore, the ROC curve confirmed that the risk signature can effectively predict the 1-, 2-, 3-, and 5- year survival rates of HCC patients. Univariate and multivariate Cox analyses confirmed the independent prognostic value of the risk signature. Several studies in recent years have identified metabolism-related risk signatures for effectively predicting OS and have uncovered the importance of metabolism-related genes in the process of HCC development (Hu et al., 2020; Wu et al., 2021). Zhu's study built a lipid metabolism-related prognostic signature and revealed that lipid metabolism-related genes are

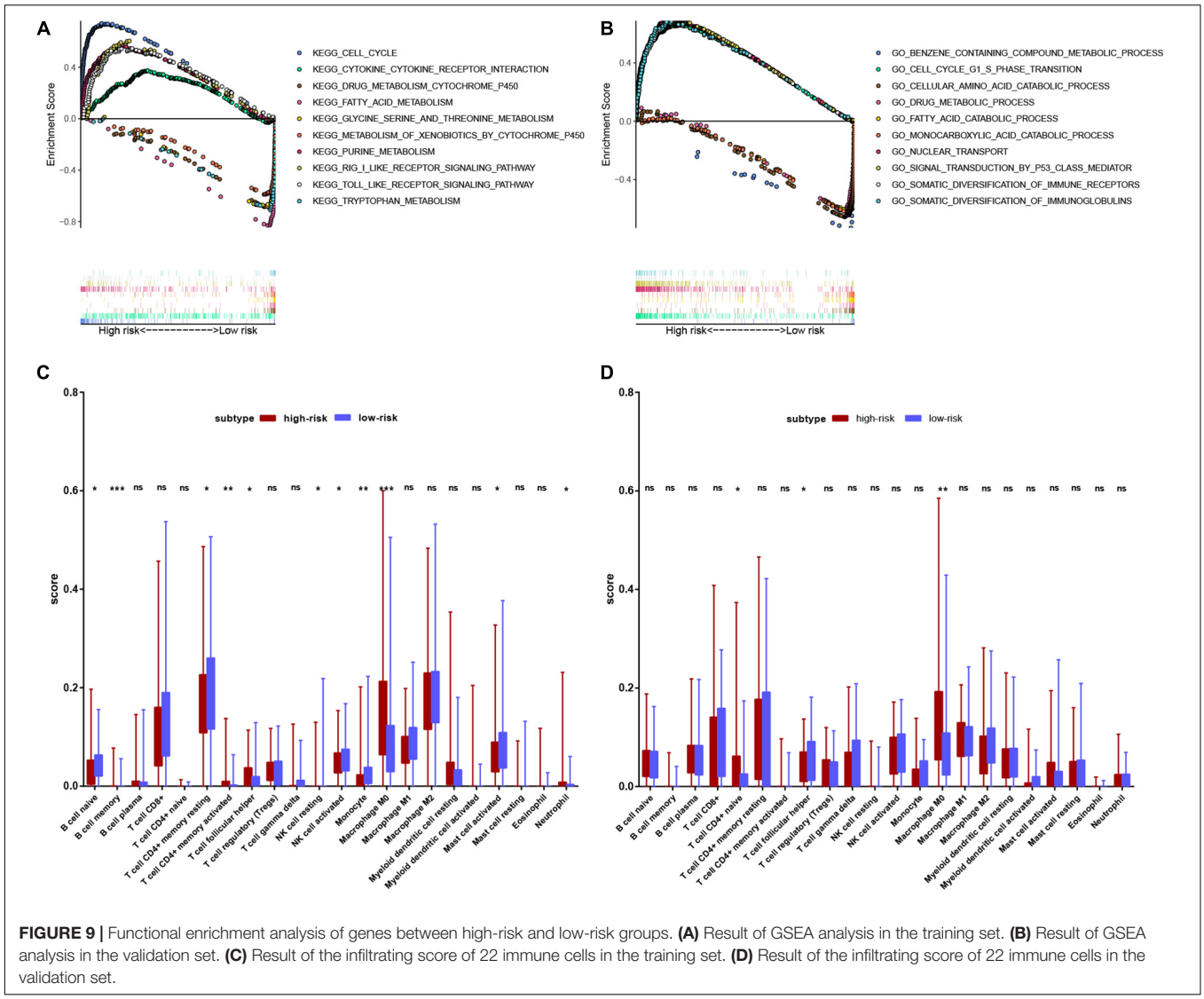

FIGURE 9 | Functional enrichment analysis of genes between high-risk and low-risk groups. **(A)** Result of GSEA analysis in the training set. **(B)** Result of GSEA analysis in the validation set. **(C)** Result of the infiltrating score of 22 immune cells in the training set. **(D)** Result of the infiltrating score of 22 immune cells in the validation set.

closely correlated with clinical characteristics, immune cells, and multiple biological functions of HCC (Zhu et al., 2021). However, this study did not build a predictive nomogram. Our study not only built the risk signature but also built nomograms based on the training set and validation set. Wu's study (Wu et al., 2021) built a six-gene metabolism risk signature, which mainly focuses on nucleotide metabolism and lipid metabolism. However, our study mainly focuses on amino acid metabolism. Liu's study built an amino acid metabolism-related prognostic signature of glioma and verified that risk scores closely correlated to different aspects of the malignancy of glioma (Liu et al., 2019). Consistently, our study verified the importance of energy metabolism disorders in HCC. We also emphasized that the amino acid metabolism-related genes played a vital role in the process of HCC development. Our study built a 9-gene signature that could effectively predict the OS of HCC patients in both the training set and validation set, and more importantly, it is a risk factor that is independent of clinicopathological factors.

Beta-1, 3-glucuronyltransferase 3 (B3GAT3) promotes the proliferation, metastasis and epithelial mesenchymal transition (EMT) process of the human HepG2 liver cancer cell line (Zhang Y. L. et al., 2019). Selenophosphate synthetase 1 (SEPHS1) promotes the expression of SMADs in liver cancer cells and stimulates the migration and invasion of tumors induced by TGF-β, which is negatively correlated with the OS and RFS of HCC patients (Yang et al., 2021). Glucosamine-6-phosphate deaminase 1 (GNPDA1) and procollagen-lysine (PLOD2) are upregulated in liver cancer and promote tumor proliferation and migration, which are correlated with poor prognosis (Du et al., 2017; Xia et al., 2021). Mutation of Beta-1, 4-galactosyltransferase 2 (B4GALT2) leads to abnormal glycosylation of proteins, promoting the development of colon cancer (Venkitachalam et al., 2016). Downregulation of glutamic-oxaloacetic transaminase 2 (GOT2) activates oxidative stress in human pancreatic ductal adenocarcinoma (PDAC) cells and inhibits the proliferation of pancreatic

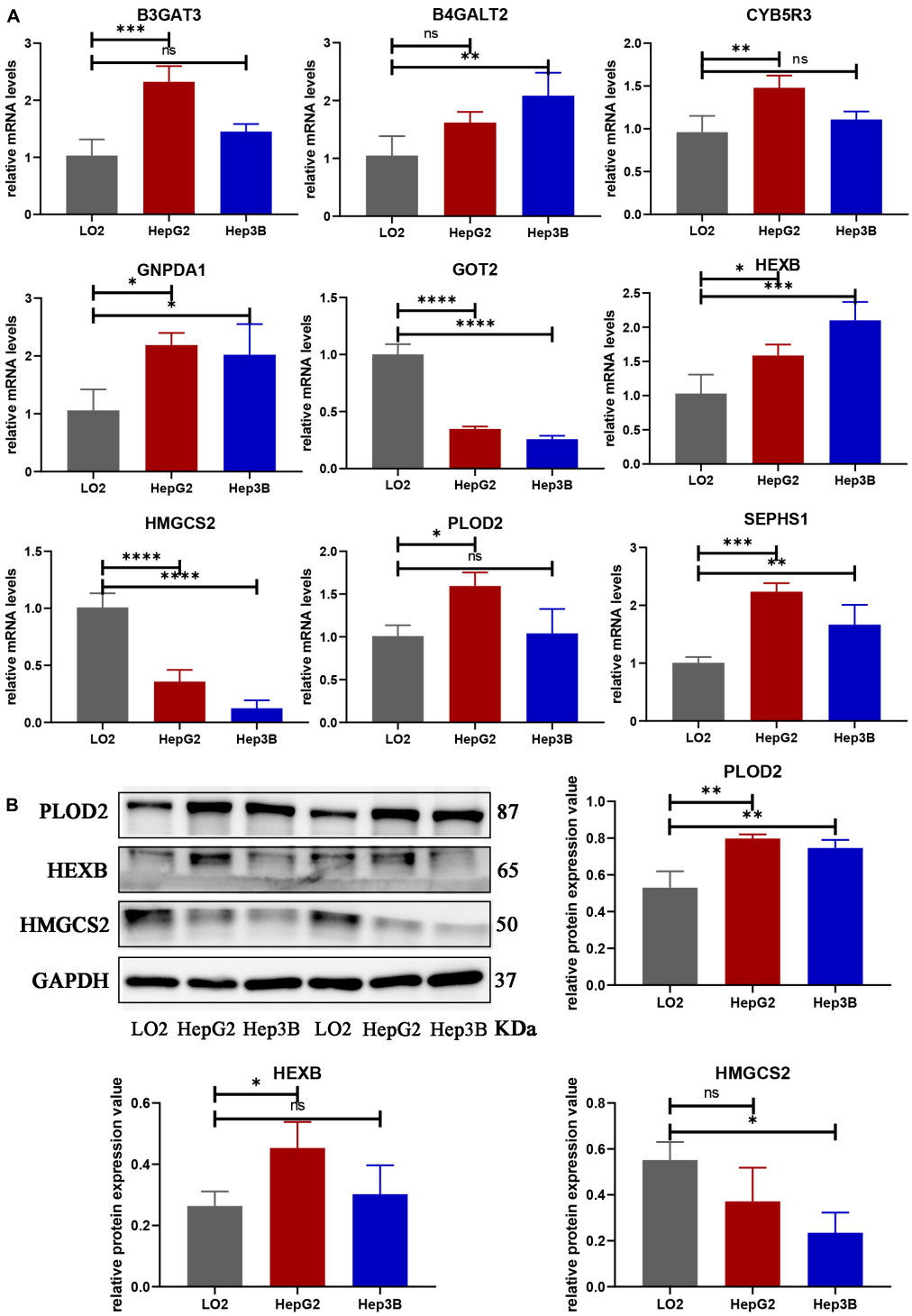

FIGURE 10 | The mRNA and protein expression of prognostic genes in LO2 cells, HepG2 cells and Hep3B cells. **(A)** The mRNA expression of nine genes analyzed by qRT-PCR. **(B)** The total protein expression of PLOD2, HEXB and HMGCS2 analyzed by western blot. Data are shown as mean ± SD, $^{*}p < 0.05$, $^{**}p < 0.01$, $^{***}p < 0.001$, $^{****}p < 0.0001$ vs. LO2 cells.

cancer (Yang et al., 2018). Downregulation of 3-hydroxy-3-methylglutaryl-CoA synthase 2 (HMGCS2) reduces ketone production, enhances the c-Myc/cyclinD1 and EMT signaling pathways, and inhibits caspase-dependent apoptosis pathways, which promotes tumor proliferation, migration and xenograft tumorigenesis in various cancers (Tang et al., 2017). The

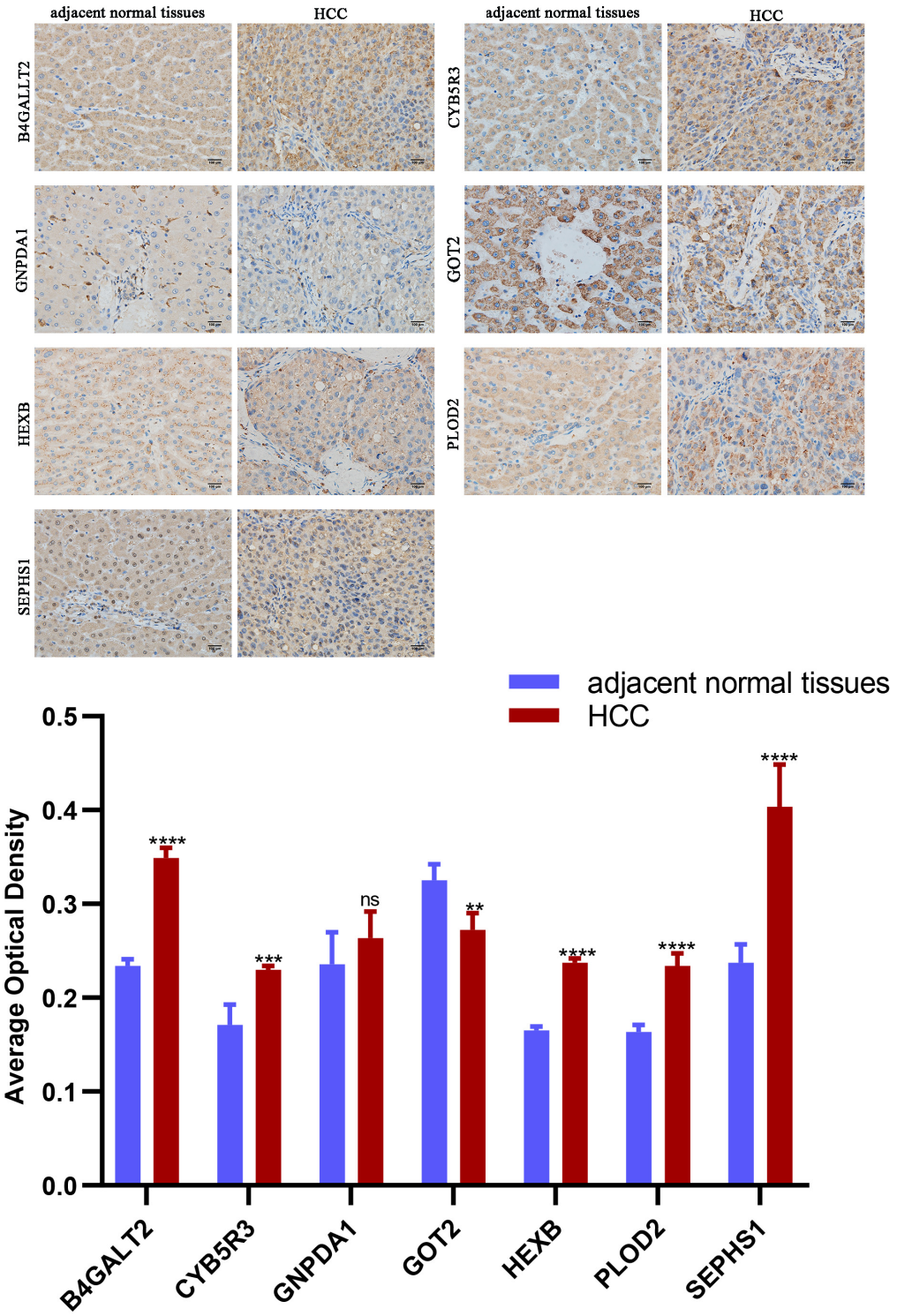

FIGURE 11 | Representative images of immunohistochemistry staining of prognostic genes in HCC and adjacent normal tissues. Data are shown as mean ± SD, $^{**}p < 0.01$, $^{***}p < 0.001$, $^{****}p < 0.0001$ vs adjacent normal tissues.

function of membrane-bound cytochrome b5 reductase 3 (CYB5R3) and hexosaminidase subunit beta (HEXB) on cancers is still unclear.

Combining several databases, our study found that the mRNA levels of B3GAT3, B4GALT2, CYB5R3, GNPDA1, HEXB, PLOD2, and SEPHS1 were increased in HCC tissues while mRNA

levels of GOT2 and HMGCS2 were decreased in HCC tissues. In addition, the protein expression was consistent with the mRNA expression. Moreover, the expression of nine genes correlated with the prognosis of HCC patients. Interestingly, we noticed that PLOD2 and HMGCS2 had no difference between CHOL and normal liver tissues. These results may indicate that the risk signature is specific for HCC rather than other subtypes of liver cancer. We also verified the mRNA and protein expression of nine genes in HCC patient samples and cell lines, which showed consistent results with the public database mining results. In brief, our results verified the importance of B3GAT3, SEPHS1, PLOD2, and GNPDA1 in HCC development again. However, previous studies have lacked an exploration of B4GALT2, GOT2, and HMGCS2 changes in HCC. Our study disclosed the prognostic value of B4GALT2, GOT2, and HMGCS2 in HCC. CYB5R3 functions in drug metabolism, cholesterol biosynthesis, desaturation of fatty acids, and mitochondrial electron transport chain (ETC) activity (Fan et al., 2020). HEXB participates in catalyzing the degradation of the ganglioside GM2 (Kuil et al., 2019). No influence of two genes (CYB5R3 and HEXB) in cancers has been reported, but our study found that upregulation of CYB5R3 and HEXB was significantly linked to the poor prognosis of HCC patients. Next, we developed nomograms for predicting the 1-, 2-, 3-, and 5-year OS of HCC patients according to risk scores and clinicopathological characteristics.

We further performed pathway enrichment analysis. GSEA revealed that cell cycle regulation and synthesis of biological macromolecules were active in high-risk patients, which discloses the importance of amino acid metabolism-related genes in the energy metabolism process for tumor proliferation. Amino acid and fatty acid catabolic processes and toxin and drug metabolic processes were inhibited in high-risk patients, which indicates that amino acid metabolism-related genes may participate in tumorigenesis. We also noticed that immune response-related pathways were enriched. In our study, infiltration of memory B cells, activated memory $CD4^+$ T cells, T follicular helper (Tfh) cells, and naive $CD4^+$ T cells was upregulated while infiltration of naive B cells was downregulated in high-risk patients. It was reported that there was more B cells infiltration in HCC patients than in patients with cirrhosis and healthy people (Zhang et al., 2020). Upregulation of plasma cells and lower expression of naive B cells correlated with poorer prognosis (Zhang Z. et al., 2019). In addition, recent studies found that lower expression of $CD8^+$ T cells can lead to immune dysfunction in HCC patients. Higher expression of Treg cells can interfere with cell cycle checkpoints and inhibit effector T cells, and promote the progression of HCC, which are factors related to poor prognosis of HCC. Consistently, our results revealed that changes in amino acid metabolism-related genes influence the ratio of different B and T cell subtypes, leading to an influence on prognosis. Our findings also show that high-risk patients have lower NK cell infiltration. It was reported that increased catabolism of Trp and Arg can induce apoptosis of NK cells, leading to tumor immune escape (Grohmann and Bronte, 2010). Therefore, abnormal expression of amino acid metabolism-related genes may promote immune escape by influencing NK cells in HCC proliferation. In addition, the proportion of neutrophils and M0 macrophages increased in high-risk patients in this study. Neutrophils influence tumor progression by releasing cytokines and chemokines with tumorigenic or antitumor functions (Haider et al., 2019). Zhou's study also found that neutrophils can recruit macrophages and Treg cells to promote HCC proliferation and drug resistance (Zhou et al., 2016). It was found that M0 and M1 macrophages were significantly correlated with RFS in HBV-HCC and HCV-HCC (Hsiao et al., 2019). Combined with our results, abnormalities in amino acid metabolism-related genes may affect neutrophil function and the interaction between neutrophils and macrophages to promote HCC proliferation.

CONCLUSION

In conclusion, our study screens out amino acid metabolism-related genes which serve as potential prognostic biomarkers and builds a novel risk signature that is independently related to the overall survival of HCC. The findings provide an effective prediction of HCC prognosis and personalized therapy for liver cancer patients. The mechanisms related to amino acid metabolism-related genes and immune regulation during HCC development need further exploration.

DATA AVAILABILITY STATEMENT

The raw data supporting the conclusions of this article will be made available by the authors, without undue reservation.

ETHICS STATEMENT

The studies involving human participants were reviewed and approved by the Medical Ethics Committee of Tongji Medical College of Huazhong University of Science and Technology. The patients/participants provided their written informed consent to participate in this study. Written informed consent was obtained from the individual(s) for the publication of any potentially identifiable images or data included in this article.

AUTHOR CONTRIBUTIONS

KX and JZ conceived and designed the study. YZ and SW performed the data analysis. YZ, JZ, and QJ wrote the manuscript. All authors read and approved the manuscript.

FUNDING

This study was supported by the National Natural Science Foundation of China (Nos. 81900520 and 81670515).

SUPPLEMENTARY MATERIAL

The Supplementary Material for this article can be found online at: https://www.frontiersin.org/articles/10.3389/fcell.2021.731790/full#supplementary-material

REFERENCES

Boroughs, L. K., and DeBerardinis, R. J. (2015). Metabolic pathways promoting cancer cell survival and growth. *Nat. Cell Biol.* 17, 351–359. doi: 10.1038/ncb3124

Di Poto, C., Ferrarini, A., Zhao, Y., Varghese, R. S., Tu, C., Zuo, Y., et al. (2017). Metabolomic characterization of hepatocellular carcinoma in patients with liver cirrhosis for biomarker discovery. *Cancer Epidemiol. Biomark. Prev.* 26, 675–683. doi: 10.1158/1055-9965.EPI-16-0366

Du, H., Pang, M., Hou, X., Yuan, S., and Sun, L. (2017). PLOD2 in cancer research. *Biomed. Pharmacother.* 90, 670–676. doi: 10.1016/j.biopha.2017.04.023

Fan, J., Du, W., Kim-Muller, J. Y., Son, J., Kuo, T., Larrea, D., et al. (2020). Cyb5r3 links FoxO1-dependent mitochondrial dysfunction with β-cell failure. *Mol. Metab.* 34, 97–111. doi: 10.1016/j.molmet.2019.12.008

Feng, M., Xiong, G., Cao, Z., Yang, G., Zheng, S., Qiu, J., et al. (2018). LAT2 regulates glutamine-dependent mTOR activation to promote glycolysis and chemoresistance in pancreatic cancer. *J. Exp. Clin. Cancer Res.* 37:274. doi: 10.1186/s13046-018-0947-4

Forner, A., Reig, M., and Bruix, J. (2018). Hepatocellular carcinoma. *Lancet* 391, 1301–1314. doi: 10.1016/S0140-6736(18)30010-2

Grohmann, U., and Bronte, V. (2010). Control of immune response by amino acid metabolism. *Immunol. Rev.* 236, 243–264. doi: 10.1111/j.1600-065X.2010.00915.x

Haider, C., Hnat, J., Wagner, R., Huber, H., Timelthaler, G., Grubinger, M., et al. (2019). Transforming growth factor-β and axl induce CXCL5 and neutrophil recruitment in hepatocellular carcinoma. *Hepatology* 69, 222–236. doi: 10.1002/hep.30166

Hsiao, Y. W., Chiu, L. T., Chen, C. H., Shih, W. L., and Lu, T. P. (2019). Tumor-Infiltrating leukocyte composition and prognostic power in hepatitis B- and hepatitis C-Related hepatocellular carcinomas. *Genes (Basel)* 10:630. doi: 10.3390/genes10080630

Hu, B., Yang, X. B., and Sang, X. T. (2020). Construction of a lipid metabolism-related and immune-associated prognostic signature for hepatocellular carcinoma. *Cancer Med.* 9, 7646–7662. doi: 10.1002/cam4.3353

Kuil, L. E., López, M. A., Carreras, M. A., van den Bosch, J. C., van den Berg, P., van der Linde, H. C., et al. (2019). Hexb enzyme deficiency leads to lysosomal abnormalities in radial glia and microglia in zebrafish brain development. *Glia* 67, 1705–1718. doi: 10.1002/glia.23641

Li, L., and Wang, H. (2016). Heterogeneity of liver cancer and personalized therapy. *Cancer Lett.* 379, 191–197. doi: 10.1016/j.canlet.2015.07.018

Li, Z., and Zhang, H. (2016). Reprogramming of glucose, fatty acid and amino acid metabolism for cancer progression. *Cell. Mol. Life Sci.* 73, 377–392. doi: 10.1007/s00018-015-2070-4

Liu, G. M., Xie, W. X., Zhang, C. Y., and Xu, J. W. (2020). Identification of a four-gene metabolic signature predicting overall survival for hepatocellular carcinoma. *J. Cell. Physiol.* 235, 1624–1636. doi: 10.1002/jcp.29081

Liu, Y. Q., Chai, R. C., Wang, Y. Z., Wang, Z., Liu, X., Wu, F., et al. (2019). Amino acid metabolism-related gene expression-based risk signature can better predict overall survival for glioma. *Cancer Sci.* 110, 321–333. doi: 10.1111/cas.13878

Locasale, J. W. (2013). Serine, glycine and one-carbon units: cancer metabolism in full circle. *Nat. Rev. Cancer* 13, 572–583. doi: 10.1038/nrc3557

Long, J., Wang, A., Bai, Y., Lin, J., Yang, X., Wang, D., et al. (2019). Development and validation of a TP53-associated immune prognostic model for hepatocellular carcinoma. *EBioMedicine* 42, 363–374. doi: 10.1016/j.ebiom.2019.03.022

Lukey, M. J., Katt, W. P., and Cerione, R. A. (2017). Targeting amino acid metabolism for cancer therapy. *Drug Discov. Today* 22, 796–804. doi: 10.1016/j.drudis.2016.12.003

Matés, J. M., Campos-Sandoval, J. A., de Los, S. J., and Márquez, J. (2020). Glutaminases regulate glutathione and oxidative stress in cancer. *Arch. Toxicol.* 94, 2603–2623. doi: 10.1007/s00204-020-02838-8

Sano, A., Tsuge, S., Kakazu, E., Iwata, T., Ninomiya, M., Tsuruoka, M., et al. (2021). Plasma free amino acids are associated with sarcopenia in the course of hepatocellular carcinoma recurrence. *Nutrition* 84:111007. doi: 10.1016/j.nut.2020.111007

Sun, C., Sun, H. Y., Xiao, W. H., Zhang, C., and Tian, Z. G. (2015). Natural killer cell dysfunction in hepatocellular carcinoma and NK cell-based immunotherapy. *Acta Pharmacol. Sin.* 36, 1191–1199. doi: 10.1038/aps.2015.41

Tajiri, K., and Shimizu, Y. (2013). Branched-chain amino acids in liver diseases. *World J. Gastroenterol.* 19, 7620–7629. doi: 10.3748/wjg.v19.i43.7620

Tang, C., Ma, J., Liu, X., and Liu, Z. (2020). Identification of a prognostic signature of nine metabolism-related genes for hepatocellular carcinoma. *PeerJ* 8:e9774. doi: 10.7717/peerj.9774

Tang, H., Wu, Y., Qin, Y., Wang, H., Jia, Y., Yang, S., et al. (2017). Predictive significance of HMGCS2 for prognosis in resected Chinese esophageal squamous cell carcinoma patients. *Onco Targets Ther.* 10, 2553–2560. doi: 10.2147/OTT.S132543

Thakur, C., and Chen, F. (2019). Connections between metabolism and epigenetics in cancers. *Semin. Cancer Biol.* 57, 52–58. doi: 10.1016/j.semcancer.2019.06.006

Vander, H. M., and DeBerardinis, R. J. (2017). Understanding the intersections between metabolism and cancer biology. *Cell* 168, 657–669. doi: 10.1016/j.cell.2016.12.039

Venkitachalam, S., Revoredo, L., Varadan, V., Fecteau, R. E., Ravi, L., Lutterbaugh, J., et al. (2016). Biochemical and functional characterization of glycosylation-associated mutational landscapes in colon cancer. *Sci. Rep.* 6:23642. doi: 10.1038/srep23642

Vettore, L., Westbrook, R. L., and Tennant, D. A. (2020). New aspects of amino acid metabolism in cancer. *Br. J. Cancer* 122, 150–156. doi: 10.1038/s41416-019-0620-5

Villanueva, A. (2019). Hepatocellular carcinoma. *N. Engl. J. Med.* 380, 1450–1462. doi: 10.1056/NEJMra1713263

Wu, X., Lan, T., Li, M., Liu, J., Wu, X., Shen, S., et al. (2021). Six metabolism related mRNAs predict the prognosis of patients with hepatocellular carcinoma. *Front. Mol. Biosci.* 8:621232. doi: 10.3389/fmolb.2021.621232

Xia, R., Tang, H., Shen, J., Xu, S., Liang, Y., Zhang, Y., et al. (2021). Prognostic value of a novel glycolysis-related gene expression signature for gastrointestinal cancer in the Asian population. *Cancer Cell Int.* 21:154. doi: 10.1186/s12935-021-01857-4

Xu, L. X., He, M. H., Dai, Z. H., Yu, J., Wang, J. G., Li, X. C., et al. (2019). Genomic and transcriptional heterogeneity of multifocal hepatocellular carcinoma. *Ann. Oncol.* 30, 990–997. doi: 10.1093/annonc/mdz103

Yang, S., Hwang, S., Kim, M., Seo, S. B., Lee, J. H., and Jeong, S. M. (2018). Mitochondrial glutamine metabolism via GOT2 supports pancreatic cancer growth through senescence inhibition. *Cell Death Dis.* 9:55. doi: 10.1038/s41419-017-0089-1

Yang, S., Zhang, H., Yang, H., Zhang, J., Wang, J., Luo, T., et al. (2021). SEPHS1 promotes SMAD2/3/4 expression and hepatocellular carcinoma cells invasion. *Exp. Hematol. Oncol.* 10:17. doi: 10.1186/s40164-021-00212-7

Ye, J., Fan, J., Venneti, S., Wan, Y. W., Pawel, B. R., Zhang, J., et al. (2014). Serine catabolism regulates mitochondrial redox control during hypoxia. *Cancer Discov.* 4, 1406–1417. doi: 10.1158/2159-8290.CD-14-0250

Zhang, S., Liu, Z., Wu, D., Chen, L., and Xie, L. (2020). Single-Cell RNA-Seq analysis reveals microenvironmental infiltration of plasma cells and hepatocytic prognostic markers in HCC with cirrhosis. *Front. Oncol.* 10:596318. doi: 10.3389/fonc.2020.596318

Zhang, Y. L., Ding, C., and Sun, L. (2019). High expression B3GAT3 is related with poor prognosis of liver cancer. *Open Med. (Wars)* 14, 251–258. doi: 10.1515/med-2019-0020

Zhang, Z., Ma, L., Goswami, S., Ma, J., Zheng, B., Duan, M., et al. (2019). Landscape of infiltrating B cells and their clinical significance in human hepatocellular

carcinoma. *Oncoimmunology* 8:e1571388. doi: 10.1080/2162402X.2019.1571388

Zhou, S. L., Zhou, Z. J., Hu, Z. Q., Huang, X. W., Wang, Z., Chen, E. B., et al. (2016). Tumor-Associated neutrophils recruit macrophages and T-Regulatory cells to promote progression of hepatocellular carcinoma and resistance to sorafenib. *Gastroenterology* 150, 1646–1658. doi: 10.1053/j.gastro.2016.02.040

Zhu, P., Li, F. F., Zeng, J., Tang, D. G., Chen, W. B., and Guo, C. C. (2021). Integrative analysis of the characteristics of lipid metabolism-related genes as prognostic prediction markers for hepatocellular carcinoma. *Eur. Rev. Med. Pharmacol. Sci.* 25, 116–126. doi: 10.26355/eurrev_202101_24355

Zou, R. C., Xiao, S. F., Shi, Z. T., Ke, Y., Tang, H. R., Wu, T. G., et al. (2019). Identification of metabolism-associated pathways and genes involved in male and female liver cancer patients. *J. Theor. Biol.* 480, 218–228. doi: 10.1016/j.jtbi.2019.08.011

Conflict of Interest: The authors declare that the research was conducted in the absence of any commercial or financial relationships that could be construed as a potential conflict of interest.

Publisher's Note: All claims expressed in this article are solely those of the authors and do not necessarily represent those of their affiliated organizations, or those of the publisher, the editors and the reviewers. Any product that may be evaluated in this article, or claim that may be made by its manufacturer, is not guaranteed or endorsed by the publisher.

frontiers in Oncology

ORIGINAL RESEARCH
published: 09 September 2021
doi: 10.3389/fonc.2021.682710

SLC25A21 Suppresses Cell Growth in Bladder Cancer *via* an Oxidative Stress-Mediated Mechanism

Yong Wang[1,2†], *Jiawen Gao*[3,4†], *Shasha Hu*[3,4†], *Weiting Zeng*[3,4], *Hongjun Yang*[3,4], *Hui Chen*[3] *and Shuang Wang*[3,4*]

[1] Department of Urology, Jilin Province People's Hospital, Changchun, China, [2] Department of Pathophysiology, College of Basic Medical Sciences, Jilin University, Changchun, China, [3] Department of Pathology, Nanfang Hospital, Southern Medical University, Guangzhou, China, [4] Department of Pathology, School of Basic Medical Sciences, Southern Medical University, Guangzhou, China

Background: Bladder cancer (BCa) is a commonly diagnosed malignancy worldwide that has poor survival depending on its intrinsic biologic aggressiveness and a peculiar radio- and chemoresistance features. Gaining a better understanding of tumorigenesis and developing new diagnosis and treatment strategies for BCa is important for improving BCa clinical outcome. SLC25 family member 21 (SLC25A21), a carrier transporting C5-C7 oxodicarboxylates, has been reported to contribute to oxoadipate acidemia. However, the potential role of SLC25A21 in cancer remains absolutely unknown.

Methods: The expression levels of SLC25A21 in BCa and normal tissues were examined by real-time PCR and immunohistochemistry. Gain-of- and loss-of-function experiments were performed to detect the biological functions of SLC25A21 *in vitro* and *in vivo* by CCK-8 assay, plate colony formation assay, cell migration, invasion assay and experimental animal models. The subcellular distribution of substrate mediated by SLC25A21, mitochondrial membrane potential and ROS production were assessed to explore the potential mechanism of SLC25A21 in BCa.

Results: We found that the expression of SLC25A21 was downregulated in BCa tissues compared to normal tissues. A significant positive correlation between decreased SLC25A21 expression and poor prognosis was observed in BCa patients. Overexpression of SLC25A21 significantly inhibited cell proliferation, migration and invasion and induced apoptosis *in vitro*. Moreover, the enhanced SLC25A21 expression significantly suppressed tumor growth in a xenograft mouse model. Furthermore, we revealed that SLC25A21 suppressed BCa growth by inducing the efflux of mitochondrial α-KG to the cytosol, decreasing to against oxidative stress, and activating the ROS-mediated mitochondrion-dependent apoptosis pathway.

Conclusions: Our findings provide the first link between SLC25A21 expression and BCa and demonstrate that SLC25A21 acts as a crucial suppressor in BCa progression, which may help to provide new targets for BCa intervention.

Keywords: SLC25A21, bladder cancer, α-ketoglutarate, ROS, apoptosis

OPEN ACCESS

Edited by:
Yongguang Tao,
Central South University, China

Reviewed by:
Agnese Po,
Sapienza University of Rome, Italy
Ali Vaziri-Gohar,
Case Western Reserve University, United States
Qianjin Liao,
Central South University, China

****Correspondence:***
Shuang Wang
shuangw@126.com

[†]These authors have contributed equally to this work

Specialty section:
This article was submitted to Molecular and Cellular Oncology, a section of the journal Frontiers in Oncology

Received: *19 March 2021*
Accepted: *20 August 2021*
Published: *09 September 2021*

Citation:
Wang Y, Gao J, Hu S, Zeng W, Yang H, Chen H and Wang S (2021) SLC25A21 Suppresses Cell Growth in Bladder Cancer via an Oxidative Stress-Mediated Mechanism. Front. Oncol. 11:682710. doi: 10.3389/fonc.2021.682710

BACKGROUND

Bladder cancer (BCa) is one of the most common malignancies of the urinary system, with approximately 900,000 new cancer cases and 250,000 mortalities worldwide each year (1). Approximately 70% of all newly diagnosed BCa cases are non-muscle-invasive BCa (nmiBCa). However, up to 30% of nmiBCa patients will relapse or develop progression to muscle-invasive BCa (miBCa) (2, 3). Additionally, in 5-15% of patients with BCa, unresectable or metastatic disease is found at the time of diagnosis (4). The poor survival of BCa patients is related to the intrinsic biologic aggressiveness of this tumor and its peculiar radio- and chemoresistance. Therefore, efforts to gain a deep understanding of the pathogenic mechanisms contributing to BCa carcinogenesis to identify new effective targets for therapy are strongly suggested.

Mitochondria are in fact the gatekeepers of the eukaryotic cell viability through regulating programmed cell death and controlling nuclear functions *via* the production of reactive oxygen species (ROS) (5), the modulation of calcium levels (6), and the trafficking of small molecule metabolites (7). The transfer of metabolites through mitochondrial membranes is a vital process that is highly controlled and regulated by the inner mitochondrial membrane (IMM). To fulfill its functions, a myriad of mitochondrial carriers are properly expressed, located and folded in the IMM (8). Mitochondrial carriers constitute a large family of transport proteins that play important roles in the intracellular translocation of metabolites, nucleotides and coenzymes. Solute carrier family 25 (SLC25) is a six-transmembrane-helix mitochondrial inner membrane protein family that includes 53 members (8). SLC25 facilitates the transport of molecules involved in the urea and citric acid cycle, oxidative phosphorylation, and iron metabolism among other processes (9). Growing evidence shows that some members of the SLC25 family can also be involved either directly or indirectly in pathological states, including cancer (10–13). The major role of SLC25 family member 21 (SLC25A21), also known as the oxoadipate carrier (ODC), is to mediate the import of 2-oxoadipate into the mitochondrial matrix in exchange for 2-oxoglutarate (α-ketoglutarate, α-KG) out. Previous studies have reported that the SLC25A21 defects may contribute to oxoadipate acidemia, a neurological disorder that is characterized by excessive amounts of oxoadipate and aminoadipate (14). Deletion of the 14q13.3 region, which contains the SLC25A21 gene, has also been reported in lung cancer (15). However, little is known about the potential role of SLC25A21 in cancer, especially BCa.

The present study was designed to explore the effects of SLC25A21 on BCa progression and the potential mechanisms. We identified that the expression levels of SLC25A21 were downregulated in BCa tissues by real-time PCR and immunohistochemistry. We further demonstrated the effects of SLC25A21 on cellular biological behaviors both *in vitro* and *in vivo* by gain- and loss-of-function experiments. We further presented evidence that SLC25A21 induces the efflux of mitochondrial α-KG to the cytosol and activates the ROS-mediated apoptosis pathway. Our findings provide novel insights into the roles of SLC25A21 in the tumorigenesis and progression of BCa, which may help to provide new therapeutic targets for BCa.

Abbreviations: BCa, Bladder cancer; nmiBCa, non-muscle-invasive BCa; miBCa, muscle-invasive BCa; ROS, reactive oxygen species; IMM, the inner mitochondrial membrane; SLC25, Solute carrier family 25; SLC25A21, SLC25 family member 21; α-KG, α-ketoglutarate; $\Delta\psi m$, Mitochondrial membrane potential; MMP, mitochondrial membrane permeabilization; TCGA, The Cancer Genome Atlas; GEO, the Gene Expression Omnibus.

METHODS AND MATERIALS

Ethics Statement

The use of tissues for this study has been approved by the ethics committee of Nanfang Hospital, Southern Medical University (Guangzhou, China). All of the patients signed an informed consent before the use of these clinical materials for research purposes. Moreover, the animal experiments were performed in strict accordance with the recommendations in the Guide for the Care and Use of Laboratory Animals of the National Institutes of Health. The protocol was approved by the Committee on the Ethics of Animal Experiments of Southern Medical University.

Cell Lines and Tissue Specimens

The human normal ureter epithelial cell line (SV-HUC-1) and bladder cancer T24, EJ, BIU-87 and UMUC3 cells were obtained from American Type Culture Collection (ATCC, Manassas, VA, USA). UMUC3 cells were maintained in DMEM (Gibco, Gaithersburg, MD, USA) and T24, EJ and BIU-87 cells were maintained in RPMI-1640 medium (Gibco) supplemented with 10% fetal bovine serum (FBS Gibco) and 1% penicillin G sodium/streptomycin sulfate. SV-HUC-1 cells were cultured in F-12K medium (Gibco) with 10% FBS, 2 mmol/L L-glutamine and 1500 mg/L sodium bicarbonate. All of the cell lines were cultured at 37°C and 5% CO_2 in a humidified incubator. All cell lines were used at early passages.

The tissue samples used for this study were obtained from randomly selected patients with a diagnosis of primary BCa from biopsy, transurethral resection of bladder tumor or radical cystectomy in Nanfang Hospital, Southern Medical University. Freshly frozen samples from BCa patients were selected for real-time PCR. 56 formalin-fixed paraffin-embedded BCa tissues and 20 adjacent non-tumor tissues were used to construct a tissue microarray (TMA) for investigating the expression of SLC25A21 protein using immunohistochemistry (IHC). One 0.6 mm tissues core had been punched out from representative regions of each tissue block, and was transferred into a TMA format as previously described (16). Tumor grade and stage assessments were made according to the World Health Organization (WHO) 2004 standard and Union for International Control Cancer (UICC) TNM system. The time of follow-up range from 3-82 months. The clinicopathological features of the case cohort are list in **Table 1**.

GEO Data Analysis

Microarray datasets were downloaded from public GEO database (https://www.ncbi.nlm.nih.gov/geo/) and normalized using the

TABLE 1 | Correlation between the clinicopathological features and expression of SLC25A21 in BCa.

Characteristics	n	SLC25A21 protein expression		
		low (%)	high (%)	*P* value
Gender				
Male	46	28 (60.1)	18 (39.9)	0.078
Female	10	9 (90)	1 (10)	
Age(years)				
<69	26	18 (69.2)	8 (30.8)	0.642
≥69	30	19 (63.3)	11 (36.7)	
Tumor diameter (cm)				
<5	34	22 (64.7)	12 (35.3)	0.788
≥5	22	15 (68.2)	7 (31.8)	
Tumor grade				
Low	18	9 (50.0)	9 (50.0)	0.080
High	38	28 (73.7)	10 (26.3)	
Invasion				
No	15	6 (40.0)	9 (60.0)	0.013
Yes	41	31 (75.6)	10 (24.4)	
T stage				
T_a+T_{is}+T_1	17	7 (41.2)	10 (58.8)	0.008
T_2	15	14 (93.3)	1 (6.7)	
T_3+T_4	24	16 (66.7)	8 (33.3)	
N stage				
N_0	50	33 (66.0)	17 (34.0)	0.974
N_{1-3}	6	4 (66.7)	2 (33.3)	

robust multichip average (RMA) with R/Bioconductor packages including affy (17). GSE3167 and GSE68020 datasets are analyzed in present study. GSE3167 dataset includes superficial transitional cell carcinoma (sTCC) with surrounding CIS (13 patients), without surrounding CIS lesions (15 patients), in muscle invasive carcinomas (mTCC; 13 patients). GSE68020 includes 30 high-grade urothelial carcinoma and 20 benign tissues.

RNA Isolation and Real- Time PCR

Total RNA from tissues and cell lines were extracted using Trizol reagent (Takara, Dalian, China) according to the manufacturer's protocol. The cDNA was synthesized with 500 ng total RNA by using PrimeScript RT Reagent Kit (Takara). Real-time PCR was carried out using SYBR® Rremix Ex TaqTM (Takara) as described previously (18). GAPDH was used as an internal control. The assay was performed in triplicate. All primer sequences are listed in **Supplement Information S1**.

IHC Staining and Scoring

IHC was performed on 3-μm sections of paraffin-embedded tissue samples. The sections were deparaffinized with xylene and rehydrated with descending ethanol concentrations, and then were treated with Peroxidase Blocking Reagent (Dako, Glostrup, Denmark) for 5 min, followed by incubation with SLCA5A21 primary antibody (1:80, Affinity Biosciences, OH, USA, Cat# DF4172) at 4°C overnight. After incubation with the secondary antibody at room temperature for 1 h. Immunodetection was performed with the diaminobenzidine (DAB) reagent (Dako) according the manufacturer's protocol, and the reaction time of each section was consistent, followed by counterstaining with hematoxylin.

The IHC-stained tissue sections were reviewed and scored separately in a double-blinded manner. Scores were determined based on both the intensity and proportion of SLC25A21-positive cells as described previously (19, 20). The staining score ranged from 0 to 4, corresponding to the percentage of immunoreactive tumor cells (0%, 1-25%, 26-50%, 51-75%, or 76-100%). The staining intensity scores were as follows: negative (0), weak (score = 1), medium (score = 2) or strong (score = 3). A total score of 0 to 12 was calculated by multiplying the staining degree score by the intensity score. The final staining score of ≥ 3 was considered to indicate high level of SLC25A21.

Construction of Cell Lines With Stably Overexpressed SLC25A21

The full-length open reading frame of human SLC25A21 was amplified and cloned into the pcDNA3.1 vector. BCa cell lines EJ and T24 were transfected with pcDNA3.1-SLC25A21 using Lipofectamine 3000 reagent (Thermo Fisher Scientific, IL, USA). The empty pcDNA3.1 vector was used as the control. G418 was used to select stable SLC25A21-overexpressing cells. The expression levels of SLC25A21 were determined by real-time PCR and western blotting analysis.

Oligonucleotide Transfection

The siRNAs targeting SLC25A21 and negative control siRNA (silencer negative control siRNA) were synthesized (GenePharma, Shanghai, China). Oligonucleotides transfection was performed with Lipofectamine 3000 following the manufacturer's protocol. Target sequences for siRNAs were shown in **Supplement Information S2**.

Cell Proliferation

Cell proliferation was assessed using the Cell Counting Kit-8 kit (Dojindo Laboratories, Kyushu Island, Japan) according to the manufacturer's instructions. In brief, BCa cells were seeded in 96-well plates at 8×10^2 cells per well. The results are reflected in the form of the absorbance optical density at 450 nm using a microplate reader (BioTek, VT, USA). The experiments were conducted in triplicate.

Colony Formation Assay

Colony formation assays *in vitro* were performed according to standard protocols as previously described (21, 22). In brief, BCa cells were seeded in 6-well plates at 2×10^2 cells per well and cultured in medium containing 10% FBS. After 2 weeks of culture, cell colonies were fixed with methanol for 30 min and stained with Giemsa for 15 min. The surviving colonies (≥50 cells per colony) were then counted under a microscope. The experiments were performed at least in triplicate.

Cell Cycle Analysis and Apoptosis Analysis

Apoptosis analysis was performed by flow cytometry by a BD FACSCanto II Flow Cytometer (BD Bioscience, San Jose, CA, USA). The cells were collected and washed twice with ice-cold PBS, resuspended in 200 μl binding buffer and stained with the Annexin V-FITC Detection Kit (Genechem, Shanghai, China) according to the manufacturer's instructions. Early apoptosis was

determined based on the percentage of cells with annexin V^+/PI^- staining, while late apoptosis was determine based on the percentage of cells with annexin V^+/PI^+ staining. The experiments were performed at least in triplicate.

For cell cycle, cells were harvested after 48 h transfection and fixed in ice-cold 70% ehanol at 4°C overnight. Cells were then resuspended in propidium iodide solution (Genechem) according to the manufacturer's protocol and subjected to analysis using flow cytometry (BD).

Wound Healing Assays

A wound healing assay was conducted to measure the migration of BCa cells. Cell migration was assessed by measuring the movement of cells into a scraped, acellular area by a 200 μL pipette tube in 6-well plates. The spread of wound closure was observed every 24 h. Migration ability was quantified by measuring the rate of cell migration toward the original wound field. The rate of cell migration were measured according to the formula: R_M (Rate of cell migration (μm/h)) = $(W_i - W_f)/t$, W_i indicates initial wound width (μm), W_f indicates final wound width (μm) and t indicates duration of migration (hour), as described previously (23).

Transwell Invasion Assays

Cell invasion assays were performed in Transwell chambers (BD Biosciences, San Jose, CA, USA) containing 8-μm pores in 24-well plates. A total of 1×10^5 cells were starved overnight and seeded into the upper chamber of the transwell, which had been pretreated with 60 μl Matrigel for 4 h, in 200 μl of serum-free medium. The lower chamber was supplemented with 500 μl of medium with 10% FBS. After incubation at 37°C for 24 to 72 h, noninvading cells in the upper chamber were scraped off with a cotton swab, and invading cells stuck to the lower surface of the membrane were fixed in 100% methanol for 30 min and stained with Giemsa solution for 15 min. The cells were counted randomly for five fields of each membrane under a light microscope. The experiments were performed at least in triplicate.

In Vivo Functional Assays in Nude Mouse Models

Male, 4- to 6-week-old Balb/C-nu/nu nude mice were obtained from the Laboratory Animal Centre of Southern Medical University. Stably overexpressing SLC25A21 EJ cells and control cells were used to produce subcutaneous xenograft models. The nude mice were divided randomly into two groups (5 mice per group). A total of 2×10^6 SLC25A21-overexpressing EJ cells or control cells were subcutaneously injected into the right flank of mice, respectively. Tumor growth was measured every 3 days with a digital caliper. Tumor volume was calculated according to the formula: V (volume) = $(D \times d^2)/2$ (D indicates the longest diameter and d indicates the shortest diameter). After 30 days of monitoring, the mice were sacrificed by cervical dislocation, and the xenografts were removed and subjected to histological examination. This investigation was carried out in strict accordance with ethical standards in the Guide for the Care and Use of Laboratory Animals of the National Institutes of Health. The protocol was approved by the Committee on the Ethics of Animal Experiments of Southern Medical University.

Mitochondria Isolation and Determination of α-KG

Mitochondria extraction was conducted according to the instructions of the Mitochondria Isolation Kit (Beyotime Biotechnology, Jiangsu, China). Briefly, at least 2×10^7 cells were harvested and then centrifuged at 600 × g at 4°C for 5 min. Mitochondrial isolation buffer was used to resuspend the pellet. The mixture was placed on ice for 15 min and then ground and centrifuged at 1000 × g at 4°C for 10 min. The supernatant was collected and centrifuged at 3500 × g at 4°C for 10 min. The pellet contained the mitochondria. The supernatant was collected and centrifuged at 12,000 × g at 4°C for 10 min. The supernatant contained the cytosolic fraction. Mitochondria were resuspended in mitochondria isolation buffer and centrifuged again at 3500 × g at 4°C for 10 min to obtain purified mitochondria. The levels of α-KG in the mitochondria and cytosolic fraction were determined using α-ketoglutarate (α-KG) enzyme-linked immunosorbent assay (ELISA) kits according to the documents of the manufacturer (JianglaiLab, Shanghai, China). In brief, 10 μL cell lysate and 40 μL sample diluent were added to the ELISA kit wells containing solid-phase antibody. After incubation at 37°C for 30 min, all the wells were washed five times with wash solution. Then, except for the blank wells, 50 μL horseradish peroxidase-conjugate reagent was added to each well. After incubation at 37°C for 30 min, all the wells were washed five times with wash solution again, and then 50 μL chromogen solution A and 50 μL chromogen solution B were added to each well. The reaction mixture was incubated at 37°C for 15 min in the dark. Finally, 50 μL stop solution was added to each well to stop the reaction, and read the absorbance at 450 nm within 15 min. The concentrations of α-KG in the mitochondria and cytosolic fraction were calculated according to the standard curve prepared following the direction of the kit. Data were expressed as mean ± standard deviation (SD) of three separate measurements.

Mitochondrial Membrane Potential ($\Delta\psi m$)

Changes in the Δψm during the early stages of apoptosis were assayed using the Mitochondrial Membrane Potential Assay kit with JC-1 (Beyotime, Shanghai, China) as described previously (24). Briefly, 5×10^4 cells were harvested and incubated with JC-1 at 37°C for 20 min in the dark. The stained cells were washed with ice-cold working solution twice and then analyzed by flow cytometry (BD). JC-1 aggregates in the polarized mitochondrial matrix and forms J-aggregates, which emit red fluorescence at 595 nm when excited at 525 nm. However, JC-1 cannot aggregate in the depolarized mitochondrial matrix and exists as JC-1 monomers, which emit green fluorescence at 525 nm when excited at 485 nm. Mitochondrial depolarization is indicated by a decrease in the red/green fluorescence intensity ratio.

ROS Production

The ROS levels were detected with the Human ROS ELISA Kit and analyzed with a microplate reader according to the documents of the manufacturer (JianglaiLab, Shanghai, China).

Western Blotting

Cells were lysed in prechilled RIPA buffer containing phosphatase inhibitors, protease inhibitors and PMSF. The protein extracts were loaded on each line of a 10% SDS-PAGE gel and transferred to polyvinylidene fluoride (PVDF) membranes (Millipore, Darmstadt, Germany). The membranes were blocked in 5% skimmed milk in 1 × PBS-T (0.5% Tween-20) and incubated overnight at 4°C with the following primary antibodies: anti-SLC25A21 (1:500; Affinity Biosciences), anti-cytochrome C (1:500; Affinity Biosciences), anti-caspase-9 (1:800; Affinity Biosciences), anti-cleaved caspase-9 (1:800; Affinity Biosciences), anti-caspase-3 (1:800; Affinity Biosciences), and anti-cleaved caspase-3 (1:800; Affinity Biosciences). Anti-tubulin (1:1000; Proteintech Group, Wuhan, China) was used as protein-loading control. Blots were incubated with HRP-conjugated secondary antibodies for 1 h at room temperature, and visualized with ECL Western Blotting Substrate (ThermoFisher Scientific).

Statistical Analysis

All statistical analyses were performed using SPSS version 16.0 software (SPSS, Chicago, Illinois, USA). Differences between groups were identified using a two-tailed Student's *t*-test. Associations between SLC25A21 expression and clinicopathological characteristics were determined by the χ^2 test. Survival curves were plotted by the Kaplan–Meier method and compared by the log-rank test. The significance of various variables for survival was analyzed by the Cox proportional hazards model for multivariate analyses. A probability value of 0.05 or less was considered to be significant.

RESULTS

SLC25A21 Is Downregulated in BCa and Is Negatively Associated With Poor Prognosis in BCa Patients

To evaluate the expression levels of endogenous SLC25A21 in BCa, we first examined SLC25A21 mRNA expression in 20 BCa tissues and their pair-matched noncancerous tissue samples using real-time PCR. As shown in **Figure 1A**, SLC25A21 mRNA was significantly downregulated in BCa tissues compared to nontumor tissues ($P<0.001$). Meanwhile, SLC25A21 mRNA levels was down-regulated in all the BCa cell lines compared with a normal cell line (SV-HUC-1) cells ($P<0.05$, **Supplementary Figure S1**). To further confirm the levels of SLC25A21 expression in BCa, we also analyzed the SLC25A21 expression in public datasets from The Cancer Genome Atlas (TCGA) and the Gene Expression Omnibus (GEO) database. By analyzing the TCGA, we also found that SLC25A21 was lower expressed in transcript levels in BCa than in normal bladder mucosa according to a Gene Expression Profiling Interactive Analysis website (GEPIA) (gepia.cancer-pku.cn/) (**Figure 1B**). In addition, consistent with our results, SLC25A21 was expressed at lower levels in BCa tissues than in normal tissues in GSE3167 and GSE68020 datasets (**Figures 1C, D**).

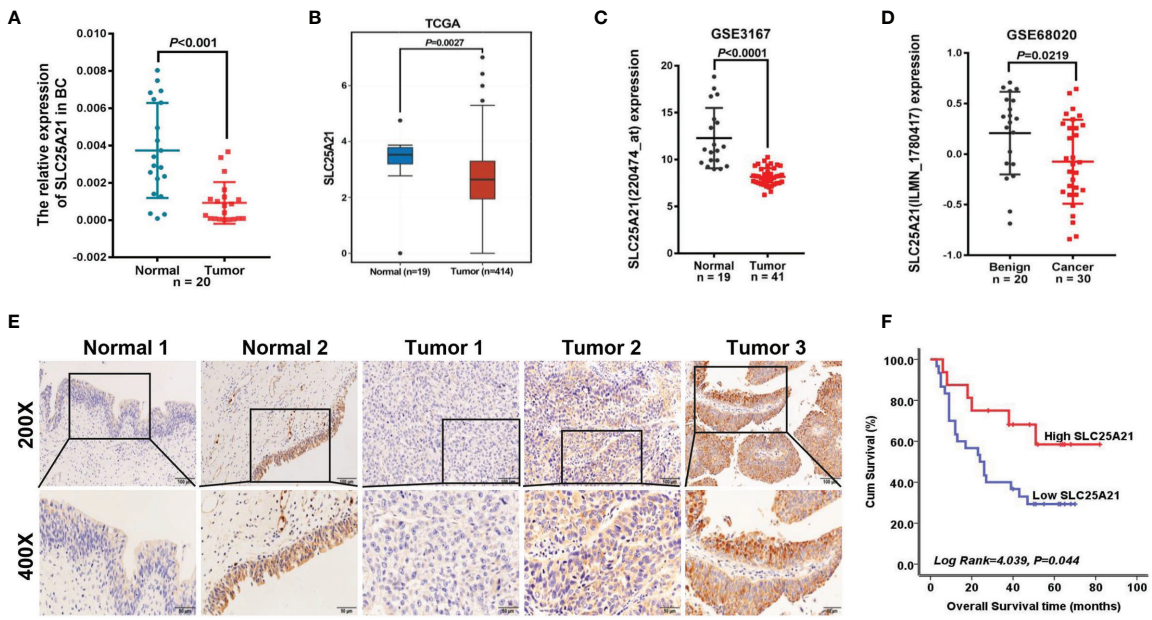

FIGURE 1 | SLC25A21 is downregulated in BCa and negatively associated with poor prognosis in BCa patients. **(A)** Expression levels of SLC25A21 mRNA in BCa and pair-matched noncancerous tissue samples. **(B–D)** Analysis of SLC25A21 expression in BCa compared with noncancerous tissue according to RNA-seq in TCGA database and BCa microarray profile (GSE3167 and GSE68020) **(E)** Expression analysis of SLC25A21 protein in BCa and normal bladder mucosa tissues by IHC. Scale bars, 100 μm (200x) or 50 μm (400x). **(F)** Correlation between SLC25A21 protein expression and overall survival in BCa patients (log-rank $P=0.044$).

To evaluate whether SLC25A21 expression was associated with the clinicopathologic features of BCa patients, we further performed immunostaining with SLC25A21 antibody in tissue microarrays using IHC and observed that SLC25A21 was highly expressed in 60.00% (12 of 20) of normal tissues and only in 33.93% (19 of 56) of BCa samples. The levels of SLC25A21 were significantly downregulated in BCa tissues (P =0.042, **Figure 1E**). The SLC25A21 immunoreactivity scores showed that the lower levels of SLC25A21 expression were associated with tumor invasion and T stage (**Table 1**). In addition, we also analyzed the prognostic significance of SLC25A21 expression in patients with BCa. As shown in **Figure 1F**, it was revealed that low expression of SLC25A21 was significantly correlated with poor survival in BCa patients (log rank P = 0.044). Taken together, these findings suggest that SLC25A21 expression is downregulated in BCa and that low SLC25A21 expression is a poor prognostic biomarker for patients with BCa, which indicates that SLC25A21 might behave as a suppressor in BCa.

Overexpression of SLC25A21 Inhibits the Growth, Migration and Invasion of BCa Cells *In Vitro*

To investigate whether SLC25A21 plays an important role in the biological behavior of BCa carcinogenesis, we established stable SLC25A21-overexpressing BCa cells and SLC25A21-depleted BCa cells. EJ and T24 cells which have relatively low endogenous mRNA expression were used to establish two BCa cell lines with stable SLC25A21 overexpression. Real-time PCR and western blotting analyses revealed that the relative level of SLC25A21 in BCa cells was significantly increased compared to that in control cell lines (**Figures 2A, B**). CCK8 assays revealed a significantly slower

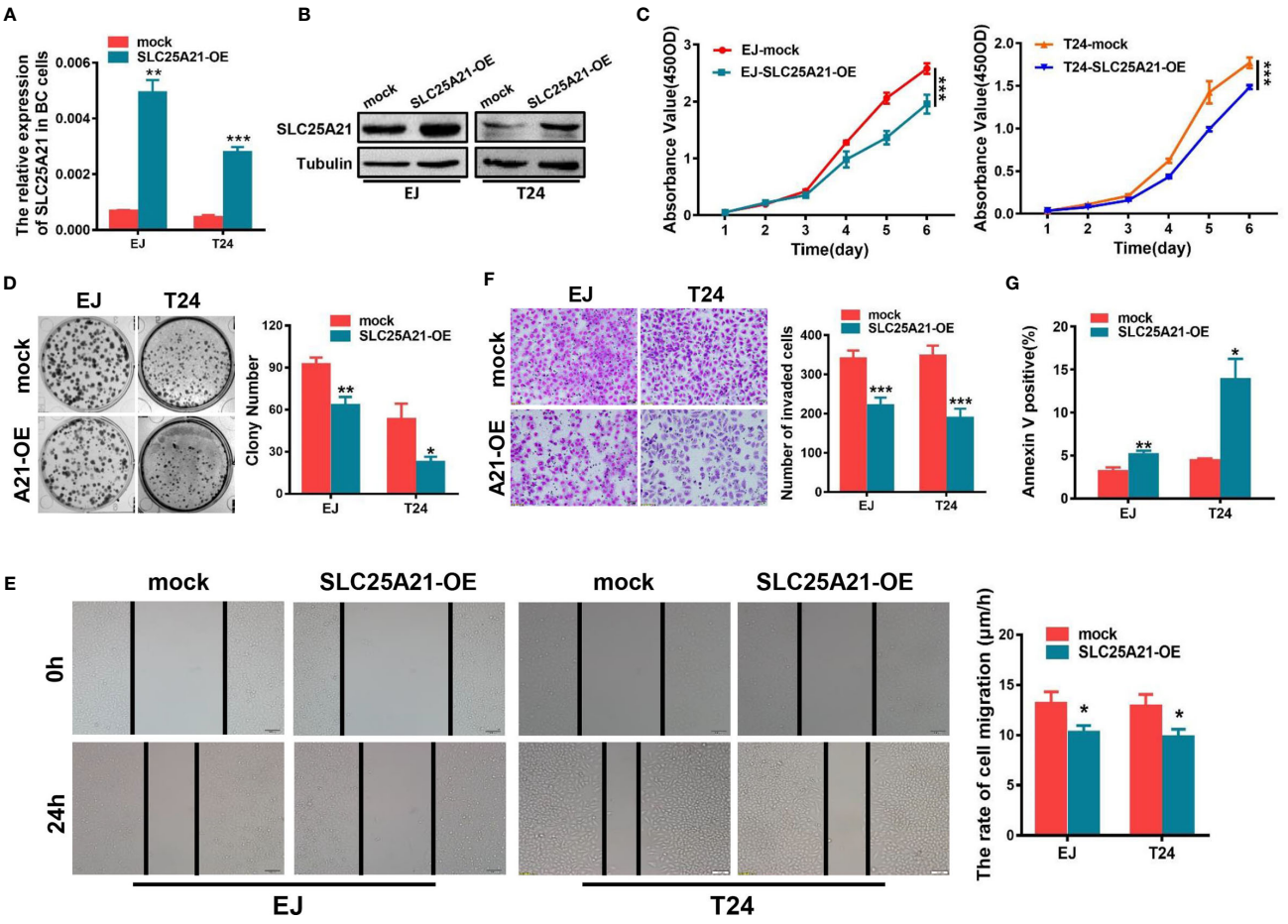

FIGURE 2 | SLC25A21 overexpression inhibits the cell proliferation, migration and invasion and induces the apoptosis of BCa cells *in vitro*. **(A, B)** Increased expression of SLC25A21 after transfection of the pcDNA3.1-SLC25A21 vector was confirmed in two BCa cell lines by real-time RT-PCR **(A)** and western blotting **(B)**. **(C)** SLC25A21 overexpression inhibits the proliferation of EJ and T24 cells. **(D)** SLC25A21 overexpression decreased the colony formation capacity of EJ and T24 cells. **(E)** The migration ability of BCa cells overexpressing SLC25A21 was decreased, as indicated by the wound healing assay. **(F)** Matrigel invasion chamber assays showed that SLC25A21 overexpression inhibited the invasiveness of both EJ and T24 cells. Representative images (left) and quantitative analyses (right) are shown. **(G)** SLC25A21 overexpression induced the apoptosis rate relative to control cells. Data are presented as the mean ± SD. The results were reproducible in three independent experiments. *P < 0.05, **P < 0.01, and ***P < 0.001.

proliferation rate in SLC25A21-overexpressing EJ and T24 cells than in control cells (P<0.001, **Figure 2C**). In the colony formation assay, both SLC25A21 overexpression obviously suppressed colony formation in both BCa cell lines (EJ, P = 0.0028 and T24, P = 0.0103, **Figure 2D**).

We also examined the effects of SLC25A21 overexpression on BCa cell migration and invasion. Wound healing assays were performed to explore the effects on the migration ability of BCa cells after enforcing the expression of SLC25A21. The results suggested that SLC25A21 upregulation inhibited the rate of migration of BCa cells (EJ cells, P=0.0211 and T24 cells, P=0.0181, **Figure 2E**). Cell invasion analysis demonstrated that the exogenous SLC25A21 overexpression in two different BCa cell lines significantly inhibited cancer cell invasion through Matrigel, a basement-membrane- like extracellular matrix (P<0.001, **Figure 2F**).

Overexpression of SLC25A21 Induces Cell Apoptosis in BCa Cells

Based on the results of CCK-8 and colony formation assays, we next investigated the potential mechanisms underlying the growth-inhibitory effects of SLC25A21 overexpression. The results of the flow cytometry cell cycle assays in two SLC25A21-overexpressing cell lines were inconsistent. SLC25A21 overexpression induced G_1 phase cell cycle arrest in EJ cells (P=0.0043) and reduced the G_1 phase cell population in (P=0.0079, **Supplementary Figure S2**). However, the upregulation of SLC25A21 expression resulted in an increased percentage of early apoptosis (EJ, P = 0.0092 and T24, P = 0.0138, **Figure 2G** and **Supplementary Figure S3**) in both BCa cell lines compared with controls. In short, these data indicate that the SLC25A21-mediated decrease in cell proliferation is modulated by apoptosis, rather than by the G_1-S checkpoint.

SLC25A21 Overexpression Suppressed Tumor Growth of BCa Cells *In Vivo*

In light of our *in vitro* findings, we also assessed the effects of SLC25A21 overexpression on the growth of xenograft tumors *in vivo*. EJ cells with SLC25A21-overexpressing and control cells were subcutaneously inoculated into nude mice. As shown in **Figures 3A, B**, compared with control cells, SLC25A21 overexpression significantly inhibited BCa cell growth *in vivo* (*P=0.0392*). The tumor weight was lower in the stable SLC25A21overexpression group than in the control groups (*P=0.0293*, **Figure 3C**). These results suggest that SLC25A21 exerts a significant inhibitory effect on BCa tumorigenesis *in vivo*.

SLC25A21 Knockdown Promotes BCa Cell Proliferation, Migration and Invasion and Inhibits Cell Apoptosis *In Vitro*

To assess the effect of reducing SLC25A21 expression in BCa, we next knocked down SLC25A21 levels by siRNA transfection in BIU-87 and UMUC3 cells, which have relatively high endogenous SLC25A21 expression. A considerable reduction in SLC25A21 was observed in both SLC25A21-depleted BCa cell lines (**Figures 4A, B**). The results of CCK8 and colony formation assays showed that both BCa cell lines with SLC25A21 knocked down had a significant growth advantage over the respective cells transfected with negative control siRNA (P<0.01, **Figures 4C, D**). Moreover, SLC25A21 knockdown inhibited cell apoptosis in BIU-87 (P=0.0014) and in UMUC3 cells (P<0.0001, **Figure 4E**). In addition, markedly higher migration rates and stronger invasiveness were observed in SLC25A21-depleted BIU-87 and SLC25A21-depleted UMUC3 cells, as revealed by the wound healing assay (BIU-87 cells, P=0.0254 and UMUC3 cells, P=0.0214, **Figure 4F**) and Transwell migration assay (P<0.0001, **Figure 4G**).

SLC25A21 Overexpression Induces Cell Apoptosis by the α-KG-Mediated ROS Pathway in BCa

We next studied the molecular mechanisms by which SLC25A21 affects proliferation. Because the function of SLC25A21 is linked to the transport of C5-C7 oxodicarboxylates, including α-KG, across the IMM, we speculated that aberrant SLC25A21 expression directly changes α-KG levels in the mitochondria. Therefore, we assessed the subcellular distribution of α-KG mediated by SLC25A21. SLC25A21 overexpression significantly increased α-KG levels in the cytosol and

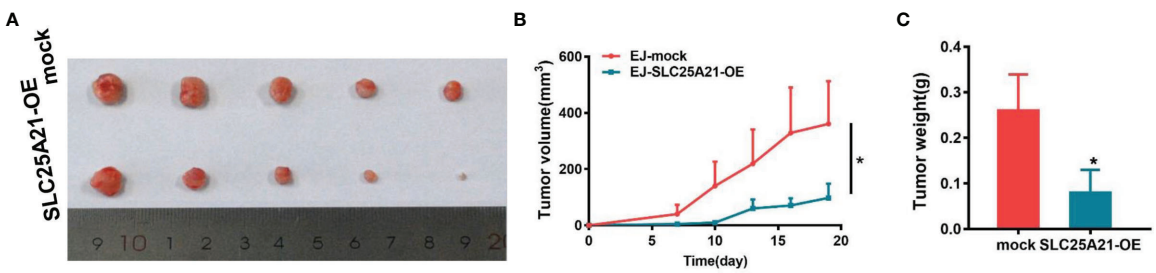

FIGURE 3 | SLC25A21 overexpression suppresses BCa cell proliferation *in vivo*. **(A)** SLC25A21 overexpression inhibited subcutaneous tumor formation in nude mice. EJ cells with SLC25A21 upregulation and control cells were inoculated into nude mice (n = 5 per group). **(A)** The xenografts of 30 days after ectopic-subcutaneous implantation of with SLC25A21 overexpressing and control cells into nude mice. **(B, C)** The effect of SLC25A21 overexpression on BCa tumor growth was evaluated based on tumor volume **(B)** and tumor weight **(C)** in the two groups. *P < 0.05.

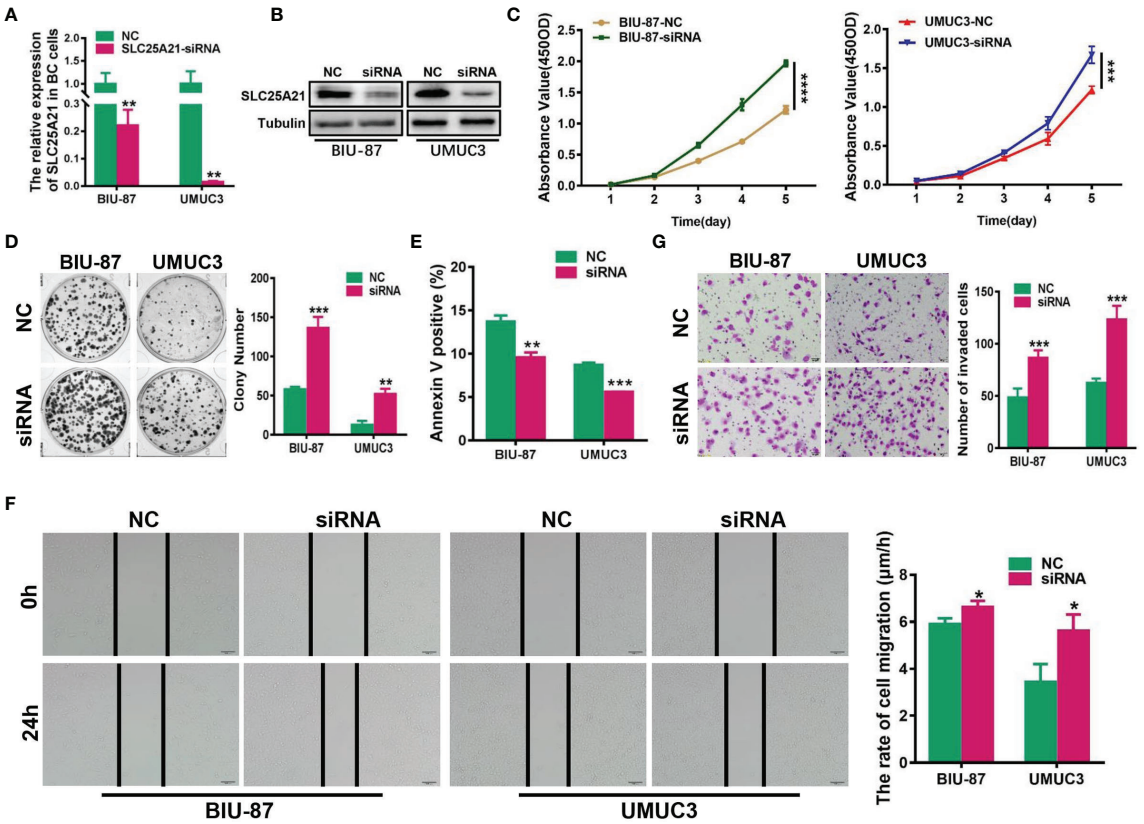

FIGURE 4 | siRNA-mediated knockdown of SLC25A21 promotes BCa cell proliferation, migration and invasion, and represses cell apoptosis *in vitro*. **(A, B)** Depletion of SLC25A21 after transient transfection of siRNA targeting SLC25A21 was confirmed in two BCa cell lines by real-time RT-PCR **(A)** and western blotting **(B)**. **(C, D)** The effects of SLC25A21 downregulation on BCa cell proliferation by CCK-8 **(C)** and colony formation assays **(D)**. **(E)** The effects of SLC25A21 depletion on cell apoptosis **(E)** by flow cytometry. **(F)** The effects of SLC25A21 depletion on the migration ability of BCa cells by using a wound healing assay. **(G)** Invasion assays were used to determine the effects of SLC25A21 depletion on the invasion ability of BCa cells. Representative images (left) and quantitative analyses (right) are shown. Data are expressed as the means ± SD of three independent experiments. $^{*}P < 0.05$, $^{**}P < 0.01$, $^{***}P < 0.001$, and $^{****}P < 0.0001$.

decreased α-KG levels in the mitochondria in T24 cells (cytosol, P=0.0150 and mitochondria, P=0.0284, **Figure 5A**, left). Moreover, SLC25A21 knockdown mediated by siRNA significantly elevated α-KG levels in the mitochondria of UMUC3 cells compared those after transfection with a negative control siRNA (P<0.001, **Figure 5A**, right). The oxidative metabolism of α-KG produces succinate in the mitochondria. Indeed, decreased levels of the succinate were observed in the mitochondria of BCa cells with SLC25A21 overexpressing (P=0.0032, **Figure 5B**, left). In contrast, the levels of succinate in the mitochondria were reduced in SLC25A21-depleted UMUC3 cells, further supporting the view that upregulation of SLC25A21 promoted the efflux of α-KG from mitochondria (P=0.0028, **Figure 5B**, right).

Because ROS generation is augmented by mitochondrial dysfunction, we next investigated whether SLC25A21 induces ROS production. The results showed that with the reduction of α-KG levels in the mitochondria, the upregulation of SLC25A21 in the two cell lines resulted in significantly higher ROS accumulation compared with the corresponding control group, which indicated a weaker ability to survive oxidative stress (T24 cells, P=0.0341 and EJ cells, P=0.0348, **Figure 5C**). We also evaluated the effects of SLC25A21 on Δψm in both SLC25A21-overexpressing cells by flow cytometry. As shown in **Figure 5D**, a decreased Δψm was observed in both SLC25A21-overexpressing BCa cell lines. T24 cells with SLC25A21-overexpressing exhibited a Δψm decline of more than 36.3% (P<0.0001), and EJ cells showed a 13.3% decline (P=0.0012) compared to the control. It has been reported to participate in triggering caspase-dependent apoptosis by regulating Δψm. The results of western blotting showed that SLC25A21 induced cytochrome C (cyto C) transfer from mitochondria to the cytosol in BCa cells. In addition, we also found that SLC25A21 overexpression increased the activation of caspase-3 and caspase-9 in BCa cell lines and xenografts tissues (**Figures 5E, F**), suggesting that SLC25A21 triggers mitochondrial apoptotic pathways in BCa. Hence, these data indicate that SLC25A21 activates the mitochondrial apoptosis pathway by inducing α-KG efflux

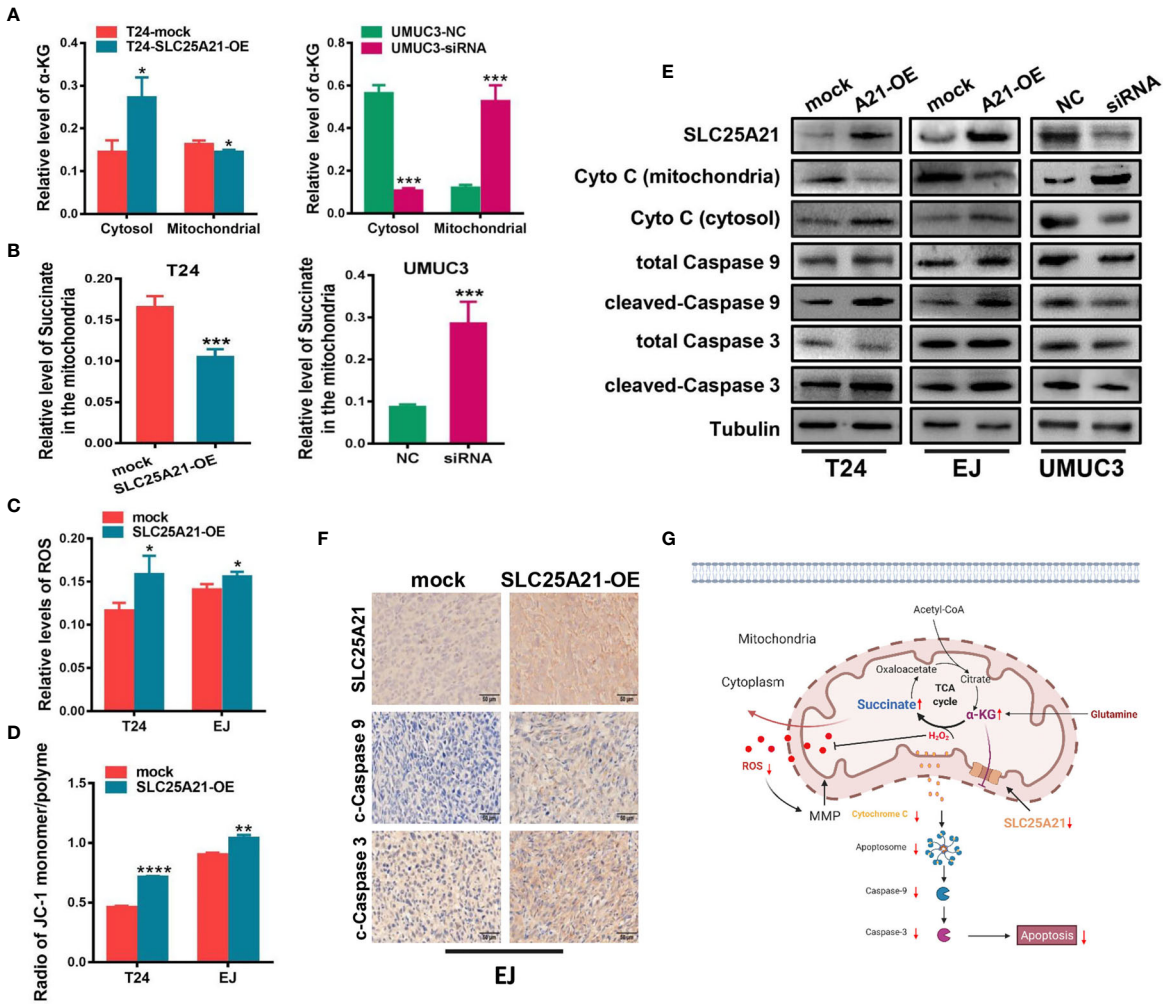

FIGURE 5 | SLC25A21 overexpression induces cell apoptosis by the α-KG-mediated ROS pathway in BCa. **(A)** SLC25A21 promoted the efflux of α-KG from the mitochondria to the cytosol. **(B)** The levels of α-KG in the mitochondria affected succinate production. **(C)** The upregulation of SLC25A21 promoted ROS accumulation in BCa cells. **(D)** The upregulation of SLC25A21 decreased Δψm in both BCa cell lines. **(E)** Western blot assays showed that SLC25A21 induced cyto C transfer from the mitochondria to the cytosol and increased the activation of caspase-9 and caspase-3 in BCa cells. **(F)** Immunohistochemistry showed that SLC25A21 increased the activation of caspase-9 and caspase-3 in BCa xenograft tissues. **(G)** Schematic diagram showing the mechanism of action of SLC25A21 on cell apoptosis in BCa. The results were reproducible in three independent experiments. $^{*}P < 0.05$, $^{**}P < 0.01$, $^{***}P < 0.001$ and $^{****}P < 0.0001$.

from the mitochondria to the cytosol, and then increasing ROS levels, thereby activating cell apoptosis (**Figure 5G**).

DISCUSSION

In the present study, we illustrated that the downregulation of SLC25A21 plays a key role in promoting human BCa development. Our data showed that SLC25A21 is strongly downregulated in BCa tissues and is especially positively correlated with an invasion and poor outcome in BCa patients. We validated SLC25A21 as an important tumor suppressor gene in BCa by gain- and loss-of-function experiments *in vitro* and *in vivo*. Interestingly, we also found that SLC25A21 promoted the efflux of α-KG from the mitochondria and increased ROS levels, resulting in the activation of the mitochondrial apoptosis pathway. Thus, our study provides strong evidence supporting the tumor suppressor roles of SLC25A21 in BCa.

SLC25 is a large family of nuclear-encoded transporters embedded in the IMM and, in a few cases, other organelle membranes. The members of this superfamily are widespread in eukaryotes and are involved in numerous metabolic pathways and cell functions (9). In recent years mutations in the SLC25 genes have been shown to be responsible for some diseases (9), highlighting the important role of SLC25 in physiological and pathological implications.

Human SLCA25A21 is ubiquitously expressed with very little variation between tissues (14). The best substrates for SLC25A21

are 2-oxoadipate and α-KG (14). The physiological role of SLC25A21 involves in 2-oxoadipate acidemia, which is accompanied by the accumulation and excretion of large amounts of 2-oxoadipate, 2-aminoadipate and 2-hydroxyadipate in urine (14). Harris and colleagues first reported that the deletion of SLC25A21 appears to be associated with lung cancer (15). However, the effects and mechanisms responsible for these diseases have not been characterized. In the present study, we revealed that the SLC25A21 expression are significantly downregulated in BCa tissues compared with normal bladder epithelial tissues, in accordance with the results from our real-time RT-PCR, IHC and TCGA and GSEA database analyses, and we determined that low expression of SCL25A21 is significantly associated with invasion and poor survival in BCa patients. These data indicate that the downregulation of SLCA25A21 expression could serve as a predictor of a higher risk of BCa progression.

To highlight the function of SLC25A21 in BCa, we further explored the critical effects of SLC25A21 on cell behaviors in BCa by gain- and loss-of-function experiments. Our results identified that SLC25A21 acts as a tumor suppressor results from the overexpression of SLC25A21 inhibits cell growth and facilitates cell apoptosis in BCa *in vitro* and *in vivo*. To the best of our knowledge, our study provides the first evidence that SLC25A21 plays a critical role in tumors, especially BCa, which suggesting SLC25A21 as a potential predictor and therapeutic target for BCa progression.

Many new functions have been ascribed to SLC25 in tumors from data generated over the last year (10, 12). For example, SLC25A22, a glutamate carrier that facilitates the transport of glutamate across the IMM into the mitochondria matrix, promotes cell proliferation and tumor progression of colorectal cancer with KRAS mutations *via* intracellular synthesis of aspartate (10). The knockdown of SLC25A10 changes the growth properties to a less malignant phenotype and causes increased glutamine dependency and sensitivity to oxidative stress in human lung adenocarcinoma cells, suggesting SLC25A10 as a novel target for anticancer strategies (13). However, the mechanisms by which SLC25A21 mediates the progression of BCa remain unknown.

The main physiological function of human SLC25A21 is probably to catalyze the uptake of 2-oxoadipate into the mitochondria and the efflux of α-KG from the mitochondria to the cytosol. α-KG is an intermediate of the tricarboxylic acid cycle (TAC) that plays important roles in cell metabolism and physiology. As a biological substance, α-KG is essential for the oxidation of fatty acids, amino acids and glucose, and serves as the carbon skeleton for the synthesis of glutamate and glutamine (25). Additionally, it has been established that α-KG can act as a true antioxidant, because it directly reacts with hydrogen peroxide (H_2O_2) to form succinate, water, and carbon dioxide (26, 27). The supplementation of α-KG can directly or indirectly stimulate endogenous antioxidant defense (28, 29). Therefore, we speculated that SLC25A21 depletion-mediated α-KG arrest in mitochondria may reduce ROS generation in BCa. Indeed, when higher levels of mitochondrial α-KG are present in SLC25A21-depleted BCa cells, ROS production is significantly decreased, accompanied by an increase in succinate in the mitochondria and *vice versa*. These results suggest that SLC25A21 can directly protect against oxidative stress by restricting the efflux of α-KG in the mitochondria.

ROS may exhibit a dual role in promoting or suppressing cancer formation. Although upregulation of ROS is known to promote tumorigenesis, growing evidence suggests that excessive accumulation of ROS leads to cell apoptosis (30, 31). Apoptosis, a type of programmed cell death, is an important pathway for regulating homeostasis and morphogenesis and is associated with various diseases, especially cancer. Apoptosis is controlled by two principal pathways, including the death receptor-mediated extrinsic pathway and the mitochondrion-dependent intrinsic pathway (30). The intrinsic pathway is much more protean but mitochondrial membrane permeabilization (MMP) is a crucial step in the signaling cascade. MMP is triggered by a variety of stimuli, such as hypoxia, oxidative stress, DNA damage, and so on. All of them can induce Δψm loss in the mitochondria. The mitochondrial apoptosis pathway starts with mitochondrial depolarization, triggering the release of cyto C into the cytosol, thereby activating caspase-9 and caspase-3, and ultimately leading to apoptosis (32). Here, we also found that SLC25A21 reduced MMP and induced the subsequent following efflux of mitochondrial cyto C to the cytosol and activation of caspase 9 and caspase 3. The elevation of intracellular ROS levels mediated SLC25A21 overexpression-induced apoptosis in BCa cell lines, which may explain why SLC25A21 overexpression decreased the cell proliferation and colony formation ability of BCa cells *in vitro* and *in vivo*. In addition, our results also revealed that SCL25A21 downregulation is significantly associated with invasion state of BCa patients and promoted tumor cell migration and invasion. Recently, Wu et al. founded that cancer-derived succinate promotes macrophage polarization and cancer metastasis in murine and human lung cancer cells (33). Moreover, previous studies have reported that the accumulation of fumarate in mouse and human cells elicits an epithelial-to-mesenchymal-transition (EMT) (34). Frezza et al. reported that the fumarate inhibits Tet-mediated demethylation of a regulatory region of the antimetastastic miRNA cluster, leading to the expression of EMT-related transcription factors and enhanced migratory properties in renal cancer (35). In TAC reaction, α-KG is oxidized and decarboxylated to succinyl CoA mediated by the α-KG dehydrogenase complex, which in turn producing succinate. Then, succinate is oxidized and hydrated to fumarate. Here, we observed that higher levels of mitochondrial α-KG promoted the accumulation of succinate in the mitochondria in SLC25A21-depleted BCa cells. Therefore, we speculated that SLC25A21 depletion-mediated α-KG arrest in mitochondria may result in an increase of succinate and fumarate, thereby promoting cell invasion, and metastasis in BCa. These data indicate that the downregulation of SLCA25A21 expression could serve as a predictor of a higher risk of BCa progeression. The mechanisms by which SLC25A21 mediates invasion inhibition present an interesting issue for further investigation.

CONCLUSIONS

Our research demonstrated that SLC25A21 is downregulated in BCa tissues and that its downregulation might play a promoting role in BCa tumorigenesis and progression through the ROS-mediated mitochondrion-dependent apoptosis pathway. These results indicate that the overexpression of SLC25A21, which specifically induces ROS-mediated apoptosis in cancer cells, could be used to develop a highly effective treatment strategy for BCa patients.

DATA AVAILABILITY STATEMENT

The original contributions presented in the study are included in the article/**Supplementary Material**. Further inquiries can be directed to the corresponding author.

ETHICS STATEMENT

The use of tissues for this study has been approved by the ethics committee of Nanfang Hospital, Southern Medical University by NFEC-2021-108. The animal study was reviewed and approved by SCXK2016-0041.7.

AUTHOR CONTRIBUTIONS

SW designed research. YW, JG, SH, WZ, and HC contributed in the experimental procedures. HY and SW analyzed data. SW and HY supervised all the work. All authors contributed to the article and approved the submitted version.

FUNDING

This work was supported by the National Natural Science Foundation of China (81972754), the Guangdong Basic and Applied Basic Research Foundation (2019A1515012226) and Guangdong Province Rural Science and Technology special commissioner project (KTP20190277).

SUPPLEMENTARY MATERIAL

The Supplementary Material for this article can be found online at: https://www.frontiersin.org/articles/10.3389/fonc.2021.682710/full#supplementary-material

REFERENCES

1. Antoni S, Ferlay J, Soerjomataram I, Znaor A, Jemal A, Bray F. Bladder Cancer Incidence and Mortality: A Global Overview and Recent Trends. *Eur Urol* (2017) 71(1):96–108. doi: 10.1016/j.eururo.2016.06.010
2. Kukreja JB, Shah JB. Advances in Surgical Management of Muscle Invasive Bladder Cancer. *Indian J Urol: IJU: J Urol Soc India* (2017) 33(2):106–10. doi: 10.4103/0970-1591.203416
3. Abufaraj M, Gust K, Moschini M, Foerster B, Soria F, Mathieu R, et al. Management of Muscle Invasive, Locally Advanced and Metastatic Urothelial Carcinoma of the Bladder: A Literature Review With Emphasis on the Role of Surgery. *Trans Androl Urol* (2016) 5(5):735–44. doi: 10.21037/tau.2016.08.23
4. Kamat AM, Hegarty PK, Gee JR, Clark PE, Svatek RS, Hegarty N, et al. ICUD-EAU International Consultation on Bladder Cancer 2012: Screening, Diagnosis, and Molecular Markers. *Eur Urol* (2013) 63(1):4–15. doi: 10.1016/j.eururo.2012.09.057
5. Berg KB, Schaeffer DF. SATB2 as an Immunohistochemical Marker for Colorectal Adenocarcinoma: A Concise Review of Benefits and Pitfalls. *Arch Pathol Lab Med* (2017) 141(10):1428–33. doi: 10.5858/arpa.2016-0243-RS
6. Pisoschi AM, Pop A. The Role of Antioxidants in the Chemistry of Oxidative Stress: A Review. *Eur J Med Chem* (2015) 97:55–74. doi: 10.1016/j.ejmech.2015.04.040
7. Yu Q, Lu Z, Tao L, Yang L, Guo Y, Yang Y, et al. ROS-Dependent Neuroprotective Effects of Nahs in Ischemia Brain Injury Involves the PARP/AIF Pathway. *Cell Physiol Biochem: Int J Exp Cell Physiol Biochem Pharmacol* (2015) 36(4):1539–51. doi: 10.1159/000430317
8. Gutierrez-Aguilar M, Baines CP. Physiological and Pathological Roles of Mitochondrial SLC25 Carriers. *Biochem J* (2013) 454(3):371–86. doi: 10.1042/BJ20121753
9. Palmieri F. The Mitochondrial Transporter Family SLC25: Identification, Properties and Physiopathology. *Mol Aspects Med* (2013) 34(2-3):465–84. doi: 10.1016/j.mam.2012.05.005
10. Wong CC, Qian Y, Li X, Xu J, Kang W, Tong JH, et al. SLC25A22 Promotes Proliferation and Survival of Colorectal Cancer Cells With KRAS Mutations and Xenograft Tumor Progression in Mice *via* Intracellular Synthesis of Aspartate. *Gastroenterology* (2016) 151(5):945–60.e6. doi: 10.1053/j.gastro.2016.07.011
11. Sun X, Liu S, Chen P, Fu D, Hou Y, Hu J, et al. Mir-449a Inhibits Colorectal Cancer Progression by Targeting SATB2. *Oncotarget* (2017) 8(60):100975–88. doi: 10.18632/oncotarget.10900
12. Vozza A, Parisi G, De Leonardis F, Lasorsa FM, Castegna A, Amorese D, et al. UCP2 Transports C4 Metabolites Out of Mitochondria, Regulating Glucose and Glutamine Oxidation. *Proc Natl Acad Sci USA* (2014) 111(3):960–5. doi: 10.1073/pnas.1317400111
13. Zhou X, Paredes JA, Krishnan S, Curbo S, Karlsson A. The Mitochondrial Carrier SLC25A10 Regulates Cancer Cell Growth. *Oncotarget* (2015) 6 (11):9271–83. doi: 10.18632/oncotarget.3375
14. Fiermonte G, Dolce V, Palmieri L, Ventura M, Runswick MJ, Palmieri F, et al. Identification of the Human Mitochondrial Oxodicarboxylate Carrier. Bacterial Expression, Reconstitution, Functional Characterization, Tissue Distribution, and Chromosomal Location. *J Biol Chem* (2001) 276 (11):8225–30. doi: 10.1074/jbc.M009607200
15. Harris T, Pan Q, Sironi J, Lutz D, Tian J, Sapkar J, et al. Both Gene Amplification and Allelic Loss Occur at 14q13.3 in Lung Cancer. *Clin Cancer Res* (2011) 17(4):690–9. doi: 10.1158/1078-0432.CCR-10-1892
16. Bubendorf L. High-Throughput Microarray Technologies: From Genomics to Clinics. *Eur Urol* (2001) 40(2):231–8. doi: 10.1159/000049777
17. Gautier L, Cope L, Bolstad BM, Irizarry RA. Affy–Analysis of Affymetrix Genechip Data at the Probe Level. *Bioinformatics* (2004) 20(3):307–15. doi: 10.1093/bioinformatics/btg405
18. Jiang H, Wang Y, Ai M, Wang H, Duan Z, Zhao L, et al. Long Noncoding RNA CRNDE Stabilized by Hnrnpul2 Accelerates Cell Proliferation and Migration in Colorectal Carcinoma *via* Activating Ras/MAPK Signaling Pathways. *Cell Death Dis* (2017) 8(6):e2862. doi: 10.1038/cddis.2017.258
19. Wang S, Zhou J, Wang XY, Hao JM, Chen JZ, Zhang XM, et al. Down-Regulated Expression of SATB2 Is Associated With Metastasis and Poor Prognosis in Colorectal Cancer. *J Pathol* (2009) 219(1):114–22. doi: 10.1002/path.2575
20. Yang MH, Zhao L, Wang L, Ou-Yang W, Hu SS, Li WL, et al. Nuclear Lncrna HOXD-AS1 Suppresses Colorectal Carcinoma Growth and Metastasis *via* Inhibiting HOXD3-Induced Integrin Beta3 Transcriptional Activating and

MAPK/AKT Signalling. *Mol Cancer* (2019) 18(1):31. doi: 10.1186/s12943-019-0955-9
21. Zhang F, Li K, Pan M, Li W, Wu J, Li M, et al. Mir-589 Promotes Gastric Cancer Aggressiveness by a LIFR-PI3K/AKT-C-Jun Regulatory Feedback Loop. *J Exp Clin Cancer Res* (2018) 37(1):152. doi: 10.1186/s13046-018-0679-5
22. Wang YQ, Jiang DM, Hu SS, Zhao L, Wang L, Yang MH, et al. SATB2-AS1 Suppresses Colorectal Carcinoma Aggressiveness by Inhibiting SATB2-Dependent Snail Transcription and Epithelial-Mesenchymal Transition. *Cancer Res* (2019) 79(14):3542–56. doi: 10.1158/0008-5472.CAN-18-2900
23. Grada A, Otero-Vinas M, Prieto-Castrillo F, Obagi Z, Falanga V. Research Techniques Made Simple: Analysis of Collective Cell Migration Using the Wound Healing Assay. *J Invest Dermatol* (2017) 137(2):e11–6. doi: 10.1016/j.jid.2016.11.020
24. Chen G, Zhang X, Zhao M, Wang Y, Cheng X, Wang D, et al. Celastrol Targets Mitochondrial Respiratory Chain Complex I to Induce Reactive Oxygen Species-Dependent Cytotoxicity in Tumor Cells. *BMC Cancer* (2011) 11:170. doi: 10.1186/1471-2407-11-170
25. Wu G, Bazer FW, Davis TA, Kim SW, Li P, Marc Rhoads J, et al. Arginine Metabolism and Nutrition in Growth, Health and Disease. *Amino Acids* (2009) 37(1):153–68. doi: 10.1007/s00726-008-0210-y
26. He L, Xu Z, Yao K, Wu G, Yin Y, Nyachoti CM, et al. The Physiological Basis and Nutritional Function of Alpha-Ketoglutarate. *Curr Protein Pept Sci* (2015) 16(7):576–81. doi: 10.2174/1389203716666150630140157
27. Long LH, Halliwell B. Artefacts in Cell Culture: Alpha-Ketoglutarate can Scavenge Hydrogen Peroxide Generated by Ascorbate and Epigallocatechin Gallate in Cell Culture Media. *Biochem Biophys Res Commun* (2011) 406 (1):20–4. doi: 10.1016/j.bbrc.2011.01.091
28. Bayliak MM, Shmihel HV, Lylyk MP, Vytvytska OM, Storey JM, Storey KB, et al. Alpha-Ketoglutarate Attenuates Toxic Effects of Sodium Nitroprusside and Hydrogen Peroxide in Drosophila Melanogaster. *Environ Toxicol Pharmacol* (2015) 40(2):650–9. doi: 10.1016/j.etap.2015.08.016
29. He L, Wu J, Tang W, Zhou X, Lin Q, Luo F, et al. Prevention of Oxidative Stress by Alpha-Ketoglutarate *via* Activation of CAR Signaling and Modulation of the Expression of Key Antioxidant-Associated Targets *In Vivo* and *In Vitro*. *J Agric Food Chem* (2018) 66(43):11273–83. doi: 10.1021/acs.jafc.8b04470
30. Cui L, Bu W, Song J, Feng L, Xu T, Liu D, et al. Apoptosis Induction by Alantolactone in Breast Cancer MDA-MB-231 Cells Through Reactive Oxygen Species-Mediated Mitochondrion-Dependent Pathway. *Arch pharmacal Res* (2018) 41(3):299–313. doi: 10.1007/s12272-017-0990-2
31. Chen X, Xu Z, Zhu Z, Chen A, Fu G, Wang Y, et al. Modulation of G6PD Affects Bladder Cancer *via* ROS Accumulation and the AKT Pathway *In Vitro*. *Int J Oncol* (2018) 53(4):1703–12. doi: 10.3892/ijo.2018.4501
32. Cory S, Adams JM. The Bcl2 Family: Regulators of the Cellular Life-or-Death Switch. *Nat Rev Cancer* (2002) 2(9):647–56. doi: 10.1038/nrc883
33. Wu JY, Huang TW, Hsieh YT, Wang YF, Yen CC, Lee GL, et al. Cancer-Derived Succinate Promotes Macrophage Polarization and Cancer Metastasis *via* Succinate Receptor. *Mol Cell* (2020) 77(2):213–27.e5. doi: 10.1016/j.molcel.2019.10.023
34. De Craene B, Berx G. Regulatory Networks Defining EMT During Cancer Initiation and Progression. *Nat Rev Cancer* (2013) 13(2):97–110. doi: 10.1038/nrc3447
35. Sciacovelli M, Goncalves E, Johnson TI, Zecchini VR, da Costa AS, Gaude E, et al. Fumarate Is an Epigenetic Modifier That Elicits Epithelial-to-Mesenchymal Transition. *Nature* (2016) 537(7621):544–7. doi: 10.1038/nature19353

Conflict of Interest: The authors declare that the research was conducted in the absence of any commercial or financial relationships that could be construed as a potential conflict of interest.

Publisher's Note: All claims expressed in this article are solely those of the authors and do not necessarily represent those of their affiliated organizations, or those of the publisher, the editors and the reviewers. Any product that may be evaluated in this article, or claim that may be made by its manufacturer, is not guaranteed or endorsed by the publisher.

frontiers in Oncology

ORIGINAL RESEARCH
published: 23 September 2021
doi: 10.3389/fonc.2021.734708

Purified Vitexin Compound 1 Serves as a Promising Antineoplastic Agent in Ovarian Cancer

Kewen Ma[1,2], *Kuansong Wang*[1,2*], *Yingjun Zhou*[3], *Nian Liu*[4,5], *Wei Guo*[1], *Jialin Qi*[2], *Zhenmin Hu*[2], *Shitong Su*[1], *Ping Tang*[2] *and Xunjian Zhou*[1]

[1] *Department of Pathology, Xiangya Hospital, Central South University, Changsha, China,* [2] *Department of Pathology, School of Basic Medical Sciences, Central South University, Changsha, China,* [3] *School of Pharmaceutical Science, Central South University, Changsha, China,* [4] *Department of Dermatology, Xiangya Hospital, Central South University, Changsha, China,* [5] *Hunan Key Laboratory of Skin Cancer and Psoriasis, Xiangya Hospital, Central South University, Changsha, China*

OPEN ACCESS

Edited by:
Yongbin Chen, Kunming Institute of Zoology (CAS), China

Reviewed by:
Xiaojing Guo, Tianjin Medical University Cancer Institute and Hospital, China
Ma Lili, Changzhi Medical College, China
Cai-Wen Duan, Shanghai Children's Medical Center, China

***Correspondence:**
Kuansong Wang
13787146109@126.com

Specialty section:
This article was submitted to Molecular and Cellular Oncology, a section of the journal Frontiers in Oncology

Received: *01 July 2021*
Accepted: *24 August 2021*
Published: *23 September 2021*

Citation:
Ma K, Wang K, Zhou Y, Liu N, Guo W, Qi J, Hu Z, Su S, Tang P and Zhou X (2021) Purified Vitexin Compound 1 Serves as a Promising Antineoplastic Agent in Ovarian Cancer. Front. Oncol. 11:734708. doi: 10.3389/fonc.2021.734708

Ovarian cancer is a common gynecologic aggressive neoplasm. The mortality of ovarian cancer is top among gynecologic malignancies due to the insidious onset, atypical early symptoms, and chemoresistance. Therefore, it is urgent to seek another promising treatment for ovarian cancer. Purified vitexin compound 1 (VB1) is a kind of neolignan from the seed of traditional Chinese herb vitex negundo that possessed diverse pharmacological effects. VB1 can exhibit anti-neoplastic activities against various cancers. However, the role of VB1 in ovarian cancer treatment has not been elaborated, and the mechanism is unknown. The aim of this study was to investigate the therapeutic effects of VB1 in ovarian cancer cells both *in vitro* and *in vivo*, along with the molecular mechanism of action. *In vitro*, VB-1 can effectively suppress the proliferation, induce apoptosis, and block cell cycle at G2/M phase with a concentration dependent manner in ovarian cancer cells. Western blot assay showed that VB1 induce apoptosis *via* upregulating expression of cleaved-caspase3 and block cell cycle at G2/M phase through upregulating expression of P21. Meanwhile, VB1 can effectively inhibit tumor growth in xenograft mouse model. Our research indicated that VB1 can significantly exert its anti-neoplastic effects and may represent a new class of agents in ovarian cancer therapy.

Keywords: vitexin compound 1, ovarian cancer, antineoplastic agent, therapy, apoptosis and cell cycle

INTRODUCTION

Ovarian cancer (OC) is a kind of highly heterogeneous disease that affects women globally, known as "silent killer", and the overall mortality generally is higher than other gynecologic malignancies. It is estimated that 22,240 new cases will be diagnosed and 14,070 women will die of ovarian cancer in the United States in 2018 (1, 2). Most patients are being diagnosed in an advanced stage because ovarian cancer is often silent in its early stages (3). Ovarian cancer usually leads to peritoneal carcinoma (PC), which is another reason why the mortality of ovarian cancer is extremely high (4). Currently, cytoreductive surgery, chemotherapy, and targeted therapy have been applied to treat ovarian cancer and improve prognosis of patients with ovarian cancer to some extent (5, 6).

Nevertheless, approximately 65% of patients with advanced-stage ovarian cancer relapse within 2 years after initial therapy (7). Ovarian cancer patients (15–25%) develop primary treatment resistance, and most of the remaining patients occur to chemotherapy resistance (8). Therefore, the development of more effective cancer therapy remains an ongoing challenge in ovarian cancer.

In China, traditional Chinese medicine is widely being used in the majority of hospitals and plays an active role in multiple diseases including cancers (9). Vitex negundo L is a powerful tonic traditional Chinese herb, possessing a wide range of biological activity against bacteria, tumor, rheumatism, etc. (10, 11). Vitexin compound 1 (VB1) is the most abundant Vitexin compound in EVn-50 which is derived from Vitex negundo L. It showed strong anti-neoplastic potential in cancers including colorectal cancer, hepatocellular carcinoma, and choriocarcinoma (12–16). Studies have shown that VB1 can suppress the tumor growth and angiogenesis by inactivating Akt signaling in hepatocellular carcinoma (17). VB1 can inhibit melanoma cell growth through DNA damage *via* increasing ROS levels (18).

Yet, for now, the effects and underlying mechanisms of VB1 on human ovarian cancers are largely unknown. The purpose of our study was to evaluate VB1 as anti-gynecological cancer herbs and to explore the molecular mechanism of anticancer activity. The result gained by our research may significantly contribute to the development of new and effective therapy for ovarian cancer.

MATERIALS AND METHODS

Chemical

VB1 termed 6-hydroxy-4-(4-hydroxy-3-methoxypheny1)-3-hydroxymethy1-7-methoxy-3,4-dihydro-2-naphthaldehyde, a purified compound, was extracted from the seed of the Chinese herb Vitex negundo and was supplied by the College of Pharmacy of Central South University (Changsha, China) (**Figure 1A**). VB1 was dissolved in dimethylsulfoxide (DMSO, Sigma) and diluted with pure water to a concentration of 10 mmol/L, which was packed and stored at 4°C. DMSO's final concentration in each sample was less than 0.1% (vol/vol).

Cell Lines and Culture Conditions

Human ovarian cancer cell lines HO8910 and SKOV3 were derived from American Type Culture Collection (ATCC). H08910 cell line was maintained in RPMI1640 medium (BI, Israel) supplemented with 10% fetal bovine serum (BI, Israel) at 37°C in a 5% carbon dioxide atmosphere. SKOV3 cell line was grown in McCoy's5a medium (Gibco, USA) containing 10% fetal bovine serum (BI, Israel) at 37°C and 5% CO_2.

Cell Viability Assay

Cells were seeded into 96-well plates (5×10^3 cells per well) and cultured at 37°C in media containing 10% FBS for 24 h. Cells were exposed to VB1 (0 μM), 0.1% DMSO, or various concentrations of VB1 (2.5, 5, 10, and 20 μM) for 24, 48, and 72 h, respectively. The cell viability (%) was determined by CCK-8 assay (7 sea biotech, China) with the manufacturer's instructions. In detail, the reagent (10 μl) was added into each well of the 96-well assay plate containing the samples in 100 ml of culture medium and incubated for another 4 hours, after 24, 48, and 72 h individually. The absorbance at a wavelength of 450 nm was measured using a microplate absorbance reader (Eppendorf, GER). The half-maximal inhibitory concentration (IC50) values were generated using the SPSS software.

Morphological Observation

Cells were seeded into six-well plates (3×10^5 cells per well) and cultured at 37°C in media containing 10% FBS and 5% CO_2 for 24 h. Subsequently, cells were subjected to VB1 (0 μM), 0.1% DMSO, or different concentrations of VB1 (2.5, 5, 10, and 20 μM) for 24 h. Cell morphological changes after treatment with VB1 were observed, and exact images were acquired using a microscope (Olympus, Japan).

Hoechst 33258 Staining Assay

Cells were seeded into six-well plates (3×10^5 cells per well) and cultured at 37°C in media containing 10% FBS for 24 h. Separately, cells were exposed to VB1 (0 μM), 0.1% DMSO, or various concentrations of VB1 (2.5, 5, 10, and 20 μM) for 24 h. After processing, cells were washed with PBS and fixed with 4% formaldehyde for 20 min. The fixed cells were stained with Hoechst 33258 for 10 min and washed with PBS. Finally, the apoptotic cells were observed and fluorescent micrographs were obtained using a fluorescent microscope (Olympus, Japan).

Detection of Apoptotic Cells by Flow Cytometry

Cells were seeded into six-well plates (3×10^5 cells per well) and incubated overnight at 37°C in media containing 10% FBS. Then, they were treated with VB1 (0 μM), 0.1% DMSO, or VB1 (2.5, 5, 10, and 20 μM) with the different concentrations for 24 h. The cells were harvested by trypsinization without EDTA after 24 h. The collected cells were suspended and washed with cold PBS, centrifuged, and stained with 5 μl AnnexinV and 5 μl propidium iodide for 15 min at room temperature in dark place according to Annexin V-FITC/PI Apoptosis Detection Kit (Becton, Dickinson and Company, USA) with the manufacturer's instructions. The number of apoptotic cells was detected by flow cytometry and analyzed using the Flowjo software.

Cell Cycle Assay

Cells were seeded into six-well plates (3×10^5 cells per well) and incubated overnight at 37°C in media containing 10% FBS. Then, they were treated with VB1 (0 μM), 0.1% DMSO, or various of concentrations of VB1 (2.5, 5, 10, and 20 μM). The cells were harvested by trypsinization after 24 h. The collect cells were suspended and washed with cold PBS, centrifuged, and fixed in 70% ethanol at 4°C overnight. The next day, the fixed cells were suspended and centrifuged again; cells were incubated with 500 μl

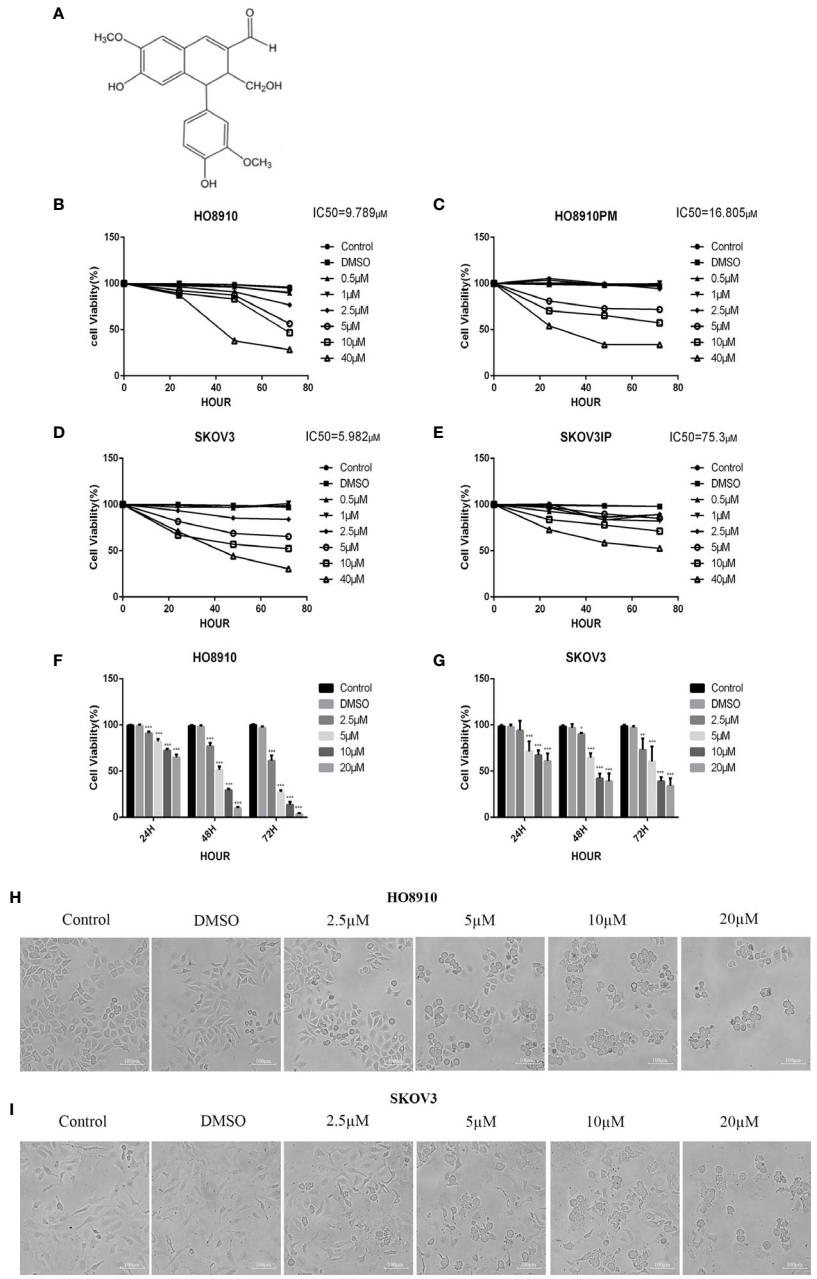

FIGURE 1 | VB1 suppressed the viability of human ovarian cancer cells. **(A)** Chemical structure of VB1. **(B–E)** The four cell lines were treated with VB1 for various times and dosages, respectively, and the cell viability was tested by CCK-8. **(F)** HO8910 cells were treated with VB1 (0 μM) (control), 0.1% DMSO, and VB1 (2.5–20 μM) for 24, 48, and 72 h, and the cell viability was measured using CCK-8 assay. **(G)** SKOV3 cells were treated with VB1 (0 μM), 0.1% DMSO, and VB1 (2.5–20 μM) for 24, 48, and 72 h; the cell viability was measured using CCK-8 assay. **(H)** The cell morphologic changes of HO8910 cells after treatment with VB1 (0 μM), 0.1% DMSO, and VB1 (2.5–20 μM) for 24 h (magnification ×100). **(I)** The cell morphological changes after treatment with VB1 (0 μM), 0.1% DMSO, and VB1 (2.5–20 μM) for 24 h in SKOV3 cells (magnification ×100). The data represent the mean ± SD of three independent experiments, *P < 0.05, ***P < 0.001 compared with control.

propidium iodide (PI) for 15 min at room temperature and protected from light according to the manufacturer's instructions (Becton, Dickinson and Company, USA). The cell cycle was measured by flow cytometry and analyzed using ModFit software.

Immunoblotting

SKOV3 cells were lysed in RIPA buffer (CWBIO, China) containing protease inhibitor cocktail (CWBIO, China) and phosphatase inhibitor cocktail (CWBIO, China) and incubated on ice for 20 min. Protein concentrations were determined using

a BCA protein assay kit (DingGuo, China). Total protein extracted from SKOV3 cells were separated by 8–12% SDS-polyacrylamide gel electrophoresis (SDS-PAGE) and transferred to polyvinylidene fluoride membranes (Millipore, USA). After blocking in 5% non-fat dry milk in TBS at room temperature for 1 h, the membranes were incubated with primary antibodies including cleaved caspase3, caspase3, and P21 (Cell Signaling, Denver, MA) and β-actin (Proteintech, USA) overnight at 4°C. Subsequently, the membranes were washed with TBST and incubated with HRP-conjugated secondary antibody (Proteintech, USA) for 1 h at room temperature. Finally, the protein expression was imaged using a gel image analysis system (Bio-Rad, USA).

Xenograft Tumor Model

The animal experiments were approved by the Animal Research Ethics Committee of Central South University. Twelve female BALB/c pathogen-free athymic nude mice at the age of 5 to 6 weeks were injected with a total of 5×10^6 HO8910 cells subcutaneously into the right flank to establish a xenograft tumor model. When the tumors reached 5 mm^3 or larger, the tumor-bearing mice were randomly divided into two groups and received vehicle or 80 mg/kg of VB1 by intraperitoneal injection twice a day for a month, with six mice in each group. Sizes of tumor were measured using a caliper every 3 days, and the tumor volume was calculated with the formula V = 1/2 (length × $width^2$). Then the mice were sacrificed, and tumors were dissected and stored in liquid nitrogen or fixed in formalin for further histological analysis. All experiments were performed according to Guidelines for the Care and Use of Laboratory Animals prepared by the Institutional Animal Care and Use Committee of Central South University, Chang Sha, China. All Animal experimental protocols were approved by the Institutional Animal Care and Use Committee of Central South University (approval no. 2018sydw0225).

Statistical Analysis

The data were expressed as the mean ± SD of three independent experiments. Statistical differences in the data were evaluated using a Student's t-tests and ANOVA tests. $P < 0.05$ was considered as statistically significant.

RESULTS

VB1 Suppressed the Viability of Human Ovarian Cancer Cells

In order to evaluate effect of VB1 on viability in ovarian cancer cell lines, we executed CCK-8 assay to measure cell viability after exposing them to 0.1% DMSO or increasing concentrations of VB1 for 24–72 h. HO8910 and SKOV3 have the most significant inhibitory effect, and their IC50 values of VB1 were 9.789 and 5.982 μM, respectively (**Figures 1B–E**). So we used HO8910 and SKOV3 as the test subjects. Results showed that VB1 possessed ability to suppress viability in ovarian cancer cell lines with a dose-dependent and time-dependent manner (**Figures 1F, G**). Compared with the VB1 (0 μM) group (Control) and 0.1% DMSO group, the cell viability of the VB1 group was significantly decreased. HO8910 cells were cultured with various concentrations of VB1 (2.5, 5, 10, and 20 μM) for 72 h, and the cell viability was 61.5%, 27.3%, 13.7%, and 3.5%, separately. In response to 20 μM of VB1 for 24, 48, and 72 h, the 20 μM VB1-treated H08910 cell viability was 64.8%, 9.9%, and 3.5%. SKOV3 cells were treated with VB1 (2.5–20 μM) for 72 h, and the cell survival rates were 73.1%, 60.5%, 39.1%, and 34.1%. SKOV3 cells in response to VB1 (20 μM) for 24, 48, and 72 h, the cell viability was 61.0%, 39.0%, and 34.1%. Meanwhile, VB1 treatment led to morphological changes in H08910 and SKOV3 cells (**Figures 1H, I**). Compared with the VB1 (0 μM) and 0.1% DMSO group, H08910 and SKOV3 cells were incubated with increasing concentrations of VB1 for 24 h, and the cell density decreased gradually. Adhered cells became small and round, and part of them were lysed after VB1 treatment. From the above data, we concluded that VB1 effectively suppressed the viability of human ovarian cancer cells, and VB1 may act as a promising anti-neoplastic agent in ovarian cancer.

VB1 Provoked Apoptosis in Human Ovarian Cancer Cells With a Caspase Signaling Pathway

Our preliminary data showed that VB1 could effectively suppress the viability of human ovarian cancer cells in a concentration way, so we speculate that whether VB1 inhibit the viability by provoking apoptosis? Firstly, we observed the apoptotic morphological changes of HO8910 and SKOV3 cells that were exposed to VB1 (0 μM), 0.1% DMSO, and VB1 (2.5–20 μM) for 24 h using a microscope. Typical apoptotic features were observed by us, such as nuclear debris, aberrant nuclear shape, and nuclear division. Apoptotic cells show strong blue staining, and exact images were observed in **Figures 2A, B**. Subsequently, after treatment with VB1 (0 μM), 0.1% DMSO, or VB1 (2.5–20 μM) for 24 h in both HO8910 and SKOV3 cells, apoptosis was detected by the flow cytometry. Compared with the group of VB1 (0 μM) (control) and 0.1% DMSO, the number of apoptotic cells significantly increased in a dose-dependent manner (**Figures 2C–F**). After processing with VB1 (2.5–20 μM) for 24 h, the apoptosis rate of HO8910 cells was 4.91%, 5.28%, 15.87%, and 31.46%, respectively. The percentage of apoptotic cells in SKOV3 cells were 5%, 9%, 19.85%, and 30.6%, separately. Furthermore, in order to determine the molecular mechanisms of VB1-induced apoptosis in HO8910 cells and SKOV3 cells, we explored the expression of apoptosis-related proteins including caspase-3 and cleaved caspase-3 by Western blotting. After treatment with VB1 (0–20 μM) for 24 h, groups of various concentrations of VB1 showed caspase-3 decreased and cleaved

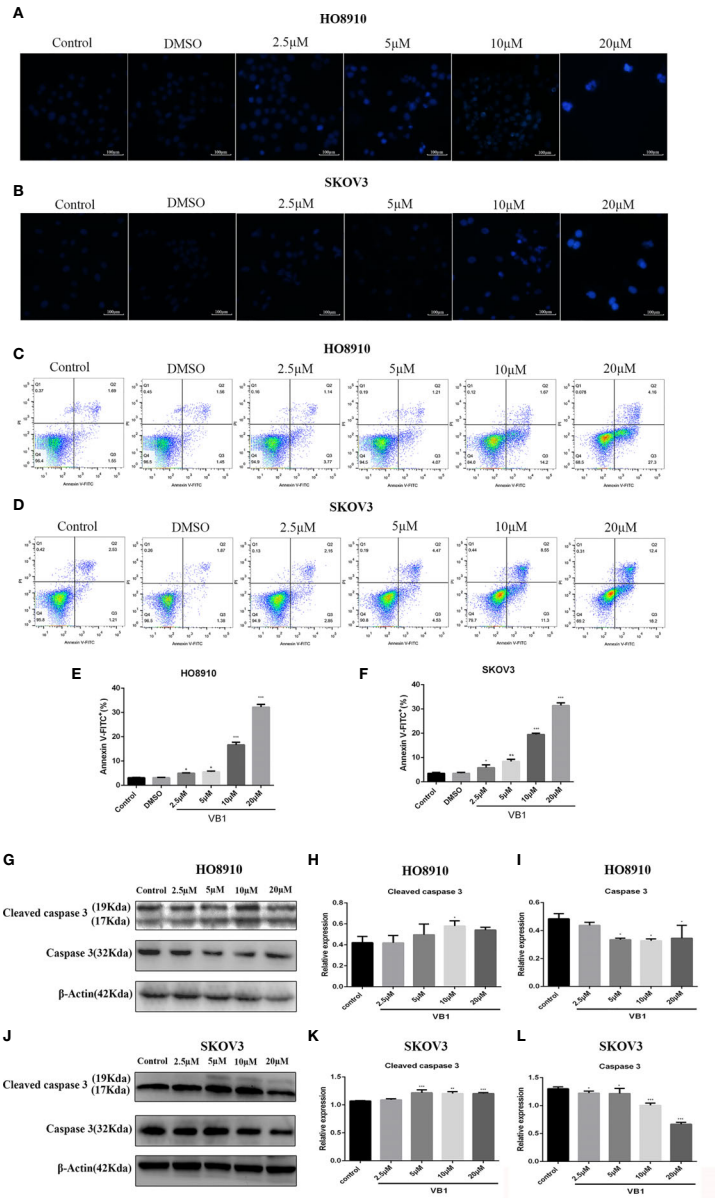

FIGURE 2 | VB1 provoked apoptosis in human ovarian cancer cells with a caspase signaling pathway. **(A, B)** HO8910 cells and SKOV3 cells were exposed to VB1 (0 μM), 0.1% DMSO, or VB1 (2.5–20 μM) for 24 h; after 24 h, the treated cells were subjected to Hoechst 33258 staining and apoptotic morphological changes were observed using a microscope (magnification ×100). **(C–F)** HO8910 cells and SKOV3 cells were handled with VB1 (0 μM), 0.1% DMSO, and VB1 (2.5–20 μM) for 24 h; the flow cytometry with Annexin V-FITC/PI staining was performed to detect apoptosis. **(G–I)** HO8910 cells were exposed to VB1 (0-20 μM) for 24 h; the expression of apoptotic protein was determined by Western blotting. **(J–L)** SKOV3 cells were exposed to VB1 (0–20 μM) for 24 h, and the expression of apoptotic protein was determined by Western blotting. Data represent the mean ± SD of three independent experiments. *P < 0.05, **P < 0.01, ***P < 0.001 compared with the control group.

caspase-3 increased in HO8910 cells (**Figures 2G–I**). Similarly, VB1 (0–20 μM) treatment for 24 h decreased caspase-3 and increased cleaved caspase-3 in SKOV3 cells with a concentration-dependent manner, compared with the VB1 (0 μM) group (**Figures 2J–L**). In conclusion, our findings were enough to prove VB1 exactly induced apoptosis with a caspase signaling pathway.

VB1 Induces G2/M Arrest in Human Ovarian Cancer Cells

To delineate the effects of VB1 on cell cycle in HO8910 and SKOV3 cells, cell cycle assay was conducted by the flow cytometry. Compared with the group of VB1 (0 μM) and 0.1% DMSO, we found that VB1 could dramatically induce G2/M arrest in a concentration-dependent way (**Figures 3A–D**).

HO8910 cells were treated with VB1 (2.5–20 μM) for 24 h, and the percentage of cells arrested in G2/M phase were 14.21%, 41.14%, 60.94%, and 96.38%, respectively. Parallelly, the arrest rant of SKOV3 cells was 17.19%, 32.75%, 44.99%, and 68.17%, individually. Our data suggested that VB1 markedly blocked cell cycle at G2/M phase by decreasing the distribution of G0/G1 phase. To the best of our knowledge, cyclin B and CDK1 play a significant role in regulation of progression of G2/M phase. P21, a downstream molecule of P53, could inhibit activity of cyclin-dependent kinases and arrest cell cycle at G2/M phase by connecting with cyclinB-CDK1 complex. Therefore, we next examined the expression of P21 by Western blotting. The results showed that the expression of P21 was elevated after treatment with the increasing concentrations of VB1 for 24 h in SKOV3 and HO8910 cells (**Figures 3E–H**). These data indicated that VB1 induces G2/M arrest *via* upregulation of the expression of p21.

VB1 Can Inhibit Tumor Growth in a Xenograft Tumor Model

Our data showed that VB-1 could effectively suppress the proliferation of HO8910 and SKOV3 cells, as well as induce apoptosis and block cell cycle at G2/M phase *in vitro*. Hence, we guessed that VB1 whether could inhibit tumor growth *in vivo*? We assessed VB1's antitumor effects *in vivo* by an animal model study. Similarly, VB1 could also significantly inhibit tumor growth, compared with the vehicle-treated group (**Figures 4A, B**). The tumor size of vehicle-treated group increased gradually during treatment, and the average tumor size was 118.7mm^3 after treatment. Tumor size of 80 mg/kg doses of VB1-treated group has no significant change, and the average tumor size was 19.0mm^3 which was smaller than the vehicle-treated group (**Figure 4C**). Meanwhile, we found a tumor of tumor-bearing mice disappeared in VB1-treated group. Consistent with the results *in vitro*, the data from experiment *in vivo* indicated the inhibitory effect of VB1 on tumor growth.

DISCUSSION

In our study, we found that VB1 extracted from traditional Chinese herb vitex negundo possesses powerful anti-neoplastic effects on human ovarian cancer. Cell viability assay showed that VB1 could effectively suppress the proliferation of ovarian cancer cell lines in a time-dependent and dose-dependent manner. Flow cytometry analysis indicated that VB1 suppress the proliferation of human ovarian cancer cells by provoking apoptosis and blocking cell cycle at G2/M phase. Hoechst 33258 staining assay suggested that typical apoptotic features emerged after VB1 treatment in HO8910 and SKOV3 cells. Furthermore, Western blot analysis revealed underlying molecular mechanisms of anti-tumor effects of VB1 on HO8910 and SKOV3 cells. VB-1 exerted its anti-neoplastic effects through upregulating the expression of cleaved-caspase3 and p21. Not only could VB1 possess inhibitory activities *in vitro*, but also inhibit tumor growth in a ovarian cancer subcutaneous xenograft tumor model of nude mice.

Apoptosis, the process of programmed cell death, is usually characterized by specific morphological and distinct biochemical and genetic pathways (19). Apoptosis play a vital role in healthy balance between cell survival and cell death (20, 21). The classic channels of provoking apoptosis by caspase cascade include endogenous mitochondrial signaling pathway and exogenous death receptor signaling pathway. Once activation of cellular stress signals in mitochondrial signaling pathway, outer mitochondrial membrane integrity will be destroyed, and cytochrome c will be released from mitochondria to cytoplasm. Then, oligomerized adaptor protein Apaf-1 recruits initial caspase (caspase 9) to active downstream executioner caspases (caspase 3) and triggers apoptosis by cleaving poly ADP-ribose polymerase (22, 23).

The exogenous pathway, a receptor-mediated pathway, and these related death receptors are members of the tumor necrosis factor (TNF) receptor gene superfamily (24). The death-inducing signaling complex (DISC) is composed of receptor, corresponding ligand, adapter protein, and procaspase-8. When exogenous pathway was activated by death signal, the receptors will bind to homologous ligand, and the connection ligand and receptor results in recruitment of adapter protein, adapter protein further connecting procaspase-8. Subsequently, the DISC activated executioner caspases by cleaved target proteins and further led to the cell death (25). In our study, Western blot analysis showed that VB1 induced the elevated expression of cleaved caspase 3 in SKOV3 cell line and HO8910 cell line after VB1 treatment, which suggested that VB1 induce apoptosis of ovarian cancer with a caspase signaling pathway by participating endogenous mitochondrial and exogenous death receptor signaling pathway.

As we have seen, cell cycle is modulated by various cyclin/cyclin-dependent kinases complexes in eukaryotes, and each cyclin/cdk complex exerts specific effects on individual cell cycle phase. Cyclin B and CDK1 play a crucial role in regulating G2/M phase process. CyclinB–CDK1 complex was recognized as a M phase-promoting factor (MPF); it is capable of starting the G2/M phase transition and promotion of mitotic entry (26, 27). P53, a tumor suppressor and transcription factor, is involved in progresses and developments of malignancy cells. In p21Waf1/Cip1, a downstream molecule of P53, the connection between p21Waf1/Cip1 and cyclinB–CDK1 complex inhibits cyclin-dependent kinases and arrests cell cycle at G2/M phase (28). Western blot analysis showed that VB1 markedly increased the level of P21 with a dose-dependent manner, which implied that P53 may participate in the process of cell cycle after VB1 treatment in ovarian cancer.

Our study proved that VB1 could effectively suppress activities of ovarian cancer *in vitro* and *in vivo*; however, cellular toxicity of VB1 in human ovarian epithelial cells is unclear. If VB1 show little influence on normal ovarian epithelial cells, intolerable toxicity or side effects of VB1 are slighter than chemotherapeutic drugs.

In summary, our present study demonstrated that VB1 exerted anti-neoplastic activities *in vitro* by inhibiting proliferation,

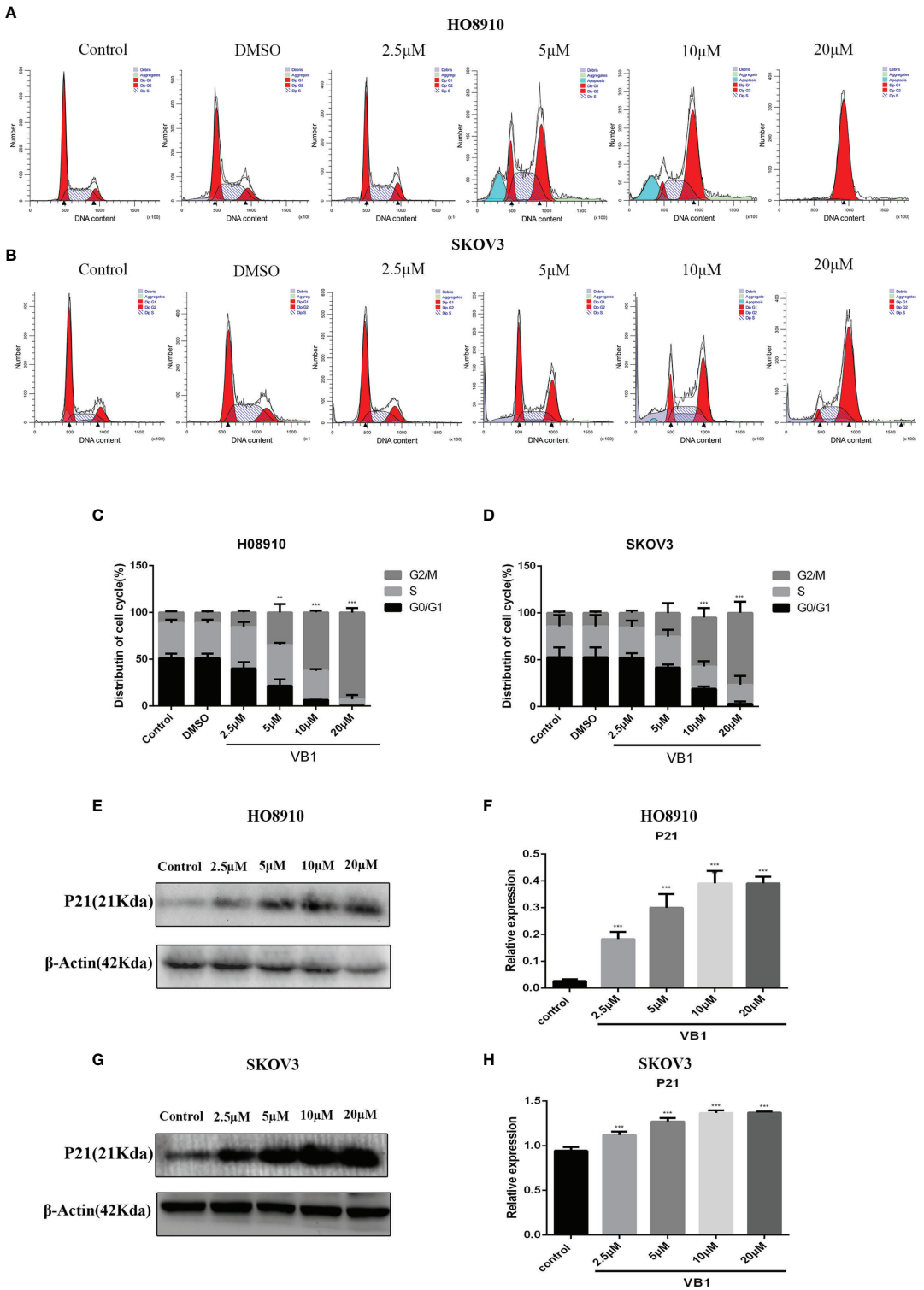

FIGURE 3 | VB1 induces G2/M arrest in human ovarian cancer cells. **(A–D)** H08910 and SKOV3 cells were exposed to VB1 (0 μM), 0.1% DMSO, and VB1 (2.5–20 μM) for 24 h; the flow cytometry was performed to detected distribution of cell cycle. **(E, F)** The expression of P21 in HO8910 cells which were treated with VB1 (0–20 μM) for 24 h. Western blotting was performed by p21 antibody. **(G, H)** The expression of P21 in SKOV3 cells which were treated with VB1 (0–20 μM) for 24 h, Western blotting was performed by p21 antibody. The results represent the mean ± SD of three independent experiments. **P < 0.01, ***P < 0.001 compared with the control group.

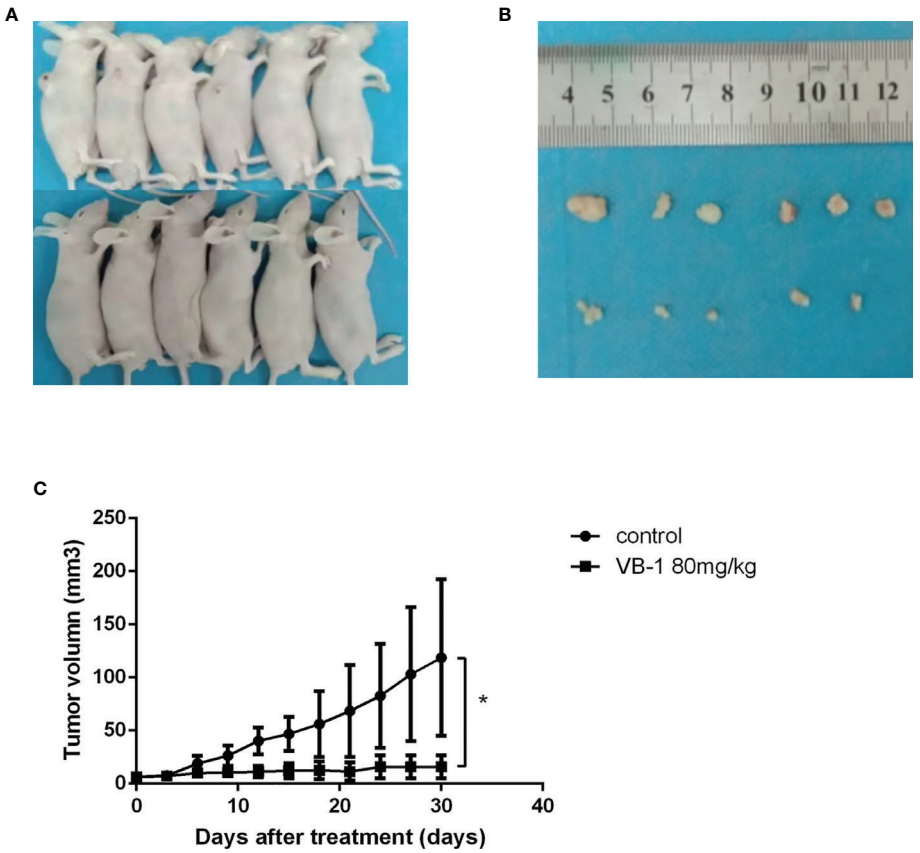

FIGURE 4 | VB1 can inhibit tumor growth in a xenograft tumor model. **(A)** Tumor-bearing nude mouse model after treatment. **(B)** VB1-treated mice demonstrated a dramatically reduced tumor volume as compared with vehicle-treated mice. **(C)** Tumor growth curves indicate a poor tumor growth in VB1-treated mice compared with vehicle-treated mice. The results represent the mean ± SD per group. *P < 0.05 compared with the control group.

inducing apoptosis, and arresting cell cycle at G2/M phase. Meanwhile, VB1 suppressed tumor growth in a subcutaneous xenograft tumor model of nude mice. Further investigation showed that VB-1 may be *via* upregulating expression of cleaved-caspase3 and P21 to induce apoptosis and block cell cycle at G2/M phase. The data from our experiments suggested that VB1 was qualified to be a promising candidate for the therapy of human ovarian cancer in the future.

DATA AVAILABILITY STATEMENT

The original contributions presented in the study are included in the article/supplementary material. Further inquiries can be directed to the corresponding author.

ETHICS STATEMENT

The animal study was reviewed and approved by Animal Care and Use committee of Central South University.

AUTHOR CONTRIBUTIONS

KM and NL were responsible for the design of the study, KM, JQ, and ZH performed the experiments. KW contributed to the review and revision of the manuscript. YZ extracted and purified drugs. KM, JQ, and PT wrote the first draft of the manuscript. WG, SS, and XZ analyzed the data. All authors discussed the results and commented on the manuscript. All authors contributed to the article and approved the submitted version.

FUNDING

This work was supported by the Natural Science Foundation of China (Grant No. 81972490).

ACKNOWLEDGMENTS

We thank the College of Pharmacy of Central South University for providing the VB1.

REFERENCES

1. Torre LA, Trabert B, DeSantis CE, Miller KD, Samimi G, Runowicz CD, et al. Ovarian Cancer Statistics, 2018. *CA Cancer J Clin* (2018) 68(4):284–96. doi: 10.3322/caac.21456
2. Kossaï M, Leary A, Scoazec J, Genestie C. Ovarian Cancer: A Heterogeneous Disease. *Pathobiology* (2018) 85(1-2):41–9. doi: 10.1159/000479006
3. Chobanian N, Dietrich CS. Ovarian Cancer. *Surg Clin N Am* (2008) 88 (2):285–99. doi: 10.1016/j.suc.2007.12.002
4. Al-Shammaa HA, Li Y, Yonemura Y. Current Status and Future Strategies of Cytoreductive Surgery Plus Intraperitoneal Hyperthermic Chemotherapy for Peritoneal Carcinomatosis. *World J Gastroenterol* (2008) 14(8):1159–66. doi: 10.3748/wjg.14.1159
5. Polom K, Roviello G, Generali D, Marano L, Petrioli R, Marsili S, et al. Cytoreductive Surgery and Hyperthermic Intraperitoneal Chemotherapy for Treatment of Recurrent Ovarian Cancer. *Int J Hyperthermia* (2016) 32 (3):298–310. doi: 10.3109/02656736.2016.1149233
6. Liu J, Matulonis UA. New Strategies in Ovarian Cancer: Translating the Molecular Complexity of Ovarian Cancer Into Treatment Advances. *Clin Cancer Res* (2014) 20(20):5150–6. doi: 10.1158/1078-0432.CCR-14-1312
7. Delqado G, Oram DH, Petrilli ES. Stage III Epithelial Ovarian Cancer the Role of Maximal Surgical Reduction. *Gynecol Oncol* (1984) 18(3):293–8. doi: 10.1016/0090-8258(84)90040-4
8. Christie EL, Bowtell DDL. Acquired Chemotherapy Resistance in Ovarian Cancer. *Ann Oncol* (2017) 28(suppl_8):viii13–5. doi: 10.1093/annonc/mdx446
9. Li X, Yang G, Li X. Traditional Chinese Medicine in Cancer Care: A Review of Controlled Clinical Studies Published in Chinese. *PloS One* (2013) 8(4): e60338. doi: 10.1177/15347354211031650
10. Zheng CJ, Tang WZ, Huang BK, Han T, Zhang QY, Zhang H, et al. Bioactivity-Guided Fractionation for Analgesic Properties and Constituents of Vitex Negundo L. Seeds. *Phytomedicine* (2009) 16(6-7):560–7. doi: 10.1016/j.phymed.2008.12.001
11. Zheng C, Li H, Ren S, Xu C, Rahman K, Qin L, et al. Phytochemical and Pharmacological Profile Ofvitex Negundo. *Phytother Res* (2015) 29(5):633–47. doi: 10.1002/ptr.5303
12. Xin H, Kong Y, Wang Y, Zhou Y, Zhu Y, Li D, et al. Lignans Extracted From Vitex Negundo Possess Cytotoxic Activity by G2/M Phase Cell Cycle Arrest and Apoptosis Induction. *Phytomedicine* (2013) 20(7):640–7. doi: 10.1016/j.phymed.2013.02.002
13. Zhou Y, Liu YE, Cao J, Zeng G, Shen C, Li Y, et al. Vitexins, Nature-Derived Lignan Compounds, Induce Apoptosis and Suppress Tumor Growth. *Clin Cancer Res* (2009) 15(16):5161–9. doi: 10.1158/1078-0432.CCR-09-0661
14. Chen J, Zhong J, Liu Y, Huang Y, Luo F, Zhou Y, et al. Purified Vitexin Compound 1, a New Neolignan Isolated Compound, Promotes PUMA-Dependent Apoptosis in Colorectal Cancer. *Cancer Med* (2018) 7(12):6158–69. doi: 10.1002/cam4.1769
15. Wang J, Zheng X, Zeng G, Zhou Y, Yuan H. Purified Vitexin Compound 1 Induces Apoptosis Through Activation of FOXO3a in Hepatocellular Carcinoma. *Oncol Rep* (2014) 31(1):488–96. doi: 10.3892/or.2013.2855
16. Tan Z, Zhang Y, Deng J, Zeng G, Zhang Y. Purified Vitexin Compound 1 Suppresses Tumor Growth and Induces Cell Apoptosis in a Mouse Model of Human Choriocarcinoma. *Int J Gynecol Cancer* (2012) 22(3):360–6. doi: 10.1097/IGC.0b013e31823de844
17. Wang J, Zheng X, Zeng G, Zhou Y, Yuan H. Purified Vitexin Compound 1 Inhibits Growth and Angiogenesis Through Activation of FOXO3a by Inactivation of Akt in Hepatocellular Carcinoma. *Int J Mol Med* (2014) 33 (2):441–8. doi: 10.3892/ijmm.2013.1587
18. Liu N, Wang KS, Qi M, Zhou YJ, Zeng GY, Tao J, et al. Vitexin Compound 1, a Novel Extraction From a Chinese Herb, Suppresses Melanoma Cell Growth Through DNA Damage by Increasing ROS Levels. *J Exp Clin Canc Res* (2018) 37(1):269. doi: 10.1186/s13046-018-0897-x
19. Elmore S. Apoptosis: A Review of Programmed Cell Death. *Toxicol Pathol* (2016) 35(4):495–516. doi: 10.1080/01926230701320337
20. Cotter TG. Apoptosis and Cancer: The Genesis of a Research Field. *Nat Rev Cancer* (2009) 9(7):501–7. doi: 10.1038/nrc2663
21. Kerr JF, Wyllie AH, Currie AR. Apoptosis: A Basic Biological Phenomenon With Wide-Ranging Implications in Tissue Kinetics. *Brit J Cancer* (1972) 26 (4):239–57. doi: 10.1038/bjc.1972.33
22. Acehan D, Jiang X, Morgan DG, Heuser JE, Wang X, Akey CW. Three-Dimensional Structure of the Apoptosome: Implications for Assembly, Procaspase-9 Binding, and Activation. *Mol Cell* (2002) 9(2):423–32. doi: 10.1016/S1097-2765(02)00442-2
23. Baliga B, Kumar S. Apaf-1/Cytochrome C Apoptosome: An Essential Initiator of Caspase Activation or Just a Sideshow? *Cell Death Differ* (2003) 10(1):16–8. doi: 10.1038/sj.cdd.4401166
24. Locksley RM, Killeen N, Lenardo MJ. The TNF and TNF Receptor Superfamilies: Integrating Mammalian Biology. *Cell* (2001) 104(4):487–501. doi: 10.1016/S0092-8674(01)00237-9
25. Kischkel FC, Hellbardt S, Behrmann I, Germer M, Pawlita M, Krammer PH, et al. Cytotoxicity-Dependent APO-1(Fas/CD95)-Associated Proteins From a Death-Inducing Signaling Complex (DISC) With the Receptor. *EMBO J* (1995) 14: (22):5579–88. doi: 10.1002/j.1460-2075.1995.tb00245.x
26. Smits VAJ, Medema RH. Checking Out the G2/M Transition. *Biochim Biophys Acta* (2011) 1519(1-2):1–12. doi: 10.1016/s0167-4781(01)00204-4
27. Cho HJ, Oh YJ, Han SH, Chung HJ, Kim CH, Lee NS, et al. Cdk1 Protein-Mediated Phosphorylation of Receptor-Associated Protein 80 (RAP80) Serine 677 Modulates DNA Damage-Induced G2/M Checkpoint and Cell Survival. *J Biol Chem* (2013) 288(6):3768–76. doi: 10.1074/jbc.M112.401299
28. Sancar A, Lindsey-Boltz LA, Unsal-Kacmaz K, Linn S. Molecular Mechanisms of Mammalian DNA Repair and the DNA Damage Check- Points. *Annu Rev Biochem* (2004) 73:39–85. doi: 10.1146/annurev.biochem.73.011303.073723

Conflict of Interest: The authors declare that the research was conducted in the absence of any commercial or financial relationships that could be construed as a potential conflict of interest.

frontiers in Cell and Developmental Biology

ORIGINAL RESEARCH
published: 04 November 2021
doi: 10.3389/fcell.2021.744992

RETSAT Mutation Selected for Hypoxia Adaptation Inhibits Tumor Growth

Xiulin Jiang[1,2†], Yaomei He[1,2†], Qiushuo Shen[1], Lincan Duan[3], Yixiao Yuan[3], Lin Tang[3], Yulin Shi[1,2], Baiyang Liu[1,2], Haoqing Zhai[1,2], Peng Shi[4,5], Cuiping Yang[1,2]* and Yongbin Chen[1,2,5]**

[1]Key Laboratory of Animal Models and Human Disease Mechanisms of Chinese Academy of Sciences and Yunnan Province, Kunming Institute of Zoology, Kunming, China, [2]Kunming College of Life Science, University of Chinese Academy of Sciences, Beijing, China, [3]The Third Affiliated Hospital of Kunming Medical University, Kunming, China, [4]State Key Laboratory of Genetic Resources and Evolution, Kunming Institute of Zoology, Chinese Academy of Sciences, Kunming, China, [5]Center for Excellence in Animal Evolution and Genetics, Chinese Academy of Sciences, Kunming, China

OPEN ACCESS

Edited by:
Yih-Cherng Liou,
National University of Singapore, Singapore

Reviewed by:
Fuming Li,
Fudan University, China
Stephen B. Keysar,
University of Colorado Anschutz Medical Campus, United States

***Correspondence:**
Yongbin Chen
ybchen@mail.kiz.ac.cn
Cuiping Yang
cuipingyang@mail.kiz.ac.cn
Peng Shi
ship@mail.kiz.ac.cn

[†]These authors have contributed equally to this work

Specialty section:
This article was submitted to Molecular and Cellular Oncology, a section of the journal Frontiers in Cell and Developmental Biology

Received: 21 July 2021
Accepted: 18 October 2021
Published: 04 November 2021

Citation:
Jiang X, He Y, Shen Q, Duan L, Yuan Y, Tang L, Shi Y, Liu B, Zhai H, Shi P, Yang C and Chen Y (2021) RETSAT *Mutation Selected for Hypoxia Adaptation Inhibits Tumor Growth. Front. Cell Dev. Biol. 9:744992. doi: 10.3389/fcell.2021.744992*

Hypoxia occurs not only in natural environments including high altitude, underground burrows and deep sea, but also in human pathological conditions, such as hypoxic solid tumors. It has been well documented that hypoxia related signaling pathway is associated with a poor clinical outcome. Our group has recently identified multiple novel genes critical for solid tumor growth comparing the genome-wide convergent/parallel sequence evolution of highland mammals. Among them, a single mutation on the retinol saturase gene (*RETSAT*) containing amino acid switch from glutamine (Q) to arginine (R) at the position 247 was identified. Here, we demonstrate that RETSAT is mostly downregulated in multiple types of human cancers, whose lower expression correlates with worse clinical outcome. We show that higher expression of RETSAT is positively associated with immune infiltration in different human cancers. Furthermore, we identify that the promoter region of *RETSAT* is highly methylated, which leads to its decreased expressions in tumor tissues comparing to normal tissues. Furthermore, we show that RETSAT knockdown promotes, while its overexpression inhibits, the cell proliferation ability of mouse embryonic fibroblasts (MEFs) and B16 *in vitro*. In addition, the mice carrying homozygous Q247R mutation (RETSATR/R) is more resistant to xenograft tumor formation, as well as DMBA/TPA induced cutaneous keratinocyte carcinoma formation, compared to littermate wild-type (RETSATQ/Q) mice. Mechanistic study uncovers that the oncogenic factor, the prolyl isomerase (PPIase) Pin1 and its related downstream signaling pathway, were both markedly repressed in the mutant mice compared to the wild-type mice. In summary, these results suggest that interdisciplinary study between evolution and tumor biology can facilitate identification of novel molecular events essential for hypoxic solid tumor growth in the future.

Keywords: retinol saturase (RETSAT), hypoxia adaptation, evolution, Pin1, skin cutaneous melanoma (SKCM)

INTRODUCTION

High altitude is one of the most extreme environments worldwide, and mammals living in high altitude evolve adaptation traits including respiratory, cardiovascular, and metabolic systems compared to reciprocal lowlanders (Brutsaert, 2008; Scheinfeldt et al., 2012; Rademaker et al., 2014; Storz and Scott, 2021). The genetic signals after hypoxia positive selection are the major factors contributing to the hypoxia tolerant physiological traits, some of which have been indicated to be critical for transcriptional regulation under hypoxic conditions (Beall et al., 2010; Yi et al., 2010). Hemoglobin levels and oxygen saturation in the blood are two physiological characteristics important for oxygen sense, which are thoroughly studied in highlanders. Hemoglobin concentration is elevated, but oxygen saturation is reduced in high-altitude Andean populations, compared to African population as well as other low-altitude populations (Beall et al., 2002).

Hypoxia occurs not only in natural environments including high altitude, underground burrows and deep sea, but also in human pathological conditions, such as diabetes and hypoxic solid tumors (De Bels et al., 2011; Cheviron and Brumfield, 2012; Yang et al., 2020; Storz and Scott, 2021). However, hypoxia cannot be simply defined by a fixed oxygen concentration, since some tissues function normally at 5% oxygen equivalent to normoxia, and others as low as 1% oxygen (Schödel and Ratcliffe, 2019). Hypoxia related signaling molecules have been documented to function as a major regulator during tumorigenesis (Kang et al., 2018; Xiong et al., 2020). These factors include hypoxia-inducible factors (HIFs), the von Hippel–Lindau (VHL) and prolyl hydroxylases (PHD1/2/3 or so-called EglN1/2/3, respectively) of the 2-oxoglutarate (or α-ketoglutarate) dioxygenase super-family (Schödel and Ratcliffe, 2019), which provide valuable therapeutic targets for various types of human cancers (Lee et al., 2020). Increasing evidence has revealed that hypoxic solid tumors are not sensitive to clinical treatment due to reduced reactive oxygen species (ROS) and DNA damage in the case of ionizing radiation and certain chemotherapies (Brustugun, 2015). However, it is important to note that hypoxia in solid tumors is not completely the same as that in high altitude. For example, some hypoxic tumor regions have near 0% oxygen, while the oxygen level will only drop to ~60% of sea level at ~4,000 m highland.

Based on the similarities between high altitude hypoxia adaptation and hypoxic solid tumors, we have developed an interdisciplinary study to identify novel biomarkers involved in tumorigenesis. For examples, we did parallel large-scale genomic data generated from Tibetan domestic mammals and corresponding lowland species, and identified multiple hypoxia adaptation selected genes including YTHDF1 and C10orf67 (Shi et al., 2019; Wu et al., 2020). Furthermore, we found that YTHDF1 expression is decreased in highland mammals compared to lowlanders, which promotes non-small cell lung cancer (NSCLC) progression by activating the translational efficiency of m6A modified CDK2 and CDK4 mRNAs (Shi et al., 2019). Recently, we uncovered that the retinol saturase gene (*RETSAT*) contains a single parallel amino acid change from glutamine (Q) to arginine (R) at position 247 in QTP (Qinghai-Tibet Plateau) mammals (Xu et al., 2021). RETSAT has been identified to be an NADH/NADPH- dependent oxidoreductase, which is highly expressed in liver, adipose tissue and kidney (Moise et al., 2004). Previous studies have shown that RETSAT saturates the 13-14 double bond of all-trans-retinol to produce all-trans-13-14-dihydroretinol, a product important for vitamin A metabolism, which then regulates lipid metabolism, and production of reactive oxygen species (Moise et al., 2005). Furthermore, RETSAT was uncovered to modulate lipid metabolism and the production of reactive oxygen species (ROS) (Pang et al., 2017). RETSAT promotes adipogenesis and is downregulated in obesity by suppressing PPARγ and retinoid X receptor α (RXRα) responses (Ziouzenkova et al., 2007; Schupp et al., 2009).

Previous studies demonstrated that all-trans retinoic acid (ATRA), the active metabolite of vitamin A, could be used for the treatment of acute promyelocytic leukemia (APL) (Gottardi et al., 2020). Another study showed that all-trans retinoic acid stealth liposomes prevent the metastasis of breast cancer and glioblastoma tumor growth (Li et al., 2011; Mirani et al., 2019). However, whether or not RETSAT play any role in human cancers is still unknown. In this study, we decided to verify the expression and mutation patterns of RETSAT in various human cancers, and compared the xneograft or chemical induced-tumor formation in RETSAT mutant and wild-type mice.

RESULTS

RETSAT Expression Patterns in Different Types of Human Cancers

We firstly examined the mRNA expression patterns of RETSAT in different types of human cancers using the Tumor Immune Estimation Resource (TIMER) online database (Li et al., 2017). The consistent lower expression of RETSAT was observed in BRCA (Breast invasive carcinoma), CHOL (Cholangiocarcinoma), COAD (Colon adenocarcinoma), HNSC (Head and Neck squamous cell carcinoma), KICH (Kidney Chromophobe), KIRC (Kidney renal clear cell carcinoma), LUAD (Lung adenocarcinoma), LUSC (Lung squamous cell carcinoma), PCPG (Pheochromocytoma and Paraganglioma), PRAD (Prostate adenocarcinoma), READ (Rectum adenocarcinoma) and THCA (Thyroid carcinoma) compared with the corresponding normal tissues (**Figure 1A**). The above results showed that RETSAT expression is commonly decreased in most human cancers, indicating that RETSAT may function as a tumor suppressor.

Based on the fact that mammals living in high altitude are exposed to both hypoxic and intensive ultra violet conditions, we decided to validate the expression pattern of RETSAT in skin cutaneous melanoma (SKCM), and identified lower RETSAT transcripts in cancerous tissues than that in normal skin tissues, by using the gene expression profile

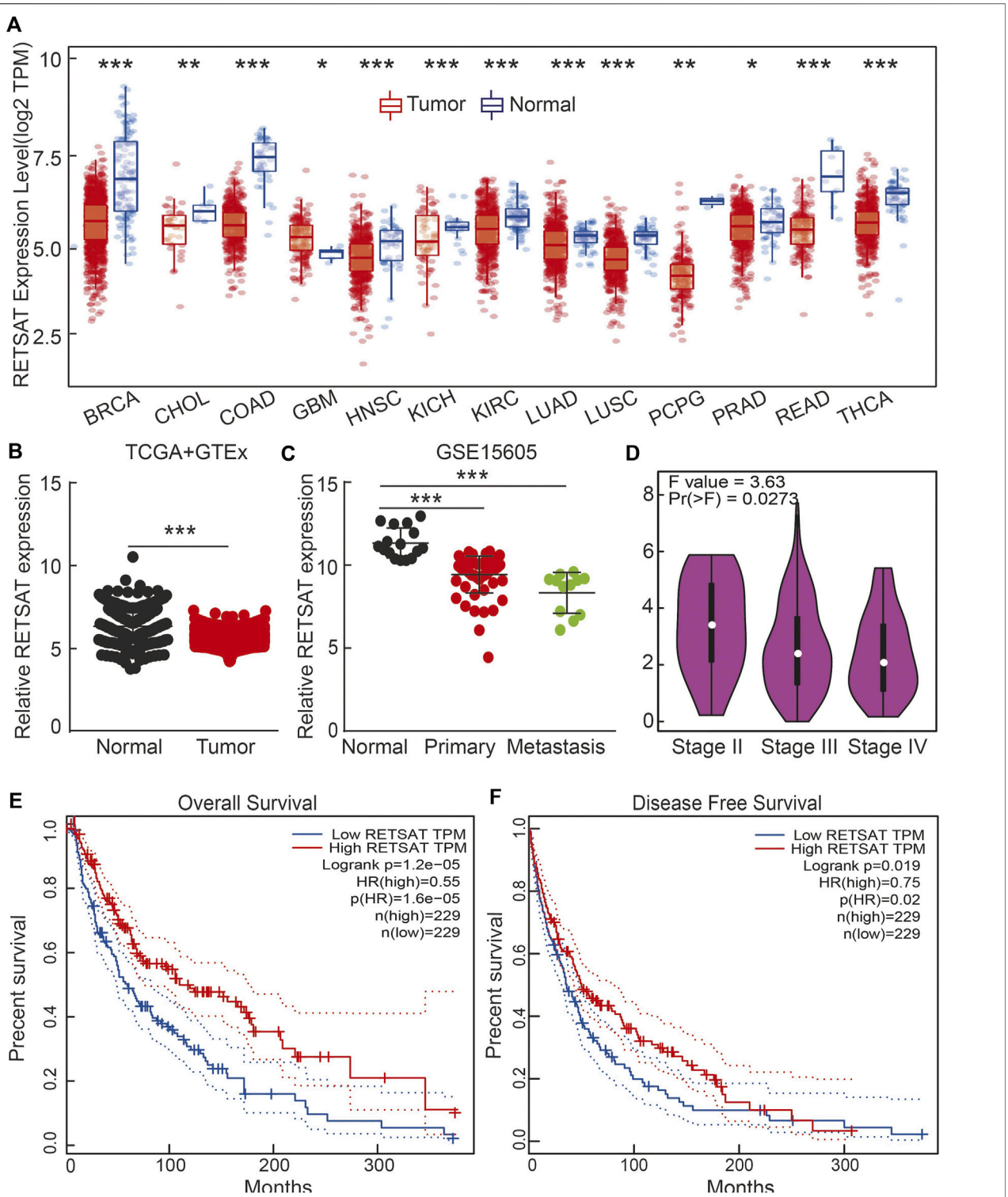

FIGURE 1 | RETSAT expression patterns in human cancers. **(A)** RETSAT expression of different types of human cancers using the TIMER database. Red: tumors; blue: normal tissues. **(B)** The expression pattern of RETSAT, comparing the profiles from SKCM in (TCGA) and GTEx (Genotype-Tissue Expression, mostly for normal tissues). **(C,D)** The expression patterns of RETSAT in SKCM using the GEO databases and the GEPIA database **(D)**. **(E)** The overall survival (OS: E) and the disease-free survival (DFS: F) tests for RETSAT in SKCM in GEPIA database. *$p < 0.05$, **$p < 0.01$, ***$p < 0.001$.

TABLE 1 | RETSAT mutations in SKCM determined by cBioportal database.

Cancer type	Change	Mutation type	Copy change	Mut sample
Cutaneous Melanoma	*G536R*	Missense	Gain	35
Cutaneous Melanoma	*A533V*	Missense	Gain	35
Cutaneous Melanoma	*G536R*	Missense	Gain	110
Cutaneous Melanoma	*A533V*	Missense	Gain	110
Cutaneous Melanoma	*P270T*	Missense	Diploid	154
Acral Melanoma	*G536R*	Missense	Diploid	248
Acral Melanoma	*A533V*	Missense	Diploid	248
Cutaneous Melanoma	*S601F*	Missense	Diploid	313
Cutaneous Melanoma	*S601F*	Missense	ShallowDel	322
Cutaneous Melanoma	*S601F*	Missense	ShallowDel	325
Melanoma	*S492F*	Missense	Diploid	346
Cutaneous Melanoma	*P215L*	Missense	Diploid	389
Cutaneous Melanoma	*P215Q*	Missense	Diploid	421
Melanoma	*W146**	Nonsense	ShallowDel	443
Cutaneous Melanoma	*W146**	Nonsense	ShallowDel	448
Cutaneous Melanoma	*L180F*	Missense	ShallowDel	499
Cutaneous Melanoma	*V258A*	Missense	Diploid	510
Cutaneous Melanoma	*P292T*	Missense	Diploid	510
Cutaneous Melanoma	*V258A*	Missense	Diploid	517
Cutaneous Melanoma	*P292T*	Missense	Diploid	517
Cutaneous Melanoma	*V258A*	Missense	Diploid	517
Cutaneous Melanoma	*P292T*	Missense	Diploid	517
Cutaneous Melanoma	*G536R*	Missense	Diploid	525
Cutaneous Melanoma	*A533V*	Missense	Diploid	525
Cutaneous Melanoma	*L180F*	Missense	Diploid	528
Cutaneous Melanoma	*L180F*	Missense	Diploid	576
Cutaneous Melanoma	*L3H*	Missense	ShallowDel	579
Melanoma	*L3H*	Missense	ShallowDel	582
Cutaneous Melanoma	*L3H*	Missense	ShallowDel	587
Melanoma	*S34F*	Missense	ShallowDel	743
Cutaneous Melanoma	*M420I*	Missense	Diploid	779
Cutaneous Melanoma	*P292S*	Missense	ShallowDel	854
Melanoma	*S34F*	Missense	ShallowDel	855
Cutaneous Melanoma	*R133C*	Missense	Diploid	867
Cutaneous Melanoma	*P292S*	Missense	Diploid	869
Cutaneous Melanoma	*R482W*	Missense	ShallowDel	949
Cutaneous Melanoma	*R482W*	Missense	Diploid	961
Cutaneous Melanoma	*R482W*	Missense	Diploid	966
Cutaneous Melanoma	*P292S*	Missense	Diploid	1,005
Cutaneous Melanoma	*G124W*	Missense	Diploid	1,088
Cutaneous Melanoma	*V54I*	Missense	ShallowDel	1,354
Cutaneous Melanoma	*L315I*	Missense	Diploid	1,369
Cutaneous Melanoma	*G172**	Nonsense	Diploid	1,436
Cutaneous Melanoma	*P168H*	Missense	Diploid	1,445
Skin Cancer	*P455S*	Missense	ShallowDel	1,521
Cutaneous Melanoma	*W450C*	Missense	ShallowDel	1,610
Cutaneous Melanoma	*G250W*	Missense	ShallowDel	1,630
Cutaneous Melanoma	*P448S*	Missense	Gain	1,718
Cutaneous Melanoma	*P305H*	Missense	ShallowDel	1,749
Cutaneous Melanoma	*Q418*	Splice	ShallowDel	1,804
Skin Cancer	*P292S*	Missense	ShallowDel	1,806
Skin Cancer	*S60L*	Missense	ShallowDel	1,836
Cutaneous Melanoma	*P506S*	Missense	ShallowDel	1,901
Cutaneous Melanoma	*Y176Tfs*20*	FS del	ShallowDel	1,937
Cutaneous Melanoma	*P506S*	Missense	Gain	1,938
Cutaneous Melanoma	*P506S*	Missense	Gain	1,967
Cutaneous Melanoma	*R164**	Nonsense	Diploid	2,068
Melanoma	*G204**	Nonsense	Diploid	2,156
Cutaneous Melanoma	*T388I*	Missense	ShallowDel	3,224
Cutaneous Melanoma	*P168S*	Missense	ShallowDel	3,330
Skin Cancer	*P465L*	Missense	ShallowDel	3,403
Cutaneous Melanoma	*P152S*	Missense	ShallowDel	3,536
Cutaneous Melanoma	*P233L*	Missense	ShallowDel	3,843
Melanoma	*F25Y*	Missense	Diploid	5,023

(Continued on following page)

TABLE 1 | (*Continued*) RETSAT mutations in SKCM determined by cBioportal database.

Cancer type	Change	Mutation type	Copy change	Mut sample
Cutaneous Melanoma	*S238F*	Missense	Diploid	5,836
Cutaneous Melanoma	*R293**	Nonsense	Diploid	7,335
Cutaneous Melanoma	*H207Y*	Missense	Diploid	15,530
Cutaneous Melanoma	*H207Y*	Missense	Diploid	15,834

Notes: *p < *0.05*, **p < *0.01*, ***p < *0.001*.

from TCGA and GETx dataset (**Figure 1B**). Consistently, we also verified the downregulation of RETSAT in tumor tissues in the GEO database (**Figure 1C**). The correlation between RETSAT and SKCM tumor stage was further tested using the GEPIA online tool (Tang et al., 2017). We found that lower expressions of RETSAT transcripts correlate with higher tumor stages (**Figure 1D**). In line with this finding, we revealed that patients with SKCM containing higher RETSAT expression exhibited longer overall survival (OS) and disease-free survival (DFS) time, compared to SKCM patients with lower RETSAT expression levels (**Figures 1E,F**). In addition, we identified many RETSAT mutations in SKCM by applying the cBioPortal web resource (**Table 1**) (Gao et al., 2013). The above results suggest that RETSAT is decreased in SKCM, indicating its inhibitory role during SKCM tumor progression.

The Promoter Region of *RETSAT* is Highly Methylated in Multiple Tumors

To further elucidate the mechanism by which RETSAT is commonly downregulated in tumors, we firstly examined the methylation status of *RETSAT* promoter region, which is major cause for repressing gene expression in tumors. By using the methSurv analysis (Modhukur et al., 2018), we found that there are many methylation sites in the promoter region of *RETSAT*, and the differential methylation regions were indicated in the heatmaps (**Figure 2A**). Importantly, by using the shiny methylation analysis resource tool (SMART) analysis (Li et al., 2019) we uncovered that the methylation of RETSAT was significantly higher in SKCM cancerous tissues compared to that in normal tissues (**Figure 2B**). Consistently, we found that the methylation levels on the specific methylation site (cg05514932) within *RETSAT* promoter region negatively correlated with its expression in SKCM (**Figures 2C,D**). Furthermore, we showed that the elevated methylation levels on cg05514932 site correlates with worse OS in the TCGA-SKCM cohorts, using the methSurv dataset (**Figure 2E**). Therefore, we hypothesized that the highly methylation in *RETSAT* promoter DNA fragment might cause its decreased expressions in multiple types of human cancers, including SKCM (**Figure 2F**). In addition, we treated B16 cells with 5-Azacytidine, the specific inhibitor for DNA methylases (Christman, 2002), and revealed that *RETSAT* mRNA expression level was dramatically increased (**Figure 2G**).

RETSAT Expression Correlates With Immune Infiltration in SKCM

Since RETSAT might function as a tumor suppressor and immune infiltration was considered as a promising independent prognostic factor in cancers, we next used the TIMER database to investigate the correlation between RETSAT expression and immune infiltration (Li et al., 2017). Specifically, *RETSAT* CNV significantly correlates with infiltrating levels of B cells, $CD8^+$ T cells, macrophages, neutrophils and dendritic cells (**Figure 3A**). Next, we analyzed the correlation between RETSAT expression and six types of infiltrating immune cells, including B cells, $CD8^+$ T cells, $CD4^+$ T cells, macrophages, neutrophils and dendritic cells. The results demonstrated that the expression level of RETSAT was positively correlated with the infiltration level of B cells ($r = 0.597$, $p = 3.63e\text{-}48$), $CD8^+$ T cells ($r = 0.422$, $p = 2.09e\text{-}22$), $CD4^+$ T cells ($r = 0.671$, $p = 1.25e\text{-}64$), macrophages ($r = 0.478$, $p = 4.55e\text{-}29$), neutrophils ($r = 0.744$, $p = 2.67e\text{-}86$), and dendritic cells ($r = 0.837$, $p = 3.66e\text{-}129$) in SKCM (**Figure 3B**). Next, we used TISIDB database to further explore the relationship between RETSAT expression level and immunostimulators and immunoinhibitors, respectively in SKCM (Ru et al., 2019). We found that RETSAT was mostly positively, but negatively, associated with the expression of immunostimulators and the immunoinhibitors, respectively (**Tables 2**, **3**). These results strongly implicate that RETSAT could serve as a key regulator for tumor immune infiltration in SKCM.

RETSAT Q247R Mutation Inhibits Tumor Growth *in vitro* and *in vivo*

To examine the functional role of RETSAT in SKCM cells, RETSAT was inhibited by two independent lenti-viral shRNAs in B16 cells and mouse embryonic fibroblasts (MEFs), and the knockdown and overexpression efficiencies were verified by Real-time RT-PCR, cell line expressing scramble shRNA was used as control. As expected, RETSAT knockdown promoted the cell proliferation ability of B16 and MEFs (**Figures 4A–D,I,J,L**), while RETSAT overexpression led to the opposite effect (**Figures 4E–H,K,M**). Taken together, these data suggest that RETSAT functions as a tumor suppressor in SKCM.

To verify the *in vivo* functional role of RETSAT during tumorigenesis, we performed both the xenograft tumor formation and DMBA/TPA induced cutaneous keratinocyte carcinoma formation assays. Five-weeks old male mice of

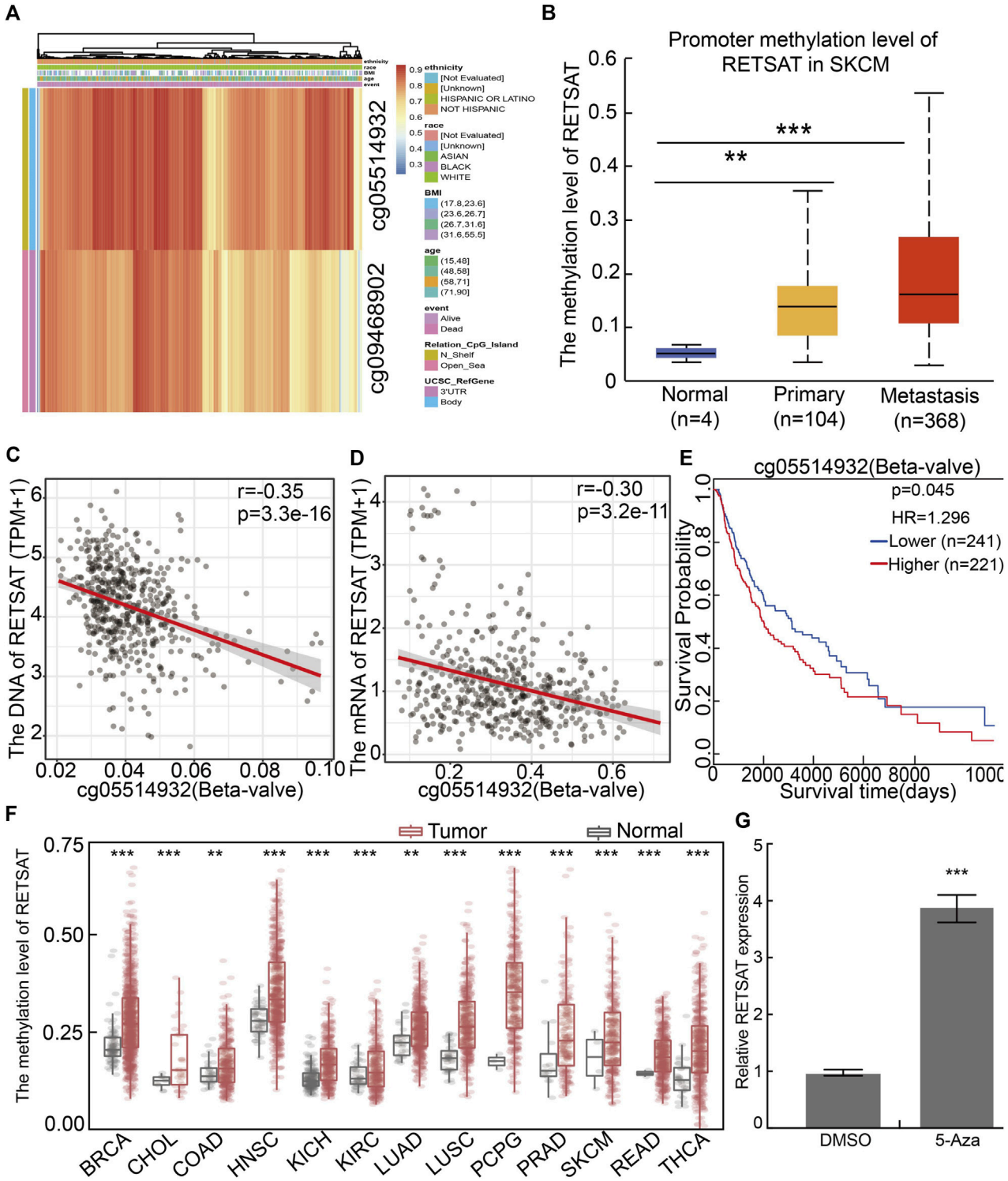

FIGURE 2 | The methylation pattern in RETSAT promoter. **(A)** Critical methylation sites within RETSAT promoter region were indicated in the heatmap. The gradient color bars indicate the different methylation levels of the two methylation sites (cg05514932, cg09468902) within RETSAT promoter region in each SKCM sample, the browner the color is, the higher methylation level is. **(B)** The methylation level in RETSAT promoter region positively correlates with SKCM stages in ualcan database. **(C,D)** Both the DNA **(C)** and mRNA **(D)** expressions of RETSAT negatively correlate with the methylation level using SMART database. **(E)** Kaplan-Meier analysis of OS (overall survival) considering RETSAT methylation level using the TCGA SKCM dataset. **(F)** The methylation level of RETSAT in different types of human cancers compared with that in normal tissues using SMART database. **(G)** The relative expression of RETSAT mRNA in B16 cells after 5-azacytidine treatment, examine by Real time RT-PCR assay. $*p < 0.05$, $**p < 0.01$, $***p < 0.001$.

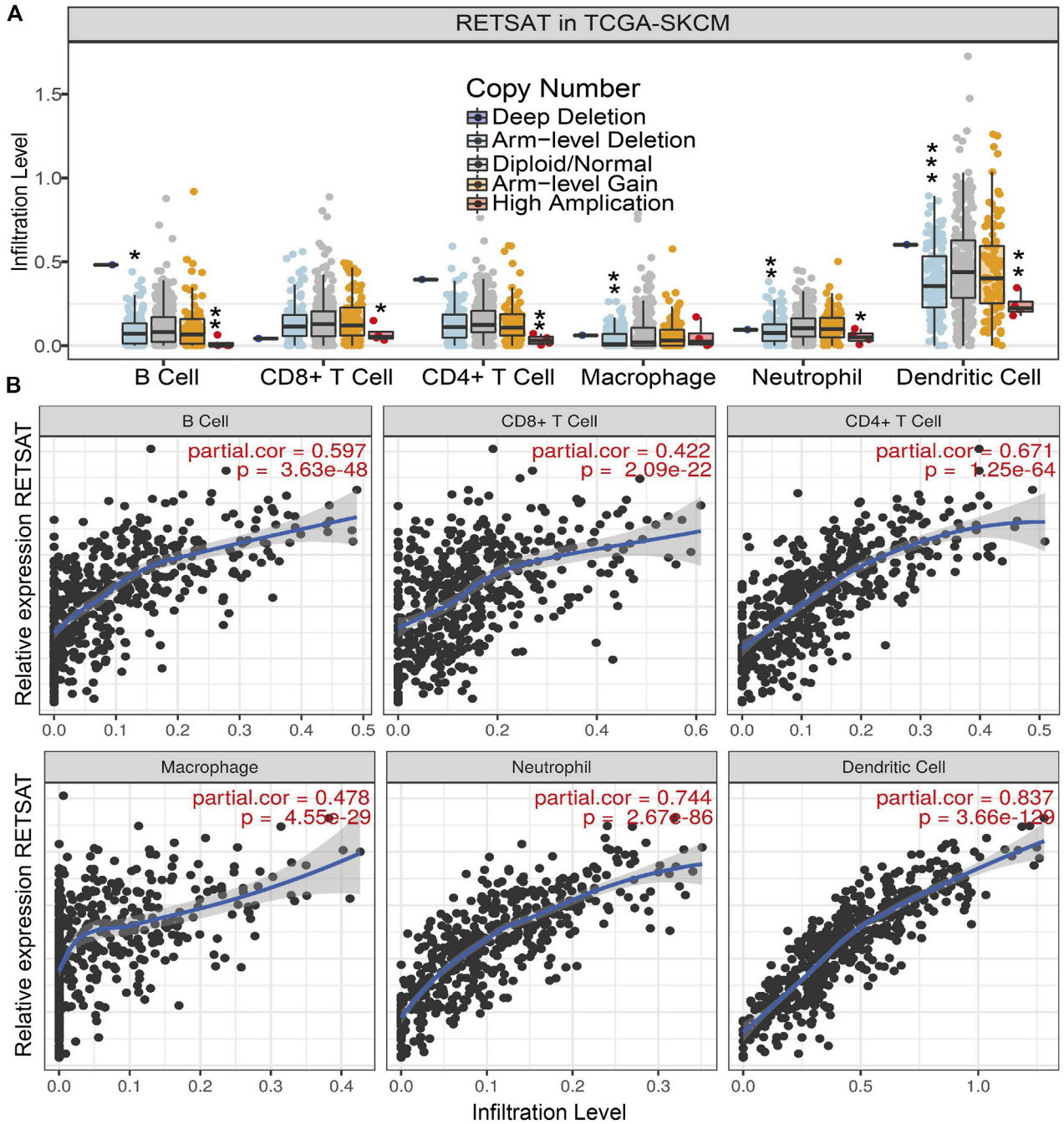

FIGURE 3 | RETSAT correlates with immune cell infiltration in tumors. **(A)** The infiltration levels of various immune cells correlate with RETSAT mutations in SKCM using the TIMER database. **(B)** The correlation of RETSAT expression level with B cell, $CD8^+$ T cell, $CD4^+$ T cell, macrophage, neutrophil or dendritic cell infiltration level in SKCM analyzed by TIMER database. $^*p < 0.05$, $^{**}p < 0.01$, $^{***}p < 0.001$.

$RETSAT^{R/R}$ mutant and wild-type littermates were randomly divided into indicated groups, and B16 cells were injected subcutaneously (2×10^5 cells/point). As expected, the subcutaneous tumors in the wild-type littermates ($RETSAT^{Q/Q}$) were detected quickly, whereas the xenograft tumors were markedly retarded in $RETSAT^{R/R}$ mice, which was visualized by the reduced tumor mass and volume compared to the control group (**Figures 5A–C**). Consistently, significant lower proliferation as measured by Ki67 immunohistochemistry (IHC) staining in the xenograft tumor sections from $RETSAT^{R/R}$ group was detected, compared to control group (**Figures 5D,E**). In addition, by using the DMBA/TPA induced cutaneous keratinocyte carcinoma formation assay, better overall survival rate was observed in

TABLE 2 | The correlation analysis between RETSAT and the expression of immunostimulators in SKCM validated by TIMER database.

Immunostimulators	r	p	Immunostimulators	r	p
C10ORF54	0.723	***	TNFRSF9	0.845	***
CD27	0.807	***	KLRC1	0.658	***
CD28	0.804	***	KLRK1	0.74	***
CD40	0.668	***	LTA	0.81	***
CD40LG	0.755	***	MICB	0.355	***
CD48	0.823	***	NT5E	0.183	***
CD70	0.436	***	TMEM173	0.253	***
CD80	0.831	***	TMIGD2	0.609	***
CD86	0.881	***	TNFRSF13B	0.685	***
CXCL12	0.699	***	TNFRSF13C	0.411	***
CXCR4	0.694	***	TNFRSF17	0.668	***
ENTPD1	0.516	***	TNFRSF18	0.586	***
ICOS	0.778	***	TNFSF14	0.756	***
ICOSLG	0.532	***	TNFRSF4	0.491	***
IL2RA	0.809	***	TNFRSF8	0.684	***

Notes: *p < *0.05*, **p < *0.01*, ***p < *0.001*.

TABLE 3 | The correlation analysis between RETSAT and the expressions of immunoinhibitors in SKCM validated by TIMER database.

Immunoinhibitors	r	p
ADORA2A	–0.295	***
BTLA	–0.199	***
CD160	–0.252	***
CD244	–0.133	***
CD96	–0.248	***
CSF1R	–0.258	***
HAVCR2	–0.19	***
IDO1	–0.268	***
IL10	–0.157	***
KDR	–0.203	***
LAG3	–0.15	***
LGALS9	–0.15	***
PDCD1	–0.116	***
PDCD1LG2	–0.264	***
TIGIT	–0.188	***

Notes: *p < *0.05*, **p < *0.01*, ***p < *0.001*.

$RETSAT^{R/R}$ mice compared to the littermate wild-type $RETSAT^{Q/Q}$ mice (**Figures 5F,G**).

RETSAT Q247R Mutation Inhibits Pin1 Related Signaling Pathway

To further explore the molecular events affected by $RETSAT^{R/R}$ mutation in SKCM, a protein-protein interaction (PPI) network for RETSAT was created using the STRING database (Szklarczyk et al., 2017) (**Figure 6A**). Among the interacting proteins, Pin1 and Akt1 caught our attention. The oncogenic factor PIN1 has been well demonstrated to promote the occurrence and development of various cancers (Min et al., 2016; Rustighi et al., 2017; Chen et al., 2018; Nakatsu et al., 2020; Yu et al., 2020). Previous study also documented that Pin1 inhibition using small molecule inhibitor such as ATRA or short hairpin RNA, reduces tumor growth via inhibiting PI3K/AKT signaling pathways (Sun et al., 2019). In addition, we revealed that RETSAT is involved in regulating PI3K/AKT signaling pathway by GSEA dataset analysis (Subramanian et al., 2005), suggesting that RETSAT could inhibit the oncogenic effect mediated by Pin1 in SKCM (**Figure 6B**).

Therefore, we decided to validate the correlation between RETSAT expression and Pin1 related signaling (Sun et al., 2019). We showed that RETSAT expression was significantly negatively correlated with Pin1 in SKCM ($r = -0.29$, $p = 2.9e\text{-}10$) (**Figure 6C**). To validate the signaling axis, we used various adult mouse tissues, including brain, heart, liver and lung, and uncovered that the markedly reduced Pin1 and phosphorylated Akt1 proteins in $RETSAT^{R/R}$ background could only be detected in MEFs, liver and lung, but not in brain and heart, suggesting that the inhibitory effect could be cellular context or developmental stage dependent (**Figures 6D–H**). Furthermore, we revealed that $RETSAT^{R/R}$ mutation inhibits Pin1 expressions in B16 xenograft tumors, compared to the $RETSAT^{Q/Q}$ wild-type control groups, detected by immunohistochemistry (IHC) staining (**Figures 6I,J**).

DISCUSSION

Melanoma incidence rates have sky rocketed in the past decades, and there are recurrent somatic mutations that appear frequently in most types of melanoma (Scolyer et al., 2011; Read et al., 2016). Driving mutations have been linked to signaling pathways that regulate proliferation (BRAF, NF1 and PTEN), cellular apoptosis (TP53), and cell cycle control (CDKN2A) (Scolyer et al., 2011; Read et al., 2016). Melanoma cells quickly adapt to the immune response due to the highly mutagenic nature (Lee et al., 2016). Recent studies have demonstrated that melanoma can be efficiently overcome by treating with antibodies against PD1, PD-L1/2 and CTLA-4 (Koller et al., 2016).

Numerous studies focusing on RETSAT have demonstrated its critical role for liver metabolism (Schupp et al., 2009; Heidenreich et al., 2017). RETSAT depletion has been shown to reduce the activity of carbohydrate response element binding protein (ChREBP), a cellular hexose-phosphate sensor and inducer of lipogenesis (Heidenreich et al., 2017). Ectopic expression of RETSAT with an intact, but not a mutated, FAD/NAD dinucleotide-binding motif, increased endogenous PPARgamma transcriptional activity and promoted adipogenesis (Schupp et al., 2009). Previous results showed that all-trans retinoic acid (ATRA), one of the active metabolites of vitamin A, could successfully treat patients with acute promyelocytic leukemia (APL) (Gottardi et al., 2020). Another study uncovered that ATRA prevented the relapse of breast cancer via promoting the differentiation of cancer stem cells (Li et al., 2011). In addition, ATRA has been applied to inhibit tumor cell growth in glioblastoma (Mirani et al., 2019). 9-cis RA (9-cis-13,14-dihydroretinic acid) is a potential activator of RARs and RXRs, which has been uncovered to inhibit tumor progression (Gottardis et al., 1996; Christov et al., 2002; Karsy et al., 2010).

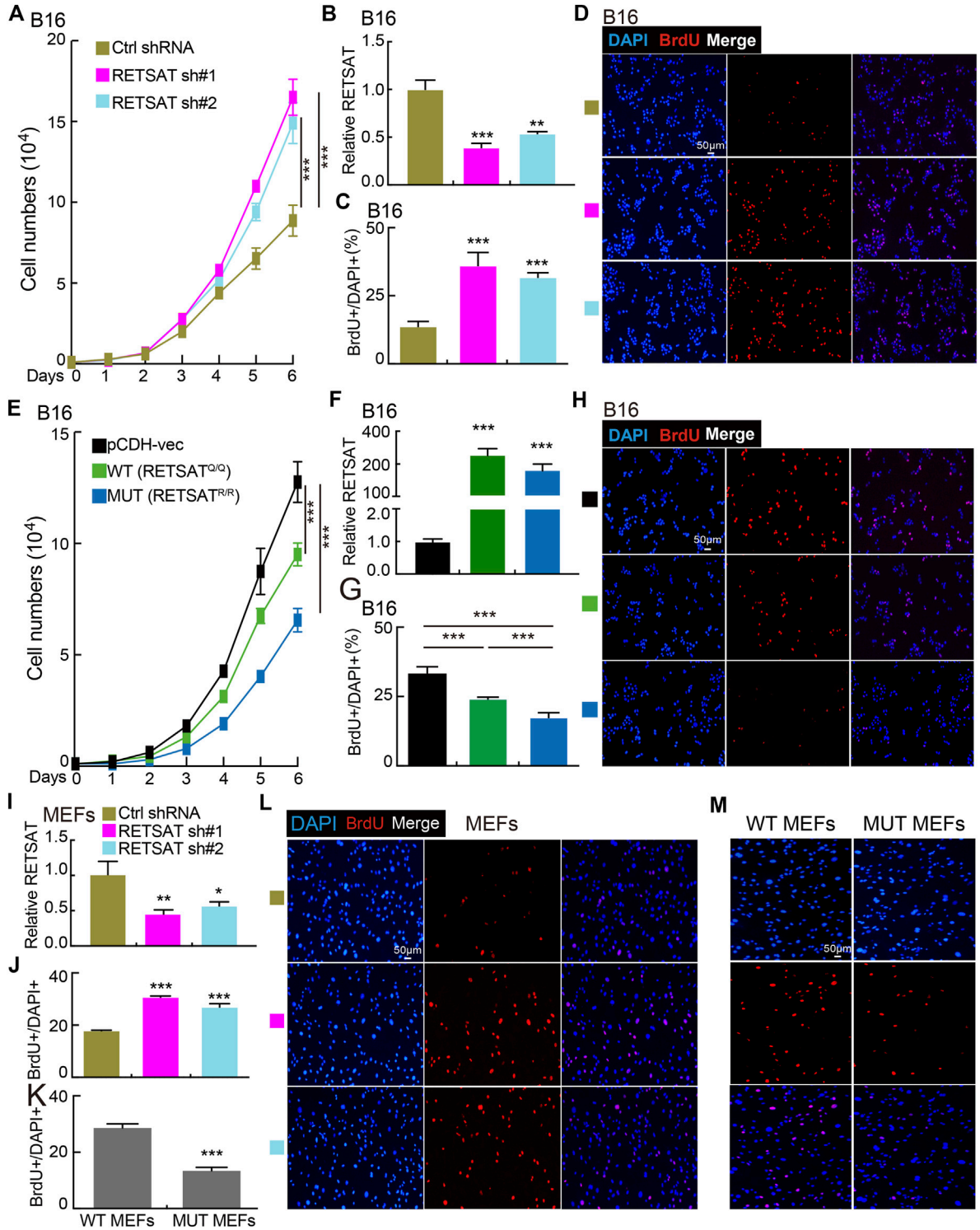

FIGURE 4 | RETSAT knockdown promotes cell proliferation. **(A)** Knockdown of RETSAT promotes B16 cell growth examined by growth curve assay. **(B)** RETSAT targeting shRNA knockdown efficiency in B16 cells was verified by Real-time RT-PCR assay, scramble shRNA was used as control. sh#1 = shRNA#1, sh#2 = shRNA#2, Ctrl = control. **(C,D)** Knockdown of RETSAT promotes B16 cell proliferation examined by BrdU incorporation assay, **(C)** is the quantification data for **(D)**. Scale bar = 50 μm. **(E)** Overexpression of RETSAT inhibits B16 cell proliferation examined by growth curve assay. **(F)** RETSAT overexpression efficiency in B16 cells was verified by Real-time RT-PCR assay. **(G,H)** RETSAT overexpression inhibits B16 cell proliferation examined by BrdU incorporation assay, **(G)** is the quantification data for **(H)**. Scale bar = 50 μm. **(I)** RETSAT targeting shRNA knockdown in wild-type MEFs was verified by Real-time RT-PCR assay. **(J,L)** RETSAT inhibition promotes cell proliferation in MEFs examined by BrdU incorporation assay, **(L)** is the quantification data for **(J)**. Scale bar = 50 μm. **(K,M)** RETSATR/R mutant MEFs exhibit higher proliferation rate compared to wild type RETSATQ/Q MEFs, **(M)** is the quantification data for **(L)**. Scale bar = 50 μm. WT = wild type (RETSATQ/Q). MUT = mutant (RETSATR/R).*$p < 0.05$, **$p < 0.01$, ***$p < 0.001$.

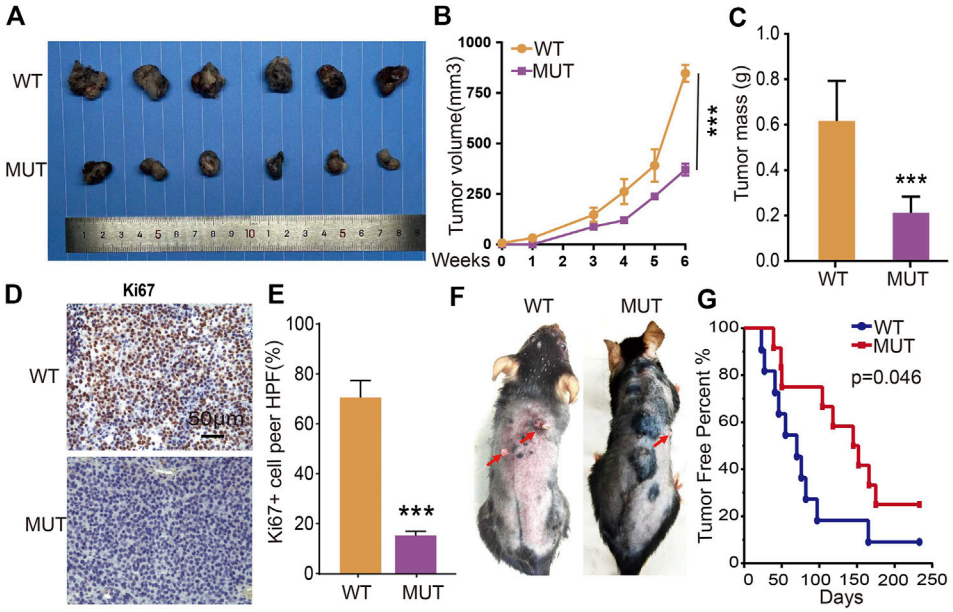

FIGURE 5 | RETSAT (Q247R) mutation inhibits tumor growth *in vivo*. **(A–C)** RETSAT mutation inhibits xenograft tumor formation *in vivo*. Representative xenograft tumor images **(A)**, tumor masses **(B)** and tumor volumes **(C)**. **(D,E)** Representative IHC staining of Ki67 for indicated xenograft tumors. **(F)** Representative mice images after DMBA/TPA treatment. WT = wild type (RETSATQ/Q). MUT = mutant (RETSATR/R). **(G)** The overall survival (OS) analysis for RETSAT mutation and RETSAT WT mice after DMBA/TPA induced cutaneous keratinocyte carcinoma. $^{*}p < 0.05$, $^{**}p < 0.01$, $^{***}p < 0.001$.

Peptidyl-prolyl *cis*-trans isomerase NIMA-interacting 1 (Pin1) was originally identified in 1996 (Ping Lu et al., 1996), which functions as an enzyme specifically catalyzing the isomerization of phosphorylated serine-proline or phosphorylated threonine-proline (pSer/Thr-Pro) motifs (Zhou and Lu, 2016). Emerging evidence has demonstrated that Pin1-mediated prolyl isomerization plays pivotal roles under both physiological and pathological conditions, including in human cancers (Sacktor, 2010; Tun-Kyi et al., 2011). Pin1 is aberrantly increased or constitutively activated in multiple tumors (Chen et al., 2018), and high expression of Pin1 is closely correlated to poor clinical prognosis (Zhou and Lu, 2016). Pin1 regulates the self-renewal of Cancer Stem Cells (CSCs) by maintenance the stability of Nanog, octamer-binding protein 4 (OCT4), and MYC (Nishi et al., 2011; Farrell et al., 2013). Importantly, recent study also showed that Pin1 inhibition by ATRA or short hairpin RNA, reduces cancer development by inhibiting Wnt/β-catenin and PI3K/AKT signaling pathways in gastric cancer (Zhang et al., 2019).

In this study, we showed that hypoxia adaptation selection mutant form of RETSAT$^{R/R}$ inhibits xenograft tumor cell growth (Xu et al., 2021), and DMBA/TPA induced cutaneous keratinocyte carcinoma formation *in vivo*. However, higher expression of RETSAT was observed in gliomas (**Figure 1A**), suggesting that RETSAT may have differential role in the central nervous system. Multiple mutations on *RETSAT* were also identified in SKCM (**Table 1**), but none of them is Q247R mutation, which is more likely a gain-of-function mutation based on the *in vitro* enzymatic assay (Xu et al., 2021). Previous evidence has shown that RETSAT saturates the 13-14 double bond of all-trans-retinol to produce all-trans-13-14-dihydroretinol, a product important for vitamin A metabolism. While, all-trans retinoic acid (ATRA), the active metabolite of vitamin A and the downstream bio-product of RETSAT, has recently been used to inhibit and degrade Pin1, leading to reduced APL and triple negative breast cancer growth (Moise et al., 2004; Wei et al., 2015). Therefore, the extrinsic inhibitory function of RETSAT$^{R/R}$ mutant might result from the increased generation of its downstream bio-products (Xu et al., 2021) or/and increased immune infiltration level (**Figures 3A,B**). In addition, we showed that RETSAT is closely associated with Pin1 and Akt1 by PPI network analysis, and also involved in PI3K/Akt signaling pathway by GSEA analysis (**Figures 6A,B**). Together with the findings that RETSAT knockdown promotes, while RETSAT overexpression inhibits, mouse B16 and fibroblast cell proliferation (**Figures 4A–M**), and RETSAT$^{R/R}$ mutation reduces Pin1 and phosphorylated Akt1 protein expressions (**Figures 6D–H**), we hypothesized that the intrinsic inhibitory role of RETSAT could be mediated by protein-protein interaction. Therefore, to further explore the extrinsic and intrinsic mechanisms of RETSAT repressing tumor progression, the gene/protein interacting network as well as the expression profiles of the downstream bio-products, should be thoroughly characterized in the future.

Regard to our findings that RETSAT might play as a tumor suppressor in most types human cancers, we hypothesized that the somatic mutations on RETSAT in SKCM tissues mostly cause loss-of-function. Retinol has six biologically active isoforms, including all-trans, 11-cis, 13-cis, 9,13-di-cis, 9-cis, and 11,13-

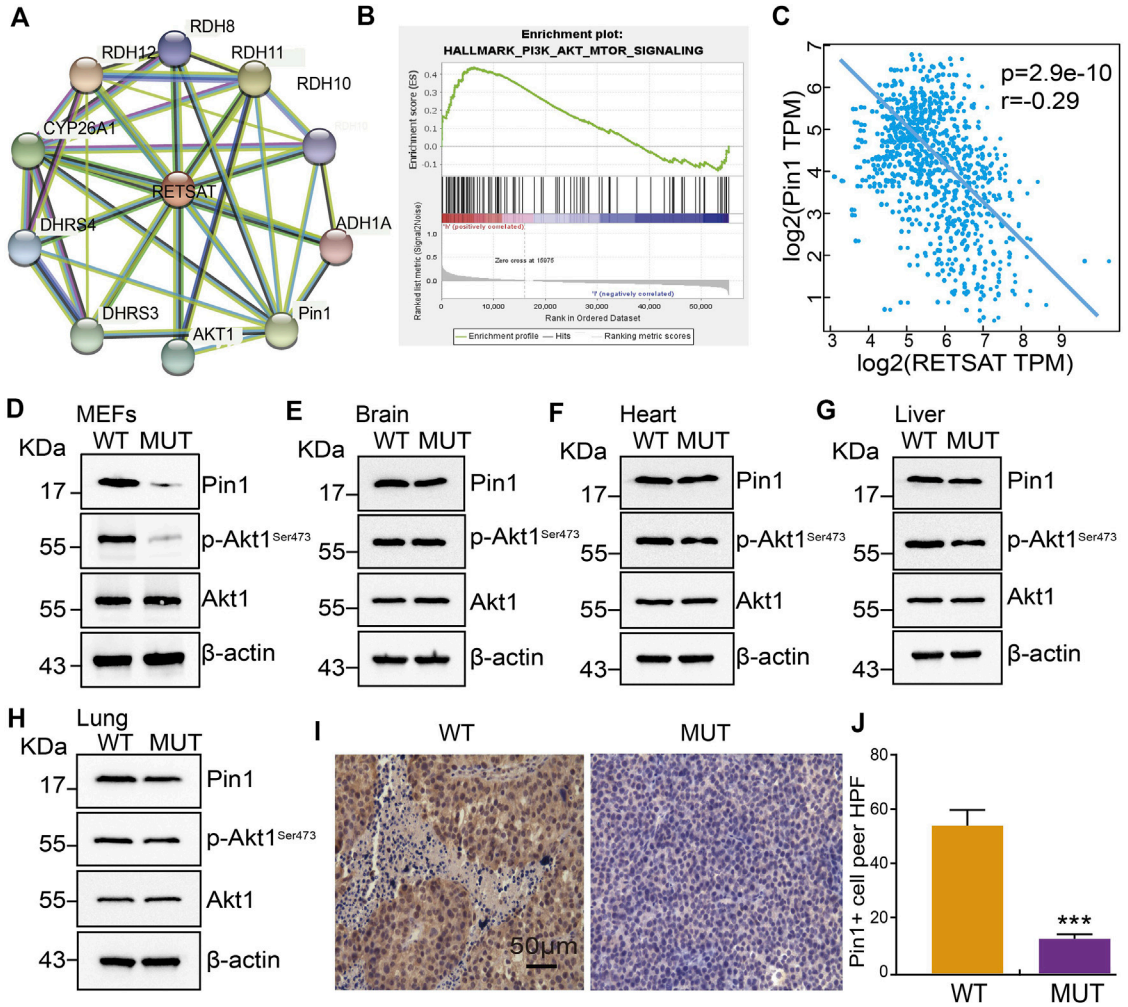

FIGURE 6 | RETSAT (Q247R) mutation represses Pin1 related signaling pathway. **(A)** The protein interaction network of RETSAT was generated using STRING database. **(B)** Enrichment plots from GSEA showing the PI3K/Akt signaling pathway associated with RETSAT expression in SKCM. **(C)** The spearman correlation analysis revealed a correlation between RETSAT and Pin1 expression in TCGA-SKCM database. **(D–H)** Examining the relative protein expressions by immunoblot in MEFs **(D)**, Brain **(E)**, Heart **(F)**, Liver **(G)** and Lung **(H)** isolated from of wild-type and mutant mice, respectively. **(I–J)** Representative IHC staining of PIN1 for indicated xenograft tumors after RETSAT mutation. $^{*}p < 0.05$, $^{**}p < 0.01$, $^{***}p < 0.001$.

di-cis, with all-trans being the predominant form (Rhee and Plutzky, 2012). Exploring the potential anti-cancer roles of the precursors of vitamin A metabolism will pave a new way treating SKCM patients, especially those with advanced stages. Therefore, to improve the clinical outcome for SKCM patients, it will be critical to identify new drugs or strategy to stabilize and activate RETSAT in the future.

MATERIALS AND METHODS

Immune Infiltration Analysis

We employed the TIMER to analyze the correlation between RETSAT expression and immune infiltration (Li et al., 2017). The TISIDB database was employed analyzing the association between RETSAT and immune regulators (immunostimulators or immunoinhibitors) (Ru et al., 2019). GEPIA and UALcan databases were employed to analyze the expression and prognosis of RETSAT in TCGA SKCM (Chandrashekar et al., 2017; Tang et al., 2017).

Cell Culture and Reagents

Mouse embryonic fibroblasts (MEFs) were generated from $RETSAT^{R/R}$ (mutant) or $RETSAT^{Q/Q}$ (wild-type) mice, and B16 cells were cultured in DMEM medium (Corning) supplemented with 10% fetal bovine serum (FBS) and 1% penicillin/streptomycin. Cells were all incubated in a humidified atmosphere with 5% CO_2 at 37°C.

Constructs, Transfection and Lenti-Viral Infection

As described before (Xu et al., 2021), RETSAT CDS (or mutant CDS DNA fragment) was sub-cloned into pCDH-MSCV-E2F-eGFP lenti-viral vector with a 3×Flag tag at the C-terminus. Independent shRNAs targeting RETSAT mRNA were synthesized and sub-cloned into the lenti-viral vector pLKO.1 (Addgene, Cambridge, United States). Cells were transfected with indicated shRNAs or control scramble shRNA using Lipofectamine 2000 (Invitrogen), and then collected for various experiments, mouse mRETSAT-shRNA#1: GTGGTGTCCTCCCTCCTACAG, mRETSAT-shRNA#2: AGCAATTCCTTGCACATATAA.

Real-Time RT-PCR Assay

For Real-time RT-PCR assay, indicated cells were lysed by RNAiso Plus (Takara Bio, Beijing, China, Cat. 108-95-2). Total RNAs were extracted according to the manufacturer's protocol, and then reverse transcribed using RT reagent Kit (Takara Bio, Beijing, China, Cat. RR047A; TIANGEN Biotech, Beijing, China, Cat. KR211-02). Real-time PCR was performed by FastStart Universal SYBR Green Master Mix (Roche, Cat. 04194194001; TIANGEN Biotech, Beijing, China, Cat. FP411-02) using an Applied Biosystems 7500 machine. The primers used in this study are: mRETSAT-qPCR-F: CCCATCAAGCAAGGATCC AA, mRETSAT-qPCR-R: ATGGGTACCAGCGCAGTCA.

Cell Proliferation

The cell proliferation assay was performed as previously described (Xu et al., 2020). For cell growth assay, indicated cells were plated into 12-well plates and the cell numbers were subsequently counted each day. For BrdU incorporation assay, indicated cells were cultured in 8-well plates for 24 h, pulsed with 10 μM BrdU (Abcam, Cat# ab142567) for 20 min, and fixed with 4% PFA (paraformaldehyde). Cells were then incubated with BrdU (Cell Signaling Technology, Cat# 5292s, dilution 1:1,000) primary antibody followed by secondary antibody detection (Abclonal, Cat# 61303, dilution 1:500). Cell nuclei were stained with DAPI (4′, 6-diamidino-2-phenylindole).

Xenograft Tumor Formation Assay

The transgenic mice ($RETSAT^{R/R}$) and their wild-type littermates ($RETSAT^{Q/Q}$) were derived from C57BL/6 mouse. About 4–6 weeks old age mice were subcutaneously injected with B16 cell lines (2 × 105 cells), 3 weeks later, all mice were sacrificed. The xenograft tumors from indicated groups were harvested and weighted. The mice were monitored every other day, xenograft tumor weights and volumes were measured with a sliding caliper, and tumor volumes were calculated using the formula (L×W2)/2. All animals were kept in a SPF environment and the protocols were pre-approved and conducted under the policy of Animal care and Use Committee at the Kunming Institute of Zoology, CAS.

DMBA/TPA Induced Cutaneous Keratinocyte Carcinoma

The assay was performed as previously described (Darido et al., 2011; Jiang et al., 2017). Briefly, 25 μg DMBA (Sigma Aldrich) in 200 μl acetone were applied to the dorsal skin after shaving. After 2 weeks, TPA (10 nmol) in 200 μl was applied to the same area twice weekly for up to 30 weeks. Skin specimens were collected 5 and 8 weeks after DMBA treatment, and when papilloma and SCC formed. The number of tumors per mouse was counted each week as palpable mass >1 mm in size.

Western Blot

To detect the protein expressions of Pin1, Akt1 and P-Akt1, cells were lysed in IP lysis buffer, supplemented with complete protease inhibitor cocktail (Complete Mini, Roche). Indicated proteins were detected with indicated antibodies by western blot. Proteins were resolved on SDS polyacrylamide gels, and then transferred to a polyvinylidene difluoride membrane. After blocking with 5% (w/v) milk, the membrane was stained with indicated primary antibodies as follows: Pin1(Catalog number, R25374, Dilution, 1:1,000, Supplier, ZENBIO), (Akt, Catalog number, 9272, Dilution, 1:1,000, Supplier, Cell Signaling Technology), (p-S473-Akt, Catalog number, 9271, Dilution, 1:1,000, Supplier, Cell Signaling Technology), β-actin (Catalog number, 60008-1-1g, Dilution, 1:20,000, Supplier Proteintech).

Immunohistochemistry Assay

For immunohistochemical staining, the sections were deparaffinized in xylene and rehydrated through graded ethanol. Antigen retrieval was performed for 20 min at 95°C with sodium citrate buffer (pH 6.0). After quenching endogenous peroxidase activity with 3% H_2O_2 and blocking non-specific binding with 1% bovine serum albumin buffer, sections were incubated overnight at 4°C with indicated primary antibodies: Pin1(Catalog number, R25374, Dilution, 1:1,000, Supplier, ZENBIO), Ki67 (Catalog number, 170, Dilution, 1:400, Supplier, NOVUS). Following several washes, the sections were treated with HRP conjugated secondary antibody for 40 min at room temperature, and stained with 3, 3-diaminobenzidine tetrahydrochloride (DAB). Slides were photographed with microscope (Olympus BX43F, Japan). The photographs were analyzed with the Image-Pro Plus 7.0 software (Media Cybernetics, Inc., Silver Spring, MD, United States).

Statistics

All data are presented as the mean ± SEM. All experiments were performed at least three times. All analyses were performed using GraphPad Prism 7 (GraphPad Software). Two-tailed Student's *t*-test was used for statistical analysis for experiments with two comparisons. *p*-values less than 0.05 were considered statistically significant. For all figures, $^{*}p < 0.05$, $^{**}p < 0.01$, $^{***}p < 0.001$.

DATA AVAILABILITY STATEMENT

The original contributions presented in the study are included in the article/**Supplementary Material**, further inquiries can be directed to the corresponding authors.

ETHICS STATEMENT

The animal study was reviewed and approved by All animals were kept in a SPF environment and the protocols were pre-approved and conducted under the policy of Animal care and Use Committee at the Kunming Institute of Zoology, CAS.

AUTHOR CONTRIBUTIONS

YC and PS initiated the project. YC and CY supervised and wrote the manuscript. XJ and YH performed the *in vitro* and *in vivo* functional assays. QS, LD, YY, LT, YS, BL, HZ, helped the bioinformatics and immunoblot assays.

FUNDING

This study was supported by National Nature Science Foundation of China (U1902216, 81772996, 82173110, 82002439), Yunnan Applied Basic Research Projects (2019FJ009, 202001AS070037, 2019HB076). CY was supported by Youth Innovation Promotion Association, CAS; Yunnan Ten Thousand Talents Plan Young and Elite Talents Project. YC was supported by grant from CAS, YJKYYQ20190048; Science and Technology Department of Sichuan Province Research Program (2020YFSY0009).

SUPPLEMENTARY MATERIAL

The Supplementary Material for this article can be found online at: https://www.frontiersin.org/articles/10.3389/fcell.2021.744992/full#supplementary-material

REFERENCES

Beall, C. M., Cavalleri, G. L., Deng, L., Elston, R. C., Gao, Y., Knight, J., et al. (2010). Natural Selection on EPAS1 (HIF2) Associated with Low Hemoglobin Concentration in Tibetan Highlanders. *Proc. Natl. Acad. Sci.* 107, 11459–11464. doi:10.1073/pnas.1002443107

Beall, C. M., Decker, M. J., Brittenham, G. M., Kushner, I., Gebremedhin, A., and Strohl, K. P. (2002). An Ethiopian Pattern of Human Adaptation to High-Altitude Hypoxia. *Proc. Natl. Acad. Sci.* 99, 17215–17218. doi:10.1073/pnas.252649199

Brustugun, O. T. (2015). Hypoxia as a Cause of Treatment Failure in Non-small Cell Carcinoma of the Lung. *Semin. Radiat. Oncol.* 25, 87–92. doi:10.1016/j.semradonc.2014.11.006

Brutsaert, T. D. (2008). Do high-altitude Natives Have Enhanced Exercise Performance at Altitude? *Appl. Physiol. Nutr. Metab.* 33, 582–592. doi:10.1139/h08-009

Chandrashekar, D. S., Bashel, B., Balasubramanya, S. A. H., Creighton, C. J., Ponce-Rodriguez, I., Chakravarthi, B. V. S. K., et al. (2017). UALCAN: A Portal for Facilitating Tumor Subgroup Gene Expression and Survival Analyses. *Neoplasia* 19, 649–658. doi:10.1016/j.neo.2017.05.002

Chen, Y., Wu, Y.-r., Yang, H.-y., Li, X.-z., Jie, M.-m., Hu, C.-j., et al. (2018). Prolyl Isomerase Pin1: a Promoter of Cancer and a Target for Therapy. *Cell Death Dis* 9, 883. doi:10.1038/s41419-018-0844-y

Cheviron, Z. A., and Brumfield, R. T. (2012). Genomic Insights into Adaptation to High-Altitude Environments. *Heredity* 108, 354–361. doi:10.1038/hdy.2011.85

Christman, J. K. (2002). 5-Azacytidine and 5-Aza-2′-Deoxycytidine as Inhibitors of DNA Methylation: Mechanistic Studies and Their Implications for Cancer Therapy. *Oncogene* 21, 5483–5495. doi:10.1038/sj.onc.1205699

Christov, K. T., Moon, R. C., Lantvit, D. D., Boone, C. W., Steele, V. E., Lubet, R. A., et al. (2002). 9-cis-retinoic Acid but Not 4-(hydroxyphenyl)retinamide Inhibits Prostate Intraepithelial Neoplasia in Noble Rats. *Cancer Res.* 62, 5178–5182.

Darido, C., Georgy, S. R., Wilanowski, T., Dworkin, S., Auden, A., Zhao, Q., et al. (2011). Targeting of the Tumor Suppressor GRHL3 by a miR-21-dependent Proto-Oncogenic Network Results in PTEN Loss and Tumorigenesis. *Cancer cell* 20, 635–648. doi:10.1016/j.ccr.2011.10.014

De Bels, D., Corazza, F., and Balestra, C. (2011). Oxygen Sensing, Homeostasis, and Disease. *N. Engl. J. Med.* 365, 1845–1846. doi:10.1056/NEJMc1110602

Farrell, A. S., Pelz, C., Wang, X., Daniel, C. J., Wang, Z., Su, Y., et al. (2013). Pin1 Regulates the Dynamics of C-Myc DNA Binding to Facilitate Target Gene Regulation and Oncogenesis. *Mol. Cel Biol* 33, 2930–2949. doi:10.1128/mcb.01455-12

Gao, J., Aksoy, B. A., Dogrusoz, U., Dresdner, G., Gross, B., Sumer, S. O., et al. (2013). Integrative Analysis of Complex Cancer Genomics and Clinical Profiles Using the cBioPortal. *Sci. Signal.* 6, pl1. doi:10.1126/scisignal.2004088

Gottardi, M., Sperotto, A., Ghelli Luserna Di Rorà, A., Padella, A., Cangini, D., Giannini, M. B., et al. (2020). Gemtuzumab Ozogamicin in Acute Myeloid Leukemia: Past, Present and Future. *Minerva Med.* 111, 395–410. doi:10.23736/S0026-4806.20.07019-6

Gottardis, M. M., Lamph, W. W., Shalinsky, D. R., Wellstein, A., and Heyman, R. A. (1996). The Efficacy of 9-cis Retinoic Acid in Experimental Models of Cancer. *Breast Cancer Res. Tr* 38, 85–96. doi:10.1007/bf01803787

Heidenreich, S., Witte, N., Weber, P., Goehring, I., Tolkachov, A., von Loeffelholz, C., et al. (2017). Retinol Saturase Coordinates Liver Metabolism by Regulating ChREBP Activity. *Nat. Commun.* 8, 384. doi:10.1038/s41467-017-00430-w

Jiang, L. P., Shen, Q. S., Yang, C. P., and Chen, Y. B. (2017). Establishment of Basal Cell Carcinoma Animal Model in Chinese Tree Shrew (Tupaia Belangeri Chinensis). *Zool Res.* 38, 180–190. doi:10.24272/j.issn.2095-8137.2017.045

Kang, J., Shin, S.-H., Yoon, H., Huh, J., Shin, H.-W., Chun, Y.-S., et al. (2018). FIH Is an Oxygen Sensor in Ovarian Cancer for G9a/GLP-Driven Epigenetic Regulation of Metastasis-Related Genes. *Cancer Res.* 78, 1184–1199. doi:10.1158/0008-5472.can-17-2506

Karsy, M., Albert, L., Tobias, M. E., Murali, R., and Jhanwar-Uniyal, M. (2010). All-trans Retinoic Acid Modulates Cancer Stem Cells of Glioblastoma Multiforme in an MAPK-dependent Manner. *Anticancer Res.* 30, 4915–4920.

Koller, K. M., Wang, W., Schell, T. D., Cozza, E. M., Kokolus, K. M., Neves, R. I., et al. (2016). Malignant Melanoma-The Cradle of Anti-neoplastic Immunotherapy. *Crit. Rev. oncology/hematology* 106, 25–54. doi:10.1016/j.critrevonc.2016.04.010

Lee, N., Zakka, L. R., Mihm, M. C., Jr., and Schatton, T. (2016). Tumour-infiltrating Lymphocytes in Melanoma Prognosis and Cancer Immunotherapy. *Pathology* 48, 177–187. doi:10.1016/j.pathol.2015.12.006

Lee, P., Chandel, N. S., and Simon, M. C. (2020). Cellular Adaptation to Hypoxia through Hypoxia Inducible Factors and beyond. *Nat. Rev. Mol. Cel Biol* 21, 268–283. doi:10.1038/s41580-020-0227-y

Li, R.-J., Ying, X., Zhang, Y., Ju, R.-J., Wang, X.-X., Yao, H.-J., et al. (2011). All-trans Retinoic Acid Stealth Liposomes Prevent the Relapse of Breast Cancer Arising from the Cancer Stem Cells. *J. Controlled Release* 149, 281–291. doi:10.1016/j.jconrel.2010.10.019

Li, T., Fan, J., Wang, B., Traugh, N., Chen, Q., Liu, J. S., et al. (2017). TIMER: A Web Server for Comprehensive Analysis of Tumor-Infiltrating Immune Cells. *Cancer Res.* 77, e108–e110. doi:10.1158/0008-5472.can-17-0307

Li, Y., Ge, D., and Lu, C. (2019). The SMART App: an Interactive Web Application for Comprehensive DNA Methylation Analysis and Visualization. *Epigenetics & Chromatin* 12, 71. doi:10.1186/s13072-019-0316-3

Min, S.-H., Zhou, X. Z., and Lu, K. P. (2016). The Role of Pin1 in the Development and Treatment of Cancer. *Arch. Pharm. Res.* 39, 1609–1620. doi:10.1007/s12272-016-0821-x

Mirani, B., Pagan, E., Shojaei, S., Duchscherer, J., Toyota, B. D., Ghavami, S., et al. (2019). A 3D Bioprinted Hydrogel Mesh Loaded with All-Trans Retinoic Acid for Treatment of Glioblastoma. *Eur. J. Pharmacol.* 854, 201–212. doi:10.1016/j.ejphar.2019.04.007

Modhukur, V., Iljasenko, T., Metsalu, T., Lokk, K., Laisk-Podar, T., and Vilo, J. (2018). MethSurv: a Web Tool to Perform Multivariable Survival Analysis Using DNA Methylation Data. *Epigenomics* 10, 277–288. doi:10.2217/epi-2017-0118

Moise, A. R., Kuksa, V., Blaner, W. S., Baehr, W., and Palczewski, K. (2005). Metabolism and Transactivation Activity of 13,14-dihydroretinoic Acid. *J. Biol. Chem.* 280, 27815–27825. doi:10.1074/jbc.m503520200

Moise, A. R., Kuksa, V., Imanishi, Y., and Palczewski, K. (2004). Identification of All-Trans-Retinol:all-Trans-13,14-Dihydroretinol Saturase. *J. Biol. Chem.* 279, 50230–50242. doi:10.1074/jbc.m409130200

Nakatsu, Y., Yamamotoya, T., Ueda, K., Ono, H., Inoue, M.-K., Matsunaga, Y., et al. (2020). Prolyl Isomerase Pin1 in Metabolic Reprogramming of Cancer Cells. *Cancer Lett.* 470, 106–114. doi:10.1016/j.canlet.2019.10.043

Nishi, M., Akutsu, H., Masui, S., Kondo, A., Nagashima, Y., Kimura, H., et al. (2011). A Distinct Role for Pin1 in the Induction and Maintenance of Pluripotency. *J. Biol. Chem.* 286, 11593–11603. doi:10.1074/jbc.m110.187989

Pang, X.-Y., Wang, S., Jurczak, M. J., Shulman, G. I., and Moise, A. R. (2017). Retinol Saturase Modulates Lipid Metabolism and the Production of Reactive Oxygen Species. *Arch. Biochem. Biophys.* 633, 93–102. doi:10.1016/j.abb.2017.09.009

Ping Lu, K., Hanes, S. D., and Hunter, T. (1996). A Human Peptidyl-Prolyl Isomerase Essential for Regulation of Mitosis. *Nature* 380, 544–547. doi:10.1038/380544a0

Rademaker, K., Hodgins, G., Moore, K., Zarrillo, S., Miller, C., Bromley, G. R. M., et al. (2014). Paleoindian Settlement of the High-Altitude Peruvian Andes. *Science* 346, 466–469. doi:10.1126/science.1258260

Read, J., Wadt, K. A. W., and Hayward, N. K. (2016). Melanoma Genetics. *J. Med. Genet.* 53, 1–14. doi:10.1136/jmedgenet-2015-103150

Rhee, E.-J., and Plutzky, J. (2012). Retinoid Metabolism and Diabetes Mellitus. *Diabetes Metab. J.* 36, 167–180. doi:10.4093/dmj.2012.36.3.167

Ru, B., Wong, C. N., Tong, Y., Zhong, J. Y., Zhong, S. S. W., Wu, W. C., et al. (2019). TISIDB: an Integrated Repository portal for Tumor-Immune System Interactions. *Bioinformatics (Oxford, England)* 35, 4200–4202. doi:10.1093/bioinformatics/btz210

Rustighi, A., Zannini, A., Campaner, E., Ciani, Y., Piazza, S., and Del Sal, G. (2017). PIN1 in Breast Development and Cancer: a Clinical Perspective. *Cell Death Differ* 24, 200–211. doi:10.1038/cdd.2016.122

Sacktor, T. C. (2010). PINing for Things Past. *Sci. Signal.* 3, pe9. doi:10.1126/scisignal.3112pe9

Scheinfeldt, L. B., Soi, S., Thompson, S., Ranciaro, A., Woldemeskel, D., Beggs, W., et al. (2012). Genetic Adaptation to High Altitude in the Ethiopian highlands. *Genome Biol.* 13, R1. doi:10.1186/gb-2012-13-1-r1

Schödel, J., and Ratcliffe, P. J. (2019). Mechanisms of Hypoxia Signalling: New Implications for Nephrology. *Nat. Rev. Nephrol.* 15, 641–659. doi:10.1038/s41581-019-0182-z

Schupp, M., Lefterova, M. I., Janke, J., Leitner, K., Cristancho, A. G., Mullican, S. E., et al. (2009). Retinol Saturase Promotes Adipogenesis and Is Downregulated in Obesity. *Proc. Natl. Acad. Sci.* 106, 1105–1110. doi:10.1073/pnas.0812065106

Scolyer, R. A., Long, G. V., and Thompson, J. F. (2011). Evolving Concepts in Melanoma Classification and Their Relevance to Multidisciplinary Melanoma Patient Care. *Mol. Oncol.* 5, 124–136. doi:10.1016/j.molonc.2011.03.002

Shi, Y., Fan, S., Wu, M., Zuo, Z., Li, X., Jiang, L., et al. (2019). YTHDF1 Links Hypoxia Adaptation and Non-small Cell Lung Cancer Progression. *Nat. Commun.* 10, 4892. doi:10.1038/s41467-019-12801-6

Storz, J. F., and Scott, G. R. (2021). Phenotypic Plasticity, Genetic Assimilation, and Genetic Compensation in Hypoxia Adaptation of High-Altitude Vertebrates. *Comp. Biochem. Physiol. A: Mol. Integr. Physiol.* 253, 110865. doi:10.1016/j.cbpa.2020.110865

Subramanian, A., Tamayo, P., Mootha, V. K., Mukherjee, S., Ebert, B. L., Gillette, M. A., et al. (2005). Gene Set Enrichment Analysis: a Knowledge-Based Approach for Interpreting Genome-wide Expression Profiles. *Proc. Natl. Acad. Sci.* 102, 15545–15550. doi:10.1073/pnas.0506580102

Sun, B., Zhang, Y., Zhou, L., Yin, L., Li, F., Li, C., et al. (2019). The Proliferation of Cervical Cancer Is Promoted by miRNA-125b through the Regulation of the HMGA1. *Ott* 12, 2767–2776. doi:10.2147/ott.s197740

Szklarczyk, D., Morris, J. H., Cook, H., Kuhn, M., Wyder, S., Simonovic, M., et al. (2017). The STRING Database in 2017: Quality-Controlled Protein-Protein Association Networks, Made Broadly Accessible. *Nucleic Acids Res.* 45, D362–d368. doi:10.1093/nar/gkw937

Tang, Z., Li, C., Kang, B., Gao, G., Li, C., and Zhang, Z. (2017). GEPIA: a Web Server for Cancer and normal Gene Expression Profiling and Interactive Analyses. *Nucleic Acids Res.* 45, W98–W102. doi:10.1093/nar/gkx247

Tun-Kyi, A., Finn, G., Greenwood, A., Nowak, M., Lee, T. H., Asara, J. M., et al. (2011). Essential Role for the Prolyl Isomerase Pin1 in Toll-like Receptor Signaling and Type I Interferon-Mediated Immunity. *Nat. Immunol.* 12, 733–741. doi:10.1038/ni.2069

Wei, S., Kozono, S., Kats, L., Nechama, M., Li, W., Guarnerio, J., et al. (2015). Active Pin1 Is a Key Target of All-Trans Retinoic Acid in Acute Promyelocytic Leukemia and Breast Cancer. *Nat. Med.* 21, 457–466. doi:10.1038/nm.3839

Wu, D.-D., Yang, C.-P., Wang, M.-S., Dong, K.-Z., Yan, D.-W., Hao, Z.-Q., et al. (2020). Convergent Genomic Signatures of High-Altitude Adaptation Among Domestic Mammals. *Natl. Sci. Rev.* 7, 952–963. doi:10.1093/nsr/nwz213

Xiong, Q., Liu, B., Ding, M., Zhou, J., Yang, C., and Chen, Y. (2020). Hypoxia and Cancer Related Pathology. *Cancer Lett.* 486, 1–7. doi:10.1016/j.canlet.2020.05.002

Xu, D., Yang, C., Shen, Q., Pan, S., Liu, Z., Zhang, T., et al. (2021). *A Single Mutation Underlying Phenotypic Convergence for Hypoxia Adaptation on the Qinghai-Tibetan Plateau*. London, England: Cell research.

Xu, P., Jiang, L., Yang, Y., Wu, M., Liu, B., Shi, Y., et al. (2020). PAQR4 Promotes Chemoresistance in Non-small Cell Lung Cancer through Inhibiting Nrf2 Protein Degradation. *Theranostics* 10, 3767–3778. doi:10.7150/thno.43142

Yang, G., Shi, R., and Zhang, Q. (2020). Hypoxia and Oxygen-Sensing Signaling in Gene Regulation and Cancer Progression. *Int. J. Mol. Sci.* 21. doi:10.3390/ijms21218162

Yi, X., Liang, Y., Huerta-Sanchez, E., Jin, X., Cuo, Z. X. P., Pool, J. E., et al. (2010). Sequencing of 50 Human Exomes Reveals Adaptation to High Altitude. *Science* 329, 75–78. doi:10.1126/science.1190371

Yu, J. H., Im, C. Y., and Min, S.-H. (2020). Function of PIN1 in Cancer Development and its Inhibitors as Cancer Therapeutics. *Front. Cel Dev. Biol.* 8, 120. doi:10.3389/fcell.2020.00120

Zhang, Z., Yu, W., Zheng, M., Liao, X., Wang, J., Yang, D., et al. (2019). Pin1 Inhibition Potently Suppresses Gastric Cancer Growth and Blocks PI3K/AKT and Wnt/β-catenin Oncogenic Pathways. *Mol. Carcinog* 58, 1450–1464. doi:10.1002/mc.23027

Zhou, X. Z., and Lu, K. P. (2016). The Isomerase PIN1 Controls Numerous Cancer-Driving Pathways and Is a Unique Drug Target. *Nat. Rev. Cancer* 16, 463–478. doi:10.1038/nrc.2016.49

Ziouzenkova, O., Orasanu, G., Sharlach, M., Akiyama, T. E., Berger, J. P., Viereck, J., et al. (2007). Retinaldehyde Represses Adipogenesis and Diet-Induced Obesity. *Nat. Med.* 13, 695–702. doi:10.1038/nm1587

Conflict of Interest: The authors declare that the research was conducted in the absence of any commercial or financial relationships that could be construed as a potential conflict of interest.

Publisher's Note: All claims expressed in this article are solely those of the authors and do not necessarily represent those of their affiliated organizations, or those of the publisher, the editors and the reviewers. Any product that may be evaluated in this article, or claim that may be made by its manufacturer, is not guaranteed or endorsed by the publisher.

Advantages of publishing in Frontiers

OPEN ACCESS
Articles are free to read for greatest visibility and readership

FAST PUBLICATION
Around 90 days from submission to decision

HIGH QUALITY PEER-REVIEW
Rigorous, collaborative, and constructive peer-review

TRANSPARENT PEER-REVIEW
Editors and reviewers acknowledged by name on published articles

Frontiers
Avenue du Tribunal-Fédéral 34
1005 Lausanne | Switzerland

Visit us: www.frontiersin.org
Contact us: frontiersin.org/about/contact

REPRODUCIBILITY OF RESEARCH
Support open data and methods to enhance research reproducibility

DIGITAL PUBLISHING
Articles designed for optimal readership across devices

FOLLOW US
@frontiersin

IMPACT METRICS
Advanced article metrics track visibility across digital media

EXTENSIVE PROMOTION
Marketing and promotion of impactful research

LOOP RESEARCH NETWORK
Our network increases your article's readership